

**THREE-DIMENSIONAL FLOW  
IN RANDOM POROUS MEDIA**

by

**Rachid Ababou**

**Dr. Ing. Fluid Mechanics,  
University of Grenoble and  
Institut National Polytechnique of Grenoble, France  
(1981)**

**Submitted in Partial Fulfillment of the  
Requirements for the Degree of  
Doctor of Philosophy**

**at the**

**MASSACHUSETTS INSTITUTE OF TECHNOLOGY**

**January 1988**

**© Massachusetts Institute of Technology, 1988**

**Signature of Author**.....  
Department of Civil Engineering  
January, 1988

**Certified by**.....  
Lynn W. Gelhar  
Thesis Supervisor

**Accepted by**.....  
Ole S. Madsen  
Departmental Graduate Committee  
Department of Civil Engineering



ARCHIVE

THREE-DIMENSIONAL FLOW  
IN RANDOM POROUS MEDIA

by

Rachid Ababou

Submitted to the Department of Civil Engineering  
on January 1988 in partial fulfillment of the requirements  
for the Degree of Doctor of Philosophy in Civil Engineering

**ABSTRACT**

Large scale subsurface flow in heterogeneous porous formations is studied using a three-dimensional (3D) random field representation of local hydraulic properties, assuming for the most part that the medium is homogeneous/ergodic. Both analytical and numerical methods are used to characterize the physical behaviour of 3D flow fields, based on the statistical properties of solutions of stochastic partial differential equations.

The first order spectral theory is applied to the case of flow in stratified aquifers, revealing a nearly isotropic head correlation structure in vertical planes, in contrast with the anisotropy of conductivity and velocity. Thus, the vertical head correlation is large, and the infinite domain spectral solutions may only be applicable for large aquifer thickness, say over a few tens of horizontal conductivity scales. Also, non-perturbative spectral equations derived from mass conservation and statistical symmetries relate the flux and head spectra for isotropic media, independently of small parameter expansions. The new relations are satisfied by the current spectral solutions in any dimension. In the 2D case, we establish a statistical identity between head gradient and flux, or head and stream function (statistical conjugacy). Other results in the literature inspired a simple conjecture for the effective conductivity tensor with arbitrary 3D anisotropy of the random conductivity field, which fits all results known to be exact. Finally, a modified flux spectrum is developed using an approximate spectral solution of equations governing the flux instead of head. The new expressions for velocity variance and solute macrodispersivity appear to follow more realistic behaviours at high variability.

The conceptual approach of "spectral conditioning" is developed to describe finite size effects, particularly for evolving subsurface phenomena. Porous medium heterogeneity inferred from borehole conductivity data is represented by self-similar random fields. The flow equation is solved for small scale fluctuations up to domain scale, conditioned on larger scale fluctuations (effective variability versus uncertainty). Closed-form results for 1D flow show that the uncertainty of finite domain statistics, such as effective conductivity and head variance, decreases with domain size. Preliminary results also

indicate the scale dependence of the 3D effective conductivity and macrodispersivity of a growing contaminant plume.

Direct numerical simulations are developed for single realizations of homogeneous/ergodic random medium properties, using the 3D turning band method for random field generation, and a special purpose numerical code for solving 3D finite difference saturated and unsaturated flow equations, with spatially variable and nonlinear coefficients. In the case of stochastic groundwater flow, a novel method of truncation error analysis shows that the discrete solution is a consistent approximation of the exact one, however with a lower order of accuracy if the random coefficients are noisy rather than smooth. The root-mean-square errors on head and velocity are respectively proportional to the powers  $3/2$  and  $1/2$  of the mesh-correlation scale ratio in the noisy case (exponential covariance). The convergence of the iterative "strongly implicit procedure" solver is studied, and the nonlinear stability of transient unsaturated flow systems is analyzed (Peclet number condition).

The single realization approach is applied to the following flow problems, using a Cray2 supercomputer for the largest simulations: steady groundwater flow in statistically isotropic or anisotropic media (up to 1 million nodes); transient strip source infiltration and steady rainfall infiltration in unsaturated soils with random conductivity-pressure curves (up to 300,000 nodes). The simulated flow fields are statistically analyzed by spatial averaging methods under weak assumptions of homogeneity. For groundwater flow, the results compare favourably with spectral solutions, especially for the head variance, effective conductivity, and velocity correlation tensor, up to large standard deviation of the natural logarithm of conductivity (2.3). The numerical velocity variances agree with the spectral theory at moderate variability (isotropic case), but increase faster with conductivity variance. The discrepancy is milder for the new flux-based spectral theory. Numerical head correlations tend to be smaller than theoretical ones due to finite size effects, particularly for shallow stratified aquifers.

For unsaturated flow, simulation results indicate sensitivity of flow behaviour depending on the variability and anisotropy of the random soil. In the case of transient strip source infiltration/drainage in a statistically anisotropic soil, there is a pronounced lateral spreading of the edges of the moisture plume. This behaviour is in qualitative agreement with available spectral solutions. The case of steady "rainfall" infiltration shows a quantitative agreement with the head variance and vertical unsaturated effective conductivity from the spectral theory. Some questions remain open, notably concerning the range of validity of the homogeneity and ergodicity hypotheses for highly nonlinear and evolving flow systems.

Thesis Supervisor: Lynn W. Gelhar  
Title: Professor of Civil Engineering

#### ACKNOWLEDGEMENTS

This research has benefited from the support of a number of persons and institutions over the course of four years. First of all, I wish to acknowledge the support, guidance, and advisorship of Lynn Gelhar. His many contributions and his keen physical insight were essential to this work, from start to finish. Dennis McLaughlin also contributed to many aspects of this work and acted as supervisor during Lynn's sabbatical. His friendly support, and availability for enriching debates, are gratefully acknowledged. Benoit Mandelbrot initiated me to the theory of fractal geometry and selfsimilar randomness in his well attended course at Harvard, and generated much food for thought through stimulating discussions. I wish to thank him for his far reaching comments and for participating to this committee in spite of a tight schedule. The help and advice of Michael Celia and Anthony Patera at various stages of this work are also gratefully acknowledged. The five committee members, named just above, had to browse through a fairly large document. I wish to thank them collectively for their collaboration.

This research was part of a team work and has benefited at times from contributions of Andrew Tompson, Wendy Craham, and Don Polmann, to name a few. Conversations with many other fellow

students and faculty, both within the hydrology group of Parsons Laboratory and outside, also helped shape this research. In addition, I wish to acknowledge the computational support provided by Parsons Laboratory (microvax'es), the Minnesota Supercomputer Center and the NASA-Ames Research Center (Cray2's). The National Science Foundation (grants ECE-8311786 and ECE-8544457) and the Nuclear Regulatory Commission (contract NRC-04-83-174) funded portions of this research; this support is gratefully acknowledged. I wish to thank in particular Tom Nicholson of N.R.C. for his coordinating efforts and enlivening meetings.

The typing of this dissertation was no small task: Mary and Nancy (M & N) Toscano typed and organized most of this nearly one thousand page document with skill and speed. The material support of the staff at Parsons Laboratory was also invaluable all along this research.

Finally, I wish to thank Martine Gavinet, my wife, who provided much needed help at odd times and in more ways than one. This thesis could not have been completed without her support, patience, and energy. Martine also gave birth to our son, Yacine, as this thesis was near completion. This work is dedicated to both of them and to my parents.

Thanks, Yacine, for your first smile.

TABLE OF CONTENTS

	Page
ABSTRACT.....	2
ACKNOWLEDGEMENTS.....	4
TABLE OF CONTENTS.....	6
LIST OF FIGURES.....	11
LIST OF TABLES.....	25
CHAPTER 1: INTRODUCTION.....	27
1.1 Subsurface Contamination and Field Heterogeneity.....	27
1.2 Scope and Objectives.....	36
1.3 Thesis Preview.....	43
CHAPTER 2: REVIEW OF STOCHASTIC APPROACHES TO SUBSURFACE FLOW.....	51
2.1 Overview of Past and Current Approaches to Field Problems.....	51
2.1.1 Empirical models.....	51
2.1.2 Probabilistic models without spatial correlation.....	53
2.1.3 Stochastic models with spatially correlated fields.....	54
2.2 The Single-Realization Approach.....	57
2.2.1 Objectives and method.....	57
2.2.2 Generation of random fields by the Turning Band Method.....	64
2.3 Brief Survey of Field Data.....	73
2.3.1 Hydraulic properties of heterogeneous aquifers.....	73
2.3.2 Constitutive relations of hetero- geneous unsaturated soils.....	79
CHAPTER 3: FIRST ORDER SPECTRAL SOLUTIONS FOR STOCHASTIC FLOW IN SATURATED MEDIA.....	92
3.1 Formal Solution of Spectral Perturbation Equations .....	92

3.2	Discussion of Admissible Log-conductivity Spectra.....	108
3.3	Head and Flux Moments for the 3D Isotropic Markov Spectrum.....	117
3.4	Head and Flux Moments for the Anisotropic 3D Anisotropic Markov Spectrum.....	127
3.5	Discussion of the Anisotropic Case (Stratified Flow Systems).....	136
3.6	Head Moments for the Hole-Markov Spectrum and Low Wavenumber Effects.....	149

CHAPTER 4: EXTENSIONS OF SPECTRAL THEORY: NON-PERTURBATIVE SOLUTIONS, SPECTRAL CONDITIONING AND UNCERTAINTY

4.1	Introduction: Sources of Errors in Standard Spectral Solutions.....	156
4.2	Non-Perturbative Spectral Solutions and Statistical Symmetries.....	165
4.2.1	Summary.....	165
4.2.2	Mass conservation relation.....	166
4.2.3	Statistical axial symmetry for 3D flow in isotropic media.....	169
4.2.4	Conjugacy property for 2D flow in isotropic media.....	187
4.2.5	Geometric mean effective conductivity for 2D isotropic media.....	199
4.2.6	Effective conductivity for general 3D anisotropic media.....	204
4.3	New Closed Form Perturbative Solutions for the Flux Spectrum.....	211
4.4	Finite Size Effects: Band-Pass Self-Similar Spectra, Spectral Conditioning and Uncertainty.....	221
4.4.1	Motivation and approaches.....	221
4.4.2	Band-pass self-similar spectra and field data.....	226
4.4.3	Stochastic flow solutions for band-pass self-similar spectra.....	235
4.4.4	Uncertainty and "spectral conditioning".....	242

CHAPTER 5:	NUMERICAL METHOD FOR LARGE SINGLE-REALIZATION SOLUTIONS OF STOCHASTIC FLOW IN SATURATED OR UNSATURATED MEDIA.....	259
5.1	Governing Equations and Finite Difference Approximations.....	259
5.1.1	Governing equation and numerical requirements.....	259
5.1.2	Finite difference in space for saturated steady flow.....	264
5.1.3	Finite difference in space-time for transient unsaturated flow.....	277
5.2	Statistical Truncation Error Analysis for Linear Random Flow Problems.....	299
5.2.1	Governing equation for the numerical head error.....	300
5.2.2	Statistical analysis of the numerical head error.....	313
5.2.3	Numerical error on the flux vector	326
5.2.4	Summary and discussion.....	336
5.3	Iterative Matrix Solver and Convergence Analysis for Linear Random Flow Problems.	343
5.3.1	Review of iterative and preconditioned matrix solvers.....	343
5.3.2	Formulation of the strongly implicit procedure (SIP solver).....	360
5.3.3	Convergence analysis for large 3D random systems of saturated flow.	371
5.4	Development and Analysis of the Nonlinear Iterative Solver for Transient Unsaturated Flow.....	402
5.4.1	Nonlinear SIP solver and nested Picard iterations.....	402
5.4.2	Truncation errors, nonlinear stability, and space-time resolution requirements.....	414
5.4.3	Numerical experiments and test of problem solving capabilities.....	429
5.5	Summary and Conclusions on Numerics.....	474
CHAPTER 6	THREE-DIMENSIONAL SINGLE-REALIZATION SIMULATIONS OF SATURATED FLOW IN RANDOM POROUS MEDIA.....	481
6.1	Scope, Model Problems, and Methodology...	481
6.2	Preliminary Analysis of 3D Isotropic Flow Simulations (130,000 nodes).....	506
6.3	Statistical Analysis of 3D Isotropic Flow Simulations (1 Million nodes).....	533



6.4	Summary Analysis of 3D Anisotropic Flow Simulations (220,000 nodes).....	588
6.5	Summary and Discussion.....	610
CHAPTER 7	THREE-DIMENSIONAL SINGLE-REALIZATION SIMULATIONS OF UNSATURATED INFILTRATION IN RANDOM SOILS.....	617
7.1	Scope and Objectives.....	617
7.2	Strip source infiltration in statistically isotropic soils (25,000 nodes).....	623
7.2.1	Model Problems and input Data.....	623
7.2.2	Simulation results.....	633
7.3	Strip source infiltration in a statistically anisotropic soil (300,000 nodes).....	643
7.3.1	Model problem and input data.....	643
7.3.2	Simulation results.....	656
7.4	Steady "Rainfall" infiltration in a statistically anisotropic soil (300,000 nodes).....	681
7.4.1	Model problem and input data.....	681
7.4.2	Simulation results and statistical analysis.....	684
7.5	Summary and discussion.....	698
CHAPTER 8	CONCLUSIONS.....	705
REFERENCES.....		746
APPENDIX 2A	UNCERTAINTY OF SAMPLE STATISTICS FOR RANDOM VARIABLES AND RANDOM FIELDS.....	760
APPENDIX 3A	CLOSED FORM EVALUATION OF THE HEAD GRADIENT VARIANCES FOR THE 3D ISOTROPIC MARKOV SPECTRUM..	767
APPENDIX 3B	CLOSED FORM EVALUATION OF VARIANCES AND CROSS-COVARIANCES OF FLUX COMPONENTS AT LAG ZERO, FOR THE 3D ISOTROPIC MARKOV SPECTRUM.....	771
APPENDIX 3C	CLOSED FORM EVALUATION OF CERTAIN CORRELATION FUNCTIONS OF THE FLUX AND HEAD GRADIENT VECTORS FOR THE 3D ISOTROPIC MARKOV SPECTRUM.....	775
APPENDIX 3D	HEAD COVARIANCE FUNCTION FOR THE 3D ANISOTROPIC MARKOV SPECTRUM (INDICATIONS).....	780
APPENDIX 3E	QUASI-ANALYTICAL EVALUATION OF THE HEAD COVARIANCE $R_{hh}(0,0,\xi_3)$ FOR THE 3D ANISOTROPIC MARKOV SPECTRUM WITH SMALL ANISOTROPY RATIO.....	784

APPENDIX 3F	CLOSED FORM EVALUATION OF THE FLUX VARIANCE FOR THE 3D ANISOTROPIC MARKOV SPECTRUM WITH SMALL ANISOTROPY RATIO.....	788
APPENDIX 3G	CLOSED FORM EVALUATION OF THE HEAD VARIANCE AND COVARIANCE FUNCTION FOR THE 3D HOLE-MARKOV SPECTRUM (ISOTROPIC AND ANISOTROPIC CASES).....	796
APPENDIX 5A	CLOSED FORM EVALUATION OF THE NUMERICAL HEAD ERROR $\sigma(\delta H)$ FOR THE 3D MARKOV SPECTRUM OF LOG-CONDUCTIVITY.....	803
APPENDIX 5B	CLOSED FORM EVALUATION OF THE HEAD ERROR $\sigma(\delta H)$ FOR THE 3D HOLE-GAUSSIAN SPECTRUM OF LOG-CONDUCTIVITY.....	810
APPENDIX 5C	CLOSED FORM EVALUATION OF THE NUMERICAL ERRORS ON THE FLUX AND HEAD GRADIENT FOR THE 3D MARKOV SPECTRUM OF LOG-CONDUCTIVITY.....	816
APPENDIX 5D	"BIGFLO" CODE ABSTRACT.....	824

LIST OF FIGURES

No.		Page
1.1	Examples of log-conductivity records $\ln K(x)$ in one spatial dimension: (a) data from vertical borehole (Gelhar, 1976), (b) synthetic realization of a one-dimensional Gauss-Markov process with exponential covariance function.....	34
2.1	Turning band method: projection of the $i$ -th line process $f_1^{(i)}(x)$ onto an arbitrary point $\underline{x}$ in three-dimensional space (from Tompson, Ababou, Gelhar, 1987).....	70
2.2	Log-conductivity contours in a vertical plane. The upper part is reproduced from Sudicky, 1986 (measured at the Borden tracer site). The lower part of the figure was obtained by simulation, using the Turning Band Method with an anisotropic spectrum.	77
2.3	(a) Normally distributed random function $Z = \ln Y$ ( $-\infty < \ln Y(x) < +\infty$ ).....	85
	(b) Log-normally distributed random function $Y$ ( $0 < Y(x) < +\infty$ ).....	86
2.4	Unsaturated hydraulic conductivity versus capillary tension head for the Maddock sandy loam. Each curve corresponds to a different spatial location (from Yeh et al., 1982).....	88
2.5	Typical horizontal and vertical movement of liquids in Hanford formation sediments under partially saturated conditions. Taped area outlines position of water addition (from Routson et al., 1979).....	91
3.1	Head correlation function along the coordinate axes for the 3D isotropic markov spectrum of log-conductivity..	120
3.2	Longitudinal flux correlation function along the coordinate axes for the 3D isotropic Markov spectrum of log-conductivity.....	122
3.3	Transverse flux correlation functions along the coordinate axes for the 3D isotropic Markov spectrum of log-conductivity.....	123

3.4	Head correlation function $R_{hh}(\xi)$ along the three principal directions for the 3D ellipsoidal Markov spectrum of log-conductivity with different values of the anisotropy ratio ( $\epsilon = \ell_3/\ell_1$ ) as $\ell_1$ increases.....	130
3.5	Sketch of a statistically layered porous medium. The ellipses represent contours of constant correlation length (Anisotropy ellipses in different planes, or anisotropy ellipsoid in 3D Space) for the log-conductivity field.....	137
3.6	Anisotropy ellipses for: (a) the log-conductivity field, (b) the hydraulic head, and (c) the flux vector in a statistically layered aquifer.....	140
3.7	Schematic representation of the fluctuation scales of the hydraulic head (top) and of the flux vector (bottom) in a stratified aquifer.....	141
4.1	The cross-covariance function of the head gradient and flux vectors vanish along certain directions in a 3D isotropic medium.....	175
4.2	Illustration of the conjugacy property for stochastic flow in a 2D isotropic medium ( $K^*$ is the dual conductivity with respect to $K$ ).....	190
4.3	Illustration of finite-size effects:	
	(a) contamination plume.....	224
	(b) log-conductivity field sample function.....	224
	(c) Band-pass self-similar spectrum.....	224
4.4	(a) Measured one-dimensional spectrum of log-conductivity at a borehole (circles), in the Mt. Simon aquifer from Bakr (1976). The straight line corresponds to a self-similar spectrum with exponent $\alpha = 1$ .....	227
	(b) Same as Figure 4.4a, for another set of data. The straight line corresponds to a self-similar spectrum with exponent $\alpha = 1$ .....	228
	(c) Same as Figure 4.4a and 4.4b; for another set of data. The straight line corresponds to a self-similar spectrum with exponent $\alpha = 1$ .....	229
4.5	Illustration of the spectral conditioning method:	
	(a) Spectral density versus wavenumber on a log-log plot.....	245
	(b) Sample function of log-conductivity in space (Mt. Simon Data).....	245

5.1	Seven-point centered finite difference molecule for a three-dimensional orthogonal grid of mesh points.....	267
5.2	Structure of the coefficient matrix for the seven-point centered finite difference scheme, illustrated here for a 3D cubic grid with 27 internal nodes (cubic domain of side $4\Delta x$ ). The matrix is symmetric and has only seven non-zero diagonal lines.....	272
5.3	(a) Soil water retention curve $\theta(h)$ for the "Dek sand" of Senegal. The solid line represents the Van Genuchten function fitted to data points (from Ababou, 1981).....	283
	(b) Unsaturated conductivity curve $K(h)$ for the "Dek sand" of Senegal. The solid line represents the exponential conductivity curve fitted to data point (from Ababou, 1981).....	284
5.4	(a) Soil water retention curve $\theta(h)$ for the Montfavet silt, a loess soil from the south of France. The Van Genuchten curve (solid line) was fitted to data points (Ababou, 1981).....	285
	(b) Unsaturated conductivity curve $K(h)$ for the Montfavet silt. The exponential conductivity curve (solid line) was fitted to data points (Ababou, 1981).....	286
5.5	Schematic representation of the SIP approximate factorization (top), and structure of the product $M = LU$ approximating $A$ (bottom). The dashed lines indicate extra diagonals not present in the original matrix $A$ ..	362
5.6	Asymmetric SIP molecule corresponding to the approximate LU factorization of the symmetric finite difference matrix $A$ (top: 2D case; bottom: 3D case)...	364
5.7	A posteriori analysis of convergence of the SIP solver: residual error norm versus number of iterations on a semi-log plot. In the convergent case (iii), the final residual error $\hat{\ e\ }$ and the convergence rate $r$ can be used to estimate the true error $\ e\ $ as explained in the text.....	382
5.8	(a) Euclidean norm of the residual error versus number of iterations on a semi-log plot for problem A (1 Million nodes). The three subproblems $\sigma=1,1.7, 2.3$ were solved sequentially on a Cray 2 computer	392

	(b)	Comparison of the asymptotic convergence rates for $\sigma=1$ and $\sigma=2.3$ of the 1 Million node problem A: same as Figure (5.8a) except that the residual errors have been scaled.....	393
5.9	(a)	Euclidean norm of the scaled residual error versus number of iterations for problem D, on a semi-log plot. The two subproblems $\sigma=1$ , $\sigma=2.3$ were solved separately on a Microvax.....	394
	(b)	Comparison of the Euclidean norm and absolute maximum norm of the scaled residual error for problem D with $\sigma_f = 1.0$ .....	395
5.10	(a)	Evolution of the time step size (plotted against number of outer iterations) for one-dimensional infiltration in a dry sand with fixed pressure $h = 0$ at soil surface.....	436
	(b)	Evolution of the time step size (plotted against number of outer iterations) for two-dimensional infiltration with fixed pressure $h = 0$ on a strip source (same soil as 5.10a).....	437
	(c)	Evolution of the time step size (plotted against number of outer iterations) for two-dimensional infiltration with fixed flux $q = 12$ cm/day on a strip source (two-layered sandy soil, top layer same as in 5.10a and b).....	438
5.11		Representation of the "variable domain" procedure in the case of infiltration from a strip source. The thick arrows indicate the movement of artificial boundaries. In this example, the soil surface is the only fixed boundary.....	441
5.12	(a)	Pressure head contours obtained after 1 day of infiltration with the variable domain procedure for 2D strip source infiltration $q = 12$ cm/day on the Dek sand with initial pressure $h = - 150$ cm..	443
	(b)	Pressure head contours after 1 day of infiltration with fixed domain size $150 \times 150$ cm and mesh size $\Delta x = 3$ cm (same case as Figure 5.12a).....	444
5.13	(a)	Pressure head contour surface ( $h = - 90$ cm) obtained after 1 day of infiltration with the variable domain procedure: 3D strip-source infiltration ( $q = 2$ cm/day) on the Dek sand with random $K_s$ and $\alpha$ parameter, and initial pressure $h = - 150$ cm.....	445

(b)	Pressure head contour surface ( $h = - 90$ cm) after 1 day of infiltration with fixed domain size $140 \times 400 \times 400$ cm and mesh size $\Delta x = 10$ cm (same case as Figure 5.13a).....	446
5.14	Example of numerical pressure contour map for 2D strip-source infiltration in a homogeneous soil with exponential $K(h)$ and $\theta(h)$ curves having the same slope ( $\alpha = \beta = 0.1 \text{ cm}^{-1}$ ). Time $t = 1$ day.....	451
5.15	Comparison of numerical and analytical solutions for 2D strip-source infiltration in a homogeneous soil with exponential $K(h)$ and $\theta(h)$ curves having the same slope ( $\alpha = \beta = 0.1 \text{ cm}^{-1}$ ). Pressure contours at time $t = 0.5$ day .....	452
5.16	Numerical and analytical solutions for the transient 1D diffusion equation with constant coefficients. The numerical solutions obtained in the saturated or unsaturated modes, with fixed or variable time steps, were undistinguishable from the analytical solution. One of the numerical solutions is shown here for times $t = 0.01, 0.10, 0.5, 1,$ and $t \geq 5$ (quasi-steady state)	455
5.17	Vertical pressure profile at times $t = 0.005$ and $0.1$ day for one-dimensional infiltration with zero pressure at soil surface (Dek sand with $h_{in} = - 111$ cm). The vertical mesh size is $\Delta x = 3$ cm and the total length of the column is $L = 300$ cm.....	459
5.18	Vertical pressure profile at time $t = 0.1$ day for a two-dimensional infiltration with a saturated strip source. The vertical transect coincides with the axis of symmetry (see Figure 5.19).....	460
5.19	Pressure head contour lines at time $t = 0.1$ day for 2D infiltration with a saturated strip source (Dek sand with $h_{in} = - 111$ cm). The source width is $33$ cm, the mesh size is $3$ cm, and the domain size $150 \times 150$ cm.....	461
5.20	Vertical pressure profiles at times $t = 0.1, 0.3$ and $0.6$ day for a two-dimensional infiltration with a constant flux strip-source. The vertical transect coincides with the axis of symmetry (see Figure 5.21).....	462

- 5.21 Pressure head contour lines for 2D infiltration with a constant flux strip source  $q_0 = 12$  cm/day (Dek sand with  $h_{in} = -111$  cm). The source width is 33 cm, the mesh size 3 cm, and the domain size 150 x 150 cm. Times:  $t = 0.1, 0.3, 0.6$  and 1.0 day.....463
- 5.22 (a) Pressure head contour lines for 2D strip-source infiltration ( $q = 12$  cm/day) in a horizontally layered sand/sand system, at time  $t = 1$  day. The mesh size is 3 cm, the domain size 150 x 150 cm, the strip width 33 cm, and the alternate layers thickness 9 cm. The initial pressure head was  $h_{in} = -150$  cm ..... 467
- (b) Same as Figure 5.22.a, but with a less dry initial state ( $h_{in} = -90$  cm)..... 468
- 5.23 Pressure head contour lines for 2D strip-source infiltration ( $q = 12$  cm/day) in a horizontally layered sand/silt system, at time  $t = 1$  day. The mesh size is 3 cm, the domain size 150 x 150 cm, the strip width 33 cm, and the alternate layers thickness 9 cm. The initial pressure was  $h_{in} = -150$  cm.....469
- 5.24 Same as Figure 5.23, but with a coarser mesh size  $\Delta x = 9$  cm equal to the layer thickness.....471
- 5.25 Vertical pressure profiles through the axis of symmetry of the strip source for the sand/silt system at times  $t = 0.3$  and 1 day. The crosses correspond to the fine mesh simulation (Figure 5.23 with  $\Delta x = 3$ cm) and the square boxes to the coarse mesh simulation (Figure 5.24 with  $\Delta x = 9$  cm).....472
- 5.26 Vertically layered sand/silt soil system (strip source infiltration-time = 1 day).....473
- 6.1 Schematic representation of flow domain geometry and boundary conditions used for single-realization simulations of steady-state saturated flow.....484
- 6.2 Typical high-resolution contour map of three-dimensional isotropic Markov log-conductivity field in a square two-dimensional slice. Only the low contour values  $K/K_G = 1$  to  $1/100$  are represented ( $\sigma_f = 1., \Delta x_i/\lambda_i = 1/3, L_i/\lambda_i = 43$ ).....491



- 6.3 Illustration of the spatial averaging procedures used to detrend the hydraulic head field and the flux vector field: (a) Cross-flow averaging, (b) Nonlinear trend  $\bar{H}(x_1)$ , and (c) Approximately constant mean  $\bar{Q}_1$ .....498
- 6.4 Sketch of the two-dimensional slices used for contour plots of the three-dimensional flow fields. The mean flow direction is  $x_1$ . From top to bottom: (a) Horizontal slice parallel to flow, (b) Vertical slice parallel to flow, and (c) Vertical slice orthogonal to flow .....509
- 6.5 Two-dimensional excursion regions of the 3D random conductivity field in a slice (problem B with  $\sigma_f = 2.3025$ ). The black and white patches indicate regions where  $K/K_G \leq 0.1$  and  $K/K_G \geq 10$ , respectively.....510
- 6.6 Three-dimensional excursion regions of the 3D random conductivity field in a cubic domain with 130,000 grid points (problem B with  $\sigma_f = 2.3025$ ). The regions correspond to high values of the conductivity such that  $K/K_G \geq 10$ .....512
- 6.7 Same as Figure (6.6) except that  $K/K_G \geq \sqrt{10}$ .....513
- 6.8 Hydraulic head contours in a horizontal slice parallel to the mean flow for problem B with  $\sigma_f = 2.3025$ . There are 10 contour lines of equally spaced head values, including the right and left boundaries. Low conductivity contours are shown in the background ( $\log_{10}(K/K_G) = 0, -0.5, -1, -1.5, -2$ ).....515
- 6.9 Comparison of hydraulic head contours in a horizontal slice parallel to flow for  $\sigma_f = 1$  (top) and  $\sigma_f \approx 2.3025$  (bottom) (Problem B). There are 21 contour lines of equally spaced head values, including the right and left boundaries.....517

6.10	One-dimensional representation of the spatial fluctuations of the hydraulic head (Problem B - $\sigma_f \approx 2.3$ ):	
	(a) Comparison of computed trend $\bar{H}(x_1)$ with hypothetical linear profile.....	519
	(b) Fluctuations of the head field around the trend for a particular transect parallel the mean flow.....	519
6.11	Longitudinal flux component $Q_1$ along a transect parallel to the mean flow direction $x_1$ (isotropic Problem B, $\sigma_f = 2.3025$ ).....	525
6.12	Transverse flux component $Q_2$ along a transect parallel to the mean flow direction $x_1$ (isotropic Problem B, $\sigma_f = 2.3025$ ).....	526
6.13	Transverse flux component $Q_3$ along a transect $x_3$ transverse to the mean flow (isotropic Problem B, $\sigma_f = 2.3025$ ).....	527
6.14	Contour lines of the longitudinal flux component $Q_1$ in a vertical slice transverse to the mean flow (isotropic Problem B, $\sigma_f = 2.3025$ ). The isovalues are equally spaced, from $Q_1 = 0$ up; the black patches correspond to high values of $Q_1$ well above the mean $\bar{Q}_1$ .....	528
6.15	Contour lines of the longitudinal flux component $Q_1$ in a horizontal slice parallel to the mean flow (isotropic Problem B, $\sigma_f = 2.3025$ ). The isovalues are equally spaced, from $Q_1 = 0$ up; the black patches correspond to high values of $Q_1$ well above the mean $\bar{Q}_1$ .....	529
6.16	(a) Contour lines of the three-dimensional hydraulic head field in a horizontal slice parallel to the mean flow (pointing right). There are 11 iso-value contours including the left and right boundaries (equally spaced values). Flow problem A with 1 Million nodes: (a) Case $\sigma_f = 1.0$ .....	540
	(b) Same as (a), with $\sigma_f = 1.732$ .....	541

(c) Same as (a), with  $\sigma_f = 2.305$ .....542

6.17 (a) One-dimensional representation of the head field  
(sample function  $H(x_1)$ , and nonlinear trend  
 $\bar{H}(x_1)$ ) along a transect parallel to the mean  
flow direction. Flow problem A with 1 Million  
nodes: (a) Case  $\sigma_f = 1.0$ .....543

(b) Same as (a), with  $\sigma_f = 1.732$ .....544

(c) Same as (a), with  $\sigma_f = 2.3205$ .....545

6.18 (a) Numerical head correlation functions along  
three directions, for the 1 Million node  
"isotropic" problem A ( $\sigma_f = 1.0$ ).....564

(b) Same as (a), with  $\sigma_f = 1.732$ .....565

(c) Same as (a), with  $\sigma_f = 2.3025$ .....566

6.19 Comparison of numerical and theoretical (spectral)  
head correlation functions in the longitudinal and  
transverse directions  $\xi_1$  and  $\xi_2$  (1 Million node isotropic  
Problem A, with  $\sigma_f = 1.0$ ).....567

6.20 Subset of vector-vector flux correlation functions,  
restricted to the diagonal components of the  
correlation tensor and to separation vectors  
parallel to the principal axes.....572

6.21 Flux correlation functions  $R_{Q_1Q_1}(\xi_j)$  for  $\sigma_f = 1.0$   
(solid lines: spectral theory; crosses: numerical  
simulation).....573

6.22 Flux correlation functions  $R_{Q_2Q_2}(\xi_j)$  for  $\sigma_f = 1.0$   
(solid lines: spectral theory; crosses: numerical  
simulation).....574

6.23 Verification of statistical symmetries on the  
numerical flux correlation functions ( $\sigma_f = 1.0$ ):  
 $R_{Q_1Q_1}(\xi_2) \approx R_{Q_1Q_1}(\xi_3)$ .....575

6.24	Verification of statistical symmetries of the numerical flux correlation functions ( $\sigma_f = 1.0$ ): $R_{Q_2Q_2}(\xi_1)$ , $R_{Q_2Q_2}(\xi_2)$ , $R_{Q_3Q_3}(\xi_1)$ , $R_{Q_3Q_3}(\xi_3)$ are nearly identical.....	576
6.25	Verification of statistical symmetries on the numerical flux correlation functions ( $\sigma_f = 1.0$ ): $R_{Q_2Q_2}(\xi_3) \approx R_{Q_3Q_3}(\xi_2) \approx R_{Q_1Q_1}(\xi_1)$ .....	577
6.26	Numerical flux correlation functions $R_{Q_1Q_1}(\xi_2)$ and $R_{Q_1Q_1}(\xi_3)$ for $\sigma_f \approx 1.0, 1.7$ and $2.3$ .....	578
6.27	Numerical flux correlation functions $R_{Q_2Q_2}(\xi_1)$ and $R_{Q_2Q_2}(\xi_2)$ for $\sigma_f \approx 1.0, 1.7$ , and $2.3$ .....	579
6.28	Numerical flux correlation function $R_{Q_2Q_2}(\xi_3)$ for $\sigma_f \approx 1.0, 1.7$ , and $2.3$ . The solid line corresponds to the result of the spectral theory, independent of $\sigma_f$ .....	580
6.29	(a) Hydraulic head contours in a horizontal slice parallel to the mean flow, for a "shallow stratified aquifer" (Problem E).....	591
	(b) Same as (a), for a "deep stratified aquifer" (Problem F).....	592
6.30	(a) Hydraulic head contours in a vertical slice parallel to the mean flow, for a "shallow stratified aquifer" (Problem E).....	593
	(b) Same as (a), for a "deep stratified aquifer" (Problem F).....	594
6.31	(a) Hydraulic head contours in a vertical slice transverse to the mean flow, for a "shallow stratified aquifer" (Problem E).....	595
	(b) Same as (a), for a "deep stratified aquifer" (Problem F).....	596
6.32	(a) Sample function of the head field $H(x_1)$ along a selected transect parallel to the mean flow, and cross flow average $\bar{H}(x_1)$ : case of the "shallow aquifer" Problem E.....	598

(b)	Same as (a) for the "deep aquifer" Problem F.....	599
6.33 (a)	Computed log-conductivity correlation functions for the single-realization anisotropic Problem E (shallow aquifer, fine grid).....	602
(b)	Computed log-conductivity correlation functions for the single-realization anisotropic Problem F (deep aquifer, coarse grid).....	603
6.34 (a)	Computed head correlation functions for the single-realization anisotropic flow Problem E (shallow aquifer, fine grid).....	605
(b)	Computed head correlation functions for the single-realization anisotropic flow problem F (deep aquifer, coarse grid).....	606
(c)	Theoretical head correlation functions as predicted by the spectral theory for anisotropy ratio $\epsilon = 1/4$ ( $\lambda_i = 1, 1, 0.25$ ).....	607
7.1	Illustration of a strip-source infiltration problem having one spatial direction of statistical homogeneity (longitudinal direction).....	620
7.2	Schematic representation of unsaturated log-conductivity variability in two cases. On top, the parameters $\ln K_s$ and $\ln \alpha$ are perfectly correlated (Case 2 in the text). On bottom, they are perfectly uncorrelated (Case 3 in the text).....	631
7.3	Two perspective views of the pressure contour surface $h = -90$ cm at $t = 2$ days for strip-source infiltration in a statistically isotropic soil with initial pressure $h_{in} = -150$ cm (Case 1: $K_s$ random, $\alpha$ constant).....	634
7.4	Two perspective views of the pressure contour surface $h = -90$ cm at $t = 2$ days for strip-source infiltration in a statistically isotropic soil with initial pressure $h_{in} = -150$ cm (Case 2: $K_s$ and $\alpha$ random, perfectly correlated).....	635

7.5	Two perspective views of the pressure contour surface $h = -90$ cm at $t = 2$ days for strip-source infiltration in a statistically isotropic soil with initial pressure $h_{in} = -150$ cm (Case 3: $K_s$ and $\alpha$ random, perfectly independent).....	636
7.6	Pressure head contour lines in a vertical plane transverse to the strip source for cases (1), (2), (3) as in Figures (7.3), (7.4), (7.5). The pressure contours are labelled every 10 cm, e.g., contour #6 corresponds to $-60$ cm, and contour #9 to $-90$ cm.....	638
7.7	Pressure head contour lines in a vertical plane parallel to the strip source for case (2) as in Figure (7.4). The pressure contours are labelled every 10 cm, e.g., contour #6 corresponds to $-60$ cm, and contour #9 to $-90$ cm.....	642
7.8	Schematic representation of the flow domain geometry for the 300,000 node simulation of strip-source infiltration in a statistically anisotropic soil ("trench experiment"). The numerical solution was sampled along certain slices ( $Y=2, 4.8, 9.8$ m and $X = 0$ ).....	645
7.9	Water retention curve (tension versus volumetric moisture content) for the soil of the strip-source simulation ("trench experiment", Wierenga et al., 1986).....	650
7.10	Mean unsaturated conductivity curve $K(h)$ for the soil of the strip-source "trench experiment": the straight line corresponds to the exponential model actually used in the numerical simulation; the other curve is the Mualem-Van Genuchten model indirectly fitted to field data by Wierenga et al., 1986.....	652
7.11	Contour lines of pressure head in three vertical-transverse slices during the simulated strip-source experiment after 5 days of infiltration ( $t=5$ days). From top to bottom: slices $Y = 2$ m, $Y = 4.8$ m, $Y = 9.8$ m.....	660
7.12	Contour lines of pressure head in three vertical-transverse slices during the simulated strip-source experiment after 10 days of infiltration ( $t=10$ days). From top to bottom: slices $Y = 2$ m, $Y = 4.8$ m, $Y = 9.8$ m.....	661

- 7.13 Contour lines of pressure head in three vertical-transverse slices during the simulated strip-source experiment after 10 days of infiltration and 5 days of drainage ( $t=15$  days). From top to bottom: slices  $Y = 2\text{m}$ ,  $Y = 4.8\text{ m}$ ,  $Y = 9.8\text{ m}$ .....662
- 7.14 Contour lines of pressure head in three vertical-transverse slices during the simulated strip-source experiment after 10 days of infiltration and 10 days of drainage ( $t=20$  days). From top to bottom: slices  $Y = 4.8\text{ m}$  and  $Y = 9.8\text{ m}$ ..... 663
- 7.15 Contour lines of pressure head in the vertical transverse slice located near the free edge of the strip ( $Y = 9.8\text{ m}$ ) at three different times. From top to bottom:  $t = 5$  days,  $t = 10$  days, and  $t = 15$  days (10 days infiltration + 5 days drainage)..... 665
- 7.16 Contour lines of pressure head in the vertical-longitudinal slice ( $X = 0$ ) at three different times. From top to bottom:  $t = 5$  days,  $t = 10$  days, and  $t = 15$  days (10 days infiltration and 5 days drainage).....666
- 7.17 (a) Contour lines of pressure head in a horizontal slice at shallow depth  $Z = 0.5\text{ m}$ . Time  $t = 15$  days (10 days of infiltration and 5 days drainage).....668
- (b) Same as (a), for a horizontal slice at a larger depth  $Z = 2.0\text{ m}$ .....669
- 7.18 Pressure head profiles in the vertical direction during infiltration (times  $t = 1.0, 2.5, 5.0$  and  $10$  days). The vertical transect is located near the geometric center of the strip ( $X = 0, Y = 4.8\text{m}$ )...671
- 7.19 Pressure head profiles in the vertical direction during drainage (times  $t = 10, 15$  and  $20$  days). The vertical transect is located near the geometric center of the strip ( $X = 0, Y = 4.8\text{m}$ ).....672
- 7.20 (a) Pressure head profiles in the horizontal-transverse direction during drainage (times  $t = 10, 15$  and  $20$  days). The transect is located at depth  $Z = 0.5\text{m}$  beneath the strip-source.....673
- (b) Same as (a), for a larger depth  $Z = 2.0\text{m}$ .....674

- 7.21 (a) Pressure head profiles in the horizontal-longitudinal direction during drainage (times  $t = 10, 15,$  and  $20$  days). The transect is located at depth  $Z = 0.5\text{m}$ .....675
- (b) Same as (a), for a larger depth  $Z = 2.0\text{m}$ .....676
- 7.22 Vertical pressure head profiles obtained at different times during the transient simulation towards a steady state solution of the "rainfall infiltration" problem. Times  $t = 4.9$  day,  $14.4$  day and  $114$  day: the crosses indicate the quasi-steady solution at  $t = 114$  days. The vertical transect is near the center of the domain.....683
- 7.23 Pressure head contour lines in a vertical slice for the steady state "rainfall" infiltration in a statistically anisotropic soil (300,000 nodes). The slice approximately crosses the geometric center of the domain ( $Y = 7.4\text{m}$ ).....685
- 7.24 Pressure head contour lines in a horizontal slice for the steady state "rainfall" infiltration in a statistically anisotropic soil (300,000 nodes). The slice is approximately located at the mid-point between soil surface and bottom boundary ( $z = 2.5\text{m}$ ).....686
- 7.25 Pressure head profile in the vertical direction for the steady state "rainfall" infiltration simulation. The transect is located near the geometric center of the domain ( $X = 0, Y = 7.4\text{m}$ ).....691
- 7.26 (a) Pressure head profile in the horizontal direction for the steady state "rainfall" infiltration simulation. The transect crosses the center of the domain and is oriented in the "transverse" direction ( $Y = 7.4\text{m}, Z = 2.5\text{m}$ ).....692
- (b) Same as (a), for another horizontal transect crossing the center of the domain and oriented in the "longitudinal" direction ( $X = 0, Z = 2.5\text{m}$ ).....693



LIST OF TABLES

No.	Page
2.1	Statistical properties of measured three-dimensional log-conductivities ( $\ln K$ ) in saturated formations, from Hufschmied (1985) and Sudicky (1986)..... 76
2.2	Summary of some field data on the spatial variability of unsaturated soils from the literature..... 81
3.1	Isotropic and anisotropic spectra for 2 and 3-dimensional random log-conductivity fields.....109
3.2	Admissible log-conductivity fields for steady flow in 1,2,3 dimensions and 3D solute transport.....112
5.1	Order of accuracy of the stochastic finite difference approximation.....338
5.2	Relative numerical error on the hydraulic head and flux vector, in the case of the 3D isotropic Markov log-conductivity spectrum.....338
5.3	List of matrix solvers and references.....344
5.4	Convergence rate of the SIP solver: summary of numerical experiments for 3D steady state saturated flow with statistically isotropic random conductivities.....386
6.1	Synopsis of single-realization problems of steady-saturated flow with 3D random field conductivities (see also Table 5.4).....482
6.2	Comparison of numerical and spectral theory statistics for the "isotropic" flow Problem B of Table 6.1 ( $N = 130,000$ nodes). The spectral theory results are shown in parenthesis.....521
6.3	Comparison of theoretical (ensemble) and computed (spatial) moments, for the single replica of the isotropic 3D Markov log-conductivity field generated by the Turning Band Method (1 Million node flow problem).....537
6.4	Summary of analytical expressions for various statistics from the first order ( $\cdot$ ) and higher order ( $(\cdot)$ ) spectral solutions, as a reference for Tables 6.5 and 6.6. (Case of isotropic 3D Markov log-conductivity).....547

6.5	Summary of computed statistics obtained for the 1 Million node flow simulations (Problem A with three values of log-conductivity standard deviation), and comparison to spectral theory (in parenthesis). The statistical quantities are defined in the text.....	548
6.6	Comparison of first order ( $\cdot$ ) and higher order ( $(\cdot)$ ) spectral solutions. The numbers in parenthesis give the relative error on $\sigma_H$ and $\sigma_{q_i}$ with respect to the values obtained by numerical simulation.....	550
6.7	Truncation errors and discrepancy between the spectral and numerical solutions, for the flux standard deviations $\sigma_{q_i}$ (1 Million nodes, $\sigma_f = 1.00$ , $\Delta x/\lambda=1/3$ )...	556
6.8	Correlation scales of the hydraulic head field along three directions: comparisons of spectral solution with the numerical results of the 1 Million node "isotropic" flow problem A.....	569
6.9	Correlation scales of the flux vector components along three directions ( $R_{Q_i Q_i}(\xi_j)$ ): Comparison of spectral solution with the numerical results of the 1 Million node "isotropic" flow Problem A.....	585
6.10	Comparison of preliminary "anisotropic flow simulations" with the results of the spectral theory: head standard deviation and correlation scales (220,000 node flow problems E and F, $\sigma_f=1$ , $\epsilon=1/4$ ).....	600
7.1	Summary of input data for the single-realization simulations of strip-source infiltration in statistically isotropic soils (25,000 nodes).....	626
7.2	Summary of input data for the single-realization simulation of strip-source infiltration in a statistically anisotropic soil ("trench experiment")....	647
7.3	Single-point moments and correlation function of the pressure head field for the single-realization "rainfall infiltration" simulation on a statistically anisotropic soil (300,000 node grid).....	689

## CHAPTER 1: INTRODUCTION

### 1.1 Subsurface Contamination and Field Heterogeneity

There has been significant progress during the past decade in our conceptual understanding of the physics of flow and mass transport in naturally heterogeneous or random porous media. Stochastic concepts were introduced to represent the natural variability of porous (non-fractured) subsurface formations and soils, leading to new mathematical formulations of the classical equations describing subsurface flow and transport phenomena, which in turn influenced current stochastic approaches to data collection.

This area of research has gradually grown into a field of its own, known as "stochastic subsurface hydrology". The basic ingredients of this approach are, on the mathematical side, the theory of random functions of multidimensional space (random fields) and of stochastic partial differential equations; the concept of "effective" transport coefficients (macro-scale conductivity and dispersivity); and advanced linear estimation/optimization theory for the collection of noisy field data. Similar concepts have been used in the past, notably in the statistical theory of homogeneous turbulence (random velocity fields) and in the mathematical theory of "homogenization".

where interest focuses on the existence and uniqueness of effective transport properties for a variety of physical problems.

The field of stochastic subsurface hydrology has become an active area of research for applications to toxic and radioactive waste contamination, with the increasing public and governmental awareness of the gravity and ubiquity of the toxic waste problem (North America and Western Europe). Because water is the main carrier of toxic species underground, e.g., in dissolved form, the study of subsurface water flow is an essential preliminary step towards a better understanding of toxic solute transport in complex environments.

The complexity of natural subsurface flow systems can be reduced somewhat by considering separately two distinct types of flow regimes: purely saturated flow with positive water pressures (aquifers), and purely unsaturated flow with negative water pressures below atmospheric pressure (unsaturated soils and vadose zone). In this work, we will be mainly concerned with the physics of water flow under these two distinct regimes, with particular emphasis on the effects of random-like heterogeneities of the porous medium.

[a] Subsurface contamination:

It may be useful to consider briefly how research on heterogeneous flow systems relates to actual field contamination problems. Low-level radioactive or toxic chemicals are usually disposed of above the ground or buried at shallow depths. Examples of hazardous waste sites of this type are landfills, surface impoundments (e.g. lined evaporation ponds), and uranium mill tailings buried at shallow depths. Another situation of interest concerns the case of potentially harmful chemicals applied over large surfaces at relatively small concentrations, such as may occur in irrigated areas (fertilizers dissolved in irrigation water). In these cases, contaminant transport will presumably take place in the unsaturated flow regime when a leak occurs. Except for controlled experiments, leakage is usually not detected until after the contaminant has reached a major, extensively monitored groundwater system, or until it has caused major damage (e.g. contamination of local communities via drinking water).

Large-scale controlled experiments of contaminant migration through the vadose zone are scant (see the extensive review of Gelhar et. al. 1984). One notable exception is the experimental study of an evaporation pond by Trauntwein et. al. (1983) and Kent et. al. (1982). These authors found that, after

20 years of leakage in the unsaturated zone, water reached a depth of 100 meters, and extended laterally over a distance of 2 kilometers. The surprisingly large lateral spread could be explained by the presence of horizontal clay lenses, leading perhaps to the formation of perched water zones (Gelhar et. al., 1984). The flow system in this case is complex and inherently three-dimensional in nature.

Another type of application concerns the case of high-level radioactive wastes. Currently, a number of options are being (re)considered for their disposal, particularly in the United States. One of these options is the deep burial of sealed canisters into saturated formations of very low permeability, such as unfractured basalt, tuff, or granite. Another option which has been proposed, but not yet implemented to our knowledge, is the burial of radioactive wastes into very dry unsaturated porous formations located in arid (and poorly populated) regions. Winograd (1981), one of the proponents of this option, discusses the possibility of burying high-level wastes at depths of 15 m to 85 m in valley-fill deposits inside the man-made Sedan crater at Yucca Flat, Nevada. In that particular environment the annual rainfall is only 125 mm/year (5 inches/year) and the water table is 600 meters deep. Winograd estimated that the downward percolation rate (velocity) through

the unsaturated valley-fill could be roughly on the order of 2 mm/year, i.e., 200 meters per hundred thousand years. Incidentally, this gives also an idea of the large time scale of interest for high-level, slowly decaying radioactive wastes. In this case of very slow flow and extremely dry conditions, it is not at all clear what the effect of local heterogeneities could be on the overall pattern of dispersion of a contaminant at the scale of thousands to several hundred thousand of years.

Of more immediate concern is the potential hazard from existing waste facilities. For instance, a major leak was detected in 1973 beneath one of the tanks located at the storage facility of Hanford, Washington state. The total amount that leaked into the vadose zone was evaluated as one fifth of the 500,000 gallons ( $2000 \text{ m}^3$ ) of high-level radioactive liquid waste initially contained in the tank. The contaminant movement at this site is now being extensively monitored. In 1978, significant radionuclide concentrations were detected as far as 30 meters in depth, and 25 meters from the edge of the tank, laterally (Rouston, et. al., 1979).

Considering all the possible options and scenarios of subsurface contamination, it is always possible that, in case of a leak, the contaminant will eventually reach a major (regional) groundwater flow system, where transport takes place in the

saturated flow regime. There have been intense monitoring of contamination plumes in a number of groundwater systems worldwide. However, the groundwater velocities are generally not directly accessible to measurements. Thus, to predict the fate of contaminants in groundwater flow systems requires a priori a reliable modelization of groundwater velocities based on other types of information more accessible to measurement. The current practice is a subtle and complex combination of numerical modeling and model fitting, e.g., from measurement of hydraulic heads and concentrations on the site. For unsaturated flow and transport, however, there have been very few observations of the flow and contamination patterns at the large scale. The report by Gelhar et. al. (1984) contains a comprehensive review and interpretation of field data for both types of flow/transport problems, saturated and unsaturated. A major conclusion from their review is that models based on a simple extrapolation of small scale data often fail to predict phenomena occurring over large space-time scales.

[b] Field heterogeneity and implications:

One essential feature of subsurface formations, on which we have chosen to focus in this dissertation, is spatial variability. With the increasing body of literature devoted to the measurement and identification of various properties of



natural formations, it appears clear that heterogeneities occur at many scales, from "grain size" up to large geological structures. For most practical purposes, the micro-scale or "grain size" variations of a discontinuous nature can be filtered out. The formation is then viewed as a porous continuum, whose bulk properties reflect implicitly the granular nature of the medium (e.g. porosity, storage capacity, conductivity, and coefficient of mechanical dispersion of tagged fluid particles).

It should be recognized, however, that this simplified view may not always be realistic for soils with fissures or macropores, for fractured rocks, or for karstic formations. Such irreducibly discontinuous media will be ignored in this work. On the other hand, there is now ample evidence that the bulk properties of natural porous media, even without the presence of fractures or other large scale discontinuities, may vary quite erratically in space. It has been progressively recognized that such variability plays a major role in phenomena like solute dispersion at the large scale (macrodispersion).

Figure (1.1a) from Gelhar (1976) depicts the vertical variation of the log-saturated conductivity measured from small cores taken from a borehole. The conductivity fluctuates, apparently at random, over four orders of magnitude. It is

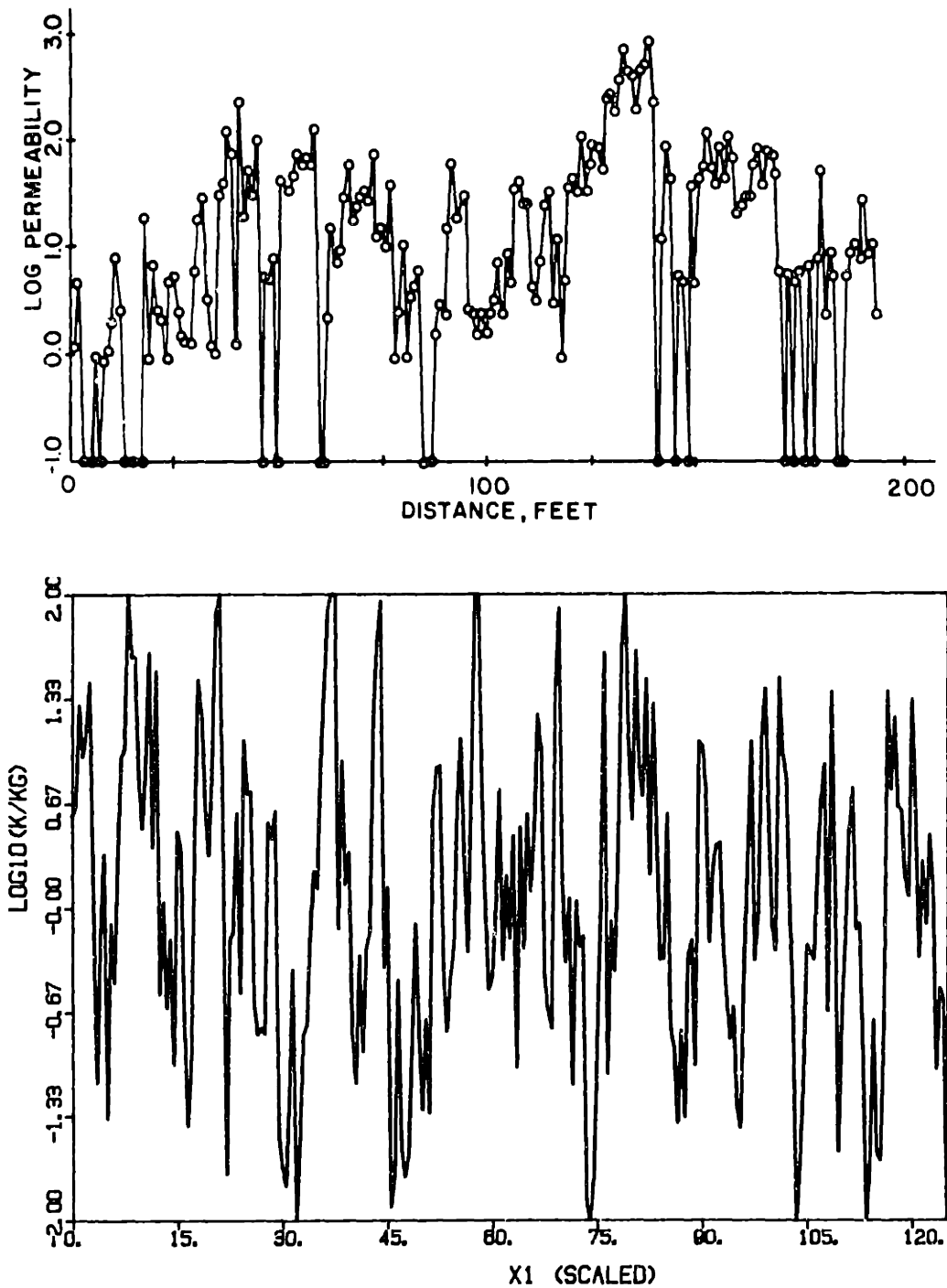


Figure 1.1: Examples of log-conductivity records  $\ln K(x)$  in one spatial dimension: (a) data from vertical borehole (Gelhar, 1976), (b) Synthetic realization of a one-dimensional Gauss-Markov process with exponential covariance function.

instructive to compare these data to the generated random function depicted in Figure (1.1b). The variance and correlation scale of the synthetic random function in (b) were adjusted to fit those of the observed record in (a). In many other cases as well, random functions appear to be adequate models of natural variability. Relevant data for aquifers can be found for example in papers by Freeze (1975), Delhomme (1979), and Hoeksema and Kitanidis (1985). Their work indicates that the log-saturated conductivity ( $\ln K$ ) is normally distributed, with standard deviations ranging from 0.5 to 3.5 (see review in Chapter 2).

The hydraulic properties of unsaturated soils also exhibit seemingly random variation in space. In this case, however, spatial variability is more difficult to characterize because unsaturated soil conductivity and moisture content are functions of soil water pressure. These functional relations are usually measured either on small soil samples in the laboratory, or on small field plots (1-10 m<sup>2</sup>, with a vertical resolution of 10-20 cm). Parameters such as porosity, saturated conductivity, and shape factors appear to be log-normally distributed whenever variability is high enough to distinguish a skewed distribution. Experimental evidence supporting this assertion can be found in Nielsen et. al. (1973), Warrick et. al. (1977), Sharma et. al. (1980), Gelhar et. al. (1982), and Russo (1983). A review of

available field data will be presented in Chapter 2.

In summary, there is ample evidence of seemingly random variations of hydraulic properties in space. Moreover, data like those shown in Figure (1.1) seem to exhibit a definite spatial structure (scale of fluctuation) that could be identified as the correlation length of a stationary random function. We recognize however that the correlation scale may not be uniquely identifiable in practice. In some experimental studies, the correlation scale was found negligible (or ignored altogether, as in Nielsen et. al., 1973). In others, it was found almost as large as the region under investigation, i.e. statistically meaningless. Finally, studies like those of Scisson and Wierenga (1981), Gajem et. al. (1981), and others, seem to indicate sensitivity of the observed variance and correlation scale with respect to the scale of measurement and size/spacing of measurement network. This, we feel, is an important issue that deserves a more thorough discussion. The topic will be touched upon at other places in this work.

## 1.2 Scope and Objectives:

### [a] Motivation and background:

The present work is based, for the most part, on the

premise that a realistic description of naturally heterogeneous porous media can be achieved by representing the local hydraulic properties in the form of statistically homogeneous random fields in three-dimensional space. Previous research under this assumption have led to useful statistical characterizations of the global behavior and spatial structure of heterogeneous flow and solute transport. In particular, the spectral theory developed by Gelhar and co-workers (Gelhar, 1984 and 1987; Gelhar and Axness, 1983) has led to closed form relations describing in a compact form the statistical behavior of heterogeneous groundwater flow systems, including the cases of statistically isotropic and statistically anisotropic (stratified) aquifers. The global/statistical properties of interest for applications are the effective conductivity, the macrodispersion of a convected solute, and the degree of variability and spectral content of the random head and velocity fields. Parallel results have also been obtained by other stochastic approaches, which will be reviewed in Chapter 2.

The spectral theory provides particularly simple results due to the assumptions of infinite-domain and statistical homogeneity/ergodicity of the solutions of the stochastic flow and transport equations. These key assumptions, by reducing further the complexity of the problem, permitted to obtain *approximate* expansion solutions of the stochastic groundwater

flow equation (similar to a "heat equation" with random conductivities) and of the solute transport equation ("convection-diffusion equation" with a random velocity field) in terms of spectral densities in Fourier space. These spectral solutions give all the information there needs to know about the covariance structure of the variables of interest (hydraulic head and groundwater velocities). However, the validity of the approximations involved in the spectral theory has yet to be ascertained for a wide range of field conditions. The same remark holds for other analytical stochastic theories proposed in the literature. In general, the available stochastic solutions (spectral or other) rely on some kind of small parameter expansion, where the small parameter corresponds to the degree of variability of the underlying porous formation (e.g., standard deviation of the random log-conductivity field). In the case of the spectral theory, the accuracy of the small parameter expansion and the validity of the homogeneity/ergodicity hypothesis need to be checked for realistic situations.

Moreover, the application of stochastic concepts to the case of unsaturated flow in heterogeneous porous media has encountered serious difficulties, both technical and conceptual, due to the highly *nonlinear* nature of the hydraulic properties of unsaturated media (moisture capacity and hydraulic conductivity functions of water pressure). Although the results obtained by

the linearized spectral approach (Yeh et al. 1985, Mantoglou et. al. 1987) are qualitatively appealing, it is not at all clear yet what the range of applicability of their results could be. In view of our poor understanding of the complex interactions between nonlinear effects and spatial variability, there is a strong motivation for investigating the operational range of the linearized spectral theory of unsaturated flow in the vadose zone, notably concerning the predicted shape, anisotropy, and hysteresis of the unsaturated conductivity tensor as a function of mean water pressure. Even a more qualitative description of actual or *simulated* heterogeneous unsaturated flow patterns could be useful.

At the present date, the available data concerning the large scale pattern of heterogeneous unsaturated flow systems are too scant (as noted previously) to allow for a verification of the linearized spectral results, except perhaps in a very qualitative and speculative fashion. On the other hand, there are now enough experimental observations to indicate that the findings of the spectral theory, among other stochastic approaches, may provide an adequate description of the variability of certain groundwater flow systems and its effect on contaminant macrodispersion (Gelhar, 1986). However, these indications still remain subjective, as too many undetermined parameters enter into play, notably the three-dimensional

correlation structure, fluctuation scales, and statistical anisotropy of the hypothetically random log-conductivity field.

Therefore, there arises the need for an independent verification of the analytical results of the spectral theory in more closely controlled situations, where the actual spatial variability of the underlying porous medium is known with reasonable accuracy.

[b] Present approach and objectives:

In this work, we aim at obtaining accurate solutions of the equations governing flow in hypothetically random porous media, based on the "postulate" of statistical homogeneity of the hydraulic properties of saturated or unsaturated media. In the case of *saturated groundwater flow* in particular, we will seek to refine and extend further the analytical results previously obtained by the first order spectral theory of Gelhar et al. There are several new approaches involved in the proposed refinements. In one instance, we explore higher order and non-perturbative solutions of the stochastic flow equation, while still retaining the infinite domain/ergodicity hypothesis. In another, we extend the spectral theory further to treat explicitly the influence of domain size on the statistical behavior of the flow system at some finite scale. However, the



latter approach will require the same approximation of "small variability" as in the infinite-domain approach.

On the other hand, we also develop and apply a numerical solution method in view obtaining, as accurately as possible, the solution of the three-dimensional saturated flow equation for finite discrete realizations of random medium properties. When the size of the domain is sufficiently large, the numerical solution of this equation should have the same statistical properties as predicted by the spectral theory if the latter was correct. Moreover, only one large single realization of the random medium should suffice to represent the ensemble statistics of the flow field, if the homogeneity/ergodicity hypothesis of the spectral theory holds true. Therefore, the numerical/single realization approach should provide an independent check of the accuracy of infinite-domain spectral solutions, and of its applicability in practical cases where the domain of investigation is necessarily finite.

Finally, the same numerical approach will be used to treat the case of three-dimensional *unsaturated flow systems* in random soils, i.e., with random coefficients intervening in the nonlinear constitutive properties (random unsaturated conductivity-pressure curve as a function of space). However, in this case, the approximations involved in the linearized

spectral theory are too severe, and the numerical requirements on the discrete grid size are too constraining, to allow for a precise statistical comparison between the spectral and single-realization approaches. Nevertheless, the large numerical experiments discussed in this work will appear useful for a preliminary screening of the complex behavior of heterogeneous unsaturated flow systems.

In summary, this dissertation focuses on the mathematical description of subsurface flow fields under the postulate that the natural variability of hydraulic properties can be characterized in the form of statistically homogeneous random fields in three-dimensional space. For the case of saturated flow, the variety of techniques that were used to solve the stochastic flow equation may reflect our attempts at minimizing the set of postulates and approximations required to achieve tractable results. On the other hand, our rather empirical approach of stochastic unsaturated flow reflects the difficulty of developing truly nonlinear yet tractable analytical models of heterogeneous flow systems in that case. Whenever possible, we have used the indications of the linearized spectral theory for interpretation. Finally, it may be relevant here to emphasize that, as in the case of turbulent flows, exact solutions to the saturated and unsaturated stochastic flow equations are not known. Thus, even approximate indications on

the robustness of existing theories can be extremely valuable.

### 1.3 Thesis Preview:

This dissertation was broken down into eight chapters, including this introductory part. The next chapter, Chapter 2, contains a brief literature review, a survey of available field data, and a general presentation of the single-realization approach, particularly in relation with the hypotheses of the spectral theory of stochastic flow. This chapter provides a background for subsequent developments. Chapters 3 and 4 are exclusively devoted to the obtention of tractable solutions of stochastic ground water flow by analytical means. Chapter 5 focuses on numerical issues related to the single-realization approach. This Chapter develops at length the various aspects of a saturated-unsaturated flow simulator, to be used as a tool in Chapters 6 and 7. The results of large saturated flow simulations in randomly heterogeneous media are presented in Chapter 6. The emphasis there is on the statistical analysis of the numerical flow fields for comparisons with the predictions of the spectral theory. Chapter 7 presents in a more qualitative fashion the results of large unsaturated flow simulations in random soils. The overall conclusions of this work are given in Chapter 8.

Because the amount of material presented in Chapters 3 - 7 is quite large, we have found it convenient to summarize the contents of each of these chapters in a compact form, as shown below:

Chapter 3:

The first order spectral theory of Gelhar and Axness (1983) is used to obtain a more complete picture of the statistical properties of the flow. Some new analytical results are derived by integrating the spectra to obtain ensemble moments, such as some closed form expressions for the variances of the flux vector components in the case of extreme anisotropy. A remarkable result concerns the near isotropy of the head field in statistically anisotropic media. The implications of these findings are discussed (shallow/deep stratified aquifers and finite size effects). The role of the low wavenumber fluctuations of the conductivity field is also briefly examined. The discussion focuses on the physical meaning and possible limitations of the spectral solutions.

Chapter 4:

In this chapter are developed several new analytical approaches related to the standard spectral theory of saturated flow in stochastic porous media. A new non-perturbative analysis

of the stochastic flow equation is developed independently of the "small variability" approximation of the spectral theory. In the restricted case of statistically isotropic conductivity, it is shown that the spectral theory of Gelhar and Axness (1983) satisfies all the fundamental conservation and symmetry properties of the flow in any number of dimensions. These properties lead to an exact statistical identity between the flux and head gradient vectors in the 2D isotropic case (statistical conjugacy). In the 3D isotropic case, the flux-head gradient relation contains a few undetermined functions. In the more general case of 3D anisotropic media, an extrapolation of previous results by Matheron (1967) and Gelhar and Axness (1983) leads to a simple closed form expression for the anisotropic effective conductivity tensor. A modification of the Gelhar-Axness spectral solutions to include higher order terms in the flux spectrum is developed, by using a stochastic system of equations governing the flux vector rather than the hydraulic head. Finally, we propose a generalization of the spectral approach to take into account the effects of finite domain size. The generalization is based on the new concept of "spectral conditioning", used to quantify explicitly the relative amounts of uncertainty and spatial variability with respect to the scale of the problem. The method combines ideas related to the concept of self-similarity (Mandelbrot, 1983), renormalization group methods (Wilson, 1975), and spectral solution method (Gelhar,

1984). Closed form results are obtained in particular for one-dimensional saturated flow. Some implications for three-dimensional flow and solute transport are also discussed in view of preliminary results.

#### Chapter 5:

This chapter is devoted to the development and analysis of a numerical method for solving large single realizations of saturated and unsaturated flow in three-dimensional random porous media. In the linear case, a new approach for evaluating finite difference truncation errors with stochastic coefficients is used to show that the classical centered finite difference scheme is consistent, at least in the mean-square sense. For the flux vector, the order of accuracy is equal to one for a smooth conductivity field, but drops to one half for a noisy field. The leading order terms of the head error and flux error are explicitly evaluated as functions of grid resolution for different kinds of random conductivity fields. We then focus on the practical implementation of an iterative matrix solver (SIP). Numerical experiments are presented for large random flow problems on the order of 0.1-1 million nodes (convergence rate analysis). An upper bound for the true solution error is given as a function of convergence rate and final residual error. The convergence rate appears proportional to the inverse square-root

of the condition number. Finally, we also develop a nonlinear system solver for unsaturated flow problems (nonlinear SIP). Preliminary numerical simulations of infiltration in some uniform and heterogeneous soil systems are used to demonstrate the problem solving capabilities of the unsaturated flow simulator. The conclusions regarding the numerical feasibility of the single realization approach are quite favorable in the saturated flow case. However, we also conclude that there could be some severe restrictions on the mesh size (Peclet number condition) and/or time step size in the case of transient unsaturated flow, particularly for dry heterogeneous soils.

#### Chapter 6:

This chapter is devoted to the interpretation and statistical analysis of large single realization simulations of three-dimensional saturated flow in random porous formations. The random conductivity fields are generated on the finite difference grid of the flow simulator by using the 3D turning band method. We begin with a preliminary analysis of "medium size" flow problems (130,000 nodes) in the case of statistically isotropic conductivities, with emphasis on the qualitative features of the head and flux fields, and some comparisons with the predictions of the spectral theory. We then move on to a more extensive statistical analysis of large flow simulations on

a 1 million node grid, again with statistically isotropic conductivities. The comparison with spectral results is quite favorable for a wide range of log-conductivity ( $\ln K$ ) standard deviations, up to  $\sigma = 2.3$ . The discrepancies observed for the flux variances are analyzed, and a further modification of the spectral solution is proposed to account for high order effects on flux variability. The agreement is quite good for other flow characteristics (head variability, flux correlation structure, effective conductivity) but the numerical head correlation ranges appear shorter due to finite size effects. We also investigate finite size effects for the case of statistically anisotropic media. The covariance structure of the head field is analyzed for two flow simulations mimicking the case of shallow and deep stratified aquifers with moderate anisotropy (grid size 220,000 nodes). The chapter ends with a summary of findings and conclusions on the range of validity of spectral solutions of stochastic groundwater flow.

#### Chapter 7:

This chapter presents a qualitative analysis of large single realization simulations of three-dimensional infiltration in random unsaturated soils. The random field coefficients of the exponential conductivity-pressure curve were generated by the turning band method. A preliminary analysis of strip source



infiltration for modest size realizations of statistically isotropic soils (25,000 nodes) revealed the effect of the variability of the slope of the conductivity-pressure curve and of its correlation with the saturated conductivity. Maximum variability of the moisture patterns was observed when both these parameters were random, and uncorrelated. We then moved on to the case of infiltration in statistically anisotropic soils. An unusually large single realization of strip source infiltration was simulated (300,000 node grid), under conditions similar to an on-going field experiment. Both the slope and the saturated value of the conductivity curve were taken random. Thus, a different conductivity curve was generated at each node of the grid. A detailed inspection of the pressure head field, sampled along transects and slices during 10 days of infiltration and 10 days of natural drainage, seemed to confirm some of the predictions of the linearized spectral theory (enhanced lateral spreading and pressure dependent anisotropy). Finally, we developed a more quantitative analysis for another large simulation in the case of steady "rainfall" infiltration on the same random soil realization (300,000 nodes). Spatial averaging estimates of pressure variability and unsaturated effective conductivity appeared fairly close to linearized spectral solutions. The chapter ends with a "summary and discussion" section, including a discussion of the current limitations and

future prospects of numerical and analytical approaches in the case of complex nonlinear flow systems.

This ends our description of the contents of chapters 3, 4, 5, 6, and 7. In summary, this dissertation was organized in three main topics: analytical/spectral approaches (Chapters 3 and 4), numerical analysis (Chapter 5), and statistical/physical interpretation of numerical simulations of random flow problems (Chapters 6 and 7). The conclusive Chapter 8 focuses on the implications of our findings for practical subsurface flow and contamination problems, and discusses some of the contributions of this work towards our conceptual understanding of stochastic flow and mass transport in heterogeneous porous media.

## CHAPTER 2: REVIEW OF STOCHASTIC APPROACHES TO SUBSURFACE FLOW

### 2.1 Overview of Past and Current Approaches to Field Problems

#### 2.1.1 Empirical models:

In view of the complexity of subsurface flow systems, most predictions were and still are based on empirical model calibration. Practitioners in the field of subsurface hydrology use numerical models based on local mass conservation, Darcy's law, and Fick's law. These are distributed-parameter models, usually two or three dimensional. Most frequently, natural variability is partially taken into account by dividing the flow domain into a few subdomains, with different conductivities. Layering within each block is also implicitly taken into account by specifying anisotropic conductivities, with a larger conductivity in the direction parallel to natural stratification, most often horizontal. The hydraulic and dispersive properties to be used in the model are further adjusted for a best fit between numerical and measured values (heads, concentrations). This calibration process has proved most expedient for addressing specific problems, but rather limited in scope. The typical situation is that accurate answers are obtained only for the particular conditions under which the model was calibrated.

Predictions made for hypothetical environmental conditions (different from those prevailing at the time of calibration) appear to be of limited value.

The limitations of current engineering practice are even more drastic concerning solute transport predictions. Dispersion coefficients obtained by way of model calibration appear much greater than those measured on small samples in the laboratory. Furthermore, they are found to increase as the contaminant spreads and more concentration data are made available for new calibrations. This inadequacy may be due to the fact that the velocity field predicted from the flow model, is much smoother than indicated by field observations (conductivity variability). Ignoring the small scale fluctuations of the flow field leads to inadequate prediction of the mechanical dispersion of convected species. Overall, it would seem that empirical calibration of these models does not allow for reliable predictions of contaminant migration over large time and length scales.

These remarks apply as well to black-box or zero-dimensional models. Jury et. al. (1982, 1986) proposed this type of model for the transport of solute in unsaturated soils. Briefly, their model isolates a soil unit (the black-box) and seeks to characterize a transfer-function that relates input and

output for that particular unit. This is analogous to the "Unit Hydrograph" method used in surface hydrology. Unfortunately, the data presented by Jury et al. (1982) indicate that the transfer functions calibrated for certain conditions do not extrapolate to other conditions, time scales, and length scales (see discussion in Gelhar et al. 1984).

### 2.1.2 Probabilistic models without spatial correlation:

There have been also a number of attempts at modelling unsaturated flow and transport by using the idea of independent soil columns. These approaches can be viewed as distributed-parameter models in one dimension. They take into account the horizontal variability of soil properties through a few random parameters, such as a random scaling factor in Warrick and Amoozegar (1979), Sharma et al. (1980), and Vauclin (1982); or the random saturated conductivity in the work by Dagan and Bresler (1983). These authors all assumed in effect that horizontal fluctuations of velocity were unimportant (one-dimensionality). The soil properties were assumed uncorrelated in the horizontal (statistically independent columns) but perfectly correlated in the vertical (homogeneous soil columns). However, other results obtained for fully three dimensional random properties indicate that dimensionality and correlation scales have a crucial influence on the overall

features of the flow field. The reduced dimensionality of the models mentioned above implies a smaller degree of freedom for the movement of fluid particles, whereas natural heterogeneities create fluid pathways that are inherently three-dimensional. In addition the assumption of statistically independent soil columns does not seem to make sense for columns of diameter smaller than the observed correlation scales. In fact, because of these simplifying assumptions the adequate inputs to be used in such models are difficult to evaluate. What are the average or effective parameters for each column? How are they related to small scale measurements?

### **2.1.3 Stochastic models with spatially correlated fields:**

In view of the difficulties just mentioned, approaches based on the theory of random functions have been developed in an attempt to capture the essential features of flow and transport processes in heterogeneous media. In these stochastic approaches, local properties such as the hydraulic conductivity, or the storage coefficient are viewed as homogeneous random functions of space, with translation-invariant means, variances, and correlation functions, determined from field data. In actual practice, the data need only be approximately homogeneous. For instance, Ababou et al. (1985) argue that a statistically meaningful identification of a log-conductivity field must

satisfy a requirement of the type  $\lambda \ll L \ll \mathcal{L}$ , where  $\lambda$  is the correlation length or fluctuation scale,  $L$  is the size of the measurement network, and  $\mathcal{L}$  is some scale of inhomogeneity (for instance  $\mathcal{L} = d \ln K_G / dx$  characterizes the length scale of inhomogeneity in the mean). In this framework, the governing equations (local mass conservation, Darcy's law, Fick's law) have stochastic solutions which can be characterized, in principle, in terms of their ensemble statistics (e.g. first and second order moments of heads, velocities and concentrations).

The infinite-domain spectral theory developed by Gelhar and others aims specifically at obtaining a large-scale characterization of spatially variable flow and concentration fields. By using ergodic arguments, they assume the equivalence between ensemble expectations and spatial averages. Their final results include close-form expressions for the head variance, velocity variance, effective conductivity and macrodispersion in a variety of situations (Bakr et al. 1978; Gelhar and Axness 1983; Gelhar 1984, 1986, and 1987). The "effective" transport properties were defined in connection with the "large scale" Darcy and Fick laws, relating mean fluxes to mean gradients (similar to the Onsager relations used in thermodynamics). The validity of these phenomenological equations have been traditionally investigated at the small scale only. What is emphasized here is that these equations may be extrapolated to

describe large scale phenomena, but with different coefficients. The effective conductivity and macrodispersion coefficients obtained from the spectral theory directly incorporate the spatial structure of the observed heterogeneities, in terms of the variance and correlation structure of the local hydraulic conductivities.

Other methods for solving stochastic flow and transport equations include the approximate Green's function method (Dagan, 1982), the direct numerical solution of approximate equations for first and second order moments (Townley, 1983; McLaughlin, 1985), and direct Monte-Carlo simulations (Freeze, 1975, Smith and Freeze 1979, Delhomme 1979, Ma et al. 1987). These methods apply in particular to the case of flow in bounded domains, and in the presence of local sources or sinks such as pumping wells. In the latter case, the ensemble moments of the stochastic flow field are to be interpreted in a Bayesian framework, i.e., they represent the uncertainty among many possible realizations or locations, rather than the large scale spatial variability of a single flow system (variance of heads near a pumping well at an unspecified location). This view was sometimes implicitly adopted, e.g. in the "well problem" treated by Dagan (1982). The case of semi-infinite aquifers was tackled by Naff and Vecchia (1986) through a combination of Green's function and spectral representation.



Some authors used Monte-Carlo simulations for checking analytical or other solutions. In most cases, comparisons were limited to fairly small conductivity variance (Freeze, 1975; McLaughlin, 1985). Indeed the number of realizations needed to obtain accurate answers could be prohibitive for the large conductivity variances observed in certain field sites, requiring the numerical solution of perhaps 10,000 or more flow problems in three dimensions (see discussion in McLaughlin, 1985). On the other hand, there are also questions about the range of validity of the perturbation-based solution methods just discussed (Gelhar, 1984; Dagan, 1982; McLaughlin, 1985): these are all in some sense "first order approximations", which are only valid asymptotically as the input variability becomes small. Even approximate indications on the robustness of these approximations would be extremely valuable, since exact solutions are not known.

## **2.2 The Single-Realization Approach:**

### **2.2.1 Objectives and method:**

In this section, we define briefly the single-realization approach which will be used in conjunction with a numerical solution method (Chapter 5) to obtain

representative solutions of stochastic flow problems (Chapters 6 and 7). It is relevant here to discuss in more rigorous terms what a "representative" solution means. The idea of the single-realization approach is that the statistical properties of the flow field can be evaluated by computing the spatial moments of one large realization of the flow, rather than the ensemble moments across a large number of realizations. The single-realization and ensemble approaches should be conceptually equivalent if the single solution is obtained on a sufficiently large domain, and if the ergodic hypothesis holds, as assumed in the spectral theory of Gelhar and others (see Chapter 3).

It may be useful here to briefly examine how large must "large" be in order to ensure the equivalence of ensemble and spatial moments of three-dimensional flow fields (e.g. hydraulic head or groundwater velocity vector). Consider a single finite realization of an ergodic flow field  $Y(\underline{x})$  in three-dimensional space. Note that we do not question here the ergodicity hypothesis. Let us now focus on the behavior of spatial sample moments, say mean and covariance, as the size  $L_i$  of the three-dimensional domain varies. If  $\lambda_i$  is the correlation length of  $Y(\underline{x})$  along  $x_i$ , and if  $Y(\underline{x})$  is indeed statistically homogeneous along all three directions ( $i=1,2,3$ ), it seems reasonable to define the sample size, or "equivalent number of independent samples", as:

$$N_Y = \frac{L_1 L_2 L_3}{\lambda_1 \lambda_2 \lambda_3} \quad (2.1)$$

Thus, as in the case of Monte-Carlo simulations, the classical theory of sampling errors can be used to determine the uncertainty on the computed spatial moments due to insufficient sample size. The relative errors on the mean and standard deviations  $\bar{Y}$  and  $\sigma_Y$  are defined as:

$$\begin{aligned} \epsilon(\bar{Y}) &= \frac{\sqrt{\text{Var}(\bar{Y})}}{\sigma_Y} \\ \epsilon(\sigma_Y) &= \frac{\sqrt{\text{Var}(\sigma_Y)}}{\sigma_Y} \end{aligned} \quad (2.2)$$

According to classical results of sampling theory (for a population of independent normal random variables) these quantities are both proportional to the inverse square-root of the equivalent sample size (see for instance Kendall and Stuart, 1977):

$$\begin{aligned} \epsilon(\bar{Y}) &\simeq \frac{1}{\sqrt{N_Y}} \\ \epsilon(\sigma_Y) &\simeq \frac{1}{\sqrt{2N_Y}} \end{aligned} \quad (2.3)$$

However, the error on the covariance function  $R_{YY}(\xi)$  will increase with lag-distance. To evaluate this effect in a very approximate manner, consider how the available number of samples decreases with lag-distance along, say, the  $x_1$ -axis:

$$\xi = (\xi_1, 0, 0)$$

$$N_Y(\xi_1) = \frac{(L_1 - \xi_1)L_2L_3}{\lambda_1 \lambda_2 \lambda_3}$$

For an isotropic field ( $\lambda_1 = \lambda_2 = \lambda_3$ ) and a cubic domain ( $L_1 = L_2 = L_3$ ), the available number of samples that can be used to compute the covariance function at lag-distance  $\xi$  is then simply:

$$N_Y(\xi) = \left(\frac{L}{\lambda} - \frac{\xi}{\lambda}\right) \cdot \left(\frac{L}{\lambda}\right)^2 \quad (2.4)$$

Now, we expect that the relative error on the covariance function:

$$\epsilon(R_{YY}) = \frac{\sqrt{\text{Var}(R_{YY})}}{R_{YY}} \quad (2.5)$$

will behave like:

$$\epsilon(R_{YY}(\xi)) \approx \frac{1}{\sqrt{N_Y(\xi)}} \quad (2.6)$$

Although these estimations of the uncertainty of sample

statistics are very approximate, they should suffice for our purpose here. More precise statements on sample statistics can be found in Appendix 2A, which will be used later in this work.

Let us now illustrate these approximate relations for a simple example: a cubic domain of size 5 correlation scales in each direction. The relative errors on the samples mean and standard deviation are reasonably low in this case (respectively 9% and 6%). However, the relative error on the sample covariance function increases with lag-distance: 10% at  $\xi = \lambda$ , 14% at  $\xi = 3\lambda$ , and over 20% for  $\xi \geq 4\lambda$ . Obviously, to obtain a reliable evaluation of the spatial structure of the flow field from a single realization, the flow domain must be taken much larger than the largest correlation scales of the variables describing the flow. In addition, the effects of artificial boundary conditions, anisotropic behavior, and intrinsic inhomogeneity of the flow along certain directions (e.g. parallel to flow) may lead to revise the size requirement up. This will be investigated more specifically in Chapter 6, using some of the sample statistics developed in Appendix 2A.

The requirement on the size of the single-realization flow problem (to ensure the equivalence of spatial and ensemble moments) is not unlike the Monte-Carlo method's requirement of a

large number of realizations in ensemble space. However, there is an essential difference, that has led us to favor the single-realization approach over Monte-Carlo. In the single-realization method, the spatial variability of a more or less homogeneous random phenomenon is studied at the large scale, and advantage is taken of the large size of the domain to sample the variables of interest over many fluctuation scales in physical space. In the Monte-Carlo method on the other hand, the large number of realizations required to obtain reliable ensemble moments is, in practice, incompatible with the study of large scale flow or transport phenomena by numerical methods. The Monte-Carlo method seems best adapted to the study of localized phenomena affected by uncertainty (uncertain drawdown near a pumping well, depending on its location in a heterogeneous aquifer). Note that our arguments are based on a two-sided interpretation of the effects of spatial variability, depending on the nature of the hydrologic problem and on the size of the domain of interest. We will touch upon this subject again in Chapter 4 (Section 4.4) with the idea of "spectral conditioning".

Furthermore, in cases where the ergodic hypothesis does not hold or is only approximately satisfied, the single realization approach can still be viewed as a direct simulation of plausible field conditions, where only one spatial realization of a particular heterogeneous flow system is actually available

for observation (over a finite domain). In contrast with the spectral theory, the numerical single realization approach does not postulate a priori the statistical homogeneity and ergodicity of the solution (although the assumption of a homogeneous/ergodic random porous medium is still retained). This brings the single realization approach closer to a realistic representation of natural field conditions. However, the statistical interpretation of just one spatial replica of a flow field may not make sense in situations where the solution appears to be strongly inhomogeneous, as would be the case for instance in the presence of some local source (single pumping well) or some inherent inhomogeneity at the domain-scale (geologic structure). A difficulty of this nature will be encountered for instance in the single-realization simulations of transient infiltration from a strip source (Chapter 7). In this case, the random flow solution is inherently inhomogeneous, especially at early times where there is a relatively well defined wetting front separating a wet and dry region. Nevertheless, even in the case of a moving front, the single-realization approach is still interesting because it provides, by direct simulation, a detailed picture of *one possible flow system* as may occur in natural conditions.

In summary, the numerical single realization approach of naturally heterogeneous flow systems seems to be a natural way to obtain, by direct simulation of the flow field, a realistic

picture of the effects of (random) spatial variability on the flow pattern, with a degree of detail that cannot be achieved by direct subsurface measurements in the field. More importantly, the simulated flow field can be statistically analyzed in space and compared to the ensemble results of the spectral theory, in cases where there is enough statistical homogeneity for such a comparison to make sense. This method of analysis will be applied systematically to the numerical solutions obtained for steady state groundwater flow (Chapter 6), and also for a problem of steady state infiltration (Chapter 7). As mentioned above, the case of transient infiltration from a local source (Chapter 7) produces inherent inhomogeneities in the flow pattern, and, precisely for this reason, a statistical analysis will not be attempted there. Nevertheless, some qualitative comparisons with the results of the linearized spectral theory will be developed based on visual observations of the spatial pattern and evolution of the wet zone.

### **2.2.2 Generation of Random Fields by the Turning Band Method:**

To be useful, the numerical single-realization method also requires the accurate generation of random field hydraulic properties on a relatively fine three-dimensional grid. The mesh size of the grid must be small enough that the statistical properties of inputs (e.g. log-conductivity) and outputs (e.g.



heads and water velocities) be preserved in the discrete representation. Without going into details, it seems reasonable at first sight to require that:

$$\Delta x/\lambda \ll 1 \quad (2.7)$$

where  $\lambda$  is a typical fluctuation scale of the flow. This requirement is similar to the sampling theorem in signal theory: a temporal signal of period  $T$  must be sampled at time intervals  $\Delta\tau \ll T/2$  in order to avoid aliasing. In the present case, the fluctuation scale  $\lambda$  plays the role of the half-period  $T/2$ .

A more quantitative interpretation of the resolution constraint (2.7) can be developed by evaluating the behavior of the local integral of the random field of interest over the discrete cell of size  $\Delta x$ . The resolution of the grid must be fine enough that the statistical properties of the locally integrated field  $\bar{Y}(\underline{x})$  be close to the random field  $Y(\underline{x})$  defined in continuous space. For a given value of  $\Delta x/\lambda$ , there is a reduction in variance and an increase in the correlation scale of  $\bar{Y}(\underline{x})$  compared to the point process  $Y(\underline{x})$ . For instance, in the simple case of a one-dimensional process  $Y(x)$  with exponential covariance function, it is not difficult to see that the statistics  $(\sigma_{\Delta x}^2, \lambda_{\Delta x})$  of the locally integrated process:

$$\bar{Y}(x) = \frac{1}{\Delta x} \int_{x - \frac{\Delta x}{2}}^{x + \frac{\Delta x}{2}} Y(x') dx' \quad (2.8)$$

are related to the  $(\sigma^2, \lambda)$  statistics of the point process  $Y(x)$  by:

$$\frac{\sigma_{\Delta x}^2}{\sigma^2} = 2 \frac{\lambda}{\Delta x} \left\{ 1 - \frac{\lambda}{\Delta x} (1 - e^{-\Delta x/\lambda}) \right\} \quad (2.9)$$

$$\frac{\lambda \Delta x}{\lambda} = \frac{\sigma^2}{\sigma_{\Delta x}^2}$$

Thus, the distortion in the variance and correlation scale of  $Y(x)$  upon local integration over a mesh of size  $\Delta x = \lambda/4$  is about 10%. This may give a rough idea of the quantitative meaning of the inequality constraint (2.7): it seems reasonable to accept a grid resolution equal to a fraction of unity, i.e not necessarily "much smaller than" unity. A more precise analysis of the grid resolution requirement will be developed in Chapter 5 in connection with the numerical issues pertaining to the discretized solution of stochastic flow equations.

At any rate, once the mesh size has been chosen, it is also important to be able to generate a representative realization of statistically homogeneous random field hydraulic

properties with specified single-point and n-point moments. We used for this purpose a three-dimensional version of the "turning band" random field generator, recently developed by Tompson, Ababou and Gelhar (1987). The idea of the turning band method was brought up by Matheron (1973) for multidimensional homogeneous and isotropic random fields. Its practical implementation was developed by Mantoglou and Wilson (1982), particularly for two-dimensional random fields. The case of three-dimensional isotropic and anisotropic fields is treated at length in Tompson et al. (1987), including a number of numerical experiments. Ababou (1986) also discusses in an unpublished report some possible extensions of the method to treat the case of self-similar random fields, and Mantoglou (1987) elaborates on the case of statistically homogeneous vector fields.

Let us briefly describe the principle of the turning band method in the case of a statistically homogeneous random field  $f(\underline{x})$  having a zero-mean Gaussian distribution, and an isotropic or ellipsoidal covariance function in three-dimensional space. The method relies on the representation of  $f(\underline{x})$  in Fourier space (see Chapter 3):

$$\begin{aligned} f(\underline{x}) &= \int_{-\infty}^{+\infty} e^{i\underline{kx}} dZ_f(\underline{k}) \\ R_{ff}(\underline{\xi}) &= \int_{-\infty}^{+\infty} e^{i\underline{kx}} S_{ff}(\underline{k}) d\underline{k} \end{aligned} \quad (2.10)$$

where  $R_{ff}(\xi)$  is the covariance function,  $dZ_f(\underline{k})$  the complex Fourier-Stieltjes increment, and  $S_{ff}(\underline{k})$  the spectral density of  $f(\underline{x})$  defined by:

$$S_{ff}(\underline{k}) \cdot d\underline{k} = \langle |dZ_f(\underline{k})|^2 \rangle \quad (2.11)$$

In particular, in the 3D isotropic case, the covariance function in (2.10) can be expressed directly in terms of a radial spectrum as follows (Adler, 1981):

$$R_{ff}(\xi) = 2 \int_0^{\infty} \frac{\sin(k\xi)}{k\xi} E(k) dk \quad (2.12)$$

$$E(k) = \int_{\mathcal{G}(k)} S(\underline{k}) d\sigma(\underline{k}) = 4\pi k^2 S(k)$$

where the integral defining the radial spectrum  $E(k)$  is taken over the sphere of radius  $k$  in  $\mathbb{R}^3$ . Note that  $k$  and  $\xi$  are the radial wavenumber and separation distance, respectively.

The idea of the turning band method is that it is possible to find a one-dimensional process  $f_1(x)$  generated independently along lines having many different orientations in space:

$$f(\underline{x}) = \lim_{L \rightarrow \infty} \frac{1}{\sqrt{L}} \sum_{i=1}^L f_1^{(i)}(\underline{x} \cdot \underline{u}_i) \quad (2.13)$$

Each line (i) is defined by its direction vector  $\underline{u}_i$ , and  $f_1^{(i)}(\underline{x})$  is the sample function of process  $f_1$  generated along line (i) as illustrated in Figure (2.1). The 1D sample functions are generated independently of each other, and the line direction vectors  $\underline{u}_i$  are drawn from a random unit vector having a uniform distribution on the sphere (see Tompson et al. 1987). In these conditions, it is not difficult to see that the covariance function of the 3D field defined by (2.13) takes the form:

$$R_{ff}(\underline{\xi}) = \lim_{L \rightarrow \infty} \frac{1}{L} \sum_{i=1}^L R_1(\underline{\xi} \cdot \underline{u}_i) \quad (2.14)$$

where  $R_1(\underline{\xi})$  is the covariance function of the 1D process  $f_1(\underline{x})$ . With additional assumptions of homogeneity and ergodicity, on which we do not elaborate here, the sum in (2.14) can be replaced by an ensemble average over all possible realizations of the random direction vector  $\underline{u}_i$  as follows:

$$R_{ff}(\underline{\xi}) = \langle R_1(\underline{\xi} \cdot \underline{u}) \rangle \quad (2.15)$$

Finally, with a uniform distribution of  $\underline{u}$  on the sphere, equation

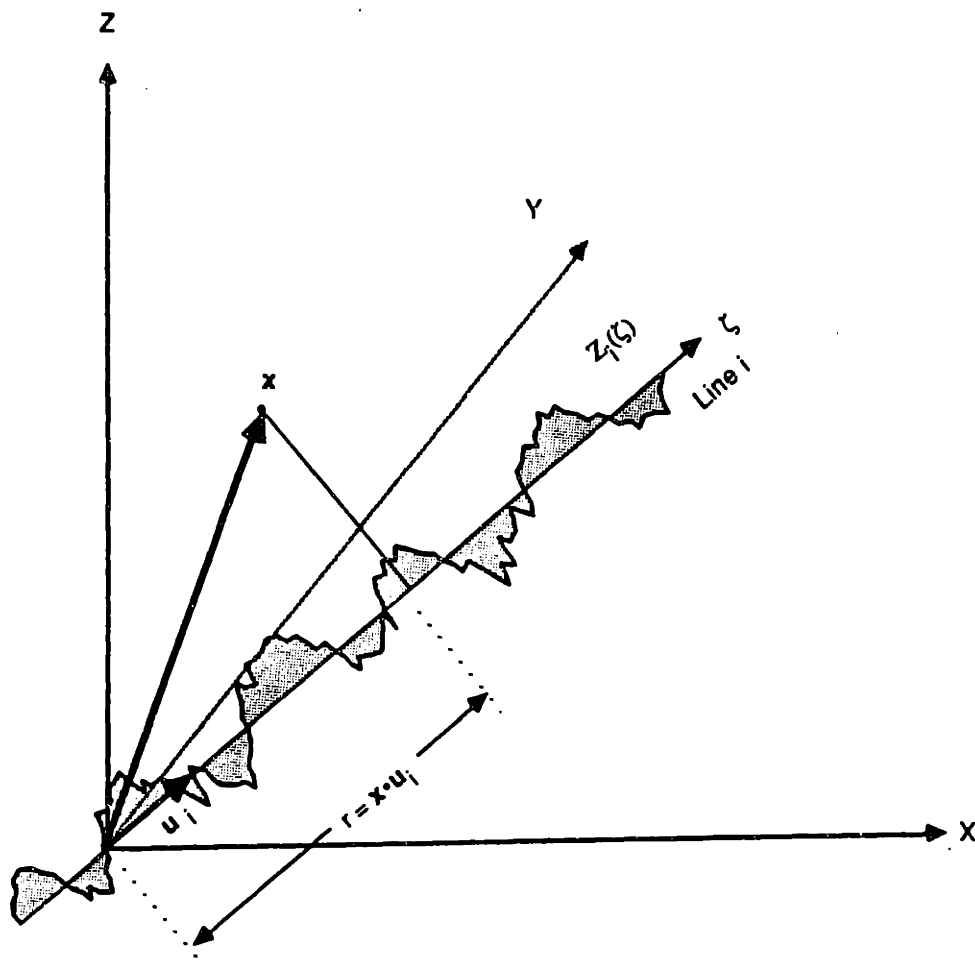


Figure 2.1: Turning band method: projection of the  $i$ -th line process  $f_i^{(1)}(x)$  onto an arbitrary point  $\underline{x}$  in three-dimensional space (from Tompson, Ababou, Gelhar, 1987).

(2.15) leads to an explicit relation between the covariance function of the line process and the desired covariance function of the isotropic random field to be generated:

$$\begin{aligned} R_{ff}(\xi) &= \frac{1}{4\pi} \int_0^{2\pi} d\theta \int_0^{\pi} R_1(\xi \cos\phi) \sin\phi \, d\phi \\ &= \frac{1}{\xi} \cdot \int_0^{\xi} R_1(s) \, ds \end{aligned}$$

whence:

$$\boxed{R_1(\xi) = \frac{d}{d\xi} (\xi R_{ff}(\xi))} \quad (2.16)$$

Equation (2.16) gives explicitly the covariance of the line-process such that the projection operator (2.13) yields the desired 3D isotropic covariance  $R_{ff}(\xi)$ , asymptotically as the number of lines  $L$  goes to infinity. The method used in the turning band algorithm to generate each line process is the spectral decomposition method of Shinozuka and Jan (1972). Details are given in Tompson et al. (1987). In actual practice, the number of lines need not be very large to obtain relatively accurate single-realizations as far as first and second moments are concerned. In particular, it seems that the number of lines

L required to be consistent with the resolution of the grid may only grow like some fractional power of the total number of nodes of the grid. This empirical observation seems to be confirmed by the results of Tompson et al. 1987, and those obtained in this work: see Chapter 6 (Section 6.3) for a realization of the log-conductivity field on a 1 million node grid using the turning band generator with 1000 lines.

Finally, the case of ellipsoidal anisotropic random fields does not require any modification of the above method. For any isotropic field with covariance function  $R_{ff}(\xi)$  and fluctuation scale  $\lambda$ , an ellipsoidal field can be constructed by rescaling the three coordinates as follows:

$$\xi'_i = \frac{\lambda}{\lambda_i} \xi_i \quad (2.17)$$

Thus, the new ellipsoidal covariance function  $R'_{ff}(\xi)$  with fluctuation scales  $(\lambda_i)$  is simply given by:

$$R'_{ff}(\xi) = R_{ff}(\sqrt{\sum (\frac{\lambda}{\lambda_i} \xi_i)^2}) \quad (2.18)$$

This simple relation was used in Chapters 6 and 7 to obtain single-realizations of statistically anisotropic (ellipsoidal) random hydraulic properties. For other applications such as



those involving space-time processes, more general classes of anisotropic random fields may be needed. Tompson et al. (1987) discussed this case as well, and Sivapalan and Wood (1986) used the 3D turning band generator to simulate anisotropic space-time rainfall intensity fields.

## 2.3 Brief Survey of Field Data

### 2.3.1 Hydraulic properties of heterogeneous aquifers

In the case of groundwater flow, the local hydraulic properties of interest are the saturated conductivity  $K$  (m/s) and the specific storativity  $S_s$  ( $m^{-1}$ ), or their two-dimensional equivalents, the transmissivity  $T$  ( $m^2/s$ ) and the storage coefficient or specific yield  $S_y$  (dimensionless).

The spatial variability of hydraulic conductivity and transmissivity have been the object of intensive experimental studies in the recent past, in an effort to characterize their variability in a statistical rather than purely descriptive fashion. Gelhar (1986) reviews some of the available field data. Most experimental studies of aquifer variability actually focused on the horizontal variability of the transmissivity or of some depth-averaged conductivity determined from well pumping tests (Delhomme 1979, Binsariti 1980, Devary and Doctor 1982, Hoeksema

and Kitanidis 1985). Their results could be summarized as follows: the standard deviation of log-transmissivity ( $\ell nT$ ) ranged between 0.6 (sandstone aquifer of Hoeksema and Kitanidis) to 2.3 (limestone aquifer of Delhomme), with correlation ranges on the order of 1 km to several tens of kilometers. The domain sizes were on the order of 5 km to several hundred kilometers.

Other studies concerned the local hydraulic conductivities obtained from small scale measurements, usually along vertical boreholes (Bakr 1976, Hufschmied 1985, Sudicky 1986). In these three studies of aquifer variability, the standard deviation of log-conductivity ( $\ell nK$ ) ranged from 0.6 to 2.2, with correlation ranges on the order of 0.1 to 1.0 meters in the vertical. The length of the vertical transects (boreholes) was 20 to 100 meters. The studies of Hufschmied (1985) and Sudicky (1986) are particularly remarkable because these authors actually determined, by different methods, the *three-dimensional* variability of the log-conductivity field. Hufschmied used a relatively sophisticated flowmeter measurement of conductivities in 16 wells, for twenty 1 meter thick layers in each well. The statistics of the point process  $\ell nK(\underline{x})$  in the vertical were then obtained by using statistical identities relating the point process to the local average process. Information obtained among different wells was used indirectly to infer the horizontal covariance structure of  $\ell nK(\underline{x})$ . On the other hand, Sudicky

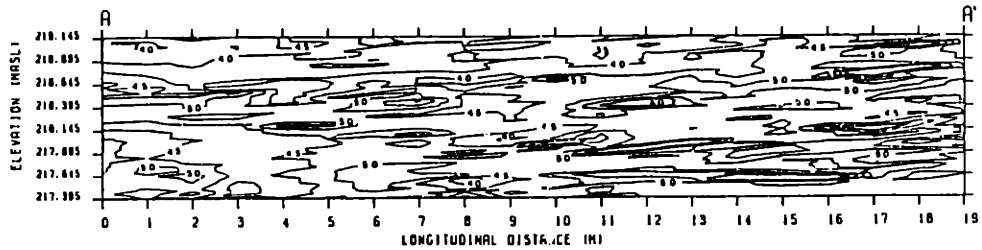
(1986) measured the conductivities from small core samples along a number of vertical boreholes organized along two perpendicular planes. This particular choice allowed them to estimate the covariance structure of  $\ln K$  in three-dimensional space.

The statistical results obtained by Hufschmied (1985) and Sudicky (1986) are summarized in Table 2.1. In addition, Figure (2.2) (top) shows the log-conductivity contours obtained by Sudicky (1986) along the vertical plane aligned with the natural hydraulic gradient at the Borden site. For comparison, the bottom part of Figure (2.2) displays an artificially generated anisotropic random field obtained by the turning band method described previously. Note that both Hufschmied and Sudicky's data show a significant statistical anisotropy between the horizontal and vertical directions.

The data reviewed above indicate that the conductivities and transmissivities can vary over several orders of magnitudes in natural formations. In addition, the work of Hufschmied (1985) and Sudicky (1986) clearly shows that the conductivities follow a log-normal probability distribution more closely than a normal distribution. Finally, it is also clear that in most cases, there is a relatively strong anisotropy in the vertical/horizontal correlation scales of the log-conductivity (Table 2.1). However, it is also possible that

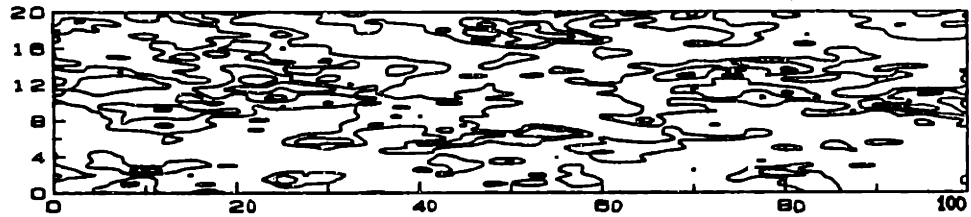
TABLE 2.1: STATISTICAL PROPERTIES OF MEASURED THREE-DIMENSIONAL LOG-CONDUCTIVITIES ( $\ln k$ ) IN SATURATED FORMATIONS, FROM HUFSCHMIED (1985) AND SUDICKY (1986)

	Hufschmied (1985)	Sudicky (1986)
Site	Aeflingen, Switzerland	Borden site, Ontario
Formation	20 m thick, sand and gravel	Outwash sand
Covariance	Anisotropic exponential	Anisotropic exponential
$K_G$	$(6 \cdot 10^{-3} \text{ m/s})$	$7.17 \cdot 10^{-5} \text{ m/s}$
$\sigma_f$	1.92	0.54 - 0.62
$\lambda_1$	15 - 20 m	2.8 m
$\lambda_2$	15 - 20 m	2.8 m
$\lambda_3$	0.5 m	0.12 m



Location of measurements and distribution of  $-\ln(K)$  along A-A' (contour interval = 0.5; vertical exaggeration = 2;  $K < 10^{-3}$  cm/s in stippled zones).

(a): Measured



(b): Simulated by the Turning Band Method

Figure 2.2 Log-conductivity contours in a vertical plane. The upper part is reproduced from Sudicky, 1986 (measured at the Borden tracer site). The lower part of the figure was obtained by simulation, using the Turning Band Method with an anisotropic spectrum.

the anisotropy observed by these authors be due in part (or depend in part) on the discrepancy between the horizontal and vertical scales of the domain under investigation (12 m × 3 m in the study of Sudicky, 1986). Indeed, some of the other studies mentioned above suggest that the supposedly stationary correlation structure of porous formations may not be well defined for certain sites and/or for certain domain sizes. This is suggested for instance by the statistical analysis of Hoeksema and Kitanidis (1985). These authors found in a number of cases that the correlation scale was either small (on the order of measurement spacing) or large (on the order of domain size). In addition, both the correlation structure and the degree of variability may be strongly influenced by certain subjective choices, such as empirical detrending (an example can be found in Devary and Doctor, 1982). These difficulties show that the measured statistical properties of supposedly homogeneous conductivity fields may be in fact scale-dependent in certain situations. In our view, this is not necessarily an obstacle to the application of stochastic concepts as long as the fact is recognized, and that adequate methods be designed to "pass" from one scale of analysis to another. The need for variable scale analysis may arise for predicting contaminant migration over large time scales. This particular question will be examined in Chapter 4 (Section 4.4).

For completeness, let us mention the papers by Clifton and Neuman (1982) and Hoeksema and Kitanidis (1985) concerning the spatial variability of the specific storativity of aquifers. The first authors found a positive correlation between log-transmissivity and log-capacity, with a slope close to unity. The specific capacity does not play a role in the present work, since only steady state problems will be considered in our analyzes of stochastic groundwater flow.

### 2.3.2 Constitutive relations of heterogeneous soils:

In this work, we will be concerned with both transient and steady state flow problems in unsaturated soils (Chapter 7). To describe these phenomena, two constitutive relations need to be determined:

- the water retention curve  $\theta(h)$  relating volumetric moisture content to pressure head.
- the unsaturated conductivity curve  $K(h)$  relating hydraulic conductivity to pressure head.

Our particular choice of functional relationships for  $\theta(h)$  and  $K(h)$  will be defined in Chapter 5 (Section 5.1). However, experimentators have used a variety of functional shapes to describe the  $\theta(h)$  and  $K(h)$  relationship in view of analyzing

their spatial variability. This makes it quite difficult to synthesize their findings in a compact form.. Nevertheless, we have attempted to summarize in a table some of the most significant results on natural soil variability in the literature.

Table 2.2 gives information on the probability distribution function and the correlation structure of the hydraulic parameters intervening in the constitutive relationships  $\theta(h)$  and  $K(h)$ . It should be mentioned that these results correspond to different scales of analysis and different schemes of data collection, so they are not always directly comparable. However, some common features seem to emerge as a whole. First of all, it should be emphasized that only one author (Russo, 1983) analyzed the correlation structure of the whole conductivity curve  $K(h)$ , including in particular the correlation structure of the saturated conductivity  $K_s(x)$  as well as that of the shape parameter:

$$\alpha(x) = \left. \frac{\partial \ln K}{\partial h} \right|_x$$

His results indicate that both  $\alpha$  and  $K_s$  are log-normally distributed, and that the correlation range of  $\ln \alpha(x)$  is significantly larger than that of  $\ln K_s(x)$ .



TABLE 2.2: SUMMARY OF SOME FIELD DATA ON THE SPATIAL VARIABILITY OF UNSATURATED SOILS FROM THE LITERATURE

$\gamma$	$\bar{\gamma}$	$CV_{\gamma}$	$\sigma_{\ln \gamma}$	$\tau_{\gamma}$	$\lambda_{\gamma}$	Ref. and Remarks
$K_o$ (cm/h)	1.96	0.71	0.64	2.49	a = 38 m $\lambda = 17m$ Spherical variogram	Russo, 1983 Hamra Red Mediterranean $K(h) = K_o e^{-ah}$ A = 2 + 2.5 ha N = 25 + 6 plots
$\alpha$ ( $cm^{-1}$ )	.0286	0.43	0.41	1.36	a = 51 m $\lambda = 72 m$ Exponent. variogram	1 plot = 3m x 3m n = 5 depths a = range of variogram $\lambda =$ integral corr. length
$\theta_s$	.338	0.08	0.08	(0.23)	76m	Russo, Bresler 1981 Hamra Red Mediterranean
$\theta_r$	.030	0.30	0.29	(0.93)	39 m	$\frac{\theta - \theta_r}{\theta_s - \theta_r} = \left(\frac{h_w}{h}\right)^{\beta}$
$K_o$ (cm/h)	22.0	0.41	0.39	(1.2)	34m	$\frac{K}{K_o} = \left(\frac{h_w}{h}\right)^{\eta}$
$\beta$	1.160	0.68	0.62	2.35	23m	$\eta = 2\beta + 2$ A = 0.8 ha N = 30 locations
$h_w$ (cm)	-7.2	0.22	0.22	(0.7)	48m	n = 4 depths (depth z=0 shown here)
$\theta_s$	.397	0.10	0.10	(0.29)	---	Nielsen et al., 1973
$K_o$ (cm/h)	0.85	1.06	0.87	4.37	---	Panoche soil A = 150 ha N = 20 plots n = 6 depths (depth z $\approx$ 30 cm shown here)

TABLE 2.2: SUMMARY OF SOME FIELD DATA ON THE SPATIAL VARIABILITY OF UNSATURATED SOILS FROM THE LITERATURE (CONTINUED)

Y	$\bar{Y}$	$CV_Y$	$\sigma_{\ln Y}$	$\tau_Y$	$\lambda_Y$	Ref. and Remarks
$K_o$ (cm/h)						Scisson, Wierenga, 1961  A = 40m <sup>2</sup> 3 infiltration rings: Diameter      Number $\phi_1 = 5\text{cm}$ $N_1 = 625$ $\phi_2 = 25\text{cm}$ $N_2 = 125$ $\phi_3 = 127\text{cm}$ $N_3 = 25$
(1)	0.27	0.70	0.63	2.45	0.13m	
(2)	0.35	0.54	0.51	1.79	---	
(3)	0.36	0.22	0.22	0.68	---	
$K_o$ (cm/h)	0.70	0.40	0.38	(1.26)	50 m (10-50m)	Vieira et al., 1961  A = 0.88 ha N = 1280 plots 160 plots/transect 55 transects
$K_o$ (cm/h)	1.46	0.60	0.56	2.02	---	Sharma et al. 1980  Watershed A = 9.6 ha N = 26 plots
$K_o$ (cm/h)	0.13	1.02	0.84	4.10	0-2 m	Luxmoore et al. 1961  A = 192 m <sup>2</sup> N = 48 plots

The log-normality of  $K_s$ ,  $\alpha$ , and other inherently positive unsaturated soil parameters, seems to be confirmed by other authors. For convenience, we have listed in Table 2.2 the skewness coefficient  $\gamma$ . When indicated in parenthesis, the skewness was computed by us based on the assumption of log-normality instead of the normal distribution assumed by the authors (references are given in the right-most column). Thus, in all cases, the skewness  $\gamma_Y$  was computed from the classical identity:

$$\gamma_Y = 3 CV_Y + (CV_Y)^3 \quad (2.19)$$

where  $CV_Y$  is the coefficient of variation of the log-normal random variable  $Y$ . In addition, we also used the following identities:

$$(CV_Y)^2 = \frac{\sigma_Y^2}{\bar{Y}^2} = \exp(\sigma_{\ln Y}^2) - 1 \quad (2.20)$$

$$\bar{Y} = Y_G \exp(\sigma_{\ln Y}^2/2) \quad (2.21)$$

where  $Y_G$  is the geometric mean defined by:

$$Y_G = \exp(\overline{\ln Y}).$$

These relations (2.19 - 2.21) can be found for instance in Vanmarcke (1983). They were used to compute the  $\ln Y$ -statistics in Table 2.2, when not provided by the authors themselves. It appears that a number of authors adopted the normality assumption precisely in those cases where the variability was too mild to be able to distinguish a normal from a log-normal distribution. Overall, we conclude that all the parameters listed in the table were in fact more or less positively skewed, and are presumably better represented by log-normal distributions. Figure (2.3) illustrates the difference between a normal and a log-normal random function (artificially generated for illustration). Note the sharp maxima and smooth minima typical of a positively skewed process.

Another feature that emerges from Table 2.2 is that the unsaturated conductivity curve seems in general to have greater variability than the water retention curve (although this is not always verified for a given site). The coefficient of variation of  $K_s$  was larger than unity in four cases, whereas the coefficient of variation of parameters involved in the  $\theta(h)$  relation was always below or at most equal to 0.6.

The data of Table 2.2 do not contain any information on the correlation structure of soil properties in the vertical

Figure 2.3(a): Normally distributed random function  $Z = \ln Y$   
( $-\infty < \ln Y(x) < +\infty$ ).

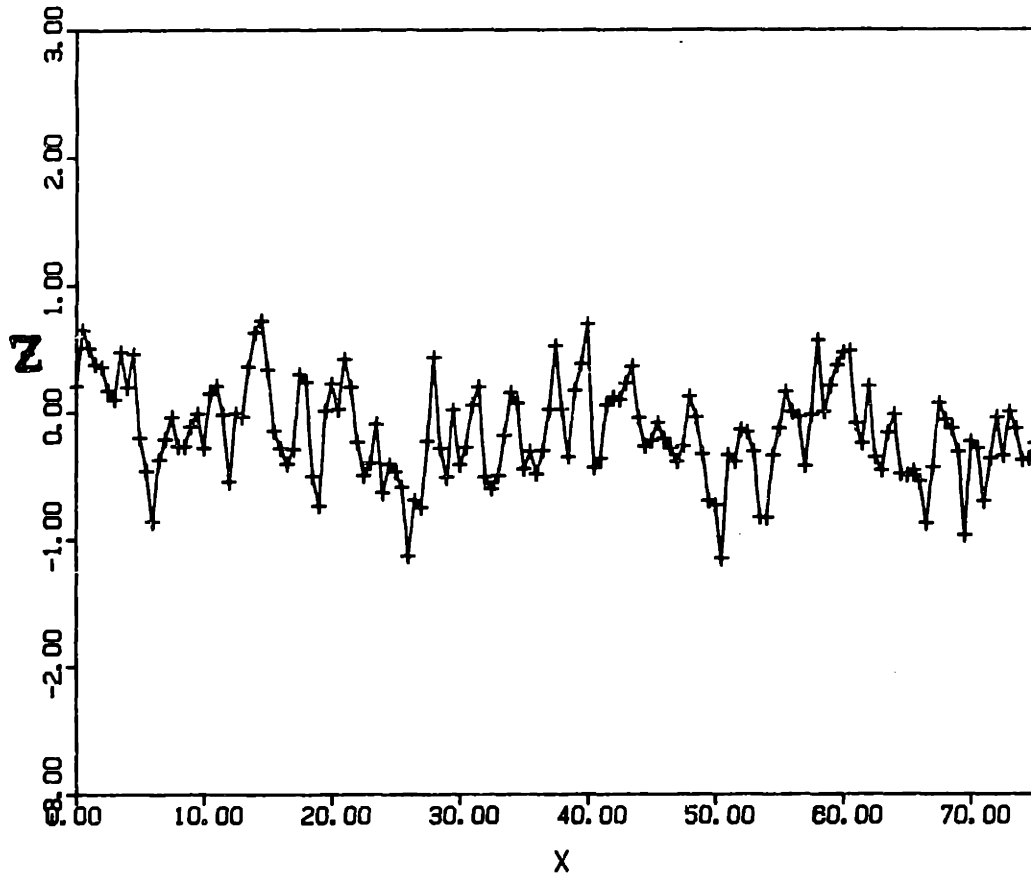


Figure 2.3(a): Normally distributed random function  $Z = \ln Y$   
( $-\infty < \ln Y(x) < +\infty$ ).

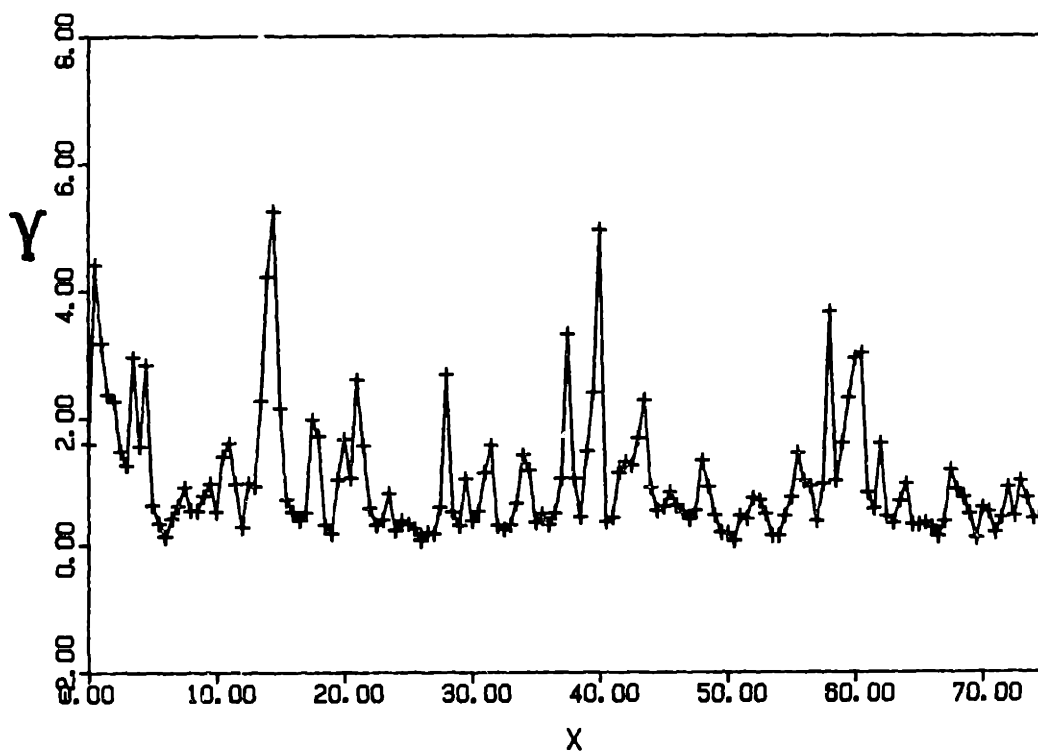


Figure 2.3(b) Log-normally distributed random function  $Y$   
( $0 < Y(x) < +\infty$ ).

direction. The horizontal correlation scales range from 10 cm to a few tens of meters. These numbers should be taken "with a grain of salt", as the apparent correlation scales are most probably influenced by the density and size of the measurement networks. In addition, the results of Scisson and Wierenga (1981) indicate that the scale of the instrument (infiltration ring) has a definite effect on variability. Finally, it should also be noted that the correlation structures were only determined for relatively small domains, on the order of 1 hectare for Russo and Bresler 1981, Vieira et al. 1981, and Russo 1983. The largest domain of investigation was the 150 ha site of Nielsen et al. 1973; however these authors did not determine any correlation structure.

In order to illustrate more concretely the spatial variability of soil properties, we have reproduced in Figure 2.4 the unsaturated conductivity curves obtained by Nielsen et al. (1973) on the Panoche silty clay loam. This figure indicates that both the saturated conductivity and the slope of the  $\ln K(h)$  curve are fairly variable. The figure does not seem to indicate a strong degree of correlation between these two parameters, although some correlation could be expected on physical grounds: coarser soils are generally more permeable at saturation and have a steeper  $\ln K(h)$ -slope (Ababou, 1981). The effect of correlation between  $K_s$  and the  $\ln K(h)$ -slope will be investigated by way of



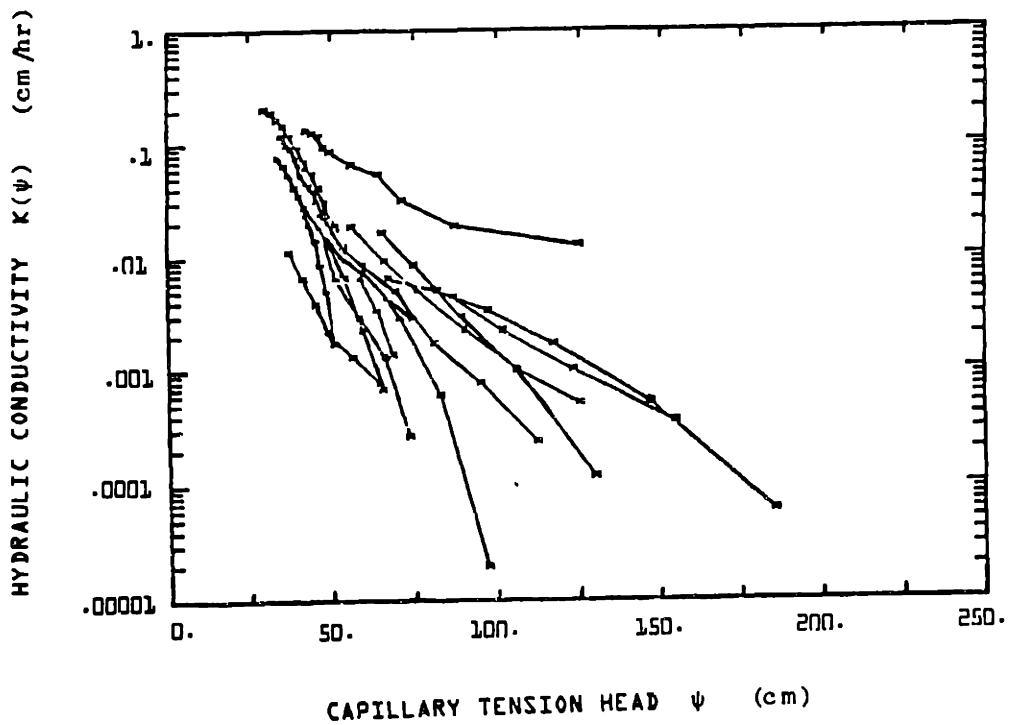


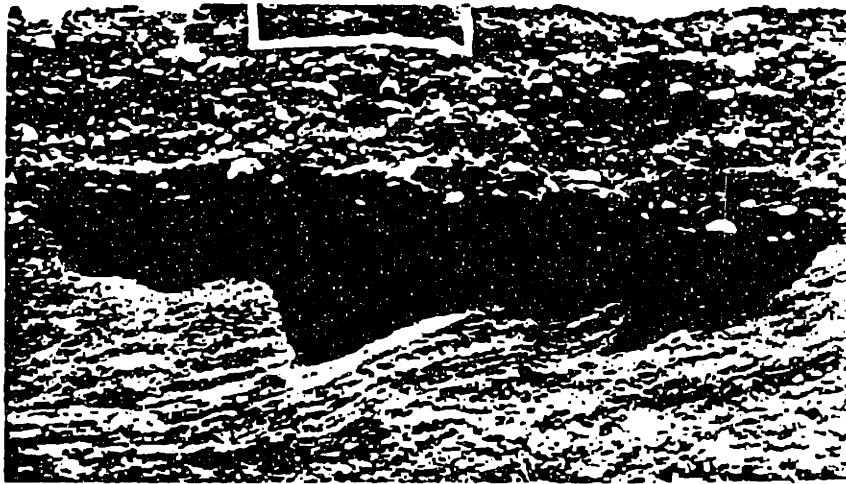
Figure 2.4: Unsaturated hydraulic conductivity versus capillary tension head for the Maddock sandy loam. Each curve corresponds to a different spatial location (from Yeh et al., 1982).

numerical experimentation in Chapter 7 (Section 7.2). Additional data and references concerning an on-going strip-source infiltration at the University of New Mexico at Las Cruces will be given in Chapter 7 (Section 7.3).

Our literature review, partially summarized in Table 2.2, indicated that available data are too scant to completely characterize the spatial variability of unsaturated soils hydraulic properties in terms of random field parameters. The variability of the unsaturated conductivity curve in particular seems to have important effects on the behavior of unsaturated flow (Mantoglou and Gelhar, 1987). Unfortunately, no comprehensive study of the three-dimensional spatial structure of  $\ln K(h)$  has yet been undertaken. However, some of the missing data could be inferred directly by correlating, for instance, the shape of the  $\ln K(h)$  curve to the value of the saturated conductivity for different types of soils. Other alternative approaches of this kind have had some success, for instance those relying on the "similar media" postulate. This latter approach reduces the characterization of spatial variability of  $\theta(h)$  and  $K(h)$  to just one spatially random scaling factor: cf. experimental studies of Warrick et al. (1977), Simmons et al. (1979), Russo and Bresler (1980), Vauclin et al. (1981), and Sharma et al. (1980). The field remains open: future research could focus on such correlations or similarity assumptions, as a

means of characterizing in a more comprehensive fashion the spatial variability of the nonlinear constitutive relations of unsaturated media.

At any rate, the complexity of unsaturated flow processes in heterogeneous formations should not be overlooked. Figure 2.5 shows the spatial structure and evolution of the wetted zone during an infiltration experiment in the Hanford sediments (from Routson et al., 1979). The wetted zone in this case is remarkably asymmetric and has pronounced lateral spreading. To explain these features statistically requires a model of three-dimensional variability that includes the effects of stratification, e.g., statistical anisotropy. Similar effects of asymmetry and spreading will be observed in the numerical simulations of Chapter 7 (Section 7.3) with fully three-dimensional and statistically anisotropic random conductivity curves.



(a) After 6 hours



(b) After 24 hours

Figure 2.5 Typical horizontal and vertical movement of liquids in Hanford formation sediments under partially saturated conditions. Taped area outlines position of water addition (from Routson et al., 1979).

### CHAPTER 3: FIRST ORDER SPECTRAL SOLUTIONS FOR STOCHASTIC FLOW IN SATURATED MEDIA

#### 3.1 Formal Solution of Spectral Perturbation Equations:

In this section, we develop approximate solutions for the stochastic equation of steady state flow in random saturated media, following the first order spectral theory previously developed by *Bakr et al.* 1978, and *Gelhar and Axness* 1983. The assumptions made at each step will be clearly stated, in anticipation of subsequent discussions on the approximate nature of perturbative spectral solutions.

Our point of departure is the partial differential equation governing flow in a saturated porous medium with spatially variable conductivity  $K(\underline{x})$ . This equation is obtained from the steady state mass conservation equation and the local Darcy equation, (Darcy, 1856) respectively:

$$\nabla \underline{Q} = 0. \quad (3.1)$$

$$\underline{Q} = -K(\underline{x}) \cdot \nabla H. \quad (3.2)$$

Here,  $\underline{Q}$  represents the specific discharge rate (Darcy velocity), and  $H$  the hydraulic head potential. Using (3.2) in (3.1) leads to the familiar groundwater flow equation:

$$\nabla(K(\underline{x}) \cdot \nabla H) = 0. \quad (3.3)$$

Let us assume that the conductivity  $K(\underline{x})$  in (3.3) is a second order stationary random function in 3D space, with a log-normal distribution. Therefore, the statistical properties of the log-conductivity  $F(\underline{x})$  are entirely described by its first and second order moments, i.e., its mean  $\bar{F}$  and covariance function  $R_{ff}$  as defined below:

$$\begin{cases} F(\underline{x}) = \ln K(\underline{x}) \\ \langle F(\underline{x}) \rangle = \bar{F} = \ln K_G \\ \langle F(\underline{x}) - \bar{F} \cdot (F(\underline{x}') - \bar{F}) \rangle = R_{ff}(\underline{\xi}), \quad \underline{\xi} = \underline{x} - \underline{x}' \end{cases}$$

where  $K_G$  is the geometric mean conductivity, and  $\underline{\xi}$  a separation vector. The flow equation (3.3) can be decomposed to be expressed in terms of  $F$  as follows:

$$\boxed{\nabla^2 H + \nabla F(\underline{x}) \cdot \nabla H = 0.} \quad (3.4)$$

Equation (3.4) will be used for the subsequent spectral perturbation analysis. Observe that (3.4) is a stochastic partial differential equation, due to the random character of the log-conductivity gradient vector  $\nabla F(\underline{x})$ , even in the case of deterministic boundary conditions.

Let us now express (3.4) in terms of ensemble averages and perturbations. The perturbations of the random fields log-conductivity and hydraulic head are defined as:

$$f(\underline{x}) = f(\underline{x}) - \langle f(\underline{x}) \rangle = \ln [K(\underline{x})/K_G]$$

$$h(\underline{x}) = H(\underline{x}) - \langle H(\underline{x}) \rangle$$

The governing flow equation can be separated into a mean equation and a perturbation equation, by substituting  $H = \langle H \rangle + h$  and  $F = \langle F \rangle + f$  in (3.4) and applying ensemble averaging operators. The mean equation obtains directly by ensemble averaging equation (3.4):

$$\nabla^2 \langle H \rangle + \nabla \langle f \rangle \cdot \nabla \langle H \rangle = - \langle \nabla f \cdot \nabla H \rangle$$

and the perturbation equation obtains by subtracting the above mean equation from (3.4):

$$\nabla^2 h + \nabla \langle F \rangle \cdot \nabla h + \nabla f \cdot \nabla \langle H \rangle = - \{ \nabla f \cdot \nabla h - \langle f \cdot \nabla h \rangle \}.$$

Finally, using the assumption that the mean log-conductivity  $\langle F \rangle$  is constant ( $K_G$  constant), we obtain:

$$\nabla^2 \langle H \rangle = - \langle \nabla f \cdot \nabla h \rangle \quad (\text{mean eq.}) \quad (3.5.a)$$

$$\nabla^2 h + \nabla f(\underline{x}) \cdot \nabla \langle H \rangle = - \{ \nabla f \cdot \nabla h - \langle \nabla f \cdot \nabla h \rangle \} \quad (\text{perturbation eq.}) \quad (3.5.b)$$

Observe that equations (3.5) form a system of two stochastic equations with three unknowns:  $h(\underline{x})$ ,  $\langle H(\underline{x}) \rangle$ , and the second order term  $\langle \underline{\nabla} f \cdot \underline{\nabla} h \rangle$ . A complete solution would involve solving an infinite hierarchy of equations governing higher order moments. This turns out to be an impossible task in the general case. Various expansion methods have been proposed in the literature in order to arrive at approximate close-form solutions (see review in Chapter 2). We develop below first order perturbation approximations following the work of Gelhar and others quoted above, although in a slightly different manner.

One way to obtain a first order solution is to expand the solution  $H(\underline{x})$  in powers of  $\sigma_f$ , the "small parameter" in the expansion (the possibly divergent character of this expansion will be discussed in Section 4.1). Accordingly, let:

$$H = H_0 + \sigma H_1 + \sigma^2 H_2 + \dots .$$

On the other hand, note that the random field  $f(\underline{x})$  in (3.4) is proportional to  $\sigma_f = \sigma$ , its standard deviation. For a correct perturbative analysis, we must use instead a normalized random field  $g(\underline{x})$  with unit variance and zero mean:

$$g(\underline{x}) = f(\underline{x})/\sigma .$$



The conductivity is simply related to  $g(\underline{x})$  by:

$$K(\underline{x}) = K_G \exp(\sigma g(\underline{x})).$$

Plugging  $g(\underline{x})$  in equation (3.4) and assuming  $K_G$  constant gives:

$$\nabla^2 H + \sigma \nabla g \cdot \nabla H = 0.$$

Plugging the expansion for  $H$  in this equation yields the infinite hierarchy of equations:

$$\begin{cases} \text{Order } \sigma^0: & \nabla H_0 & = 0 \\ \text{Order } \sigma^1: & \nabla^2 H_1 + \nabla g \cdot \nabla H_0 & = 0 \\ & \vdots & \\ & \vdots & \end{cases}$$

Comparing the zero-order equation to the mean equation (3.5a) shows that  $H_0$  is just an approximation for the mean head  $\langle H \rangle$ , to first order in  $\sigma$ . Likewise, the first order term ( $\sigma H_1$  in the series expansion) is just an approximation for the head perturbation  $h$ , to second order in  $\sigma$ . Accordingly, we obtain:

$$\nabla^2 \langle H \rangle = 0 \quad (\sigma)$$

$$\nabla^2 h + \nabla f \cdot \nabla \langle H \rangle = 0(\sigma^2).$$

These equations appear tractable if the high order terms on the right-hand side are neglected (requiring  $\sigma$  small), and the mean hydraulic gradient is constant. Note that  $\langle \nabla H \rangle$  is indeed constant to first order. This can be seen by observing that the mean head satisfies the Laplace equation to first order:

$$\nabla^2 \langle H \rangle = 0$$

which yields a linear solution for  $\langle H(x) \rangle$  if the flow domain is a rectangular prism, with Dirichlet conditions on two opposite faces, and zero Neumann conditions on all other faces. As the size of the domain becomes infinite, these boundary conditions becomes equivalent to specifying a constant mean hydraulic gradient:

$$\underline{J} = - \langle \nabla H \rangle . \quad (3.6.a)$$

In practice, this kind of "boundary condition" corresponds to the case of a uniform flow field at the large scale.

The perturbative equation can now be expressed, to second order in  $\sigma$ , as follows:

$$\nabla^2 h - \underline{J} \cdot \nabla f = 0 \quad (3.6.b)$$

where the term  $\underline{J} \cdot \underline{\nabla} f(\underline{x})$  is a known random field. Note that equation (3.6b) is a stochastic Poisson equation governing the head perturbation  $h(\underline{x})$ .

We proceed to solve the stochastic Poisson equation (3.6b) in the Fourier space, by using Fourier-Stieltjes representations for both  $f(\underline{x})$  and  $h(\underline{x})$  as shown below:

$$f(\underline{x}) = \iiint_{-\infty}^{+\infty} e^{j\underline{k}\underline{x}} dZ_f(\underline{k})$$

(3.7)

$$h(\underline{x}) = \iiint_{-\infty}^{+\infty} e^{j\underline{k}\underline{x}} dZ_h(\underline{k}).$$

Such a representation exists and is unique for any zero-mean stationary random field (Yaglom 1962; Loève 1963). In particular, this implies that the two-point covariance function depends only on the separation vector between the two points. By writing the representation (3.7) for  $h(\underline{x})$ , we therefore assume that  $h(\underline{x})$  is stationary, i.e., statistically invariant under translation. The validity of this assumption will be discussed at a later stage.

The usefulness of the representation (3.7) lies in the fact that it is "orthogonal". The random  $dZ$  terms are zero-mean

complex Fourier-Stieltjes increments which have the property of being uncorrelated for distinct wavenumbers:

$$\langle dZ(\underline{k}) dZ^*(\underline{k}') \rangle = 0 \quad \text{for } \underline{k} \neq \underline{k}'.$$

In addition, the real and imaginary parts of  $dZ(\underline{k})$  are uncorrelated and identically distributed; the real part is even in  $\underline{k}$ , while the imaginary part is odd:

$$dZ(-\underline{k}) = dZ^*(\underline{k}) \quad .$$

Finally, the variance of  $|dZ|$  corresponds to the spectral content of fluctuations occurring in the wavenumber range  $(\underline{k}, \underline{k}+d\underline{k})$ . More precisely, it is easily seen that:

$$\langle |dZ(\underline{k})|^2 \rangle = S(\underline{k})d\underline{k}$$

where  $S(\underline{k})$  is the spectral density, i.e., the Fourier transform of the covariance function  $R(\underline{\xi})$  (see equation 3.10 below).

Plugging (3.7) into (3.6) yields, by the uniqueness of the spectral representations, a simple relation between the complex Fourier increments of  $h(\underline{x})$  and  $f(\underline{x})$ :

$$dZ_h(\underline{k}) \cong -j \frac{(J_{\underline{\rho}} \cdot \underline{k}_{\underline{\rho}})}{k^2} dZ_f(\underline{k}). \quad (3.8)$$

Multiplying both sides by  $dZ_f^*(\underline{k})$  and averaging, gives the spectral density of  $h(\underline{x})$  as a function of that of  $f(\underline{x})$ :

$$\boxed{S_{hh}(\underline{k}) = \frac{(J_{\ell} k_{\ell})^2}{k^4} S_{ff}(\underline{k})} \quad (3.9)$$

where we used Einstein's implicit summation over repeated indices, and  $k$  is the radial wavenumber  $\sqrt{k_1^2 + k_2^2 + k_3^2}$ . Finally, the covariance function of  $h(\underline{x})$  can be obtained by an inverse Fourier Transform of its spectrum:

$$R_{hh}(\underline{\xi}) = \iiint_{-\infty}^{+\infty} e^{j \cdot \underline{k} \cdot \underline{\xi}} S_{hh}(\underline{k}) d\underline{k} \quad (3.10)$$

The spectral densities for the *head gradient* obtain easily from the well-known relations between a stationary field and its derivative. Denoting  $h_i$  the *i*th-component of  $\underline{v}h$ :

$$dZ_{h_i}(\underline{k}) = j k_i dZ_h(\underline{k}) = k_i \frac{(J_{\ell} k_{\ell})}{k^2} dZ_f(\underline{k}) \quad (3.11)$$

which gives the spectral density tensor of the head gradient vector( $h_i$ ):

$$\boxed{S_{h_i h_j}(\underline{k}) = \frac{k_i k_j (J_{\ell} \cdot k_{\ell})^2}{k^4} S_{ff}(\underline{k})} \quad (3.12)$$

The tensor of covariance functions  $R_{h_i h_j}(\underline{\xi})$  could be obtained by Fourier-transforming the tensor spectrum in (3.12). Alternatively, the same result can be obtained directly from  $R_{hh}(\underline{\xi})$  by applying simple differentiation rules as shown below (let  $\underline{\xi} = \underline{x}' - \underline{x}$ ):

$$R_{hh}(\underline{\xi}) = R_{hh}(\underline{x}, \underline{x}') = \langle h(\underline{x})h(\underline{x}') \rangle$$

$$\frac{\partial R_{hh}}{\partial x_i} = \langle \frac{\partial h}{\partial x_i}(\underline{x})h(\underline{x}') \rangle$$

$$\frac{\partial^2 R_{hh}}{\partial x_i \partial x'_j} = \langle \frac{\partial h}{\partial x_i}(\underline{x}) \cdot \frac{\partial h}{\partial x'_j}(\underline{x}') \rangle.$$

Using  $\underline{x}' = \underline{x} + \underline{\xi}$  and the fact that  $R_{hh}$  depends only on  $\underline{\xi}$ , this leads to:

$$\frac{\partial^2 R_{hh}}{\partial \xi_i \partial \xi'_j} = - \langle \frac{\partial h}{\partial x_i}(\underline{x}) \cdot \frac{\partial h}{\partial x'_j}(\underline{x} + \underline{\xi}) \rangle.$$

Thus, the head gradient covariance tensor is simply given by:

$$\boxed{R_{h_i h_j}(\underline{\xi}) = - \frac{\partial^2 R_{hh}(\underline{\xi})}{\partial \xi_i \partial \xi_j}} \quad (3.12')$$

Finally, we follow Gelhar and Axness (1983) by using the local Darcy equation to obtain the spectral density tensor of the flux vector. It turns out that an additional approximation is needed in order to obtain this result. Indeed, the Darcy equation must first be expressed in terms of the log-conductivity  $f(\underline{x})$ :

$$\underline{Q}(\underline{x}) = - K_G \cdot e^{f(\underline{x})} \cdot \underline{\nabla} H. \quad (3.13)$$

The exponential dependence on  $f(\underline{x})$  is the source of the trouble, since the spectral representation method is only useful when the random fields appear linearly. Gelhar and Axness (1983) propose linearizing the exponential around  $f(\underline{x}) = 0$ , although we will see later that this additional approximation could be avoided. Following for now the method of Gelhar and Axness, let us compute the flux moments based on the "linearized" Darcy equation. Using the expansion  $e^f = 1 + f + f^2/2 + \dots$  gives:

$$\underline{Q}(\underline{x}) \simeq - K_G (-\underline{J} + \underline{\nabla} h - \underline{J} \cdot f + f \cdot \underline{\nabla} h - \underline{J} \cdot f^2/2).$$

The mean flux is obtained by taking the ensemble average:

$$\langle \underline{Q} \rangle = + K_G [-\langle f \cdot \underline{\nabla} h \rangle + J(1 + \sigma_f^2/2)].$$

The ensemble average term  $\langle f \cdot \underline{\nabla} h \rangle$  can be worked out by using the relation between  $dZ_{h_i}$  and  $dZ_f$  given in (3.11). From the spectral representation theorem (3.7) we have:

$$\begin{aligned} \langle f(\underline{x}) \cdot \frac{\partial h(\underline{x})}{\partial x_i} \rangle &= \iiint_{-\infty}^{+\infty} \langle dZ_f \cdot dZ_{h_i}^* \rangle \\ &= \iiint_{-\infty}^{+\infty} \frac{k_i(J_j k_j)}{k^2} \langle dZ_f dZ_f^* \rangle \\ &= \iiint_{-\infty}^{+\infty} \frac{k_i(J_j k_j)}{k^2} S_{ff}(\underline{k}) d\underline{k} \end{aligned}$$

so that we can express the mean flux  $\langle Q_i \rangle$  in terms of an effective conductivity tensor  $\hat{K}_{ij}$  as follows:

$$\begin{aligned} \bar{Q}_i &= \hat{K}_{ij} \cdot \bar{J}_j \\ \hat{K}_{ij} &= K_G \left[ - \iiint_{-\infty}^{+\infty} \frac{k_i k_j}{k^2} S_{ff}(\underline{k}) d\underline{k} + \left(1 + \frac{\sigma_f^2}{2}\right) \delta_{ij} \right] \end{aligned} \tag{3.14}$$

The effective conductivity  $\hat{K}_{ij}$  given in (3.14) is a second rank symmetric tensor, provided that the spectral density



function  $S_{ff}(\mathbf{k})$  is even in each of the wavenumber components  $k_i$ , e.g. in the case of ellipsoidal anisotropy. However, this holds only as a first order approximation, implying that the tensorial property may not hold for large values of  $\sigma_f$ . Equation (3.14) was obtained by Gelhar and Axness [1983-Eq. 52], who developed close-form expressions for  $\hat{K}_{ij}$  in specific cases.

In order to obtain also the *flux spectrum*, we need to expand again the  $e^f$  term as explained earlier (after Gelhar and Axness). The flux perturbation equation obtains by subtracting the mean:

$$\begin{aligned} Q(\underline{x}) &= K_G [1+f+f^2/2+\dots][-\underline{v}h+J] \\ \langle Q(\underline{x}) \rangle &= K_G [(1+\sigma_f^2/2+\dots)\bar{J} - \langle f \cdot \underline{v}h \rangle + \dots] \end{aligned}$$

which gives for the flux-perturbation:

$$\begin{aligned} q(\underline{x}) = Q - \langle Q \rangle &= K_G \cdot \{ [(1+f+f^2/2+\dots) - (1+\sigma_f^2/2+\dots)] J \\ &\quad - \underline{v}h(1+f+f^2/2+\dots) + (\langle f \cdot \underline{v}h \rangle + \dots) \} \end{aligned}$$

where the dots represent higher order terms. By neglecting perturbations of products, such as  $[f^2/2 - \sigma_f^2/2]$ ,  $[f \cdot \underline{v}h]$ , and all higher order perturbations as well, we obtain the "first order approximation":

$$\underline{q}(\underline{x}) \approx K_G \{ \underline{J} \cdot \underline{f}(\underline{x}) - \underline{v}h \}. \quad (3.15)$$

For completeness, let us also write a third order approximation, of  $\underline{q}(\underline{x})$  excluding only terms like  $[f^4 - \langle f^4 \rangle]$ , etc. This gives:

$$\begin{aligned} \underline{q}(\underline{x}) \approx K_G \cdot \{ \underline{J}f - \underline{v}h + \langle \underline{v}h \cdot \underline{f} \rangle - \underline{v}h \cdot \underline{f} + (f^2 - \langle f^2 \rangle) \underline{J} / 2 \\ + \underline{J}f^3 / 6 + \langle \underline{v}h \cdot f^2 / 2 \rangle - \underline{v}h \cdot f^2 / 2 \}. \end{aligned} \quad (3.16)$$

Using the flux perturbation approximation (3.15) as in Gelhar and Axness leads finally to the spectral density tensor. By the representation theorem (3.7) and previous results, equation (3.15) gives:

$$\boxed{S_{q_i q_j}(\underline{k}) \approx K_G^2 \cdot J_m J_n (\delta_{im} - k_i \cdot k_m / k^2) \cdot (\delta_{jn} - k_j \cdot k_n / k^2) \cdot S_{ff}(\underline{k})}. \quad (3.17)$$

This is a second rank symmetric tensor, being the spectral density tensor of a vector whose components are stationary random fields.

In view of the results obtained so far, it is worth noting that the flow field appears to be inherently anisotropic. Indeed, the spectral density functions  $S_{hh}$  and  $S_{q_i q_j}$  are generally anisotropic (and so is the tensor  $S_{q_i q_j}$ ), even in the

case where the input spectrum  $S_{ff}$  is isotropic.

We end this section by specializing the spectral solutions (3.9) - (3.17) for the case where the log-conductivity spectrum is of "ellipsoidal type" (as defined by Van Marcke, 1983). In this important case, the spectrum and covariance of the log-conductivity are of the form:

$$S_{ff}(\underline{k}) = S_{ff}(\lambda_i^2 k_i^2)$$

$$R_{ff}(\underline{\xi}) = R_{ff}(\lambda_i^{-2} \xi_i^2)$$

in the coordinate system coinciding with the axes of statistical anisotropy of  $f(\underline{x})$ . In this case, recall that the effective conductivity  $\hat{K}_{ij}$  obtained from the first order analysis is a symmetric tensor.

Let us focus in particular on the case where the mean head gradient is aligned with one of the principal axes of  $f(\underline{x})$ . Accordingly, let the  $x_1$  axis coincide with the mean head gradient vector  $\underline{J}$  and also with the principal axis corresponding to the principal value  $\lambda_1$  ( $\lambda_1$  is the correlation scale along  $x_1$ , in a sense to be precised later). The spectral solutions (3.9) - (3.17) can now be written as follows:

$$\begin{aligned}
 S_{hh}(\underline{k}) &= \frac{J_i^2 k_i^2}{k^4} S_{ff}(\underline{k}) \\
 S_{h_i h_j}(\underline{k}) &= \frac{k_i k_j J_i^2 k_i^2}{k^4} S_{ff}(\underline{k}) \\
 S_{q_i q_j}(\underline{k}) &= K_G^2 J_1^2 \left[ \delta_{i1} - \frac{k_i k_{i1}}{k^2} \right] \left[ \delta_{j1} - \frac{k_j k_{j1}}{k^2} \right] S_{ff}(\underline{k})
 \end{aligned}
 \tag{3.18}$$

where the indices vary from 1 to m (the dimension of space). In addition, the effective conductivity tensor is now diagonal; this comes from the fact that the ellipsoidal spectrum  $S_{ff}$  is even in each of the wavenumber components, so that the integral in (3.14) vanishes for  $i \neq j$ . Following Gelhar and Axness (1983), equation (3.14) gives in this case:

$$\begin{aligned}
 \hat{K}_{ij} &= 0 \text{ for } i \neq j \\
 \hat{K}_{ii} &= K_G [-\sigma_f^2 g_{ii} + (1 + \sigma_f^2/2)] \approx K_G \cdot \exp[\sigma_f^2 (1/2 - g_{ii})] \\
 g_{ii} &= \iiint_{-\infty}^{+\infty} \frac{k_i^2 S_{ff}(\underline{k})}{k^2 \sigma_f^2} d\underline{k}
 \end{aligned}
 \tag{3.19}$$

Note that the exponential formula for  $\hat{K}_{ii}$  in (3.19) was proposed by Gelhar and Axness, 1983, after examination of special cases of quasi one-dimensional flow for which the effective conductivity is known exactly.

In order to obtain more concrete results, such as the covariance functions of heads and fluxes we need to introduce a specific model for the spectral density function of the log-conductivity field. There exists a wide class of ellipsoidal spectral density functions, but we will see that certain spectra lead to divergence of second order moments of the flow solution, thus violating the stationarity assumption. This is discussed in the next section below.

### 3.2 Discussion of Admissible Log-conductivity Spectra

In this section, we analyze certain restrictions for admissible  $\ln K$ -spectra based on results obtained in the literature. Table 3.1 summarizes some of the input log-conductivity spectra and the corresponding covariance functions used in the literature for 2- and 3-dimensional stochastic flow problems. These particular spectra were chosen for several reasons:

- (i) Some of the spectra in Table 3.1 were fitted to field data; for instance *Bakr* (1976) observed a good fit between the 1D marginal spectrum obtained by integrating the 3D Isotropic Markov Spectrum over two wavenumber components, and the 1D Spectral density of the log-conductivity measured at a borehole;

Table 3.1: Isotropic and Anisotropic Spectra for 2 and 3-Dimensional Random Log-Conductivity Fields

Spectral Model	SPECTRAL DENSITY FUNCTION $S_{ff}$	COVARIANCE FUNCTION $R_{ff}$	REFERENCES
3D Ellipsoidal Markov	$\frac{\sigma^2 \ell_1 \ell_2 \ell_3}{\pi^2 \cdot (1+u^2)^2}$	$\sigma^2 e^{-s}$	Bakr et al. 1978 and Gelhar and Axness, 1983
3D Ellipsoidal Hole-Markov	$\frac{4\sigma^2 \ell_1 \ell_2 \ell_3 \cdot u^2}{3\pi^2 (1+u^2)^3}$	$\sigma^2 (1-s/3) \cdot e^{-s}$	Naff 1978 and Vomvoris, 1986
3D Anisotropic Hole-Markov (non-ellips.)	$\frac{4\sigma^2 \ell_1 \ell_2 \ell_3 u_3}{\pi^2 (1+u^2)^3}$	$\sigma^2 \cdot (1-s_3^2 s) e^{-s}$	Naff 1978 and Gelhar and Axness, 1983
2D Ellipsoidal Markov	$\frac{\sigma^2 \ell_1 \ell_2}{\pi (1+u^2)^2}$	$\sigma^2 \cdot s \cdot K_1(s)$ (Bessel Function $K_1$ )	Mizell et al. 1982 ( $\ell_1 = \ell_2$ )
2D Ellipsoidal Hole-Markov	$\frac{2\sigma^2 \ell_1 \ell_2 u^2}{\pi (1+u^2)^3}$	$\sigma^2 \left\{ \frac{s}{2} K_1\left(\frac{s}{2}\right) - \frac{s^2}{4} K_0\left(\frac{s}{2}\right) \right\}$	Mizell et al. 1982 ( $\ell_1 = \ell_2$ )

Note:  $u_i$  represents the rescaled wavenumber  $\lambda_i k_i$  (here without summation) and  $u^2 = u_1^2 + u_2^2 + u_3^2$ ; similarly  $s_i$  represents the rescaled separation vector  $s_i = \xi_i / \lambda_i$ , and  $s^2 = s_1^2 + s_2^2 + s_3^2$ .

- (ii) The proposed spectra are fairly simple rational functions of the wavenumber, so that closed form solutions can be obtained for at least some of the statistics of interest, such as variances and covariance functions;
- (iii) Certain properties of the log-conductivity spectrum, in particular concerning the behaviour at zero wavenumber, are required in order to obtain physically realistic solutions for stochastic flow and convection-dispersion problems.

The last statement may require some explanation. Previous applications of the spectral solutions (3.18) in the literature have shown that certain quantities of interest may go to infinity (see references in Table 3.2). The divergence problem manifests itself by the appearance of a divergent integral, the integrand being typically the product of the log-conductivity spectrum by a certain transfer function which depends on the statistical quantity of interest. Such divergences are in fact a common problem in statistical physics. Two different types of divergence may be distinguished, as explained below:

(i) Low-Wavenumber divergence:

The statistical quantity of interest may diverge because of a singularity of the spectral integrand at zero wavenumber. This has been dubbed "Infrared Catastrophe". Physically, such divergence is caused by the persistence of fluctuations at increasingly large scales (low wavenumbers).

(ii) Large-Wavenumber divergence

On the other hand, certain statistical quantities diverge as the spectral integral is carried out to infinite wavenumbers, because the integrand does not decay rapidly enough at large wavenumbers. This type of divergence is known as "Ultraviolet Catastrophe". Physically, this means that the statistical quantity diverges because of the persistence of fluctuations at infinitely small scales (large wavenumbers).

Now, such divergence problems do occur in certain cases with the infinite domain spectral theory of stochastic flow and solute transport. Table 3.2 summarizes some of the results obtained in the literature, along with the relevant references. The table shows that certain constraints on the log-conductivity spectrum are needed in order to avoid the low-wavenumber divergence of hydraulic heads (for steady saturated flow) and of concentrations (for steady solute transport in a steady flow).



Table 3.2: Admissible Log-Conductivity Fields for Steady Flow in 1, 2, 3 Dimensions and 3D Solute Transport(\*)

	CONDITION ON COVARIANCE (REFERENCES)	EXAMPLE OF ADMISSIBLE $\ell_n K$	INTERPRETATION
1D flow ( $W=1/K$ )	$\int_0^\infty \xi \cdot R_{WW}(\xi) d\xi < 0$ Gutjahr, Gelhar 1981	$R_{WW}(\xi) = \sigma_W^2 \left(1 - \frac{ \xi }{\ell}\right) e^{- \xi /\ell}$ 1D Hole-Exponential Covariance	Requires strongly negative hole-covariance with negative integral scale.
2D flow ( $f = \ell_n K$ isotropic)	$\int_0^\infty \xi \cdot R_{ff}(\xi) d\xi = 0$ Mizell, Gutjahr, and Gelhar, 1982	$S_{ff}(k) = \frac{2\sigma_f^2 a^2}{\pi} \cdot \frac{k^2}{(k^2 + a^2)^2}$ 2D Markov Spectrum with Multidirectional Hole	Requires weakly negative hole-covariance, or hole-spectrum with zero integral scale.
3D flow ( $f = \ell_n K$ isotropic)	$\int_0^\infty \xi \cdot R_{ff}(\xi) d\xi < \infty$ Gelhar, Axness 1983 Gutjahr, Gelhar 1981	$S_{ff}(k) = \frac{\sigma_f^2 \lambda^3}{\pi^2} + \frac{1}{(1 + \lambda^2 k^2)^2}$ 3D Gauss-Markov Spectrum	No Hole Spectrum is required. Any 3D isotropic field with $R_{ff}(\xi) \geq 0$ and finite integral scale is satisfactory.
3D Solute Transport ( $f = \ell_n K$ isotropic)	$S_{ff}(0) = 0$ , i.e.: $\int_0^\infty \xi^2 \cdot R_{ff}(\xi) d\xi = 0$ Vomvoris 1986	$S_{ff}(k) = \frac{4\sigma_f^2 \lambda^3}{3\pi^2} \frac{\lambda^2 k^2}{(1 + \lambda^2 k^2)^2}$ 3D Gauss-Markov with Multidirectional Hole	Requires Hole-spectrum with zero integral scale

(\*) The table gives necessary and sufficient conditions for stationary solutions of the 1D, 2D, 3D flow problems with an isotropic  $\ell_n K$  field. For the 3D solute transport problem the given condition is sufficient, but may not be necessary.

In order to understand the requirements of Table 3.2, it is useful to note the relation between the integral correlation scale and the spectral density at zero wavenumber. For an  $m$ -dimensional isotropic random field (Vanmarcke, 1983) the correlation length  $\lambda_{mD}$  satisfies:

$$(\lambda_{mD})^m = c' \cdot \int_0^{\infty} \xi^{m-1} \frac{R(\xi)}{\sigma_f^2} d\xi = c'' \cdot \frac{S(0)}{\sigma_f^2}$$

Now, Table 3.2 shows that in order to avoid the low-wavenumber (large scale) divergence of the head field, a zero integral scale of  $\ln K$  is required in the 2D case. In 3D, the requirement is much milder: it is easily shown for instance that if then any  $\ln K$  field with finite correlation scale and positive covariance function will be satisfactory. Finally, in 1D, the requirement is much more stringent: the  $\ln K$  correlation function must have strongly negative values and its "integral scale" must usually be negative. It has no physical meaning in this case.

Such requirements on the shape of the input spectrum could be viewed as an artefact of the infinite domain spectral theory. They can be explained by observing that the head field appears as the result of band-pass filtering of the  $\ln K$  field

in the low-wavenumber range [see Figure 6.12 of Bakr, 1976]. When the flow is constrained, e.g., when the dimensionality of space is decreased from 3D to 2D or 1D, the large scale fluctuations taking place in the remaining dimensions are effectively amplified, with significant fluctuations persisting at infinitely large scales. This leads to divergent solutions in the case of steady flow in low-dimensional space (consider for instance a 3D flow channelized between two impervious walls). Such divergence can only be avoided by eliminating the large scale fluctuations of the conductivity, e.g., using "Hole-Spectra" as those shown in Table 3.1.

Table 3.2 also shows that a low-wavenumber divergence of the *solute concentration* field will occur in 3D, unless the log-conductivity field had a zero correlation scale (Vomvoris, 1986, p. 45). This shows that the problem of divergence due to large scale fluctuations may arise even if the fully 3-dimensional nature of space is taken into account (here for the solute transport problem). One possible interpretation is that the large scale divergence of solute concentrations results from the inadequate assumption that there exist *steady* solutions which are *spatially stationary*. Some insight on this question could be

gained by examining the fully non-steady flow/transport problem in three dimensions. This will not be attempted here.

We conclude that the *low-wavenumber or large-scale divergence of stochastic quantities may result from the inadequacy of the assumption that there exist stationary and ergodic solutions to the flow and transport problems in the steady state.* The results of the first order spectral perturbations theory (Table 3.2) clearly show that this is not always the case, depending on the spatial structure of the porous medium. In general, the  $\ln K$  field must be taken to be "almost periodic" at some large but finite scale in order to obtain useful results. Furthermore, it turns out that the  $\ln K$  field must be taken more strongly "periodic", with smaller "wavelength", as the dimensionality of space decreases. In our view, this indicates that the conditions for the existence of steady stationary solutions become more and more restrictive as the degree of freedom of flow decreases in physical space.

Finally, let us briefly mention the appearance of *large wavenumber divergences of the steady solute concentration field*, as this may be relevant to the steady flow problem itself. One example of small scale divergence is the divergence of the concentration variance as the local dispersion coefficient (length scale) goes to zero. A second case of small scale

divergence or near-divergence was found by Vomvoris, 1986: the correlation scale of the concentration along the mean flow direction appeared to be very sensitive to the rate of decay of the  $\ln K$  spectrum at large wavenumbers. In order to obtain physically reasonable results, the  $\ln K$  spectrum must decay exponentially at large wavenumbers. In our view, this suggests that the  $\ln K$  spectrum should be truncated at some large wavenumber  $k \simeq \alpha^{-1}$ , where  $\alpha$  represents the length scale of the mechanical dispersion process taking place at small scales. In other words,  $\alpha$  represents the small scale dispersivity, or sub-grid dispersivity with respect to the measurement grid. Accordingly, we argue that the spectral density models of Table 3.1 should be truncated at  $k \leq \alpha^{-1}$  for use in the solute transport equations. The proposed approach assumes that the effect of small scales heterogeneities is correctly modeled by the local dispersivity term, which should be measured independently at the laboratory scale.

Based on the previous analysis, both the Markov and Hole-Markov spectra appear to be admissible for stationary first order flow solutions in an isotropic three dimensional medium. Presumably, this also holds in the anisotropic case. Thus, we develop in the next sections a number of closed form results for these spectra with various degrees of anisotropy in three dimensions. Recall however that the proposed spectra may not be

meaningful in the case of stochastic solute transport, unless they be truncated at some low and high wavenumbers. The Hole model realizes a kind of smooth truncation at low wavenumbers, but seems somewhat arbitrary. This problem suggested the idea of a finite domain approach based on band-pass self-similar spectra, eventually leading to a systematic analysis of finite size effects in a later part of this work (Section 4.4 of Chapter 4).

### 3.3 Head and Flux Moments for the 3D Isotropic Markov Spectrum

In the isotropic case, simple closed form results can be obtained for the head variance, head correlation function, effective conductivity, and the variance of the head gradient and flux vectors. We present all these results below. The quantities  $\sigma_h^2$ ,  $R_{hh}(\xi)$ ,  $\hat{K}_{ii}$ , were obtained by Bakr et al., 1978. The head gradient variance  $\sigma_{h_i}^2$  and the flux variance  $\sigma_{q_i}^2$  are easily obtained by spectral integration (see Appendices 3.A and 3.B). Finally, the flux covariance functions  $R_{q_i q_j}(\xi)$  can be obtained either by numerical integration or analytically (Wendy Graham, personal communication, and Appendix 3.C). All the relevant quantities were computed by using the 3D Gauss-Markov spectrum of Table 3.1 with  $\lambda_1 = \lambda_2 = \lambda_3$ . Thus, the log-conductivity spectrum is:

$$S_{ff}(\underline{k}) = \frac{\sigma_f^2 \lambda^3}{\pi^2} \cdot \frac{1}{(1+\lambda^2 k^2)^2} \quad (3.20)$$

The head covariance obtains from:

$$R_{hh}(\underline{k}) = \iiint e^{jk\xi} S_{hh}(\underline{k}) d\underline{k}$$

and the flux covariance from:

$$R_{q_i q_j}(\underline{k}) = \iiint e^{jk\xi} S_{hh}(\underline{k}) d\underline{k}$$

where the spectra appearing in the integrands were given in equation (3.18). The effective conductivity  $\hat{K}_{ii}$  is similarly evaluated from (3.19). The results are the following:

(i) Hydraulic head (from Bakr et al. 1978):

$$\sigma_h = \frac{1}{\sqrt{3}} \sigma_f \lambda J_1 \quad (3.21.a)$$

$$R_{hh}(\xi) = \left(\frac{3}{2}\right) \sigma_h^2 \cdot \{ (\cos^2 \chi - 1) \cdot [e^{-\xi/\lambda} + 2(e^{-\xi/\lambda} - 1) \cdot (\xi/\lambda)^{-1}] + (3\cos^2 \chi - 1) \cdot [ (1 - e^{-\xi/\lambda}) \cdot (\xi/2\lambda)^{-3} - e^{-\xi/\lambda} (1 + 2(\xi/2\lambda)^{-1} + 2(\xi/2\lambda)^{-2}) ] \} \quad (3.21.b)$$

where  $\chi$  is the angle between the separation vector  $\underline{\xi}$  and the mean flow direction. The corresponding

correlation function is plotted in Figure 3.1 for two angles:  $\chi = 0$  (along the mean flow) and  $\chi = \pi/2$  (across the mean flow). Note  $\cos\chi = \xi_1/\xi$   $\xi = \sqrt{\xi_1^2 + \xi_2^2 + \xi_3^2}$ , so that  $\chi = 0$  corresponds to  $\xi = (\xi_1, 0, 0)$  and  $\chi = \pi/2$  to  $\xi = (0, \xi_2, \xi_3)$ .

(ii) Head gradient vector (Appendices 3.A and 3.C):

$$\sigma_{h_1} = \frac{1}{\sqrt{5}} \sigma_f J_1 \quad (3.22)$$

$$\sigma_{h_2} = \sigma_{h_3} = \frac{1}{\sqrt{15}} \sigma_f J_1$$

The head gradient covariance functions  $R_{h_i h_j}(\xi)$  can be obtained as indicated in Appendix 3.C.

(iii) Mean flux and effective conductivity (from Gelhar and Axness, 1983):

$$\hat{K}_{ii} = K_G \cdot \exp(\sigma_f^2 / 6) \quad \forall i = 1, 2, 3 \quad (3.23)$$

$$\langle Q_1 \rangle = \hat{K}_{11} \cdot J_1, \quad \langle Q_2 \rangle = \langle Q_3 \rangle = 0.$$



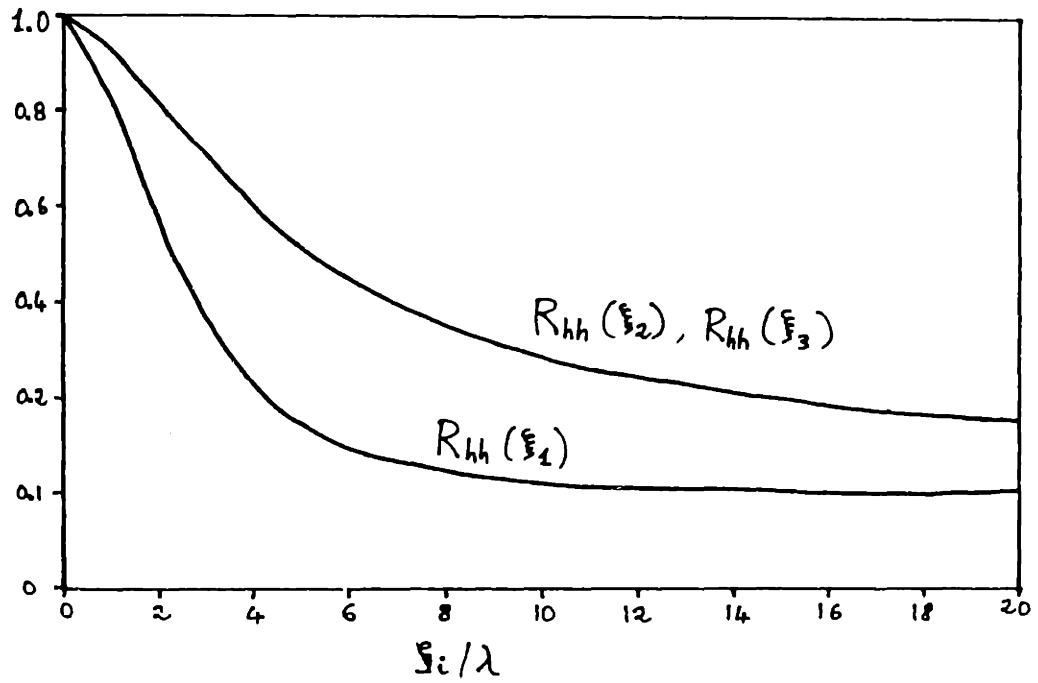


Figure 3.1 Head correlation function along the coordinate axes for the 3D Isotropic Markov spectrum of log-conductivity

(iv) Flux vector variances and covariance functions  
(cf. Appendices 3.B and 3.C)

$$\sigma_{q_1} = \sqrt{8/15} K_G \sigma_f J_1 \quad (3.24)$$

$$\sigma_{q_1} = \sigma_{q_2} = \sqrt{1/15} K_G \sigma_f J_1$$

$$R_{q_i q_j}(\underline{0}) = 0 \quad \text{for } i \neq j$$

The covariance tensor  $R_{q_i q_j}(\underline{\xi})$  is defined by:

$$R_{q_i q_j}(\underline{\xi}) = \langle (Q_i(\underline{x}) - \bar{Q}_i) \cdot (Q_j(\underline{x} + \underline{\xi}) - \bar{Q}_j) \rangle$$

The components of this tensor are plotted along the three coordinates axes ( $\underline{\xi}$  parallel to  $\underline{x}_i$ ) in Figures (3.2) and (3.3). These plots were obtained from analytical integration of the flux spectrum of equation (3.18). The integrations were carried out by Wendy Graham (personal communication) for all but the covariance  $R_{q_2 q_2}(\underline{\xi}_2)$  given in Appendix 3.C.

The results in equations (3.21)-(3.24) and Figures (3.1)-(3.3) can be interpreted as follows. In terms of standard deviations, the equation for  $\sigma_H$  shows that the amplitude of head fluctuations is proportional to  $\sigma_f$  and to the mean head drop over one correlation scale ( $\lambda J_1$ ). The amplitude of the flux vector fluctuations is proportional to  $\sigma_f$  and to  $K_G J_1$  (a subsequent analysis will show that this term should be replaced by the mean flux  $\langle Q_1 \rangle$  -- see section 4.3). Similarly, the amplitude of fluctuations of the head gradient is

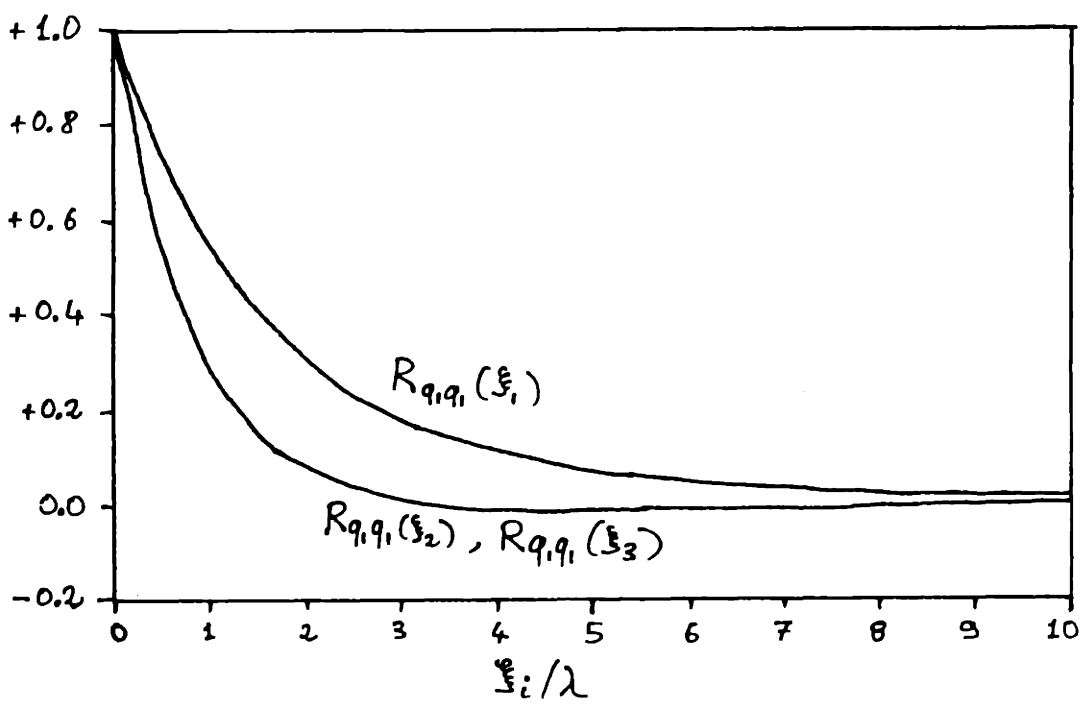


Figure 3.2 Longitudinal flux correlation function along the coordinate axes for the 3D Isotropic Markov spectrum of log-conductivity

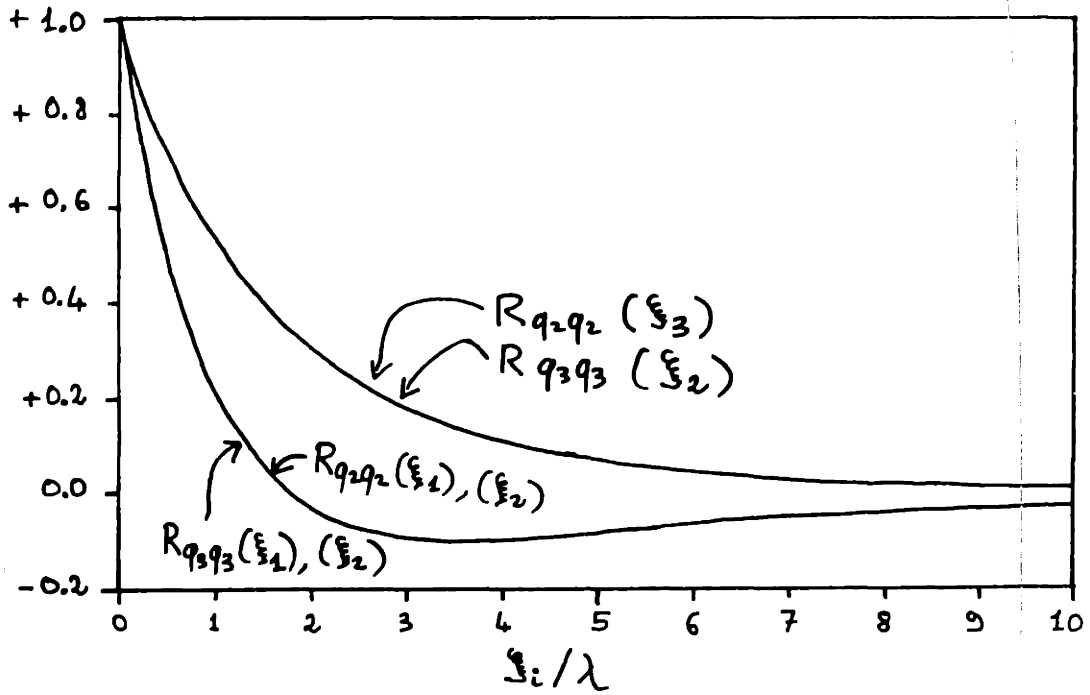


Figure 3.3 Transverse flux correlation functions along the coordinate axes for the 3D Isotropic Markov spectrum of log-conductivity

proportional to  $\sigma_f$  and to the mean head gradient  $J_1$ .

Furthermore, it appears that the longitudinal flux component has larger fluctuations than the transverse flux components, by a factor  $\sqrt{8}$ . The contrast is milder for the head gradient components (factor  $\sqrt{3}$ ). After replacing the term  $K_G J_1$  by the mean flux  $\langle Q_1 \rangle$  in (3.24), we obtain a coefficient of variation on the order of  $\sigma_f/\sqrt{2}$  for the longitudinal flux component. The coefficient of variation for the longitudinal component of the head gradient is significantly smaller, about  $\sigma_f/\sqrt{5}$ . This suggests that the range of validity of the first order solutions may not be the same for different quantities such as head gradient and flux. Taking for instance  $\sigma_f \simeq 1.5$  yields a coefficient of variation of 60% for  $\partial h/\partial x_1$ , and over 100% for  $q_1$ . It seems wise to expect some degree of inaccuracy of the perturbative solutions for such a large coefficient of variation as 100%. This example indicates that the range of validity of the spectral solutions for the flux vector could be limited to cases of moderate variability ( $\sigma_f < 1-1.5$ ).

In terms of correlation functions, it can be seen from Figure (3.1) that the hydraulic head is correlated over longer distances than the log-conductivity. Furthermore, the head correlation is stronger in the direction transverse to flow.

Defining the e-correlation length as the distance at which correlation drops below  $e^{-1}$ , we obtain a head correlation length equal to  $7.5\lambda$  transversally, compared to  $3\lambda$  in the direction of the mean flow. This clearly shows that the head field is not isotropic.

Similarly, the flux components are not isotropic. The flux correlation lengths are on the order of the conductivity scale  $\lambda$ , or nearly twice as much for certain flux components and orientations of the separation vector (see Figures (3.2) and (3.3)). Overall, it appears that the flux correlations are consistently smaller than the head correlations. This can be explained by the fact that the flux is more directly related to the conductivity fluctuations (through the local Darcy equation). Another remarkable feature is the fact that different flux components are totally uncorrelated at zero separation distance. Finally, note again that the *anisotropic* flux covariance tensor satisfies a number of symmetry relations and other identities (mass conservation), which will be analyzed in a later part of this work (Section 4.2).

We end this section by focusing on a peculiar feature of the flux spectral solution which does not seem to have been observed in the literature. According to equations (3.23) and

(3.24), it appears that the ratios  $\sigma_{q_i} / \langle Q_1 \rangle$  have a maximum at  $\sigma_f = \sqrt{3}$ , and they converge to zero as  $\sigma_f$  goes to infinity. Indeed, from (3.23) and (3.24) we have:

$$\frac{\sigma_{q_1}}{\langle Q_1 \rangle} = \sqrt{8/15} \sigma_f e^{-\sigma_f^2/6} \quad (3.25)$$

$$\frac{\sigma_{q_2}}{\langle Q_1 \rangle} = \frac{\sigma_{q_2}}{\langle Q_1 \rangle} = \sqrt{1/15} \sigma_f e^{-\sigma_f^2/6}$$

Surprisingly, these quantities have a maximum at  $\sigma_f = \sqrt{3}$ :

$$\left. \frac{\sigma_{q_1}}{\langle Q_1 \rangle} \right|_{\max} = 0.557$$

$$\left. \frac{\sigma_{q_2}}{\langle Q_1 \rangle} \right|_{\max} = \left. \frac{\sigma_{q_2}}{\langle Q_1 \rangle} \right|_{\max} = 0.271.$$

Unfortunately, there seems to be no obvious physical reason for such a behavior. Rather, one would expect that the coefficient of variation  $\sigma_{q_1} / \langle Q_1 \rangle$  be a monotonously increasing function of  $\sigma_f$ . We will show in Chapter 4 (section 4.3) that a more physical behavior obtains by an alternative perturbation analysis which avoids linearization approximations of the type  $e^f \simeq 1 + f + \dots$ . The new spectral solution obtains simply by replacing the term  $K_G J_1$  by  $\langle Q_1 \rangle$  in the flux variance (3.24).

Therefore, the exponential term  $e^{-\sigma^2/6}$  disappears from (3.25), and the coefficients of variations of the flux components appear now to increase linearly with  $\sigma_f$ , which seems to be a more realistic behavior. Accordingly, we propose that equation (3.24) be modified as follows:

$$\boxed{\begin{aligned} \sigma_{q_1} &= \sqrt{8/15} \sigma_f \langle Q_1 \rangle \\ \sigma_{q_2} = \sigma_{q_3} &= \sqrt{1/15} \sigma_f \langle Q_1 \rangle . \end{aligned}} \quad (3.26)$$

This modification of the spectral flow solutions of Gelhar and Axness (1983) has also implications on the solute transport problem, as explained later (Section 4.3 of Chapter 4).

---

### 3.4 Head and Flux Moments for the 3D Anisotropic Markov Spectrum

The first order spectral solutions (3.18) are now applied to the case of the ellipsoidal Markov log-conductivity spectrum (Table 3.1) with  $\ell_1 = \ell_2 = \ell$  and  $\ell_3 \neq \ell$ . We assume that the mean head gradient is parallel to the principal direction of anisotropy ( $x_1$ ). The vertical/horizontal anisotropy ratio:

$$\epsilon = \ell_3 / \ell$$

will usually be taken to be less than one, as this is a case of practical interest for most horizontally layered porous media. In addition, certain results become simpler when  $\epsilon \ll 1$  holds,



which is the case of perfectly stratified media. However, this assumption is not needed in the calculations that follow.

The log-conductivity spectrum for the case at hand is:

$$S_{ff}(\underline{k}) = \frac{\sigma_f^2 \ell^2 \ell_3}{\pi^2} \cdot \frac{1}{[1 + \ell^2(k_1^2 + k_2^2) + \ell_3^2 k_3^2]^2}$$

Plugging this into (3.10), we obtain the head covariance function in the form:

$$R_{hh}(\underline{k}) = \left[ \frac{\pi}{8} \sigma_f^2 \cdot J_1^2 \ell \ell_3 \right] \cdot I(\xi) \quad (3.27.a)$$

where  $I(\xi)$  is the triple-integral:

$$I(\xi) = \left[ \frac{2}{\pi \ell} \right]^3 \cdot \int_{-\infty}^{+\infty} \int_{-\infty}^{+\infty} \int_{-\infty}^{+\infty} \frac{k_1^2 \cos(\underline{k}\xi)}{k^4 [\ell^{-2} + (k_1^2 + k_2^2) + \ell_3^2 k_3^2]^2} d\underline{k}$$

We show in Appendix 3.D that that this can be reduced to the double-integral:

$$I(\xi) = \frac{2}{\pi^2} \cdot \int_0^{2\pi} \cos^2 \theta \, d\theta \int_0^{\pi} F(\theta, \varphi) \, d\varphi \quad (3.27.b)$$

where

$$F(\theta, \varphi) = \sin^3 \varphi \cdot \left[ \frac{1+C(\theta, \varphi)}{B(\varphi)} \right] \cdot e^{-C(\theta, \varphi)}$$

$$C(\theta, \varphi) = \frac{1}{\ell} \cdot \left| \frac{A(\theta, \varphi)}{B(\varphi)} \right|$$

$$A(\theta, \varphi) = (\xi_1 \cos \theta + \xi_2 \sin \theta) \sin \varphi + \xi_3 \cos \varphi$$

$$B(\varphi) = \sqrt{\sin^2 \varphi + \epsilon^2 \cdot \cos^2 \varphi}$$

The double-integral above was computed by careful numerical integration, using Romberg interpolation for the most difficult inner integral (IMSL routine DCADRE), and Simpson integration for the outer integral. The calculations were carried out in double precision (64-bit words). In addition, the results were checked by using a quasi-analytical expression for  $R_{hh}(0,0,\xi_3)$  in the case  $\epsilon \ll 1$  (see [Appendix 3.E](#)). The comparison indicates that the numerical integration procedure was sound.

[Figure \(3.4\)](#) shows the resulting head covariance functions plotted for a separation vector  $\xi$  parallel to  $x_1, x_2$  and  $x_3$  respectively, for different values of the anisotropy ratio. Only the case  $\epsilon \leq 1$  is shown, as this is the most interesting case in practice (horizontal layering).

The most remarkable feature from these plots is that

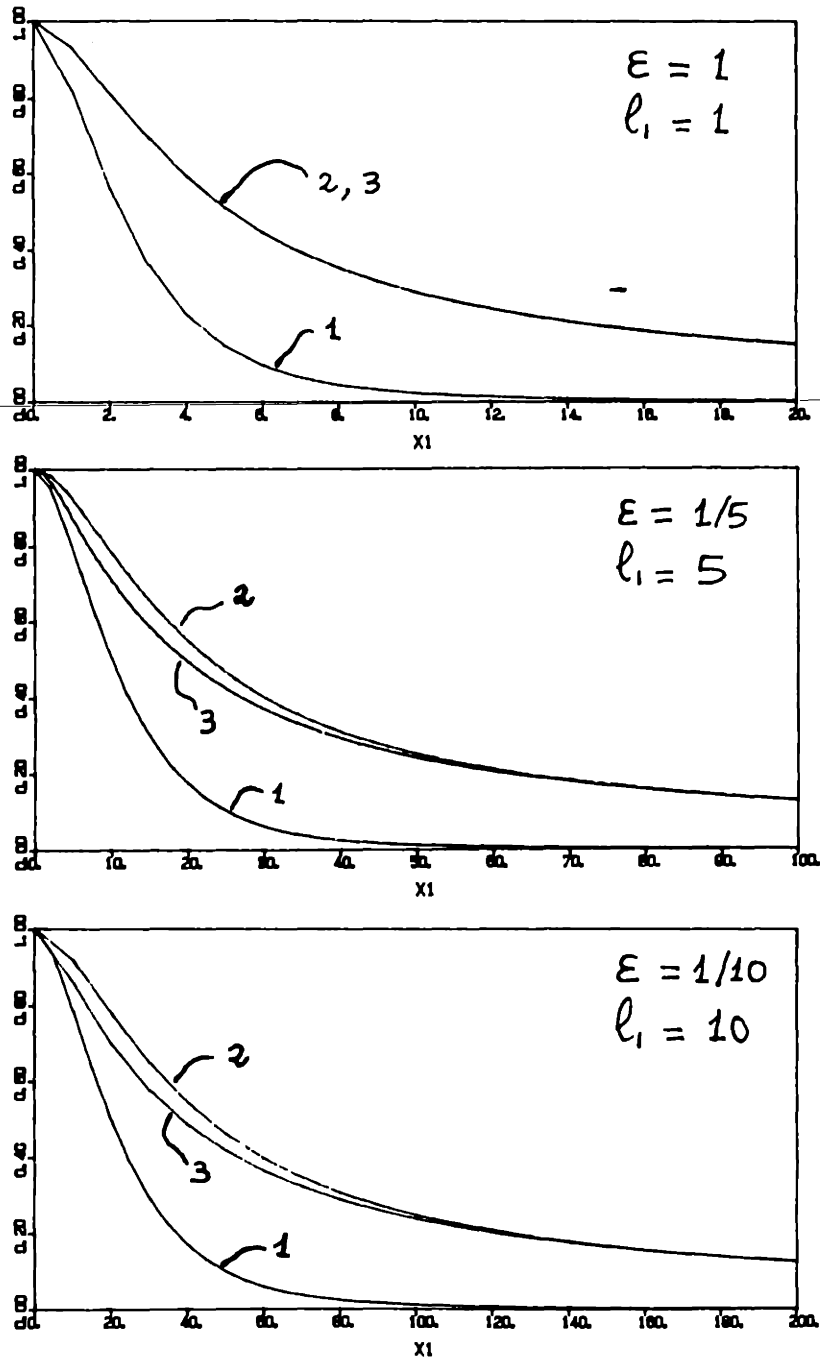


Figure 3.4 Head correlation function  $R_{hh}(\xi)$  along the three principal directions for the 3D ellipsoidal Markov spectrum of log-conductivity with different values of the anisotropy ratio ( $\epsilon = l_2/l_1$ ) as  $l_1$  increases.

the head correlation function does not change much when the vertical scale  $\ell_3$  goes to zero as the horizontal scale  $\ell$  remains fixed. Indeed, the vertical correlation scale of heads only decreases slightly as  $\ell_3$  decreases from  $\ell_3 = \ell$  (isotropic) to  $\ell_3 \simeq 0$  (perfectly stratified) while  $\ell$  is fixed. Physically, this means that the head process in a layered medium has a vertical scale of fluctuation much larger than the "layers" thickness, and does not decrease appreciably as the layers thickness decreases. Thus, as  $\epsilon \rightarrow 0$ , the ratio of the vertical head scale versus the vertical log-conductivity scale tends to infinity.

Furthermore, the ensemble head variance may be obtained analytically by evaluating the integral  $I(\xi)$  at  $\xi = 0$ . This was computed by *Naff and Vecchia (1986)* for the case  $\epsilon \leq 1$ :

$$\sigma_h^2 = \frac{\pi}{8} \sigma_f^2 J_1^2 \ell_G^2 \cdot G(\epsilon) \quad (3.28)$$

where:

$$G(\epsilon) = \frac{1}{\gamma} \left\{ \left( 1 - \frac{\epsilon^2}{\gamma^2} \right) + \frac{2}{\pi} \frac{\epsilon}{\gamma} \right\} + \frac{1}{\epsilon^2} \cdot \left( \frac{1}{\gamma^3} - \frac{3}{\gamma} + 2\gamma \right) \cdot \left( 1 - \frac{2}{\pi} \tan^{-1} (\gamma/\epsilon) \right)$$

and:

$$\begin{aligned} \gamma &= \sqrt{1-\epsilon^2} \\ \epsilon &= \ell_3/\ell \leq 1 \\ \ell_G &= \sqrt{\ell\ell_3}. \end{aligned}$$

It is easily seen that  $G(\epsilon) \rightarrow 1$  as  $\epsilon \rightarrow 0$ . This gives immediately the asymptotic result for perfectly stratified media as follows:

$$\boxed{\sigma_h \approx \sqrt{\frac{\pi}{8}} \sigma_f J_1 \ell_G \quad \text{for } \epsilon \ll 1.} \quad (3.29)$$

Note that  $\ell_G = \sqrt{\ell\ell_3}$  is the geometric mean of the horizontal and vertical correlation scales. This shows that the head standard deviation tends to a finite constant (neither zero nor infinity) if the anisotropy ratio decreases while the geometric mean correlation scale  $\ell_G$  remains constant.

Finally, let us analyze the statistics of the flux vector. In the asymptotic case of perfect stratification ( $\epsilon \ll 1$ ), a few close-form results can be obtained. Recall for instance that equation (3.19) gives the general form of the effective conductivity in the anisotropic case (after Gelhar and Axness, 1983). For  $\epsilon \ll 1$ , in particular, equation (3.19) yields the geometric mean and the harmonic mean, respectively, for the effective conductivity components parallel and transverse to stratification:

$$\begin{aligned}
 \hat{K}_{11} &\approx K_G \\
 \hat{K}_{22} &\approx K_G \\
 \hat{K}_{33} &\approx K_H = K_G e^{-\sigma_f^2/2}
 \end{aligned}
 \tag{3.30}$$

We show in Appendix (3.F) that closed form expressions can be obtained as well for the variance of the flux components ( $\sigma_{q_i}^2$ ) in the limit of perfect stratification  $\epsilon \rightarrow 0$ :

$$\boxed{
 \begin{aligned}
 \sigma_{q_1} &\approx \sqrt{1 - \frac{13}{32} \pi \epsilon} \cdot \sigma_f K_G J_1 \\
 \sigma_{q_2} &\approx \sqrt{\frac{\pi}{32} \epsilon} \cdot \sigma_f K_G J_1 \\
 \sigma_{q_3} &\approx \sqrt{\frac{\pi}{8} \epsilon} \cdot \sigma_f K_G J_1
 \end{aligned}
 }
 \tag{3.31}$$

These approximate relations were obtained for the 3D anisotropic Markov spectrum with  $\ell_1 = \ell_2 = \ell$  and assuming  $\epsilon = \ell_3/\ell$  small (they are thought to be adequate for  $\epsilon \leq 1/5$  or so).

It appears from equations (3.31) that both transverse flux variances vanish in the limit of perfect stratification, while the longitudinal flux variance tends to a constant value about twice larger than would be obtained in the isotropic case (compare equations 3.31 and 3.24). Accordingly, the transverse flux components  $Q_i$  ( $i = 2,3$ ) appear to vanish identically when

$\epsilon = 0$ , resulting in a one-dimensional flow. However, the mass conservation equation shows that  $Q_1$  must be constant in one-dimensional flow, which seems contrary to the limit result  $\sigma_{q_1} \neq 0$ ,  $\sigma_{q_2} = \sigma_{q_3} = 0$ . This difficulty can be resolved by considering the fact that the transverse flux components have smaller scales of fluctuations than the longitudinal component.

The correlation length scales of the flux components can be evaluated qualitatively by considering the mass conservation equation in relation to equation (3.31). Using the fact that the mean flux vector is constant, mass conservation simply requires that the flux perturbation be "divergence free", that is:

$$\frac{\partial q_1}{\partial x_1} + \frac{\partial q_2}{\partial x_2} + \frac{\partial q_3}{\partial x_3} = 0.$$

A standard "scale analysis" of this equation leads to:

$$\frac{\sigma_{q_1}}{\Lambda_{11}} u_1(\underline{x}) + \frac{\sigma_{q_2}}{\Lambda_{22}} u_2(\underline{x}) + \frac{\sigma_{q_3}}{\Lambda_{33}} u_3(\underline{x}) = 0$$

where  $\Lambda_{ii}$  is the correlation length of  $q_i$  along the  $x_i$  axis. and the  $u_i(\underline{x})$  are normalized zero-mean random fields having variances on the order of unity. This formulation suggests that the constant coefficients in the above equation must be roughly

of equal magnitude:

$$\frac{\sigma_{q_1}}{\Lambda_{11}} \approx \frac{\sigma_{q_2}}{\Lambda_{22}} \approx \frac{\sigma_{q_3}}{\Lambda_{33}}.$$

Using the  $\sigma_{q_i}$ 's given in (3.31), and assuming that the longitudinal flux has a correlation length on the order of  $\ell$  (the conductivity scale in the horizontal) leads to rough estimates for the flux correlation scales as follows:

$$\Lambda_{11} \approx \ell$$

$$\Lambda_{22} \approx \sqrt{\frac{\pi}{32} \epsilon} \ell \approx 0.3 \sqrt{\ell \ell_3} \quad (3.32)$$

$$\Lambda_{33} \approx \sqrt{\frac{4\pi}{32} \epsilon} \ell \sim 0.6 \sqrt{\ell \ell_3}.$$

Thus, although the transverse flux components have very small variances, their fluctuation scale is also very small. As a consequence, the terms  $\partial q_i / \partial x_i$  ( $i=2,3$ ) appearing in the mass conservation equation may not be negligible. This explains why the "perfectly stratified" flow might appear nearly one-dimensional in the large, while still retaining three-dimensional features at the local scale.



The actual spatial structure of the flux vector field is probably more complex than the above analysis would suggest. However, it is sufficient here to observe that the flux vector has sharply contrasting scales of fluctuations in different directions and components, while the hydraulic head field is only slightly anisotropic (as can be seen from Figure 3.4). The practical implication of these findings for groundwater flow in stratified subsurface formations is now examined.

### 3.5 Discussion of the Anisotropic Case (Stratified Flow Systems)

Some of the new results developed above have direct implications for field problems, as most subsurface formations exhibit some degree of horizontal or near-horizontal layering (see Figure 3.5). The spatial structure of the flow field for statistically anisotropic conductivities was not fully understood, it seems, although stochastic solutions were available from the work of Gelhar and Axness (1983) and others. In order to illustrate our findings, we will consider the case of an aquifer with significant vertical-to-horizontal anisotropy, say  $\ell_3/\ell_1 = 1/5$ , and isotropy in the horizontal plane of stratification. The mean flow is assumed, as before, to be parallel to the plane of stratification. The log-conductivity spectrum is assumed to be the 3D anisotropic Markov model. For illustration, we will use typical length scale values as follows:

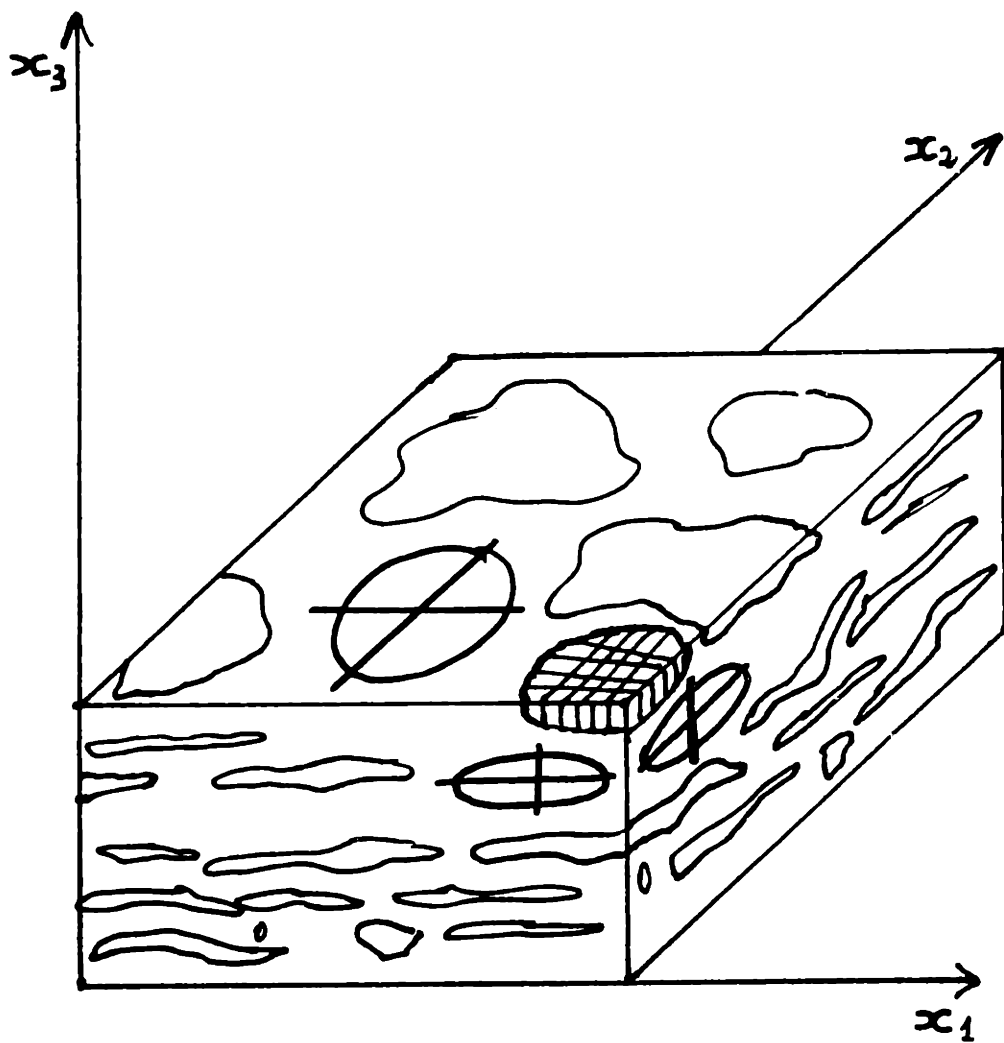


Figure 3.5: Sketch of a statistically layered porous medium. The ellipses represent contours of constant correlation length (anisotropy ellipses in different planes, or anisotropy ellipsoid in 3D space) for the log-conductivity field.

$$\ell_1 = \ell_2 \simeq 1\text{m}, \ell_3 \simeq 0.20\text{ m.}$$

We now discuss some of the most salient features of the flow field, based on the statistical analysis of spectral solutions developed in this section. Perhaps the most important point to be made here concerns the *correlation structure* of the flow field, in terms of hydraulic head and flux: see figures (3.5), (3.6) and (3.7). The hydraulic head exhibits near-perfect isotropy in the cross-flow plane (perpendicular to stratification). For the example above, the correlation scale of the head perpendicular to strata would be about 7 m, that is about 40 times larger than the conductivity scale in the same direction ( $\ell_3 = 0.20\text{m}$ ). The correlation scale of head in the horizontal direction across flow is on the same order, about 7.5 m. Finally, the correlation scale of head along the mean flow direction is half smaller, about 3m. These numbers are very close to those obtained for the isotropic case  $\ell_1 = \ell_2 = \ell_3 = 1\text{m}$ . Thus, it appears that *the spatial structure of the hydraulic head is not sensitive to the anisotropy ratio*. Furthermore, for the anisotropic case at hand, the head will be very strongly correlated over distances on the order of one or a few meters. In fact, the hydraulic head should appear nearly constant vertically over a few layer thicknesses.

In contrast, we have seen that the vertical flux component  $q_3$  has a scale of fluctuation presumably on the order of 0.20m along  $x_3$  perpendicular to stratification. This is just the same as the conductivity correlation scale  $\ell_3$ , or "layer thickness". Figure (3.6) shows that the transverse flux component  $q_2$  also has a small correlation scale (0.10m) along  $x_2$ , parallel to stratification. On the other hand, the longitudinal flux  $q_1$  presumably has a much smaller scale of fluctuation transverse to the mean flow (0.20m) than along the mean flow (1m). Thus, the flux vector field appears strongly anisotropic as illustrated on the bottom parts of Figures (3.6) and (3.7). This is in contrast with the near isotropic character of the head field (except for a ratio 1:2 in the horizontal plane).

Consider now a very shallow aquifer ( $L_3 \leq 3m$ ) and a deep aquifer ( $L_3 \geq 100m$ ), with correlation scales  $\ell_1 = \ell_2 = 1m$  and  $\ell_3 = 0.20m$  as before. Because the vertical head correlation scale is about 7m, the head will appear nearly constant vertically in the shallow aquifer:

$$Q_3 = -K \frac{\partial H}{\partial x_3} \simeq 0. \quad (3.33)$$

Upon vertical averaging, head field in the shallow aquifer system behaves nearly two-dimensionally, (or one-dimensionally) as aquifer thickness decreases. However, the intermediate case of

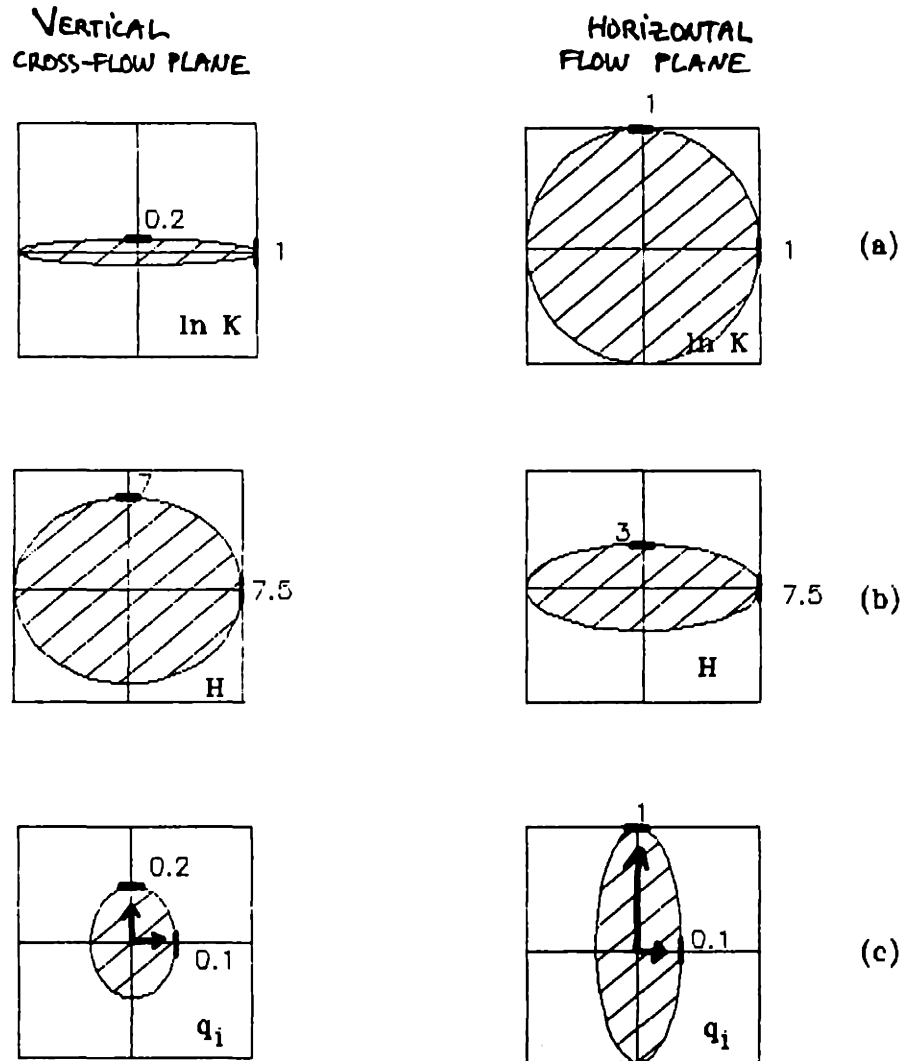


Figure 3.6: Anisotropy ellipses for (a) the log-conductivity field, (b) the hydraulic head, and (c) the flux vector in a statistically layered aquifer.

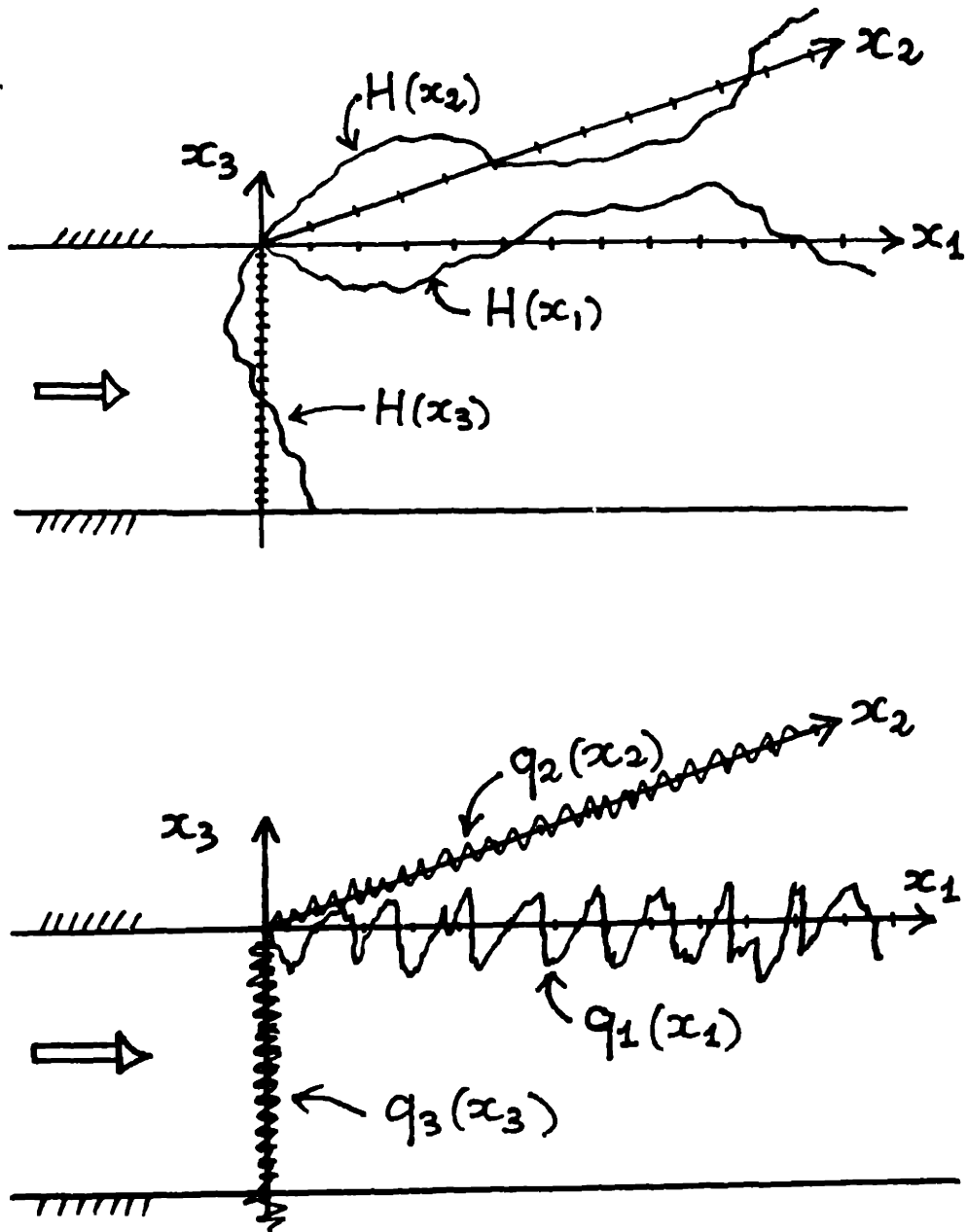


Figure 3.7: Schematic representation of the fluctuation scales of the hydraulic head (top) and of the flux vector (bottom) in a stratified aquifer

moderately shallow aquifers is more complex, as this case falls between the nearly two-dimensional case and the case of deep aquifers covered by the spectral theory. This intermediate class of flow systems is characterized by aquifer thickness in the range  $3m \ll L_0 \ll 100m$  for the case at hand.

For deep aquifers on the other hand, the hydraulic head fluctuates many times in the vertical direction. The infinite domain spectral theory holds in this case, and predicts that the flow system behaves one-dimensionally at the large scale, with the effective conductivity in the mean flow direction equal to the arithmetic mean conductivity. This result indicates that the vertical fluctuations of the conductivity and of the longitudinal head gradient are effectively decoupled. Indeed, the same result could be obtained by vertically averaging the Darcy equation:

$$Q_1 = -K \frac{\partial H}{\partial x_1}$$

and assuming that the fluctuations of  $K$  and  $\partial H/\partial x_1$  are independent of each other in the vertical.

The limitations of the infinite domain approach for the case of aquifers of finite thickness have been recognized in the past. Naff and Vecchia (1986) developed quasi-analytical

solutions for confined stratified aquifers with finite thickness. They found that the head variance increases to infinity as the ratio of layer thickness to aquifer thickness ( $\ell_3/L_3$ ) increases. This is in accordance with the fact that the flow system becomes two dimensional (in this case a Hole-Spectrum is needed in order to obtain finite head variance -- see Table 3.2). However, these authors do not seem to recognize the fact that the vertical head correlation in an infinite domain is large ( $7\ell$ ) and nearly independent of the anisotropy ratio. This finding provides a simple criterion for evaluating the range of aquifer thickness for which the infinite domain theory applies: aquifer thickness must be on the order of several tens of horizontal conductivity scales or more. This simple rule does not seem to have been recognized in the past. On the other hand, for very shallow aquifers with thickness on the same order as the horizontal conductivity scale, a two-dimensional theory based on vertical averages could perhaps be used as a first approximation.

Let us now focus exclusively on the case of deep stratified aquifers for which the spectral theory holds. In these cases, the hydraulic head standard deviation appears to be proportional to the geometric mean of horizontal and vertical correlation scales ( $\sqrt{\ell_1 \ell_3}$ ), independently of the anisotropy ratio ( $\ell_3/\ell_1$ ). Thus, two different types of aquifers such as ( $\ell_1 = 1\text{m}$ ,  $\ell_3 = 0.2\text{m}$ ) and ( $\ell_1 = 4\text{m}$ ,  $\ell_3 = 0.05\text{m}$ ) lead to the same head



variance -- although the detailed structure of the flow field may be very different. This shows that the value of head variance does not indicate the degree of anisotropy of the velocity field in stratified aquifers.

It is particularly instructive to examine the limit cases  $\ell_1, \ell_2 \rightarrow \infty$  and  $\ell_3 \rightarrow 0$  (the anisotropy ratio goes to zero in both cases: limit of perfect stratification). The first case,  $\ell_1 \rightarrow \infty$ , corresponds to an infinite horizontal correlation scale. We have seen that the vertical head correlation length is proportional to  $\ell_1$ , so that it must also become infinite. Therefore, the spectral theory will not hold in this case for any finite aquifer thickness, however large. One must dismiss the case  $\ell_1 \rightarrow \infty$  as pathological. Examine now the case  $\ell_3 \rightarrow 0$  corresponding to infinitely small layer thickness. In this case the infinite domain theory seems to apply, and equation (3.3.1) shows that:

$$\begin{aligned}\sigma_h &\rightarrow 0 \\ \sigma_{q_2}, \sigma_{q_3} &\rightarrow 0 \\ \sigma_{q_1} &= \sigma_f K_G J_1.\end{aligned}\tag{3.34}$$

Note that  $\sigma_{q_2}$  and  $\sigma_{q_3}$  vanish, implying that the transverse flux components vanish identically, and the head remains constant in vertical planes across the mean flow direction. Thus the flow

field appears inherently one-dimensional, which explains why the ensemble head variance vanish (consider the equivalence of ensemble mean and 3D averages: the 3D averaged variance of a 1D process must vanish). However, this result turns out to be inconsistent, as mass balance would require that  $Q_1$  be constant for one-dimensional flow. This clearly contradicts the result ( $\sigma_{Q_1} \neq 0$ ) obtained above. Again, this case is a singular limit of the three-dimensional spectral theory and must be dismissed.

In summary, we have shown that the limit cases  $\ell_1 = \infty$  and  $\ell_3 = 0$  are meaningless in the framework of the three-dimensional, infinite domain theory. Nevertheless, the asymptotic analysis of strongly stratified aquifers ( $\epsilon \ll 1$ ) remains valid as long as  $\epsilon \neq 0$ . The asymptotic solutions (3.31) hold for small anisotropy ratios, provided that the aquifer thickness be "significantly larger" than about  $10 \ell_1$ , where  $\ell_1$  is the horizontal conductivity scale. Concerning the flux vector, it is instructive to note that the longitudinal flux component has a variance about twice as large as for the isotropic case, and is independent of  $\epsilon$  for  $\epsilon$  small. The variance of the transverse flux components is much smaller, on the order of  $\epsilon$ , so that nearly one-dimensional flow obtains at the large scale for deep stratified aquifers.

It may be useful to end this section with some remarks concerning the meaning of the so-called "anisotropy ratio". All along, we assumed implicitly that the length scale ratio  $\epsilon = \ell_3/\ell_1$  expresses to some kind of anisotropy in the conductive properties of the statistically layered formation. We will show in fact that  $\epsilon$  is equivalent to the square root of some kind of conductivity anisotropy ratio to be defined shortly.

The interpretation of  $\epsilon$  in terms of a conductivity anisotropy ratio is obtained by re-scaling the coordinate system in such a way that the random conductivity field becomes isotropic in the rescaled coordinates:

$$x'_i = x_i/\ell_i. \quad (3.35)$$

Starting with an ellipsoidal log-conductivity field  $F(\underline{x})$  with covariance function:

$$R_{FF}(\underline{\xi}) = R_{FF}(\sqrt{\xi_1^2/\ell_1^2 + \xi_2^2/\ell_2^2 + \xi_3^2/\ell_3^2})$$

we obtain indeed an isotropic field  $F(\underline{x}')$  in the new coordinates:

$$R_{FF}(\underline{\xi}') = R_{FF}(\sqrt{\xi_1'^2 + \xi_2'^2 + \xi_3'^2})$$

Furthermore, the governing flow equation (3.3) written in the rescaled coordinates takes the form:

$$\frac{\partial}{\partial x'_i} (K_{ij}(\underline{x}') \cdot \frac{\partial H}{\partial x'_j}) = 0 \quad (3.36)$$

where the  $K_{ij}(\underline{x}')$  tensor appears as the product of a deterministic anisotropic conductance tensor and a statistically isotropic random field conductivity, as shown below:

$$K_{ij}(\underline{x}') = \begin{bmatrix} \frac{K_G}{K_{11}} & 0 & 0 \\ 0 & \frac{K_G}{K_{22}} & 0 \\ 0 & 0 & \frac{K_G}{K_{33}} \end{bmatrix} \cdot K(\underline{x}') \quad (3.37)$$

$$K_{11} = \left[ \frac{\ell_1}{\ell_3} \right]^2 K_G$$

$$K_{22} = \left[ \frac{\ell_2}{\ell_3} \right]^2 K_G$$

$$K_{33} = K_G$$

In the case of isotropy in the plane of stratification ( $\ell_1 = \ell_2$ ), this yields a formal equivalence between length scale

anisotropy and local deterministic conductivity anisotropy in the form:

$$\epsilon = \frac{\ell_3}{\ell_1} = \sqrt{\frac{K_{33}}{K_{11}}} \quad - \quad (3.38)$$

This suggests that a typical "deterministic anisotropy" on the order  $K_{33}/K_{11} \simeq 1/100$ , corresponds to a "length scale anisotropy" on the order  $\epsilon = 1/10$ . However, this interpretation of anisotropy should be taken "with a grain of salt": the *deterministic* anisotropy defined above should be distinguished from the concept of a large scale *effective* anisotropy. Indeed, the spectral solutions developed by Gelhar and Axness (1983) show that the effective conductivity anisotropy is in fact independent from  $\epsilon$  when  $\epsilon$  is small, being asymptotically equal to the ratio of harmonic to geometric means. In any case, it is still instructive to think of the length scale ratio  $(\ell_3/\ell_1)$  as equivalent to the square root of some deterministic conductivity ratio. The form of the scaled flow equation (3.36) also suggests more generally that water flow in a stratified heterogeneous formation results from complex local interactions between purely isotropic random effects and deterministic anisotropy effects.

### 3.6 Head Moments for the Hole-Markov Spectrum and Low Wavenumber Effects

In order to ascertain that the previous results are physically meaningful, we investigate in this section the behaviour of the head process for a different input spectrum: the Hole-Markov spectrum Table 3.1. The effect of the "hole" here is to reduce the low-wavenumber content of the log-conductivity field, compared to the Markov model used previously. This may affect the behaviour of the head field, particularly by reducing its correlation range.

Assuming again  $\ell_1 = \ell_2 = \ell$  and  $\epsilon = \ell_3 / \ell$ , the 3D anisotropic Hole-Markov spectrum for  $\ln K$  can be written as:

$$S_{ff}(\mathbf{k}) = \frac{4\sigma_f^2 \ell^2 \ell^3}{3\pi^2} \cdot \frac{(\ell^2 (k_1^2 + k_2^2) + \ell_3^2 k_3^2)}{[1 + \ell^2 (k_1^2 + k_2^2) + \ell_3^2 k_3^2]^3}$$

Plugging this into (3.10) gives the head covariance in the form

$$R_{hh}(\xi) = \left(\frac{\pi}{8} \sigma_f^2 J_1^2 \ell \ell_3\right) \cdot I(\xi) \quad (3.39)$$

$$I(\xi) = (2/\pi\ell)^3 \cdot \iiint_{-\infty}^{+\infty} \frac{k_1^2 (k_1^2 + k_2^2 + \epsilon^2 k_3^2) \cdot \cos(k\xi)}{k^4 [\ell^{-2} + (k_1^2 + k_2^2) + \epsilon^2 k_3^2]^3} \cdot d\mathbf{k}$$

The head variance obtains by evaluating the  $I(\xi)$  integral analytically at  $\xi = 0$ . The computation is detailed in Appendix 3.G, and the result is:

$$\sigma_h^2 = \frac{1}{16} \left(\frac{\pi}{2}\right)^6 \sigma_f^2 J^2 \ell_G^2 \cdot G(\epsilon) \quad (3.40)$$

with:

$$G(\epsilon) = \frac{1}{\epsilon} \cdot \frac{\epsilon^2}{\epsilon^2-1} \left\{ -1 + \frac{2\epsilon^2-1}{\epsilon\sqrt{\epsilon^2-1}} \ln \left[ \frac{\epsilon+\sqrt{\epsilon^2-1}}{\epsilon-\sqrt{\epsilon^2-1}} \right] \right\} \quad \text{for } \epsilon > 1$$

$$G(\epsilon) = 4/3 \quad \text{for } \epsilon = 1$$

$$G(\epsilon) = \frac{1}{\sqrt{1-\epsilon^2}} \cdot \left\{ \frac{\epsilon}{\sqrt{1-\epsilon^2}} + \frac{1-2\epsilon^2}{1-\epsilon^2} \cdot \arcsin(\sqrt{1-\epsilon^2}) \right\} \quad \text{for } \epsilon < 1.$$

When the geometric scale  $\ell_G = \sqrt{\ell_1 \ell_3}$  is kept fixed, this gives the following asymptotic results for the strongly anisotropic cases  $\epsilon \gg 1$  (vertical layers) and  $\epsilon \ll 1$  (horizontal layers):

$$\epsilon \rightarrow \infty: \quad \sigma_h^2 \approx \frac{1}{16} \left(\frac{\pi}{2}\right)^6 \sigma_f^2 J^2 \ell_G^2 \cdot \frac{4\ln(2\epsilon)-1}{\epsilon} \rightarrow 0 \quad (3.41)$$

$$\epsilon \rightarrow 0: \quad \sigma_h^2 \approx \frac{1}{16} \left(\frac{\pi}{2}\right)^7 \sigma_f^2 J^2 \ell_G^2 \quad (3.42)$$

In the isotropic case ( $\epsilon = 1$ ), the head variance is:

$$\epsilon = 1: \sigma_h^2 = \frac{1}{12} \left(\frac{\pi}{2}\right)^6 \sigma_f^2 J^2 \ell_G^2 \quad (3.43)$$

The results obtained for the isotropic case ( $\ell_3 = \ell_1$ ) and the anisotropic case ( $\ell_3 \ll \ell_1$ ) resemble those previously obtained with the Markov spectrum without a hole. The following table summarizes the different values of  $\sigma_H$  obtained for the Markov and Hole-Markov spectra for various degrees of anisotropy.

Anisotropy $\epsilon = \ell_3 / \ell_1$	Markov Spectrum ( $\lambda_i$ ): $\sigma_h / (\sigma_f J \lambda_G)$	Hole-Markov Spectrum ( $\ell_i$ ): $\sigma_h / (\sigma_f J \ell_G)$
$\epsilon \ll 1$ :	$\sqrt{\pi/8} \approx 0.63$	$(\pi/2)^{7/2}/4 \approx 1.21$
$\epsilon = 1$ :	$1/\sqrt{3} \approx 0.58$	$\sqrt{1/12} (\pi/2)^3 \approx 1.12$
$\epsilon \gg 1$ :	-----	$\frac{4 \ln(2\epsilon)}{\epsilon} \rightarrow 0$

The comparative table above shows that the head standard deviations will not be the same if the  $\ell_i$ -scales of the Hole-Markov are taken equal to the  $\lambda_i$ -scales of the Markov spectrum. Remarkably, it appears that the same head variances are obtained with the two spectra by taking the length scales of the Hole-Markov spectrum to be half the correlation scales of the Markov spectrum, i.e.:



$$\ell_1 = \lambda_1/2.$$

Furthermore, it appears that the head variance for strongly anisotropic formations (such that  $\ell_3 \ll \ell_1$ ) is approximately equal to the head variance obtained for an equivalent isotropic medium with correlation scale  $\ell_G = \sqrt{\ell_1 \ell_3}$ . Recall that the same observation holds for the Markov model. In addition, the table also shows that the head variance vanishes in the limit for strongly anisotropic vertical formations ( $\ell_3 \gg \ell_1$ ) if  $\ell_G$  is kept constant.

In order to complete the comparison between the Markov and Hole-Markov spectral models, it may be instructive to compare the head correlation functions obtained in the two cases. This would help quantify the influence of the input log-conductivity spectrum (or correlation function) upon the spatial structure of the head field. Specifically here, one may expect that the "Hole" model (spectrum with a low wavenumber hole) produces a head field with smaller correlation length. The question is: how important is this effect? And finally: how sensitive is the spatial structure of the solution with respect to the assumed shape of the log-conductivity spectrum?

For the Hole-Markov model, Appendix (3.G) develops a

close-form expression for the transverse correlation function  $R_{hh}(0,0,\xi)$  in the isotropic case  $\epsilon=1$ . The final result is reproduced below:

$$\epsilon = 1: \frac{R_{hh}(0,0,\xi_3)}{\sigma_h^2} = \frac{12}{s_3} \left\{ \frac{2}{s_3} \left[ \frac{1-e^{-s_3}}{s_3} - e^{-s_3} \right] - \left( 1 + \frac{s_3}{4} \right) e^{-s_3} \right\} \quad (3.44)$$

One way to compare the Markov and Hole-Markov models is to evaluate the e-correlation lengths, i.e., separation distance at which the correlation drops below  $e^{-1}$ . The e-correlation length of head is about  $7\lambda$  for the Markov-model, and about  $3\ell$  for the Hole-Markov model. This indicates that the head correlation across flow is about half smaller for the Hole model, based on  $\lambda_i = \ell_i$ . On the other hand, recall that the head variances obtained for the two models become equal if one chooses  $\ell_i = \lambda_i/2$ . With this choice, the head correlation would appear 4 times smaller when using the Hole model. Perhaps the most rational approach is to choose the scales  $\ell$  and  $\lambda$  in such a way that the e-correlation scales of the two random fields coincide. It can be shown that this particular choice corresponds to  $\ell = \lambda/0.723$  (from Table 2.2 of Vomvoris, 1986). It does not seem that this choice leads to a better agreement between the head solutions obtained by the two models.

We conclude that the spatial structure of the head field is fairly sensitive to the choice of the log-conductivity spectrum. For the 3D isotropic case, the head correlation lengths are increased with increasing spectral density at low wavenumbers, all other quantities being held constant (fixed head variance). On the other hand, remember that the head random field becomes non-stationary with infinite correlation length in two dimensions, unless the spectral density of log-conductivity vanishes at zero wavenumber (see Table 3.2). This indicates that the effect of large scale conductivity fluctuations becomes more significant as the degree of freedom of flow decreases from 3 to 2-dimensional flow. One may think of 3D anisotropy as an intermediate case between the 2 and 3-dimensional isotropic cases.

Our finding that the large scale fluctuations of the conductivity field have a significant effect on the spatial structure of the head field raises new questions about the appropriate determination of conductivity spectra from field measurements. In our view, the available spectral analysis of field-measured conductivities (Bakr, 1976) do not lead to favor the Hole-Markov over the Markov-spectrum or vice-versa. This is

due to the fact that the low wavenumber range of the spectrum cannot be determined with reasonable confidence for wavenumbers near or below the inverse domain size (standard estimates of spectral confidence interval also break down in this range). Rather, we feel that the size of the domain of interest should be used as an extra parameter to determine the appropriate cut-off of the "measured" log-conductivity spectrum at some low wavenumber, in such a way that essentially all fluctuations larger than the inverse domain size be removed. The Hole-Markov model is just one way of carrying on the cut-off procedure in an implicit way. However, a different approach, which departs from the "infinite domain" postulate, will be developed in Section 4.4 of Chapter 4 in order to clarify the effects of finite domain size.

**CHAPTER 4: EXTENSIONS OF SPECTRAL THEORY:  
NON-PERTURBATIVE SOLUTIONS, SPECTRAL CONDITIONING AND UNCERTAINTY**

**4.1 Introduction: Sources of Errors in Standard Spectral  
Solutions**

This chapter is devoted to the improvement and generalization of the spectral perturbation solutions of saturated flow developed earlier (Chapter 3). By exploring the stochastic flow problem from a somewhat broader viewpoint, we hope to shed some light on the approximations involved in the standard spectral solutions (see also Chapter 6 for a comparison with direct numerical simulations). More importantly, our goal is to develop alternative approaches for obtaining realistic yet tractable solutions of stochastic flow, and related phenomena like dispersive solute transport.

One of the major advantages of the spectral perturbation theory, as it stands, is its high potential for producing tractable closed form results. On the other hand, this theory presumably suffers some drawbacks due to the approximations that were made. In the forthcoming sections, we will develop *non-perturbative* solutions method (Section 4.2), as well as new *perturbative* solutions (Section 4.3), and suggest possible extensions of the spectral theory to include non-stationarity or finite-size effects (Section 4.4). In the preliminary study that

follows, we review some of the most significant sources of "errors" in order to clarify the weak points of the current spectral theory.

There are two levels of approximations involved in the standard spectral solution method: first, the "solution errors" due to the approximate solution of the postulated stochastic flow equation, and second, the "model errors" due to the approximate representation of real world heterogeneities by stationary and ergodic random fields. The perturbation approximations belong to the first category, while the basic assumptions of infinite domain, statistical homogeneity, and ergodicity of the log-conductivity field, belong to the second category. Let us now review in some detail the potential inaccuracies of the current spectral theory, due to approximations made at the "solution" level and at the "model" level, respectively.

Solution errors can be identified through a formal, qualitative comparison of spectral and exact solutions, assuming that the basic premises of the spectral theory are true. Hence, in keeping with the spectral approach, let us assume for the moment that the flow field is indeed governed by the stochastic equation (3.1), that the domain is infinite, and the log-conductivity  $\ln K(\underline{x})$  is a Gaussian, stationary and ergodic random field, with first and second order moments invariant by

translation. Based on these premises, the standard spectral perturbation approach (Chapter 3) requires some additional hypotheses and approximations in order to arrive at closed form solutions:

- (i) All second order and higher order terms  $O(\sigma^p)$ ,  $p \geq 2$ , are neglected in the flow equation governing head.
- (ii) The random fields  $h$ ,  $\nabla H$  and  $Q$  are assumed to be stationary and ergodic in the first and second moments (recall that  $h$  is the head perturbation  $H - \langle H \rangle$ ).
- (iii) The random fields  $h$ ,  $\nabla H$  and  $Q$  are implicitly assumed to be nearly Gaussian, so that knowledge of their first and second moments (mean and covariance function) suffices to determine their statistical properties entirely.

Intuitively, the validity of all three requirements depends on  $\sigma_f$  being small. This is particularly obvious for (i), but not as obvious for (ii) and (iii). Some results in the literature suggest that stationarity and normality (for heads) are satisfied asymptotically as  $\sigma_f \rightarrow 0$ , but may not hold as  $\sigma_f$  increases. Specifically, Gutjahr and Gelhar (1981) showed that if  $\sigma_f \ll 1$  then the head field is stationary in the case of three-dimensional isotropic  $\Omega_n K$  fields whose covariance function satisfies:

$$\int_0^{\infty} \xi R_{ff}(\xi) d\xi < \infty.$$

This relation is satisfied in particular for any isotropic  $R_{ff}(\xi)$  that is positive everywhere and has finite integral correlation length (see Table 2, Chapter 3). Also by looking at the head covariance (3.22) obtained for a Markov spectrum, one can see that:

$$\lim_{\xi \rightarrow \infty} R_{hh}(\xi) = 0$$

which is a sufficient condition for ergodicity in the first and second order increments (cf. Yaglom, 1962, 1.4). Unfortunately, this only proves that  $h(\underline{x})$  is asymptotically stationary and ergodic as  $\sigma_f \rightarrow 0$  -- since a perturbation method was used to establish the proof. In fact, it appears from the detailed perturbation analysis (3.4-3.6) that the apparent stationarity in the mean head gradient results from neglecting second order terms  $O(\sigma^2)$  in the equations. This suggests that the solution may not be stationary unless  $\sigma_f$  is small.

Similarly, Gutjahr (1984) showed that the first order spectral perturbation solutions are exact for arbitrary  $\sigma_f$  if it can be assumed that  $(\underline{\nabla}H, f)$  are jointly Gaussian. However, the point is precisely that the random fields  $\underline{\nabla}H$  and  $Q$  become increasingly skewed (non-Gaussian) as  $\sigma_f$  increases. In turn,



this implies that the standard spectral perturbation method becomes increasingly inaccurate as the skewness of the solution increases with  $\sigma_f$ . Indeed, non-Gaussian random fields cannot be completely characterized with first and second moments alone. Some of the numerical experiments of Chapter 6 will confirm the non-Gaussian character of the flux or velocity field.

In summary, we argue that a large log-conductivity variance could yield non-negligible high order terms in the perturbation equations. This in turn produces two types of effects that cannot be captured by the first order spectral perturbation solution:

- (i) non stationary behavior of first and second moments
- (ii) non Gaussian distribution of the random field solution.

At first sight, it seems natural to try developing higher order perturbation expansions in order to predict more accurately the statistical behavior of highly variable flow fields. An effort in this direction was pursued by Dagan (1985). However, this author did not obtain third or higher order moments, as would be needed to characterize a non-Gaussian behavior. In addition, it should be kept in mind that the perturbation expansion admittedly may not converge at all for  $\sigma_f > 0$ , even though the first order term does converge to the

exact solution as  $\sigma_f \rightarrow 0$ .

The distinction between convergent and asymptotic expansion is well documented in the literature (see Bender and Orszag, 3.8, 1978). Consider for instance the following expansion of the head perturbation  $h$  in the small parameter  $\sigma$ :

$$h^{(N)} = h_0 + \sigma h_1 + \sigma^2 h_2 + \dots + \sigma^N h_N \quad (4.1)$$

The  $N$ th-order approximation  $h^{(N)}$  may possibly be asymptotic to the exact solution  $h$ , i.e.:

$$|h^{(N)} - h| \ll \sigma^N \text{ as } \sigma \rightarrow 0, N \text{ fixed}$$

... even though the series diverges, i.e.:

$$\lim_{N \rightarrow \infty} |h^{(N)} - h| \neq 0, \sigma > 0 \text{ fixed.}$$

Accordingly, one should not expect too much improvement from higher order solutions beyond the first few terms; there is even the possibility that "higher order" approximations be less accurate for a given, fixed value of  $\sigma$ . In fact, the work by Dagan (1985) shows that the head covariance is not changed much by using second order rather than first order expansions. For instance, the head variance obtained by numerical integration of

Dagan's spectral solution for a 3D isotropic Markov field is only slightly decreased as follows (Lynn Gelhar, personal communication):

$$\text{Var}(h)_2 = \frac{1}{3} (1-0.058 \sigma_f^2) \sigma_f^2 J^2 \lambda^2 \quad (4.2)$$

compared to the first order result (Eq. 3.21):

$$\text{Var}(h)_1 = \frac{1}{3} \sigma_f^2 J^2 \lambda^2.$$

The difference between these two expressions is quite mild for log-conductivity standard deviations on the order of unity. This indicates that the head variance is relatively unaffected by high order interactions. However, the most interesting high order effects may have been "missed", as only three-point covariance functions can capture the "skewness effects" due to large  $\sigma_f$ . Moreover, it is also worth noting that the type of higher order spectral perturbation such as used by Dagan (1985) does not address the "large variance nonstationarity effects" discussed above.

In the present work, we will not pursue the classical approach of developing higher order expansions. Rather we develop a more general non-perturbative approach based on exact statistical identities in order to assess the validity of the

standard first order spectral solutions (Section 4.2). This will lead us also to propose a new perturbation solution for the flux spectrum (Section 4.3).

Let us now focus briefly on the second category of errors, the so-called "model errors" defined earlier. In view of real field situations, it would seem that it is not always possible to identify uniquely a stationary  $\Omega_n K$  field with a definite correlation scale. Thus, the ideal case postulated in Chapter 3 may not be encountered often in actual practice. In our view, this type of identification problem may be due in practice to inadequate sampling of field data (geometry and spacing of measurement network), and/or to the particular spatial structure of the subsurface formation, which may involve some large scale inhomogeneities. This kind of situation could lead to inconsistent random field identification, for instance with apparent correlation scales on the order of domain size (see some of the results reported by Hoeksema and Kitanidis, 1985). With proper detrending, however, it is often possible to identify a definite correlation length based on the assumption that the detrended field is stationary. Nevertheless, the correlation scale determined in this manner may still depend on the particular subregion of investigation, as suggested by some field studies. The reader is referred to the data review of Chapter 2 for more details and references.

Another related situation of interest is the case where the flow or transport process of interest takes place on increasingly larger regions as time evolves. This occurs in a number of cases of great importance for contamination studies, for instance in the case of a contaminant plume spreading from a local source in an aquifer, or an unsaturated moisture plume spreading from a local infiltration area. In both cases, the "global scale" of interest evolves in time, and it is conceivable that the most dominant contributions from spatial heterogeneities occur at varying length scales, as the size of the plume evolves. This idea could be related to our earlier observation that the formation's heterogeneity is only *locally* stationary around some given trend, and with a given correlation scale, both depending on the size of the region. This type of finite scale problem will be approached in the last section of this chapter (Section 4.4) by using band-pass self-similar spectra, and by developing the idea of *spectral conditioning*. The preliminary results obtained there will show explicitly the scale dependence and uncertainty of the head variance, effective conductivity, and macrodispersivity for flow and transport phenomena taking place over finite domains.

## 4.2 Non-Perturbative Spectral Solutions and Statistical Symmetries

### 4.2.1 Summary:

In this lengthy section, we show that a stationary solution of the stochastic flow equation, if it exists, must satisfy a certain set of statistical relations, notably in terms of the spectrum of the flux vector and head gradient. These statistical identities are derived directly from the continuity equation, and by taking into account the inherent symmetries of the flow system in any number of dimensions, particularly in the case of 3D and 2D isotropic media. These relations are used to "test" the standard spectral solutions. In the special 2D isotropic case, the effective conductivity must be identical to the geometric mean, and an exact relation is found between the flux spectrum and head spectrum. Both results are based on a conjugacy property relating the flux and head gradient in two-dimensional space with isotropic Gaussian log-conductivity. The problem of determining a general relation for the effective conductivity tensor in 3D anisotropic media is also investigated, leading to a general closed form relation in terms of the log-conductivity variance and two anisotropy length scale ratios. Note that the spectral relation obtained in the 2D case also suggested a modification of the standard spectral solutions, to be developed in a forthcoming section (4.3).

#### 4.2.2 Mass Conservation Relation:

The mass conservation or "continuity" equation for steady flow in  $m$ -dimensional space is:

$$\frac{\partial Q_i}{\partial x_i} = 0 \quad (i = 1, \dots, m) \quad (4.3)$$

where the implicit Einstein summation convention was used. We now assume that the basic premises of the standard spectral theory hold, i.e., the flux  $Q_i$  is a stationary random vector field. Whence the mean  $\bar{Q}_i = \langle Q_i(x) \rangle$  is a constant vector, and the perturbation  $q_i(\underline{x}) = Q_i(\underline{x}) - \bar{Q}_i$  is zero mean stationary. For all practical purposes here, second order stationarity suffices.

By averaging the continuity equation (4.3) and then subtracting, one obtains an equation for the mean and another equation for the perturbation, of identical form:

$$\frac{\partial \bar{Q}_i}{\partial x_i} = 0 \quad (i = 1, \dots, m) \quad (4.4)$$

$$\frac{\partial q_i}{\partial x_i} = 0 \quad (i = 1, \dots, m). \quad (4.5)$$

Because these equations are stochastically linear, and the flux

$Q_i$  was assumed stationary, the spectral representation theorem (3.7) can be used to obtain an exact relation on the spectrum of  $q_i$  from equation (4.5). The Fourier increments satisfy:

$$j k_i dZ_{q_i}^*(\underline{k}) = 0. \quad (j = \sqrt{-1}) \quad (4.6)$$

Multiplying by  $dZ_{q_j}^*(\underline{k})$  and averaging yields:

$$k_i \cdot S_{q_i q_j}(\underline{k}) = 0 \quad (j = 1 \dots m) \quad (4.7)$$

where  $S_{q_i q_j}$  is the tensor spectrum of the flux vector, whose Fourier Transform is the tensor covariance function  $R_{q_i q_j}(\underline{\xi})$ . The equivalent mass conservation condition on  $R_{q_i q_j}(\underline{\xi})$  is easily obtained by Fourier-transforming (4.7):

$$\frac{\partial R_{q_i q_j}(\underline{\xi})}{\partial \xi_i} = 0 \quad (j = 1 \dots m). \quad (4.8)$$

Now, it is easily seen that the standard first order spectral solutions developed in Chapter 3 verify mass conservation both in the mean and second order moments. The mean equation (4.4) is automatically satisfied since  $\bar{Q}_i$  is constant; and the equation (4.7) for  $S_{q_i q_j}$  is satisfied by the spectrum given in (3.17), as can be easily verified. We conclude that the



standard spectral solutions are self-consistent with respect to mass conservation, as far as first and second moments are concerned. Incidentally, we obtain for the special 1D case:

$$k S_{qq}(k) = 0$$

which shows that  $S_{qq}(k) = 0$  is a solution, i.e., the flux  $q$  must be a deterministic constant. It may seem that a flux spectrum of the form  $S_{qq}(k) = \sigma_q^2 \delta(k)$  could also be solution, i.e., the flux  $q$  could be a spatially constant random variable with variance  $\sigma_q^2$ . However this gives rise to an indeterminacy in the limit  $kS_{qq}(k)$  as  $k \rightarrow 0$  (this can be seen by replacing  $\delta(k)$  by any sequence of functions that converges to  $\delta(k)$ ). Therefore, it seems that the case  $\sigma_q \neq 0$  should not be accepted as a valid "stationary" solution in the 1D case. Gutjahr and Gelhar (1981) adopted a different view in their discussion of stationary and non-stationary two-point boundary value flow problems with  $\sigma_q \neq 0$ .

Finally, let us point out a result mentioned in Batchelor (1953). By using the continuity condition (4.7) along with the usual properties of a spectral density tensor:

$$S_{q_i q_j}(\underline{k}) = S_{q_j q_i}(-\underline{k}) \quad (4.9)$$

he obtained the following spectrum:

$$S_{q_i q_j}(\underline{k}) = \beta^2(\underline{k}) \cdot \left[ \delta_{ij} - \frac{k_i k_j}{k^2} \right] + \alpha_i(\underline{k}) \alpha_j^*(\underline{k}) \left[ 1 - \frac{\beta^2(\underline{k})}{\alpha^2(\underline{k})} \right]. \quad (4.10)$$

Here, the complex vectors  $\alpha_i(\underline{k})$ ,  $\beta_i(\underline{k})$  are mutually orthogonal, and orthogonal with the wavenumber vector (i.e.,  $\underline{\alpha} \cdot \underline{\beta} = \underline{\alpha} \cdot \underline{k} = \underline{\beta} \cdot \underline{k} = 0$ ). The scalar quantities  $\alpha^2, \beta^2, k^2$  denote the squared modulus of the vectors  $\underline{\alpha}$ ,  $\underline{\beta}$ ,  $\underline{k}$ , respectively. We will see that one can arrive at more useful special forms of the flux spectrum by considering, along with the continuity equation, the invariance of the tensor under certain transformations arising from spatial symmetries of the random flow problem, particularly for statistically isotropic conductivities in 2D and 3D space.

#### 4.2.3 Statistical Axial Symmetry for 3D Flow in Isotropic Media:

Here we consider the case of flow in a statistically isotropic formation in the infinite 3D space. The log-conductivity  $F = \ln K$  is a statistically isotropic homogeneous Gaussian random field, implying in particular that the covariance function  $R_{ff}(\underline{\xi})$  depends only on the radial separation distance  $\xi = \sqrt{\xi_1^2 + \xi_2^2 + \xi_3^2}$  (similarly the spectrum  $S_{ff}(\underline{k})$  depends only on  $k = \sqrt{k_1^2 + k_2^2 + k_3^2}$ ). We now examine the consequences of this symmetry, assuming as before that the solution ( $h$ ,  $\underline{v}H$ , and  $\underline{q}$ ) is

statistically homogeneous in space. In particular, we seek relations on the flux covariance  $R_{q_i q_j}(\xi)$  or on the spectral tensor  $S_{q_i q_j}(\underline{k})$ , in a manner somewhat similar to previous work on the statistical theory of isotropic turbulence (see the books by Batchelor 1953, Monin and Yaglom 1965, and Landahl and Mollo-Christensen 1986). However, note that the case at hand is different from isotropic turbulence in one important respect: the flow driven by a mean gradient in a random porous medium cannot be represented realistically as a statistically isotropic field in all three space dimensions, even when the underlying medium is fully isotropic. Rather, the flow field can be thought of as having statistical *axial symmetry* with respect to the mean flow direction.

In order to clarify this notion, we turn back to the basic flow equations expressed in terms of "detrended" random fields. The perturbation equations for the head and the flux vector are, respectively:

$$\begin{aligned} \frac{\partial^2 h}{\partial x_i \partial x_i} + \frac{\partial f}{\partial x_i} \frac{\partial h}{\partial x_i} - \bar{J}_1 \frac{\partial f}{\partial x_1} &= 0 \\ \bar{Q}_i &= K_G J_1 \delta_{1i} e^{\sigma^2/2} - K_G \langle e^f \frac{\partial h}{\partial x_i} \rangle \\ q_i &= K_G (e^f - e^{\sigma^2/2}) (J_1 \delta_{1i} - \frac{\partial h}{\partial x_i}) - K_G e^{\sigma^2/2} \frac{\partial h}{\partial x_i} - (\bar{Q}_i - K_G e^{\sigma^2/2}) \end{aligned} \quad (4.11)$$

where we used the stochastic Darcy equation for obtaining  $\bar{Q}_i$  and

$q_i$ . Recall that  $h$  and  $q_i$  are the statistically homogeneous perturbations of the head and the flux vector,  $\bar{J}_1$  is the only non-zero component of the constant mean hydraulic gradient (by choice of the  $x_1$  axis), and  $\bar{Q}_i$  is the  $i$ -th component of the mean flux vector. Recall also that the log-conductivity perturbation  $f(\underline{x})$  is Gaussian, and  $R_{ff}(\underline{\xi})$  is invariant under translations and rotations in the  $\underline{\xi}$ -space. In addition, all higher order moments of  $f(\underline{x})$  are expressible in terms the covariance of  $R_{ff}$ , and the  $N$ -point covariance  $\langle f(\underline{x}_1) \cdots f(\underline{x}_N) \rangle$  is also invariant under translations and rotations in  $\underline{x}$ -space. The form taken by (4.11) implies that  $h(\underline{x})$  must then be statistically invariant under rotations in the  $(x_2, x_3)$  plane, as well as invariant under reflections through the  $x_1$  axis. In particular  $R_{hh}(\underline{\xi})$  is isotropic in  $(\xi_2, \xi_3)$ , and invariant when  $(\xi_1)$  is changed into  $(-\xi_1)$ . In addition, we expect that the vectors  $g_i = -\frac{\partial h}{\partial x_i}$ , and perhaps  $q_i$ , be also invariant under such transformations. We now explore this in more detail, beginning with the head gradient vector  $g_i$ .

By using the fact that  $g_i$  is a special kind of "potential" vector, being the gradient of a scalar quantity  $h(\underline{x})$  that is statistically isotropic in the  $(x_2, x_3)$  plane, one can obtain explicit relations on the covariance tensor  $R_{g_i g_j}(\underline{\xi})$ . Indeed, it is well known that, if  $h$  is a homogeneous field, then  $g_i = \frac{\partial h}{\partial x_i}$  has the covariance tensor:

$$R_{g_i g_j}(\xi) = - \frac{\partial^2 R_{hh}(\xi)}{\partial \xi_i \partial \xi_j}. \quad (4.12)$$

On the other hand,  $R_{hh}(\xi)$  is isotropic in the  $(\xi_2, \xi_3)$  plane as explained earlier. Thus we can write: -

$$R_{hh}(\xi) = R_{hh}(\xi_1, r) \quad (4.13)$$

where  $R$  is an even function of  $\xi_1$ , and  $r$  is the 2D radial separation distance  $(\xi_2^2 + \xi_3^2)^{1/2}$  in the cross-flow-plane. By applying the chain rule of differentiation, and using the fact that  $\partial r / \partial \xi_i = \xi_i / r$  for  $i = 2$  and  $3$ , we obtain finally the head gradient covariance in terms of the head covariance:

$$R_{g_1 g_1}(\xi) = - \frac{\partial^2 R_{hh}}{\partial \xi_1^2}$$

$$j \neq 1: R_{g_1 g_j}(\xi) = R_{g_j g_1}(\xi) = - \frac{\xi_j}{r} \cdot \frac{\partial^2 R_{hh}}{\partial r \partial \xi_1} \quad (4.14)$$

$$i \neq 1, j \neq 1: R_{g_i g_j}(\xi) = R_{g_j g_i}(\xi) = - \frac{\delta_{ij}}{r} \frac{\partial R_{hh}}{\partial r}$$

$$- \frac{\xi_i \xi_j}{r^2} \left[ \frac{\partial^2 R_{hh}}{\partial r^2} - \frac{1}{r} \frac{\partial R_{hh}}{\partial r} \right].$$

These equations give the general form of the hydraulic gradient covariance tensor for the case of flow in a 3D isotropic medium. Note that  $R_{g_i g_j}$  is a symmetric tensor and an even function of  $(\xi)$  for all  $(i,j)$ , so that the identity  $R_{g_i g_j}(\xi) = R_{g_j g_i}(-\xi)$  is satisfied, as it should for any tensor covariance of a statistically homogeneous vector field. In addition, it can be seen by inspection of (4.14) that  $R_{g_i g_j}(\xi)$  is invariant under the rotation-reflexion group restricted to the transverse flow plane  $(x_2, x_3)$ . Here, rotational invariance is to be understood in the sense of tensor invariance: the tensor function is invariant when expressed in the new coordinates according to tensor transformation rules. For the case of pure rotations we have:

$$[a_{ij}] = \begin{bmatrix} 1 & 0 & 0 \\ 0 & \cos\theta & -\sin\theta \\ 0 & \sin\theta & \cos\theta \end{bmatrix}$$

with transformation rules:

$$x'_j = a_{ij} x_i; \quad x_i = a_{ji} x'_j \quad (4.15)$$

$$\frac{\partial \bullet}{\partial x_i} = a_{ij} \frac{\partial \bullet}{\partial x'_j}; \quad T_{ij} = a_{mi} a_{lj} T'_{ml}$$

The same transformation rules apply for pure reflexions, defined

as:

$$[a_{ij}] = \begin{bmatrix} 1 & 0 & 0 \\ 0 & -1 & 0 \\ 0 & 0 & 1 \end{bmatrix} \text{ or } \begin{bmatrix} 1 & 0 & 0 \\ 0 & 1 & 0 \\ 0 & 0 & -1 \end{bmatrix}.$$

Invariance is verified by checking directly from (4.14) that  $R_{g_i g_j}$  indeed transforms according to:

$$R_{g_i g_j}(\xi) = a_{i' i} a_{j' j} R_{g_{i'} g_{j'}}(\xi').$$

For the reflexions in particular, this implies that the two-point covariance of the head gradient is invariant under transformation  $\xi_2 \rightarrow -\xi_2$  or  $\xi_3 \rightarrow -\xi_3$ . In addition, it can be seen from (4.14) that  $R_{g_i g_j}(\xi)$  is also invariant under reflexions through the  $x_1$  axis ( $\xi_1 \rightarrow -\xi_1$ ). Finally, it is worth noting that the cross-covariances vanish along certain lines or planes, as can be seen in Figure 4.1:

$$R_{g_1 g_2}(\xi_1, 0, \xi_3) = 0$$

$$R_{g_1 g_3}(\xi_1, \xi_2, 0) = 0 \tag{4.16}$$

$$R_{g_2 g_3}(\xi_1, 0, 0) = 0$$

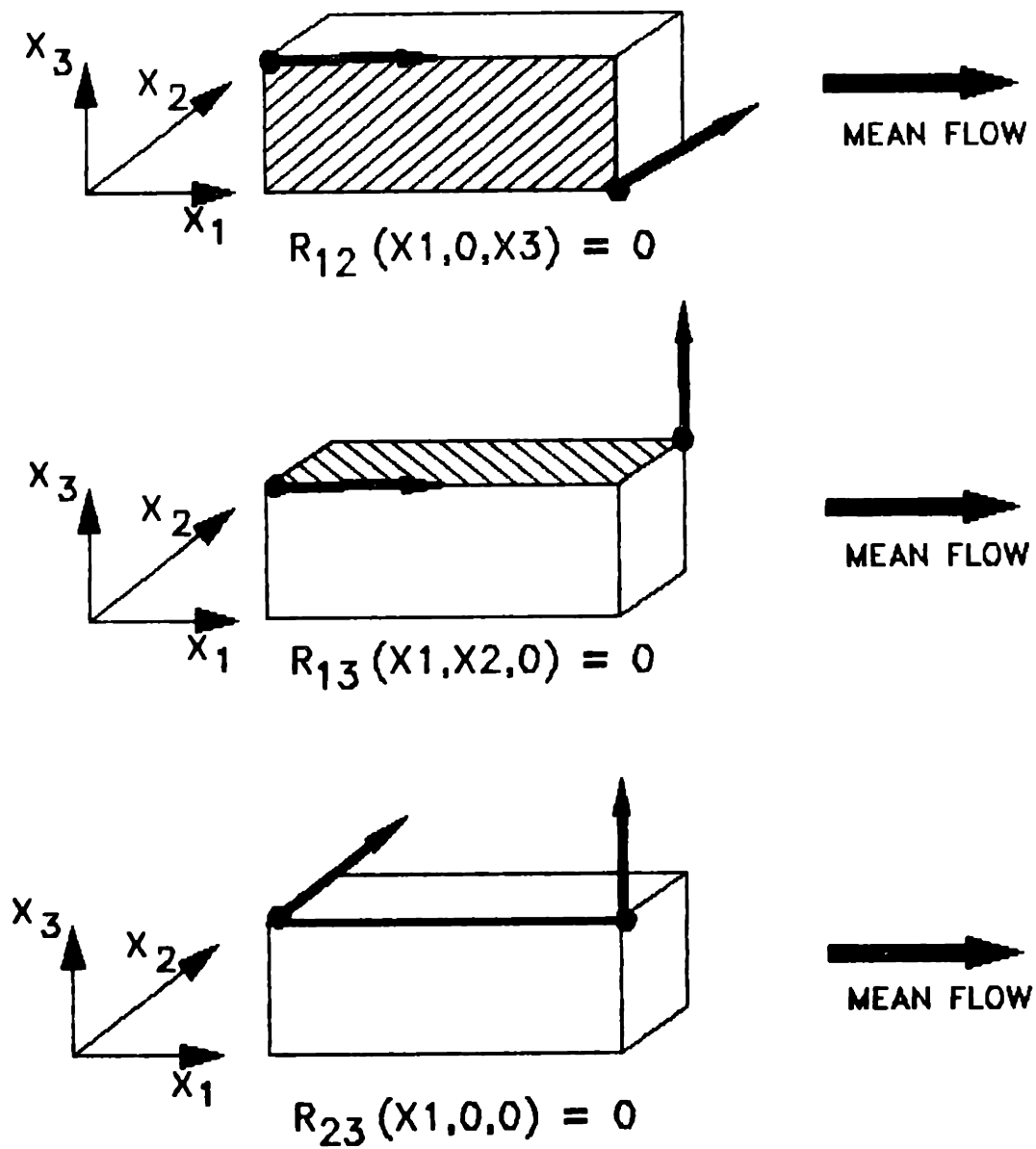


Figure 4.1 The cross-covariance function of the head gradient and flux vectors vanish along certain directions in a 3D isotropic medium.



Note in particular that all the cross-covariances at lag zero ( $\xi = 0$ ) are null. The result in (4.16) can be found by inspection of (4.14), or by looking directly at the consequences of invariance under reflexions and rotations of the  $R_{g_i g_j}(\xi)$ .

The results obtained so far can be summarized as follows:

- (i) For a 3D isotropic medium, the covariance tensor  $R_{g_i g_j}(\xi)$  of the head gradient is symmetric, invariant under rotations and reflexions in the plane transverse to flow, and under reflexions through the mean flow direction. Invariance is understood to hold under transformations of the coordinate system provided application of the usual tensor transformation rules.
- (ii) The general form of  $R_{g_i g_j}(\xi)$  is given by (4.14), and the cross-covariances in particular vanish along certain directions according to (4.16).

It is important to keep in mind that all the symmetry relations developed above are independent of the small variance approximations that were used to obtain first order spectral solutions. We now show that the first-order solutions previously

obtained for  $R_{hh}$  and  $R_{g_i g_j}$  do satisfy the symmetry properties (4.14, 4.16). This can be easily seen by observing that the  $R_{hh}(\xi)$  given in (3.22) is indeed statistically isotropic in the transverse plane, and so is the spectrum  $S_{hh}(\underline{k})$ . As a consequence, the covariance and spectrum of  $g_i = \partial h / \partial x_i$  obtained from the first order theory satisfy indeed all the invariance properties outlined above. Incidentally, note that the covariance  $R_{g_i g_j}(\xi)$  can be obtained in close form from the first order solution  $R_{hh}(\xi)$  by using (3.22) and (4.14), thus avoiding some difficult Fourier integral.

Finally, it can be shown by using the properties of the Fourier Transform that the spectrum tensor  $S_{g_i g_j}(\underline{k})$  shares the same invariance properties as  $R_{g_i g_j}(\xi)$ . More precisely, it is easily seen from  $g_i = \partial h / \partial x_i$  that  $S_{g_i g_j}$  must be of the form:

$$S_{g_i g_j}(\underline{k}) = -k_i k_j S_{hh}(\underline{k}) \quad (4.17)$$

where the spectrum  $S_{hh}$  must be invariant under rotations and reflexions in the transverse plane  $(k_2, k_3)$  -- and reflexions through the longitudinal direction  $k_1$ . All the symmetry properties previously established for  $R_{g_i g_j}$  could be deduced from (4.17) by plugging  $S_{hh}(\underline{k}) = S(k_1, \underline{k})$  and using Fourier Transforms.

We now focus our interest on the flux vector perturbation  $q_i$ , which is the physical quantity of interest for applications to contaminant transport. The Darcy equation can be used to decompose  $q_i$  into a sum of terms involving the random field perturbations:  $p(\underline{x}) = e^{f(\underline{x})} - e^{\sigma^2/2}$  and  $g_i = \partial h / \partial x_i$ . Using equation (4.11) and decomposing leads to:

$$q_i(\underline{x}) = q_i^{(1)}(\underline{x}) + q_i^{(2)}(\underline{x})$$

$$q_i^{(1)}(\underline{x}) = -K_G \{ p(\underline{x}) J_i \delta_{1i} - e^{\sigma^2/2} \cdot g_i(\underline{x}) \} \quad (4.18)$$

$$q_i^{(2)}(\underline{x}) = -K_G \{ p(\underline{x}) \cdot g_i(\underline{x}) - \langle p(\underline{x}) \cdot g_i(\underline{x}) \rangle \}.$$

The term  $K_G p(\underline{x})$  is the perturbation of the log-normal conductivity field  $K(\underline{x}) = K_G \exp(f(\underline{x}))$ , and  $g_i(\underline{x})$  is the perturbation of the head gradient vector as before. The first term  $q_i^{(1)}$  in (4.18) represents the flux perturbation produced by the separate contributions from the conductivity and head gradient fluctuations while the second term  $q_i^{(2)}$  involves the stochastic interactions between them.

The covariance tensor  $R_{q_i q_j}(\underline{\xi})$  could be worked out in principle by computing all the terms involved in  $\langle q_i(\underline{x}) \cdot q_j(\underline{x} + \underline{\xi}) \rangle$ . This leads to an expression involving third and fourth order moments of the augmented vector  $(p(\underline{x}), g_i(\underline{x}))$ . Assuming that

$(p(\underline{x}), g_i(\underline{x}))$  is jointly statistically homogeneous, up to at least fourth order moments, one obtains triple-point and four-point covariances of the form:

$$\langle u(\underline{x})v(\underline{x}+\underline{\xi}_v) w(\underline{x}+\underline{\xi}_w) \rangle = R_{uvw}(\underline{\xi}_v, \underline{\xi}_w)$$

$$\langle u(\underline{x})v(\underline{x}+\underline{\xi}_v) w(\underline{x}+\underline{\xi}_w) z(\underline{x}+\underline{\xi}_z) \rangle = R_{uvwz}(\underline{\xi}_v, \underline{\xi}_w, \underline{\xi}_z).$$

With these definitions in mind, we obtain from equation (4.18) a general expression for the flux covariance tensor:

$$R_{q_i q_j}(\underline{\xi}) = R_{ij}^{11}(\underline{\xi}) + R_{ij}^{12}(\underline{\xi}) + R_{ij}^{22}(\underline{\xi}) \quad (4.19.a)$$

where:

$$R_{ij}^{11} = K_G^2 \cdot \{ J_1^2 \cdot \delta_{1i} \delta_{1j} R_{pp}(\underline{\xi}) + e^{\sigma^2} \cdot R_{g_i g_j}(\underline{\xi}) - e^{\sigma^2/2} J_1 (\delta_{1i} R_{pq_j}(\underline{\xi}) + \delta_{1j} R_{pg_i}(-\underline{\xi})) \}$$

$$R_{ij}^{12} = K_G^2 \{ J_1 \delta_{1i} (R_{ppg_j}(\underline{\xi}, \underline{\xi}) + R_{ppg_j}(-\underline{\xi}, -\underline{\xi})) - e^{\sigma^2/2} \cdot (R_{pg_i g_j}(\underline{0}, \underline{\xi}) + R_{pg_i g_j}(\underline{0}, -\underline{\xi})) \} \quad (4.19.b)$$

$$R_{ij}^{22} = K_G^2 \{ R_{pg_i pg_j}(\underline{0}, \underline{\xi}, \underline{\xi}) - R_{pg_i}(\underline{0}) \cdot R_{pg_j}(\underline{0}) \}.$$

Despite the complicated form taken by the flux covariance tensor above, it appears that it should remain invariant under the transformations which leave  $p(\underline{x})$  and  $g_i(\underline{x})$  jointly invariant. Note that  $p(\underline{x})$  is just the scaled perturbation of the conductivity  $K(\underline{x})$ . Without any rigorous proof, we will assume that  $K(\underline{x})$  and  $g_i(\underline{x})$  are jointly axisymmetric random fields (we know this is true for the log-conductivity and for  $g_i(\underline{x})$  separately). Accordingly, the flux covariance should remain invariant under rotations-reflexions in the transverse plane, and reflexions through the longitudinal direction as explained earlier. This also implies that  $R_{q_i q_j}$  is a symmetric tensor. For completeness, observe that  $R_{q_i q_j}$  given by (4.19) does satisfy the mass conservation relation (4.8) as required.

Now, by using only the symmetry properties due to statistical isotropy (invariance to rotations and reflexions, as defined above) as well as the mass conservation relation, it is possible to come up with the general form of the covariance or spectrum of  $q_i(\underline{x})$  independently of the detailed formula given in (4.19). For instance, Batchelor (1953) gives the general form of the covariance tensor of a vector field which is *statistically axisymmetric*. By applying his results [Eqs. 3.3.9, page 43] and adding the condition of invariance under reflexions through the axis of symmetry, we obtain:

$$\begin{aligned}
 R_{q_i q_j}(\xi) = & \\
 & A(\xi_1, r) \frac{\xi_i \xi_j}{r^2} + B(\xi_1, r) \delta_{ij} \\
 & + C(\xi_1, r) \delta_{1i} \delta_{1j} + D(\xi_1, r) \cdot (\xi_i \delta_{1j} + \xi_j \delta_{1i})
 \end{aligned}
 \tag{4.20}$$

where  $r$  is the radial lag distance  $(\xi_2^2 + \xi_3^2)^{1/2}$  in the transverse plane, and  $A, B, C, D$  are even functions of  $\xi_1$ . Note that the case of spherical isotropy for  $R_{q_i q_j}(\xi)$  obtains by taking  $C = D = 0$ . This suggests that the  $A$  and  $B$  terms account for the fully isotropic part of velocity fluctuations, while the  $C$  and  $D$  terms account for those fluctuations driven by the mean head gradient (the driving force responsible for anisotropic behavior).

Similarly, by using properties of the Fourier Transform, it can be shown that the tensor of spectral densities  $S_{q_i q_j}(\underline{k})$  must be of the same form as (4.20), namely:

$$\begin{aligned}
 S_{q_i q_j}(\underline{k}) = & A \cdot \frac{k_i k_j}{k^2} + B \cdot \delta_{ij} \\
 & + C \cdot \delta_{1i} \delta_{1j} + D \cdot (k_i \delta_{1j} + k_j \delta_{1i})
 \end{aligned}
 \tag{4.21}$$

where  $A, B, C, D$  are functions of  $k_1$  and  $k_R = (k_2^2 + k_3^2)^{1/2}$ , and are even in  $k_1$ .

We now apply the mass conservation condition in its spectral form (4.7) to obtain additional conditions on  $A, B, C$  and  $D(k_1, k_R)$  as follows. Combining equation (4.7):

$$k_i S_{q_i q_j}(\underline{k}) = 0$$

with equation (4.21) above gives:

$$\begin{aligned} & (A + B) k_j \\ & + (k^2 \cdot D + k_1 \cdot C) \delta_{1j} \\ & + k_1 k_j D = 0 \end{aligned}$$

where  $k^2 = k_1^2 + k_2^2 + k_3^2 = k_1^2 + k_R^2$ , and  $j = 1, 2, 3$  respectively.

These conservation conditions on  $A, B, C, D$  can be rewritten as follows:

$$\begin{aligned} (1): & k_1 \cdot A + k_1 B + k_1 C + (k^2 + k_1^2) D = 0 \\ (2): & k_2 \cdot A + k_2 B + k_1 k_2 D = 0 \\ (3): & k_3 \cdot A + k_3 B + k_1 k_3 D = 0 \end{aligned} \tag{4.22}$$

Multiplying each equation by  $k_i$  and summing, we obtain the equivalent system of equations:

$$A + B + \frac{k_1^2}{k^2} C + 2k_1 D = 0$$

$$A + B + C + \frac{k^2 + k_1^2}{k_1^2} k_1 D = 0$$

$$A + B + k_1 D = 0.$$

This leads after some manipulations to just two independent relations:

$$k^2 D + k_1 C = 0$$

(4.23)

$$A + B = \frac{k_1^2}{k^2} C.$$

Plugging (4.23) into (4.21) finally gives the general form of the flux spectrum  $S_{q_i q_j}$  that satisfies the properties of axial symmetry (as defined earlier) and mass conservation:

$$S_{q_i q_j}(\underline{k}) = \left[ \frac{k_i k_j}{k^2} - \delta_{ij} \right] \cdot A(k_1, k_R) + \left[ \delta_{1i} \delta_{1j} + \frac{(k_1)^2}{k^2} \delta_{ij} - \frac{k_1 k_i}{k^2} \delta_{1j} - \frac{k_1 k_j}{k^2} \delta_{1i} \right] \cdot C(k_1, k_R)$$

(4.24)



where  $k$  is the spherical-radial wavenumber, and  $k_R$  is the cylindrical-radial wavenumber in the transverse plane  $(k_2, k_3)$ . Note again that  $A$  and  $C$  are even functions of  $k_1$ .

The general result given in (4.24) may now be compared to specific solutions, such as the first order spectral solutions derived in Chapter 3. Equation (4.24) also applies to isotropic turbulence by taking  $C = 0$  (recall that the case  $C = 0$  corresponds to spherical symmetry). In this case, equation (4.24) gives the correct result, with  $A(k)$  being the 3D radial spectrum of kinetic energy (see for instance Monin and Yaglom, 1965, Eq. 12.73). Let us now compare equation (4.24) with the first order spectral solution (3.18) for the case where the spectrum of log-conductivities is isotropic ( $S_{ff} = S_{ff}(k)$ ). Let us first decompose both equations (4.24) and (3.18) for a term by term comparison. This is shown below, denoting  $S_{q_i q_j}$  the general solution and  $S_{q_i q_j}^{(1)}$  the first order solution:

$$S_{q_i q_j}(\underline{k}) = C \left\{ \delta_{i1} \delta_{j1} - \delta_{i1} \frac{k_1 k_j}{k^2} - \delta_{j1} \frac{k_1 k_i}{k^2} + \frac{A}{C} \cdot \frac{k_i k_j}{k^2} + \left[ \frac{(k_1)^2}{k^2} - \frac{A}{C} \right] \delta_{ij} \right\} \quad (4.25)$$

$$S_{q_i q_j}^{(1)}(\underline{k}) = K_G^2 J_i^2 S_{ff}(k) \cdot \left\{ \delta_{i1} \delta_{j1} - \delta_{i1} \frac{k_1 k_j}{k^2} - \delta_{j1} \frac{k_1 k_i}{k^2} + \frac{(k_1)^2}{k^2} \cdot \frac{k_i k_j}{k^2} \right\}, \quad (4.26)$$

The comparison shows that the first order solution  $S_{q_i q_j}^{(1)}$  satisfies the general form of the spectrum given in (4.24) or (4.25), with the choice:

$$C(k_1, k_R) = C(k) = K_G^2 J_i^2 S_{ff}(k) \quad (4.27)$$

$$A(k_1, k_R) = A(k_1, k) = \frac{(k_1)^2}{k^2} \cdot C(k).$$

The form of the flux covariance tensor can also be found by applying a Fourier Transform to both sides of (4.24). It is worth noting that the flux covariance  $R_{q_i q_j}(\underline{\xi})$  as well as the head gradient covariance  $R_{g_i g_j}(\underline{\xi})$  must vanish along certain lines or planes when  $i \neq j$  (see Figure (4.1) above). This is due solely to certain symmetries under rotations or reflexions, and the same should hold for any solution satisfying the stationarity hypothesis. Again, we find that the first order solutions of Chapter 3 do satisfy the relations depicted in Figure (4.1).

In summary, we have obtained the general form of the spectrum of the flux vector independently of any particular perturbation approximation, assuming only that the log-conductivity field is statistically isotropic, and the flow field is statistically homogeneous (stationary). This general solution includes as a special case the first order spectral solutions of Chapter 3 (Bakr et al. 1978, Gelhar and Axness 1983). More generally, we believe that any approximate solution should yield a flux spectrum of the form (4.24) in order to be consistent with the basic statistical properties of the governing flow equation.

Finally, it is worth noting that most of the results in this section may be applied to the 2D isotropic case as well, by letting  $i = (1,2)$  rather than  $i = 1,2,3$  in tensorial expressions. For example, applying (4.24) with  $i = (1,2)$  gives the general form of the  $S_{q_i q_j}$  spectrum in the 2D case, with  $A$  and  $C$  even functions of  $\underline{k} = (k_1, k_2)$ . In fact, we will show that the form of the solutions in the special 2D case can be narrowed down further by using the special symmetry inherent to the 2D space -- leading to a conjugacy relation between flux and head gradient. This is examined next.

#### 4.2.4 Conjugacy property for 2D flow in isotropic media:

For the case of flow in a two-dimensional random porous medium, we use the streamfunction formulation to show that the stochastic flow field must satisfy a conjugacy condition (in probability) between the flux and head gradient vectors.

For details on the streamfunction formulation, the reader is referred to Bear (1972), among others. Briefly, the streamlines are defined as the set of curves tangent to the velocity field at every point in space. Note that the velocity and flux vectors are equivalent in a medium of constant porosity (normalized to unity for convenience). Thus the equation for the streamlines can be written in terms of the flux vector field as follows:

$$\frac{dx_1}{Q_1(\underline{x})} = \frac{dx_2}{Q_2(\underline{x})}.$$

The streamfunction  $\psi(\underline{x})$  is defined as:

$$\begin{aligned} Q_1(\underline{x}) &= - \frac{\partial \psi}{\partial x_2} \\ Q_2(\underline{x}) &= + \frac{\partial \psi}{\partial x_1}. \end{aligned} \tag{4.28}$$

It is easily seen that the curves  $\Psi(\underline{x}) = c$  describe the set of streamlines in the flow. The equipotentials  $H(\underline{x}) = c$  similarly describe the level curves of the hydraulic head ("potential") field. Finally, note that the flux vector in (4.28) automatically satisfies the conservation equation  $\partial Q_i / \partial x_i = 0$ .

We now seek a flow equation based solely on the streamfunction  $\Psi$ . The Darcy equation implies that  $(\underline{Q}/K)$  is a potential vector:

$$\underline{Q}/K = - \underline{\nabla} H$$

whose curl must vanish, i.e.:

$$\underline{\nabla} \times (\underline{Q}/K) = \underline{0}.$$

In fact, only the third component of the curl is of interest here, giving:

$$\frac{\partial}{\partial x_1} (Q_2/K) - \frac{\partial}{\partial x_2} (Q_1/K) = 0. \quad (4.29)$$

Plugging (4.28) in (4.29) leads to the required  $\Psi$ -based equation:

$$\underline{\nabla} \cdot \left( \frac{1}{K} \underline{\nabla} \Psi \right) = 0. \quad (4.30)$$

Equivalently, by using the log-conductivity  $F(\underline{x}) = \ell n K(\underline{x})$ , we obtain the desired equation for the streamfunction:

$$\nabla^2 \psi - \underline{\nabla} F \cdot \underline{\nabla} \psi = 0. \quad (4.31)$$

In comparison, the equivalent equation for the hydraulic head "potential" was:

$$\nabla^2 H + \underline{\nabla} F \cdot \underline{\nabla} H = 0. \quad (4.32)$$

The idea of conjugacy arises from the observation that the governing equation for the streamfunction  $\psi$  can be obtained simply by reversing the sign of  $F(\underline{x}) = \ell n K(\underline{x})$  in the equation governing the head field. We now examine the implications of this "duality" in the case where the log-conductivity is a *Gaussian isotropic random field* in 2D space.

Consider the case of a finite square domain, with fixed heads on two opposite boundaries, and zero normal flux on the other boundaries (Figure 4.2). We now use equation (4.28), along with the Darcy equation, to express these boundary conditions in terms of the streamfunction. This is summarized below:

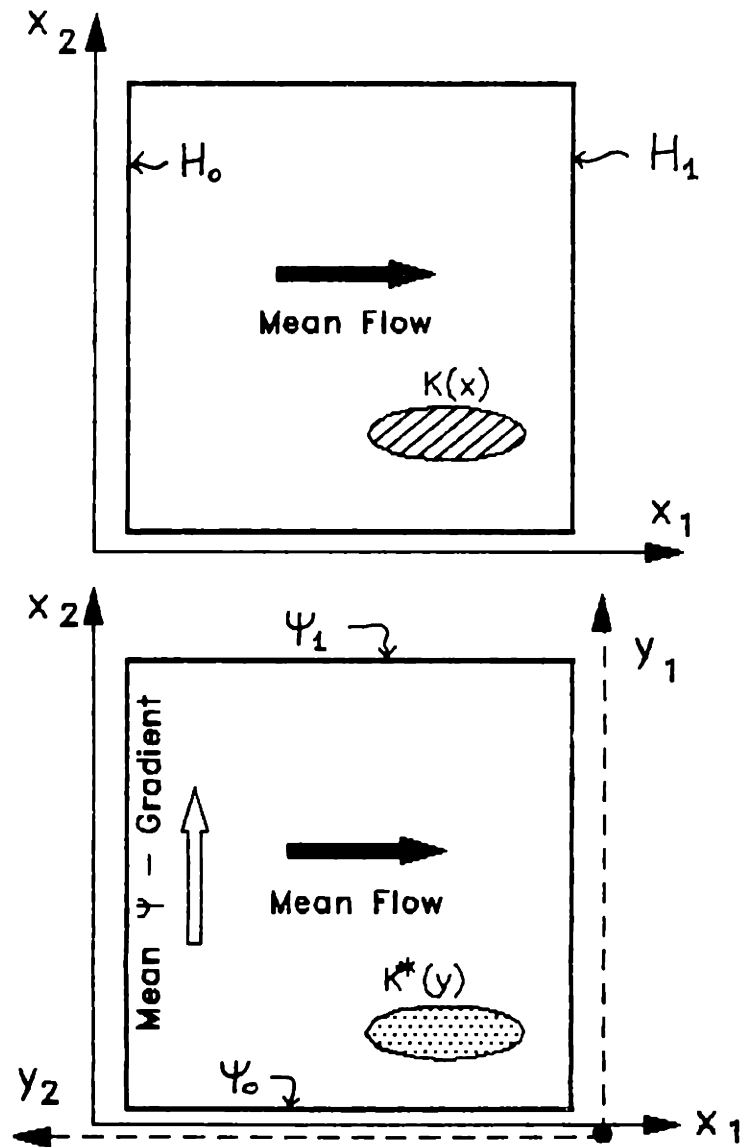


Figure 4.2 Illustration of the conjugacy property for stochastic flow in a 2D isotropic medium ( $K^*$  is the dual conductivity with respect to  $K$ )

(i) On the fixed head boundaries (e.g., at  $x_1 = 0$ ):

$$H(0, x_2) = H_0 \Rightarrow \frac{\partial H}{\partial x_2}(0, x_2) = 0 \Rightarrow \frac{\partial \psi}{\partial x_2}(0, x_2) = 0.$$

(ii) On the zero-flux boundaries (e.g. at  $x_2 = 0$ ):

$$Q_2(0, x_1) = 0 \Rightarrow \frac{\partial \psi}{\partial x_1}(0, x_1) = 0 \Rightarrow \psi(0, x_1) = \psi_0.$$

This clearly shows that the boundary conditions for the streamfunction equation are of the same type as those for the head equation, provided a 90 degree rotation of the flow domain (see Figure 4.2). Furthermore, observe that the global hydraulic gradient is, by construction:

$$\frac{-(H_1 - H_0)}{L} = \bar{J}_1$$

while the global streamfunction gradient is:

$$\frac{-(\psi_1 - \psi_0)}{L} = \frac{1}{L} \int_{x_2=0}^{x_2=L} Q_1 dx_2 = \bar{Q}_1.$$

Based on these remarks, the boundary value problem for 2D flow can be expressed indifferently in terms of  $H$  or  $\psi$  as shown below. First, we need to define new dimensionless variables:



$$\tilde{H} = \frac{H-H_0}{\bar{J}_1 L} \quad (4.33)$$

$$\tilde{\psi} = \frac{\psi - \psi_0}{\bar{Q}_1 L}$$

Second, let us define the dual conductivity, dual log-conductivity, and dual log-conductivity perturbation as follows:

$$K^*(x_1, x_2) = 1/K(-x_2, +x_1) \quad (4.34)$$

$$F^*(x_1, x_2) = -F(-x_2, +x_1)$$

$$f^*(x_1, x_2) = -f(-x_2, +x_1).$$

It is easily seen that equations (4.31) and (4.32) are mutually "conjugate", or "dual", i.e., the normalized streamfunction  $\tilde{\psi}$  is solution of the conjugate boundary-value problem involving the dual conductivity field as shown below:

$$\frac{\partial^2 \tilde{\psi}}{\partial y_i \partial y_i} + \frac{\partial F^*}{\partial y_i} \cdot \frac{\partial \tilde{\psi}}{\partial y_i} = 0$$

$$\tilde{\psi}(0, y_2) = 0; \quad \tilde{\psi}(L, y_2) = 1 \quad (4.35)$$

$$\frac{\partial \tilde{\psi}}{\partial y_2}(y_1, 0) = \frac{\partial \tilde{\psi}}{\partial y_2}(y_1, L) = 0$$

where  $(y_1, y_2) = (x_2, -x_1)$ . The equation for the normalized head potential  $\tilde{H}$  is identical:

$$\frac{\partial^2 \tilde{H}}{\partial x_1 \partial x_1} + \frac{\partial F}{\partial x_1} \frac{\partial \tilde{H}}{\partial x_1} = 0$$

$$\tilde{H}(0, x_2) = 0; \quad \tilde{H}(L, x_2) = 1 \quad (4.36)$$

$$\frac{\partial \tilde{H}}{\partial x_2}(x_1, 0) = \frac{\partial \tilde{H}}{\partial x_2}(x_1, L) = 0.$$

The next step in this analysis consists in letting the domain size  $L$  become infinite, while the mean hydraulic gradient  $\bar{J}_1$  remains finite. Furthermore, we now use the assumption that  $F(\underline{x})$  is a stationary, Gaussian, and isotropic random field. Taken together, statistical isotropy and normality imply that the log-conductivity perturbation ( $f$ ) must have all its moments invariant under rotations and reflexions, as well as invariant under the transformation  $f \rightarrow -f$  (due to the symmetry of the Gaussian distribution). This implies that the dual field  $f^*(\underline{x})$  defined in (4.34) is identical in probability to  $f(\underline{x})$ . Thus, equations (4.35) and (4.36) imply that the normalized random fields  $\tilde{\psi}(\underline{y})$  and  $\tilde{H}(\underline{x})$ , expressed in different coordinate systems, are identical in probability. Note that the  $\underline{y}$  coordinate system obtains by rotating  $\underline{x}$ , such that  $(y_1, y_2) = (-x_2, +x_1)$ .

The above results can be simply stated in one single equation:

$$\boxed{\tilde{\Psi}(-x_2, +x_1) \stackrel{\Delta}{=} \tilde{H}(x_1, x_2)} \quad (4.37)$$

where the " $\stackrel{\Delta}{=}$ " sign stands for equality in probability, meaning that all the moments up to arbitrary order must be equal. The above equation simply means that the random patterns of streamlines and equipotentials are statistically identical in a 2D isotropic medium, provided proper normalization of variables and rotation of the coordinates by a 90 degree angle. This is the property we call "conjugacy", to be understood in a statistical sense. Thus, according to equation (4.37), the streamfunction and head potential are statistically "conjugates" of each other.

We now use the conjugacy property (4.37) along with the flux-streamfunction relation (4.28) to show that the flux and head gradient vectors must also be conjugate. First, by plugging (4.33) in (4.37) we obtain, in terms of dimensional quantities:

$$\psi(y_1, y_2) - \psi_0 \stackrel{\Delta}{=} \frac{Q_1}{J_1} \cdot \frac{H(x_1, x_2) - H_0}{J_1}$$

where  $(y_1, y_2) = (-x_2, +x_1)$ . Using (4.28) and applying standard differentiation rules, this gives:

$$Q_i(x_1, x_2) \triangleq -\frac{\bar{Q}_i}{\bar{J}_i} \cdot \frac{\partial H}{\partial x_i}(x_2, -x_1) \quad (4.38)$$

where the gradient vector  $\partial H / \partial x_i$  should be evaluated by differentiating  $H$  with respect to the  $(x_1, x_2)$  system before substituting  $(x_2, -x_1)$ . Equation (4.38) shows that the flux and head gradient vectors, normalized by their mean values, are statistically identical upon rotation of the coordinate system by a 90 degree angle.

We now use this important result to obtain an exact relation between the covariance functions or the spectral density functions of the flux and head gradient vector fields. Equation (4.38) immediately leads to:

$$\begin{aligned} R_{q_i q_j}(\xi_1, \xi_2) &= \hat{K}^2 \cdot R_{g_i g_j}(\xi_2, -\xi_1) \\ S_{q_i q_j}(k_1, k_2) &= \hat{K}^2 \cdot S_{g_i g_j}(k_2, -k_1) \end{aligned} \quad (4.39)$$

where  $\hat{K} = \bar{Q}_1/\bar{J}_1$  is the *effective conductivity*. Again note that the tensors  $R_{g_i g_j}$  on the right-hand-side should be evaluated in the  $(\xi_1, \xi_2)$  system before substituting for  $(\xi_2, -\xi_1)$ ; similarly for  $S_{g_i g_j}$ .

Finally, the head spectrum can be introduced on the right hand side of equation (4.39). Indeed, using the fact that  $g_i(\underline{x})$  is a potential vector (gradient of the scalar field  $h(\underline{x})$ ), one may express directly the flux spectrum in terms of the head spectrum as shown below:

$$S_{q_i q_j}(\underline{k}) = \hat{K}^2 \cdot k'_i k'_j S_{hh}(\underline{k}')$$

where  $(k'_i, k'_j) = (k_2, -k_1)$ . To obtain a more explicit relation, let us rewrite the transformed wavenumber system as:

$$k'_i = -(1-\delta_{i1}) k_1 + (1-\delta_{i2}) k_2.$$

This gives:

$$\begin{aligned} S_{q_i q_j}(k_1, k_2) = & \\ & \hat{K}^2 \cdot \{ (1-\delta_{i1})(1-\delta_{j1}) k_1^2 + (1-\delta_{i2})(1-\delta_{j2}) k_2^2 \\ & - [(1-\delta_{i1})(1-\delta_{j2}) + (1-\delta_{i2})(1-\delta_{j1})] k_1 k_2 \} \cdot S_{hh}(k_2, -k_1). \end{aligned}$$

This expression can be simplified further by defining the radial wavenumber  $k = (k_1^2 + k_2^2)^{1/2}$  and using certain properties of the Kronecker symbol such as:

$$(1 - \delta_{i1})(1 - \delta_{j2}) + (1 - \delta_{i2})(1 - \delta_{j1}) = 1 - \delta_{ij}.$$

This gives finally a general expression for the flux spectrum in a 2D isotropic medium, independently of any perturbative approximation other than the stationarity hypothesis:

$$\begin{aligned} S_{q_i q_j}(k_1, k_2) &= \hat{K}^2 \cdot \{(1 - \delta_{i1})(1 - \delta_{j1})k_1^2 \\ &+ (1 - \delta_{i2})(1 - \delta_{j2})k_2^2 \\ &- (1 - \delta_{ij})k_1 k_2\} \cdot S_{hh}(k_2, -k_1). \end{aligned} \quad (4.40)$$

Using the radial wavenumber  $k = (k_1^2 + k_2^2)^{1/2}$ , let us give explicitly each component of the symmetric  $S_{q_i q_j}$  tensor:

$$\begin{aligned} S_{q_1 q_1}(k_1, k_2) &= \hat{K}^2 \cdot \left(1 - \frac{k_1^2}{k^2}\right) k^2 S_{hh}(k_2, -k_1) \\ S_{q_2 q_2}(k_1, k_2) &= \hat{K}^2 \cdot \left(1 - \frac{k_2^2}{k^2}\right) k^2 S_{hh}(k_2, -k_1) \\ S_{q_1 q_2}(k_1, k_2) &= \hat{K}^2 \cdot \left(-\frac{k_1 k_2}{k^2}\right) k^2 S_{hh}(k_2, -k_1) \end{aligned} \quad (4.40')$$

Equation (4.40) is an important new result, since it gives the relation between the flux and head spectrum based

solely on the stationarity hypothesis (no small parameter expansion involved). Furthermore, this result can be checked by comparing it to the more general form (4.24) which was derived for 3D isotropic media -- and remains valid for 2D isotropic media as well. Indeed the spectrum (4.40) does satisfy the condition (4.24), with  $A = 0$  and  $C = \hat{K}^2 k^2 S_{hh}(k_2, -k_1)$ . Finally, it is instructive to compare (4.40) with the first order spectral solutions from Chapter 3. By applying equations (3.18) for the 2D isotropic case, it is easily seen that the first order approximation for  $S_{q_i q_j}$  is just equation (4.40) with  $\hat{K}$  replaced by  $K_G$ .

We conclude that the first order spectral solutions (3.18) are consistent with the conjugacy condition (4.40), at least up to a constant factor ( $\hat{K}/K_G$ ). We will show next that the effective conductivity  $\hat{K}$  must be precisely equal to the geometric mean  $K_G$  in a 2D isotropic medium, assuming only the existence of  $\hat{K}$  (i.e., stationary flow field). Therefore, we may conclude here that the first order spectral solution is consistent, in the sense that it satisfies exactly the conjugacy property of two-dimensional isotropic flow systems. Note that any higher-order stationary solutions should also satisfy the conjugacy property in order to be consistent. The conjugacy relations were given by (4.40) for second order moments only, but equation (4.38) could be used to derive similar conjugacy

conditions on higher order moments.

#### 4.2.5 Geometric mean effective conductivity for 2D isotropic media:

In order to complete the previous analysis, we show here that the effective conductivity, if it exists, must be exactly equal to the geometric mean in a 2D isotropic medium. Consider again equations (4.28) to (4.37), and denote  $\phi$  the head potential  $H$ , and  $\phi^*$  the streamfunction  $\psi$  expressed in the rotated coordinates  $(y_1, y_2) = (x_2, -x_1)$ . Restating previous results, we have that  $\phi(x)$  and  $\phi^*(y)$  are governed by the dual equations:

$$\nabla_{\mathbf{x}}^2 \phi + \nabla_{\mathbf{x}} F \cdot \nabla_{\mathbf{x}} \phi = 0$$

$$\nabla_{\mathbf{y}}^2 \phi^* + \nabla_{\mathbf{y}} F^* \cdot \nabla_{\mathbf{y}} \phi^* = 0 .$$

Furthermore, the Darcy law:

$$\underline{Q}(\underline{x}) = -K(\underline{x}) \cdot \underline{\nabla} \phi(\underline{x})$$

has also its dual counterpart:

$$\underline{Q}^*(y) = -K(\underline{y}) \cdot \underline{\nabla} \phi^*(y)$$



where, according to previous definitions:

$$K^*(\underline{y}) = -1/K(\underline{x}). \quad (4.41.a)$$

This leads us to define two "effective conductivities", one for the original  $\phi$ -equation, and one for the dual  $\phi^*$ -equation:

$$\hat{K} = \frac{\langle K(\underline{x}) \cdot \frac{\partial \phi}{\partial x_1}(\underline{x}) \rangle}{\langle \frac{\partial \phi}{\partial x_1}(\underline{x}) \rangle} \quad (4.41.a)$$

$$\hat{K}^* = \frac{\langle \frac{1}{K^*(\underline{y})} \cdot \frac{\partial \phi^*}{\partial y_1}(\underline{y}) \rangle}{\langle \frac{\partial \phi^*}{\partial y_1}(\underline{y}) \rangle}.$$

We now borrow an argument from Matheron's indications of a similar proof (Matheron, 1967 and 1984). First, observe that the effective conductivity and its dual satisfy by construction:

$$\hat{K}^* = 1/\hat{K}$$

as can be seen from equations (4.28) to (4.38). Second, note that the effective conductivities  $\hat{K}$  and  $\hat{K}^*$  must take the form of a functional  $\mathcal{F}$  involving possibly all the moments of  $K(\underline{x})$ . Furthermore, this functional must be of the same form in the two cases, because the governing equations for  $\phi$  and  $\phi^*$  are formally

identical, that is  $\phi(\mathbf{x})$  depends on  $K(\mathbf{x})$  in the same manner that  $\phi^*(\mathbf{y})$  depends on  $K^*(\mathbf{x})$ . Whence:

$$\hat{K} = \mathcal{F}(K(\underline{\mathbf{x}})) \quad (4.42)$$

$$\hat{K}^* = \mathcal{F}(1/K(\underline{\mathbf{x}})) = 1/\hat{K}.$$

The functional in (4.42) must behave linearly with respect to multiplication by a constant, e.g.  $\mathcal{F}(\alpha K(\underline{\mathbf{x}})) = \alpha \mathcal{F}(K(\underline{\mathbf{x}}))$ : try equation (4.42) with  $\alpha K(\underline{\mathbf{x}})$ . We now use a special property of the log-normal distribution, namely that  $K/\langle K \rangle$  and  $K^{-1}/\langle K^{-1} \rangle$  have identical distributions in terms of all N-points moments ( $N = 1, 2, \dots$ ). This will in fact hold for any conductivity field whose logarithm has a symmetric distribution. The required result follows directly from equation (4.42), along with the symmetry of the  $\ln K$  distribution, and the invariance of  $\hat{K}$  with respect to coordinates:

$$\begin{aligned} \hat{K}^*/\hat{K} &= \mathcal{F}(K^{-1}(\mathbf{y})) \\ &= \mathcal{F}(K(\mathbf{y}) \cdot \frac{\langle K^{-1} \rangle}{\langle K \rangle}) \\ &= \frac{\langle K^{-1} \rangle}{\langle K \rangle} \cdot \mathcal{F}(K(\mathbf{y})) \\ &= \frac{\langle K^{-1} \rangle}{\langle K \rangle} \cdot \hat{K}. \end{aligned}$$

From the previous identity  $\hat{K}^* = 1/\hat{K}$ , this gives immediately:

$$\hat{K} = \sqrt{\langle K \rangle / \langle K^{-1} \rangle} \quad (4.43)$$

Now, by using also the properties of the log-normal distribution:

$$\begin{aligned} f(\underline{x}) &= \ln (K(\underline{x})/K_G) \\ K_G &= \exp\langle \ln K \rangle && \text{(geometric mean)} \\ \langle K \rangle &= K_G e^{\sigma^2/2} && \text{(arithmetic mean)} \\ \langle K^{-1} \rangle^{-1} &= K_G e^{-\sigma^2/2} && \text{(harmonic mean)} \end{aligned}$$

we obtain finally the announced result:

$$\boxed{\hat{K} = K_G} \quad (4.43')$$

Incidentally, it is interesting to note that a similar proof was obtained for electric networks, by using the concept of a dual conductivity network (Marchant and Gabillard, 1975).

The fact that the effective conductivity is equal to the geometric mean for a 2D isotropic medium with a symmetric probability distribution of  $\ln K$ , was mentioned by Matheron (1967), Marchant and Gabillard (1975), and Matheron (1984). The proof given above follows and expands on a review published by Matheron (1984). It seems natural to ask whether an exact closed form relation for the effective conductivity could be obtained in

more than 2 dimensions. An interesting formula for the case of statistically isotropic log-normal conductivity in  $m$ -dimensional space was suggested by Matheron (1967, Chapt. VI, p. 132), however with no proof. In terms of log-conductivities, Matheron's conjecture can be re-stated as follows:

$$\ln(\hat{K}) = \left(1 - \frac{1}{m}\right) \ln K_A + \frac{1}{m} \ln K_H \quad (4.44)$$

where  $K_A$  is the arithmetic mean  $\langle K \rangle$ , and  $K_H$  the harmonic mean  $\langle K^{-1} \rangle^{-1}$ . This equation is indeed exact for  $m = 1$  and 2 dimensions, giving respectively the harmonic mean and the geometric mean  $K_G = \sqrt{K_A \cdot K_H}$ . For 3-dimensions, Matheron's conjecture gives exactly the same result as the first order spectral theory:  $\hat{K} = K_G \exp(\sigma_f^2/6)$ . It is remarkable that these approximations obtained by two different methods match exactly, even though they might be inaccurate for large values of  $\sigma_f$ . Furthermore, as the number of dimensions goes to infinity, the effective conductivity (4.44) converges to its upper bound, the arithmetic mean  $K_A$ . Thus, as the "dimensionality" of flow increases from one to infinity, the effective conductivity increases monotonically from its lower bound  $K_H = K_G e^{-\sigma^2/2}$  to its upper bound  $K_A = K_G e^{+\sigma^2/2}$ . This is indeed an attractive feature of Matheron's formula. Incidentally, the proof that the effective conductivity is bounded by  $K_H$  and  $K_A$  was given by Matheron (1967) based on energy arguments.

In our view, the question of the adequacy of current estimates of the effective conductivity tensor  $\hat{K}_{ij}$  for realistic three-dimensional flow problems remains open. However, anticipating the results of numerical simulations with 3D isotropic media (Chapter 6), we stress the fact that the effective conductivity predicted by the spectral theory (or by Matheron's conjecture) agreed very well with the numerical simulation results for a wide range of log-conductivity variability, up to  $\sigma_f = 2.3$ . Based on this encouraging result, we now investigate how Matheron's conjecture (4.44) could be generalized to include the case of statistically anisotropic media.

#### 4.2.6 Effective conductivity for general 3D anisotropic media:

The proposed generalization of (4.44) is based on the observation that the parameter  $m$  should be interpreted as the number of degrees of freedom of fluid particles, rather than the dimensionality of space. When the log-conductivity is a three-dimensional ellipsoidal random field with anisotropic length scales  $(\lambda_1, \lambda_2, \lambda_3)$ , it seems reasonable to assume that the degree of freedom of flow will depend solely on these three length scales. Furthermore, the first order spectral results obtained by Gelhar and Axness (1983) for various anisotropy ratios  $(\lambda_1/\lambda_3, \text{etc.})$  suggest that equation (4.44) could be

generalized in the form:

$$\ln \hat{K}_{ii} = \alpha_{ii} \ln K_A + \beta_{ii} \ln K_H \quad (4.45)$$

where the coefficients  $\alpha_{ii}$  and  $\beta_{ii}$  must be somehow related to the degrees of freedom available for flow in "parallel" mode ( $K_A$ ) and flow in "perpendicular" mode ( $K_H$ ), for each of the three principal axes of anisotropy ( $i=1,2,3$ ).

We now show how  $\alpha_{ii}$  and  $\beta_{ii}$  should depend on the length scales ( $\lambda_1, \lambda_2, \lambda_3$ ) for a few special cases, assuming for convenience that the mean head gradient  $\underline{J}$  is aligned with one of the principal axes ( $x_1, x_2, x_3$ ). In this case,  $\hat{K}_{ij}$  is a diagonal tensor. The more general case of arbitrary orientation of  $\underline{J}$  will follow by using tensorial transformation rules under rotations, assuming that  $\hat{K}_{ij}$  indeed behaves like a second rank symmetric tensor (see Matheron 1967, and Gelhar and Axness, 1983).

Let us focus first on the behavior of  $\hat{K}_{11}$  in certain special cases where a close-form result is available. The results given below were deduced in part from the work of Gelhar and Axness (1983, Eqs. 4.52-4.60):

- (i)  $\lambda_1 = \lambda_2 = \lambda_3:$   

$$\ell n \hat{K}_{11} = \frac{2}{3} \ell n K_A + \frac{1}{3} \ell n K_H$$
- (ii)  $\lambda_1 = \lambda_2, \lambda_3 \rightarrow 0:$   

$$\ell n \hat{K}_{11} = 1 \cdot \ell n K_A + 0 \cdot \ell n K_H = \ell n K_A$$
- (iii)  $\lambda_1 = \lambda_2, \lambda_3 \rightarrow \infty:$   

$$\ell n \hat{K}_{11} = \frac{1}{2} \ell n K_A + \frac{1}{2} \ell n K_H = \ell n K_G$$
- (iv)  $\lambda_1 \neq \lambda_2, \lambda_3 \rightarrow \infty:$   

$$\ell n \hat{K}_{11} = \frac{\lambda_1}{\lambda_1 + \lambda_2} \ell n K_A + \frac{\lambda_2}{\lambda_1 + \lambda_2} \ell n K_H.$$

The first case above corresponds to a fully isotropic medium; the second case corresponds to a horizontally stratified medium with isotropic horizontal slices; the third case represents a vertically "stratified" medium analogous to a bundle of independent vertical columns of circular section; and the fourth case is a generalization of the previous one, with vertical columns of ellipsoidal section.

In addition, the case of horizontal flow perpendicular to vertical strata obtains by taking  $\lambda_2$  and  $\lambda_3$  infinite which yields  $\hat{K}_{11} = K_H$  as expected. Similarly, for flow parallel to horizontal strata, one obtains  $\hat{K}_{11} = K_A$  by taking  $\lambda_1$  and  $\lambda_2$  infinite.

The other principal components  $\hat{K}_{22}$  and  $\hat{K}_{33}$  may be obtained in a similar fashion. For instance in the case  $(\lambda_1 \neq \lambda_2, \lambda_3 \rightarrow \infty)$   $\hat{K}_{22}$  obtains from  $\hat{K}_{11}$  by inverting  $(\lambda_1, \lambda_2)$ , and  $\hat{K}_{33}$  by inverting  $(\lambda_1, \lambda_3)$ . The result, given below, follows from the first order spectral analysis of Gelhar and Axness (1983):

$$\underline{\lambda_1 \neq \lambda_2, \lambda_3 \rightarrow \infty:}$$

$$\hat{K}_{11} = \frac{\lambda_1}{\lambda_1 + \lambda_2} \ell n K_A + \frac{\lambda_2}{\lambda_1 + \lambda_2} \ell n K_H$$

$$K_{22} = \frac{\lambda_2}{\lambda_1 + \lambda_2} \ell n K_A + \frac{\lambda_1}{\lambda_1 + \lambda_2} \ell n K_H$$

$$K_{33} = \ell n K_A.$$

Taken together, these results indicate that the  $\alpha_{ii}, \beta_{ii}$  are functions of  $(\lambda_1, \lambda_2, \lambda_3)$  that follow a few simple rules, listed below:

- (1)  $\alpha_{ii}(\underline{\lambda})$  is identical to  $\alpha_{jj}(\underline{\lambda}')$  with  $\underline{\lambda}'$  obtained by interversion of  $\lambda_i, \lambda_j$ .
- (2)  $\alpha_{ii}(\underline{\lambda}) + \beta_{ii}(\underline{\lambda}) = 1$ .
- (3)  $\alpha_{11}(\lambda, \lambda, \lambda) = 2/3$  (4.46)
- (4)  $\alpha_{11}(\lambda, \lambda, 0) = 1$
- (5)  $\alpha_{11}(\lambda_1, \lambda_2, \infty) = \frac{\lambda_1}{\lambda_1 + \lambda_2}$  .



These remarks eventually led us to a more general rule satisfying all the requirements in (4.46):

$$\alpha_{11}(\lambda_1, \lambda_2, \lambda_3) = \frac{\lambda_1}{\lambda_1 + \frac{\lambda_2 \lambda_3}{\lambda_2 + \lambda_3}} \quad (4.47)$$

with the provision that  $\alpha_{22}$  and  $\alpha_{33}$  can be deduced from  $\alpha_{11}$  according to (4.46.1), and  $\beta_{ii} = 1 - \alpha_{ii}$  according to (4.46.2).

Finally, by using (4.45) (4.46) and (4.47), we obtain a generalization of Matheron's conjecture, applicable to the general case of 3D anisotropic media:

$$\begin{aligned} \ln \hat{K}_{ii} &= \alpha_{ii}(\underline{\lambda}) \cdot \ln K_A + (1 - \alpha_{ii}(\underline{\lambda})) \ln K_H \\ \alpha_{ii}(\underline{\lambda}) &= \frac{\lambda_i^2}{\lambda_1 \lambda_2 \lambda_3 + \frac{\lambda_i^2}{(\lambda_1 + \lambda_2 + \lambda_3) - \lambda_i}} \end{aligned} \quad (4.48)$$

Equivalently, by using the relations:

$$\begin{aligned} K_A &= K_G e^{+\sigma^2/2} \\ K_H &= K_G e^{-\sigma^2/2} \end{aligned}$$

valid in the case of a log-normal conductivity field, equation

(4.48) can be expressed in the simpler form:

$$\hat{K}_{ii} = K_G \exp \left\{ -\frac{\sigma_f^2}{2} (1 - 2\alpha_{ii}(\lambda)) \right\} \quad (4.49)$$

where  $\alpha_{ii}$  was defined in equation (4.48) above.

Furthermore, the case where the mean head gradient  $\underline{J}$  is not aligned with the anisotropy axis can be resolved by rotating the coordinate system to coincide with  $\underline{J}$  and by applying tensorial transformation rules as explained in Gelhar and Axness, 1983. This yields:

$$\hat{K}'_{ij} = a_{im} a_{jm} \hat{K}_{mm} \quad (4.50)$$

where  $\hat{K}_{mm}$  is given by (4.48) or (4.49). The matrix  $[a_{ij}]$  represents the rotation from  $\underline{J}$  to the principal axis  $x_1$ , and  $\hat{K}'_{ij}$  represents the effective conductivity tensor expressed in the  $(x_1, x_2, x_3)$  system of principal axes. Note that when the angle  $(\underline{J}, x_1)$  is zero, we obtain  $\hat{K}'_{ij} = \delta_{im} \delta_{jm} \hat{K}_{mm}$  as expected, i.e., the effective conductivity is a diagonal tensor in this case.

It is instructive to see how equations (4.48) to (4.50) apply in specific cases of practical interest. We give below the

three principal components of the effective conductivity tensor, according to (4.49), for the case of vertical-to-horizontal anisotropy:

$$\begin{aligned}\lambda_1 &= \lambda_2 = \lambda \\ a &= \lambda_3/\lambda \\ \hat{K}_{11} &= \hat{K}_{22} = K_G \exp\left\{ + \frac{\sigma^2}{2} \cdot \frac{1}{1+2a} \right\} \\ \hat{K}_{33} &= K_G \exp\left\{ - \frac{\sigma^2}{2} \cdot \frac{1-2a}{1+2a} \right\}.\end{aligned}\tag{4.51}$$

In particular, the case of imperfect horizontal stratification (horizontal slices) obtains by taking  $a < 1$ . The perfectly stratified case corresponds to  $a \rightarrow 0$ . The case  $a > 1$  is less typical, corresponding to a formation made of vertical elongated lenses of cylindrical shape (or elongated ellipsoids with circular section).

More complex cases, such as those involving three different length scales, can be worked out directly from (4.49). For example, a typical situation may involve a slight anisotropy in the horizontal plane (1:2), and a significant anisotropy in the vertical plane (1:8). Taking  $\lambda_1 = 8$ ,  $\lambda_2 = 4$ ,  $\lambda_3 = 1$  and  $K_G = 1$ ,  $\sigma_f = 2.3$ , the values 8.7, 5.4, and 0.30 for the effective conductivities  $\hat{K}_{11}, \hat{K}_{22}, \hat{K}_{33}$ , respectively.

In summary, we have extended a conjecture by Matheron (1967) in order to evaluate the effective conductivity in a three-dimensional anisotropic medium characterized by three length scales  $(\lambda_1, \lambda_2, \lambda_3)$ . The proposed formula (4.48-4.50) matches the results known to be exact for all cases where these are available: arithmetic mean for "parallel flow", harmonic mean for "perpendicular flow", and geometric mean for two-dimensional isotropic flow. In addition, the conjecture also coincides with the results of the first order spectral theory (Gelhar and Axness) in all the special cases examined, such as the case of anisotropy in the horizontal plane with the vertical length scale much larger than the horizontal. Such a general closed form expression for the effective conductivity was not available before, and could be useful for applications.

#### 4.3 New Closed Form Perturbative Solution for the Flux Spectrum:

In this section, we build on our previous analyses of the flux spectrum to suggest a new linearization of the stochastic flow equation for obtaining first order spectral solutions. Specifically, the results obtained for 2D flow, suggest that the flux spectrum in any number of dimensions could be proportional to  $\bar{Q}_1^2$  (see equations 4.24, 4.25, and 4.40), rather than the factor  $K_G^2 \bar{J}_1^2$  given by the standard spectral theory (equations 3.18 or 4.26).

Building on this observation, we will show here that the flux spectrum can be obtained directly from a linear second order PDE governing the flux vector  $q_1$ . Solving this equation by the first order perturbation method indeed leads to a factor  $\bar{Q}_1^2$  rather than  $K_G^2 \bar{J}_1^2$  in the flux spectrum. This is thought to be a more accurate result because of the "linearity" of the stochastic flux-based equation (compared to the "non-linearity" of the stochastic Darcy equation). The numerical experiments of Chapter 6 will confirm the validity of the new linearization approach. We now proceed to develop the new first order solutions in detail.

The flux-based equation can be obtained by applying linear partial differential operators to the Darcy and continuity equations:

$$\begin{aligned}\underline{Q} &= -K \underline{\nabla} H \\ \underline{\nabla} \cdot \underline{Q} &= 0.\end{aligned}\tag{4.52}$$

For clarity of notation, observe that we use the Nable operator for the gradient ( $\underline{\nabla} H$ ) as well as for the divergence (scalar product  $\underline{\nabla} \cdot \underline{Q}$ ). The next step is based on the observation that the vector  $\underline{Q}/K$  is a gradient, so that its curl must vanish:

$$\underline{\nabla} \times (\underline{Q}/K) = \underline{0}.\tag{4.53}$$

In addition, from the mass conservation equation (4.52), the gradient of the divergence of  $\underline{Q}$  vanishes:

$$\underline{\nabla}(\underline{\nabla} \cdot \underline{Q}) = \underline{0}. \quad (4.54)$$

Note that equations (4.53) and (4.54) express the fact that  $\underline{Q}/K$  is a gradient (Darcy law) and  $\underline{Q}$  is a divergence free vector (mass conservation). By using the standard rules of vector field operators (see for instance Gradshteyn and Ryzhik, 1980, 10.31), equation (4.54) gives:

$$\underline{\nabla}^2 \underline{Q} + \underline{\nabla} \times (\underline{\nabla} \times \underline{Q}) = \underline{0}. \quad (4.55)$$

The curl term in (4.55) can be decomposed as follows:

$$\begin{aligned} \underline{\nabla} \times (\underline{\nabla} \times \underline{Q}) &= \underline{\nabla} \times (\underline{\nabla} \times (K \cdot \underline{Q}/K)) \\ &= \underline{\nabla} \times [\underline{K} \underline{\nabla} \times (\underline{Q}/K) + \underline{\nabla}(K) \times \underline{Q}/K] \\ &= \underline{\nabla} \times \left( \frac{1}{K} \underline{\nabla} K \times \underline{Q} \right) \end{aligned}$$

where the last step obtains by using equation (4.53). Plugging the above identity in (4.55) gives:

$$\underline{\nabla}^2 \underline{Q} + \underline{\nabla} \times \left( \frac{1}{K} \underline{\nabla} (K) \times \underline{Q} \right) = \underline{0}.$$

This equation is nonlinear in  $K$ , but can be made linear in the

log-conductivity perturbation  $f(\underline{x}) = \ln(K(\underline{x})/K_G)$ . Indeed, by using  $K = K_G e^f$  it comes:

$$\boxed{\nabla^2 \underline{Q} + \nabla \times (\nabla f \times \underline{Q}) = \underline{0}} \quad (4.56)$$

Equation (4.56) constitutes a system of three scalar second order partial differential equations governing the flux vector components. The most remarkable feature of this simple equation is its linearity with respect to the log-conductivity field  $f(\underline{x})$ . In comparison, the standard spectral solutions were based on the "nonlinear" Darcy equation, of the form:

$$\underline{Q} = -K_G e^{f(\underline{x})} \cdot \nabla H$$

where the exponential  $e^f$  is obviously a strongly nonlinear function of  $f$ .

Equation (4.56) can be made more explicit by decomposing the curl term as follows:

$$\begin{aligned} \nabla \times (\nabla f \times \underline{Q}) &= \nabla f (\nabla \cdot \underline{Q}) - \underline{Q} (\nabla \cdot \nabla f) \\ &\quad - (\nabla f \cdot \nabla) \underline{Q} + (\underline{Q} \cdot \nabla) \nabla f. \end{aligned}$$

Using again  $\underline{\nabla} \cdot \underline{Q} = 0$  and plugging the above expression in (4.56) yields:

$$\boxed{\underline{\nabla}^2 \underline{Q} - (\underline{\nabla} f \cdot \underline{\nabla}) \underline{Q} = \underline{Q} \nabla^2 f - (\underline{Q} \cdot \underline{\nabla}) \underline{\nabla} f} \quad (4.57)$$

where  $\underline{\nabla}^2$  is the vector-Laplacian defined earlier, and  $\nabla^2$  is the usual scalar Laplacian. For convenience, let us express (4.57) in tensorial form:

$$\boxed{\frac{\partial^2 Q_i}{\partial x_j \partial x_j} - \frac{\partial f}{\partial x_j} \frac{\partial Q_i}{\partial x_j} = \frac{\partial^2 f}{\partial x_j \partial x_j} Q_i - \frac{\partial^2 f}{\partial x_i \partial x_j} Q_j} \quad (4.58)$$

It is easy to verify that (4.57) or (4.58) is indeed a valid governing equation for flow, by plugging  $\underline{Q} = -K \underline{\nabla} H$  and using  $\underline{\nabla} \cdot \underline{Q} = 0$  for mass conservation.

The linear form of the flux-based equation (4.58) suggests that the standard spectral solutions for the flux vector field could be improved by using (4.58) rather than the Darcy equation for a perturbative spectral analysis of the flux vector. In keeping with the basic premises of the spectral method, we assume now that the input log-conductivity as well as the output flux vector are stationary random fields. Defining the flux perturbation:



$$q_i = Q_i - \bar{Q}_i$$

and using the stationarity assumption ( $\bar{Q}_i$  constant), we obtain the mean equation by averaging (4.58):

$$- \left\langle \frac{\partial f}{\partial x_j} \frac{\partial q_i}{\partial x_j} \right\rangle = \left\langle \frac{\partial^2 f}{\partial x_j \partial x_j} q_i \right\rangle - \left\langle \frac{\partial^2 f}{\partial x_i \partial x_j} q_j \right\rangle. \quad (4.59)$$

Note that the mean flux components  $\bar{Q}_i$  cancel out due to the fact that  $\langle f \rangle = 0$  and  $\partial \bar{Q} / \partial x = 0$ . Next, the equation for the flux perturbation obtains by subtracting (4.59) from (4.58). This gives after some manipulations:

$$\frac{\partial^2 q_i}{\partial x_j \partial x_j} - \frac{\partial^2 f}{\partial x_j \partial x_j} \cdot \bar{Q}_i + \frac{\partial^2 f}{\partial x_i \partial x_j} \cdot \bar{Q}_j = 0(\sigma_f^2). \quad (4.60)$$

The term that was neglected on the right hand side of (4.60) is the second-order perturbation:

$$\mathcal{P} \left\{ \frac{\partial f}{\partial x_j} \frac{\partial q_i}{\partial x_j} + \frac{\partial^2 f}{\partial x_j \partial x_j} \cdot q_i - \frac{\partial^2 f}{\partial x_i \partial x_j} \cdot q_j \right\} \quad (4.61)$$

where we used the operator  $\mathcal{P}$  to denote the perturbation of a random quantity:  $\mathcal{P}(Y) = Y - \langle Y \rangle$ .

Now, the first order spectral solution for the flux field is readily obtained by applying the spectral representation theorem as in Chapter 3. This gives, from (4.60) with the terms on the right-hand side neglected:

$$\begin{aligned}
 dZq_i(\underline{k}) &= \left\{ \bar{Q}_i - \frac{k_i(k_m \bar{Q}_m)}{(k_m k_m)} \right\} dZ_f(\underline{k}) \\
 S_{q_i q_j}(\underline{k}) &= \left\{ \bar{Q}_i - \frac{k_i(k_m \bar{Q}_m)}{k^2} \right\} \cdot \left\{ \bar{Q}_j - \frac{k_j(k_m \bar{Q}_m)}{k^2} \right\} S_{ff}(\underline{k}). \quad (4.62)
 \end{aligned}$$

Note that the flux spectrum in (4.62) is entirely determined once the effective conductivity tensor is known. Recall that the effective conductivity relates the mean flux to the mean head gradient via:

$$\bar{Q}_i = \hat{K}_{im} \bar{J}_m.$$

For the particular case where the mean head gradient coincides with the principal axis of the  $\hat{K}_{ij}$  tensor (say  $x_1$ ), equation (4.62) simplifies to:

$$S_{q_i q_j}(\underline{k}) = (\bar{Q}_1)^2 \cdot \left\{ \delta_{11} - \frac{k_1 k_1}{k^2} \right\} \cdot \left\{ \delta_{1j} \frac{-k_1 k_j}{k^2} \right\} S_{ff}(\underline{k}) \quad (4.63)$$

where  $\bar{Q}_1 = \hat{K}_{11} \bar{J}_1$  should be used.

Comparing now (4.63) to the result from the standard spectral result (3.18), it appears that equation (4.63) obtains from (3.18) by replacing the factor  $(K_G J_1)$  by  $\bar{Q}_1$ . Thus, the shape of the spectrum is not affected by the new approach, and the flux correlation functions will remain unchanged. On the other hand, the flux standard deviations  $\sigma_{q_i}$  previously obtained in Chapter 3 must now be multiplied by the factor  $(\hat{K}_{11}/K_G)$  according to the new approach.

It is instructive to compare (4.63) to the standard spectral theory (3.18) by examining the behavior of the ratio  $\hat{K}_{11}/K_G$ . First note that both (3.18) and (4.63) give  $S_{qq} = 0$  for the pathological one-dimensional case ( $q$  must be constant in order to satisfy mass conservation in one dimension). For the 2D isotropic case, (3.18) and (4.63) coincide exactly since  $\hat{K}_{11} = K_G$  in this case. For the 3D isotropic case we have  $\hat{K}_{11}/K_G = \exp(\sigma_f^2/6)$  and the discrepancy will increase with  $\sigma_f$ . The discrepancy between (3.18) and (4.63) will be even higher in the case of strongly anisotropic media, such as flow perpendicular to perfect stratification ( $\hat{K}_{11}/K_G = e^{-\sigma^2/2}$ ) and flow parallel to perfect stratification ( $\hat{K}_{11}/K_G = e^{+\sigma^2/2}$ ).

Let us illustrate these remarks for two simple cases using the notation  $\sigma_q^{(1)}$  for the standard theory (3.18) and  $\sigma_q^{(2)}$  for the new result (4.63). For a 3D isotropic medium with  $\sigma_f=1$ , the ratio of  $\sigma_q^{(2)}/\sigma_q^{(1)}$  is about 1.2. In the case of flow parallel to stratification in a perfectly stratified medium, this ratio would rise to about 1.7. We conclude that the discrepancy between (3.18) and (4.63) is quite significant as far as the flux standard deviations are concerned. It seems reasonable to assume that the most accurate formula is (4.63), since it is based on a "linear" equation governing the flux vector. The forthcoming numerical experiments (Chapter 6) will confirm that the standard solution (3.18) appears to underestimate the flux variances, whereas (4.63) is in better agreement with numerical results.

Incidentally, the new result obtained here indicates that the spectral solutions of stochastic solute transport should be modified as well. In particular, the longitudinal macrodispersivity for 3D solute transport given by Gelhar and Axness (1983):

$$A_{11} = \frac{\sigma_f^2 \lambda}{\gamma^2} \quad (\gamma = \hat{K}_{11}/K_G) \quad (4.64)$$

should now be revised according to equation (4.63), as follows:

$$A_{11} = \sigma_f^2 \lambda. \quad (4.65)$$

It is interesting to note that the new macrodispersivity given by (4.65) increases monotonically with  $\sigma_f$ , whereas the expression (4.64) of Gelhar and Axness presents a maximum at some positive value of  $\sigma_f$ . Beyond this value, the macrodispersivity would decrease with increasing variability. This behavior could not be explained on physical grounds, which makes the new solution (4.65) more attractive.

Along the same lines, note that the coefficient of variation of the flux component ( $\sigma_{q_i} / \bar{Q}_i$ ) also presents a maximum with respect to  $\sigma_f$  according to the standard solution (3.18). In contrast, this coefficient increases monotonically like  $\sigma_f$  when (4.63) is used instead. Again, there seems to be no intuitive explanation for the occurrence of a maximum in  $\sigma_{q_i} / \bar{Q}_i$  as  $\sigma_f$  increases. We conclude that the proposed spectral solution for the flux (4.63) seems preferable. This conclusion is also justified by observing that the linearization of  $e^f$  used in the standard spectral perturbation method was not required in the present approach. However, it should be recognized that other linearization approximations involved in the solute transport equation were not eliminated or improved by the present approach.

#### 4.4 Finite Size Effects: Band-Pass Self-Similar Spectra, Spectral Conditioning and Uncertainty.

##### 4.4.1 Motivation and approaches:

One of the major difficulties encountered in the application of spectral methods to field cases arises from the fact that groundwater flow fields (and solute concentration fields) are not, in reality, stationary random fields over infinitely large domains. Here, the term "stationary" is understood in the usual sense of statistical homogeneity, or translation invariance in probability. Recall that the spectral solution method, based on the representation theorem of random functions in Fourier space, required assuming the existence of stationary solutions over infinite domains in order to solve the governing stochastic equations in closed form (Chapter 3, and previous sections of Chapter 4). Other methods were developed in the literature to deal explicitly with non-stationary problems, and they may be more appropriate in cases of irreducible non-stationary behavior (e.g., drawdown near a pumping well). For instance the approximate Green's function method of Dagan (1982), and the numerical solution of approximate moment equations (Townley 1983, McLaughlin 1985) can be used to obtain non-stationary solutions in the case of small variability. These solution methods have their advantages. However, they do not possess the analytical simplicity of the infinite domain spectral approach (see literature review in Chapter 2).

Due to the approximations involved, the spectral method seems best adapted to the study of "large scale" flow and transport phenomena where the effect of local inhomogeneities on the overall pattern is minimal. However, field contamination studies usually focus on phenomena occurring on a finite scale. The scale in question may well be imposed by the geologic structure itself, or by policy considerations (target time for plume prediction). Moreover, certain physical phenomena like solute transport or unsaturated infiltration from local sources necessarily take place over some finite scale evolving in time.

In addition, experimental studies published in the literature indicate that the statistical properties of conductivities or transmissivities measured at different scales (or by different researchers!) may vary greatly. This is especially true for the "correlation scale", as noted in the previous data review in Chapter 2. The reader is referred in particular to section 2.3 for more complete references on field observations and data collection.

In our view, these difficulties indicate that, at least in some cases, the apparent correlation structure of the conductivity field inferred from field data depends on the scale of the observation. This suggests that a similar phenomenon may occur physically in transient flow and/or mass transport systems

dominated by local sources. Consider for instance a contamination plume originating from a local source, and convected in a steady groundwater flow field through a heterogeneous porous formation. This is illustrated in Figure 4.3 (top). As the plume grows and invades larger regions of the porous formation, it "responds" to larger and larger heterogeneities. At early times, the plume's spreading process is being "excited" by small heterogeneities which appear large with respect to the plume. Later on, the same small heterogeneities appear as mere fluctuations, with respect to the larger plume. In summary, as the plume grows and spreads, there is a change in the typical size of those heterogeneities that affect the global trends of the plume, and those that contribute to random-like mechanical dispersion within the plume. Accordingly, the apparent macrodispersion of the plume is likely to depend on the size or time scale of interest.

The phenomenon of scale dependence may also play a role for "large scale" characterization of groundwater flow fields. Figure 4.3 (centerpiece) illustrates that the apparent mean and the trend of the log-conductivity may depend on the size of the domain of interest in a given subsurface formation. To illustrate this scale effect, we have used borehole data from the Mont Simon formation (Gelhar, 1976, and Bakr, 1976); the figure shows that, although the mean log-conductivity appears constant



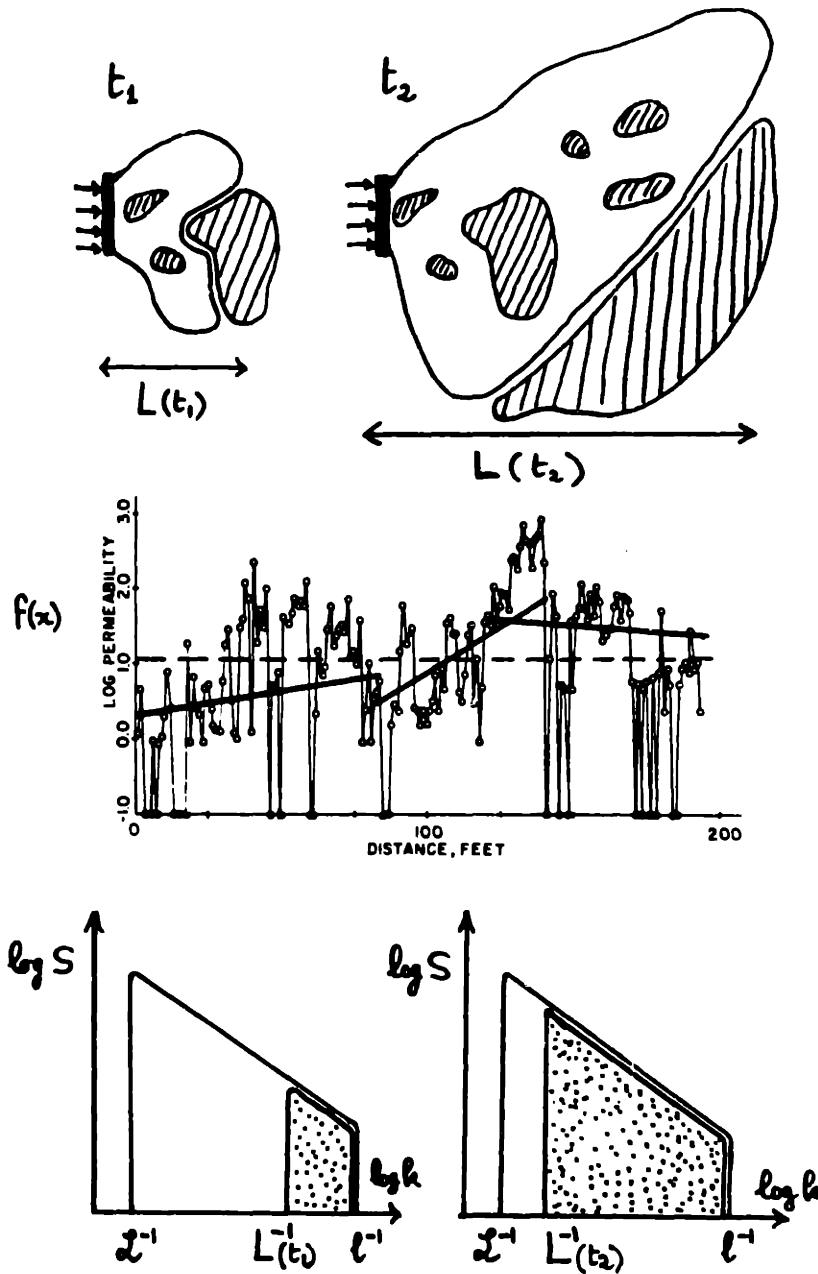


Figure 4.3: Illustration of finite-size effects:  
 (a) Contamination plume  
 (b) Log-conductivity field sample function  
 (c) Band-pass self-similar spectrum

at the scale 200 feet, there exist pronounced trends in the apparent mean log-conductivity at the scale 75 feet. This, in turn, suggests that the effective "large scale" conductivity could depend on domain size (and location) within a given regional formation.

We now briefly indicate how the standard spectral theory could be manipulated to incorporate finite-size effects. A first step in this direction consists in using band-pass spectra for the log-conductivity field, with a low wavenumber cut-off proportional to the inverse size of the domain ( $k_{\min} \approx 1/L$ ). This is illustrated on the bottom part of Figure 4.3. The high wavenumber cut-off ( $k_{\max} \approx 1/\ell$ ) takes into account the measurement spacing, or possibly the typical scale of conductivity measurements. In addition, the band-pass spectral representation of finite-scale phenomena will be considerably simplified by assuming a self-similar behavior of the spectrum within the range of scales of interest. This will be justified shortly by examining some available spectral data. Note, however, that the self-similar behavior may not hold for very large scale phenomena. In the latter case, the infinite-domain spectral theory could be applied safely provided that  $L^{-1} \ll \varrho^{-1}$ , where  $\varrho^{-1}$  is the wavenumber below which the spectral content of the log-conductivity becomes negligible. A very large measurement network may be required in order to detect

the actual value of the low wavenumber cut-off  $\varphi^{-1}$ , if such a value exists at all.

Finally, the "band-pass" spectral approach could be made more useful if it were possible to incorporate in a simple manner the dependence of the "mean" log-conductivity field with respect to the size of the domain under consideration (see centerpiece in Figure 4.3). This motivated the idea of "spectral conditioning", leading to a clear distinction between uncertainty and spatial variability. The main features of this new approach will be outlined towards the end of this section, building on the simple band-pass self-similar model.

#### 4.4.2 Band-pass self-similar spectra and field data:

Figures 4.4(a,b,c) display one-dimensional log-conductivity spectra obtained from three sets of borehole data in the Mont Simon aquifer (reproduced from Bakr's thesis, 1976). For Figure 4.4.a, the domain size was  $L = 303$  ft, with data spacing  $\ell = 1$  ft. The log-spectra density is plotted against the log-frequency in cycles/feet units (wave number =  $2\pi \times$  frequency). The frequency range shown in the figure is approximately  $5L^{-1}$  to  $0.5\ell^{-1}$  cycles. The straight line superimposed on the spectral data represents a self-similar spectrum with exponent one, that is:

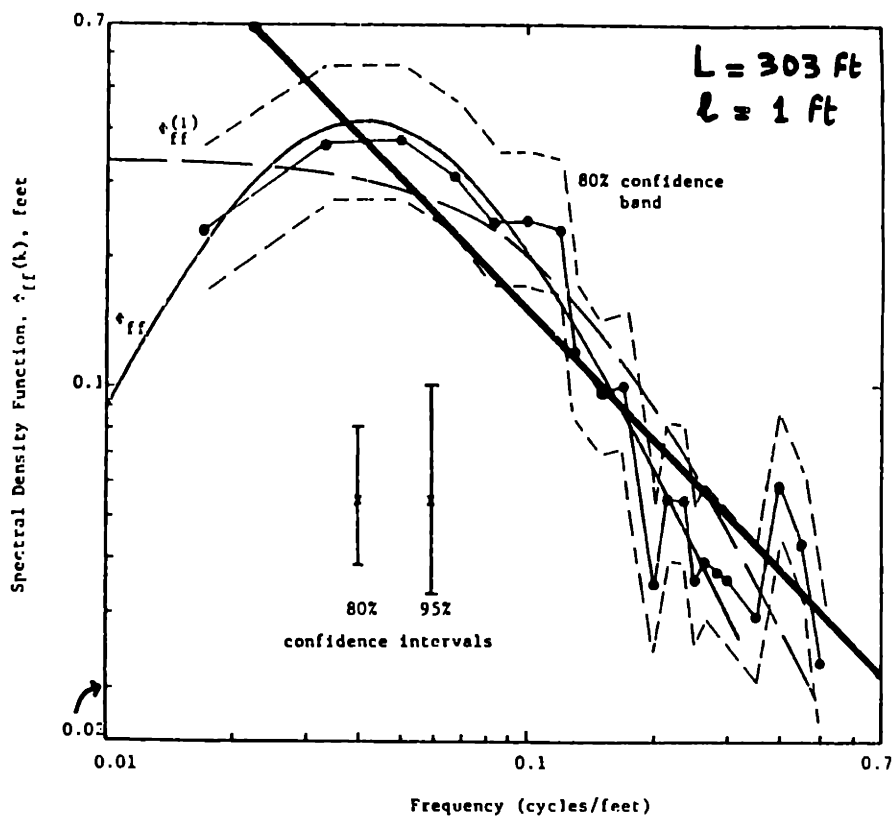


**Figure 4.4a:** Measured one-dimensional spectrum of log-conductivity at a borehole (Circles), in the Mt. Simon aquifer, from Bakr (1976). The straight line corresponds to a self-similar spectrum with exponent  $\alpha = 1$ .

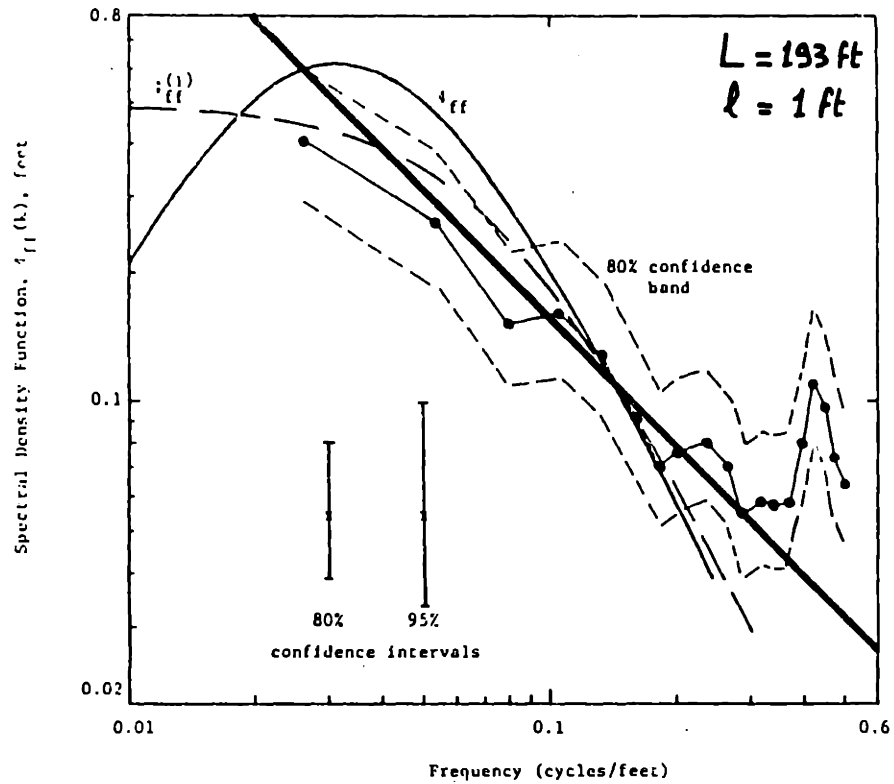


Figure 4.4.b: Same as Figure 4.4.a, for another set of data. The straight line corresponds to a self-similar spectrum with exponent  $\alpha = 1$ .

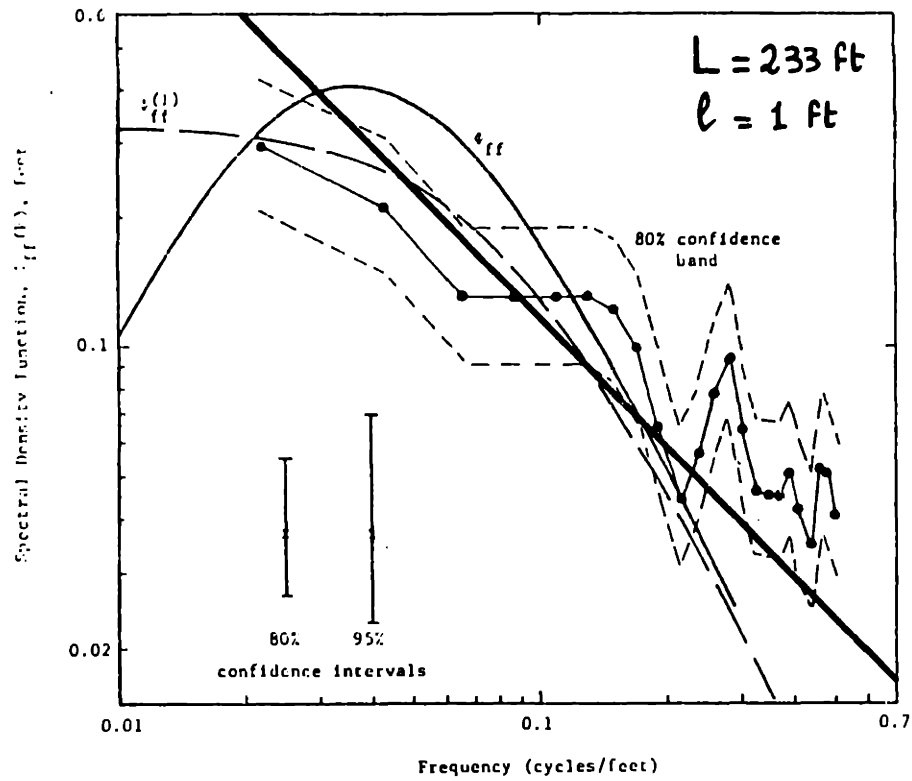


Figure 4.4.c: Same as Figure 4.4a and 4.4b, for another set of data. The straight line corresponds to a self-similar spectrum with exponent  $\alpha = 1$ .

$$S_{ff}(k) = \frac{S_0}{k^\alpha} \cdot \alpha \approx 1 \cdot \quad (4.66)$$

It may be instructive at this point to briefly analyze the concept of self-similarity, and the meaning of the coefficient  $\alpha$  (slope of the spectrum in a log-log plot). Self-similarity, or fractal behavior, can be thought of as the property of certain physical phenomena to replicate themselves on many scales. This means that certain identifiable fluctuations, structures, patterns, etc., appear to replicate themselves at different length scales, provided a simple similarity transformation. Mandelbrot (1983) exposed the theory of deterministic and *random* fractal geometry, and investigated its manifestations in nature. In particular, Mandelbrot proposed to use the Fractional Brownian Motion (FBM) as a random fractal model of landscapes, and in other applications including hydrological time series and geophysical spatial series (Mandelbrot and Wallis, 1969). More recent studies along these lines include Mandelbrot et al. 1984 (metal fracture surfaces), and Burrough 1981 (spatial analysis of soil granulometry).

The Fractional Brownian Motion is a special class of stationary-increment random process possessing the property of self-similarity (more appropriately "self-affinity"). That is, an FBM process  $f(x)$  is self-similar if its increments are statistically invariant under the transformation

$\Delta f(x) \rightarrow \lambda^{-H} \Delta f(\lambda x)$ . The parameter  $H$  is the Hurst coefficient (or Hölder coefficient, as  $\Delta f$  satisfies a Hölder condition).

A complete review of the properties of one-dimensional FBM processes can be found in Mandelbrot and Van Ness (1968). Note in particular that the usual Brownian motion corresponds to  $H = 1/2$ . The FBM processes obtained for  $1/2 < H < 1$  are "persistent" (positively correlated increments), while  $0 < H < 1/2$  gives "antipersistent" processes with negatively correlated increments. The spectrum of the FBM is precisely that of equation (4.66) with  $\alpha = 2H + 1$ . Observe that the Hurst coefficient is close to zero for the log-conductivity spectra shown in Figures (4.4), indicating a very noisy, anticorrelated behavior within the range of scales available to us (1 ft - 300 ft). This finding seems in accordance with the survey by Burrough (1981), who obtained a low Hurst coefficient for sand and clay fractions ( $H \approx 0.2$ ).

Incidentally, note that the Hurst coefficient could be evaluated directly from sample functions in physical space rather than spectral densities in Fourier space. Indeed, for an FBM process, the "core function" (variance of increments) takes the form:

$$C_H(\xi) \sim |\xi|^{2H}$$



where  $\xi$  is the lag distance. For the data of Figure 4.4, the core function would be nearly flat since  $H \approx 0$ . However, this would need to be checked directly by plotting the core function without detrending the log-conductivity data. Other methods, such as "R/S analysis", could also be applied: see Mandelbrot (1983) for reference.

At any rate, the available data shown in Figures (4.4) do indicate that the self-similar spectrum (4.66) with exponent one is a reasonable model, at least within the range of length scales 1 - 300 ft. One should keep in mind that the spectral densities obtained at wavenumbers on the order of inverse domain size or below are unreliable. In our opinion, even the estimated confidence intervals (dashed lines in Figures 4.4) cannot be trusted in the low wavenumber region of the spectrum.

According to the previous discussion, the one-dimensional spectrum of log-conductivity can be approximated as a band-pass self-similar spectrum with Hurst coefficient zero:

$$S_{ff}^{(1)}(k_1) = \begin{cases} S_0/|k_1| & \text{for } L^{-1} \leq |k_1| \leq \ell^{-1} \\ 0 & \text{otherwise} \end{cases} \quad (4.67)$$

Furthermore, we now adopt the view that the large scale cut-off  $L$  represents the size of the region in which flow or transport takes place (which may evolve in time), while  $\ell$  represents some

fixed small scale on the order of measurement spacing or perhaps sample size. The intercept of the spectrum at the origin (in a log-log plot) could be thought of as an intrinsic measure of variability of the formation independent of the particular cut-off scales  $L$  and  $\ell$ . Accordingly, we define the "intrinsic variance" of log-conductivity as:

$$\sigma_0^2 = S_0. \quad (4.68)$$

On the other hand, the "observed" variance of the log-conductivity within the range of scales  $(\ell, L)$  can be computed by integrating the 1D band-pass spectrum as follows:

$$\sigma_f^2 = 2 \int_{L^{-1}}^{\ell^{-1}} \frac{\sigma_0^2}{k_1} dk_1 = 2\sigma_0^2 \ln\left(\frac{L}{\ell}\right). \quad (4.69)$$

Note that  $\sigma_f^2$  is scale-dependent, being a slowly varying function of the ratio  $(L/\ell)$ . In particular, it is interesting to note that the "observed" variance of the log-conductivity increases logarithmically with domain size.

We now generalize this approach for the three-dimensional case, assuming that the log-conductivity is statistically isotropic. First, note that the one-dimensional spectra displayed in Figure 4.4 were obtained by Fourier

transforming the log-conductivity data sampled along a single direction. This yields a one-dimensional marginal spectrum, related to the full 3D spectrum by:

$$S_{ff}^{(1)}(k_1) = \iint S_{ff}(k_1, k_2, k_3) dk_2 dk_3$$

Let us now define a three-dimensional isotropic band-pass self-similar spectrum analogous to its one-dimensional counterpart:

$$S_{ff}(\underline{k}) = \begin{cases} \frac{\sigma_0^2}{2\pi k^3} & \text{for } L^{-1} \leq k \leq \ell^{-1} \\ 0 & \text{otherwise} \end{cases} \quad (4.70)$$

where  $k$  is the radial wavenumber:

$$k = \sqrt{k_1^2 + k_2^2 + k_3^2}.$$

By plugging equation (4.70) into the equation preceding it, one obtains the one-dimensional marginal spectrum corresponding to (4.70). It turns out that this spectrum approximates quite well the one-dimensional spectrum of (4.67), at least far enough from the cut-offs, as shown below:

$$S_1(k_1) = \sigma_0^2 \left[ \frac{1}{(k_1^2 + L^{-2})^{3/2}} - \frac{1}{(k_1^2 + \ell^{-2})^{3/2}} \right] \approx \frac{\sigma_0^2}{|k_1|} \text{ for } L^{-1} \ll k_1 \ll \ell^{-1}.$$

Since the above spectrum agrees fairly well with the 1D spectral data displayed in Figure 4.4, this justifies our choice of the 3D spectrum (4.70) -- assuming only that the formation is statistically isotropic. The more general case of anisotropic media will not be discussed here.

To complete this preliminary investigation, note that the "observed" finite-domain variance of the log-conductivity in 3D space can be obtained by integrating the isotropic spectrum (4.70), leading to the same relation as in the 1D case:

$$\sigma_f^2 = 2\sigma_0^2 \ln(L/\ell) \quad (4.71)$$

where  $L$  and  $\ell$  are now the *radial cut-off scales* in 3D space. Again, note that  $\sigma_f^2$  increases (logarithmically) with domain size. We are now ready to investigate the stochastic flow problem with the one-dimensional and three-dimensional band-pass self-similar spectra defined above.

#### 4.4.3 Stochastic flow solutions for band-pass self-similar spectra:

We now proceed to develop first order spectral solutions following the method already used in Chapter 3. It is important to note that the log-conductivity fields having band-pass

self-similar spectra (4.67) or (4.70) are, by construction, statistically homogeneous in infinite space. As in Chapter 3, we assume again that the mean log-conductivity is a uniquely defined constant, as well as the mean hydraulic gradient. However, we must emphasize the fact that these assumptions do not take into account the influence of domain size on the "observed" mean values. Admittedly, the present approach will be only of limited interest if one insists on stationarity in the mean as a requisite for obtaining tractable solutions. Postponing to a later stage this delicate point, we examine here strictly the solutions obtained by applying the standard first order spectral method with the band-pass self-similar log-conductivity spectra defined above.

For the head variance, the effective conductivity, and the longitudinal macro-dispersion of a convected solute (as defined by Gelhar and Axness, 1983), the calculations are straightforward and need not be detailed here. Recall only that  $J$  represents the constant mean hydraulic gradient (expectation or infinite domain average). For one-dimensional flow, with the log-conductivity spectrum (4.67), the head variance is found to be:

$$\sigma_h^2 = \sigma_0^2 J^2 (L^2 - \ell^2) \quad (4.72)$$

For three-dimensional flow, with the isotropic spectrum (4.70), the head variance is:

$$\boxed{\sigma_h^2 = \frac{1}{3} \sigma_0^2 J^2 (L^2 - \ell^2)} \quad (4.73)$$

In comparison, the results obtained respectively for a 1D hole-exponential model (Gutjahr and Gelhar 1981) and the 3D Markov spectrum were, respectively:

$$\sigma_h^2 = \sigma_f^2 J^2 \lambda_{3D}^2 \quad (4.74)$$

$$\sigma_h^2 = \frac{1}{3} \sigma_f^2 J^2 \lambda_{1D}^2 \quad (4.75)$$

Note that the  $\lambda$ 's do not necessarily represent the same length scale in (4.74) and in (4.75). Nevertheless, it is interesting to note that, when  $\ell \ll L$  in the band-pass models, then the results obtained with the band-pass and continuous spectra are similar in form if one replaces  $\sigma_f^2$  by  $\sigma_0^2$  and  $\lambda$  by  $L$ . Since  $L$  represents the domain size in (4.72) and (4.73), the head variance obtained with the band-pass spectra appears to depend mainly on large-scale structures, and not on small-scale fluctuations. For instance, assuming  $\ell \ll L$  in (4.73) yields the simple result:

$$\sigma_h^2 \approx \frac{1}{3} \sigma_0^2 J^2 L^2 \quad (4.76)$$

where  $\sigma_0^2$  is the "intrinsic" log-conductivity variance and does not depend on the domain size.

For the 3D effective conductivity, one obtains formally the same result as with the 3D Markov spectrum used in Chapter 3, namely:

$$\hat{K}_{11} = K_G \exp(\sigma_f^2/6). \quad (4.77)$$

However, remember that  $\sigma_f^2$  now represents the observed finite-domain variance of the log-conductivity within the range of scales ( $\ell, L$ ). Accordingly, plugging (4.71) in (4.77) gives a *scale-dependent effective conductivity*:

$$\boxed{\hat{K}_{11} = K_G \cdot \left(\frac{L}{\ell}\right)^{\sigma_0^2/3}} \quad (4.78)$$

For the data of Figure 4.4.a, the intrinsic log-conductivity variance  $\sigma_0^2$  is on the order of 0.06, so that the rate of growth of the effective conductivity with domain size is quite slow (+10% for an increase of  $L$  by 2 orders of magnitude). Note however that this example corresponds to a mildly variable formation ( $\sigma_f^2 = 0.67$  from equation 4.71 with

$\ell = 1$  ft and  $L = 300$  ft). For highly variable media, we expect values of  $\sigma_0^2$  on the order of 0.3 - 0.6. In these cases the effective conductivity (4.78) could increase by a factor of two or more as the domain size  $L$  increases by two orders of magnitude.

It is interesting to note that this "size" effect is captured by (4.78) based solely on the standard spectral theory of stationary flow fields previously developed in Chapter 3. The increase of effective conductivity with domain size can be interpreted as follows. When the size of the domain of interest is allowed to grow, larger heterogeneities are included. The high conductivity zones outweigh those of low conductivity, due to the high degree of freedom of fluid trajectories in a three-dimensional isotropic medium.

In one dimension, the situation is reversed. Indeed, the one-dimensional effective conductivity is the harmonic mean:

$$\hat{K}_{11} = K_H = K_G \exp(-\sigma_f^2/2). \quad (4.79)$$

Expressing, as before, the observed variance  $\sigma_f^2$  in terms of the intrinsic variance  $\sigma_0^2$ , we obtain the 1D effective conductivity:



$$\boxed{\hat{K}_{11} = K_G \cdot \left(\frac{L}{\ell}\right)^{-\sigma_0^2}} \quad (4.80)$$

Thus, for  $\sigma_0^2$  on the order of 0.3 - 0.6, the effective conductivity of a one-dimensional flow system will decrease by one order of magnitude when the domain size is increased by two orders of magnitude. This is due to the low degree of freedom of fluid trajectories in one dimension. As domain size is increased, larger heterogeneities are included, and the low conductivity zones outweigh the high conductivity zones (consider what happens if an impervious inclusion is placed in a 1D flow system). Finally, the two-dimensional case appears to be special. The effective conductivity is equal to the geometric mean, and does not depend on domain size, unlike the 1 and 3-dimensional cases.

The same approach can be used to evaluate the macro-dispersivity of a convected plume. Following Gelhar (1987), the longitudinal macro-dispersivity at large times is given by:

$$A_{11} = \frac{\pi}{Q_1^2} \int_{-\infty}^{+\infty} \int_{-\infty}^{+\infty} S q_1 q_1(0, k_2, k_3) dk_2 dk_3. \quad (4.81)$$

Using the flux-based flow equation (Section 4.3) and plugging the 3D Band-Pass Self-Similar spectrum eventually leads to:

$$S_{q_1 q_1}(\underline{k}) = \bar{Q}_1^2 \frac{\sigma_0^2}{2\pi} \left[ 1 - \frac{k_1^2}{k^2} \right]^2 \cdot \frac{1}{k^3} \quad (4.82)$$

with the provision that  $S_{q_1 q_1}$  vanishes outside the wavenumber range  $(L^{-1}, \ell^{-1})$ . Plugging (4.82) into (4.81) and integrating gives finally:

$$\boxed{A_{11} = \sigma_0^2 \cdot (L - \ell)} \quad (4.83)$$

This last result suggests that the macro-dispersivity could grow linearly with the size of the plume, due to the fact that a wider range of conductivity heterogeneities will contribute to mechanical dispersion as the plume grows. However, equation (4.83) is admittedly oversimplified, due to the "large time" assumption that was used. Nevertheless, the result does suggest that the macro-dispersivity could increase in time as:

$$\boxed{A_{11}(t) \simeq \sigma_0^2 \cdot L(t)} \quad (4.84)$$

where  $L(t)$  is some typical global scale characteristic of the plume. This relation indicates the occurrence of a positive

feedback: a large macro-dispersivity enhances spreading, which in turn yields a larger macro-dispersivity.

In summary, the new spectral solutions obtained with band-pass self-similar spectra reveal the influence of domain size. For a given heterogeneous formation, the analysis suggests that the 3D head standard deviation and the longitudinal macrodispersivity increase like domain size, and the 3D effective conductivity increases slowly as a small power of domain size. In one dimension, though, the effective conductivity decreases with domain size. This behavior was found to be physically realistic based on intuitive arguments.

#### 4.4.4 Uncertainty and "spectral conditioning"

We now proceed to develop further the finite-domain approach, building on previous results obtained with the Band-Pass Self-Similar spectrum. Our purpose here is to show how the effects of local trends could be taken into account by using the idea of "spectral conditioning". This will be illustrated summarily for the simple case of one-dimensional flow in a random self-similar medium, with a prescribed uniform mean flow at the regional scale.

The idea of "spectral conditioning" -- to be described shortly -- was borrowed from a similar technique used in the Fourier-Space version of the Renormalization Group Theory of critical phenomena in statistical mechanics and quantum physics (Wilson and Kogut, 1974; Wilson, 1975; Wilson, 1983). Wilson's version of the Renormalization Group Theory involves defining an average state (magnetization) over regions of a given size  $(L)$  by truncating a spectral representation to include only the low wavenumber range  $(0 \leq k \leq L^{-1})$ , and obtaining *effective properties* (a Hamiltonian) by conditionally averaging over local fluctuations  $(k > L^{-1})$ . In fact, this is just the first step of the whole renormalization procedure, which involves iterating and re-scaling to advance towards a fixed point solution. The approach proposed here does not involve the whole recursion, but uses the idea of conditioning low frequencies while solving for higher frequencies.

Consider now the one-dimensional stochastic flow equation:

$$\frac{d^2H}{dx^2} + \frac{dF}{dx} \frac{dH}{dx} = 0 \quad (4.85)$$

where the log-conductivity  $F(x)$  is a random field whose spectrum is Band-Pass Self-Similar, with cut-off wavenumbers  $(\ell^{-1} \leq k \leq \ell^{-1})$ . Suppose we are interested in finding some

statistical characteristics of the flow within a domain of size  $L$  comprised between  $\ell$  and  $\mathcal{L}$ . This is illustrated in Figure (4.5). The small scale  $\ell$  corresponds to the measurement scale or spacing; the intermediate scale  $L$  represents the size of the flow domain of interest (perhaps the size of a contaminated zone); and the large scale  $\mathcal{L}$  is a regional scale such that the log-conductivity spectrum is roughly self-similar up to fluctuation scales on the order of  $\mathcal{L}$ . If a piece of size  $L$  of the sample function  $F(x)$  is isolated as shown in Figure (4.5), it will appear that the mean value  $\bar{F}(x)$  estimated over the domain of size  $L$  is different from the regional mean  $\langle F \rangle$ . Our main purpose is to incorporate this kind of effect in the stochastic equation (4.85) by way of "spectral conditioning".

We now develop the spectral conditioning approach to solve equation (4.85). The key to this approach consists in writing the spectral representation of  $F(\underline{x})$ , a stationary-ergodic random field, in such a way that the wavenumbers above and below  $L^{-1}$  are clearly distinguished:

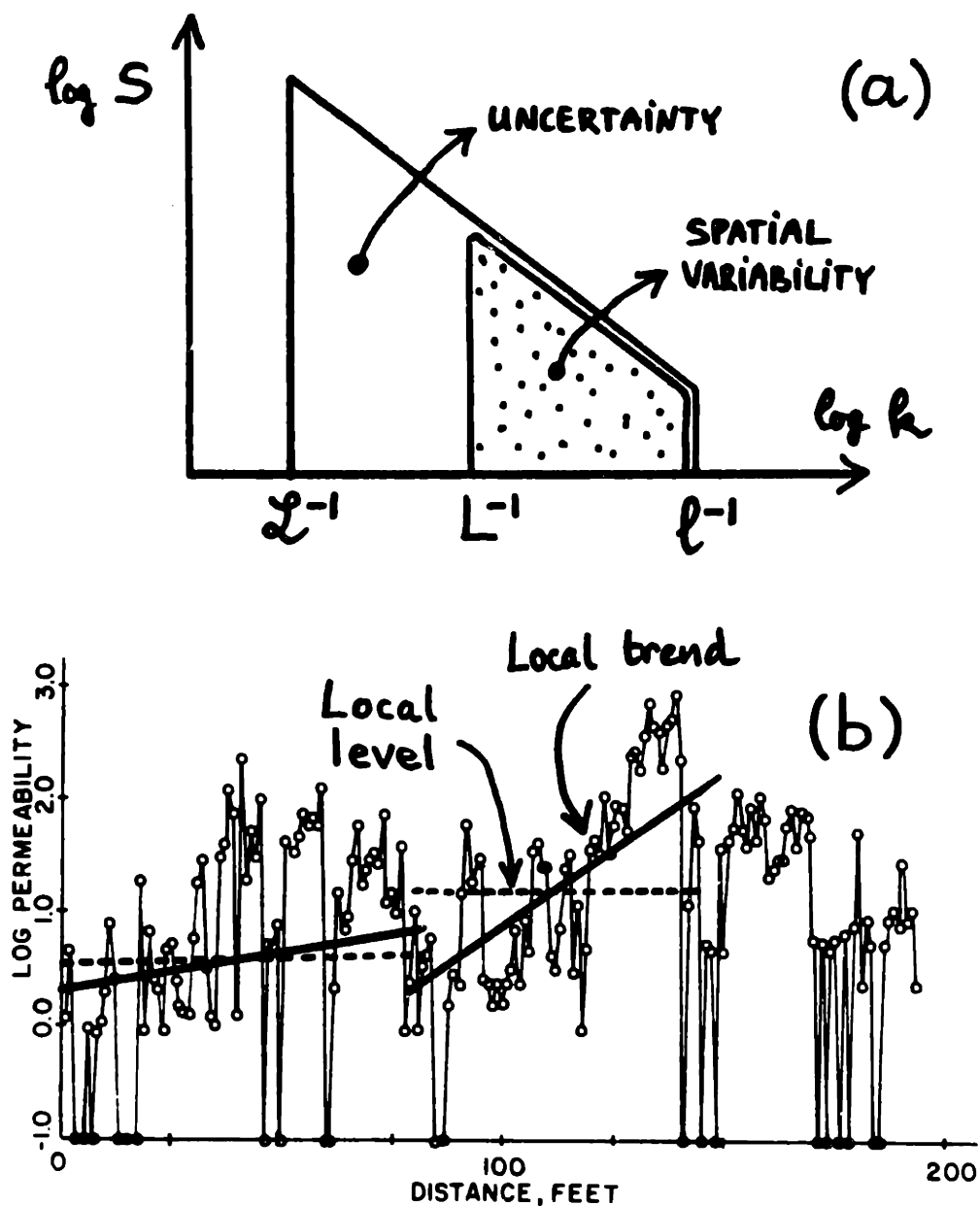


Figure 4.5: Illustration of the spectral conditioning method:  
 (a) Spectral density versus wavenumber on a log-log plot  
 (b) Sample function of log-conductivity in space (Mt. Simon data).

$$F(\mathbf{x}) = \langle F \rangle + \bar{f}(\mathbf{x}) + \tilde{f}(\mathbf{x}) = \langle F \rangle + f(\mathbf{x})$$

$$\bar{f}(\mathbf{x}) = \int_{\ell^{-1} \leq |\mathbf{k}| \leq L^{-1}} e^{j\mathbf{k}\mathbf{x}} dZ_F(\mathbf{k}) \quad (4.86)$$

$$\tilde{f}(\mathbf{x}) = \int_{L^{-1} \leq |\mathbf{k}| \leq \ell^{-1}} e^{j\mathbf{k}\mathbf{x}} dZ_F(\mathbf{k})$$

In these equations,  $\langle F \rangle$  represents the ensemble average of log-conductivity, equivalent to infinite domain average by stationarity-ergodicity of  $F(\mathbf{x})$  (in practice, this corresponds to the regional mean). The perturbation  $f(\mathbf{x})$  was split in two components. The first component is a smooth trend  $\bar{f}(\mathbf{x})$  involving only those fluctuations of scale larger than domain size  $L$ , and the second is a rapidly fluctuating component  $\tilde{f}(\mathbf{x})$  involving higher wavenumbers. As the size of the domain becomes large (on the order of the regional scale  $\ell$  or larger) this representation yields the usual infinite-domain spectral representation with:

$$\bar{f}(\mathbf{x}) \rightarrow 0$$

$$\tilde{f}(\mathbf{x}) \rightarrow f(\mathbf{x})$$

$$F = \langle F \rangle + f(\mathbf{x}).$$

Let us now "freeze" the local trend  $\bar{f}(\mathbf{x})$  by assuming that the Fourier coefficients at low wavenumbers are known. This procedure boils down to conditioning the local log-conductivity

field with respect to its large scale fluctuations and to the specific location of the local domain of interest. Say for instance that  $x_0$  defines the location of the center of the flow domain:

$$x_0 - \frac{L}{2} \leq x \leq x_0 + \frac{L}{2} .$$

Thus,  $\bar{f}(x)$  is known when the position  $x_0$  of the domain and all fluctuations on the order of domain size or larger are known. Plugging (4.86) in (4.85) while holding  $\bar{f}(x)$  fixed yields a stochastic equation driven by the local fluctuations  $\tilde{f}(x)$ , as will be seen shortly.

We now introduce a spectral representation for the head process as well. Using the same model as (4.86) gives:

$$H(x) = \langle H(x) \rangle + \bar{h}(x) + \tilde{h}(x). \quad (4.87)$$

Plugging (4.86) and (4.87) in (4.85) gives finally the stochastic flow equation in the desired form:

$$\frac{d^2 \langle H \rangle}{dx^2} + \frac{d^2 \bar{h}}{dx^2} + \frac{d^2 \tilde{h}}{dx^2} + \left[ \frac{d\bar{f}}{dx} + \frac{d\tilde{f}}{dx} \right] \left[ \frac{d \langle H \rangle}{dx} + \frac{d\bar{h}}{dx} + \frac{d\tilde{h}}{dx} \right] = 0 . \quad (4.88)$$

Upon conditional averaging (in the sense described earlier), the conditional fluctuations  $\tilde{f}$  and  $\tilde{h}$  vanish. This yields a



conditional mean equation:

$$\frac{d^2\langle H \rangle}{dx^2} + \frac{d^2\bar{h}}{dx^2} + \frac{d\bar{f}}{dx} \frac{d\langle H \rangle}{dx} + \frac{d\bar{f}}{dx} \frac{d\bar{h}}{dx} = - \left[ \overline{\frac{d\tilde{f}}{dx} \frac{d\tilde{h}}{dx}} \right]. \quad (4.89)$$

Note again that the "bar" sign stands for a conditional spectral average as defined in (4.86). By subtracting (4.89) from (4.88), one also obtains the equation governing the local head perturbations  $\tilde{h}$  conditioned on regional scale fluctuations:

$$\frac{d^2\tilde{h}}{dx^2} + \frac{d\tilde{f}}{dx} \frac{d\langle H \rangle}{dx} + \frac{d\tilde{f}}{dx} \frac{d\bar{h}}{dx} + \frac{d\bar{f}}{dx} \frac{d\tilde{h}}{dx} = - \left\{ \frac{d\tilde{f}}{dx} \frac{d\tilde{h}}{dx} - \left[ \overline{\frac{d\tilde{f}}{dx} \frac{d\tilde{h}}{dx}} \right] \right\}.$$

Neglecting the second order perturbation term on the right-hand side gives finally:

$$\frac{d^2\tilde{h}}{dx^2} + \frac{d\tilde{f}}{dx} \frac{d\langle H \rangle}{dx} + \frac{d\tilde{f}}{dx} \frac{d\bar{h}}{dx} + \frac{d\bar{f}}{dx} \frac{d\tilde{h}}{dx} \approx 0. \quad (4.90)$$

Before attempting to solve (4.90) for  $\tilde{h}(x)$ , we need some information on  $\bar{h}(x)$ . This is obtained by solving (4.89) for  $\bar{h}(x)$ , with  $\bar{f}(x)$  considered now as a *random* function (not a prescribed deterministic function). This may be called the "unconditional solution step", where  $\bar{f}(x)$  is allowed to vary randomly over all possible fluctuations larger than  $L$ , and over all possible locations  $x_0$  (midpoint of the local flow domain).

Accordingly, we now apply ensemble averages to equation (4.89) in order to obtain the *unconditional* ensemble mean and the *unconditional* perturbation equations:

$$\frac{d^2\langle H \rangle}{dx^2} = - \left\langle \frac{df}{dx} \frac{dh}{dx} \right\rangle - \overline{\left\langle \frac{df}{dx} \frac{dh}{dx} \right\rangle}$$

$$\frac{d^2\bar{h}}{dx^2} + \frac{d\bar{f}}{dx} \frac{d\langle H \rangle}{dx} = - \left\{ \frac{d\bar{f}}{dx} \frac{d\bar{h}}{dx} - \left\langle \frac{d\bar{f}}{dx} \frac{d\bar{h}}{dx} \right\rangle \right\}$$

$$- \left\{ \overline{\left\langle \frac{df}{dx} \frac{dh}{dx} \right\rangle} - \left\langle \frac{df}{dx} \frac{dh}{dx} \right\rangle \right\}.$$

We now neglect the high order perturbation terms appearing on the right-hand sides, as we did in the formal "small parameter" expansion developed in section 3.1 of Chapter 3. Thus, we obtain finally:

$$\frac{d^2\langle H \rangle}{dx^2} \approx 0 \quad (4.91)$$

and

$$\frac{d^2\bar{h}}{dx^2} + \frac{d\bar{f}}{dx} \frac{d\langle H \rangle}{dx} \approx 0. \quad (4.92)$$

Equation (4.91) implies that the ensemble mean (or regional) hydraulic gradient is constant:

$$J = - \frac{d\langle H \rangle}{dx} \quad (4.93)$$

Plugging this into equation (4.92) governing the perturbation of the local mean head, yields the simple result:

$$\frac{dh}{dx} \approx J \cdot \bar{f}(x). \quad (4.94)$$

This relation makes sense intuitively. The term  $(-\frac{dh}{dx})$  represents the perturbation of the local mean hydraulic gradient with respect to the regional gradient ( $J$ ); it is positive if the local mean log-conductivity is smaller than the regional mean ( $\bar{f}$  negative). Thus, the local mean hydraulic gradient will be higher than the regional mean if the local mean log-conductivity is lower than its regional mean (the term "local" refers to domain size  $L$ ). This behavior is suggested more directly by the form of the Darcy equation in one-dimensional space: the hydraulic gradient is inversely proportional to the conductivity.

We may now attempt a spectral solution of the conditional perturbation equation (4.90), by plugging (4.93) and (4.94) while holding  $\bar{f}(x)$  fixed (non-random). This gives the required stochastic equation for the local head perturbations:

$$\boxed{\frac{d^2 \tilde{h}}{dx^2} + \frac{d\bar{f}}{dx} \frac{d\tilde{h}}{dx} \approx J \cdot (1-\bar{f}) \cdot \frac{d\tilde{f}}{dx}} \quad (4.95)$$

It is important to note that  $\bar{f}(x)$  is by construction a slowly varying function, compared to the rapid oscillations of  $\tilde{f}(x)$ . This suggests approximating equation (4.95) by letting  $d\bar{f}/dx$  be some average slope, and  $\bar{f}$  some average level of  $\bar{f}(x)$  within the flow domain, as illustrated in Figure (4.5).

With this provision, equation (4.95) becomes a linear stochastic equation which can be solved by the standard spectral method in Fourier space. The result is given below in terms of Fourier-Stieltjes increments conditioned on the values taken by  $\bar{f}$  and  $d\bar{f}/dx$ :

$$dZ_h^{\sim}(k) \approx -J(1-\bar{f}) \frac{jk}{k^2 - j\frac{d\bar{f}}{dx}k} dZ_f^{\sim}(k). \quad (4.96)$$

This gives the conditional head spectrum:

$$\boxed{S_{hh}^{\sim}(k) \approx J^2(1-\bar{f})^2 \frac{1}{k^2 + (\frac{d\bar{f}}{dx})^2} S_{ff}^{\sim}(k)} \quad (4.97)$$

where  $S_{ff}^{\sim}(k)$  is the conditional band-pass self-similar spectrum  $\sigma_0^2/k$ , vanishing outside the range  $L^{-1} \leq k \leq \ell^{-1}$ . Note that the low wavenumber range ( $k \leq L^{-1}$ ) has been incorporated entirely into the terms  $\bar{f}$  and  $d\bar{f}/dx$ , the local mean level and local trend of log-conductivity.

The conditional head variance obtains directly from (4.97) by integrating over the wavenumber range  $(L^{-1}, \ell^{-1})$ . This gives after some manipulation and replacing  $(1-\bar{f})$  by  $e^{-\bar{f}}$ :

$$\boxed{\tilde{\sigma}_h^2 \approx \sigma_0^2 J^2 \frac{e^{-2\bar{f}}}{\left(\frac{d\bar{f}}{dx}\right)^2} \cdot \ell n \left\{ \frac{1 + \left(\frac{d\bar{f}}{dx}\right)^2 L^2}{1 + \left(\frac{d\bar{f}}{dx}\right)^2 \ell^2} \right\}} \quad (4.98)$$

Incidentally, it is interesting to note that this expression gives the correct head variance as  $L$  goes to infinity ( $L \gg \ell$ ). Indeed in this case, the local and regional means coincide, yielding  $\bar{f} \rightarrow 0$  and  $\frac{d\bar{f}}{dx} \rightarrow 0$ , and it can be seen from a Taylor development of the logarithmic term that the right-hand side of (4.98) will coincide exactly with the previous result (4.72). Recall also that the conditional log-conductivity variance, obtained by integrating the log-conductivity spectrum in the range  $L^{-1} \leq k \leq \ell^{-1}$ , depends on domain size as in equation (4.69), that is:

$$\tilde{\sigma}_f^2 = 2 \sigma_0^2 \ell n\left(\frac{L}{\ell}\right). \quad (4.99)$$

The last step of the spectral conditioning method consists in analyzing the local head variance (4.98) as a random parameter when  $\bar{f}(x)$  is viewed as a random field. Indeed, remember that  $\bar{f}$  was defined in (4.86) as the difference between

a local and regional mean: the spectral content of  $\bar{f}(x)$  coincides with the spectrum of the log-conductivity in the wavenumber range  $\varphi^{-1} \leq k \leq L^{-1}$ . Accordingly,  $\tilde{\sigma}_h^2$  can be viewed as the local head variance due to spatial variability at the local scale  $L$ ; at the same time,  $\tilde{\sigma}_h^2$  also appears to be random at the regional scale  $\varphi$ . The randomness of  $\tilde{\sigma}_h^2$  arises from uncertainty among all possible realizations of the regional formation, and should be understood in the Bayesian sense, that is in terms of risk analysis.

In order to evaluate explicitly the uncertainty on  $\tilde{\sigma}_h^2$ , let us compute the ensemble variance of the random terms appearing in (4.98) for the case  $L \leq \varphi$  :

$$\text{Var}(\bar{f}) = 2\sigma_0^2 \ln\left(\frac{\varphi}{L}\right)$$

$$\text{Var}\left(\frac{d\bar{f}}{dx}\right) = \sigma_0^2 \left(\frac{1}{L^2} - \frac{1}{\varphi^2}\right) .$$

Plugging these values into (4.98), we obtained after some manipulations a rough estimate of the coefficient of variation of the local head variance:

$$\text{C.V.}(\tilde{\sigma}_h^2) \sim 1 - \exp\{-2\sqrt{2\sigma_0^2 \ln(1/\epsilon)}\} \cdot \frac{\ln\{1+\sigma_0^2(1-\epsilon^2)\}}{\sigma_0^2(1-\epsilon^2)} \quad (4.100)$$

where  $\epsilon$  is the length scale ratio  $L/l$ . Using hypothetical data for a fairly heterogeneous formation ( $\sigma_0^2 \approx 0.5$ ) with a domain size about one order of magnitude smaller than the regional scale ( $\epsilon = 0.1$ ), yields a C.V. on the order of 100%. In addition, equation (4.98) shows more specifically that the local head variance is larger than its expectation if the local mean of the log-conductivity is smaller than the regional mean value.

A similar analysis can be carried out for the *effective conductivity*. First, the Darcy equation can be used to define a *local effective conductivity*  $\tilde{K}_{\text{eff}}$ , conditioned on regional scale fluctuations. Second, the *uncertainty* on  $\tilde{K}_{\text{eff}}$  can be computed by averaging over the unresolved fluctuations (terms involving  $\bar{f}(x)$ ). Using previous results (equation 4.94), the Darcy equation can be expressed as:

$$Q = -K_G e^{(\bar{f} + \tilde{f})} \cdot \left( -J + J \cdot \bar{f} + \frac{dh}{dx} \right)$$

where the flux  $Q$  is necessarily constant for 1D flow. Taking conditional expectations with respect to both sides (with  $\bar{f}(x)$  fixed), and linearizing the exponential term gives:

$$Q \approx -K_G \left\{ J \cdot \left( \frac{\overline{\tilde{f}^2}}{2} - 1 \right) + \overline{\tilde{f}} \cdot \frac{dh}{dx} - J \cdot \frac{\overline{\tilde{f}^2}}{2} \right\}.$$

Using previous definitions, the second term on the right can be computed by spectral integration as shown below:

$$\overline{\tilde{f} \frac{d\tilde{h}}{dx}} = \int_{L^{-1} \leq |k| \leq \ell^{-1}} jk \langle dZ_f^* \cdot dZ_h \rangle.$$

Plugging equation (4.96) for  $dZ_h$ , and using the band-pass self-similar spectrum for the log-conductivity finally leads to:

$$Q = \tilde{K}_{\text{eff}} \cdot J$$

where the local effective conductivity is given by:

$$\tilde{K}_{\text{eff}} \simeq K_G \cdot \left\{ 1 - \frac{\bar{f}^2}{2} + \sigma_0^2 \ln\left(\frac{L}{\ell}\right) - (1-\bar{f}) \cdot 2\sigma_0^2 \ln \left[ \frac{L}{\ell} \cdot \sqrt{\frac{1+a^2\ell^2}{1+a^2L^2}} \right] \right\}$$

and  $a = d\bar{f}/dx$ . After rearranging and replacing terms like  $(1-\bar{f})$  by exponentials, we obtain a more realistic expression for the local effective conductivity as follows:



$$\tilde{K}_{\text{eff}} \approx K_G \cdot \exp \left\{ (1 - 2e^{-\bar{f}}) \cdot \sigma_0^2 \ln\left(\frac{L}{\ell}\right) + e^{-\bar{f}^2/2} + e^{-\bar{f}} \sigma_0^2 \ln\left(\frac{1 + a^2 L^2}{1 + a^2 \ell^2}\right) \right\}. \quad (4.101)$$

This effective conductivity is local to the flow domain of size  $L$ , in the sense that it is conditioned on the local mean  $(K_G e^{\bar{f}})$  and the local trend  $(a = d\bar{f}/dx)$ . As the domain size increases, these parameters converge to the regional mean values  $(\bar{f} = 0 \text{ and } a = 0)$ . In that case, equation (4.101) converges to the harmonic mean:

$$K_H = K_G e^{-\sigma_0^2 \ln\left(\frac{L}{\ell}\right)} = K_G e^{-\sigma_f^2/2}$$

as expected. Moreover, equation (4.101) shows that the local effective conductivity drops below the arithmetic mean if the local mean level of  $\ln K$  happens to be smaller than the regional mean  $(\bar{f} < 0)$ . Finally, the variance of  $\tilde{K}_{\text{eff}}$  could be computed from this equation by letting  $\bar{f}(x)$  be random, and applying ensemble averages to resolve the uncertainty due to low wavenumber components (regional scale fluctuations).

In summary, the "spectral conditioning" approach based on a band-pass self-similar model of the log-conductivity spectrum was used to evaluate the effect of domain size on "large scale" flow characteristics. This led to closed form expressions for the head variance and the effective conductivity in a finite domain. Moreover, we have shown that these statistical quantities were themselves subject to uncertainty due to heterogeneities on the order of domain size or larger. The solutions obtained for the case of one-dimensional flow incorporate such uncertainty in the form of two simple random parameters:

- (i) The local mean "level" of conductivity ( $K_G e^{\bar{f}}$ );
- (ii) The local mean slope of log-conductivity ( $a = d\bar{f}/dx$ ).

These local parameters were defined by smoothing out the local fluctuations of  $\ln K$ , i.e. those fluctuations whose wavenumber is higher than the inverse domain size. Their spectral content is concentrated exclusively in the low wavenumber range, which decreases as domain size increases.

The whole approach leads to analytical results that distinguish the uncertainty and spatial variability of phenomena taking place over finite scales. This may be particularly relevant for the case of a subsurface contamination plume

spreading from a local source, where there is some uncertainty about the location of the center of mass and the extent (macro-dispersion) of the plume at early times. It would be interesting to examine how this uncertainty decreases as the time and length scales of the plume increase. Admittedly, more work is needed in order to evaluate the potential of the proposed "spectral conditioning approach" for realistic model problems of stochastic flow and dispersive transport. Last but not least, large sets of conductivity data collected over a wide range of scales may be needed in order to ascertain the validity of the proposed band-pass self-similar model. A useful range of scales for subsurface contamination problems may involve at least three to four orders of magnitude along each spatial direction.

## **CHAPTER 5 NUMERICAL METHOD FOR LARGE SINGLE-REALIZATION SOLUTIONS OF STOCHASTIC FLOW IN SATURATED OR UNSATURATED MEDIA**

### **5.1 Governing Equations and Finite Difference Approximations**

In this introductory section, we develop a Finite Difference numerical approximation for solving large single-realization stochastic flow problems in three dimensions. The choice of the finite difference (FD) discretization method is justified by considering the numerical requirements and computational work involved. The discrete form of the flow equation (finite difference system) is given in detail for steady saturated flow, and also for the more general case of transient flow in partially saturated or unsaturated media with nonlinear and spatially variable coefficients.

#### **5.1.1 - Governing equation and numerical requirements**

For simplicity, let us focus here on the case of saturated flow in the steady state, postponing to a later stage the analysis of the more general case of transient and unsaturated flow. The governing equation for the hydraulic head  $H$  is easily obtained from the Darcy equation and the continuity equation. By using implicit summation over repeated indices, this yields in three dimensions:

$$L_K(H) = - \frac{\partial}{\partial x_i} \left[ K(\underline{x}) \frac{\partial H}{\partial x_i} \right] = 0 \quad (i = 1, 2, 3). \quad (5.1)$$

Here, we emphasize once again that the flow problem to be solved is inherently stochastic, since the conductivity is assumed to be a random function of space. But, according to the single realization approach, we aim at obtaining a numerical solution of the flow equation for one particular realization of the random conductivity field  $K(\underline{x})$ , over a large finite domain with specified boundary conditions. Thus, equation (5.1) is now considered as a single realization of a stochastic partial differential equation. The flow problem "appears" to be deterministic and may be solved, in principle, by standard numerical methods.

On the other hand, recall that the idea of the single-realization approach is to obtain the statistical properties of the flow field by postulating the equivalence of spatial averages and ensemble averages. The flow statistics obtained in this manner should be unique, independent of the particular realization, provided that the flow field is statistically homogeneous and ergodic and the domain is sufficiently large. In this framework, the numerical solution of the single-realization problem requires special care regarding the numerical method to be used. The difficulty is that the local conductivity  $K(\underline{x})$  fluctuates wildly in space, which

requires a high resolution mesh in order to capture the detailed features of the flow field. On the other hand, the domain must be large compared to the largest scale of fluctuation of the flow field, in order to guarantee the equivalence of spatial and ensemble statistics by the ergodicity hypothesis. These considerations imply that the size of the computational grid may have to be unusually large to capture the fluctuations of the flow solution over a reasonably wide range of scales.

For a preliminary evaluation of statistical requirements, one may use the  $\ell_n$  K-correlation scale  $\lambda_i$  as an indication of the typical scale of fluctuation of the solution (the index  $i$  refers to the spatial direction  $x_i$ ). Let  $\Delta x_i$  be the size of the discretization cell, and  $L_i$  the size of the computational flow domain. We require for adequate statistical resolution:

$$\Delta x_i / \lambda_i \ll 1. \quad (5.2)$$

On the other hand, the computational flow domain must be large enough so that many "independent events" can be sampled. In other words, the domain size must be taken much larger than the scale of fluctuation, that is:

$$L_i / \lambda_i \gg 1. \quad (5.3)$$

Now, the number of discretization cells in each direction is:

$$n_i = L_i / \Delta x_i$$

and the total number of cells in 3 dimensions is:

$$N = n_1 n_2 n_3.$$

The requirements (5.2) and (5.3) could lead to ratios  $L_i / \Delta x_i$  on the order of 100 or more, implying that the typical size of the computational grid ( $N$ ) could be 1 Million cells or more.

Another major point of concern is the validity of classical numerical methods, such as finite differences (FD) or finite elements (FE) Methods, when applied to an equation like (5.1) with highly variable conductivities. Intuitively, one would expect that the error due to discretization decreases as  $\sigma_f$  decreases. Note for instance that as  $\sigma_f \rightarrow 0$ , equation (5.1) becomes just the Laplace equation which can be solved accurately (even exactly) with a second order accurate FD or FEM scheme. The key question is: "what happens when  $\sigma_f$  is significantly different from zero?" The truncation error analysis to be developed in the next section will show that the discretization error decreases with  $\Delta x_i / \lambda_i$  when  $\sigma_f$  is fixed. Intuitively, this means that truncation errors are small when the solution

behaves smoothly at the scale of the mesh. We conclude that the resolution constraint (5.2) is a requirement for *numerical accuracy* as well as statistical resolution.

In summary, the issues of numerical accuracy, statistical resolution, and large sampling space, all indicate the need for solving very large discrete systems (e.g., one million equations or more). This has led us to the choice of the 7-point centered finite difference scheme for spatial discretization. The reason for this choice will appear more clearly in the sequel. Let us briefly mention some of the arguments in favor of this discretization method. First of all, the resulting system of equations is very sparse, symmetric and can be solved efficiently by fast iterative methods based on matrix preconditioning, such as the Strongly Implicit Procedure (SIP) and the Incomplete-Choleski Conjugate Gradient (ICCG) methods. Moreover, the algebraic properties of the coefficient matrix arising from other discretization methods, such as Galerkin, would not be as well suited to fast solution methods. In our view, the centered finite difference scheme essentially gives the most sparse and best structured algebraic system among all discretization methods consistent with the governing flow equation. Based on these remarks, most of our efforts were devoted to developing efficient solvers for large finite difference systems having spatially variable (random)



coefficients. This will be developed in detail in Section 5.3 (for linear systems) and in Section 5.4 (for unsaturated nonlinear systems), following the truncation error analysis of linear flow systems presented in Section 5.2.

We now proceed to develop the finite difference approximations, first for the steady saturated flow equation, then for the transient unsaturated flow equation with nonlinear coefficients. The stochastic nature of the coefficients in these equations should always be kept in mind, particularly for purposes of error analysis.

### 5.1.2 - Finite difference in space for steady saturated flow

#### [a] Derivation of the Finite Difference System:

The 7-point centered finite difference approximation of the steady state flow equation (5.1) obtains by approximating the Darcy flux  $q_1 = -K(\underline{x}) \frac{\partial H}{\partial x_1}$  by the centered difference scheme:

$$q_1(x_{i+1/2, j, k}) \approx -K_{i+1/2, j, k} \left[ \frac{H_{i+1, j, k} - H_{i, j, k}}{\Delta x_1} \right] \quad (5.4)$$

Note that  $q_1$  is evaluated at the mid-nodal point  $x_{i+1/2, j, k}$  of an orthogonal grid where nodes are located at  $x_{i, j, k}$ . The derivative  $\frac{\partial q_1}{\partial x_1}$  is then approximated again by the centered

difference:

$$\frac{\partial q_1}{\partial x_1}(x_{i,j,k}) \approx \frac{q_1(x_{i+1/2,j,k}) - q_1(x_{i-1/2,j,k})}{\Delta x_1} \quad (5.5)$$

at the node points  $x_{i,j,k}$ . By repeating similar approximations for the terms  $\frac{\partial q_2}{\partial x_2}$  and  $\frac{\partial q_3}{\partial x_3}$ , one obtains the Finite Difference system governing the hydraulic head at the nodes of the orthogonal grid. For convenience, we use the triple-index notation as shown below between brackets:

$$\begin{aligned} [0] &= (i, j, k) \\ [i \pm 1/2] &= (i \pm 1/2, j, k) \\ [i \pm 1] &= (i \pm 1, j, k) \\ &\text{etc.} \end{aligned}$$

Accordingly, the FD system for heads can be expressed as:

$$\begin{aligned} \hat{L}_K(H) = & - \frac{K[i-1/2]}{(\Delta x_1)^2} \cdot H[i-1] - \frac{K[j-1/2]}{(\Delta x_2)^2} \cdot H[j-1] - \frac{K[k-1/2]}{(\Delta x_3)^2} \cdot H[k-1] \\ & + \left\{ \frac{K[i-1/2] + K[i+1/2]}{(\Delta x_1)^2} + \frac{K[j-1/2] + K[j+1/2]}{(\Delta x_2)^2} + \frac{K[k-1/2] + K[k+1/2]}{(\Delta x_3)^2} \right\} \cdot H[0] \\ & - \frac{K[i+1/2]}{(\Delta x_1)^2} \cdot H[i+1] - \frac{K[j+1/2]}{(\Delta x_2)^2} \cdot H[j+1] - \frac{K[k+1/2]}{(\Delta x_3)^2} \cdot H[k+1] = 0 \end{aligned} \quad (5.6)$$

and the Darcy flux vector (5.4) can be expressed in terms of the discrete head solution as:

$$\begin{aligned}
 q_1[i+\frac{1}{2}] &= -K[i+\frac{1}{2}] \cdot \frac{H[i+1]-H[0]}{\Delta x_1} \\
 q_2[j+\frac{1}{2}] &= -K[j+\frac{1}{2}] \cdot \frac{H[j+1]-H[0]}{\Delta x_2} \\
 q_3[k+\frac{1}{2}] &= -K[k+\frac{1}{2}] \cdot \frac{H[k+1]-H[0]}{\Delta x_3}
 \end{aligned} \tag{5.7}$$

where  $H[0]$  stands for the head at the central node  $H(i,j,k)$ .

The FD system (5.6) comprises  $N$  equations: one equation per node. Equation  $(i,j,k)$  relates the unknown at node  $(i,j,k)$  to the unknown at six neighboring nodes  $(i\pm 1, j\pm 1, k\pm 1)$  as illustrated in Figure 5.1, representing the 7-point FD molecule in space. Note that mid-nodal conductivities like  $K[i+\frac{1}{2}]$  stand for point values of  $K(\underline{x})$  at  $\underline{x} = x_{i+\frac{1}{2},j,k}$ . Since only the nodal values of  $K(\underline{x})$  are known, the mid-nodal conductivities must be approximated by some weighting scheme, such as the *geometric mean of nodal conductivities*:

$$\hat{K}[i+\frac{1}{2}] \simeq \sqrt{K[0] \cdot K[i+1]}$$

or in more explicit triple-index notation:

$$\hat{K}(i+\frac{1}{2}, j, h) \simeq \sqrt{K(i, j, k) \cdot K(i+1, j, k)} \tag{5.8}$$

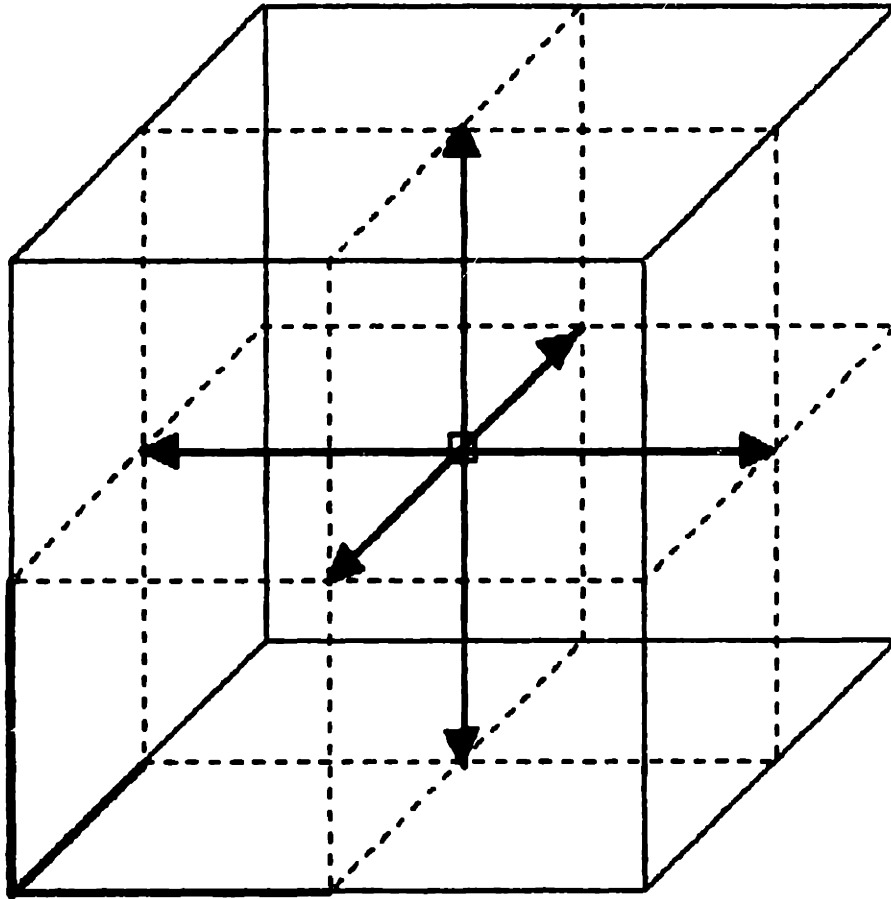


Figure 5.1 Seven-point centered finite difference molecule for a three-dimensional orthogonal grid of mesh points.

The geometric mean weighting scheme was preferred to other schemes used in the literature (such as the arithmetic mean and the harmonic mean) based on the findings of the spectral theory concerning the effective conductivity of a three-dimensional random isotropic formation:

$$K_H = K_G e^{-\sigma_f^2/2} < K_{\text{eff}} = K_G e^{\sigma_f^2/6} < K_A = K_G e^{\sigma_f^2/2} \quad (5.9)$$

Equation (5.9) shows that the flow at the large scale is governed by  $K_G$  more closely than  $K_A$  or  $K_H$ . This suggests that the flow at smaller scales is similarly governed by the local geometric mean conductivity (5.8), more closely than by arithmetic or harmonic averages. To complete this analogy, observe that the discrete conductivity field will appear more nearly isotropic at the mesh scale if the mesh size is chosen proportional to the conductivity correlation scales in all three directions ( $\Delta x_1/\lambda_1 = \Delta x_2/\lambda_2 = \Delta x_3/\lambda_3$ ). This seems to be a desirable property in order to avoid artificial grid-induced anisotropy.

Other criteria for a "best" conductivity weighting scheme were proposed in the literature (e.g., Narasimhan et al., 1978). Their arguments do not appear convincing enough to be taken into account, as truncation error analysis shows that the

weighting error  $\hat{K}[i+\frac{1}{2}] - K[i+\frac{1}{2}]$  remains of order  $O((\Delta x/\lambda)^2)$  for all consistent weighting schemes such as  $K_H, K_G, K_A$ . Intuitively, when the mesh size is such that  $\Delta x_i/\lambda_i$  is the same in all directions, the geometric mean weighting scheme appears as a good compromise between the arithmetic mean (exact for layered systems with flow parallel to layers) and the harmonic mean (exact for layered systems with flow perpendicular to layers).

We now focus on the structure of the linear FD system (5.6). In matrix notation, this system can be expressed as:

$$\underline{\underline{K}} \cdot \underline{h} = \underline{b} \quad (5.10)$$

where  $\underline{\underline{K}}$  is the coefficient matrix, or conductivity matrix of size  $N = n_1 n_2 n_3$  for the 3D case (boundary nodes excluded). The vector  $\underline{h}$  represents the nodal head values, and  $\underline{b}$  is a vector containing boundary conditions such as fixed head and fixed flux. In our implementation, this vector was formed by a technique known as "matrix condensation": the discretized boundary conditions were used to express the unknown at the boundaries in terms of the unknowns at neighboring nodes located inside the domain. All quantities such (as  $H$  or  $q$ ) specified at the boundaries were then transferred to the right-hand side of the system (vector  $\underline{b}$ ). The details of this procedure are illustrated below in the simple case of one-dimensional flow.

Consider the case of one-dimensional flow with fixed head on the left boundary and fixed flux on the right boundary. The flux condition on the right is discretized by using a centered FD approximation at the mid-node located between the last and next-to-last nodes (one may consider the physical boundary to be located precisely at the mid-node). The finite difference approximation of Darcy equation yields:

$$q(x_{n+1/2}) \approx -K_{n+1/2} \cdot \frac{H_{n+1} - H_n}{\Delta x} = q_{n+1/2} \quad (5.11)$$

On the other hand, the head condition on the left boundary can be expressed exactly as:

$$H(x_0) = H_0. \quad (5.12)$$

After implementation of boundary conditions, the one-dimensional Finite Difference system analogous to (5.10) can be written explicitly as follows:

$$\begin{aligned} i = 1: & \quad 0 + \frac{K_{1/2} + K_{1+1/2}}{\Delta x^2} \cdot H_1 - \frac{K_{1+1/2}}{\Delta x^2} \cdot H_2 = +\frac{K_{1/2}}{\Delta x^2} \cdot H_0 \\ & \quad \cdot \\ & \quad \cdot \\ & \quad \cdot \\ 1 < i < n: & \quad -\frac{K_{i-1/2}}{\Delta x^2} \cdot H_{i-1} + \frac{(K_{i-1/2} + K_{i+1/2})}{\Delta x^2} \cdot H_i - \frac{K_{i+1/2}}{\Delta x^2} \cdot H_{i+1} = 0 \\ & \quad \cdot \\ & \quad \cdot \\ i = n: & \quad -\frac{K_{n-1/2}}{\Delta x^2} \cdot H_{n-1} + \left\{ \frac{K_{n+1/2} + K_{n+1/2}}{\Delta x^2} - \frac{K_{n+1/2}}{\Delta x^2} \right\} \cdot H_n - 0 = \frac{-q_{n+1/2}}{\Delta x} \end{aligned} \quad (5.13)$$

The proposed treatment of flux boundary conditions (see the last equation above) has several advantages over other schemes proposed in the literature. First, the flux at the boundary is approximated by the same scheme as used for interior nodes (compare (5.4) to (5.11)). Second, the coefficient matrix retains the same sparsity pattern and remains symmetric after elimination of boundary values, as can be seen by inspection of (5.13). In the one dimensional case above, a tridiagonal symmetric system is obtained.

In the three-dimensional case, boundary conditions similar to (5.11) and (5.12) should be used for each node of the six planar boundaries. The resulting coefficient matrix  $\underline{K}$  is 7-diagonal symmetric, as illustrated in Figure (5.2). Each of the six off-diagonal lines contains a few zeroes corresponding to those nodes that are adjacent to one or several boundaries. For a cubic domain of size  $N = n^3$ , the number of such zeroes on the off-diagonal lines is only  $O(n^2)$ , while the size of each line is about  $O(n^3)$ . On the whole, only  $4n^3$  matrix elements need to be defined, due to the symmetry and sparsity of the matrix. This is very small compared to the total number of elements of the matrix,  $(n^3 \times n^3)$  including the zeroes. Thus, for a 1 million node grid ( $n = 100$ ), the total number of elements in the matrix is  $10^{12}$ , of which only  $4 \times 10^6$  are actually non-zero. In addition, it is important to note that the location of the



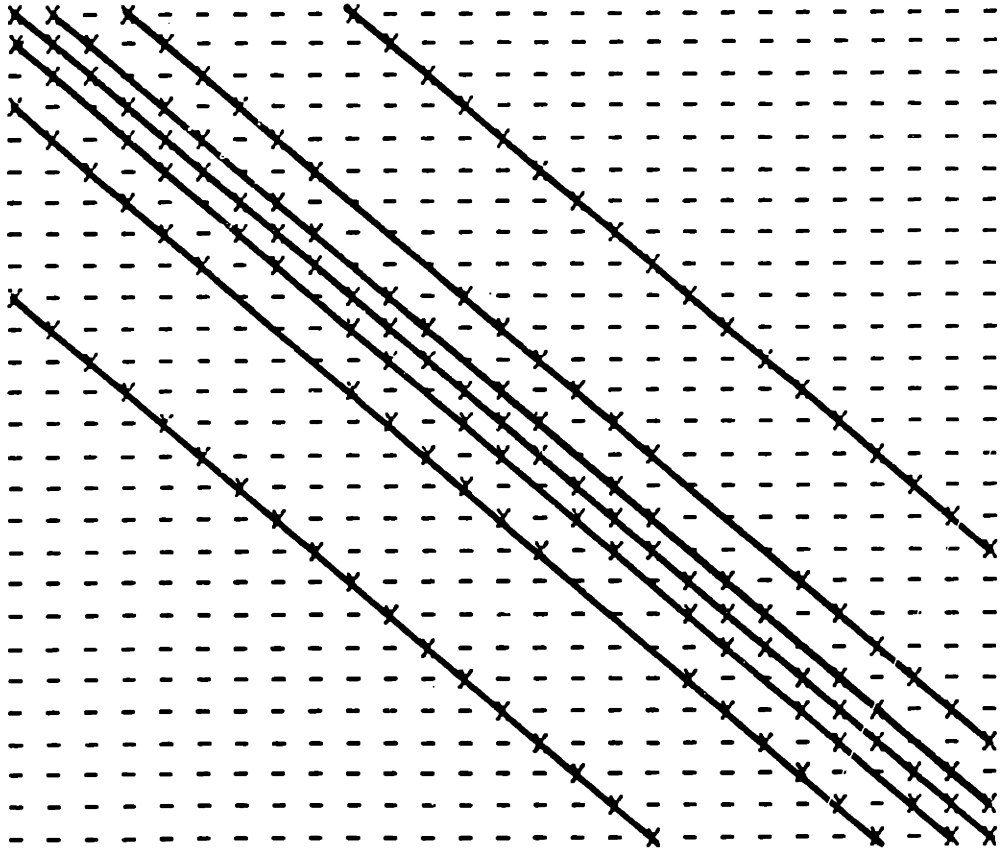


Figure 5.2 Structure of the coefficient matrix for the seven-point centered finite difference scheme, illustrated here for a 3D cubic grid with 27 internal nodes (cubic domain of side  $4\Delta x$ ). The matrix is symmetric and has only seven non-zero diagonal lines.

non-zero elements (or non-zero lines) is known exactly. This is illustrated shown in Figure (5.2), for a small matrix of size  $27 \times 27$  corresponding to  $n = 3$  interior nodes along each side of the domain.

Furthermore, it can be seen by inspection that  $\underline{K}$  is symmetric positive-definite and weakly diagonal-dominant, provided that a fixed head boundary condition be specified on at least one boundary node. The matrix becomes singular in the case where all nodal boundary conditions are "fixed flux". In this case, a solution to the steady state problem exists only if the algebraic sum of in-going and out-going fluxes is identically zero; the head solution is then only defined up to an additive constant.

Finally,  $\underline{K}$  has also the "M-matrix property", that is all diagonal elements are strictly positive and all off-diagonal elements are negative or null. This property is required for certain approximate factorization methods such as Incomplete Choleski decomposition (Meijerink and Van der Vorst, 1977). More generally, many iterative solution methods rely on the system being at least symmetric positive-definite in order to ensure optimal convergence (e.g., successive overrelaxation methods). Positive-definiteness or weak diagonal dominance is also required

for the stability to round-off errors of certain matrix factorization methods, such as the Thomas algorithm for tri-diagonal matrices. This requirement is likely to extend to more general factorization methods such as the one considered in section 5.2 for the solution of the 7-diagonal finite difference system (SIP factorization).

In conclusion, the 7-point centered FD scheme seems very well suited for the application of fast iterative methods, particularly those based on approximate factorization, due to the sparsity and special algebraic structure of the coefficient matrix.

[b] - Comparison of Finite Differences with the Galerkin Method:

It may be instructive to compare the sparse FD system with the Finite Element system obtained by using the Galerkin method with tetrahedral elements and tri-linear basis functions (details can be found for instance in Huyakorn and Pinder, 1983, pp. 88, 3.5.1). One of the simplest partitions of 3D space into tetrahedral elements is obtained from a regular partition of space into hexahedral elements, each of which is further subdivided into six tetrahedra, of distinct sizes and shapes. It may be of interest to note that there exists no regular partition of the 3D space with tetrahedra all of the same size and shape;

in contrast the 2D space can be partitioned into triangles all of the same size and shape (see for instance Coxeter's book "Regular Polytopes", 1973).

The Galerkin system for the 3D saturated flow equation (5.1) takes the form:

$$\sum_{J=1}^N a_{IJ} \cdot H_J = b_I \quad (I = 1, \dots, N)$$

where  $N = n^3$  is the total number of nodes for the regular orthogonal partition of space into identical hexahedra, and the matrix coefficients  $a_{IJ}$  are made up of weighted conductivities over the set of six tetrahedral elements forming an hexahedron. These coefficients take the form:

$$a_{IJ} = \sum_{H=1}^N \sum_{T=1}^6 \sum_{i=1}^3 \int_{\Omega_{H,T}} \alpha_I^{(i)} \alpha_J^{(i)} K(\underline{x}) \, d\underline{x} \quad (5.14)$$

where tetrahedral elements were labeled " $\Omega_{H,T}$ ". The index H runs over all hexahedral elements (same as total number of nodes), the index T runs over the six tetrahedra comprised in one hexahedron, and the index  $i = 1, 2, 3$  is related to the three independent tri-linear basis functions. It turns out that the coefficient product  $\alpha_I^{(i)} \alpha_J^{(i)}$  ( $i = 1, 2, 3$ ) is generally non-zero for 27 tetrahedra out of 6N tetrahedra on each row (equation) of the

matrix system. This yields *a priori* 27 non-zero diagonal lines in the Galerkin coefficient matrix.

In fact, most Finite Element equation solvers ignore the fine structure of the matrix, e.g. they only take into account the bandwidth of the system, (size of the band containing non-zero coefficients). The bandwidth is  $2n^2 + 1$  for a cubic domain of size  $n^3$ . Taking into account the symmetry of the matrix, this implies that the number of matrix elements to be processed for solution is about  $n^6$ , compared to  $4n^3$  for the 7 point FD system. In our view, these observations show that the solution of the Galerkin system would be impractical for large grids on the order of 1 million hexahedral cells ( $n = 100$ ). Moreover, it turns out that the Galerkin system does not satisfy the "M-matrix property" mentioned above. This seems to exclude the Galerkin system as a candidate for Incomplete Choleski, and other approximate factorization methods. Note that the SIP method in particular was specifically designed for Finite Difference systems having a simple structure.

We conclude again that the 7-point centered Finite Difference scheme appears the most suited for the solution of very large flow problems with fluctuating conductivities, due to

the special algebraic properties and sparsity of the FD system. In comparison, "higher order" discretization methods such as Galerkin lead to more complex matrix structures, particularly in the three-dimensional case. We feel that the advantage of using higher order or smoother numerical approximations may well be offset by the significant increase in computational work for three-dimensional, high resolution simulations.

#### **5.1.3: Finite difference in space-time for transient unsaturated flow**

We now extend our finite difference discretization method to the case of unsaturated flow, or more generally "partially saturated flow", in a statistically heterogeneous porous medium. In what follows, we focus particularly on the case of transient flow, as this is of interest for applications like local infiltration in unsaturated soils. However, the cases of steady unsaturated flow, mixed saturated/unsaturated flow, as well as the case of purely saturated flow studied just above, are all embodied in the general unsaturated flow problem treated in this section.

[a] Governing Equation and Constitutive Soil Properties:

The general unsaturated flow problem in a heterogeneous porous medium is governed by the continuity equation:

$$\frac{\partial}{\partial t} [S(h, \underline{x}) + \theta(h, \underline{x})] = - \frac{\partial q_i}{\partial x_i} \quad (i = 1, 2, 3) \quad (5.15)$$

and the generalized Darcy equation:

$$q_i = -K(h, \underline{x}) \cdot \frac{\partial}{\partial x_i} (h + g_j x_j) \quad (5.16)$$

where:

- $S(h, \underline{x})$  is the storage term due solely to water-soil compressibility under positive pressures ( $\text{cm}^3/\text{cm}^3$ )
- $\theta(h, \underline{x})$  is the pressure-dependent, spatially variable volumetric soil water content relative to an incompressible soil matrix ( $\text{cm}^3/\text{cm}^3$ )
- $q_i$  is the flux vector, or specific discharge rate ( $\text{cm}/\text{s}$ )
- $K(h, \underline{x})$  is the pressure-dependent, spatially variable unsaturated hydraulic conductivity ( $\text{cm}/\text{s}$ )
- $h$  is the water pressure head relative to atmospheric pressure ( $\text{cm}$ )
- $g_i$  is a cosine vector, corresponding to the unit acceleration of gravity taken with a minus sign.

The generalized Darcy equation (5.16) calls for explanations. First, note that the "gravity vector"  $g_i$  has components  $(-1,0,0)$  if the  $x_1$  axis is taken to be vertical downwards. More generally,  $g_i = (\sin\gamma, 0, \cos\gamma)$  if there is an angle  $\gamma$  between  $x_3$  and the upward vertical axis. This formulation makes it possible to simulate infiltration onto hill slopes and similar unsaturated flow problems involving sloping faces. Second, it should be observed that the hydraulic head  $H$  appears implicitly in the generalized Darcy equation (5.16), in the form:

$$H = h + g_j x_j \quad (j = 1,2,3)$$

i.e., as the sum of a pressure potential and a gravity potential. Note that the "pressure head"  $h$  may attain very large negative values in a dry soil, especially in clay soils or in the presence of active plant roots. In these cases,  $h$  should be interpreted as a thermodynamic potential. The minus hydraulic head ( $-H$ ) stands for the energy that must be produced in order to bring soil water to its free state at a plane of reference such as soil surface ( $g_i x_j = 0$ ). Soil water is in its free state when  $H = 0$ , has negative energy when  $H < 0$ , and positive energy when  $H > 0$ .

We now introduce specific constitutive relations for the unsaturated conductivity  $K(h, \underline{x})$ , the soil moisture retention



curve  $\theta(h, \underline{x})$ , and the elastic storage term  $S(h, \underline{x})$ . First of all, we assume that the elastic storage term plays no role for purely unsaturated flow, provided that positive pressures never appear within the flow domain. This may be realistic in the case of infiltration at low flow rate. On the other hand, it should be recognized that perched water tables or locally saturated zones are likely to appear in the case of high rate infiltration in a heterogeneous medium. For this reason, the elastic storage term was retained in the numerical code, assuming a simple dependence on water pressure as follows:

$$S(h, \underline{x}) = \begin{cases} S_s(\underline{x}) \cdot h & \text{if } h \geq 0 \\ 0 & \text{if } h \leq 0 \end{cases} \quad (5.18)$$

where  $S_s(\underline{x})$  is the specific storativity ( $\text{cm}^{-1}$ ) which accounts for the compressibility of water and the solid porous matrix under positive pressures. For simplicity,  $S_s$  can be taken constant when the flow system is mostly in the unsaturated regime. In this work,  $S_s$  was neglected altogether since most unsaturated flow simulations concerned the case of low rate infiltration in dry soils (Section 5.4.3 and Chapter 7).

The soil moisture retention curve  $\theta(h, \underline{x})$  was assumed to take the form of a multi-parameter nonlinear function of pressure  $h$ , possibly with spatially variable parameters. The particular

model we used for unsaturated flow simulations is the well-documented Van Genuchten model (Van Genuchten, 1978 and 1980). With spatially variable parameters, this model can be expressed as:

$$\theta(h, \underline{x}) = \theta_r(\underline{x}) + \frac{\theta_s(\underline{x}) - \theta_r(\underline{x})}{\{1 + (-\beta h)^n\}^{1-1/n}} \quad (5.19)$$

where  $\beta$  is a scale factor ( $\text{cm}^{-1}$ ),  $n$  is a real dimensionless parameter (identified as "VGN" in the flow simulator),  $\theta_s$  is the saturated soil water content, and  $\theta_r$  is the residual water content at very high negative pressures. Note that the term  $(\theta_s(\underline{x}) - \theta_r(\underline{x}))$  can be thought of as a spatially variable "effective porosity". The  $\beta$  and  $n$  parameters could also be taken spatially variable. However the results of the linearized spectral theory suggest that the effects of the spatial variability of  $\theta(h, \underline{x})$  are small compared to those due to  $K(h, \underline{x})$ : see Mantoglou 1984, and Mantoglou and Gelhar, 1987. For this reason we will assume constant parameters in the water retention curve for stochastic unsaturated flow simulations (Chapter 7), although some of the preliminary numerical experiments developed in the present chapter will include uniformly layered soil systems where both the  $\theta(h)$  and  $K(h)$  curves vary from layer to layer (section 5.4.3).

The most relevant feature of the constitutive relation

(5.19) is its nonlinear (logistic curve) shape. This is illustrated in Figures (5.3) and (5.4) for two different types of soils (from Ababou, 1981). The location of the inflexion point is of particular interest, since this is the point where the specific soil moisture capacity  $C(h) = \frac{\partial \theta}{\partial h}$  attains its maximum.

This inflexion point is given below in close form:

$$\begin{cases} h_{\max} = -\frac{1}{\beta} \cdot \left(1 - \frac{1}{n}\right)^{1/n} \\ C_{\max} = \beta \cdot (\theta_s - \theta_r) \cdot (n - 1) \cdot \frac{(m)^m}{(m + 1)^{m+1}} \end{cases} \quad (5.20)$$

where  $m = 1 - 1/n$ . For coarse or sandy soils the maximum capacity occurs at relatively high pressures ( $h_{\max}$ ) with a narrow peak compared to finer soils. For example, the maximum capacities for the Dek Sand and Montfavet Silt soils depicted in Figure (5.3) and (5.4) were, respectively:

- Sand:  $C_{\max} = 2.82 \times 10^{-3} \text{ cm}^{-1}$ ,  $h_{\max} = -24.5 \text{ cm}$
- Silt:  $C_{\max} = 0.33 \times 10^{-3} \text{ cm}^{-1}$ ,  $h_{\max} = -344. \text{cm}$

Furthermore, the shape of the  $\theta(h)$  curve indicates that the soil moisture capacity must be approximately constant in the pressure range:

$$|h - h_{\max}| \ll \beta^{-1} \quad (5.21)$$

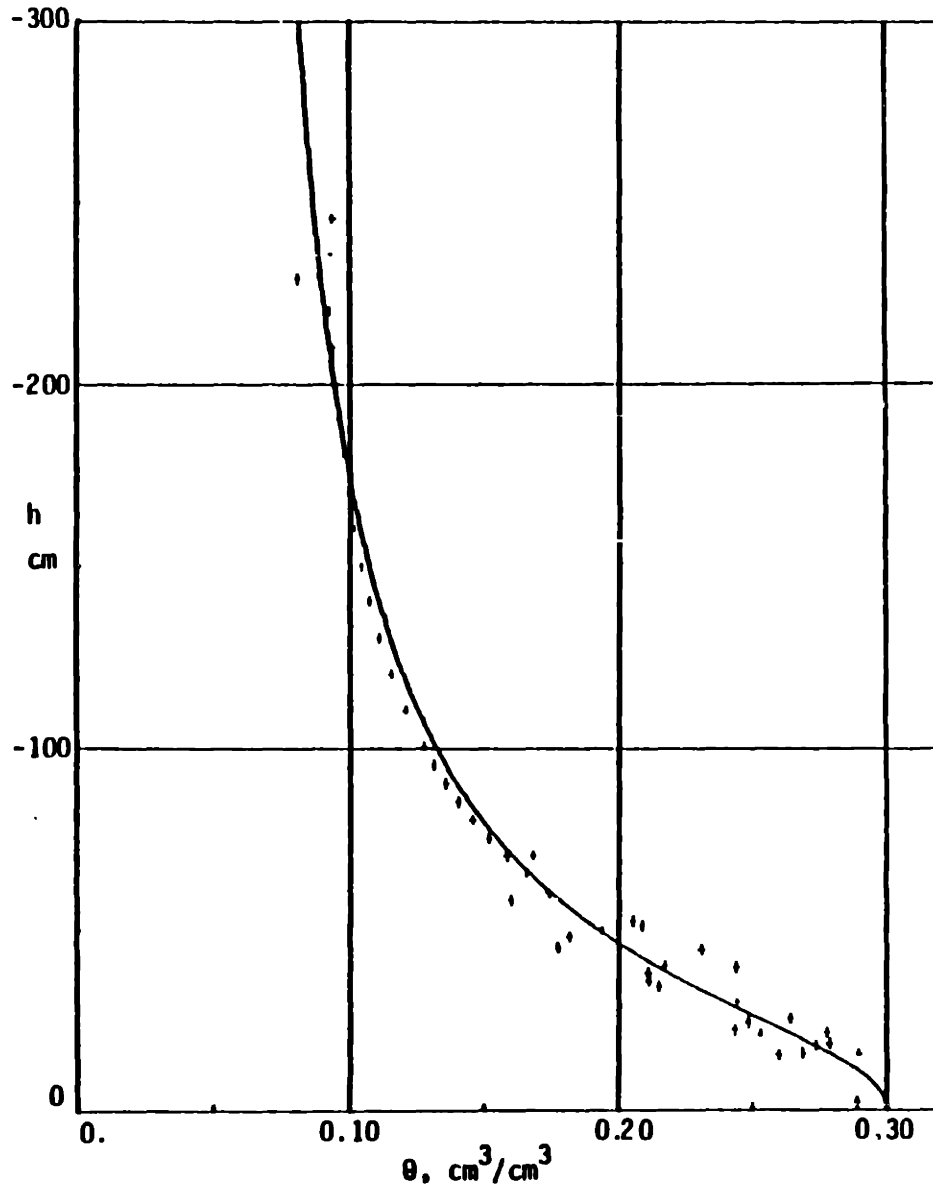


Figure 5.3(a) Soil water retention curve  $\theta(h)$  for the "Dek sand" of Senegal. The solid line represents the Van Genuchten function fitted to data points (from Ababou, 1981).

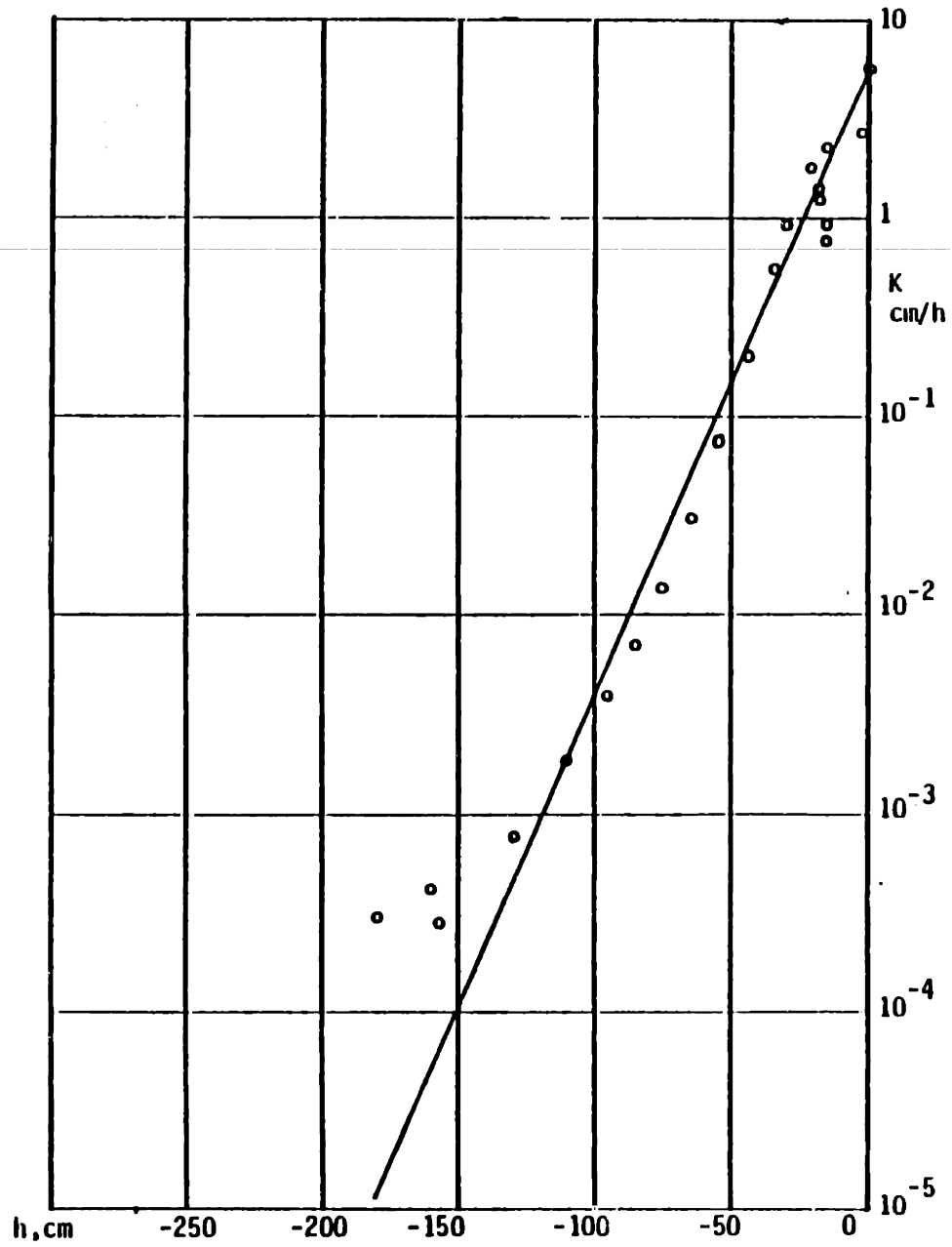


Figure 5.3 (b) Unsaturated conductivity curve  $K(h)$  for the "Dek sand" of Senegal. The solid line represents the exponential conductivity curve fitted to data points (from Ababou, 1981).

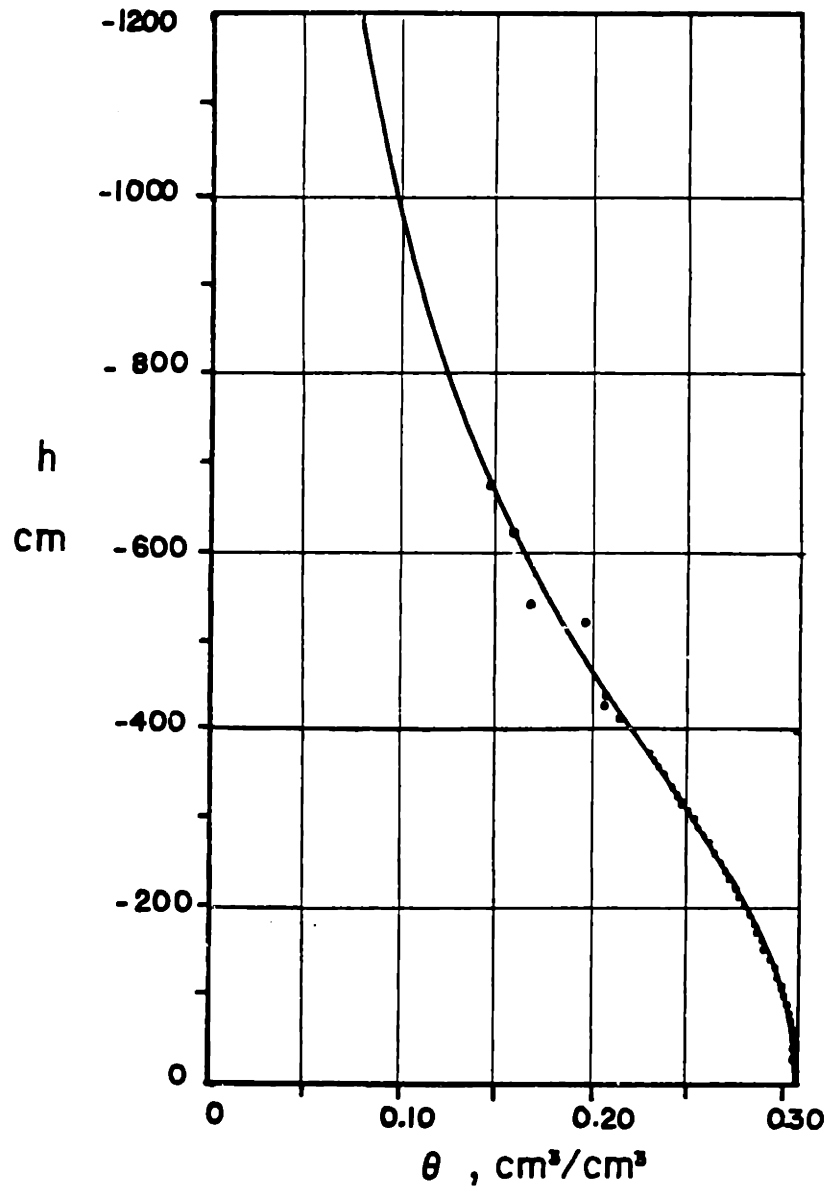


Figure 5.4 (a) Soil water retention curve  $\theta(h)$  for the Montfavet silt, a loess soil from the south of France. The Van Genuchten curve (solid line) was fitted to data points (Ababou, 1981).

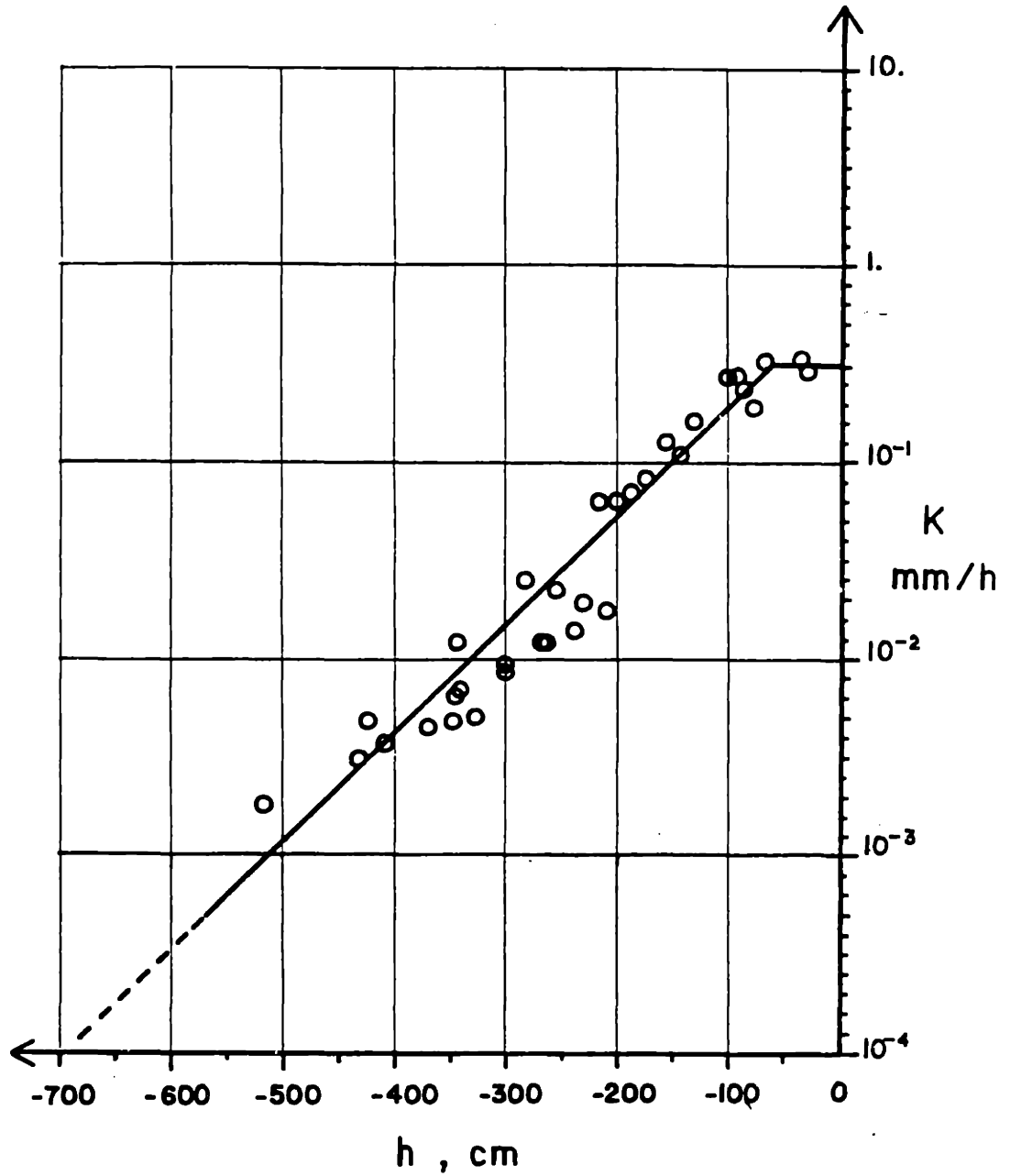


Figure 5.4 (b) Unsaturated conductivity curve  $K(h)$  for the Montfavet silt. The exponential conductivity curve (solid line) was fitted to data points (Ababou, 1981).

In the examples above,  $\beta$  was about  $2.3 \times 10^{-2}$  for the sand, and  $2.3 \times 10^{-3}$  for the silt. Accordingly, it appears that the soil moisture capacity is approximately constant and close to  $C_{\max}$  in the pressure ranges (-90cm to -10cm) and (-650cm to -150cm) respectively for the sand and silt soils. Within these ranges, the simplifying assumption of a constant capacity used by Mantoglou and Gelhar (1987) in their spectral theory of unsaturated flow appears to hold approximately.

Finally, we chose an exponential model for the unsaturated conductivity-pressure relation; as shown below:

$$K(h, \underline{x}) = \begin{cases} K_s(\underline{x}) \cdot \exp\{\alpha(\underline{x}) \cdot (h - h_b(\underline{x}))\} & \text{if } h \leq h_b(\underline{x}) \\ K_s(\underline{x}) & \text{if } h \geq h_b(\underline{x}) \end{cases} \quad (5.22)$$

When the "bubbling pressure head"  $h_b$  is taken to be null, equation (5.22) becomes identical to the model used in the spectral theory of Mantoglou and Gelhar. Figures (5.3) and (5.4) show that the exponential conductivity model is in good agreement with measured values for wet and moderately dry soils. However, these and other data also suggest that the exponential rate of decrease of  $K(h)$  is not sustained as the soil dries up below a certain pressure (e.g.,  $h \approx -600$  cm for the silt). This limitation of the exponential model will be taken into account in



our simulations of field infiltration problems, by using the field measured initial conductivity (rather than the field-measured pressure) for an estimate of the initial pressure based on the exponential conductivity model. The initial pressure obtains by plugging  $K = K_{in}$  (field-measured) into the inverse relation:

$$h = \frac{1}{\alpha} \ln\left(\frac{K}{K_s}\right)$$

where  $\alpha$  and  $K_s$  represent using mean values, in lieu of  $\alpha(\underline{x})$  and  $K_s(\underline{x})$ . This expedient procedure may be useful in cases where the field-measured initial pressure is outside the range of validity of the exponential model (very low pressure) whereas most of the unsaturated flow process occurs at higher pressures well within the range of validity of the exponential model.

In view of the results obtained by the spectral perturbation method of Mantoglou and Gelhar, our main focus will be the study of infiltration problem with the exponential conductivity curve having both  $K_s(\underline{x})$  and  $\alpha(\underline{x})$  random fields in 3D space. This, combined with the strong nonlinearity of  $K(h, \underline{x})$  with respect to  $h$ , makes the numerical solution of the unsaturated flow problem a difficult task indeed.

[b] Time Discretization:

The time discretization of the transient unsaturated flow equation is now being developed. For convenience, let us merge the elastic storage and the soil moisture terms into a single term:

$$\theta(h, \underline{x}) := S(h, \underline{x}) + \theta(h, \underline{x})$$

Plugging the Darcy equation into the continuity equation, one obtains the governing nonlinear flow equation for pressure head or "Richards equation":

$$\frac{\partial \theta(h, \underline{x})}{\partial t} = \frac{\partial}{\partial x_i} \left[ K(h, \underline{x}) \cdot \left( \frac{\partial h}{\partial x_i} + g_i \right) \right] = -L(h, \underline{x}) \quad (5.23)$$

For the time integration scheme, we choose the fully implicit (Backward Euler) two-point finite difference scheme. Denoting  $(-L(h, \underline{x}))$  the spatial operator on the right-hand side of (5.23), the fully implicit time discretization scheme can be expressed as the first order finite difference approximation:

$$\frac{\theta^{n+1}(h, \underline{x}) - \theta^n(h, \underline{x})}{\Delta t_{n+1}} \simeq -L^{n+1}(h, \underline{x}) \quad (5.24)$$

where  $\Delta t_{n+1} = t_{n+1} - t_n$ . Alternatively, this finite difference approximation could also be interpreted as a time integral approximation. Indeed, by integrating the exact equation (5.23) between times  $(t_n, t_{n+1})$  one obtains:

$$\theta^{n+1}(h, \underline{x}) - \theta^n(h, \underline{x}) = - \int_{t_n}^{t_{n+1}} L(h, \underline{x}) dt$$

and, using the mean value theorem:

$$\frac{\theta^{n+1}(h, \underline{x}) - \theta^n(h, \underline{x})}{\Delta t_{n+1}} = - \{ \gamma \cdot L^{n+1}(h, \underline{x}) + (1 - \gamma) \cdot L^n(h, \underline{x}) \} \quad (5.25)$$

where  $0 \leq \gamma \leq 1$ . In particular for  $\gamma = 1$  one obtains the fully implicit finite difference approximation (5.24). The more general class of implicit scheme corresponds to  $\frac{1}{2} \leq \gamma \leq 1$ . The Crank-Nicholson scheme in particular corresponds to the case  $\gamma = 1/2$ .

Briefly, our particular choice  $\gamma = 1$  was based on results of stability theory and various numerical experiments in the literature. First of all, it is well known that implicit schemes are unconditionally stable, whereas explicit schemes require for stability a stringent constraint on the time step.

For the simple heat equation  $\frac{\partial u}{\partial t} = D \cdot \frac{\partial^2 u}{\partial x_i \partial x_i}$ , the stability constraint takes the form (Ames, 1977):

$$\Delta t \leq \left[ 2D \cdot \sum_i \frac{1}{\Delta x_i^2} \right]^{-1}.$$

This observation holds also for more complex cases such as the nonlinear unsaturated flow equation. Of course, the exact form of the stability constraint depends in fact on the spatial discretization scheme and the linearization scheme. In any case the resulting stability constraint is qualitatively of the same form as shown above. In particular, note that the soil moisture diffusivity  $D = K/C$  may become quite large in a wet zone, so that the time step may have to be dramatically small in order to satisfy the stability constraint. Taking the Dek sand of Figures (5.3)-(5.4) as an example, and using a value of pressure corresponding to the maximum soil moisture capacity, we find that  $\Delta t \leq 4.3$  sec is needed to ensure the stability of the explicit scheme on a 3D grid with  $\Delta x_i = 5$  cm. For "wetter" conditions, the stability constraint would be even more drastic. This justifies the use of the unconditionally stable implicit scheme for time integration.

Our second remark is about the choice of the fully implicit scheme ( $\gamma = 1$ ) in preference to other implicit schemes such as Crank-Nicholson ( $\gamma = 1/2$ ). Numerical experiments tend to show that the fully implicit scheme is particularly efficient for the case of the nonlinear flow equation at hand (Vauclin et al., 1979), although there is no theoretical evidence in favor of one

type of implicit scheme over the other for strongly nonlinear equations.

[c] Linearization and Spatial Discretization:

We now focus on the nonlinear semi-discretized equation (5.24). In order to obtain a tractable linear system, we propose an approximate linearization of (5.24) by way of iterative corrections based on a modified Picard iteration scheme. The procedure is best explained in two steps: (i) linearization of the right hand side spatial operator, and (ii) linearization of the left hand side temporal operator. This is described in detail below:

(i) - We use a Picard iteration scheme to approximate the nonlinear equation (5.24) into a sequence of equations ( $k = 0, 1, 2 \dots$ ) where the conductivity appears linearly as follows:

$$\frac{\theta^{n+1,k+1}(h,x) - \theta^n(h,x)}{\Delta t_{n+1}} \simeq \frac{\partial}{\partial x_i} \left[ k^{n+1,k}(h,\underline{x}) \cdot \left[ \frac{\partial h^{n+1,k+1}}{\partial x_i} + g_i \right] \right]$$

Note that the conductivity on the right-hand side is evaluated from the previous iteration level. By substituting to both sides the "residual":

$$R^{n+1,k} = - \left\{ \frac{\theta^{n+1,k} - \theta^n}{\Delta t_{n+1}} - \frac{\partial}{\partial x_i} \left[ K^{n+1,k} \cdot \left( \frac{\partial h^{n+1,k}}{\partial x_i} + g_i \right) \right] \right\}$$

we obtain equivalently the "modified" Picard scheme:

$$\frac{\theta^{n+1,k+1} - \theta^{n+1,k}}{\Delta t_{n+1}} - \frac{\partial}{\partial x_i} \left[ K^{n+1,k} \cdot \frac{\partial}{\partial x_i} (h^{n+1,k+1} - h^{n+1,k}) \right] \simeq R^{n+1,k}. \quad (5.26)$$

which is computationally more stable with respect to round-off errors. For clarity, note that  $n$  represents the time level, while  $k$  represents the iteration level. At this point, we have only linearized the spatial operator  $\frac{\partial}{\partial x_i} [K(h) \frac{\partial}{\partial x_i} (h + g_i)]$ . However the discrete storage term involving  $\theta(h)$  is still nonlinear.

(ii) - In order to obtain a fully linear equation, the storage term is now linearized by applying the mean value theorem as follows:

$$\begin{aligned} \theta^{k+1} - \theta^k &= \int_{h^k}^{h^{k+1}} C(h) dh \\ &= (h^{k+1} - h^k) \cdot C[(1 - \gamma)h^k + \gamma h^{k+1}] \end{aligned}$$

where  $\gamma$  is some number in the interval  $[0,1]$ . The choice  $\gamma = 0$  would lead to a linear equation in  $h$ , as required. We prefer a more stable approximation similar to the chord-slope

approximations proposed by Huyakorn, et al. (1984) and Milly (1985), that is:

$$\left\{ \begin{array}{l} \frac{\theta^{k+1} - \theta^k}{\Delta t_{n+1}} \simeq \frac{\hat{C}(h^k)}{\Delta t_{n+1}} \cdot (h^{k+1} - h^k) \\ \hat{C}(h^k) = \frac{\theta(h^k) - \theta(h^0)}{h^k - h^0} \end{array} \right. \quad (5.27)$$

where all variables are for time level (n+1), except  $h^0$  which stands for "iteration level (0)". In other words,  $h^0$  is the known solution at the previous time level n.

Combining (5.26) and (5.27) we finally obtain a fully linear semi-discretized equation in terms of the incremental pressure head  $\delta h$  between successive iterations:

$$\boxed{\frac{\hat{C}^{n+1,k}}{\Delta t_{n+1}} \cdot \delta h - \frac{\partial}{\partial x_i} [K^{n+1,k} \cdot \frac{\partial}{\partial x_i} (\delta h)] \simeq R^{n+1,k}} \quad (5.28)$$

where:

$$\delta h = h^{n+1,k+1} - h^{n+1,k}$$

and:

$$R^{n+1,k} = - \left\{ \frac{\hat{C}^{n+1,k}}{\Delta t_{n+1}} (h^{n+1,k} - h^n) - \frac{\partial}{\partial x_i} \left[ K^{n+1,k} \left( \frac{\partial h^{n+1,k}}{\partial x_i} + g_i \right) \right] \right\}$$

In summary, equation (5.28) is a linearized, semi-discrete

approximation of the original unsaturated flow equation (5.23), which can be used as a starting point for further discretization in space. This is examined next.

The spatial operators appearing on the left and right-hand sides of (5.28) are now discretized by using the 7-point centered finite difference scheme, in the same fashion as in the previous section dealing with saturated flow (Eqs. 5.4-5.7). For convenience, the two spatial operators appearing in (5.28) will be designated as:

$$L_K(Y) = - \frac{\partial}{\partial x_i} \left( K \frac{\partial Y}{\partial x_i} \right)$$

$$L_G(Y) = - g_i \cdot \frac{\partial K}{\partial x_i}.$$

Applying the 7-point finite difference scheme to the  $L_K$ -operator leads to an expression similar to that obtained for saturated flow (Eqs. 5.1 and 5.6), with the mid-nodal *unsaturated* conductivities defined as:

$$K_{i+1/2, j, k} = K(h_{i+1/2, j, k}, x_{i+1/2, j, k}).$$

Furthermore, we use again the geometric mean weighting scheme to evaluate the mid-nodal conductivities:



$$\hat{K}_{i+\frac{1}{2},j,k} = \sqrt{K(h_{ijk}, x_{ijk}) \cdot K(h_{i+1,j,k}, x_{i+1,j,k})}$$

In the particular case of the exponential conductivity model (5.22) with a zero bubbling pressure, this gives:

$$\begin{aligned} \hat{K}_{i+\frac{1}{2},j,k} &= \sqrt{K_s(x_{i+1,j,k}) \cdot K_s(x_{i,j,k})} \\ &\cdot \exp \left\{ \frac{\alpha(x_{i+1,j,k}) \cdot h_{i+1,j,k} + \alpha(x_{i,j,k}) \cdot h_{i,j,k}}{2} \right\} \end{aligned} \quad (5.29)$$

This particular choice of conductivity weighting was guided by the results of the spectral theory concerning the effective conductivity in a random unsaturated soil (see Mantoglou and Gelhar, 1987). According to these authors, the effective unsaturated conductivity is of the form:

$$K_{\text{eff}} \sim K_G \cdot \exp\{\langle ah \rangle\}$$

where  $K_G$  is the ensemble geometric mean of the random saturated conductivity. The conductivity weighting scheme (5.29) may be justified by analogy with this result.

The  $L_G$ -operator may be approximated in the same fashion as the  $L_K$ -operator. Using the same index notation as before (see equation 5.6) we obtain the following centered finite difference approximation:

$$\hat{L}_G(Y) = - \left\{ \begin{aligned} & \frac{g_1}{\Delta x_1} (K[i+1/2] - K[i-1/2]) \\ & + \frac{g_2}{\Delta x_2} (K[j+1/2] - K[j-1/2]) \\ & + \frac{g_3}{\Delta x_3} (K[k+1/2] - K[k-1/2]) \end{aligned} \right\} \quad (5.30)$$

Mid-nodal conductivities like  $K[i+1/2] = K_{i+1/2,j,k}$  are as defined just above.

The fully discretized, linearized unsaturated flow system obtains by plugging  $\hat{L}_G$  of (5.30) and  $\hat{L}_K$  of (5.6) into equation (5.28). The resulting finite difference system takes the form:

$$\boxed{\left( \frac{C}{\Delta t} \cdot \underline{\underline{I}} + \underline{\underline{K}} \right)^{n+1,k} \cdot \underline{\underline{\delta h}} = \underline{\underline{r}}^{n+1,k}} \quad (5.31)$$

where  $\underline{\underline{I}}$  is the identity matrix,  $\underline{\underline{K}}$  is the unsaturated conductivity matrix,  $\delta h$  is the increment of pressure between two iteration levels  $(k,k+1)$ , and  $\underline{\underline{r}}$  is the vector of residuals including also the vector of boundary conditions. It is worth noting that the conductivity matrix  $\underline{\underline{K}}$  has exactly the same form as for the saturated flow equation, with the unsaturated mid-nodal conductivities of (5.29) replacing the saturated mid-nodal conductivities of (5.28). As a consequence, the coefficient matrix:

$$\underline{\underline{A}} = \frac{C}{\Delta t} \cdot \underline{\underline{I}} + \underline{\underline{K}}$$

has the same sparsity pattern for saturated and unsaturated flow. In both cases, the matrix is a 7-diagonal symmetric as shown in Figure (5.1).

Furthermore, the coefficient matrix is strictly diagonal-dominant in the case where the storage term ( $C/\Delta t$ ) is strictly positive for all times and all locations, as would occur for transient infiltration in a moderately dry soil. As a consequence, the iterative matrix solver could converge much faster in the transient case than in the steady state case (due to better matrix condition). This suggests that there will be a trade-off between the requirement of strong diagonal dominance for faster solution (small  $\Delta t$ ), and the need to minimize the number of time steps (large  $\Delta t$ ). In addition, a small time step may be required for fast convergence of the nonlinear-Picard iterations. The numerical experiments of section 5.4 will help determine the appropriate strategy in that respect.

## 5.2: Statistical Truncation Error Analysis for Linear Random Flow Problems

In this section, we focus on the evaluation of numerical errors due to the discretization of the stochastic flow equation. In particular, we develop in detail a *statistical truncation error analysis* of the finite difference approximation of the steady state saturated flow equation with random field conductivities. This will lead to some useful results concerning the order of accuracy of the finite difference method for a certain class of stochastic equations (random heat equations). Both the method and results appear to be new in view of the current literature on numerical analysis. The final results will be summarized and discussed at the end of this section, notably in terms of numerical requirements like grid resolution. For completeness, note that the nonlinear problem of transient unsaturated flow will be analyzed separately in a forthcoming section, however in a much more qualitative way.

Because the statistical truncation error analysis of this section is somewhat intricate, we feel that it may be useful to outline here the main features of our approach. Our purpose is to obtain a closed form statistical evaluation of the finite difference error, that is the error on the finite difference solution due solely to truncation errors, assuming

that an exact solution of the finite difference system can be achieved. The method we use is applicable to linear problems, such as the linear system arising from the stochastic saturated flow equation. Briefly, we begin by evaluating analytically the truncation error of the finite difference operator. We then obtain an equivalent partial differential equation that governs the error on the hydraulic head. This equation has the same structure as the governing equation, except that it is driven by the truncation error (forcing function). To solve this "error equation", we use a first order spectral perturbation method with the usual assumptions of stationarity and ergodicity (the "exact" solution is also evaluated by this method). This gives finally the error in the form of a random field with known spectral density. The root-mean-square error on the hydraulic head obtains by computing the variance of the random field error, and taking the square root. A similar procedure is then used to evaluate the error in the flux vector. The reader not interested in the details may jump to the "summary and discussion" given in subsection 5.2.4.

### 5.2.1 Governing equation for the numerical head error

Recall that the exact equation governing the head variable is of the form  $L(H) = 0$ , where  $L(H)$  is the partial differential operator:

$$L(H) = \frac{\partial}{\partial x_m} (K(x) \frac{\partial H}{\partial x_m}) \quad (m = 1, 2, 3)$$

The FD solution  $\hat{H}$  defined on a grid  $(I_1, I_2, I_3)$  satisfies the FD equations  $\hat{L}(\hat{H}) = 0$ , where  $L(\hat{H})$  is the difference operator:

$$\hat{L}(\hat{H}) = \sum_{m=1,2,3} \frac{1}{(\Delta x_m)^2} \left\{ \hat{K}_{I_{m+1/2}} \cdot \hat{H}_{I_{m+1}} - \left[ \hat{K}_{I_{m+1/2}} + K_{I_{m-1/2}} \right] \cdot \hat{H}_o + \hat{K}_{I_{m-1/2}} \cdot \hat{H}_{I_{m-1}} \right\}$$

Note that  $m$  indicates the three directions  $x_m$ , and we used the shorthand notations:

$$\hat{H}_o \rightarrow \hat{H}(I_1, I_2, I_3)$$

$$\hat{H}_{I_1+1} \rightarrow \hat{H}(I_1+1, I_2, I_3)$$

$$\hat{K}_{I_1+1/2} \rightarrow \hat{K}(I_1+1/2, I_2, I_3)$$

(etc.)

The mid-nodal conductivities were evaluated by the geometric mean weighting scheme:

$$\hat{K}_{I_1+1/2} = \sqrt{K(I_1, I_2, I_3) \cdot K(I_1+1, I_2, I_3)}$$

(etc.).

and the flux vector:

$$q_m = -K \frac{\partial H}{\partial x_m}$$

was evaluated at mid-nodal points by:

$$\hat{q}_{I_m+1/2} = -\hat{K}_{I_m+1/2} \cdot \frac{\hat{H}_{I_m+1} - H}{\Delta x_m}.$$

Finally, we now prescribe *Dirichlet boundary conditions* on all boundaries, since these conditions can be expressed exactly in the finite difference formulation. The introduction of Neuman conditions would complicate unnecessarily the forthcoming error analysis.

The *truncation error* is defined as the difference between the exact and approximate operators (both operating on the exact solution  $H$ ):

$$T(H) = \hat{L}(H) - L(H)$$

where  $H$  is evaluated at the grid points  $\underline{I} = (I_1, I_2, I_3)$ . Once computed as a function of  $H$ , the truncation error could also be evaluated as a function of the approximate FD solution  $\hat{H}_I$ , or more precisely as a function of an equivalent continuous FD solution  $\tilde{H}$  which takes the values of the discrete FD solution  $\hat{H}_i$  at the grid points. Thus we can write:

$$T(\tilde{H}) = \hat{L}(\tilde{H}) - L(\tilde{H})$$

where  $\tilde{H}(\underline{x})$  is a continuous function such that  $\tilde{H}(\underline{x}_I) = \hat{H}_I$ . Observe that the term  $\hat{L}(\tilde{H})$  can be eliminated since it is identically zero at the grid points (by definition of  $\hat{H}$ ). This yields immediately a partial differential equation governing the "Equivalent Continuous Finite Difference Solution":

$$\frac{\partial}{\partial x_m} \left[ K(\underline{x}) \frac{\partial \tilde{H}}{\partial x_m} \right] + T(\tilde{H}) = 0. \quad (5.32)$$

Similarly, the continuous solution error can be defined as:

$$\delta \tilde{H}(\underline{x}) = \tilde{H}(\underline{x}) - H(\underline{x}) \quad (5.33)$$

$$\delta \tilde{H}_I = \hat{H}_I - H(\underline{x}_I).$$

Ultimately, one would like to obtain an estimate for the error



$\tilde{\delta H}_I$  at the grid points. This can be achieved by developing  $\delta H(\underline{x})$  into a power series of  $(\Delta x_m)$ :

$$\delta \tilde{H}_I(\underline{x}) = \delta \tilde{H}^{(0)} + \Delta x_m \cdot \delta \tilde{H}_m^{(1)} + (\Delta x_m)^2 \cdot \delta \tilde{H}_m^{(2)} + \dots \quad (5.34)$$

Obviously, the zero-order term  $\delta H^{(0)}$  should vanish if the FD approximation is consistent. In fact it will turn out that the zero-order and all odd-order terms in the expansion vanish.

To see that  $\delta \tilde{H}^{(0)}$  vanishes, we plug the identity  $\tilde{H} = H + \delta \tilde{H}$  into (5.32) to obtain:

$$\boxed{\begin{aligned} \frac{\partial}{\partial x_m} \left[ K(\underline{x}) \cdot \frac{\partial(\delta \tilde{H})}{\partial x_m} \right] + T(H) + T(\delta \tilde{H}) &= 0 \\ \delta H &= 0 \quad \text{on all boundaries (exact BC's)} \end{aligned}} \quad (5.35)$$

where we used the fact that  $T$  is a linear function, due to the linearity of the flow equation. Combining (5.34) and (5.35), it appears that  $\delta \tilde{H}^{(0)}$  vanishes if  $\lim_{\Delta x \rightarrow 0} T(H) = 0$ , that is, provided that the finite difference scheme is a consistent approximation. We will see shortly that this is indeed the case.

We now proceed to evaluate explicitly the truncation error function  $T(H)$  in order to obtain the equation governing the

solution error  $\delta H$  (from (5.34) and (5.35)). This is done by using Taylor series expansions such as:

$$H_{i+1} - H_{i+\frac{1}{2}} = \frac{1}{2} \left( \frac{\partial H}{\partial x} \right)_{i+\frac{1}{2}} \cdot \Delta x + \frac{1}{8} \left( \frac{\partial^2 H}{\partial x^2} \right)_{i+\frac{1}{2}} \cdot \Delta x^2 + \frac{1}{48} \left( \frac{\partial^3 H}{\partial x^3} \right)_{i+\frac{1}{2}} \Delta x^3 + \dots$$

$$H_{i+\frac{1}{2}} - H_i = \frac{1}{2} \left( \frac{\partial H}{\partial x} \right)_{i+\frac{1}{2}} \Delta x - \frac{1}{8} \left( \frac{\partial^2 H}{\partial x^2} \right)_{i+\frac{1}{2}} \Delta x^2 + \frac{1}{48} \left( \frac{\partial^3 H}{\partial x^3} \right)_{i+\frac{1}{2}} \Delta x^3 + \dots$$

whence:

$$\frac{H_{i+1} - H_i}{\Delta x} = \left( \frac{\partial H}{\partial x} \right)_{i+\frac{1}{2}} + \frac{\Delta x^2}{24} \left( \frac{\partial^3 H}{\partial x^3} \right)_{i+\frac{1}{2}} + O(\Delta x^4) \quad (5.36)$$

$$\frac{Y_{i+\frac{1}{2}} - Y_{i-\frac{1}{2}}}{\Delta x} = \left( \frac{\partial Y}{\partial x} \right)_i + \frac{\Delta x^2}{24} \left( \frac{\partial^3 Y}{\partial x^3} \right)_i + O(\Delta x^4). \quad (5.37)$$

Plugging  $Y = K \frac{\partial H}{\partial x}$  into the last equation yields the flux divergence:

$$\begin{aligned} \frac{1}{\Delta x} \left[ \left( K_i \cdot \left( \frac{\partial H}{\partial x} \right)_{i+\frac{1}{2}} - K_{i+\frac{1}{2}} \cdot \left( \frac{\partial H}{\partial x} \right)_{i-\frac{1}{2}} \right) \right] = \\ \left[ \frac{\partial}{\partial x} \left( K \frac{\partial H}{\partial x} \right) \right] + \frac{\Delta x^2}{24} \cdot \left[ \frac{\partial^3}{\partial x^3} \left( K \frac{\partial H}{\partial x} \right) \right]_i + O(\Delta x^4). \quad (5.38a) \end{aligned}$$

Substituting (5.36) for the terms  $\left( \frac{\partial H}{\partial x} \right)_{i \pm \frac{1}{2}}$  appearing in the left hand side of (5.37) yields:

$$\frac{1}{\Delta x} \left\{ K_{i+1/2} \cdot \left[ \frac{H_{i+1} - H_i}{\Delta x} \right] - K_{i-1/2} \cdot \left[ \frac{H_i - H_{i-1}}{\Delta x} \right] \right\} - \left\{ \frac{\partial}{\partial x} \left[ K \left( \frac{\partial H}{\partial x} \right) \right] \right\}_i =$$

$$\left\{ \frac{\Delta x^2}{24} \cdot \frac{1}{\Delta x} \left[ K_{i+1/2} \cdot \left( \frac{\partial^3 H}{\partial x^3} \right)_{i+1/2} - K_{i-1/2} \cdot \left( \frac{\partial^3 H}{\partial x^3} \right)_{i-1/2} \right] + O(\Delta x^3) \right\} +$$

(5.38b)

$$\frac{\Delta x^2}{24} \left\{ \frac{\partial^3}{\partial x^3} \left( K \frac{\partial H}{\partial x} \right) \right\}_i + O(\Delta x^4)$$

Using again equation (5.37) with  $Y = K \frac{\partial^3 H}{\partial x^3}$  yields a Taylor development for the finite difference appearing on the right hand side above:

$$\frac{1}{\Delta x} \left[ K_{i+1/2} \cdot \left( \frac{\partial^3 H}{\partial x^3} \right)_{i+1/2} - K_{i-1/2} \cdot \left( \frac{\partial^3 H}{\partial x^3} \right)_{i-1/2} \right] = \left\{ \frac{\partial}{\partial x} \left( K \frac{\partial^3 H}{\partial x^3} \right) \right\}_i +$$

$$\frac{\Delta x^2}{24} \left\{ \frac{\partial^3}{\partial x^3} \left( K \frac{\partial^3 H}{\partial x^3} \right) \right\}_i + O(\Delta x^4).$$

Plugging this identity into the right hand side of (5.38b) yields, on the right hand side of that equation:

$$\frac{\Delta x^2}{24} \cdot \left\{ \frac{\partial}{\partial x} \left( K \left( \frac{\partial^3 H}{\partial x^3} \right)_i + \frac{\partial^3}{\partial x^3} \left( K \frac{\partial H}{\partial x} \right)_i \right\} + O(\Delta x^3)$$

Now observe that the left hand side of (5.38b) is just the one-dimensional truncation error function  $T_1(H) = L_1(H)$ .

Furthermore, the exact mid-nodal conductivities can be expressed as  $K_{i+1/2} = \hat{K}_{i+1/2} - \delta K_{i+1/2}$ , where  $\delta K_{i+1/2}$  is the error due to the approximate evaluation of  $K_{i+1/2}$  by  $\hat{K}_{i+1/2} = \sqrt{K_i \cdot K_{i+1}}$ . Thus, we obtain an intermediate formulation of the truncation error  $T(H) = \hat{L}(H) - L(H)$ , shown below for just the first of three terms ( $T = T_1 + T_2 + T_3$ ):

$$T_1(H) = \frac{1}{\Delta x} \left\{ \delta K_{i+1/2} \cdot \left[ \frac{H_{i+1} - H_i}{\Delta x} \right] - \delta K_{i-1/2} \cdot \left[ \frac{H_i - H_{i-1}}{\Delta x} \right] \right\} + \frac{\Delta x^2}{24} \cdot \left\{ \frac{\partial}{\partial x} \left[ K \frac{\partial^3 H}{\partial x^3} \right]_i + \frac{\partial^3}{\partial x^3} \left[ K \frac{\partial H}{\partial x} \right]_i \right\} + O(\Delta x^3).$$

In order to complete this evaluation, we need again to replace finite differences by differentials. Thus, using again (5.36) in the above equation gives:

$$T_1(H) = \frac{1}{\Delta x} \left\{ \delta K_{i+1/2} \cdot \left( \frac{\partial H}{\partial x} \right)_{i+1/2} - \delta K_{i-1/2} \cdot \left( \frac{\partial H}{\partial x} \right)_{i-1/2} \right\} + \frac{\Delta x^2}{24} \cdot \frac{1}{\Delta x} \left\{ \delta K_{i+1/2} \cdot \left( \frac{\partial^3 H}{\partial x^3} \right)_{i+1/2} - \delta K_{i-1/2} \cdot \left( \frac{\partial^3 H}{\partial x^3} \right)_{i-1/2} \right\} + \frac{\Delta x^2}{24} \cdot \left\{ \frac{\partial}{\partial x} \left( K \frac{\partial^3 H}{\partial x^3} \right)_i + \frac{\partial^3}{\partial x^3} \left( K \frac{\partial H}{\partial x} \right)_i \right\} + O(\Delta x^3). \quad (5.39)$$

Finally, we must use again a Taylor expansion technique to evaluate the "mid-nodal conductivity error"  $\delta K_{i+1/2}$  that appears in equation (5.39). We have from previous definitions:

$$\left\{ \begin{aligned} \delta K_{i+1/2} &= \hat{K}_{i+1/2} - K_{i+1/2} \\ &= \sqrt{K(x_i) \cdot K(x_{i+1})} - K(x_{i+1/2}). \end{aligned} \right.$$

However, it will be more convenient to use the log-conductivity process  $f(\underline{x}) = \ell n K(\underline{x})$  in order to evaluate the  $\delta K$  term. The mid-nodal log-conductivity is:

$$\left\{ \begin{aligned} \hat{f}_{i+1/2} &= \ell n \hat{K}_{i+1/2} = \frac{1}{2} (f_i + f_{i+1}) \\ f_{i+1/2} &= \ell n K_{i+1/2} \end{aligned} \right.$$

which leads to a simple expression for the mid-nodal conductivity error:

$$\delta K_{i+1/2} = K_{i+1/2} \cdot \left\{ \exp\left(\frac{f_{i+1} + f_i}{2} - f_{i+1/2}\right) - 1 \right\}. \quad (5.40)$$

Furthermore, we obtain by Taylor expansion of  $f_i$  and  $f_{i+1}$  around  $f_{i+1/2}$ :

$$\frac{f_{i+1} + f_i}{2} = f_{i+1/2} + \frac{1}{8} \left( \frac{\partial^2 f}{\partial x^2} \right)_{i+1/2} \cdot \Delta x^2 + O(\Delta x^4)$$

so that the mid-nodal conductivity error (5.40) can be expressed as:

$$\delta K_{i+1/2} = K_{i+1/2} \cdot \left\{ \exp \left[ \frac{\Delta x^2}{8} \cdot \left( \frac{\partial^2 f}{\partial x^2} \right)_{i+1/2} + O(\Delta x^4) \right] - 1 \right\} \quad (5.41)$$

This expression may be linearized under conditions which will be discussed in more detail in the sequel (these conditions require both  $\Delta x$  and  $\sigma_f$  to be small):

$$\boxed{\delta K_{i+1/2} \simeq K_{i+1/2} \cdot \left\{ \frac{\Delta x^2}{8} \cdot \left( \frac{\partial^2 f}{\partial x^2} \right)_{i+1/2} + O(\Delta x^4) \right\}} \quad (5.42)$$

Plugging this into the expression (5.39) for the truncation error, we obtain:

$$\begin{aligned} T_1(H) &= \frac{\Delta x^2}{8} \cdot \frac{1}{\Delta x} \left[ \left( \frac{\partial^2 f}{\partial x^2} \right) \cdot \left( K \frac{\partial H}{\partial x} \right) \right]_{i-1/2}^{i+1/2} + \\ &\quad \frac{\Delta x^2}{24} \cdot \left\{ \frac{\partial}{\partial x} \left( K \frac{\partial^3 H}{\partial x^3} \right) + \frac{\partial^3}{\partial x^3} \left( K \frac{\partial H}{\partial x} \right) \right\}_i + O(\Delta x^3). \end{aligned}$$

The first term is a finite difference which can be evaluated by a Taylor expansion similar to that of equation (5.38):

$$\frac{1}{\Delta x} \left[ \left( \frac{\partial^2 f}{\partial x^2} \right) \cdot K \frac{\partial H}{\partial x} \right]_{i-1/2}^{i+1/2} = \frac{\partial}{\partial x} \left[ \left( \frac{\partial^2 f}{\partial x^2} \right) K \frac{\partial H}{\partial x} \right]_i + O(\Delta x^2).$$

This gives finally in closed form the truncation error function  $T_1(H)$  evaluated at the grid point  $x = x_i$  for the one-dimensional flow operator. The result is the same for  $T_m(H)$  with  $m = 1, 2, 3$  corresponding to the spatial operators  $L_1 = \frac{\partial}{\partial x_1} (K \frac{\partial}{\partial x_1})$ , etc. The total truncation error in the 3D case obtains by summing:

$$T(H) = T_1(H) + T_2(H) + T_3(H) \quad (5.43)$$

where:

$$T_1(H) = \frac{\Delta x_1^2}{24} \left\{ 3 \frac{\partial}{\partial x_1} \left[ \frac{\partial^2 f}{\partial x_1^2} \cdot K \frac{\partial H}{\partial x_1} \right] + \frac{\partial}{\partial x_1} \left[ K \frac{\partial^3 H}{\partial x_1^3} \right] + \frac{\partial^3}{\partial x_1^3} \left[ K \frac{\partial H}{\partial x_1} \right] \right\} + O(\Delta x_1^3)$$

(5.44)

and similar expressions hold for  $T_2$  and  $T_3$ .

We may now use this result in order to solve the partial differential equation governing the "equivalent" solution error  $\tilde{\delta H}$ . Using the  $\Delta x$ -expansion (5.34) and plugging (5.44) into equation (5.35), we find that:

- (i) At order zero,  $\tilde{\delta H}^{(0)}$  satisfies the flow equation with boundary conditions  $\tilde{\delta H}^{(0)} = 0$  so that  $\tilde{\delta H}^{(0)}$  vanishes identically over the whole domain.

- (ii) Since  $T(H)=O(\Delta x^2)$ , all the odd-order error terms  $\delta\tilde{H}^{(1)}$ ,  $\delta\tilde{H}^{(3)}$ , etc., vanish.
- (iii) The leading error term is  $\delta\tilde{H}^{(2)}$ , second order in  $\Delta x$ .

In the three-dimensional case, the leading order solution error can be expressed formally as:

$$\delta\tilde{H} = \sum_{i=1}^3 \left\{ \delta\tilde{H}_m^{(2)} \cdot (\Delta x_m)^2 + O(\Delta x_m^4) \right\} \quad (5.45)$$

and  $\delta\tilde{H}$  is governed by equation (5.35) without the term  $T(\delta\tilde{H}) = O(\Delta x^4)$ , which can be neglected. This leads to a tractable governing equation for the solution error, of the form:

$$\frac{\partial}{\partial x_m} \left[ K(\underline{x}) \cdot \frac{\partial(\delta\tilde{H})}{\partial x_m} \right] = -T(H) + O(\Delta x^4) \quad (5.46)$$

Upon substituting the expression for  $T(H)$  given in (5.43)-(5.44), we obtain an equation which can be broken into three spatial component of the leading error term ( $\delta\tilde{H}_m^{(2)}$ ,  $m = 1,2,3$ ). For convenience, we show here only the term on the left-hand side of the equation corresponding to the first spatial direction  $m = 1$ :



$$\begin{aligned} \Delta x_1^2 \cdot \frac{\partial}{\partial x_1} \left[ K(\underline{x}) \frac{\partial E_1}{\partial x_1} \right] + \frac{\Delta x_1^2}{24} \left\{ 3 \frac{\partial}{\partial x_1} \left[ \frac{\partial^2 f}{\partial x_1^2} \cdot K \frac{\partial H}{\partial x_1} \right] \right. \\ \left. + \frac{\partial}{\partial x_1} \left[ K \frac{\partial^3 H}{\partial x_1^3} \right] + \frac{\partial^3}{\partial x_1^3} \left[ K \frac{\partial H}{\partial x_1} \right] \right\} + O(\Delta x_1^3) \end{aligned} \quad (5.47)$$

where the notation  $E_1 = \tilde{\delta H}_1^{(2)}$  was used. We also obtain similar expressions for  $E_2$  and  $E_3$ . The total solution error is:

$$\tilde{\delta H} = E_1 \Delta x_1^2 + E_2 \Delta x_2^2 + E_3 \Delta x_3^2 + O(\Delta x_m^4) \quad (5.48)$$

In the particular case where  $\Delta x_1 = \Delta x_2 = \Delta x_3$  (equal mesh sizes in all directions), the full error equation becomes simpler. Indeed we obtain the governing equation for  $E = E_1 + E_2 + E_3$  by summing over spatial directions and observing that  $\frac{\partial}{\partial x_m} (K \frac{\partial H}{\partial x_m})$  vanishes. Thus, we obtain finally the head solution error for a cubic mesh as follows:

$$\boxed{\tilde{\delta H} = E \cdot \Delta x^2 + O(\Delta x^4)} \quad (5.49)$$

where  $E(x)$  is governed by the partial differential equation:

$$\boxed{\sum_m \frac{\partial}{\partial x_m} \left[ K(\underline{x}) \frac{\partial E}{\partial x_m} \right] = - \frac{1}{24} \left\{ 3 \sum_m \frac{\partial}{\partial x_m} \left[ \frac{\partial^2 f}{\partial x_m^2} K \frac{\partial H}{\partial x_m} \right] + \frac{\partial}{\partial x_m} \left[ K \frac{\partial^3 H}{\partial x_m^3} \right] \right\} + O(\Delta x)}$$

(5.50)

with boundary conditions  $E = 0$  on all boundaries.

Equation (5.50) gives explicitly the stochastic equation governing the head solution error. The first term on the right hand side is solely due to errors in the evaluation of mid-nodal conductivities, while the second term corresponds to errors in the evaluation of the flux divergence. Note that the right hand side depends solely on the exact solution  $H$ , which must be evaluated in order to find closed form stochastic solutions for the error  $E(x)$ . Our approach assumes that the remainder  $O(\Delta x)$  can be neglected; this residual term could perhaps be loosened to  $O(\Delta x^2)$  with more work.

### 5.2.2 Statistical analysis of the numerical head error

[a] The spectrum of the head error:

We now proceed to analyze the hydraulic head solution error  $\delta\tilde{H} = E \cdot \Delta x^2$  in a stochastic framework. Following the assumptions of the spectral theory and the single realization approach, we postulate the equivalence of ensemble and spatial averages in the stochastic error equation (5.50). Furthermore, we use the first order spectral method to evaluate the statistical moments of the "exact" solution  $H(x)$  appearing on the right hand side of (5.50). The same method will then be used to

obtain the first and second order moments of the head error itself. First, equation (5.50) is re-arranged in a more tractable form by using the relation:

$$K(\underline{x}) = K_G e^{f(\underline{x})}$$

where  $f(\underline{x})$  is the perturbation of the  $\ln K$  process around its mean ( $\langle f \rangle = 0$ ). This leads to:

$$\sum_m \left\{ \frac{\partial^2 E}{\partial x_m^2} + \frac{\partial f}{\partial x_m} \frac{\partial E}{\partial x_m} = \right. \quad (5.51)$$

$$\left. \sum_m \left\{ -\frac{3}{24} \left[ \frac{\partial^3 f}{\partial x_m^3} \cdot \frac{\partial H}{\partial x_m} + \frac{\partial^2 f}{\partial x_m^2} \cdot \left( \frac{\partial H}{\partial x_m^2} + \frac{\partial f}{\partial x_m} \frac{\partial H}{\partial x_m} \right) \right] - \frac{1}{24} \left[ \frac{\partial^4 H}{\partial x_m^4} + \frac{\partial f}{\partial x_m} \cdot \frac{\partial^3 H}{\partial x_m^3} \right] \right\} \right.$$

Equation (5.51) should be interpreted as a stochastic equation in an infinite domain, i.e., with domain size much larger than correlation scales. The boundary conditions  $E = 0$  suggest that the mean error should be approximately zero in order to be consistent with the stationarity-ergodicity assumptions. We will show that this is indeed the case for  $\sigma_f$  small. Our purpose will be to determine the standard deviation, or root-mean-square norm (RMS norm) of the solution error  $\delta H = E \cdot \Delta x^2$ , in an ensemble sense. The accuracy of the finite difference approximation will then be studied by analyzing the

behavior of  $\sigma(\delta H)$  compared to  $\sigma(H)$ . The ratio of these two quantities indicates the relative amount of "numerical noise" compared to the physical noise in the solution.

In order to show explicitly how the forthcoming statistical analysis of error depends on  $\sigma_f$  being small, let us reproduce below the spectral perturbation solution of the exact flow equation (as in Chapter 3). We begin by expanding (5.53a)  $H(\underline{x})$  into a power series with  $\sigma_f$  as the "small parameter":

$$H(\underline{x}) = H_0(\underline{x}) + \sigma H_1(\underline{x}) + \sigma^2 H_2(\underline{x}) + \dots$$

Similarly, we let:

$$f(\underline{x}) = \sigma \cdot g(\underline{x})$$

or equivalently:

$$K(\underline{x}) = K_G \cdot e^{\sigma \cdot g(\underline{x})}$$

where  $g(\underline{x})$  is a zero-mean Gaussian field with unit variance. The 3D flow equation (5.1) with stochastic conductivities can now be expressed as:

$$\frac{\partial^2 H}{\partial x_m \partial x_m} + \sigma \cdot \frac{\partial g}{\partial x_m} \cdot \frac{\partial H}{\partial x_m} = 0.$$

By plugging the expansion (5.52) into this flow equation, we obtain the infinite hierarchy of equations:

$$\left. \begin{aligned} \frac{\partial^2 H_0}{\partial x_m \partial x_m} &= 0 \\ &\vdots \\ \frac{\partial^2 H_1}{\partial x_m \partial x_m} + \frac{\partial g}{\partial x_m} \cdot \frac{\partial H_0}{\partial x_m} &= 0 \\ &\vdots \\ &(\text{etc.}). \end{aligned} \right\} \quad (5.53b)$$

The zero order term ( $H_0$ ) could be interpreted as the linear mean head solution, satisfying  $\frac{\partial H_0}{\partial x_m} = -J_m$ , where  $J_m$  is the mean hydraulic gradient. Accordingly, the other terms in the expansion will have zero mean as can be easily checked. Assuming that the mean gradient is parallel to  $x_1$ , the first order term in the expansion satisfies:

$$\frac{\partial^2 H_1}{\partial x_m \partial x_m} = \frac{\partial g}{\partial x_1} \cdot J_1.$$

Comparing this to the equation for head perturbations ( $h$ ) as obtained in Chapter 3, it appears that  $H_0$  and  $H_1$  are related to the mean and first order perturbation of the head field as follows:

$$\begin{cases} \langle H \rangle = H_0(\underline{x}) = -\underline{J} \cdot \underline{x} \\ h = \sigma \cdot H_1 + 0(\sigma^2) \end{cases} \quad (5.54a)$$

Solving the equation for  $H_1$  in Fourier space gives immediately the Fourier increment and spectral density of  $H_1$ :

$$dZ_{H_1} = i J_1 \frac{k_1 dZ_g}{k^2} \quad (i = \sqrt{-1}) \quad (5.45b)$$

$$S_{H_1} = J_1^2 \frac{k_1^2}{k^4} S_g$$

We now use a similar expansion for the stochastic error in order to solve equation (5.51) by a first order spectral method:

$$E(\underline{x}) = E_0 + E_1 \cdot \sigma + E_2 \cdot \sigma^2 + \dots \quad (5.55a)$$

By plugging the expansions for  $H$  and  $E$  into (5.51) with  $f(\underline{x}) = \sigma g(\underline{x})$ , we obtain a hierarchy of equations for  $E_0$ ,  $E_1$ , etc., as shown below:

$$\left. \begin{aligned} \sigma^0: \quad & \sum_m \frac{\partial^2 E_0}{\partial x_m \partial x_m} = 0 \\ \sigma^1: \quad & \sum_m \left\{ \frac{\partial^2 E_1}{\partial x_m \partial x_m} + \frac{\partial g}{\partial x_m} \cdot \frac{\partial E_0}{\partial x_m} \right\} = \\ & - \frac{3}{24} \left[ - J_1 \cdot \frac{\partial^3 g}{\partial x_1^3} \right] - \frac{1}{24} \sum_m \frac{\partial^4 H_1}{\partial x_m^4} \\ \sigma^2: \quad & \text{(etc.).} \end{aligned} \right\} \quad (5.55b)$$

Again, the zero order equation suggests that  $E_0$  is the mean error, and that it must vanish identically over the infinite domain. This is consistent with the boundary conditions  $E = 0$  for the finite domain case. It is also consistent with the fact that all higher order terms appear to have zero mean if  $E_0 = \langle E \rangle$  holds. As a consequence, the equation governing the leading term ( $E_1$ ) becomes:

$$\boxed{\frac{\partial^2 E_1}{\partial x_m \cdot \partial x_m} = \frac{1}{8} J_1 \frac{\partial^3 g}{\partial x_1^3} - \frac{1}{24} \frac{\partial^4 H_1}{\partial x_m^2 \cdot \partial x_m^2}} \quad (5.56)$$

with implicit summation over repeated indices. Thus, the head error's leading order term in  $\Delta x$  and  $\sigma_f$  is given by:

$$\boxed{\delta H = E \cdot \Delta x^2 = E_1 \cdot \sigma_f \cdot \Delta x^2.} \quad (5.57)$$

The two equations above show that the numerical error  $\delta H$  is proportional, as a first approximation, to the product  $\sigma \Delta x^2$  times a stochastic term governed by a stochastic PDE independent of  $\sigma$  and  $\Delta x$ .

Furthermore, since equation (5.56) is linear, it can be solved easily in Fourier space, i.e., by using a spectral method as in Chapter 3. Plugging Fourier-Stieltjes representations for

$E_1$  and  $g$  in (5.56) yields:

$$k^2 \cdot dZ_{E_1} = \frac{3}{8} J_1 (ik_1)^3 dZ_g - \frac{1}{24} (k_m^2 \cdot k_m^2) dZ_{H_1}.$$

Using also equation (5.54) for  $dZ_{H_1}$ , this gives explicitly the Fourier component and spectrum of  $E_1(\mathbf{x})$  in terms of the Fourier component and spectrum of  $g(\mathbf{x})$ :

$$dZ_{E_1}(\underline{k}) = -i \frac{J_1 k_1}{24} \left\{ 3 \frac{k_1^2}{k^2} + \frac{(k_m^2 \cdot k_m^2)}{k^4} \right\} dZ_g(\underline{k}) \quad (5.58)$$

$$S_{E_1}(\underline{k}) = \frac{J_1^2}{(24)^2} k_1^2 \cdot \left[ 3 \frac{k_1^2}{k^2} + \frac{(k_m^2 \cdot k_m^2)}{k^4} \right]^2 \cdot S_g(\underline{k})$$

where we used again implicit summation over repeated indices.

Equivalently, the spectrum of  $\delta H$  can be obtained by multiplying  $S_{E_1}$  by  $\Delta x^4$  and replacing  $S_g$  by  $S_f$ . Thus, equation (5.58) gives the spectral density of the "equivalent error"  $\delta\tilde{H}(\underline{x})$ .

Note that  $\delta\tilde{H}(\underline{x})$  is a zero-mean random field defined in the continuous 3D space. However, we are only interested in the discrete error defined at the nodes of the finite difference grid. The restriction  $\hat{\delta H}_1$  of the continuous process  $\delta\tilde{H}(\underline{x})$  on the FD grid may be viewed as a lattice process, whose spectrum is identical to that of the continuous error within the range of wavenumbers:



$$0 \leq |k_m| \leq \pi/\Delta x_m \quad (m = 1, 2, 3).$$

and zero outside this range. In other words, the fluctuations of  $\tilde{\delta H}$  at scales smaller than the mesh size must be ignored. In particular, the variance of the discrete error process  $\hat{\delta H}_i$  can be obtained by integrating the spectrum (5.58) up to wavenumbers  $(\pi/\Delta x)$ . This gives the final result we were looking for, namely the variance of the head error for the 3D flow problem:

$$\text{var}(\hat{\delta H}_i) \approx \left[ J_1 \cdot \frac{\Delta x^2}{24} \right]_0^2 \cdot \int_{0 \leq k \leq \pi/\Delta x} k_1^2 \left[ \frac{3k_1^2}{k^2} + \frac{(k_m^2 \cdot k_m^2)}{k^4} \right]^2 \cdot S_{ff}(\underline{k}) \, d\underline{k} \quad (5.59)$$

[b] Head error in the one-dimensional case:

For ease of analysis, we focus first on the one-dimensional version of the flow equation. In this case, equation (5.59) becomes simpler:

$$\text{var}(\hat{\delta H}_i) \approx \left[ J_1 \frac{\Delta x^2}{6} \right]^2 \cdot \int_{0 \leq k \leq \pi/\Delta x} k_1^2 S_{ff}(k_1) dk_1. \quad (5.60)$$

It is interesting to note that, in one dimension, the variance of the head error is proportional to the spectral content of  $df/dx$  up to wavenumber  $(\pi/\Delta x)$ . For illustration, let us use the 1D

"hole-spectrum" log-conductivity as proposed by *Bakr et al.* 1978:

$$S_{ff}(k) = \sigma^2 \frac{\ell^3}{(\pi/2)} \frac{k^2}{(1+k^2\ell^2)^2}$$

$$R_{ff}(\xi) = \sigma^2 (1 - |\xi|/\ell) \cdot e^{-|\xi|/\ell}.$$

In this case, the spectral head solution is known to be stationary, with variance:

$$\text{Var}(H) = \sigma_h^2 = J_1^2 \sigma_f^2 \ell^2.$$

On the other hand, observe that the first derivative of the  $f(x)$  process used in this example has a significant spectral content at large wavenumbers, up to the wavenumber cut-off  $(\pi/\Delta x)$  corresponding to the smallest scale of fluctuations sampled by the numerical grid. The integral in (5.60) can now be obtained by using the following identities from Gradshteyn and Rhyzik, 1980 (2.174 and 2.175):

$$\int \frac{u^4}{(1+u^2)^2} du = \frac{u^3}{1+u^2} - 3 \int \frac{u^2}{(1+u^2)^2} du$$

$$\int \frac{u^2}{(1+u^2)^2} du = -\frac{2u}{4(1+u^2)} + \frac{2}{4} \cdot \int \frac{du}{1+u^2}$$

$$\int \frac{du}{1+u^2} = \text{arctg } u$$

whence the result:

$$\frac{\text{Var}(\delta\hat{H}_i)}{\text{Var}(H)} = \frac{2}{\pi} \left(\frac{1}{6}\right)^2 \cdot \left\{ \left(\frac{\Delta x}{\ell}\right)^4 + \frac{\left(\frac{\Delta x}{\ell}\right)^3 + \frac{3}{2}\left(\frac{\Delta x}{\ell}\right)^5}{\left(\frac{\Delta x}{\ell}\right)^2 + 1} - \frac{3}{2} \left(\frac{\Delta x}{\ell}\right)^4 \cdot \text{arctg} \left[ \left(\frac{\Delta x}{\ell}\right)^{-1} \right] \right\}.$$

For  $\Delta x/\ell \ll 1$ , this gives a simple expression for the ratio of the standard deviations of the head numerical error and head solution in one dimension:

$$\frac{\sigma(\delta\hat{H}_i)}{\sigma(H)} \simeq \frac{1}{6} \sqrt{2/\pi} \left(\frac{\Delta x}{\ell}\right)^{3/2} + O\left(\frac{\Delta x}{\ell}\right). \quad (5.61)$$

The most striking feature in this equation is that the "noise-to-signal ratio" appears independent of the input log-conductivity variance, and increases as a fractional power of the resolution ( $\Delta x/\ell$ ), rather than the usual  $O(\Delta x^2)$  behaviour for deterministic problems. The relative error is 2.5% for a resolution 1/3, and 7% for a resolution 2/3.

The simplicity of the 1D case allows us to study in some detail, the effect of the behaviour of  $f(x)$  at small scales or large wavenumbers. If a smoother process with 1D exponential covariance is used, equation (5.61) becomes:

$$\frac{\sigma(\hat{\delta H}_i)}{\sigma_f \cdot J \cdot \ell} \approx \frac{1}{6} \cdot \left(\frac{\Delta x}{\ell}\right)^2$$

Alternatively, using the 1D Band-Pass Self-Similar Spectrum of Chapter 4, with  $\Delta x \leq \ell \ll L$ , we obtain:

$$\frac{\sigma(\hat{\delta H}_i)}{\sigma_H} \approx \frac{1}{6} \left(\frac{\Delta x}{\sqrt{L\ell}}\right)^2.$$

On the whole, these results indicate that the relative numerical error goes to zero with  $\left(\frac{\Delta x}{\lambda}\right)$  faster in the case of a smooth  $\ell n K$  process, compared to the case where  $\ell n K$  has significant variability at the smallest scales. This observation can be stated formally as follows:

$$\frac{\sigma(\hat{\delta H}_i)}{\sigma(H)} \approx \frac{1}{6} \left(\frac{\Delta x}{\lambda}\right)^p, \quad 0 < p \leq 2 \quad (5.62)$$

where  $\lambda$  is a typical correlation scale, and  $p$  is equal to  $3/2$  for the "noisy"  $\ell n K$  process with hole-exponential covariance, while  $p = 2$  for smoother processes.

[c] Head error in the three-dimensional case:

We will now see that the relative numerical error  $\sigma(\delta H)/\sigma(H)$  follows a similar behavior in the case of 3D flow.

The variance of the three-dimensional head error given in equation (5.59) will be computed below for two different isotropic log-conductivity spectra: a "noisy" spectrum, and a "smooth" spectrum. The isotropic 3D Markov spectrum is a good candidate for a "noisy" random field, since it is non-differentiable in the mean-square sense (the variance of  $df/dx_m$  is infinite!). This noisy random field was used for all the stochastic single-realization flow simulations to be described in Chapters 6 and 7. On the other hand, the 3D Hole-Gaussian spectrum (used by Vomvoris, 1986, for analysis of stochastic solute transport) appears as a good candidate for a "smooth" random field, being infinitely differentiable.

To obtain a closed form result for  $\text{Var}(\delta H)$  in equation (5.59) requires the evaluation of complicated three-dimensional Fourier integrals. The details of this evaluation are given in Appendix 5A for the case of the Markov spectrum (noisy field), and Appendix 5B for the case of the Hole-Gaussian spectrum (smooth field). These appendices also develop the spectral solution for the head field in order to obtain  $\text{Var}(H)$ . The root-mean-square relative numerical error on the head field is given below, respectively, for the "noisy" case and the "smooth" case:

$$(a): \text{ Noisy input: } \frac{\sigma(\delta H)}{\sigma(H)} = \frac{\sqrt{3}}{12} \left(\frac{\Delta x}{\lambda}\right)^{3/2} \left(1 + O\left(\frac{\Delta x}{\lambda\pi}\right)\right)^{1/2} \quad (5.63)$$

$$(b): \text{ Smooth: } \frac{\sigma(\delta H)}{\sigma(H)} \leq \frac{\sqrt{5}}{8} \left(\frac{\Delta x}{\ell}\right)^2$$

This result confirms the behavior observed earlier in the 1D case. Indeed, equation (5.63) shows that the relative head error is proportional to the grid resolution  $\Delta x/\lambda$  with a power 3/2 for the "noisy" 3D Markov log-conductivity spectrum, and with a power 2 for the "smooth" 3D Hole-Gaussian spectrum. Note that the  $\lambda$ -scale stands for the integral correlation scale of the Markov spectrum, while the  $\ell$ -scale is a typical fluctuation scale for the Hole-Gaussian spectrum (not the integral scale). Both log-conductivity fields are assumed isotropic, and the grid has equal mesh size in all three directions. A generalization of these results to the case of anisotropic inputs and rectangular grids would be of great interest.

Equation (5.63) can be used to compute the leading order term of the relative head error in specific cases (note that the inequality in 5.63b becomes equality as the resolution ratio goes to zero). It appears that the relative error on the head field is quite small and fairly independent on the type of log-conductivity field (noisy or smooth), at least for a reasonably fine grid. Indeed, the error is only 3% in both cases

for a resolution equal to  $1/3$ . This indicates that the hydraulic head fluctuations can be accurately resolved by the finite difference flow simulator with moderate grid resolution. The situation is not so good when it comes to evaluating the Darcy flux vector, as will be seen shortly.

### 5.2.3 Numerical error on the flux vector

#### [a] Relation between flux error and head error:

The next step of the truncation error analysis focuses on the error in evaluating the flux vector  $q_m$  by the centered FD scheme (5.31). This error is defined as:

$$\delta \hat{q}_m = \hat{q}_m - q_m \quad (m = 1, 2, 3). \quad (5.64)$$

The FD solution  $\hat{q}_m$  was expressed in terms of head differences in equation (5.31). Dropping the spatial direction index ( $m$ ) for convenience, equation (5.31) gave an expression of the form:

$$\hat{q}(x_{i+1/2}) = \hat{K}_{i+1/2} \cdot \frac{\hat{H}_{i+1} - \hat{H}_i}{\Delta x}. \quad (5.65)$$

Thus, the flux error evaluated at the mid-nodal points of the grid is simply:

$$\hat{\delta q}(x_{i+1/2}) = - \left\{ K_{i+1/2} \cdot \left( \frac{\partial H}{\partial x} \right)_{i+1/2} - \hat{K}_{i+1/2} \frac{\hat{H}_{i+1} - \hat{H}_i}{\Delta x} \right\} \quad (5.66)$$

Now, we can use our previous results in order to evaluate explicitly the flux error. Indeed, let:

$$\hat{K}_{i+1/2} = K_{i+1/2} + \delta K_{i+1/2}$$

$$\hat{H}_i = H_i + \delta H_i.$$

Plugging these expressions in equation (5.66) yields:

$$\begin{aligned} \hat{\delta q}(x_{i+1/2}) = & - \left\{ K_{i+1/2} \left( \frac{\delta H}{\delta x} \right)_{i+1/2} - K_{i+1/2} \cdot \frac{H_{i+1} - H_i}{\Delta x} \right\} \\ & - \left\{ \delta K_{i+1/2} \cdot \frac{H_{i+1} - H_i}{\Delta x} \right\} - \left\{ K_{i+1/2} \frac{\delta H_{i+1} - \delta H_i}{\Delta x} \right\}. \end{aligned} \quad (5.67)$$

Using a Taylor expansion, the first term in braces takes the form:

$$- \left\{ -K_{i+1/2} \frac{\Delta x^2}{24} \left( \frac{\partial^3 H}{\partial x^3} \right)_{i+1/2} + O(\Delta x^4) \right\}.$$

To evaluate the second term, we use our previous finding concerning the mid-nodal conductivity error  $\delta K_{i+1/2}$  in (5.42).

This gives:



$$- \left\{ K_{i+1/2} \frac{\Delta x^2}{8} \left( \frac{\partial^2 f}{\partial x} \right)_{i+1/2} + O(\Delta x^4) \right\}.$$

Finally, we evaluate the third term by using a Taylor expansion of  $(\hat{\delta H}_{i+1} - \hat{\delta H}_i)$  with  $\hat{\delta H}_i$  replaced by the equivalent  $\hat{\delta H}(x)$  head error. This gives:

$$- \left\{ K_{i+1/2} \frac{\Delta x^4}{24} \left( \frac{\partial^3(\tilde{\delta H})}{\partial x^3} \right)_{i+1/2} + O(\Delta x^4) \right\}.$$

Reassembling these terms in (5.67) leads to the following expression for the equivalent flux error  $\tilde{\delta q}(\underline{x})$  defined in continuous space:

$$\begin{aligned} \tilde{\delta q}(\underline{x}) = & \\ K(\underline{x}) \cdot & \left\{ \frac{\Delta x^2}{24} \left[ \frac{\partial^3 H}{\partial x^3} + 3 \frac{\partial^2 f}{\partial x^2} \cdot \frac{\partial H}{\partial x} \right] + O(\Delta x^4) \right\} \\ & - K(\underline{x}) \cdot \left\{ \frac{\partial}{\partial x} \tilde{\delta H} + \frac{\Delta x^2}{24} \frac{\partial^3}{\partial x^3} \tilde{\delta H} + O(\Delta x^4) \right\}. \end{aligned}$$

The head error  $\tilde{\delta H}$  is known from previous results. Recall that the leading order term in  $\sigma_f$  and  $\Delta x$  was:

$$\tilde{\delta H} = E \cdot \Delta x^2 = E_1 \sigma_f \Delta x^2$$

where  $E_1(x)$  is known from equation (5.58). Similarly, the exact solution  $H(x)$  is known from previous spectral perturbation results. In particular, we have:

$$\frac{\partial H}{\partial x} = -J + \sigma_f \cdot H_1 + O(\sigma_f^2)$$

where the zero-mean  $H_1(x)$  process is known from equation (5.54). Note also that  $f(x) = \sigma_f g(x)$ . Plugging these expressions into the equation for  $\tilde{\delta q}_m(\underline{x})$ , we obtain to the leading order in  $\sigma_f$  and  $\Delta x$ :

$$\tilde{\delta q}_m(x) = \sigma_f \cdot \Delta x^2 \cdot K_G \exp(\sigma \cdot g) \left\{ \frac{1}{24} \frac{\partial^3 H_1}{\partial x_m^3} + \frac{\partial E_1}{\partial x_m} \right\}. \quad (5.68)$$

Finally, denoting  $h$  the perturbation  $h = H - \langle H \rangle$ , equation (5.68) can be expressed in a form which clearly shows the dependence of  $\delta q$  on the exact head perturbation  $h$  and the head error  $\delta H$ :

$$\boxed{\tilde{\delta q}_m(x) = K(\underline{x}) \cdot \left\{ \frac{\Delta x^2}{24} \frac{\partial^3 h}{\partial x_m^3} + \frac{\partial}{\partial x_m} \tilde{\delta H} \right\}} \quad (5.69)$$

where the first term is due solely to errors in the evaluation of the mid-nodal conductivities. A similar expression holds for the error  $\tilde{\delta G}_m$  in the hydraulic gradient  $G_m = \frac{-\partial H}{\partial x_m}$ :

$$\boxed{\tilde{\delta G}_m = -\frac{\partial}{\partial x_m} \tilde{\delta H}.} \quad (5.70)$$

[b] Spectrum of head gradient and flux errors:

The random field errors (5.69) and (5.70) are perfectly determined from previous results (head spectrum and head error spectrum). For the hydraulic gradient error, we obtain the following statistics spectrum:

$$\left\{ \begin{array}{l} \langle \delta \tilde{G}_m \rangle = 0 \\ dZ(\delta \tilde{G}_m) = \frac{\Delta x^2}{24} J_1 \cdot k_m k_1 \left[ \frac{3k_1^2}{k^2} + \frac{(k_n^2 \cdot k_n^2)}{k^4} \right] \cdot dZ_f \\ S(\delta \tilde{G}_m) = \left( \frac{\Delta x^2}{24} \right)^2 \cdot J_1^2 \cdot (k_m k_1)^2 \left[ \frac{3k_1^2}{k^2} + \frac{(k_n^2 \cdot k_n^2)}{k^4} \right]^2 \cdot S_{ff} \end{array} \right. \quad (5.71)$$

with implicit summation over repeated indices. In order to determine the statistics of the flux error  $\delta \tilde{q}$  in a similar fashion, we need to linearize the conductivity in the following fashion:

$$K = K_G e^{\sigma \cdot g} \approx K_G (1 + \sigma g + \dots).$$

Now, we recognize that this approximation may be poor if  $\sigma_f$  is larger than unity. Also, recall that a similar approximation was made for the mid-nodal conductivity error  $\delta K$  in (5.41) and (5.42). For the time being, we postpone discussing the possible

inaccuracy of this linearization approximation.

Using the latter approximation, we obtain a tractable expression for the stochastic flux error to the leading order in  $\sigma_f$  and  $\Delta x$ :

$$\tilde{\delta q}_m(x) = K_G \sigma_f \frac{\Delta x^2}{24} \left\{ \frac{\delta^3 H_1}{\partial x_m^3} + 24 \frac{\partial E_1}{\partial x_m} \right\}. \quad (5.72)$$

Finally, since the spectra of  $H_1$  and  $E_1$  are known from previous results, this gives the required statistics of the flux error vector in closed form:

$$\left. \begin{aligned} \langle \tilde{\delta q}_m \rangle &= 0 \\ dZ_{\tilde{\delta q}_m} &= K_G \cdot J_1 \cdot \frac{\Delta x^2}{24} \left\{ \frac{k_1 k_m^3}{k^2} + k_1 k_m \left[ \frac{3k_1^2}{k^2} + \frac{(k_n^2 \cdot k_n^2)}{k^4} \right] \right\} \cdot dZ_f \\ S_{\tilde{\delta q}_m} &= (\text{term above squared}) \cdot S_{ff}. \end{aligned} \right\} \quad (5.73)$$

The first equation indicates that the mean flux error is null in an infinite domain; the second equation gives the complex Fourier-Stieltjes increment of the stochastic flux error vector, and the third equation indicates how the diagonal components of its spectral density tensor can be obtained. Recall that  $S_{ff}$  is the known spectrum of the input log-conductivity field.

[c] Head gradient and flux errors in the 1D case:

In order to facilitate the analysis, we now focus on applications of previous results in the 1D case. The spectral densities of the random field errors  $\tilde{\delta G}$  and  $\tilde{\delta q}$  shown in (5.71) and (5.73) become much simpler in one dimension. Dropping the tilde ( $\sim$ ) sign for convenience, we obtain in this simple case:

$$S_{\delta G}(k) = (\sigma_f J_1 \frac{4}{24} \Delta x^2)^2 \cdot k^4 \frac{S_{ff}(k)}{\sigma_f^2} \quad (5.74)$$

$$S_{\delta q}(k) = (\sigma_f J_1 K_G \frac{5}{24} \Delta x^2)^2 \cdot k^4 \frac{S_{ff}(k)}{\sigma_f^2} \quad (5.75)$$

Now, the variances  $\text{Var}(\delta G)$ ,  $\text{Var}(\delta q)$ , can be obtained by integrating the above spectra up to wavenumber  $\pi/\Delta x$  as explained previously. It turns out that these variances are proportional to the variance of the second derivative of the log-conductivity field (after elimination of fluctuation scales smaller than the mesh size). For illustration, the relative numerical errors for the 1D Hole-Exponential Covariance log-conductivity ("noisy" field) were obtained in closed form. The result is shown below:

$$\frac{\sigma(\delta G)}{(\sigma_f J)} = \frac{\sigma(\delta q)}{\left(\frac{5}{4} \sigma_f J K_G\right)} \approx$$

$$\sqrt{2/3} \cdot \pi/6 \cdot \left(\frac{\Delta x}{\ell}\right)^{1/2} \cdot \left(1 + O\left(\frac{\Delta x}{\pi \ell}\right)\right)^{1/2} \quad (5.76)$$

The most remarkable feature in equation (5.76) is that the order of accuracy on both the *head gradient* and the *flux vector*, drops by one power of  $\left(\frac{\Delta x}{\ell}\right)$  compared to the order of accuracy on the head (equation 5.61). This is exactly the same behaviour as in the case of deterministic, spatially smooth conductivities. However here, the order of accuracy is *fractional* rather than integer, and *less than unity*.

[d] Head gradient and flux errors in the 3D case:

We now proceed to develop similar expressions for the relative error on the numerical flux and head gradient solutions in the case of three-dimensional flow with statistically isotropic conductivity fields. We focus specifically on the "noisy" Markov spectrum of log-conductivity, which is the input spectrum actually used in the numerical simulations of groundwater flow presented in Chapter 6. The present analysis of the *flux error*, due to truncations in the finite difference scheme, is of particular interest for assessing the feasibility of accurate numerical simulations of three-dimensional flow and solute transport in heterogeneous media. Indeed, the spatial

fluctuations of the flux (or groundwater velocity) are responsible for the mechanical dispersion of convected solutes. It seems clear that an accurate simulation of the velocity field is a prerequisite for obtaining reliable simulations of the convection-dispersion mechanism in groundwater contamination problems.

In order to compute the relative error on the flux and head gradient vectors in the root-mean-square sense, one needs to compute both the variance of errors and the variance of the physical quantities themselves (using known solutions). The variance of numerical errors can be computed by integrating the error spectra given in equations (5.71) and (5.73), up to wavenumbers  $|k_i| \leq \pi/\Delta x$  ( $i = 1,2,3$ ) in three-dimensional Fourier space. This can be expressed as follows, for the flux error vector ( $Y_m = \delta q_m$ ) as well as the head gradient error vector ( $Y_m = \delta G_m$ ):

$$\text{Var} (Y_m) = \iiint_{\substack{0 \leq |k_i| \leq \pi/\Delta x \\ i=1,2,3}} S_{Y_m}(\underline{k}) \cdot d\underline{k} \quad (5.77)$$

The result of integration is given in [Appendix 5.C](#), using the flux error spectrum (5.73) and the head gradient error spectrum (5.71). Note that the domain of integration in (5.77) was approximated as  $0 \leq k \leq \pi/\Delta x$ , where  $k$  is the radial wavenumber.

In addition, the error variances obtained in Appendix 5.C take particularly simple forms for moderate-to-small grid resolution ratio:

$$R = \frac{\Delta x}{\pi \lambda} \ll 1 ,$$

which is precisely the case of most interest for applications (say  $\Delta x/\lambda \leq 1/2$  in practice). Thus, we will generally assume  $R \ll 1$  in what follows.

On the other hand, the variances of the flux and head gradient random fields are known from the first order spectral solutions developed in Chapter 3 (see equations 3.21-3.24). These results are reproduced below for convenience:

$$\left\{ \begin{array}{l} \text{Var}(q_1) = \left\{ \sqrt{\frac{8}{15}} K_G \sigma_f J \right\}^2 \\ \text{Var}(q_2) = \left\{ \sqrt{\frac{1}{15}} K_G \sigma_f J \right\}^2 \\ \text{Var}(q_3) = \left\{ \sqrt{\frac{1}{15}} K_G \sigma_f J \right\}^2 \end{array} \right.$$

and

$$\left\{ \begin{array}{l} \text{Var}(G_1) = \left\{ \sqrt{\frac{3}{15}} K_G \sigma_f J \right\}^2 \\ \text{Var}(G_2) = \left\{ \sqrt{\frac{1}{15}} K_G \sigma_f J \right\}^2 \\ \text{Var}(G_3) = \left\{ \sqrt{\frac{1}{15}} K_G \sigma_f J \right\}^2 \end{array} \right.$$



The final result shown below in terms of relative root-mean-square errors was obtained by computing the ratio  $\text{Var}(\delta Y)/\text{Var}(Y)$  and taking the square root (see [Appendix 5.C](#)). The relative numerical error on the flux vector is:

$$\boxed{\begin{aligned} m = 1: \frac{\sigma(\delta q_1)}{\sigma(q_1)} &\approx \frac{2.42\pi}{24} \left(\frac{\Delta x}{\lambda}\right)^{1/2} \\ m = 2,3: \frac{\sigma(\delta q_m)}{\sigma(q_m)} &\approx \frac{1.82\pi}{24} \left(\frac{\Delta x}{\lambda}\right)^{1/2} \end{aligned}} \quad (5.78)$$

and the relative numerical error on the head gradient is:

$$\boxed{\begin{aligned} m = 1: \frac{\sigma(\delta G_1)}{\sigma(G_1)} &\approx \frac{3.51\pi}{24} \left(\frac{\Delta x}{\lambda}\right)^{1/2} \\ m = 2,3: \frac{\sigma(\delta G_m)}{\sigma(G_m)} &\approx \frac{1.39\pi}{24} \left(\frac{\Delta x}{\lambda}\right)^{1/2} \end{aligned}} \quad (5.79)$$

where  $\lambda$  is the integral correlation scale of the 3D isotropic Markov log-conductivity field.

#### 5.2.4. Summary and discussion

We have evaluated the root-mean-square norm of the

finite difference solution error on the random head and flux fields, , for both 1D and 3D saturated flow. The three-dimensional results of equations (5.78) and (5.79) confirm the behaviour already observed in the one-dimensional case (equation 5.76). In both cases, it appears that the order of accuracy on the flux vector is  $O(\Delta x/\lambda)^{1/2}$  when a "noisy" log-conductivity field is used. Recall that the order of accuracy on the hydraulic head was  $O(\Delta x/\lambda)^{3/2}$  in the "noisy" case, and  $O(\Delta x/\lambda)^2$  in the case of a "smooth" log-conductivity field. In spite of the fact that we did not compute the order of accuracy for the flux in the case of a "smooth" 3-dimensional log-conductivity field, there is little doubt that the order of accuracy will be  $O(\Delta x/\lambda)$  in that case, as shown previously for the 1-dimensional case. These findings are summarized in Table 5.1.

The most important conclusion to be drawn from the truncation error analysis developed above, is that the centered finite difference scheme is a *consistent approximation* of the stochastic flow equation, even when the log-conductivity is a "noisy" random field, such as the non-differentiable 3D Markov field. Here, "consistency" means convergence in the mean-square sense of the finite difference solution to the exact solution as

Table 5.1

Order of Accuracy of the Stochastic Finite Difference Approximation (the "Noisy" and "Smooth" Random Fields were Defined in the Text, with Examples for 1 and 3-Dimensional Flow).

ORDER OF ACCURACY $O(\Delta x/\lambda)^P$	NOISY $\ell_n$ K FIELD	SMOOTH $\ell_n$ K FIELD
Hydraulic Head (H)	$p = 3/2$	$p = 2$
Head Gradient ( $G_m$ )	$p = 1/2$	$p = 1$
Flux Vector ( $g_m$ )	$p = 1/2$	$p = 1$

Table 5.2

Relative Numerical Error on the Hydraulic Head and Flux Vector, in the Case of the 3D Isotropic Markov Log-Conductivity Spectrum ("Noisy" Random Field)

GRID RESOLUTION $(\Delta x/\lambda)$	1/10	<u>1/3</u>	1/2
Hydraulic Head (H)	0.5%	<u>3%</u>	5%
Longitudinal flux( $q_1$ )	10. %	<u>17%</u>	22%
Transverse Flux ( $q_2, q_3$ )	8. %	<u>14%</u>	17%

the grid resolution ( $\Delta x/\ell$ ) goes to zero. The length scale  $\ell$  represents the integral correlation scale or some otherwise defined fluctuation scale, of the log-conductivity field.

Furthermore, it is worth noting that the present analysis leads to explicit estimates of the leading order term of the numerical error for the variables of interest, particularly the hydraulic head and the flux vector. Table 5.2 gives the relative numerical errors on the hydraulic head and on the different components of the flux vector in the case of the 3D Isotropic Markov spectrum of log-conductivity. Recall that the relative error was defined as the ratio of the standard deviation of the numerical error  $\delta Y$ , versus the standard deviation of the variable of interest  $Y$ . For a moderate grid resolution, such as the value  $1/3$  used in the numerical experiments of Chapter 6, the error on the head appears to be fairly small (3%), while the error on the flux vector is significant but still acceptable (less than 20%).

Another important finding from the truncation error analysis is that the relative errors  $\sigma(\delta Y)/\sigma(Y)$  appear to be independent of the log-conductivity standard deviation  $\sigma_f$ . Therefore, as  $\sigma_f$  decreases, the absolute precision on  $\sigma_H$  and  $\sigma_{q_i}$  will improve, but not the relative precision. The latter

can only be improved by using higher grid resolution. This finding will be useful for the design of numerical experiments aimed at obtaining accurate second order moments of the flow field for comparison with spectral solutions (Chapter 6).

In order to put these findings in proper perspective, it may be useful to recall the various assumptions that were used in our analysis of accuracy of the finite difference scheme. First of all, note that the solution errors were evaluated by using a statistical root-mean-square norm, or standard deviation of the random field error. It was assumed that the computational domain is large enough that these statistics can be viewed equivalently as ensemble or spatial averages, provided also that both the solution and the error be stationary and ergodic. Without these assumptions, no simple closed form results could be obtained.

Second, we emphasize the fact that the results of error analysis were obtained by using a double-expansion in terms of  $\Delta x/\lambda$  and  $\sigma_f$ , respectively. Thus, the closed form results obtained above give only the *leading order term* of the root-mean-square error, with respect to the "small parameters"  $\Delta x/\lambda$  and  $\sigma_f$ . In particular, note that a linearization of the type:

$$e^f \simeq 1 + f + \dots$$

was needed in order to include the effect of inaccurate evaluation of mid-nodal conductivities by the geometric mean weighting scheme (see equations 5.40 and 5.41). This particular linearization could lead eventually to underestimating the error on the flux vector  $\sigma(\delta q_i)$  for large values of  $\sigma_f$ . However, the same type of linearization was also used to evaluate  $\sigma(q_i)$ , so that the *relative* error  $\sigma(\delta q_i)/\sigma(q_i)$  could be less dependent on the linearization approximations, even for large values of  $\sigma_f$ . As an indication, the leading order errors obtained in this section are thought to be fairly representative of the actual finite difference solution errors for values of  $\sigma_f$  up to 1-1.5 and  $\Delta x/\lambda$  up to 0.5.

In addition, it is worth noting that the present error analysis did not include finite size effects and/or non-stationary behavior of the stochastic solution (as will necessarily occur to some degree for finite domain simulations). Neither did it include the sampling errors that will occur when computing single realization flow statistics by spatial averages (rather than ensemble averages). These effects will be discussed in Chapter 6.

Finally, it should be noted that several different kinds of errors actually occur in the numerical solution procedure: truncation errors, matrix solution errors, and round-off errors. The truncation errors were defined and analyzed in this section. Solution errors arise from the approximate solution of the finite difference system (e.g., by an iterative method). Round-off errors are due to the finite precision of digital computers, usually 32 digits on mainframes and 64 digits on recent supercomputers, and they accumulate more or less rapidly depending on the type of algorithm used (certain linear system solvers are more stable to round-off errors than others). It seems important to ascertain that solution errors and round-off errors will be minimal. Indeed, the fine grid resolution required for the case at hand leads to very large finite difference systems that may be difficult to solve accurately. This will be the subject of a forthcoming section, where we will focus on a particular type of preconditioned iterative solution method (the SIP solver).

By way of closing remarks, let us mention that the proposed approach of evaluating finite difference truncation errors for a stochastic partial differential equation appears to be new, in view of the available literature on numerical analysis. Our method, based on Taylor expansions, stochastic

linearization, and Fourier space representations, could be used to analyze mesh resolution requirements for more general stochastic partial differential equations, such as parabolic convection-diffusion equations. The present work could also be used to obtain a more complete picture of the discretization errors, such as the spatial correlation structure of the errors on the hydraulic head and on the flux vector. Other possible applications could involve the study of higher order finite difference methods, finite element methods, pseudo-spectral methods, and multigrid methods for stochastic PDE's with random coefficients.

### **5.3 Iterative Matrix Solver and Convergence Analysis for Linear Random Flow Problems**

#### **5.3.1 Review of iterative and preconditioned matrix solvers**

Our survey of the literature ([Table 5.3](#)) clearly showed that large sparse matrix systems can be solved more efficiently with iterative solvers than with direct solvers such as Choleski factorization or Gauss substitution. One of the many examples of the superiority of iterative solvers, even for relatively modest



Table 5.3 List of Matrix Solvers and References

Solvers	Comments	Applications to Subsurface Hydrology and Related Problems
1 Point Jacobi	Explicit type; $O(n^2)$ iterations.	seldom used
2. Gauss Seidel	Weakly implicit; $O(n^2)$ iterations.	seldom used
3. SOR	Accelerated Gauss-Seidel $O(n)$ iterations with optimal parameter, else $O(n^2)$ iterations.	Reisenauer et al., 1981 Bjordammen and Coats, 1969 Stone 1968
4. LSOR	Line - SOR, implicit along lines; requires optimal parameter for $O(n)$ convergence.	Bjordammen and Coats, 1969 Freeze, 1971, Cooley, 1974
5 ADI	Implicit along each direction alternatively; requires near-optimal sequence of parameters.	Stone 1968 Weinstein et al., 1969 Bjordammen and Coats, 1969 Watts 1971; Cooley, 1974; Trescott and Larson 1977; Kershaw, 1978
6. ICCG	First order accurate Incomplete Choleski factorization, with Conjugate Gradient iterations (no parameter required).	Kershaw 1978 Gambolati, 1979 Kuiper 1981 and 1987 Gambolati and Perdon 1984
7. SIP	Second order accurate strongly implicit LU factorization (requiring sequence of parameters); Picard iterations.	Stone 1968, Weinstein et. al. 1969, Cooley 1974 and 1983, Trescott, 1975, Trescott and Larson 1977, McDonald and Harbaugh, 1984, Kuiper 1981 and 1987.
8. Gauss Elimination or Choleski Factorization	Fully implicit, direct solver (non-iterative).	Neuman and Davis 1983 Yeh and Luxmoore 1983

size problems, can be found in Gambolati and Perdon (1984). Our own experience with a Gauss elimination solver adapted to a banded Galerkin coefficient matrix confirmed this view. The CPU time for this direct solver was proportional to  $N^{7/3}$  for steady state 3D groundwater flow on a cubic domain discretized into  $N$  elements. On a Vax 11/782 machine, the CPU time was about one hour for  $N = 4000$  elements. However, solving a problem of size  $N = 64000$  would have required one month of CPU time on the same machine, and larger problems on the order of 1 million elements could not be solved in reasonable amounts of time even on recent supercomputers such as Cray 2. The storage would be likewise prohibitive, being proportional to  $N^{5/3}$  (number of equations  $N$  times the matrix bandwidth  $N^{2/3}$ ). Thus, the storage requirement will be 10 Gigawords for large problems on the order of 1 million elements. In comparison, the central memory of the Cray 2 is currently about 250 Megawords.

The major disadvantage of using direct solvers for the solution of large linear systems lies in the fact that the triangular matrices arising in the process of decomposition are not sparse, even though the coefficient matrix itself may be sparse. For the 7-diagonal finite difference matrix depicted in Figure 5.2, a Choleski factorization  $A = LL^T$  yields a triangular matrix  $L$  with mostly non-zero elements within the half band of width  $n^2 = N^{2/3}$  (for a cubic grid of size  $n^3 = N$ ). As

mentioned above, this yields on the order of  $N^{5/3}$  non-zero elements to be computed, compared to just  $4N$  non-zero elements in the lower half of the original matrix. This kind of observation has led numerical analysts to develop a number of iterative solution methods based on approximate sparse decompositions of the original system matrix, such that the computational work per iteration and the required storage are both proportional to  $N$ .

The sparse iterative methods can be roughly classified with respect to the approximate decomposition method used. Most of the "classical" iterative solvers are based on an approximate *splitting* of the matrix (Point Jacobi, Gauss-Seidel, successive overrelaxation (SOR), alternate directions implicit (ADI)) while the more recent "fast" iterative solvers are based on an approximate *factorization* of the matrix (strongly implicit procedure, and incomplete Choleski-conjugate gradients). The reader is referred to Jacobs (1981) for a survey of iterative solvers according to the classification proposed above, and Evans (1981) for a review of matrix-splitting preconditioners. A number of other reviews and experimentations with matrix iterative methods can be found in the collections of papers edited by Schultz (1981), Evans (1983), and Birkhoff and Schoenstadt (1984). In addition, Table 5.3 gives a list of references concerning the use of iterative solvers for subsurface flow and analogous problems; some of these studies include

numerical experiments and comparisons between different types of solvers.

Another important distinction to be made among iterative solvers is, precisely, the type of iteration used to converge to the solution of the original matrix system. Apart from the IOCG solver, all the other solvers mentioned above are based on Picard-like iterations, including in particular the SIP method. These solvers can be briefly described as follows. Consider the linear finite difference system:

$$Ah = b \quad (5.80)$$

and suppose that an approximation  $M$  of matrix  $A$  has been found ( $M$  must be easier to invert than  $A$ ). The simple manipulation shown below leads quite naturally to a Picard iteration scheme where the new system matrix  $M$  is by construction easier to invert than the original matrix  $A$ :

$$(M + A - M) h = b$$

$$Mh = b + (M-A)h$$

$$Mh^{m+1} = b + (M-A)h^m.$$

Furthermore, by subtracting  $Mh^m$  to both sides, one obtains a "modified Picard" scheme that is presumably more stable with respect to round-off errors:

$$M \cdot \delta h^{m+1} = b - Ah^m$$

where  $\delta h^{m+1} = h^{m+1} - h^m$ , and  $m$  is the iteration counter. Finally, the iterations can be overrelaxed or underrelaxed by multiplying the right-hand side residual by a "relaxation parameter"  $\omega$ :

$$\boxed{M \cdot \delta h^{m+1} = \omega \cdot (b - Ah^m)} \quad (5.81)$$

It is worth noting that (5.81) is a consistent iteration scheme with respect to the original system (5.80), in the sense that the exact solution  $h = A^{-1}b$  is obtained as  $m \rightarrow \infty$ , provided however that the iterations converge. Unfortunately, convergence is not necessarily guaranteed in the general case.

We now proceed to review various kinds of preconditioners (matrix  $M$ ). The classical iterative solvers such as Jacobi and various versions of successive overrelaxation (SOR) are based on an approximate decomposition obtained by splitting  $A$  into lower triangular, diagonal, and upper triangular

matrices:

$$A = L + D + U$$

The approximate matrix  $M$  can be expressed in the general form:

$$M = D^{-1}(D + \gamma_L L)(D + \gamma_U U) \quad (5.82)$$

When the preconditioner (5.82) is plugged into (5.81), one obtains some well known iterative solvers of the "matrix-splitting" kind:

Point Jacobi	$(\gamma_L = \gamma_U = 0, \text{ and } \omega = 1)$
Point Gauss-Seidel	$(\gamma_L = 1, \gamma_U = 0, \text{ and } \omega = 1)$
Point SOR	$(\gamma_L = 1, \gamma_U = 0, \text{ and } 1 \leq  \omega  \leq 2)$
Symmetric SOR	$(\gamma_L = \gamma_U = \gamma, \text{ and } \omega = \gamma(2-\gamma))$

Similarly, the ADI solver can be viewed as an iterative method based on matrix-splitting decomposition. As an example, the Peaceman-Rachford version of ADI for two-dimensional finite difference systems (Peaceman and Rachford, 1955), can be expressed as follows:

$$A = -L_X - L_Y$$

$$(\gamma I - L_X)(h^{M+1/2} - h^m) = b - Ah^m$$

$$(\gamma I - L_Y)(h^{m+1} - h^{m+1/2}) = b - Ah^{m+1/2}$$

where the  $L_X$  and  $L_Y$  matrices correspond to the partial differential operators in the X and Y-directions, respectively. Note that each step of ADI is similar to the basic iterative scheme (5.81). The ADI method can be extended to three-dimensional finite difference systems (Douglas, 1962). More general alternate directions operator splitting methods have also been devised for the solution of weighted residual and collocation systems (Celia and Pinder, 1985).

The convergence properties of some of the classical iterative solvers reviewed above have been thoroughly analyzed in the literature (Varga 1962, Young 1971, Golub and Van Loan 1983). For instance, it has been shown that Jacobi and Gauss-Seidel require on the order of  $n^2$  iterations to reach a given precision, where  $n$  is the unidirectional size of the grid (Laplace problem, in any number of dimensions). The SOR methods require only  $O(n)$  iterations if the optimal iteration parameter can be computed accurately. Unfortunately, this requires estimating the spectral radius of the SOR iteration matrix. For

complex problems such as the stochastic flow equation, it seems unlikely that the "optimal" relaxation parameter could be estimated accurately without dramatically increasing the total computational work. Thus, the number of iterations is likely to be  $O(n^2)$  - rather than the  $O(n)$  behaviour predicted for *optimal* SOR.

This feature is presumably shared by the iterative ADI methods. The theory for ADI convergences remains incomplete, but the work of Peaceman and Rachford (1955) and Wachspress and Habeter (1960) shows that the optimal ADI-relaxation parameter is not a constant. These authors proposed a cyclic sequence of parameters based on the eigenspectrum of the  $L_X$  and  $L_Y$  matrices defined above. The truly optimal sequence is not known, except for very special forms of the governing equation, e.g., the heat equation with spatially separable conductivity  $K(x,y)=K_x(x) \cdot K_y(y)$ . More details can be found in Varga (1962) and Ames (1977), among others.

The Jacobi, SOR, LSOR, and ADI solvers can also be compared in a slightly different way as follows. First of all, let us point out key feature shared by all the iterative methods reviewed above: the interactions among nodal variables are *partially decoupled* through the iterative solution process. At each iteration step, the solution is computed by taking into



account the interactions among a certain group of nodal values, while the remaining nodes are treated explicitly (e.g., by retaining the values obtained at the previous iteration). The computational work per iteration is roughly the same for all solvers (on the order of  $N$ ), but the "degree of implicitness" differs. In the Jacobi method, the solution at each node is computed explicitly with respect to all the remaining nodes; in the Gauss-Seidel and SOR methods, about half of the nodes are treated implicitly on average; and in the ADI method, the nodal values are coupled alternatively in the  $X$  and  $Y$ -directions, while the other direction is treated explicitly. Various devices have been proposed in the literature in order to increase the degree of implicitness, or coupling, of iterative solvers while still retaining the advantages of a sparse and easily invertible matrix approximation. Indeed, the SOR matrix-splitting can be generalized into line-SOR or more generally block-SOR splittings, which may increase the coupling along lines or among neighboring nodes (Evans, 1984).

However, our literature review indicates that the most efficient, or "strongly implicit", iterative solvers are those based on an approximate factorization of the original matrix, such as the SIP and ICCG solvers mentioned earlier. This was taken into account in the classification given in Table 5.3, where the solvers were listed according to their "degree of

implicitness", increasing from top to bottom (Jacobi, Gauss Seidel, SOR, LSOR, ADI, ICCG, SIP, and Direct Solvers). According to this classification, direct solvers are fully implicit (requiring only "one iteration") but their computational cost will be prohibitive for large systems, as explained earlier. The advantage of SIP and ICCG is that they are based on strongly implicit, yet sparse factorizations of the coefficient matrix. Thus, these two methods presumably converge faster than the solvers based on matrix-splitting, while the computational work per iteration remains on the order of  $N$ .

The numerical experiments published in the literature confirmed this view. Most of the references given in Table 5.3 above involved comparisons between LSOR, ADI, SIP, and ICCG. It appeared that ADI had the slowest convergence rate in most cases, or diverged in difficult cases such as those involving anisotropic conductivities. The LSOR solvers were reasonably efficient, provided alternate line-sweeping along different directions, but the SIP solver was usually more efficient for "difficult" problems involving heterogeneities and mild nonlinearity. In addition, the performance of SIP was not overly sensitive to the choice of its iteration parameters, whereas this was sometimes a critical issue for LSOR and ADI.

On the other hand, ICCG also appeared to be a powerful solver. The numerical experiments by Kershaw (1978) demonstrate the superiority of ICCG over ADI and LSOR for a laser fusion problem (transient diffusion equation with a radiation term). Other numerical experiments for heterogeneous confined and unconfined groundwater flow (Kuiper 1981) indicate that SIP with underrelaxation could be as efficient as ICCG for the mildly nonlinear case of unconfined flow, although ICCG usually converged faster for linear problems. In a more recent study Kuiper (1987) concludes in favor of ICCG over SIP. However, it is possible that a change in the details of implementation, especially for the nonlinear problems, could affect his conclusions. Furthermore, the SIP solver involves an adjustable sequence of iteration parameters (similar to ADI), and could also be underrelaxed to avoid divergence in difficult cases. On the other hand, ICCG does not depend on any extraneous iteration parameter. It is conceivable that the flexibility of SIP could be an advantage, rather than a drawback, when dealing with near ill-conditioned systems.

At any rate, it may be preposterous to draw definite conclusions here, since the numerical experiments mentioned above were limited to rather modest-size flow problems, below 10,000 nodes. The largest among those was the saturated-unsaturated numerical simulation by Freeze (1971) with the LSOR solver on an

8,000-node grid, but his study did not include comparisons with other solvers. Larger simulations can be found in the literature on numerical analysis, however, these focus typically on the solution of the Laplace or Poisson equations (constant coefficients). One of these studies, by Jacobs (1983), develops an adaptation of the SIP factorization in conjunction with conjugate gradient iterations, for comparison with ICG methods. The conclusions, based on two-dimensional test problems up to 40,000 nodes, were in favor of ICG over SIP-CG. However, we do not know of any numerical experiments with the *standard* SIP solver for problems of comparable size or larger.

We now focus our review on the theory of SIP and ICG, since our search in the literature indicates that these solution methods may have the best potential for large finite difference systems. The idea of using sparse approximate factorization for preconditioned iterative solvers arose in 1968, when the *SIAM Journal on Numerical Analysis* published in the same issue three papers on the approximate factorization and iterative solution of multi-dimensional finite difference systems. The first, by Stone, described the *strongly implicit procedure* (SIP) based on an approximate, non-symmetric LU factorization of the symmetric coefficient matrix  $A$ , with a Picard iteration scheme to converge to the solution of the  $A$ -matrix system. Although Stone's paper (1968) concerned only two-dimensional 5-point finite difference

systems, the SIP method was subsequently extended to three-dimensional 7-point finite difference systems (Weinstein et al, 1969). The two other papers in the 1968 *SIAM Journal*, by DuPont, Kendall, Rachford and the companion paper by Dupont, developed a symmetric  $LL^T$  approximate factorization with Picard iterations to converge to the solution. The  $LL^T$  factorization they used was similar to an incomplete Choleski factorization where the matrix  $L$  is forced to have the same sparsity pattern as  $A$ , and furthermore the row-sums of  $A$  are conserved (see Gustaffson 1978, Jackson and Robinson 1985). Thus, the iterative solvers of Stone (1968) and Dupont et al. (1968) differed essentially in the method used to obtain an approximate factorization of the finite difference matrix.

It was not until 1977 that the symmetric incomplete Choleski factorization was used as a preconditioner for conjugate gradient iterations (Mejerink and Van der Vorst, 1977). This combination, known as incomplete Choleski-conjugate gradients (ICCG), has become quite popular due to the fast convergence of the CG iterations in the case of well conditioned (preconditioned) symmetric positive-definite systems (see Kershaw, 1978, among others). It is interesting to note that the "pure" conjugate gradients method devised by Hestenes and Stiefel (1952) was viewed in the early days as an exact solver, since the method was known to converge to the exact solution in at most  $N$

iterations ( $N$  being the number of equations). However, the CG iteration did not converge fast enough to be competitive as an approximate large sparse matrix solver ( $N$  large). Thus, it should be kept in mind that the incomplete factorization is an essential ingredient of the IOCG method, required to ensure fast convergence of the conjugate gradient iterations.

On the other hand, it is worth noting that the conjugate gradients method, and the IOCG solver, can only be used to solve symmetric positive-definite systems. As a consequence, the conjugate gradients method cannot be used to accelerate the convergence of the SIP solver, as the latter is based on a non-symmetric LU factorization. This would seem to advantage the IOCG method, since the conjugate gradients iterations presumably converge faster than Picard iterations for well conditioned (preconditioned) systems. On the other hand, the non-symmetric SIP factorization appears to be a more accurate approximation of the original system matrix than the Incomplete Choleski factorization (respectively second order and first order in  $\Delta x$ : see Stone 1968 and Gustaffson 1978). This seems to advantage SIP, with a better preconditioner than IOCG.

Unfortunately, there does not appear to be any solid theoretical basis on which to compare the two methods. A formal theory of SIP convergence is still lacking, due to the complex

form of the LU factorization involved; there has not been much progress in this area since the indications given by Stone (1968) for 2-dimensional problems with constant coefficients. The theory for IOCG is more developed, but limited to constant or mildly variable coefficients. For instance, Gustaffson (1978) showed that the condition number of the iteration matrix for the Picard-Incomplete Choleski solver of Dupont, et al. (1968) was  $O(n)$ , compared to  $O(n^2)$  for the condition number of the original matrix (Laplace equation, with  $n$  the unidirectional size of the grid). On the other hand, the number of iterations required to reach a given precision grows like the square-root of this condition number, both for the Picard and the conjugate gradient iterations (Gustaffson 1978, and Golub and Van Loan 1983). This yields for the number of IOCG iterations a relation of the form:

$$m \sim n^{1/2}$$

which indicates that the IOCG method could converge quite fast for large 3D systems. Indeed, the total size of the grid is  $N = n^3$  in three dimensions, which yields:

$$m \sim N^{1/6} \tag{5.83}$$

indicating a very slow growth of the number of iterations with grid size. Note however that the theoretical analysis that led

to (5.83) was based on a number of assumptions, including the restriction to mildly variable or constant coefficients. It seems more reasonable to postulate that, in the worst case, the number of iterations could grow like the unidirectional size of the grid, for the IOCG as well as the SIP methods, i.e.:

$$m \sim n$$

This gives finally a worst case estimate of the number of iterations required for convergence of both IOCG and SIP for three-dimensional systems with highly variable coefficients:

$$\boxed{m \sim N^{1/3}} \quad (5.84)$$

In comparison, note that the non-optimal SOR method will not converge faster than  $N^{2/3}$  iterations, even for mildly variable coefficients.

We have developed a Fortran implementation of the SIP solver during the initial stages of this research. Some of the details of this implementation will be described in the next section, and a number of numerical experiments for large random flow problems will also be presented in a forthcoming section. Because the results obtained with SIP were eventually found to be quite satisfactory, it was felt that developing the IOCG solver



was not necessary. However, there is no claim that IOCG could not perform as well or perhaps better than SIP in terms of computational work (more on this later).

### 5.3.2 Formulation of the strongly implicit procedure (SIP solver)

We now proceed to describe the algebraic details of the strongly implicit procedure. Recall that SIP is based on the Picard iteration scheme (5.81):

$$M \cdot \delta h^{m+1} = \omega \cdot (b - Ah^m) \quad [(5.81)]$$

where  $M = LU$  is an approximate non-symmetric factorization of the system matrix  $A$ . In what follows, we analyse in some detail the SIP factorization for the case of the 7-diagonal symmetric coefficient matrix  $A$ , corresponding to the 7-point centered finite difference scheme in three dimensions (see Figures 5.1 and 5.2 above). The 3D version of SIP was exposed briefly by Weinstein et al. (1969), based on the 2D version previously developed by Stone (1968). Details on coding can be found for instance in McDonald and Harbaugh (1984). However, our particular implementation is exposed below.

The SIP factorization aims at obtaining a close approximation of matrix  $A$  in the form of a product of a lower and

an upper triangular matrix (L and U) that have the same sparsity patterns as the lower and upper parts of A (Figure 5.5). The difficulty is to find the matrices L and U such that the product  $M = LU$  is indeed close to A in some sense. Let us define E the error matrix:

$$E = M - A = LU - A \quad (5.85)$$

Obviously, many choices of L, U, and E are possible for a given matrix A, since the system (5.85) is undetermined. On the other hand, it is easily seen by inspection that E cannot be the zero-matrix since the system  $A = LU$  is overdetermined. We conclude that A cannot be *exactly* factored in the form LU.

The particular factorization devised by Stone and co-workers was obtained by writing explicitly the undetermined system (5.85) - with L and U as shown in Figure (5.5) - in a recursive form. The undetermined coefficients in this recursion were then obtained by manipulating the equations in such a way that the product LU appears equivalent to a non-symmetric, second order finite difference approximation of the governing partial differential equation. In two dimensions, Stone (1968) showed that LU corresponds to a 7-point symmetric FD approximation

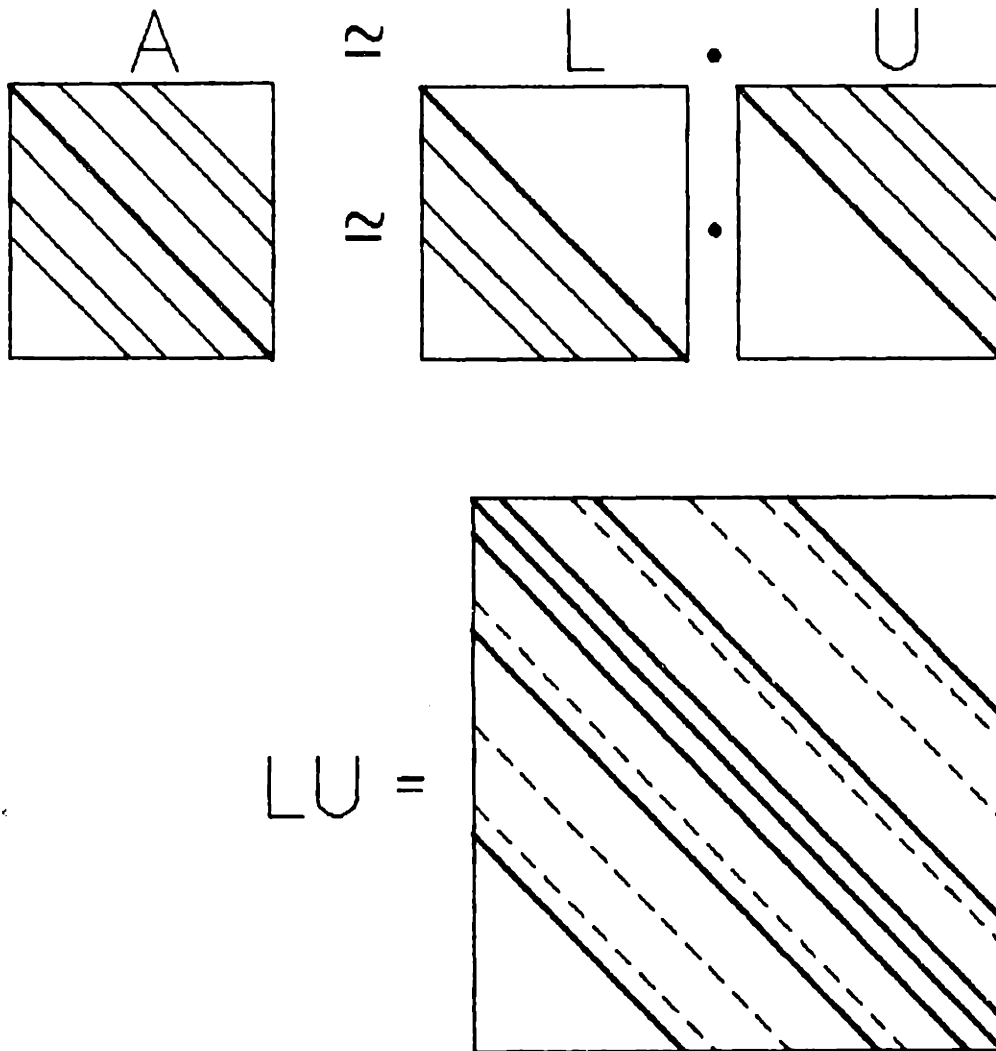


Figure 5.5 Schematic representation of the SIP approximate factorization (top), and structure of the product  $M = LU$  approximating  $A$  (bottom). The dashed lines indicate extra diagonals not present in the original matrix  $A$ .

(Figure 5.6, top) satisfying:

$$LU = A + O(\Delta x^2, \Delta y^2, \Delta x \Delta y).$$

In three dimensions, an analogous procedure devised by Weinstein et al. (1969) leads to a factorization LU that appears equivalent to a 13-point asymmetric FD approximation of the governing equation (Figure 5.6, bottom). Presumably, this corresponds to a second order approximation of the governing equation, as in the two-dimensional case.

However, it turns out that the LU factorization required an additional modification in order to ensure proper convergence of the iterations defined by (5.81). A new parameter  $\gamma$  was introduced (undetermined coefficient of the LU matrices) in such a way that the factorization described just above corresponds to the case  $\gamma = 1$ . Note that  $\gamma$  is an "iteration parameter", distinct from the relaxation parameter  $\omega$  appearing in equation (5.81). According to Stone (1968) and Weinstein et al. (1969), the best results were obtained when  $\gamma_m$  followed a cyclic sequence, with  $0 < \gamma_m < 1$ . The proposed sequence of parameters is analogous to that of the ADI method. This sequence takes the form:

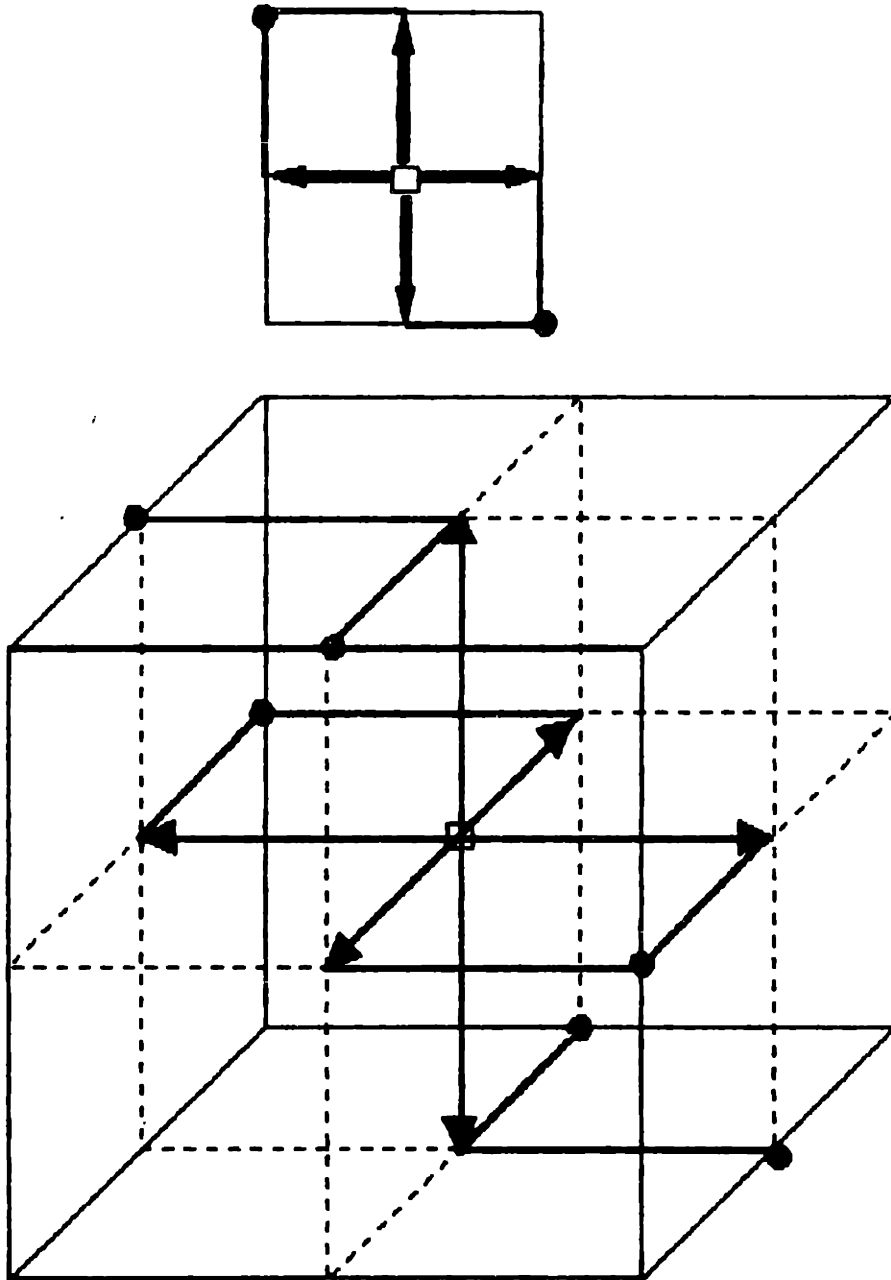


Figure 5.6 Asymmetric SIP molecule corresponding to the approximate LU factorization of the symmetric finite difference matrix  $A$  (top: 2D case; bottom: 3D case).

$$1 - \gamma_m = (1 - \gamma_{\max})^{\frac{m-1}{m_0-1}}, \quad m = 1, 2, \dots, m_0 \quad (5.86)$$

where  $m_0$  is the cycle length (taken equal to 4 in this work), and  $\gamma_{\max}$  is the maximum value of  $\gamma$  over one cycle. Correcting the erroneous formula given by Stone (1968),  $\gamma_{\max}$  is given by:

$$\gamma_{\max} = \text{Min}_{i,j,k} \left\{ \frac{\pi^2}{n_1^2 \rho_1}; \frac{\pi^2}{n_2^2 \rho_2}; \frac{\pi^2}{n_3^2 \rho_3} \right\}$$

$$\rho_1 = 1 + \left[ \frac{K_{i,j+\frac{1}{2},k}}{\Delta x_2^2} + \frac{K_{i,j,k+\frac{1}{2}}}{\Delta x_3^2} \right] / \frac{K_{i+\frac{1}{2},j,k}}{\Delta x_1^2}, \quad (\text{etc.})$$

where  $n_i$  represents the number of nodes along direction  $x_i$ . Note that  $\gamma_{\max}$  appears to be spatially variable in the case of non-constant conductivities, so that the above formula requires some further modification. In the case of 3D flow with locally isotropic (but variable) conductivities, we propose a simple elimination of the conductivities appearing in  $\rho_1$ , etc., on the grounds that neighboring mid-nodal values should not differ much on a high resolution grid. This yields finally:

$$1 - \gamma_{\max} = \text{Min}_{i=1,2,3} \left\{ \frac{\pi^2 (\sum \Delta x_j^2 - \Delta x_i^2)}{2n_i^2 \cdot \sum \Delta x_j^2} \right\} \quad (5.87)$$

where  $\Sigma \Delta x_j^2 = \Delta x_1^2 + \Delta x_2^2 + \Delta x_3^2$ . Equations (5.86) and (5.87) completely define the cyclic sequence of SIP iteration parameters used in this work, both for the linear and nonlinear flow systems. The cycle length was  $m_0 = 4$  for all simulations. To avoid confusion, we stress again the fact that  $\gamma$  is distinct from the relaxation parameter  $\omega$  appearing in the basic iteration (5.81). The parameter  $\omega$  was introduced to provide additional flexibility to the SIP solver, and will turn out later to be useful.

~~It may be instructive to briefly explain the rationale~~ behind the choice of a cyclic sequence of the  $\gamma$ -parameter. The geometric progression (5.86) was chosen intentionally in order to cover a wide range of values  $0 \leq \gamma_m \leq \gamma_{\max} < 1$ , in such a way that the values taken by  $\gamma_m$  are mostly clustered near unity (note that  $\gamma_{\max}$  is very close to one for large grids). Indeed, it turns out that for  $\gamma \simeq 1$ , the iterative smoothing of the error is only effective within a narrow wavenumber band, so that several different values of  $\gamma$  near unity are needed in order to cover a wide enough band. In addition, the precise choice of  $\gamma_{\max}$  is important for the success of the SIP method. According to equation (5.87), this parameter is close to one, but always less than one. Indeed, Fourier analysis shows that taking  $\gamma_{\max}$  exactly equal to unity would lead to divergence of the SIP iterations.

In the case of the two-dimensional Laplace equation, Stone (1968) showed that, for any constant value of  $\gamma_m$  in the vicinity of unity, there will be an amplification of the Fourier modes of the error within some wavenumber range. On the other hand, Stone also showed that for any given Fourier mode, there exists a value of  $\gamma$  between zero and one that results in the decay of the amplitude of that mode. Values of  $\gamma$  near unity tend to decay the low wavenumber components of the error (although some other modes might be amplified!), while values of  $\gamma$  near zero tend to decay the high wavenumber modes quite rapidly. The sequence of  $\gamma_m$  defined above is therefore an important ingredient of the SIP method, without which very slow convergence or even divergence could occur. Unfortunately, there exists no proof that this sequence will guarantee optimal convergence of the SIP method in the general case. The ADI method encounters the same type of problem, as explained earlier.

Another important feature of the SIP factorization that might be altered to improve convergence is its *directionality*, arising from the asymmetry of the "SIP molecule" depicted in Figure 5.6 above. Indeed, the orientation of the SIP molecule could be changed by reordering the nodes in a different fashion. In three dimensions, we have enumerated eight possible ways to do so without changing the sparsity pattern of the system matrix. The standard node ordering scheme, which sweeps first through



( $+x_1$ ), then ( $+x_2$ ), then ( $+x_3$ ), was used as the basic indexing scheme in our numerical code. However, the SIP algorithm can be manipulated to accommodate other node orderings, such as sweeping reversely through ( $-x_1$ ), then ( $-x_2$ ), then ( $-x_3$ ) in the negative directions. It has been claimed that implementing the SIP factorization with alternate ordering ( $+x_1, +x_2, +x_3$ )/( $-x_1, -x_2, -x_3$ ) from one iteration to the next, resulted in improved convergence. However we have not observed any favorable effect of the alternate ordering strategy in our preliminary numerical tests. For completeness, note that there are two ways to implement the alternate SIP method; the one we have tried without success cycled the  $\gamma$ -parameter every other iteration, so that the same value of  $\gamma$  was used for alternate sweeps. According to Weinstein et. al. (1969), the other strategy which uses different values of  $\gamma$  over alternate sweeps may work as well or better. In any case, the numerical experiments shown in this work were all performed with the standard node ordering implementation of SIP (no alternate sweeps).

The algebra of the SIP factorization is tedious and will not be reproduced in detail here. The factorization must be recomputed at each iteration step because the factored matrices L and U depend on  $\gamma_m$ , which varies cyclically as explained before. Our particular implementation used a vector representation of each non-zero diagonal line of A, L and U. We

obtained a nonlinear recursion for the coefficients of the L and U matrix, analogous to the Thomas algorithm for tridiagonal matrices, but much more complex (13 equations define the recursion). Unfortunately, this type of recursion does not appear to be fully vectorizable, except at the cost of increased storage requirements.

We have coded several implementations of the SIP solver in order to accommodate different computing environments. One of the variants is slower, but more flexible and requires less storage. Typically, the solution of a linear problem such as saturated flow with random field conductivities will require a storage of about  $10N$  words, where  $N$  is the total number of nodes. The number of equivalent additions performed at each iteration step is on the order of 50-100 per node, of which only a fraction is vectorizable. Thus, solving a single realization of the stochastic flow problem on a 3D grid on the order of 1 million nodes would require the availability of about 10 Megawords of central memory, and consume on the order of 100 MFLOP per iteration (1MFLOP = 1 million floating point operations).

In comparison, a recent supercomputer like the Cray 2 could run at 10 MFLOP/second (or several times faster) in scalar mode, and 100 MFLOP/second (or several times faster) in full

vector mode. The physical memory of the Cray 2 is currently 256 Megawords (with 64-bit words), but other supercomputers have only about 1-10 Mwords of central storage (Cray 1, Cyber 205). Nevertheless, storage should not be a real problem in the near future, since the current trend is towards larger physical memories on the order of the Gigaword ( $10^9$  words).

We conclude that the numerical solution of random flow problems on grids on the order of 1 million nodes will be feasible at reasonable cost on current supercomputers having sufficient, direct access memory, *provided that the number of iterations required to reach an accurate solution be on the order of 1000 or less.* In this case, a solution for each single-realization problem could be reached in, say, no more than a few hours of CPU time. Thus, the key question is whether the SIP solver converges at a reasonable rate in the case of large, highly variable flow problems. We will examine this question below for the case of steady state flow in saturated media. The transient and nonlinear problem of unsaturated flow is of a different nature, and its numerical analysis is postponed to a later section.

### 5.3.3 Convergence analysis for large 3D random systems of saturated flow

In this subsection, we summarize the results of a number of numerical experiments conducted with the SIP solver, for large single-realizations of the stochastic groundwater flow equation in three dimensions (up to 1 million nodes). We begin by developing an approximate theory relating the unknown solution error to other "observables" such as the residual iteration error. This will serve as a basis to interpret the numerical experiments. Note that we focus here strictly on the *convergence* of the solver, and not on the physical meaning of the solutions themselves (see Chapter 6).

#### [a] Theoretical Analysis of Convergence:

We proceed to show that the convergence rate of the SIP solver is related to the spectral radius of the so-called iteration matrix, or "Jacobi matrix"  $J$ . Furthermore, we will also show that the observable "residual error"  $(\hat{\epsilon})$  usually underestimates the true error  $(\epsilon)$  by an amount which depends on the convergence rate. Let us start with the basic Picard iteration scheme (5.81):

$$LU(h^{m+1}-h^m) = \omega \cdot (b-Ah^m) \quad [(5.81)]$$

and recall that LU is an *approximate* factorization of matrix A, which depends on the cyclic  $\gamma$ -parameter of equation (5.86). For simplicity here, we will ignore the fact that LU varies cyclically with respect to the iteration counter m. This should not be of consequence for the forthcoming analysis, e.g., the convergence rate can be interpreted as an average over the cycle length.

Let us now define a "residual error" which can be computed a posteriori by numerical experimentation:

$$\hat{\epsilon}^m = h^{m+1} - h^m \quad (5.88)$$

However, the "true error":

$$\epsilon^m = h^m - h \quad (5.89)$$

remains unknown, since the exact solution  $h$  is not known. Nevertheless, a recursive relation on  $\epsilon^m$  is easily obtained by manipulating equation (5.81); this gives:

$$\epsilon^m = (J_\omega)^m \cdot \epsilon^0 \quad (5.90)$$

where  $\epsilon^0$  is the initial error (depending on the initial guess  $h^0$ ), and  $J_\omega$  is the iteration matrix:

$$J_{\omega} = I - \omega (LU)^{-1} A \quad (5.91)$$

Furthermore, it is easily seen, by manipulating again equation (5.81), that the residual error follows a geometric progression similar -- but not identical -- to equation (5.90):

$$\hat{\epsilon}^m = (J_{\omega})^m \cdot \omega (h-(LU)^{-1}Ah^0) \quad (5.92)$$

These relations show that the SIP iterations will not converge unless the "norm" of the iteration matrix  $J_{\omega}$  is less than one, in some sense to be precised later. In the case of an *exact* LU factorization, and taking  $\omega = 1$ , the iteration matrix becomes zero and the *exact* solution will be obtained after just one "iteration". In the case of the approximate SIP factorization, we expect that the rate of convergence be directly related to the accuracy of the LU factorization, which can be represented by the norm of  $J_{\omega}$  in equation (5.91). This intuitive observation will be given a more precise meaning shortly.

Note also that equations (5.90) to (5.92) can be combined to relate the unknown error vector  $\epsilon$  to the residual error vector  $\hat{\epsilon}$  as follows:

$$\epsilon^m = (I - J_\omega)^{-1} \cdot \hat{\epsilon}^m \quad (5.93)$$

This equation indicates that the true error may be much larger than the observed residual error when the norm of the iteration matrix  $J_\omega$  is close to unity. Observe that  $J_\omega$  depends on the chosen value of the relaxation parameter. The role of  $\omega$  can be made more explicit by plugging equation (5.91) into (5.93). This yields:

$$\epsilon^m = \frac{1}{\omega} \cdot A^{-1} LU \cdot \hat{\epsilon}^m \quad (5.94)$$

The role of the relaxation parameter now appears more clearly. Taking  $\omega < 1$  (underrelaxation) does not seem a good strategy at first sight, since this will increase the ratio  $\epsilon^m / \hat{\epsilon}^m$  according to equation (5.94). On the other hand, underrelaxation might be necessary in order to avoid divergence in the case where the LU matrix is not an accurate approximation of  $A$  (the norm of  $J_\omega$  must be less than unity in equation 5.91). This suggests that there exists some optimal value of the relaxation parameter ( $\omega_{opt}$ ) which will maximize the convergence rate of the true error. It is conceivable that  $\omega_{opt}$  be greater than one in certain "easy" cases, but more likely  $\omega_{opt}$  will be less than unity for "difficult" problems characterized by a large condition number of the coefficient matrix.

Unfortunately, the relations obtained so far depend on the unknown inverse matrix  $A^{-1}$  involved in  $J_\omega$ , so they cannot be used for an a priori analysis of convergence of the SIP solver in terms of the true error  $\epsilon$ . However, it is possible to relate the norm or spectral radius of  $J_\omega$  to the  $\epsilon$ -convergence rate, at least approximately. In addition, comparing equation (5.92) to (5.90) shows that the  $\epsilon$ - and  $\hat{\epsilon}$ -convergence rates should be the same. These remarks eventually lead to an explicit expression for the true error ( $\epsilon$ ) in terms of two "observable" quantities: the residual error ( $\hat{\epsilon}$ ), and the  $\hat{\epsilon}$ -convergence rate. This is developed in more detail below.

Our starting point consists in obtaining a tractable expression for the true solution error ( $\epsilon$ ) in equation (5.93). Intuitively, this equation suggests an inequality of the form:

$$\|\epsilon^m\| \leq \frac{\|\hat{\epsilon}^m\|}{1 - \|J_\omega\|}$$

A relation of this type was used for instance by Hageman and Young (1981) to design a stopping criterion for conjugate gradient iterations. In order to show that this is indeed a reasonable approximation of (5.93), we need to define some vector and matrix norms. The reader is referred to Householder (1964) for basic definitions and inequalities on matrix norms. The



facts directly relevant to the present work can be summarized as follows. A matrix norm must satisfy the usual properties of norms, including the triangular inequalities:

$$\|A + B\| \leq \|A\| + \|B\| \quad (5.95)$$

$$\|AB\| \leq \|A\| \cdot \|B\|$$

One particularly useful matrix norm  $\|A\|$  is defined in relation with the usual Euclidean norm  $\|x\|$  for vectors, as follows:

$$\|A\| = \max_x \frac{\|Ax\|}{\|x\|} \quad (5.96)$$

Incidentally, it can be shown that  $\|A\|$  is the square-root of the maximum eigenvalue of  $AA^T$ . Now, by using the second triangular inequality in (5.95) we obtain another useful inequality:

$$\|A^m\| \leq \|A\|^m \quad (5.97)$$

On the other hand, the spectral radius  $\rho(A)$  of a matrix  $A$  is defined as its maximum absolute eigenvalue:

$$\rho(A) = \max_i |\lambda_i(A)| \quad (5.98)$$

This quantity turns out to be always smaller or equal to the Euclidean matrix norm:

$$\rho(A) \leq \|A\| \quad (5.99)$$

Finally, combining (5.97) and (5.99) yields another useful inequality:

$$\rho(A^m) \leq \|A^m\| \leq \|A\|^m \quad (5.100)$$

Let us now assume that the iterations do converge, and that the norm  $\|J_\omega\|$  of the iteration matrix is less than unity (this also implies that its spectral radius  $\rho(J_\omega)$  is less than unity). Equation (5.93) can then be approximated as follows. First, take the Euclidean vector norm on both sides of (5.93) to obtain:

$$\|\epsilon^m\| = \|(I - J_\omega)^{-1}\| \cdot \|\hat{\epsilon}^m\|.$$

Second, write a formal Taylor development of the matrix-valued function:

$$(I - J_\omega)^{-1} = I + J_\omega + J_\omega^2 + \dots$$

and use the previous inequalities to obtain:

$$\|(I - J_\omega)^{-1}\| \leq 1 + \|J_\omega\| + \|J_\omega\|^2 + \dots$$

The series on the right-hand side converges since it was assumed that  $\|J_\omega\| < 1$ . Thus, we obtain finally:

$$\|(I - J_\omega)^{-1}\| \leq \frac{1}{1 - \|J_\omega\|}$$

which gives immediately the announced result:

$$\boxed{\|\epsilon^m\| \leq \frac{\hat{\|\epsilon^m\|}}{1 - \|J_\omega\|}} \quad (5.101)$$

On the other hand, applying previous matrix norm inequalities to equations (5.90) and (5.92) gives two more inequalities:

$$\|\epsilon^m\| \leq \|J_\omega\|^m \cdot \|\epsilon^0\| \quad (5.102)$$

$$\hat{\|\epsilon^m\|} \leq \|J_\omega\|^m \cdot \omega \|h - (LU)^{-1} Ah^0\|$$

Let us now define the convergence rate:

$$r = - \frac{d \ell n \epsilon}{dm} \quad (5.103)$$

and observe that the convergence rate of the residual error is identical to that of the true error if equality holds in both relations of (5.102). In that case, the convergence rate is given by:

$$r \simeq \ell n (1/\|J_{\omega}\|). \quad (5.104)$$

However, this can only be a rough approximation (hopefully on the safe side) since in fact equations (5.102) are *inequalities*. Other authors have used a slightly different argument that leads to a similar result with  $\|J_{\omega}\|$  replaced by  $\rho(J_{\omega})$  in equation (5.104). This is reported for instance in Remson et al. (1971), following the work of Forsythe and Wasow (1960) and others. Indeed, expressing equation (5.90) in the basis ( $e_i$ ) of independent eigenvectors of  $J_{\omega}$  gives:

$$\begin{aligned} \epsilon^0 &= \sum \alpha_i e_i \\ \epsilon^m &= \sum \alpha_i \lambda_i^m e_i \end{aligned}$$

and, in the case where the largest eigenvalue  $\lambda_1 = \rho(J_{\omega})$  dominates the others, we obtain approximately:

$$\epsilon^m \simeq [\rho(J_\omega)]^m \cdot \epsilon^0$$

This finally leads to replacing  $\|J_\omega\|$  by  $\rho(J_\omega)$  in equations (5.101) through (5.104). It should be mentioned that, although we know in general that  $\rho(J) \leq \|J\|$ , the cases where these two quantities are not close to each other are somewhat pathological. Here, we can only hope that the SIP iteration matrix  $J_\omega$  is not pathological, i.e. that its spectral radius is approximately equal to its Euclidean matrix norm.

To conclude, the results of equations (5.101) - (5.104) finally lead to an upper bound on the "true" solution error, in the form:

$$\boxed{\|\epsilon^m\| \leq \frac{\|\hat{\epsilon}^m\|}{1-e^{-r}}} \quad (5.105)$$

where  $\epsilon$  is the true error vector,  $\hat{\epsilon}$  is the residual error vector, and  $r$  is the convergence rate, which can be computed from:

$$\boxed{r \simeq -\frac{d \ln \|\hat{\epsilon}^m\|}{dm}} \quad (5.106)$$

Equations (5.105)-(5.106) are applicable in the case where the computed convergence rate,  $r$ , is a positive constant. In other words, the iterations must converge, and the number of iterations must be large enough that the convergence rate reaches an asymptotic value. Figure 5.7 shows three different situations that might arise in practice:

- (i) The residual error norm  $\|\hat{\epsilon}^m\|$  increases monotonically (on average over the cycle length) after a certain number of iterations: this is a sure sign that the method diverges.
- (ii) The residual error norm  $\|\hat{\epsilon}^m\|$  decreases monotonically but does not seem to reach a constant convergence rate: the method may converge with more iterations, or may not (possibly due to accumulation of round-off errors).
- (iii) The residual error norm  $\|\hat{\epsilon}^m\|$  decreases monotonically and reaches a constant convergence rate (straight line on a semi-log plot): the method clearly converges, and the final error  $\|\epsilon^m\|$  can be evaluated a posteriori by using equation (5.105).

The methodology developed above proved to be useful in practice, especially for the solution of very large "random" flow

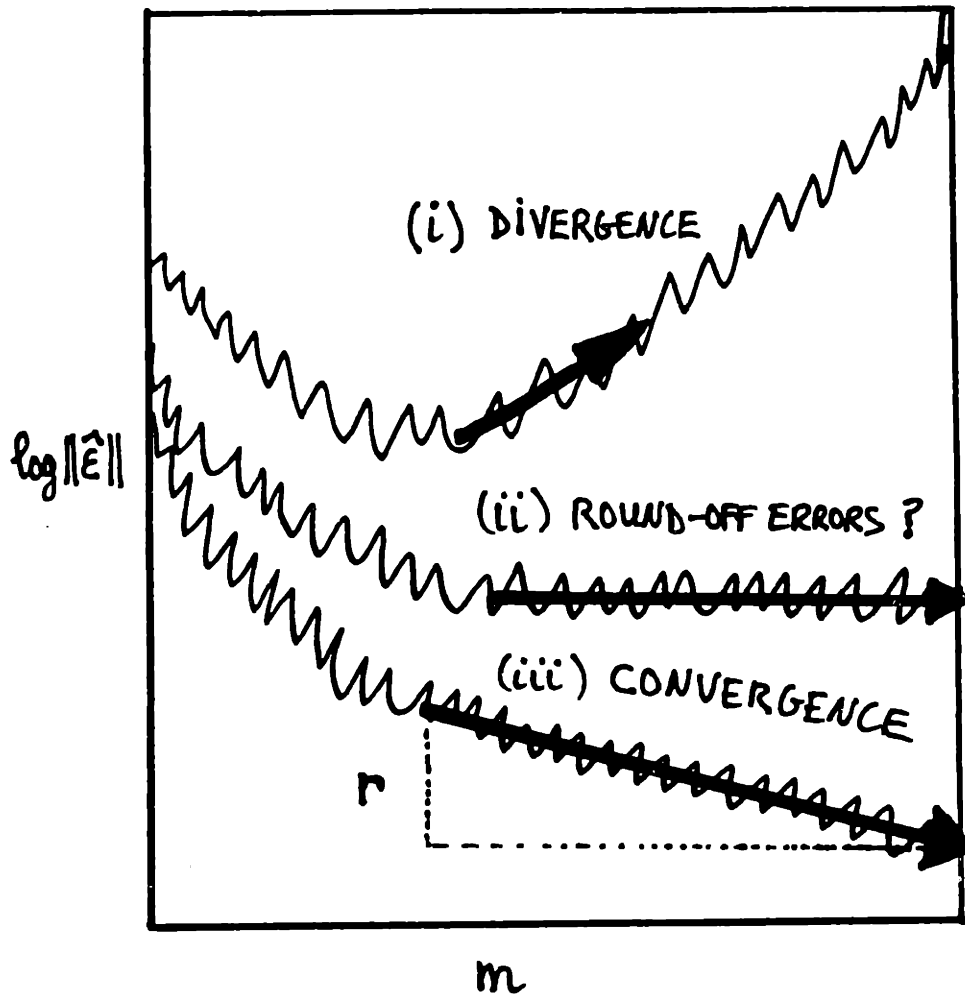


Figure 5.7 A posteriori analysis of convergence of the SIP solver: residual error norm versus number of iterations on a semi-log plot. In the convergent case (iii), the final residual error  $\|\hat{E}\|$  and the convergence rate  $r$  can be used to estimate the true error  $\|e\|$  as explained in the text.

problems. It was found that *underrelaxation* was needed in order to achieve convergence for such problems. As a consequence, the iterations converged quite slowly. Now, the simple relation in (5.105) shows that the *residual* error will largely underestimate the true solution error in these cases of slow convergence. Incidentally, let us mention that most empirical studies of iterative solvers in the literature use the residual error ( $\hat{\epsilon}^m = h^{m+1} - h^m$ ), or else the right-hand side residual ( $b - Ah^m$ ), in their evaluation of the solver's performance. The above analysis indicates that such information could be misleading, except perhaps for "academic" cases where the convergence rate is high enough that the residual error approximates well the true solution error. In the sequel, we analyze sequences of residual errors obtained from actual simulations, using equation (5.105) for a realistic evaluation of the performance of the SIP solver in terms of the "true" solution error.

[c] Numerical Experiments:

The SIP solver was applied to a model problem of saturated flow for a variety of grid sizes and different cases of log-conductivity variability. Briefly, the model problem was designed to simulate steady state saturated flow driven by a known global hydraulic gradient. The three-dimensional domain



was a rectangular prism, elongated in certain cases, cubic in other cases. The global hydraulic gradient was imposed along one of the axes of the rectangular prism (axis  $x_1$ ) by using fixed head boundary conditions on two opposite faces ( $x_1=0$  and  $x_1=L_1$ ), while zero-flux conditions were imposed on all other lateral faces. With this configuration,  $x_1$  represents the direction of the mean flow (longitudinal), while  $x_2$  and  $x_3$  are the axes transverse to the mean flow.

In the trivial case of a constant conductivity ( $\sigma_f=0$ ), the exact solution in terms of the hydraulic head is a linear function of the longitudinal coordinate:

$$H^0(\underline{x}) = H(0) + \frac{H(L_1)-H(0)}{L_1} \cdot x_1 \quad (5.107)$$

In the case of a random log-conductivity ( $\sigma_f \neq 0$ ), equation (5.107) was used as the initial guess for the SIP solver. The log-conductivity was generated at each node of the finite difference grid by using the 3-dimensional Turning Band algorithm developed by Thomson, Ababou and Gelhar (1987). This method generates single-realizations of random fields, as explained earlier (Chapter 2). The particular random field used for the numerical experiments of this section is the 3D isotropic Markov field, whose spectrum was given in Table 3.1. Let us mention that other simulations were conducted with anisotropic Markov

log-conductivity fields. The numerical solutions obtained for isotropic as well as anisotropic fields will be analyzed more thoroughly at a later stage (Chapter 6).

Table 5.4 summarizes the results obtained with SIP for 4 test problems and several values of  $\sigma_f$ . The first row gives the size and geometry of the grid. Note that the largest problem (1 million nodes) was solved on a Cray 2 machine with 64-bit words, while the other problems were solved on a minicomputer, the Microvax 2, with 32-bit words. The mesh size was the same along all three directions, and equal to one third of the conductivity correlation scale for the largest problem (one half for the others).

The second row in Table 5.4 gives the standard deviation of the log-conductivity field ( $\sigma_f$ ), which ranged between 1 and 2.3; these are fairly representative values in view of available field data (see Chapter 2). In addition, one of the simulations listed in Table 5.4 was for  $\sigma_f = 0$ , i.e. for constant conductivity (Laplace equation). The initial guess for the Laplace equation was taken to be a constant hydraulic head:

$$H(\underline{x}) = \frac{H(0)+H(L_1)}{2}$$

rather than the linear function (5.107) which is known to be the

Table 5.4

**Convergence Rate of the SIP Solver:  
Summary of Numerical Experiments for 3D Steady State  
Saturated Flow with Statistically Isotropic Random Conductivities**

Problem Label	A		B	C	D		
N	1 million		130,000	110,000	40,000		
$n_i$	(101; 101; 101)		(51; 51; 51)	(250; 21; 21)	(80; 21; 22)		
$\sigma_f$	1.0	2.3	2.3	2.3	0.	1.	2.3
$\omega$	2.5	.25	.50	.25	1.00	.50	.50
r	.0219	.0070	.0256	.0041	.0341	.0512	.0259
$(\Delta m_1)^*$	105.	330.	90.	570.	67.	45.	64.
$(s)^*$	1.2	0.4	0.7	0.3	0.9	1.4	0.7

(\*) The "iteration increment" ( $\Delta m_1$ ) and the "scaled convergence rate" (s) are defined in the text; note that  $\Delta m_1$  is the number of iterations required to decrease the true error by 1 order of magnitude.

exact solution of the Laplace equation. This particular test problem was included in order to examine the effect of conductivity variability over a wide range of  $\sigma_f$  values. In theory, the asymptotic convergence rate should not depend on the initial guess, but only on the size of the grid, the input conductivities, and certain iteration parameters.

The third row of inputs in Table 5.4 gives the relaxation parameter  $\omega$  used for simulations (see equation 5.81). The method used to search for an optimal value of  $\omega$  was rather elementary and empirical. The value  $\omega = 1$  was tried first; if divergence or very slow convergence occurred, the simulation was started again with underrelaxation. Thus, the sequence of values of the relaxation parameter used successively in the search process was  $\omega = 1$ ,  $\omega = 0.50$ ,  $\omega = 0.25$ , and  $\omega = 0.1$ .

The last three rows of Table 5.4 display the asymptotic convergence rate ( $r$ ) and two other quantities related to it. Recall that  $r$  is the rate of decrease of the logarithm of the residual error norm as defined by equation (5.106), which can be rewritten as:

$$r \simeq - \frac{d \ln \|h^{m+1} - h^m\|}{dm} \quad [(5.106)]$$

As explained earlier, this should be identical to the rate of convergence of the true error,  $\|h-h^m\|$ . The "iteration increment"  $\Delta m_1$  was defined as the average number of iterations required to decrease the error by 1 order of magnitude:

$$\Delta m_1 = \frac{\ln 10}{r} \quad (5.108)$$

Finally, the "scaled convergence rate" ( $s$ ) was obtained by dividing the convergence rate by a factor *approximately* equal to the square root of the *condition number* of the coefficient matrix  $A$ . In fact, this condition number is known only for the special case  $\sigma_f = 0$  (Laplace matrix), namely:

$$C_0 = \frac{4}{3} \frac{(n_1)^2 + (n_2)^2 + (n_3)^2}{\pi^2} \quad (5.109)$$

where  $n_i$  is the unidirectional size of the grid (number of nodes) in the direction  $x_i$ .

The condition number given by (5.109) was obtained as follows. First of all, the condition number of a symmetric matrix is defined as the ratio of the maximum versus minimum absolute eigenvalue of the matrix. The eigenspectrum of the Laplace matrix is easily obtained by solving the Laplace eigenproblem:

$$(\nabla^2 - \lambda) v = 0$$

for  $v(\underline{x})$ , and by plugging the corresponding eigenvectors  $v(i_1\Delta x_1, i_2\Delta x_2, i_3\Delta x_3)$  into the matrix eigenvalue problem:

$$(A-\lambda I)v = 0.$$

In the case where  $\Delta x_1 = \Delta x_2 = \Delta x_3$ , this gives the eigenvalue spectrum:

$$\lambda(\underline{k}) = \frac{K_G}{\Delta x^2} \cdot \sum_{i=1,2,3} \left[ 2 \sin \frac{k_i \pi}{2(n_i+1)} \right]^2$$

where  $k_i = 1, 2, \dots, n_i$ . The final result (5.109) was obtained by computing the ratio of the extreme eigenvalues ( $C_0 = \lambda_{\max} / \lambda_{\min}$ ) assuming  $n_i \gg 1$ , and the quantity "s" on the last row of Table 5.4 was defined as:

$$s = C_0^{-1/2} \cdot r \quad (5.110)$$

Thus, a constant value of  $s$  across the last row of Table 5.4 would indicate that the convergence rate is proportional to  $C_0^{1/2}$ , which is itself approximately proportional to the unidirectional size of the grid along the direction of maximum elongation (largest number of nodes). To avoid confusion, recall that  $C_0$  is the condition number of the Laplace matrix ( $\sigma_f = 0$ ), not of the

random matrix ( $\sigma_f \neq 0$ ).

The major results that emerge from Table 5.4 are the following. First of all, it appears that underrelaxation was usually required in order to achieve convergence. Second, convergence was fairly slow in general, since the number of iterations required to decrease the error by 1 order of magnitude ( $\Delta m_1$ ) was on the order of one hundred, up to several hundred iterations in the most difficult cases. Furthermore, it appears that the required number of iterations was roughly proportional to the unidirectional size of the grid as defined earlier. This can be seen by comparing problems A,B,C for  $\sigma_f = 2.3$ . On the other hand, the required number of iterations usually increased with  $\sigma_f$  for a given grid size (see problems A and D for  $\sigma_f = 1$  and 2.3).

However, the sequence of convergence rates obtained for problem D with  $\sigma_f = 0, 1$  and 2.3, indicates that the influence of  $\sigma_f$  on convergence might be fairly complex. If one accepts the conjecture that the convergence rate of SIP is proportional to  $C_A^{1/2}$ , where  $C_A$  is the condition number of the random conductivity matrix A, then the results of problem D suggest that  $C_A$  decreases with  $\sigma_f$  at low values of  $\sigma_f$ , and increases eventually for larger values. We have observed this kind of behavior for a very small matrix with random

conductivities distributed independently of each other, using a direct perturbation analysis to obtain a "geometric mean" condition number. The minimum condition number was obtained for  $\sigma_f$  around 1.00-1.25. This result is not intuitively obvious.

In any case, we infer from Table 5.4 that the convergence rate of the SIP solver behaved like:

$$r \simeq s \cdot \frac{\pi}{\sqrt{n_1^2 + n_2^2 + n_3^2}} \quad (5.111)$$

where  $n_i$  is the unidirectional size of the grid, and  $s$  is a slowly variable function of  $\sigma_f$  and  $n_i$ . According to the last row of Table 5.4, the coefficient  $s$  was roughly on the order of unity.

Figures (5.8) and (5.9) display the actual sequence of residual errors obtained during the iterative solution process for the largest and smallest problems A and D listed in Table 5.4. Figure 5.8a in particular gives the Euclidean norm of the residual error  $\|h^{m+1} - h^m\|$  versus the number of iterations ( $m$ ) on a semi-log plot for the "1 million node" problem A. The three subproblems  $\sigma_f \simeq 1.0, 1.7$  and  $2.3$  were solved sequentially



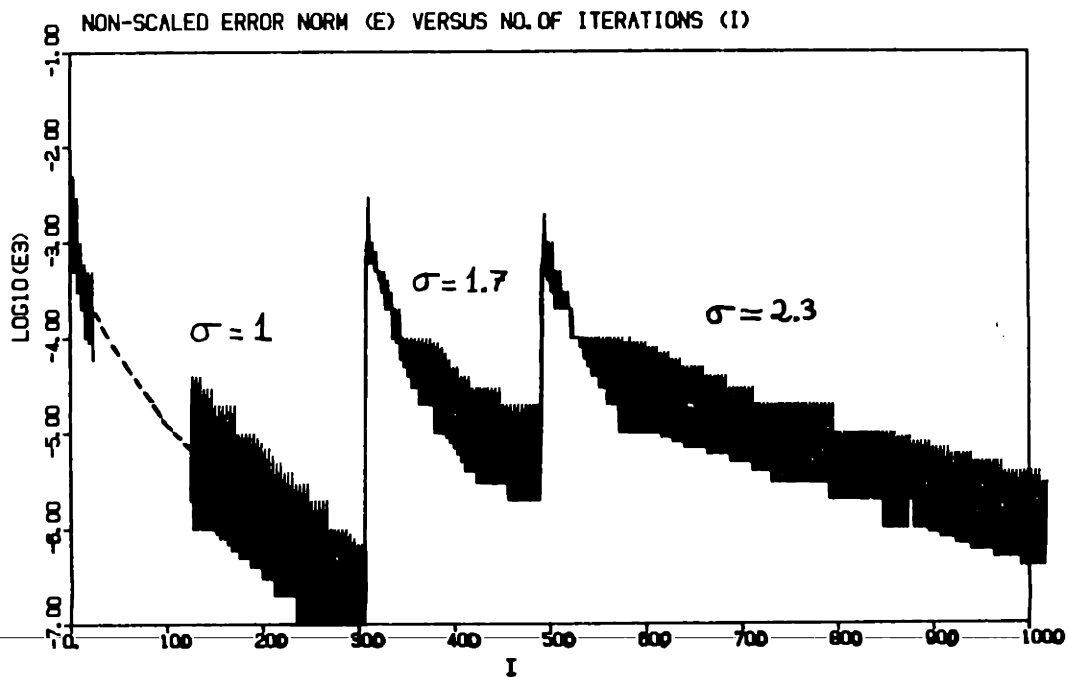


Figure 5.8 (a) Euclidean norm of the residual error versus number of iterations on a semi-log plot for problem A (1 Million nodes). The three subproblems  $\sigma=1, 1.7, 2.3$  were solved sequentially on a Cray 2 computer

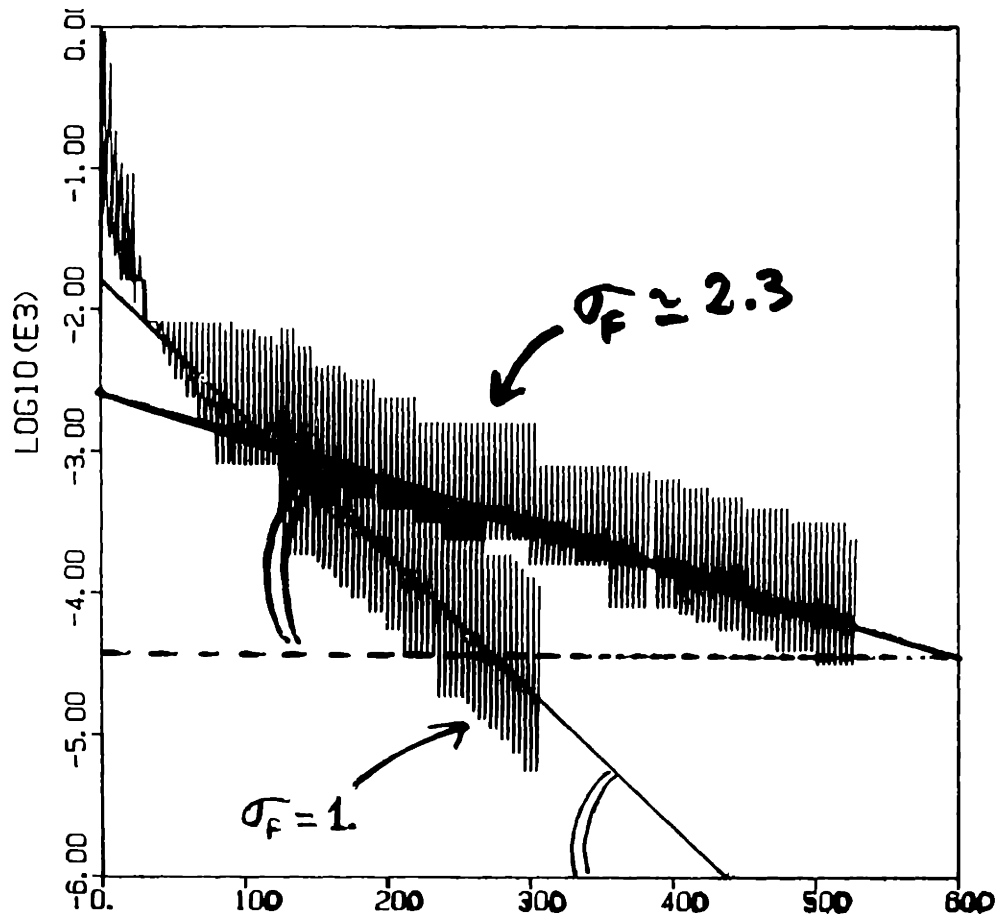


Figure 5.8 (b) Comparison of the asymptotic convergence rates for  $\sigma=1$  and  $\sigma=2.3$  of the 1 Million node problem A: same as Figure (5.8a) except that the residual errors have been scaled

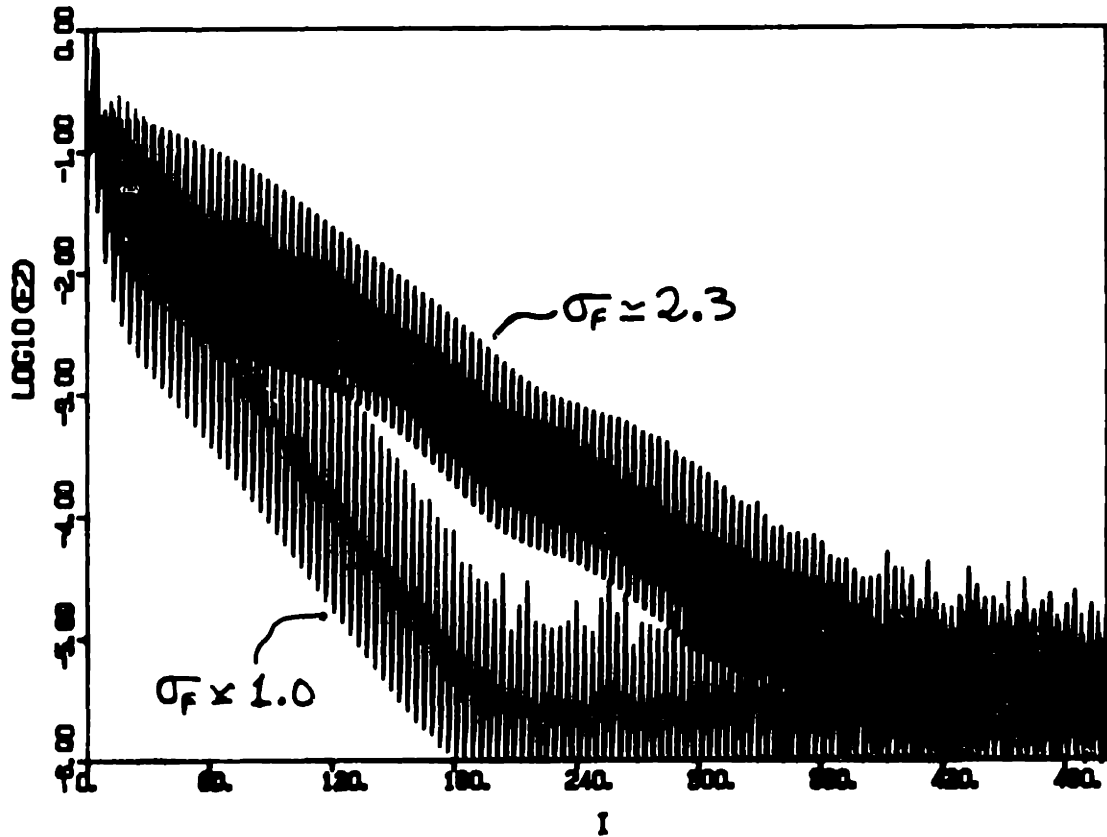


Figure 5.9 (a) Euclidean norm of the scaled residual error versus number of iterations for problem D, on a semi-log plot. The two subproblems  $\sigma=1$ ,  $\sigma=2.3$  were solved separately on a Microvax.

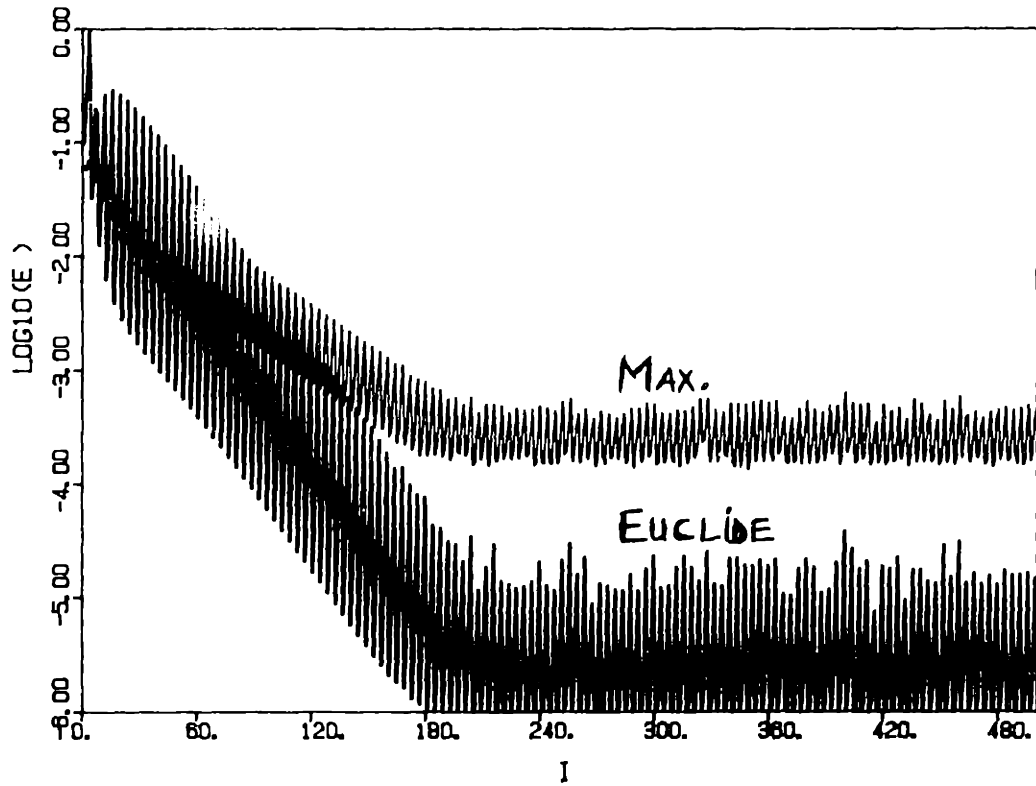


Figure 5.9 (b) Comparison of the Euclidean norm and absolute maximum norm of the scaled residual error for problem D with  $\sigma_f = 1.0$ .

on a Cray 2 machine, by using the last iterate of a subproblem as an initial guess for the next one. This procedure bears some resemblance with the so-called "continuation methods" to solve systems of equations whose solution depends continuously on a parameter  $\sigma$ : see Ortega and Rheinboldt (1970) in the context of nonlinear systems. Here the system is linear, but "difficult" to solve unless  $\sigma = 0$ ; the three subproblems  $\sigma \approx 1, 1.7, 2.3$  correspond to three "iterates" of the continuation method.

The total number of SIP iterations required to solve accurately the three subproblems of Figure 5.8a was about 1000 iterations, which consumed a total of about 4 CPU hours on the four-quadrant Cray 2 machine of the Minnesota Supercomputer Center running in "single precision" (64-bit words).

It should be noted that the Fortran code ("Bigflo") did not fully vectorize due to the nonlinear recursions of the SIP factorization algorithm, and the backward substitution of the solution algorithm. In addition, a "slow" Fortran compiler ("cft77") was used for technical reasons. As a result, the speed-up ratio between the Cray 2 and a Microvax 2 machine was moderate, about 1 CPU hour/1 CPU minute. The CPU time was found to follow the general relation:

$$T \simeq (c_0 + c_1 \cdot \frac{m}{100}) \cdot \frac{N}{10^6} \quad (5.112)$$

where  $c_0 \approx 5$  mn (overhead per million nodes) and  $c_1 \approx 23$  mn (per hundred iterations/per million nodes) for the Cray 2 machine. Recall that the number of iterations ( $m$ ) was found to be roughly proportional to the largest unidirectional size of the grid. Using equations (5.108) and (5.111) and ignoring the overhead time gives approximately the CPU time required to decrease the residual error by 1 order of magnitude, as a function of the grid size:

$$T_1 \approx c_1 \cdot \prod_{i=1,2,3} \left(\frac{n_i}{100}\right) \cdot \text{Max}_{i=1,2,3} \left\{\frac{n_i}{100}\right\} \quad (5.113)$$

For a grid with equal size  $n$  in all directions, this gives simply:

$$T_1 \approx c_1 \left(\frac{n}{100}\right)^4 \quad (5.114)$$

For the 1 million node grid ( $n = 100$ ) this yields just 23 CPU minutes on the Cray 2. However, doubling the unidirectional size of the grid ( $n = 200$ ) yields an 8 million node grid, which would require about 6 CPU hours of Cray 2 time in order to decrease the residual error by just one order of magnitude! This indicates that flow problems on the order of ten million grid points or more are presently very costly or infeasible in any "reasonable" amount of time with the SIP solver. Presumably, this assessment

also holds for most of the iterative solvers discussed in our literature review.

For the flow problems reviewed in Table 5.4, fairly accurate solutions were obtained after the initial residual error was decreased by two to three orders of magnitude. The iterations were usually stopped after the relative error (defined below) reached about  $10^{-2} - 10^{-3}$  or less. The relative solution error was evaluated a posteriori in two steps. First, the residual errors (Figure 5.8a) were normalized by a typical head variation ( $\sigma_H$ ) which was taken to be the standard deviation of head given by the approximate spectral solutions of Chapter 3. Figure 5.8b shows the sequence of scaled residual errors for the 1 million node problem A, with  $\sigma_f = 1$  and  $\sigma_f = 2.3$ . A similar graph is depicted in Figure 5.9a for the smaller problem D.

The true solution error (normalized by  $\sigma_H$ ) was then evaluated according to equations (5.105)-(5.106). As an example, let us focus on problem A with  $\sigma_f = 2.3$  (Figure 5.8b). The scaled residual error at the last iteration was:

$$\frac{\|h^{m+1} - h^m\|}{\sigma_H} \approx 10^{-4}.$$

However, the asymptotic convergence rate was quite small:

$$r = - \frac{d \ell_n \|h^{m+1} - h^m\|}{dm} \approx 0.0070.$$

According to equation (5.105), we evaluated the upper bound on the *true* solution error as follows:

$$\frac{\|h - h^m\|}{\sigma_H} \leq \frac{10^{-4}}{1 - e^{-0.007}} \approx 1.5 \cdot 10^{-2}.$$

This shows that the solution error was at most 1.5%, relative to the magnitude of fluctuations of the solution ( $\sigma_H$ ). Although this is certainly acceptable, it should be noticed that the "true" error (upper bound) appears to be almost 2 orders of magnitude larger than the residual error. The discrepancy was less marked in the case of smaller variability ( $\sigma_f = 1.0$ ), and the solution error was found to be only a fraction per cent relative to  $\sigma_h$ . Indeed, it is clear from Figures (5.8) and (5.9) that convergence was faster in the case of smaller variability ( $\sigma_f = 1$ , compared to  $\sigma_f = 2.3$ ).

We conclude that the solutions obtained with the SIP solver were highly accurate, since the solution error at the last iterate was found to be at most on the order of one percent the standard deviation of the (random) head solution itself. In our view, this is a remarkable result given the large size and high variability of the problems considered for solution (especially problem A, with 1 million nodes and  $\sigma_f=2.3$ ).



On the other hand, we have seen by extrapolating a relation on the number of iterations versus grid size, that the solution of larger random flow problems on the order of 10 million nodes or more may not be at hand. Even if convergence could be achieved, we predict that the solution of such problems could require 1 CPU day or more on recent supercomputers like the Cray 2. Furthermore, the solution process could be overwhelmed by the accumulation of *round-off errors* before reaching a satisfactory solution error. This possibility seems to be indicated by Figure 5.9b, which shows that the residual error cannot be decreased beyond a certain level. Note that Figure 5.9b is for the "small" problem D, solved on the Microvax 2 minicomputer with 32-bit words. The accumulation of round-off errors was not observed with the Cray 2 simulations, due to the higher precision on this machine (64-bit words).

Incidentally, Figure 5.9b also compares the Euclidean norm and the absolute maximum norm of the residual error. As one could expect, using the absolute maximum norm gives a more pessimistic picture of the performance of the solver. Nevertheless, we emphasize the fact that, for all problems listed in Table 5.4, the SIP solver did converge in terms of the absolute maximum norm as well, and the *maximum* head error over the grid was only a fraction of the head standard deviation in all cases. In summary, the solution error due to the approximate

matrix solver SIP was quite small in all cases considered for simulation, both in the Euclidean norm and the absolute maximum norm.

Finally, it should be kept in mind that truncation errors will necessarily compound with the matrix solution errors to yield, presumably, a larger total error. Considering the results above and those of Section 5.2 on truncation errors, it appears that the total root-mean-square error on the hydraulic head will be at most about 5% relative to the head standard deviation. Note that this evaluation is based on the one million node problem (A) of Table 5.4 with  $\sigma_f = 2.3$ . The error so estimated refers of course to the exact solution of the finite-domain single-realization problem, not to the hypothetical ergodic solution of the infinite-domain problem as assumed for instance in the spectral theory.

## 5.4 Development and Analysis of the Nonlinear Iterative Solver for Transient Unsaturated Flow

### 5.4.1 Nonlinear SIP solver and nested Picard iterations:

#### [a] Overview of Numerical Issues:

In the case of unsaturated or partially saturated flow -- as opposed to saturated flow -- a new solution strategy must be devised in order to take into account the highly *nonlinear* nature of the algebraic finite difference system. We have chosen in this work to focus our analysis on the case of *transient* flow problems, such as local infiltration in semi-infinite unsaturated media. Steady state solutions, when they exist, can be obtained by running the transient unsaturated flow simulator for large times. An example of this can be found in Chapter 7, where large scale unsaturated flow solutions are presented for both transient and steady state cases.

In the transient regime, and when the time steps are sufficiently small, the algebraic system to be solved becomes much better conditioned than its steady state counterpart (see equation 5.31). As a consequence, the SIP matrix solver is expected to converge much faster for each time step of a transient flow problem than it does for the single step of a steady flow problem. On the other hand, the nonlinearity of the

unsaturated flow system requires prior linearization in order to obtain a solvable matrix system, presumably with iterative corrections to converge to the solution of the *nonlinear* system. Now, it is likely that there will be some restriction on the time step size in order to ensure the convergence of the iterative linearization scheme. Therefore, we expect that the interplay between time step size and convergence rate of the linearization scheme will play a major role in determining the overall efficiency of the unsaturated flow simulator (perhaps more important than the rate of convergence of the SIP matrix solver). With this "warning" in mind, we proceed to describe the actual procedure used to solve the nonlinear transient flow problem.

[b] Description of the Nonlinear-SIP Solver:

The procedure which we have developed is based on a doubly-iterative Picard scheme for solving the nonlinear finite difference system at each time step. The outer Picard iteration loop is a simple iterative predictor-corrector scheme which breaks down the nonlinear system into a sequence of linear systems. This was described in Section 5.1.3, where we developed in detail the nonlinear space-time finite difference system and its linearized version (see in particular equations 5.28-5.31). The inner Picard iteration loop corresponds to the solution of

the linearized matrix system by the SIP method, for each step of the outer iteration loop. For simplicity, the whole solution procedure will be designated as "nonlinear SIP".

The linearized system (equation 5.31) can be written for each time step ( $n \rightarrow n+1$ ) and each outer iteration ( $k \rightarrow k+1$ ) as:

$$A^{n+1,k} \cdot \delta h^{n+1,k+1} = \eta \cdot r^{n+1,k} \quad (5.115)$$

where  $\eta$  is a new nonlinear relaxation parameter, and  $r$  is the residual for the outer Picard iteration loop ( $r^k \rightarrow 0$  as  $k \rightarrow \infty$ ). Note that the linearized vector of boundary conditions was absorbed in the residual. The numerical code accommodates boundary conditions of fixed pressure, fixed flux, or zero pressure gradient, for each of the nodes belonging to the boundary.

The linearized coefficient matrix  $A$  has the same sparse structure as the matrix previously obtained for the linear system of saturated flow -- a major advantage of the Picard linearization scheme over Newton-Raphson. More precisely, we have shown earlier (equation 5.31) that  $A$  takes the form:

$$\underline{\underline{A}}^{n+1,k} = \frac{C^{n+1,k}}{\Delta t_n} \cdot \underline{\underline{I}} + \underline{\underline{K}}^{n+1,k} \quad (5.116)$$

where  $C$  is the linearized storage term (for transient flow only),  $\underline{\underline{I}}$  is the identity matrix, and  $\underline{\underline{K}}$  is the linearized unsaturated conductivity matrix, formally identical to the coefficient matrix of the saturated flow system. As mentioned earlier, the condition of matrix  $A$  improves as  $\Delta t_n$  decreases, due to enhanced diagonal dominance in that case.

Plugging the standard SIP iteration scheme of equation (5.81) into the linear system (5.115) yields a doubly-iterative Picard scheme of the form:

$$\begin{array}{l} y^{k+1,m} = h^{k+1,m} - h^k = \delta h^{k+1,m} \\ y^{k+1,m+1} = h^{k+1,m+1} - h^k = \delta h^{k+1,m+1} \\ \delta y^{k+1,m+1} = y^{k+1,m+1} - y^{k+1,m} \\ L_{m+1}^k \cdot U_{m+1}^k \delta y^{k+1,m+1} = \omega \cdot (\eta \cdot r^k - A^k y^{k+1,m}) \end{array} \quad (5.117)$$

where the time index  $(n+1)$  has been dropped for clarity of

exposition. The double iteration loop (5.117) runs over  $k = 1, \dots, K$  for outer iterations, and  $m = 1, \dots, M$  for inner iterations of the SIP solver (the LU matrices vary with  $m$  because of the cyclic SIP iteration parameter  $\gamma_m$  of equation 5.86).

Now, for any given time step ( $n \rightarrow n+1$ ), let  $h^0$  be the known pressure solution at time  $t_n$ . Then, the solution at the next time step  $t_{n+1} = t_n + \Delta t_n$  is obtained as follows:

(0) Define the initial guess for outer iterations:

$$h^0 = h(t_n), \quad k = 0$$

(1) Increment the outer iteration loop  $k \rightarrow k + 1$

(Picard linearization scheme)

(2) Update nonlinear coefficients of matrices  $L^k, U^k, A^k$  and vectors  $r^k, b^k$  (all functions of  $h^k$ , known from previous outer iteration step)

(3) Define the initial guess for inner iterations:

$$y^{k+1,0} = h^{k+1,0} - h^k = 0, \quad m = 0.$$

- (4) Increment the inner iteration loop  $m \rightarrow m + 1$   
(Picard iterations of the SIP solver)
- (5) Compute the LU factorization and solve the system (5.117) by forward-backward substitution (SIP) to obtain  $\delta y^{k+1,m+1}$
- (6) Update  $y^{k+1,m+1} = y^{k+1,m} + \delta y$ , and iterate to step (4) unless  $m = M$  or  $\|\delta y\| \leq \epsilon_M$
- (7) Update  $h^{k+1} = h^k + y$ , and iterate to step (2) unless  $k = K$  or  $\|y\| = \|\delta h\| \leq \epsilon_K$ .
- (8) The last computed vector  $h$  is the desired solution  $h(t_{n+1})$  at the new time; the difference  $(h_{n+1} - h_n)$  is used to compute the next time step before incrementing the time loop (not shown here).

This algorithm defines, in an extremely condensed form, the nonlinear SIP solver which forms the backbone of the flow simulator. The actual Fortran code ("Bigflo") comprises over ten thousand lines of instructions and comments. A summary narrative of this code is given in Appendix 5.D. It should be emphasized that a single program was developed to solve both steady and transient, saturated and unsaturated, deterministic and random



flow problems. These various options are accommodated by certain parameters that act as switches (transient/steady, saturated/unsaturated, etc.). The "nonlinear SIP" algorithm described above includes all the cases just considered. For instance, in the case of steady saturated flow, the time loop and the outer iteration loop are simply bypassed, or incremented only once.

Another important feature of the numerical flow simulator is its modularity. For instance, the SIP solver intervening in Step (5) is the same for saturated or unsaturated flow. This solver, and many other parts of the code, are isolated in subroutines. It may be of interest to note that the SIP solver subroutine, although quite complex, takes only a very small fraction of the whole Fortran code. However, we have found that most of the computational work was usually consumed in that small part of the object code (typically 80%-90% of the total CPU time, as estimated by a Cray software called "flowtrace").

Let us now consider how the nested inner/outer Picard iteration loops can be controlled to optimize the nonlinear solution process. The control parameters that remain to be determined for a given flow problem and a given mesh size are the following:

- Time step size ( $\Delta t_n$ )
- Maximum number of iterations for the inner loop (M)  
and outer loop (K)
- Maximum residual error for the inner loop ( $\epsilon_M$ )  
and outer loop ( $\epsilon_K$ )
- Choice of a norm for the residual error  
(Euclidean norm? Maximum absolute norm?)
- Relaxation parameters for the inner iterations ( $\omega$ )  
and outer iterations ( $\eta$ ).

These control parameters were determined empirically on a case-by-case basis, i.e., by numerical experimentation, for a number of transient test problems of two and three-dimensional infiltration in homogeneous and heterogeneous soils, with grid sizes ranging from a few thousand to a few hundred thousand nodes. The variable time-step size was controlled automatically by following the evolution of the solution, as will be explained in a later subsection. It was found that the time-step size had to be quite small in order to ensure the convergence of the outer Picard iterations (although not as small as would be needed in the case of an explicit time discretization scheme). The relaxation parameters  $\omega$  and  $\eta$  were usually taken equal to one. Note that the inner iteration loop (SIP) was not underrelaxed because most cases of divergence seemed to have been

triggered by the growth of the outer iteration residuals. When divergence occurred, the simulations were simply resumed with smaller time steps, while the relaxation parameters were usually kept the same ( $\omega=\eta=1$ ). On the other hand, recall that for linear problems of steady saturated flow, the choice of the SIP relaxation parameter was critical, and  $\omega < 1$  was frequently required for SIP convergence. It appears that for highly nonlinear transient flow problems, the time step size is more important as a control parameter.

The remaining parameter ( $K, \epsilon_K$ ) and ( $M, \epsilon_M$ ) were used to control the number of iterations for the outer loop and inner loop, respectively. Typically, the *maximum* length allowed for each iteration loop was set for  $K=M=50$ . The *actual* length of each loop was controlled by the tolerances  $\epsilon_K$  and  $\epsilon_M$  for the outer and inner residual errors expressed in terms of pressure heads. The norm chosen for comparison was the absolute maximum of the residual errors over the grid (rather than the Euclidean norm used for steady saturated flow). The chosen tolerance was typically  $\epsilon_K \simeq 0.1$  cm for the outer iterations, and  $\epsilon_M = 0.01$  cm for the inner (SIP) iterations. This resulted in a very short iteration loop for the SIP solver (on the order of 1-10 iterations). The outer iteration loop was somewhat larger (1-20 iterations) depending on the time step size. In one example, it was found that a moderate increase in the time step

size resulted in an increase of the average number of iterations, in such a way that the total computational work was unchanged. However, divergence eventually occurred if the time step was increased by a larger amount. Thus, the simulations were successful only in those cases where the time step was small enough that the lengths of the inner and outer loops were kept small, say, no more than 10 inner iterations and 20 outer iterations on average.

For clarity, it may be useful to define more explicitly our concept of a "successful" simulation. First, the inner and outer residuals must both decrease monotonously on average. And second, the number of iterations for each loop must remain below the preset maximum, so that the residual at the last iteration be smaller than the preset tolerance (at least most of the time). Typically, a "successful" simulation of infiltration in dry heterogeneous soils resulted in a total of 50 iterations of the SIP matrix solver per time step (say 5 inner iterations and 10 outer iterations on average). Thus, the solution of a nonlinear flow problem over, say 100 time steps, typically required 5000 SIP iterations. This is more than would be required for the solution of a steady state, saturated flow problem (Section 5.3). The increased computational work for unsaturated flow is due to the highly nonlinear nature of the governing equation. Of course, we expect that the solution of steady state unsaturated

flow problems will be even more demanding, unless a good initial guess can be found.

[c] Brief Literature Review and Discussion:

The nonlinear solution procedure just described bears some resemblance with a number of methods proposed in the literature. In particular, various versions of nonlinear SIP solvers that are similar in some respects to the present method were developed by Trescott and Larson (1977), Kuiper (1981), and Kuiper (1987) for the simulation of groundwater flow with a variable watertable. In the first two papers, the standard SIP solver was implemented in such a way that the nonlinear coefficients were updated at every SIP-iteration. This is nearly equivalent to reducing the inner iteration loop of our solver to just one iteration ( $M=1$ ). The third paper (Kuiper 1987) was devoted to the comparison of a number of variants of the SIP and IOCG solvers in conjunction with various strategies for the outer linearization loop, including SIP-Picard and SIP-Newton strategies with only 1-5 inner iterations of the SIP solver. Finally, Cooley (1983) addressed the problem of partially saturated flow with seepage faces, using a complex procedure described as a combination of Newton-Raphson iteration, successive approximation, and (SIP).

It should be noted that the numerical experiments reported by these authors involved rather small, mildly nonlinear problems, with grid sizes generally below 1000 nodes. Unfortunately, we have found it quite difficult to draw conclusions from their work regarding the optimal design of the nonlinear solvers. The nonlinear systems to be solved are sometimes so complex that they could be sensitive to even minute details of implementation. One single fact seems to emerge however: most authors have chosen a solution strategy that imposes a very small number of matrix solver iterations between each nonlinear coefficient updates. This is similar to what occurred in actual practice with the more flexible nonlinear-SIP method developed in this work.

More details on certain aspects of the unsaturated flow simulator will be given below, particularly concerning the dynamic control of time step size and domain size (in cases where a variable domain evolving with the solution makes sense), as well as mass balance computation, and other related issues. A semi-empirical analysis of space-time resolution requirements will also be developed in order to obtain heuristic criteria for the choice of mesh size and time step size, particularly for ensuring the convergence of the linearization scheme. In addition, numerical experiments for a variety of test problems will be presented in order to explore the actual capabilities of

the unsaturated flow simulator. However, the analysis and physical interpretations of the numerical solutions obtained for *random* unsaturated flow problems is postponed to Chapter 7. It should be noted that the largest such problem analyzed in this work involved a three-dimensional grid size on the order of 0.3 million nodes, and over a hundred steps in time. As far as we know, this problem size is 1 to 2 orders of magnitude larger than currently available simulations of unsaturated flow published in the literature. Even for modest size problems, it does not seem that the degree of variability considered in this work, with a node-by-node variation of the random constitutive properties of unsaturated porous media, has ever been considered elsewhere for direct numerical simulations. The present flow simulator appears therefore as a unique "high resolution" tool for exploring highly heterogeneous nonlinear unsaturated flow phenomena.

#### 5.4.2 Truncation errors, nonlinear stability, and space-time resolution requirements

##### [a] Methodology

In this subsection, we attempt by various methods to evaluate the numerical requirements for convergence and accuracy of the unsaturated flow simulator. The major numerical

difficulty appears to be the highly nonlinear nature of the governing flow equation, with the soil moisture capacity and unsaturated conductivity curves given by equations (5.19) and (5.22). In the case of transient infiltration in dry soils, we have observed that the solution could diverge after just one or a few time steps if the initial time step size was taken too large. The problem becomes naturally more severe in the case of spatially variable soils: instabilities can be triggered at any time as a moving infiltration front encounters zones of higher or lower conductive properties. In this light, it seems worthwhile to look for constraints on the mesh size and time step size that will guarantee the convergence of the Picard linearization scheme (outer iteration loop of the nonlinear-SIP solver). The question of accuracy of the finite difference approximation can also be examined in terms of truncation errors. It seems however futile to draw conclusions from truncation analysis without taking into account the errors due to *linearization*. This difficult enterprise was not pursued in this work. Instead, the issues of accuracy (truncation error) and convergence (nonlinear stability analysis) will be examined separately. The latter view-point will lead to some specific numerical requirements, however without rigorous proof.



[b] Truncation Error Analysis:

Let us develop a simplified truncation error analysis for the one-dimensional, transient unsaturated flow equation with spatially constant soil properties. Note that we do not attempt to develop closed form expressions for the solution error as was done in Section 5.2 for the case of random saturated flow. Briefly, the truncation error is defined by the expression:

$$T(h_i) = \hat{L}(h_i) - L(h_i). \quad (5.118)$$

where  $L(h)$  represents the (vanishing) operator corresponding to the one-dimensional transient unsaturated flow equation:

$$L(h) = C(h) \frac{\partial h}{\partial t} + \frac{\partial}{\partial x} (K(h) \cdot (\frac{\partial h}{\partial x} + g)) = 0 \quad (5.119)$$

Note that  $g$  indicates the acceleration of gravity: take  $g = 0$  for horizontal flow, and  $g = +1$  for vertical flow with the  $x$ -axis upwards. On the other hand,  $\hat{L}(h_i)$  represents the finite difference operator defined analogously to equations (5.24)-(5.30). In this discrete operator, the midnodal unsaturated conductivity  $K(h_{i+\frac{1}{2}})$  is evaluated by the geometric mean  $\hat{K}_{i+\frac{1}{2}}$ , as in equation (5.29).

The truncation error (5.118) can be expressed formally

by using Taylor developments analogous to those of Section 5.2 (e.g., equation 5.36). The calculations are tedious but straightforward, and its details will not be reproduced here (some intermediate results can be found in Vauchin et al., 1979, p. 40). When the truncation error due to the approximate evaluation of mid-nodal conductivities ( $\hat{K}_{i+1/2}$ ) is ignored, the resulting truncation error ( $T_i^n$ ) at the nodes of the space-time grid takes the form:

$$T(h_i^n) = \frac{\Delta x^2}{24} \cdot \left\{ \frac{\partial}{\partial x} \left[ K \frac{\partial^3 h}{\partial x^3} \right] + \frac{\partial^3}{\partial x^3} \left[ K \left( \frac{\partial h}{\partial x} + g \right) \right] \right\}_i^n$$

(5.120)

$$+ \Delta t \cdot \left\{ \frac{\partial}{\partial x} \left[ K \frac{\partial}{\partial t} \left( \frac{\partial h}{\partial x} \right) \right] - \frac{1}{2} C \frac{\partial^2 h}{\partial t^2} \right\}_i^n$$

On the other hand, when  $\hat{K}_{i+1/2}$  is evaluated by the geometric mean weighting scheme, the error ( $\hat{K}-K$ ) needs also to be taken into account. Assuming an exponential conductivity - pressure relation:

$$K(h) = K_s \exp(\alpha \cdot h) \tag{5.121}$$

where both  $K_s$  and  $\alpha$  are assumed constant, the mid-nodal conductivity error takes the form:

$$\hat{K} - K = \frac{\Delta x^2}{8} \cdot \alpha K \frac{\partial^2 h}{\partial x^2} . \quad (5.122)$$

When this discrepancy is taken into account in the Taylor developments, an additional term is obtained in equation (5.120).

This new term takes the form:

$$+ \frac{\Delta x^2}{8} \cdot \frac{\partial}{\partial x} \left[ \alpha \frac{\partial^2 h}{\partial x^2} \cdot K \left[ \frac{\partial h}{\partial x} + g \right] \right] \quad (5.123)$$

and the total truncation error results from adding (5.123) to the right-hand side of (5.120).

A few remarks can be made about equations (5.120)-(5.123). First of all, we find that the order of accuracy of the finite difference approximation is  $O(\Delta x)^2$  in space and  $O(\Delta t)$  in time. However, we expect a degradation of the spatial accuracy when the coefficients are random fields instead of constants (by analogy with the results of Section 5.2). Our second remark is that the accuracy in time depends on the rate of change of the pressure gradient and on the second derivative  $\partial^2 h / \partial t^2$ . Finally, it is interesting to note that the error due to inaccurate weighting of mid-nodal conductivities (equation 5.123) is roughly proportional to  $\partial^3 h / \partial x^3$  (this is in fact exactly true in the steady state case of 1 dimension). Thus, the error is largest in regions of rapid changes of the

curvature of  $h(x)$ , which are located just above and just below the inflexion point of the wetting front.

[c] Nonlinear Stability Analysis:

Unfortunately, it appears that our formal evaluation of truncation errors does not lead to any useful estimates of space-time resolution requirements. This is due to the fact that the approximate, iterative linearization of the finite difference system was left out of the analysis. Here, we propose an indirect way of including the "linearization error" by considering only one iteration of the outer loop of the nonlinear solver. For one-dimensional flow, the corresponding finite difference system can be expressed as:

$$C_i^n \frac{h_i^{n+1} - h_i^n}{\Delta t_n} = K_{i+1/2}^n \left[ \frac{h_{i+1}^{n+1} - h_i^{n+1}}{\Delta x} \right] - K_{i-1/2}^n \left[ \frac{h_i^{n+1} - h_{i-1}^{n+1}}{\Delta x} \right] \\ + g \cdot \frac{K_{i+1/2}^n - K_{i-1/2}^n}{\Delta x} \quad (5.124)$$

where  $n$  indicates the time level, and  $g$  is zero for horizontal flow, one for vertical flow. This formulation reveals that the nonlinear gravity term, containing  $g$ , is in fact treated *explicitly* during the first outer iteration of the nonlinear solver, even though we used a so-called fully implicit

time discretization scheme. Let us now examine how this could affect the stability of the numerical solution.

One possible way of investigating the specific effects of linearization of the gravity term is to develop a Fourier stability analysis of equation (5.124) with "frozen coefficients" on the storage term and diffusive term, while the nonlinearity of the gravity term is explicitly taken into account. In the case of the exponential conductivity model (5.121), the gravity term takes the special form:

$$g \cdot \frac{K_{i+1/2}^n - K_{i-1/2}^n}{\Delta x} = g \cdot \frac{K_i^n}{\Delta x} \cdot \left\{ \exp \left[ \alpha \frac{h_{i+1}^n - h_i^n}{2} \right] - \exp \left[ \alpha \frac{h_{i-1}^n - h_i^n}{2} \right] \right\}$$

which may be approximated as:

$$g \frac{K_i^n}{\Delta x} \frac{\alpha}{2} (h_{i+1}^n - h_{i-1}^n)$$

provided that  $\alpha(h_{i+1} - h_i)$  be on the order of unity or less. Thus, we find that the FD scheme (5.124) is approximately equivalent to:

$$\begin{aligned} -R_{i-1/2} \cdot h_{i-1}^{n+1} + (1 + 2\bar{R}_i)h_i^{n+1} - R_{i+1/2}h_{i+1}^{n+1} \approx \\ -\frac{1}{2} g \alpha \Delta x R_i \cdot h_{i-1}^n + h_i^n + \frac{1}{2} g \alpha \Delta x R_i h_{i+1}^n \end{aligned} \quad (5.125)$$

where  $R$  is a dimensionless number proportional to  $\Delta t/\Delta x^2$ :

$$R_{i(\pm 1/2)} = \frac{K_{i(\pm 1/2)}}{C_i} \cdot \frac{\Delta t}{\Delta x^2} ; \bar{R}_i = \frac{R_{i-1/2} + R_{i+1/2}}{2} .$$

Now, a standard Fourier stability analysis of equation (5.125) with the  $R$  coefficients "frozen" (see for instance Ames, 1977) yields the complex time amplification factor of the Fourier modes of  $h(x)$ :

$$\rho \approx \frac{1 + j \cdot g \alpha \Delta x R_i \sin k \Delta x}{1 + (R_{i+1/2} + R_{i-1/2})(1 - \cos k \Delta x) - j \cdot (R_{i+1/2} - R_{i-1/2}) \sin k \Delta x}$$

where  $k$  is the discrete wavenumber taking values  $(\pi/L, \dots, n\pi/L)$ . After some manipulations, the square-modulus of this amplification factor takes the form:

$$|\rho|^2 \approx \frac{1 + [g \alpha \Delta x R_i \sin k \Delta x]^2}{[1 + (R_{i+1/2} + R_{i-1/2})(1 - \cos k \Delta x)]^2 + [(R_{i+1/2} - R_{i-1/2}) \sin k \Delta x]^2} \quad (5.126)$$

Clearly, when the gravitary term disappears (horizontal flow:  $g = 0$ ) the amplification factor is always less than one, and the FD scheme is then unconditionally stable. However, in the presence of the gravity term (vertical flow:  $g = 1$ ) equation

(5.126) shows that a constraint on the mesh size will be necessary in order to guarantee stability.

The exact stability condition for the case  $g \neq 0$  can be found by requiring that the denominator be larger than the numerator in (5.126). To simplify the analysis, let us assume  $R_i \simeq R_{i+1/2} \simeq R_{i-1/2}$ . The stability condition is then:

$$1 + R_i \cdot \left[1 - \left(g \frac{\alpha \Delta x}{2}\right)^2\right] \cdot (1 - \cos k \Delta x) \geq 0.$$

This condition is required for all wavenumbers ( $k = \pi/L, \dots, n\pi/L$ ) where  $n$  is the unidimensional size of the grid. Since  $R_i > 0$ , this condition is always satisfied in the case  $g = 0$ , as expected. For non-horizontal flow ( $g \neq 0$ ), it is easily seen that the inequality above will be satisfied if and only if:

$$\left(g \frac{\alpha \Delta x}{2}\right)^2 \leq 1 + (2R_i)^{-1}.$$

Plugging  $g = 1$  for vertical flow, and using the previous definition of  $R_i$  give finally the "nonlinear stability condition":

$$\boxed{\alpha \Delta x \leq 2 \cdot \sqrt{1 + \left(2 \frac{K_i \Delta t}{C_i \Delta x^2}\right)^{-1}}.} \quad (5.127)$$

The second term inside the square root corresponds to the well known stability condition for explicit time discretization schemes (whereas the discretization used in this work is of implicit type). If  $\Delta t/\Delta x^2$  is taken to be significantly larger than the inverse diffusivity  $C/K$ , the condition (5.127) becomes equivalent to a constraint on the grid Peclet number, of the form:

$$\boxed{Pe = \alpha \Delta x \leq 2} \quad (5.128)$$

For completeness, note that in the case where inequality (5.128) is not satisfied, then the stability condition (5.127) implies a rather stringent constraint on the time step:

$$\boxed{2 \frac{K_i}{C_i} \frac{\Delta t}{\Delta x^2} \leq \frac{1}{\frac{\alpha \Delta x}{2} - 1} \text{ if } \alpha \Delta x > 2} \quad (5.129)$$

In conclusion, equations (5.127)-(5.129) show that the linearized finite difference scheme used to approximate the unsaturated flow equation may not be stable unless the grid Peclet number  $Pe = \alpha \Delta x$  is less than 2. In the more general case of multidimensional space, this gives a constraint on the vertical mesh size,  $\Delta x_1$ , of the form  $\Delta x_1 \leq 2 \alpha^{-1}$ .

For heterogeneous soils however, the coefficient  $\alpha$



will be spatially variable, and the constraint will not be satisfied at every nodes of the grid in actual practice. Therefore, attention is called on the time step constraint (5.129). This condition is rather stringent, having the same form as the condition for stability of *explicit* time integration schemes. This indicates that the best strategy might be to minimize as much as possible the vertical grid Peclet number, e.g.:

$$\boxed{Pe_1 = \bar{\alpha}\Delta x_1 \ll 2} \quad (5.130)$$

where  $\bar{\alpha}$  is some average of  $\alpha(\underline{x})$  over the grid, or some mean value defined in ensemble space.

[d] Interpretation of the Peclet Constraint and Discussion:

It may be interesting to note that the inverse of  $\alpha = d\ell nK/dh$  has been interpreted in the literature as a pore size distribution index, or as the typical thickness of the capillary fringe (Yeh et al., 1985). Another interesting interpretation is that  $\alpha$  represents a "gravity/diffusion" ratio. Both types of interpretations seem qualitatively correct. Observations show that  $\alpha$  is largest in coarse soils, where gravity effects are significant and the pore size distribution is typically quite narrow. A review of various interpretations of  $\alpha$  in the literature can be found in a recent paper by White and Sully

(1987), who also contribute their own. It seems particularly useful to view  $\alpha$  as a gravity/diffusion ratio in the context of numerical analysis. Ababou (1981) suggested this interpretation by rewriting the pressure-based flow equation (5.119) in terms of the "Kirchhoff potential":

$$\phi(h) = \int_{-\infty}^h K(h') dh' ,$$

named after Kirchhoff (1894) for his work on heat conduction. In the case of an exponential conductivity relation of the type (5.121), it turns out that  $\phi = \alpha^{-1}K$ , and the multidimensional flow equations can then be expressed by using the unsaturated conductivity as the dependent variable:

$$\frac{\partial K}{\partial t} = D \cdot \{ \nabla^2 K + \alpha \cdot (\underline{g} \cdot \nabla K) \} \quad (5.131)$$

where  $D$  is a nonlinear diffusivity function ( $D = K/C$ ) and  $\underline{g}$  is the gravity vector, for instance  $\underline{g}=(1,0,0)$  for a 3D system of coordinate with the  $x_1$ -axis upwards. The so-called Kirchhoff equation has been used extensively in the area of soil water physics since the early works of Wooding (1968), Philip (1969), Raats (1971), and Parlange (1972) among others.

It is now clear that the coefficient  $\alpha$  takes the form:

$$\alpha = \frac{\alpha D}{D} = \frac{dK/d\theta}{D} = \frac{V}{D}$$

where  $\theta$  is the volumetric water content of the soil. This shows that  $\alpha$  is indeed the ratio of gravitary versus diffusive coefficients of the conductivity-based (Kirchhoff) equation given above. In particular, note that  $\alpha D$  scales like a velocity ( $V=\alpha D$ ). This finally justifies our interpretation of  $\alpha \Delta x$  as a *grid Peclet number*:

$$Pe = \alpha \Delta x = \frac{V \Delta x}{D} .$$

To complete the analogy, observe that the Kirchhoff equation (5.131) is equivalent to the equation governing heat conduction in a body that moves with velocity  $V$  with respect to the heat source (see Carslaw and Jaeger, 1959, for heat conduction problems). Similarly, the  $K$ -based equation is also equivalent to the convection-diffusion equation governing solute transport in a porous medium, with diffusion coefficient  $D$  and water velocity  $V$ . In the case of unsaturated flow,  $D$  is the soil moisture diffusivity and  $V=dK/d\theta$  gives in certain cases the rate of advance of the wetting front in the vertical direction. The proposed stability constraint on the grid Peclet number (equations 5.128 or 5.130) is most usually taken into account in the area of solute transport modeling, but does not seem to have been invoked in the context of unsaturated or two-phase flow

simulation, as we do here.

In summary, we have found that a constraint on the grid Peclet number  $Pe = \alpha \Delta x_1$ , analogous to the ratio of velocity versus diffusion coefficient in convection-diffusion problems, must be satisfied in order to ensure the stability of the finite difference approximation of the *nonlinear* unsaturated flow equation. Here, we have assigned a particular meaning to the notion of stability, such that the error due to linearizing the gravitary term of the equation is taken into account, while all other nonlinear coefficients are "frozen". In addition, our analysis was based on the assumption that only *one outer iteration* of the nonlinear solver was performed for each time step (see equation 5.124). In spite of the many approximations involved, we believe that the Peclet number constraint is meaningful and gives an approximate condition for the stability and convergence of the outer Picard iterations of the nonlinear SIP solver.

Accordingly, the Peclet number constraint (5.130) was taken into account in all of our numerical simulations. Note that the coefficient  $\bar{\alpha}$  lies in the range  $0.01-0.10 \text{ cm}^{-1}$  for natural soils (clayey soils to coarse sands). According to the Peclet constraint ( $\alpha \Delta x_1 \ll 2$ ) the vertical mesh size should not be taken greater than 10-100 cm, depending on the type of soil.

We have found this rule to be quite useful, although far from sufficient for ensuring stability without additional constraints on the time step. Indeed, equation (5.129) suggests a more pessimistic view of the numerical requirements, particularly for heterogeneous soils where the Peclet constraint may not be enforced at all nodes of the grid.

Thus, it may be interesting to examine how instabilities could be triggered locally in regions where the Peclet constraint is not satisfied. Equation (5.126) and the inequality below specifically show that the high wavenumber Fourier nodes are the most unstable (fluctuations at the mesh scale are amplified faster). Moreover, the instability will be more severe for large values of  $\Delta t/\Delta x^2$  and for large values of the local diffusivity (e.g., near saturation).

However, results from Fourier stability analysis may be too approximate to be reliable in practice. It remains unclear whether local scale instabilities, such as due to high Peclet number, will actually grow and contaminate all scales of fluctuations from mesh size to domain size. Another approach, based on the requirement that the spectral radius of the nonlinear iteration matrix be less than unity (Ortega and Rheinboldt, 1970, 7.1 and 10.1), suggested that the condition for convergence of the nonlinear iterations could be of the form:

$$Pe_m = \alpha(\underline{x}) \Delta x_m \leq 2 \cdot \left| \frac{\partial H}{\partial x_m} \right|^{-1} \quad (5.132)$$

which means that the mesh size in any direction ( $m = 1,2,3$ ) must be taken small in inverse proportion of the hydraulic gradient ( $\partial H / \partial x_m$ ) in that direction. This is obviously a more severe constraint than the standard Peclet number condition. It indicates that the presence of sharp hydraulic gradients, such as occur at a wetting front, could trigger global divergence of the nonlinear SIP solver, even when the mesh size is small enough that the Peclet condition  $\alpha \Delta x \ll 2$  is satisfied. This observation seemed to be confirmed by numerical experiments, as most cases of divergence occurred during the early times of infiltration in very dry soils (sharp fronts).

#### 5.4.3 Numerical experiments and test of problem solving capabilities:

In this last subsection, we present the results of a number of numerical experiments in order to test the problem solving capabilities of the unsaturated flow simulator. Accordingly, we focus have mainly on numerical issues, and only occasionally on physical interpretation. The numerical solutions obtained for large problems of three-dimensional infiltration in *random* soils will be presented and discussed more thoroughly in

Chapter 7). The order of presentation is as follows. We first discuss the methodology and present an overview of model problems for testing the unsaturated flow simulator. Some details of implementation of the code are then described, notably concerning the dynamic control of time step size, the variable domain size, and the algorithm used for mass balance computation. Numerical experiments are finally presented, for increasingly complex problems, in view of testing various features of the unsaturated flow simulator.

[a] Overview of Test Problems and Methodology:

The complexity of the random unsaturated flow problem is such that it does not appear possible to devise a unique, well-defined procedure to check the accuracy of the numerical solution, as was done earlier in the linear case (steady saturated flow, Sections 5.2 and 5.3). In the present case, the best approach seems to be a "divide and conquer" strategy, whereby several isolated features of the code are checked through a series of simple test problems. The particular tests considered in this work can be broadly classified as follows:

(i) Comparison with exact solutions:

Quasi-analytical solutions are available for instance in the case of two-dimensional infiltration from a

surface strip source in a homogeneous soil. However, the unsaturated soil properties must be of a special type, assuming in particular a constant soil moisture diffusivity. This is usually an unrealistic assumption for transient infiltration problems (Ababou, 1981). Nevertheless, since the conductivity-pressure function is exponential, the comparison of the numerical and analytical solutions provides a test of the ability of the nonlinear SIP solver to converge to the correct nonlinear solution. Another quasi-analytical solution for one-dimensional flow with constant coefficients was also used for debugging purposes: the flow simulator was run in the unsaturated mode with constant coefficients in order to test various algorithms such as the effect of variable time step size.

(ii) Self-benchmark procedures:

We refer to "self-benchmark" as a method for testing some special feature of the flow simulator in complex cases where no analytical solution is available (highly nonlinear and random soil properties). The most obvious self-benchmark of a numerical flow simulator is the computation of global mass balance. Our flow simulator automatically computes the mass balance by spatial integration of soil moisture and calculation of



the mass entering or leaving the system at the boundaries. Another kind of self-benchmark procedure consists in testing the sensitivity of the numerical solution with respect to mesh size and time step size, using as a reference the solution obtained with the highest space-time resolution. The obvious limitation of this kind of test is its high computational cost: thus, in actual practice, such tests were limited to fairly small domain size. A self-benchmark test was also conducted to check whether the solutions obtained with variable domain size and fixed domain size coincide. Finally, it should be kept in mind that the iterative matrix solver, which is one of the key components of the unsaturated flow code, was already tested extensively (Section 5.3). The method we used there can be viewed as a particular type of self-benchmark, conducted by running the SIP solver over a very large number of iterations and monitoring the convergence rate of residual errors, for a variety of linear flow systems. However, it does not appear feasible to test the nonlinear iterative solver in the same systematic way.

(iii) Qualitative tests:

Certain anomalies of the numerical solutions can

sometimes be detected by examining the numerical solutions visually, e.g., by looking at a plot of the pressure head contours, or at pressure profiles along one-dimensional transects. For example, in the case of strip source infiltration in a perfectly layered soil, one expects the solution to be perfectly *symmetric* about the vertical plane running through the middle of the strip. This and a number of other features based on physical principles, can be used to detect possible inaccuracies in the numerical solutions. A few simple test problems were devised for this purpose, including one-dimensional and two-dimensional infiltration in homogeneous soils (with various types of boundary conditions), and two-dimensional strip source infiltration in horizontally layered and vertically layered soil systems. In addition, some more complex infiltration problems in three-dimensional random soils are also discussed briefly (the complete analysis of these numerical solutions is postponed to Chapter 7, as mentioned earlier).

In summary, we have adopted a variety of procedures to test the problem solving capabilities and reliability of the unsaturated flow simulator, including comparisons with known analytical solutions, self-benchmark procedures, and qualitative

evaluation of the reliability of numerical solutions based on physical principles. Let us start by a description of some of the most relevant details of implementation of the flow simulator, along with some related numerical experiments.

[b] Control of Variable Time Step, Moving Boundaries, and Mass Balance:

The *variable time step size* is computed as follows. First, an initial time step is prescribed by the user (or else a very small initial time step is computed by the code). Second, the code evaluates the maximum possible value of the global spatial variation of pressure head that could occur within the flow domain ( $\Delta h_{\text{stab}}$ ). Typically, this pressure variation is estimated by taking the difference between the largest pressure at the boundaries and the initial pressure within the flow domain, that is:

$$\Delta h_{\text{stab}} = |h_{\text{surf}} - h_{\text{in}}|$$

where  $h_{\text{surf}}$  is either the fixed pressure at the infiltration surface, or, in case of a flux condition, the pressure obtained by solving the equation  $K(h) = q_{\text{surf}}$ . Finally, the variable time step size  $\Delta t_n$  for the next time step  $t_n \rightarrow t_{n+1}$  is computed by the following algorithm ( $n > 1$ ):

$$\Delta t_n = \text{Min} \left\{ \rho \cdot \Delta t_{n-1} , \frac{\|h^{n+1} - h^n\|_{\text{max}}}{\Delta h_{\text{stab}}} \cdot \Delta t_1 \right\} \quad (5.133)$$

where  $\Delta t_1$  is the first (initial) time step,  $\rho$  is an amplification ratio used for limiting the rate at which the time step may grow, and the norm  $\|h\|_{\text{max}}$  represents the absolute maximum of  $h(\underline{x})$  over the grid. In practice, the amplification ratio  $\rho$  should be only slightly greater than unity, e.g.,  $\rho = 1.05$  up to  $\rho = 1.25$  at most. Our experience for infiltration problems with initially dry soils indicates that equation (5.133) usually leads to a sharp increase of the time step at early times, reaching a sill after a relatively short time of infiltration.

Figures 5.10(a), (b), and (c) show the growth of the time step for three simulations of infiltration in dry soils (plotted against number of outer iterations rather than time). The first of these figures corresponds to a problem of one-dimensional infiltration under fixed pressure ( $h=0$ ) in a dry sand (Dek soil) whose unsaturated properties were given earlier in Figure 5.3. The second figure corresponds to a two-dimensional infiltration in the same soil, with a fixed pressure ( $h=0$ ) at the surface of a strip source. The third and last figure corresponds to a problem of two-dimensional strip source infiltration in a two-layer system of sandy soils of moderate contrast, with a relatively high flux condition

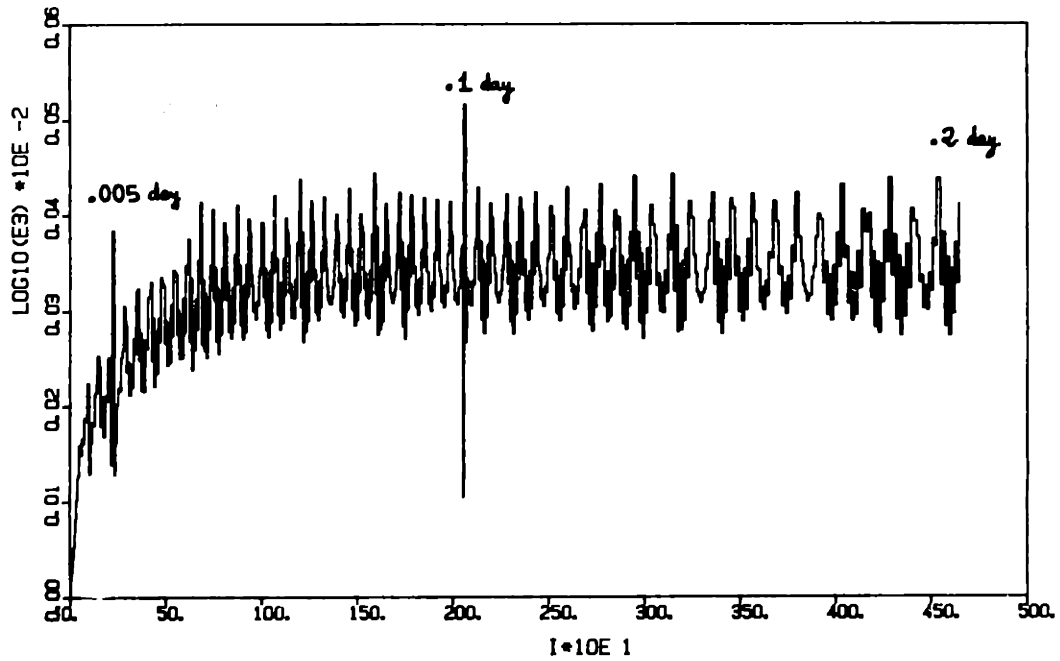


Figure 5.10 (a) Evolution of the time step size (plotted against number of outer iterations) for one-dimensional infiltration in a dry sand with fixed pressure  $h = 0$  at soil surface.

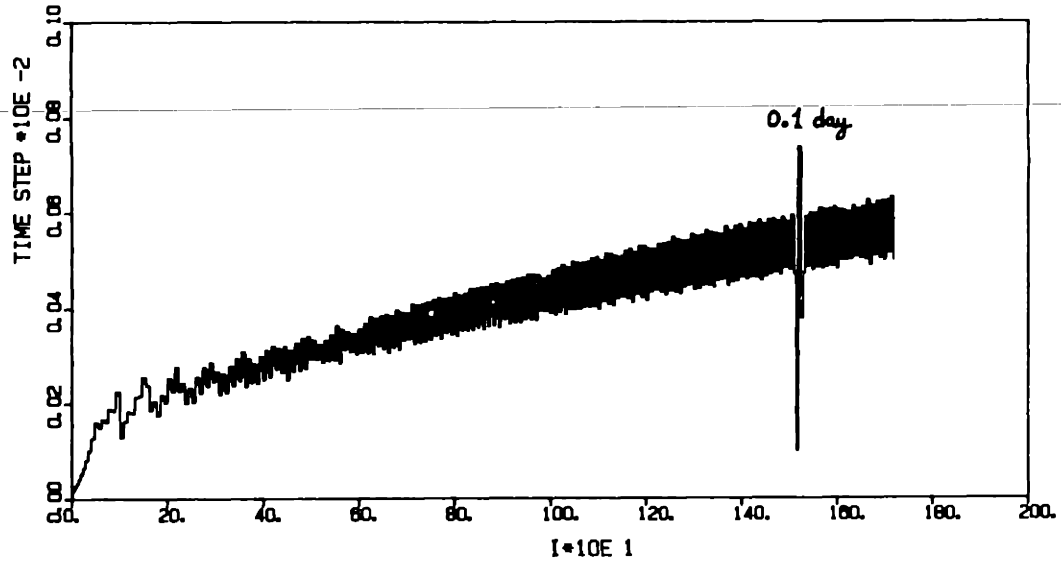


Figure 5.10 (b) Evolution of the time step size (plotted against number of outer iterations) for two-dimensional infiltration with fixed pressure  $h = 0$  on a strip source (same soil as 5.10a).

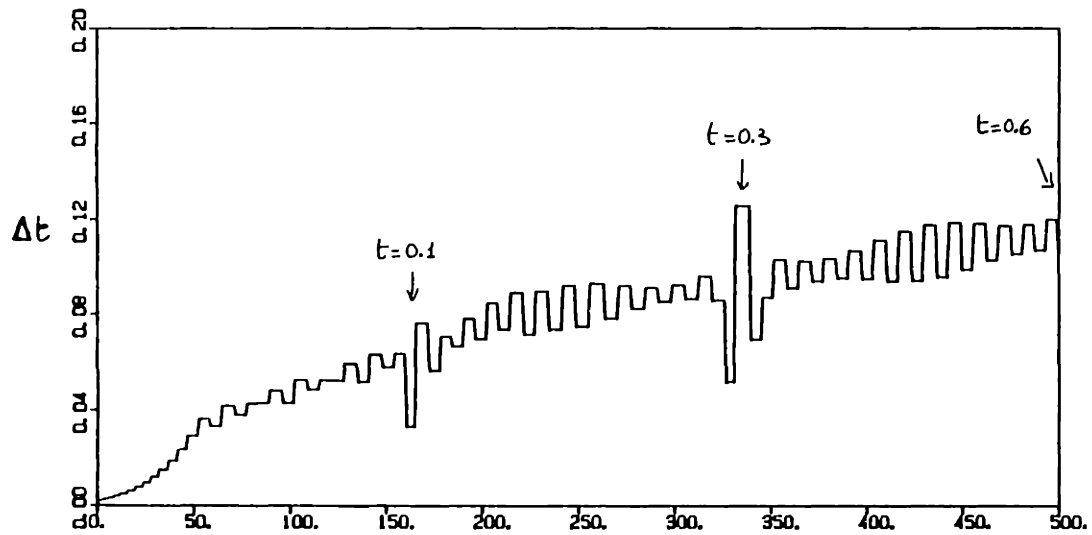


Figure 5.10 (c) Evolution of the time step size (plotted against number of outer iterations) for two-dimensional infiltration with fixed flux  $q = 12$  cm/day on a strip source (two-layered sandy soil, top layer same as in 5.10a and b)

prescribed at the surface of the strip ( $q = 12$  cm/day, one order of magnitude lower than the saturated conductivity of the top layer). In all cases, the initial pressure was on the order of -100 cm, corresponding to an initial conductivity on the order of 0.1 cm/day or less.

Based on these and other numerical experiments, the time-stepping algorithm appeared to be well-behaved, and did not generate instabilities. However, this algorithm was not flexible enough to handle properly large-time simulations. In such cases, the simulation was processed in several pieces: whenever the time step size appeared too small and did not increase, the simulation was stopped and resumed with a larger "initial" time step  $\Delta t_1$ . It is expected that a more satisfactory time-stepping algorithm could be obtained by taking into account the maximum flux over the grid (Ababou, 1981) and/or some global property of the numerical solution such as the rate of advance of the wetting front, the mean pressure gradient, or the global mass balance. Other methods of control of the time step size for similar flow problems can be found in Hanks and Bouwer (1962), Edwards (1972), Ababou (1981), and Dave and Mathis (1981). The latter authors used mass balance to adjust the time step size in their "adaptive grid" model of one-dimensional unsaturated flow.



A variable domain size was used for multidimensional infiltration problems on very dry soils. The size of the computational domain was controlled by moving the artificial boundaries in such a way that they always remained far from the "wetting front". The rationale behind this procedure is that, for any finite time, there exists a region beyond the wetting front where the pressure has not yet increased from its initial value. It should be noted however that this property holds only in the case of highly nonlinear coefficients and a very dry initial state ( $h_{in} \rightarrow \infty$ ). The second condition is not exactly satisfied in practice. There may be a significant amount of gravity-driven flow outside the wetted zone in the case of imperfectly dry soils. For heterogeneous soils, this "natural flow" will be even more complex, with gravity acting in the vertical direction and soil moisture "diffusion" in the horizontal. Nevertheless, the variable domain size algorithm was found useful in a number of cases, leading to significant savings in computational work when the soil was dry enough that the "wetting front" could be tracked accurately.

Figure 5.11 gives a schematic representation of the "variable domain" procedure in the case of strip source infiltration in two dimensions (the three-dimensional case is treated in a similar way). The procedure can be summarized as follows. A small initial domain size must be specified by the

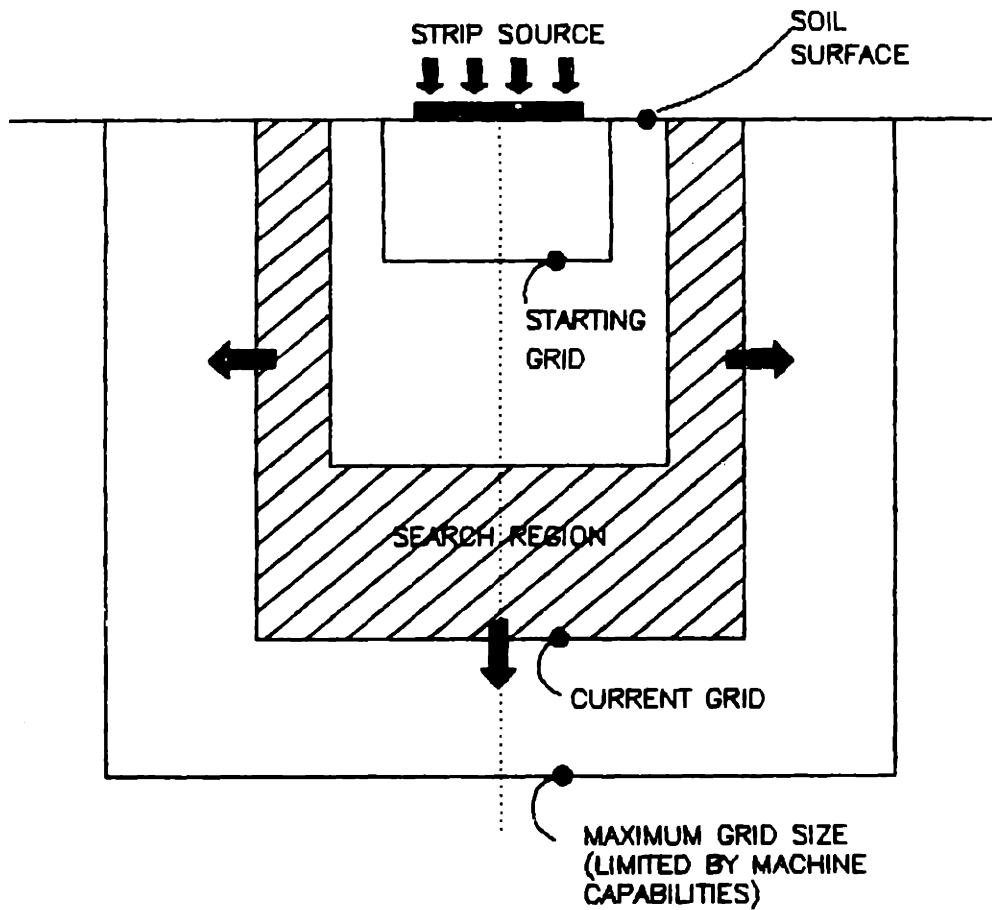


Figure 5.11 Representation of the "variable domain" procedure in the case of infiltration from a strip source. The thick arrows indicate the movement of artificial boundaries. In this example, the soil surface is the only fixed boundary.

user, along with the maximum allowable size of the domain and the definition of "artificial" (moving) boundaries, as opposed to fixed boundaries. The numerical solution at any given time step is computed based on the current domain size, with fixed pressure conditions on the artificial boundaries ( $h = h_{in}$ ). Each artificial boundary is then moved away from the wetted zone if the maximum pressure change  $\|h - h_{in}\|_{max}$  is larger than a preset tolerance (within the "search region" depicted in Figure 5.11). The algorithm is such that each boundary can move separately at its own rate, depending on the shape of the wetted zone. The displacement of a moving boundary was taken equal to the depth of the search region ( $3\Delta x$ ). It should be noted that the grid itself was not deformed in the process, i.e., the mesh ( $\Delta x_1, \Delta x_2, \Delta x_3$ ) remained constant in space as the size of the domain was increased. The design of a truly adaptive grid model would pose difficult problems of interpolation/extrapolation in the case of highly variable or random coefficients.

Figures (5.12) and (5.13) show two cases where the variable domain procedure worked well. Figure 5.12(a) shows the pressure head contours obtained for two-dimensional strip source infiltration on a dry sand, using the variable domain procedure with three moving boundaries. The solution obtained with a fixed domain size (Figure 5.12.b) is visually indistinguishable. A

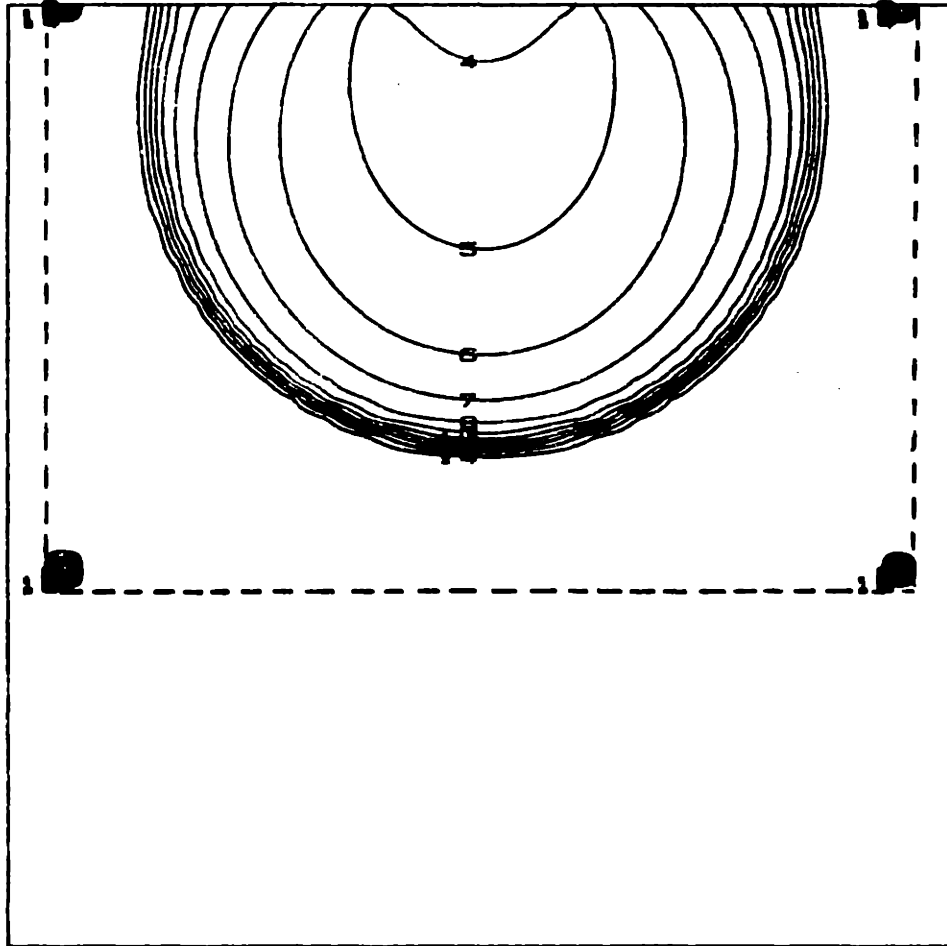


Figure 5.12 (a) Pressure head contours obtained after 1 day of infiltration with the variable domain procedure for 2D strip source infiltration  $q = 12$  cm/day on the Dek sand with initial pressure  $h = -150$  cm..

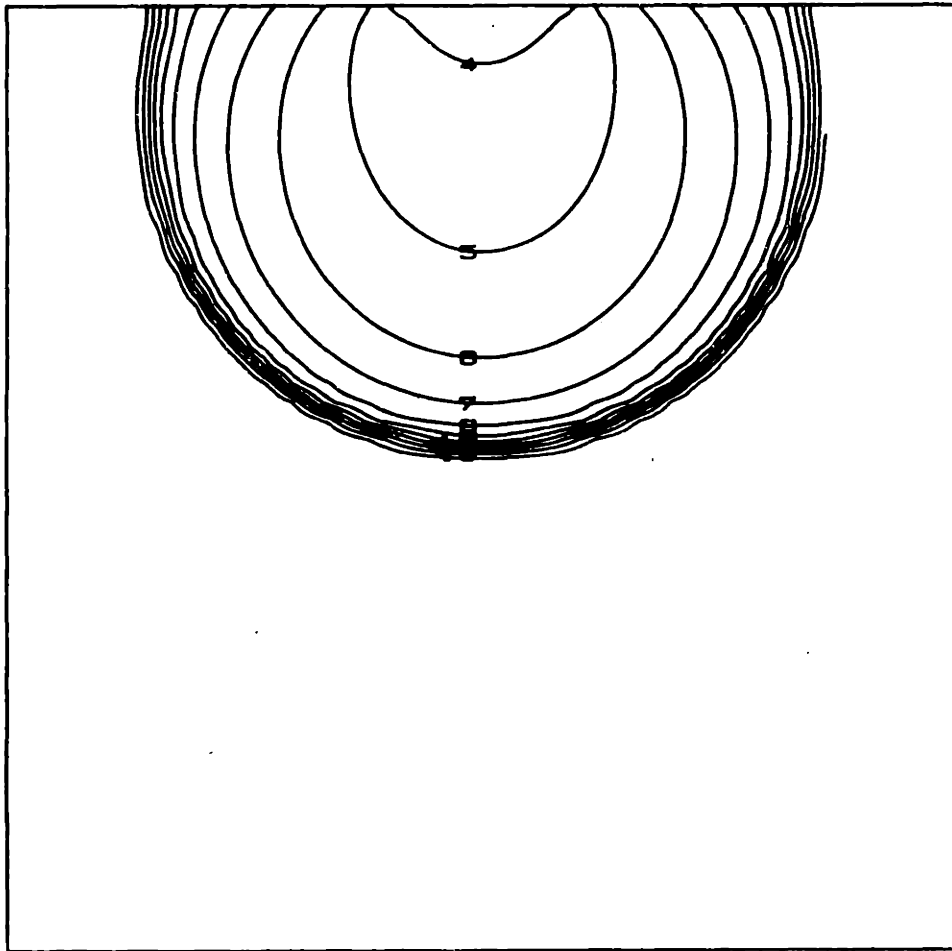


Figure 5.12(b) Pressure head contours after 1 day of infiltration with fixed domain size  $150 \times 150$  cm and mesh size  $\Delta x = 3$  cm (same case as Figure 5.12a).

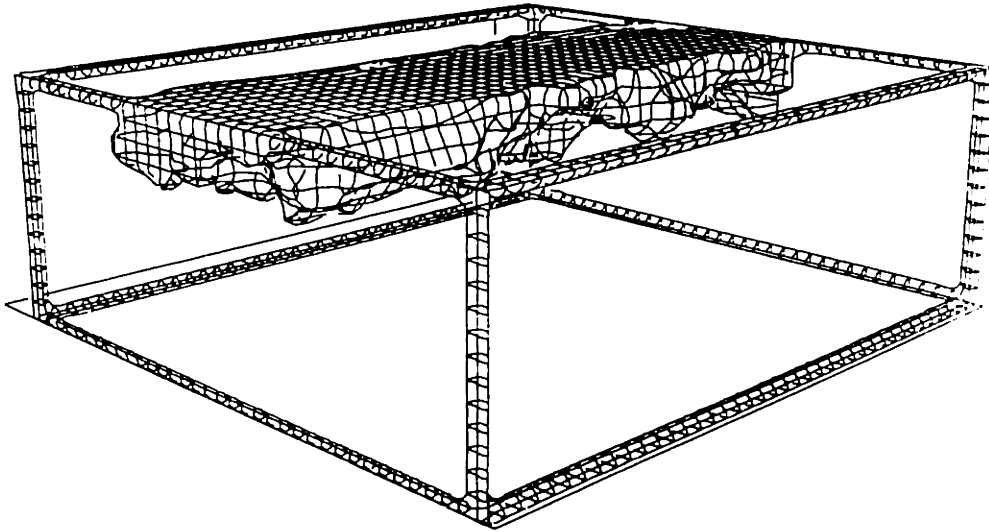


Figure 5.13 (a) Pressure head contour surface ( $h = -90$  cm) obtained after 1 day of infiltration with the variable domain procedure: 3D strip-source infiltration ( $q = 2$  cm/day) on the Dek sand with random  $K_s$  and  $\alpha$  parameter, and initial pressure  $h = -150$  cm

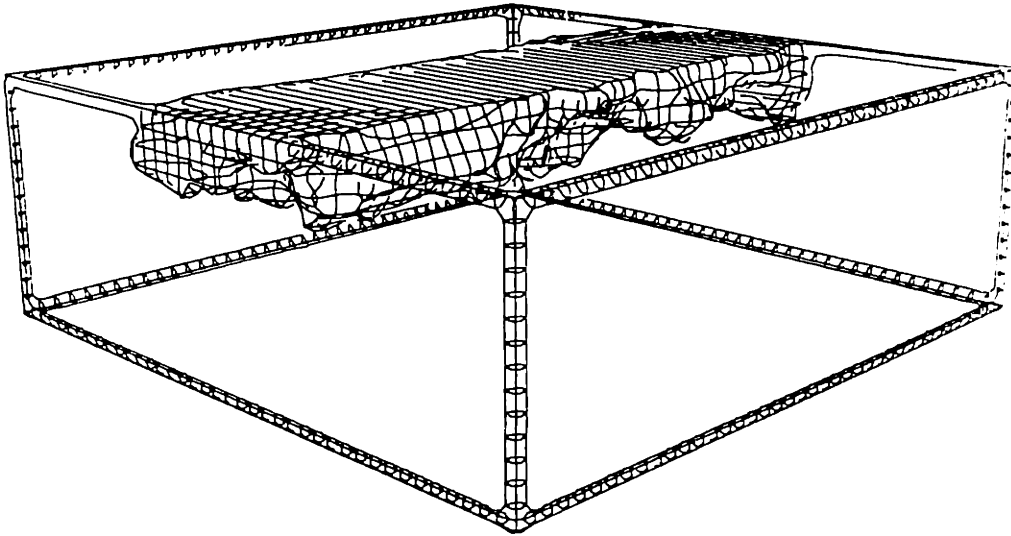


Figure 5.13 (b) Pressure head contour surface ( $h = -90$  cm) after 1 day of infiltration with fixed domain size  $140 \times 400 \times 400$  cm and mesh size  $\Delta x = 10$  cm (same case as Figure 5.13a).

similar comparison is shown on Figures 5.13(a) and (b), this time for the case of three-dimensional strip source infiltration on a random, statistically isotropic soil whose mean properties are the same as those of Figure 5.12. The same pressure contour surface ( $h = -90$  cm) is shown in both Figures 5.13(a) and (b): again the solutions for variable and fixed domain size seem undistinguishable visually. It should be noted however that, in the random case, the bottom boundary moved rapidly downwards to reach its prescribed maximum depth. This was due to the occurrence of non-negligible changes of pressure even far below the "wet zone".

Finally, the *mass balance* was computed automatically by the code at every time step based on the following algorithm. First, the computational domain for mass balance was defined as the sub-domain obtained by deleting a half-mesh size near each of the six planar boundaries (assuming here that the boundaries are fixed, for simplicity of exposition). Second, the total mass inside this subdomain was computed by integrating the volumetric moisture content  $\theta(\underline{x})$  according to a simple trapezoidal rule in three dimensions. Accordingly, the mass of a node-centered cell located at node  $(i_1, i_2, i_3)$  was calculated as follows:

$$\text{Mass}(i_1, i_2, i_3) = \theta[h(i_1, i_2, i_3)] \cdot \Delta x_1 \cdot \Delta x_2 \cdot \Delta x_3.$$



On the other hand, the total mass entering or leaving the system was obtained by summing the normal fluxes at each node of the six planar boundaries, and integrating over time. The normal fluxes were calculated according to:

$$q_{1/2} = - \hat{K}_{1/2} \cdot \left( \frac{h_1 - h_0}{\Delta x} + g \right)$$

where the index 1/2 indicates the mid-nodal location adjacent to the boundary under consideration (other indices have been omitted). In the case where all boundary conditions are of Neuman type (fixed flux), this algorithm gives the same result as would be obtained by summing directly the prescribed fluxes at the boundaries, at least within machine precision.

The accuracy of the numerical solutions was examined from the point of view of mass balance by looking at the time-dependent relative errors:

$$e(t) = \frac{Q_{\text{mass}} - (Q_{\text{in}} - Q_{\text{out}})}{Q_{\text{in}} - Q_{\text{out}}} = \frac{\delta Q}{Q} \quad (5.134)$$

$$E(t) \simeq \frac{\int_0^t \delta Q(\tau) d\tau}{\int_0^t Q(\tau) d\tau}$$

where  $Q_{\text{mass}}$  is the rate of change of total mass in the system,

and  $Q_{in}$  and  $Q_{out}$  are the discharge rates in and out of the system (both positive quantities here). The relative error on the mass rate of change ( $e$ ) usually oscillated during the early time of infiltration (this has been observed with other numerical models as well, e.g. Ababou 1981). In some of the numerical simulations presented in this work, the amplitude of oscillations could attain relatively high values (about 10%, and up to 100% in certain cases) but only for a limited number of time steps. Both error indicators  $e(t)$  and  $E(t)$  were usually very small after a sufficient number of time steps, even for fairly "difficult" cases. For instance, the relative error on total mass,  $E(t)$ , was well below 1% at time  $t = 1$  day for the infiltration problems of Figures 5.12 and 5.13, involving fixed as well as variable domain size. Figure 5.13.b in particular was for a 25,000 node grid with random soil properties.

The evolution of the relative mass balance errors  $e(t)$  and  $E(T)$  was also monitored for the more difficult infiltration problems to be analyzed in Chapter 7: see the 300,000 node grid simulations of transient strip source infiltration and steady rainfall infiltration in a random anisotropic soil (respectively sections 7.3 and 7.4). In both cases, the error on the total mass present in the flow domain rarely exceeded 10-15%. This was judged to be quite satisfactory given the high variability, nonlinearity, and large size of the system. Note that the steady

"rainfall infiltration" solution was obtained by running the flow simulator in the transient mode. The information provided by the mass balance subroutine was used to detect the convergence of the transient flow system to a steady state.

[c] Comparisons of Numerical and Analytical Solutions:

Figure 5.14 depicts the numerical solution of the 2D strip source infiltration problem (time  $t = 1$  day) for a special type of soil having nonlinear conductivity and water retention curves, but constant "moisture diffusivity". The wet zone in that case is characterized by a fairly smooth spatial variation of pressure, and the absence of a sharply defined wetting front. Figure 5.15 compares the numerical and quasi-analytical solution obtained at a shorter time  $t = 0.5$  day. The quasi-analytical solution was only possible because of the special form taken by the nonlinear constitutive properties of the soil, as shown below:

$$\begin{aligned} K(h) &= K_s \exp(\alpha h) \\ \theta(h) &= \theta_s \exp(\beta h) \\ \alpha &= \beta \end{aligned} \tag{5.135}$$

Note that the soil moisture diffusivity corresponding to the conductivity and water retention curves (5.135) is constant,

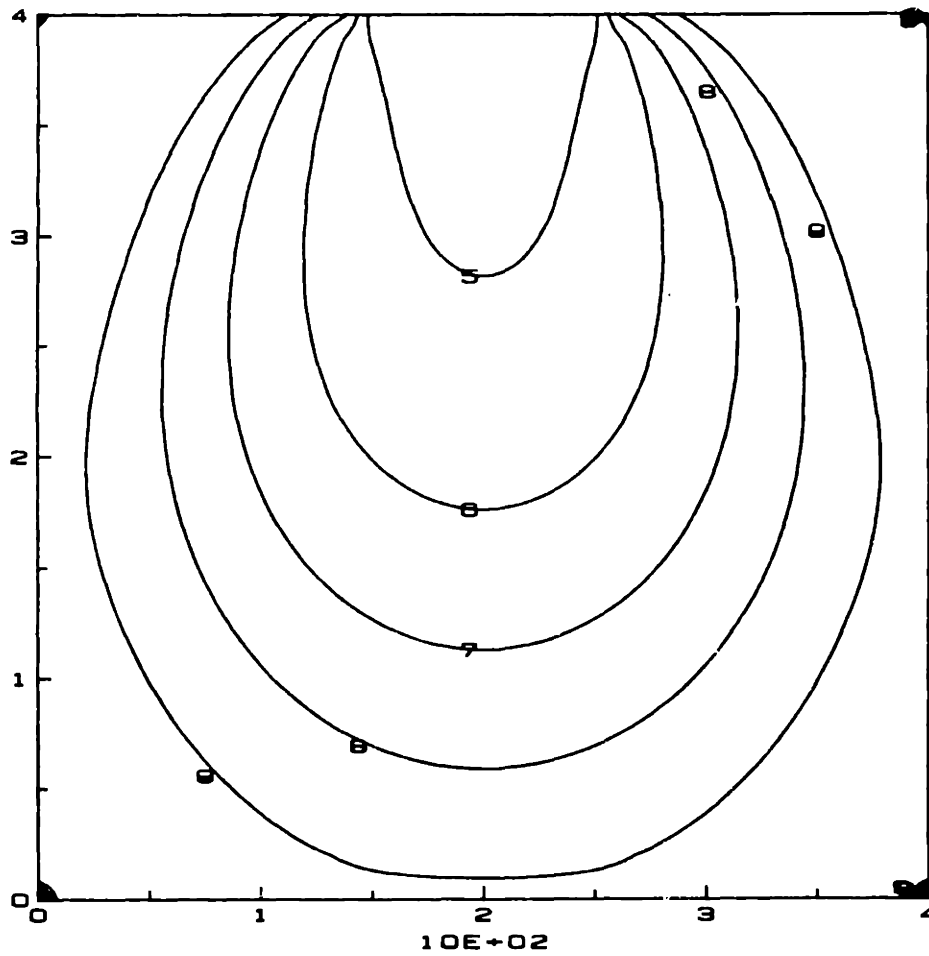


Figure 5.14 Example of numerical pressure contour map for 2D strip-source infiltration in a homogeneous soil with exponential  $K(h)$  and  $\theta(h)$  curves having the same slope ( $\alpha = \beta = 0.1 \text{ cm}^{-1}$ ). Time  $t = 1$  day.

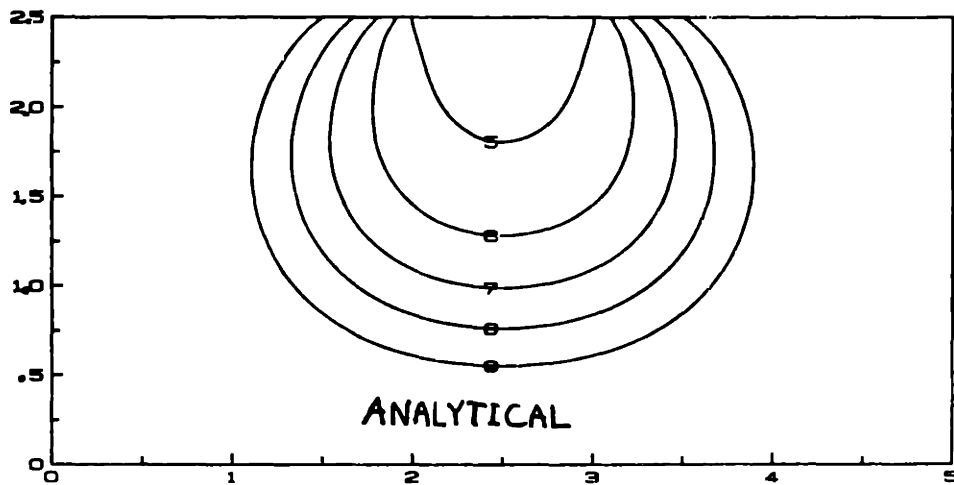
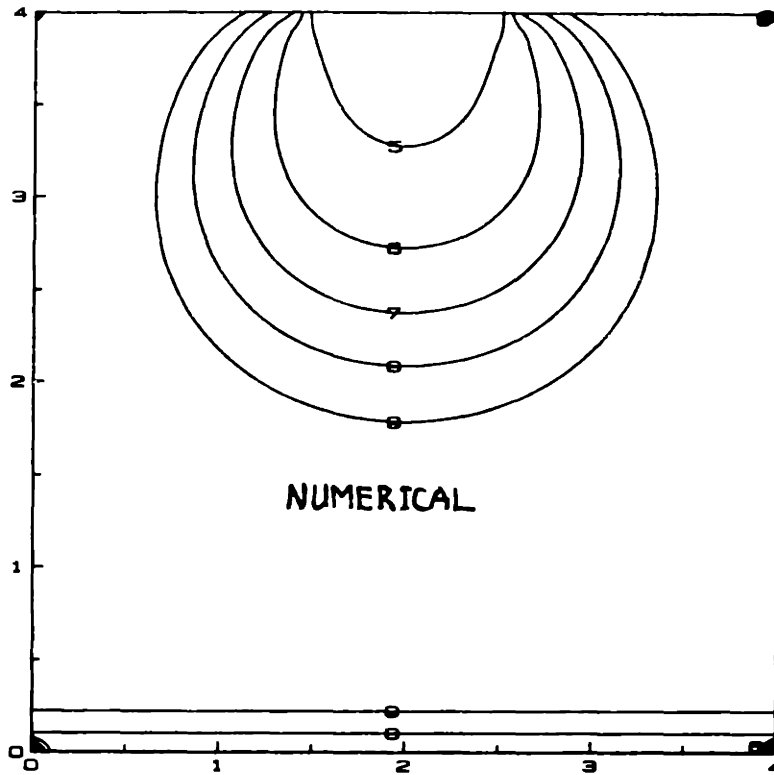


Figure 5.15 Comparison of numerical and analytical solutions for 2D strip-source infiltration in a homogeneous soil with exponential  $K(h)$  and  $\theta(h)$  curves having the same slope ( $\alpha = \beta = 0.1 \text{ cm}^{-1}$ ). Pressure contours at time  $t = 0.5$  day

independent of pressure:

$$D = K_s / (\alpha \theta_s).$$

As a consequence, the unsaturated flow equation expressed in terms of the conductivity or Kirchhoff transform (Equation 5.131) becomes linear. Warrick and Lomen (1976) developed quasi-analytical solutions for the case of strip-source and disc-source infiltration under constant flux. The particular program to calculate the strip-source solution shown in Figure 5.15 was developed by us (Ababou, 1981).

Unfortunately, the soil properties (5.135) are not realistic enough to obtain a reasonable simulation of transient infiltration phenomena, due to the fact that in general the diffusivity is far from constant (see Ababou, 1981). Another drawback is that the solution given by Warrick and Lomen (1976) is exact only in the limit of zero initial conductivity. The slight discrepancy that can be observed between the numerical and analytical solutions shown in Figure (5.15) could be due to the fact that the initial conductivity in this example was not really negligible relative to the input flux ( $K_{in}/q_0 = 4.5 \cdot 10^{-3}$ ). In addition, the quasi-analytic solution requires a numerical evaluation of integrals of special functions; the computed

pressure contours close to the initial state (far from the source) are quite sensitive to small errors of numerical integration.

Nevertheless, the agreement between the numerical and analytical solutions of Figure (5.15) seems reasonably good, especially close to the source. The two-dimensional numerical solution shown on top was obtained by shrinking the longitudinal domain size to just 5 nodes (3 internal nodes) and picking the central slice for visual display. The near-perfect symmetry of the numerical solution is an indication that the nonlinear-SIP solver worked well in that case: it should be noted indeed that the three-dimensional SIP solver is inherently asymmetric. This asymmetry would probably show up in cases of incomplete convergence.

Figure 5.16 shows the result of another comparison between numerical and analytical solutions. In this case, the flow simulator was used in both the "saturated" and "unsaturated" mode to solve the one-dimensional linear diffusion equation:

$$\begin{aligned} \frac{\partial H}{\partial t} &= D \cdot \frac{\partial^2 H}{\partial x^2}, \quad 0 \leq x \leq L \\ H(0, t) &= 1 \\ H(L, t) &= 0 \\ H(x, 0) &= 0. \end{aligned} \tag{5.136}$$

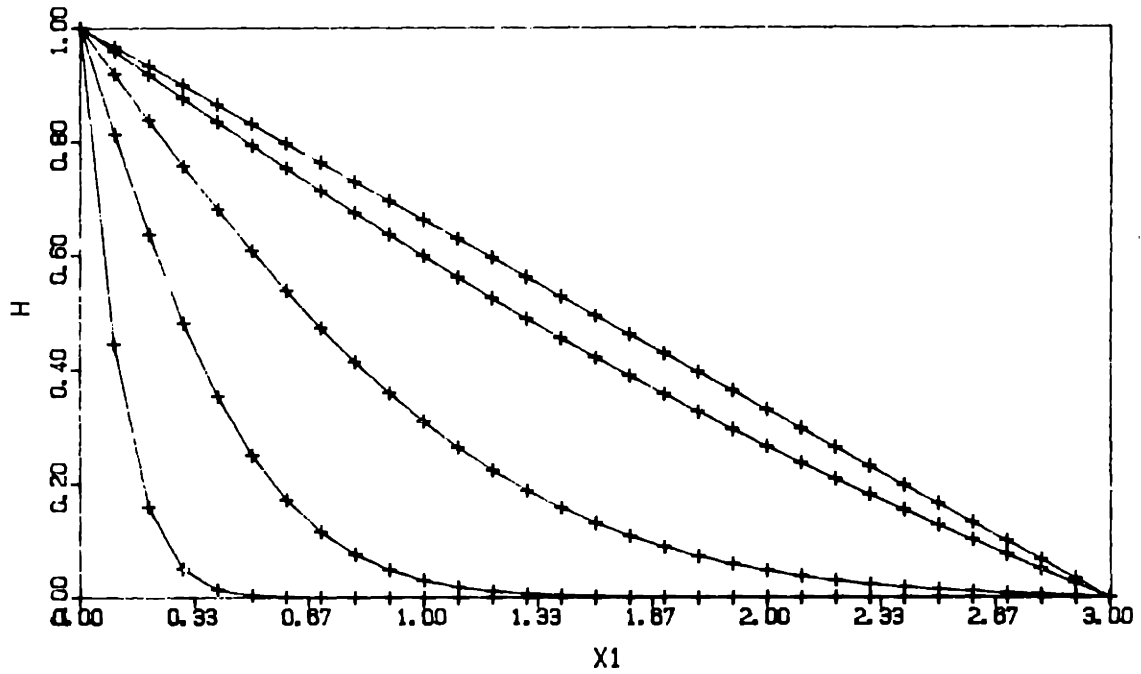


Figure 5.16 Numerical and analytical solutions for the transient 1D diffusion equation with constant coefficients. The numerical solutions obtained in the saturated or unsaturated modes, with fixed or variable time steps, were undistinguishable from the analytical solution. One of the numerical solutions is shown here for times  $t = 0.01, 0.10, 0.5, 1,$  and  $t \geq 5$  (quasi-steady state)



This equation models for instance the transient recharge of a confined aquifer with conductivity  $K$  and specific storativity  $S$ , such that  $D = K/S$ .

The analytical solution of equation (5.136) can be expressed in the form of an infinite series with sine and exponential functions (Korn and Korn, 1968, p. 325). However we have found that a very high machine precision would be needed to obtain reasonably accurate answers at early times. Another series solution was finally worked out by using a superposition of Green's functions as explained by Godunov (1973, pp. 29-41). The final result is given below in dimensionless space-time variables:

$$H(y, \tau) = \sum_{n=1}^{\infty} n \cdot (a_n - b_n)$$

$$a_n = \operatorname{erf}\left(\frac{n+y/2}{\sqrt{\tau}}\right) + \operatorname{erf}\left(\frac{n-y/2}{\sqrt{\tau}}\right) \quad (5.137)$$

$$b_n = \operatorname{erf}\left(\frac{n-1+y/2}{\sqrt{\tau}}\right) + \operatorname{erf}\left(\frac{n+1-y/2}{\sqrt{\tau}}\right)$$

where:

$$y = x/L$$

$$\tau = D \cdot t / L^2$$

and  $\operatorname{erf}(x)$  is the usual error function defined by:

$$\operatorname{erf}(x) = \frac{2}{\sqrt{\pi}} \cdot \int_0^x e^{-s^2} \cdot ds.$$

The numerical solutions obtained with both the saturated and unsaturated options of the flow simulator for a three-dimensional elongated domain, fitted perfectly the one-dimensional analytical solution computed from equation (5.137). Figure (5.16) showed only one graph of  $H(x,t)$  because the three solutions were visually indistinguishable. It should be noted that the saturated flow mode was implemented with constant time steps, while the unsaturated mode was implemented with a variable time step size. In the latter case, the constant coefficients were obtained by taking  $K(h)$  constant and  $\theta(h)$  linear. This test was useful to check the soundness of various algorithms of the flow simulator, including the variable time step procedure and the performance of the SIP matrix solver for transient problems. In other words, this particular test problem provided an accurate check on many features of the flow simulator, other than the nonlinear solver.

[c] Infiltration Experiments with Homogeneous and Layered Soils:

We now proceed to analyze, in a rather qualitative way, the numerical pressure fields obtained for a few test problems of one and two-dimensional infiltration in uniform or deterministically layered soil systems. Our intent here is merely to demonstrate that, in all cases considered, the numerical solution agrees with intuitive and/or physically based

principles. We consider first a few cases of infiltration in uniform soils, and continue our exploration with the case strip-source infiltration in two-dimensional deterministically layered soils. In the process, one of these test problems will be used to examine the effect of mesh size on the numerical solution.

The first sequence of test problems concerned one and two-dimensional infiltration on the homogeneous "Dek" sand with a relatively dry initial state ( $h_{in} = -111$  cm). The constitutive relations of this soil were given earlier in Figure (5.3). The pressure profiles obtained for one-dimensional infiltration in a 3 meter deep soil column, with zero pressure at the top, are depicted in Figure (5.17). The resolution  $\Delta x = 3$  cm was fine enough to capture the very sharp wetting fronts obtained in this case. The next two Figures (5.18) and (5.19) display the vertical pressure profile and the pressure contours obtained for 2D infiltration with zero pressure maintained at the surface of a strip-source (saturated strip). The wetting front is still very sharp, although less so than for the one-dimensional problem. In addition, it can be seen that that front moves downwards at a lesser rate due to increased dimensionality (lateral diffusion). Finally, Figures (5.20) and (5.21) display the vertical pressure profiles and the pressure contours obtained for 2D strip-source infiltration with a fixed flux ( $q_0 = 12$  cm/day) at the surface of

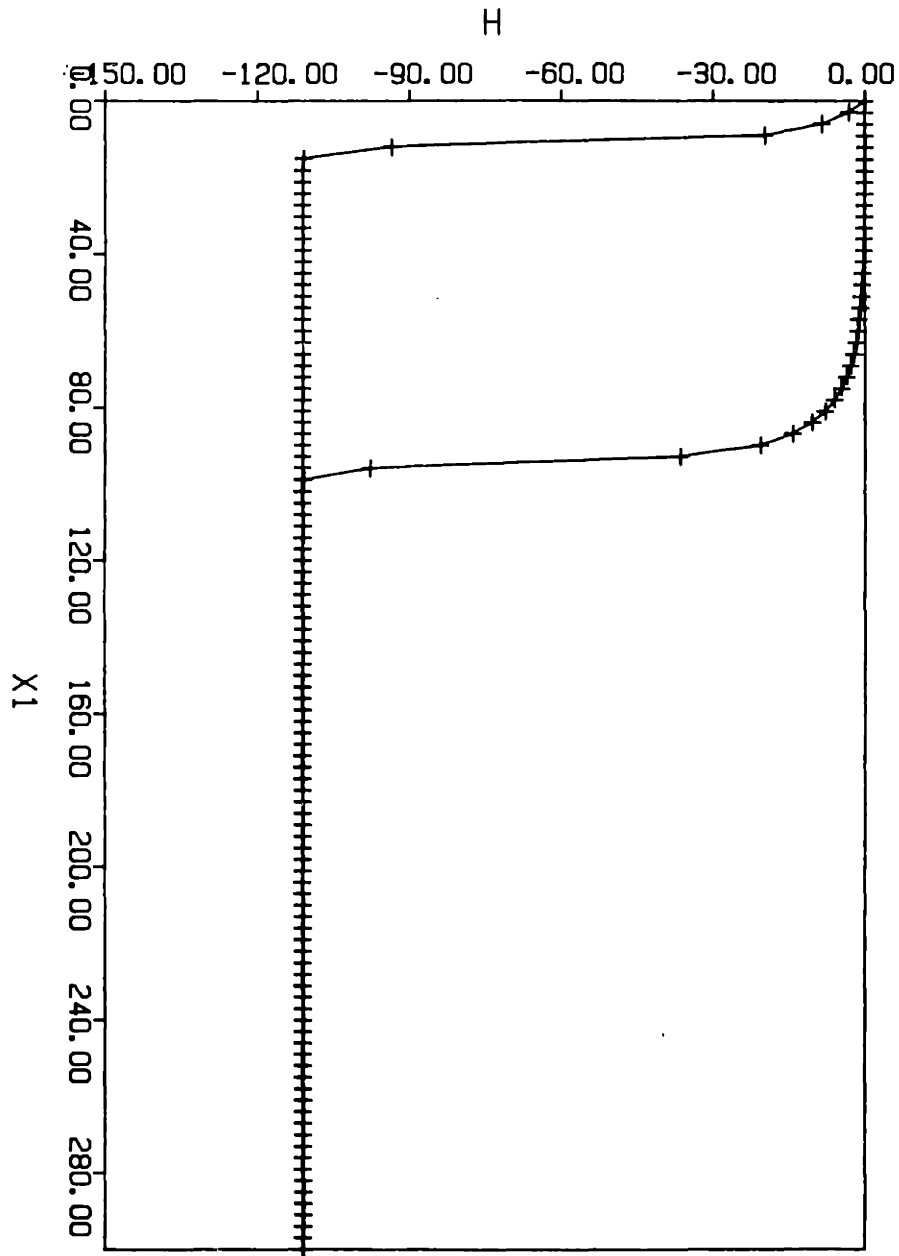


Figure 5.17 Vertical pressure profile at times  $t = 0.005$  and  $0.1$  day for one-dimensional infiltration with zero pressure at soil surface (Dek sand with  $h_{in} = -111$  cm). The vertical mesh size is  $\Delta x = 3$  cm and the total length of the column is  $L = 300$  cm.

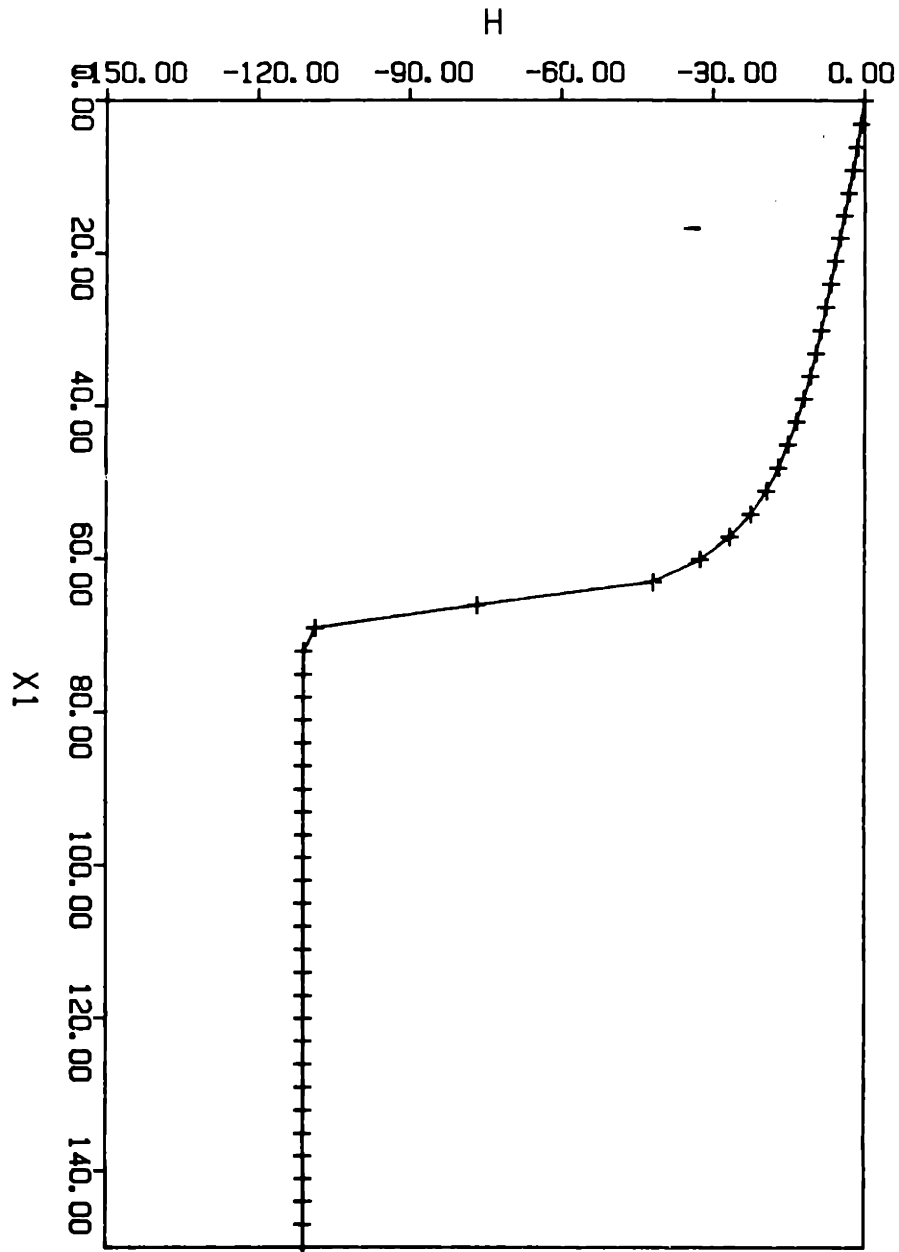


Figure 5.18 Vertical pressure profile at time  $t = 0.1$  day for a two-dimensional infiltration with a saturated strip source. The vertical transect coincides with the axis of symmetry (see Figure 5.19).

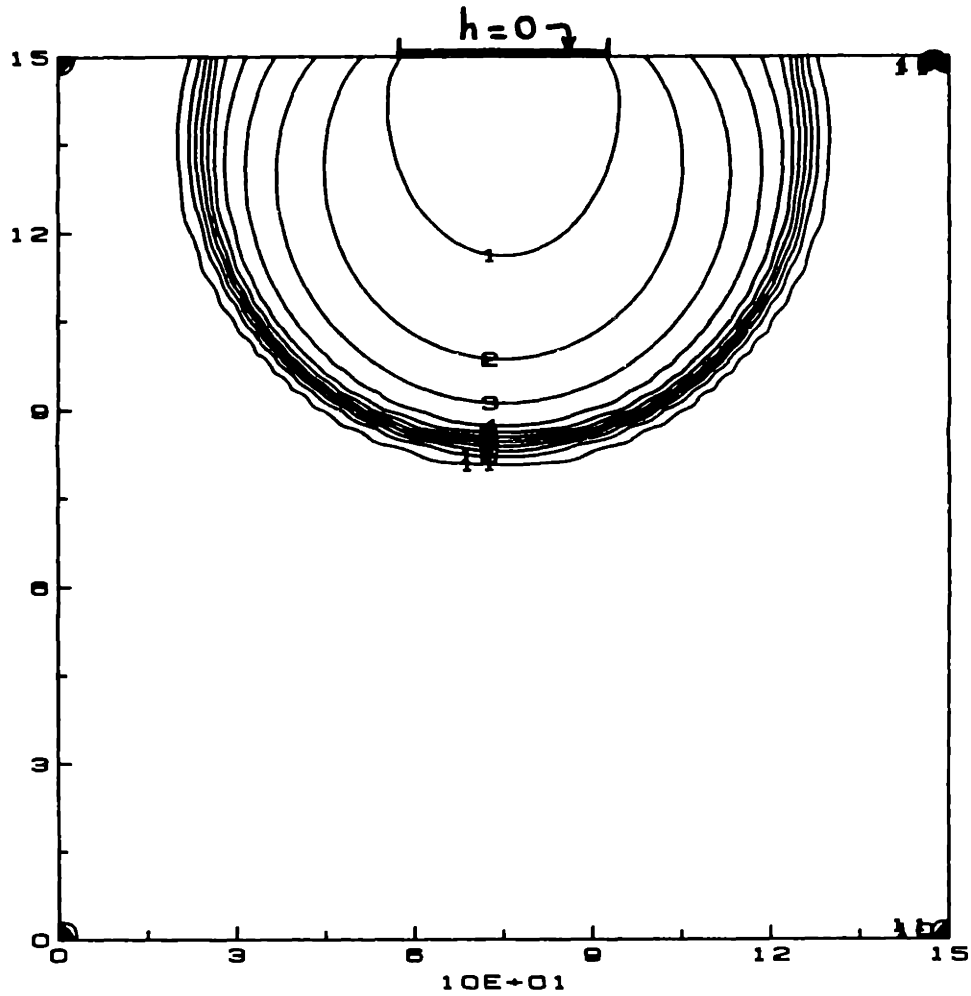


Figure 5.19 Pressure head contour lines at time  $t = 0.1$  day for 2D infiltration with a saturated strip source (Dek sand with  $h_{in} = -111$  cm). The source width is 33 cm, the mesh size is 3 cm, and the domain size  $150 \times 150$  cm.

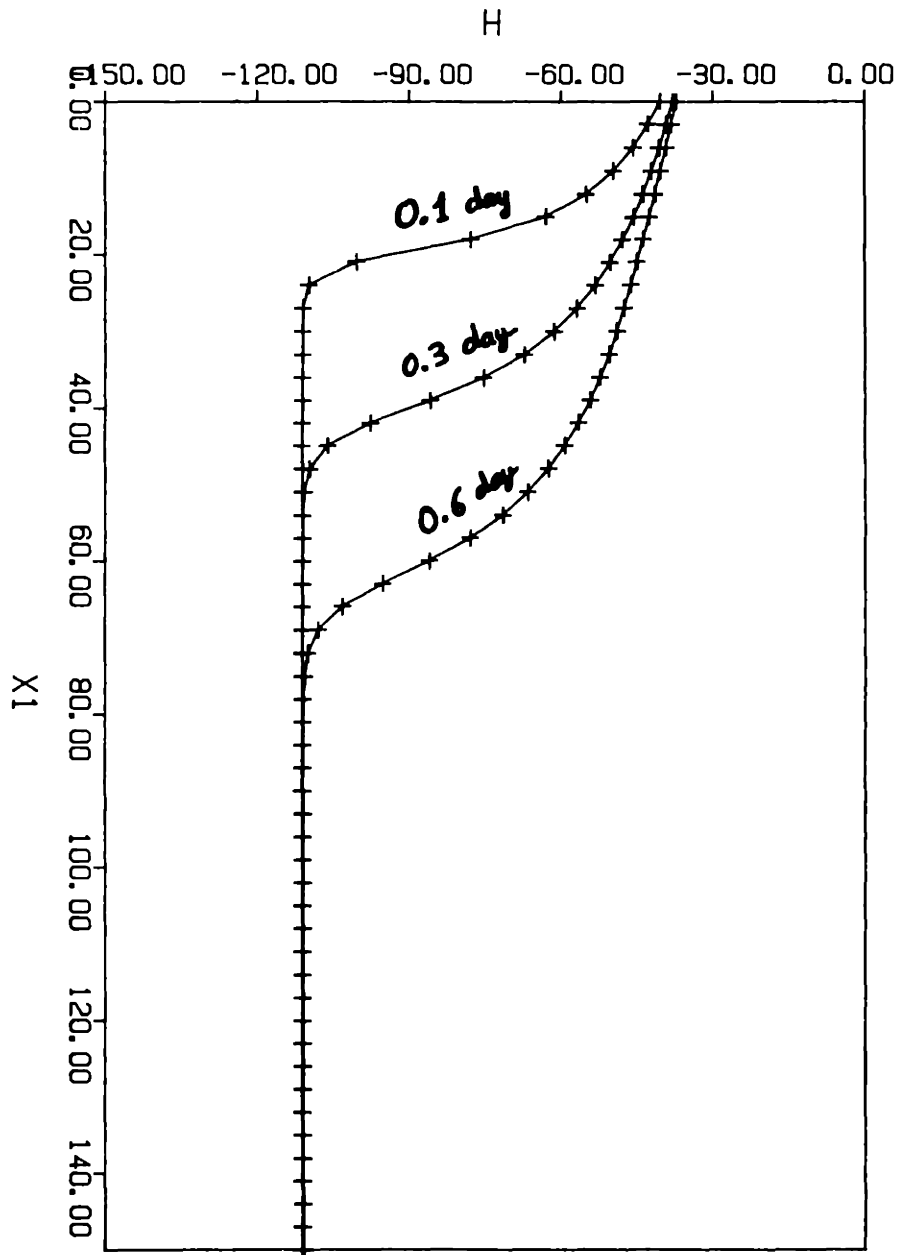


Figure 5.20 Vertical pressure profiles at times  $t = 0.1, 0.3$  and  $0.6$  day for a two-dimensional infiltration with a constant flux strip-source. The vertical transect coincides with the axis of symmetry (see Figure 5.21)

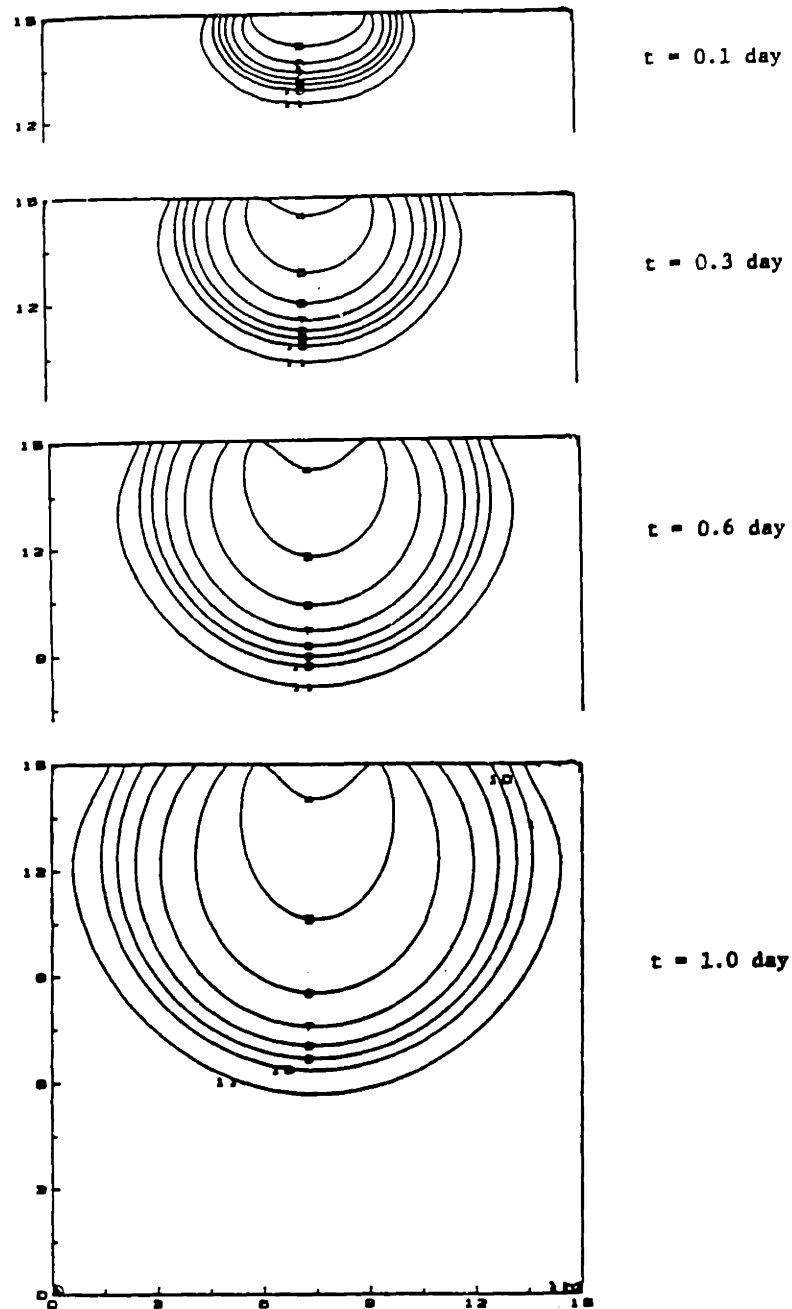


Figure 5.21 Pressure head contour lines for 2D infiltration with a constant flux strip source  $q_0 = 12$  cm/day (Dek sand with  $h_{in} = -111$  cm). The source width is 33 cm, the mesh size 3 cm, and the domain size 150 x 150 cm. Times:  $t = 0.1, 0.3, 0.6$  and 1.0 day



the strip. In this case, the wetting front appears even smoother, and the rate of growth of the wet zone is slower than in the previous case of a saturated strip (in both cases, the strip width was 33 cm). Note that the prescribed flux was 8.5% the value of the saturated conductivity, whereas the flux over the saturated strip source in the previous example was presumably much larger. Last but not least, we emphasize the fact that the numerical solutions obtained for the strip-source problems seem perfectly symmetric about the central vertical axis. This feature was not built-in the solution, but rather resulted from the convergence of the nonlinear-SIP solver towards the exact solution; it should be kept in mind indeed that the SIP factorization is not symmetric, so that the numerical solution would probably appear non-symmetric in case of incomplete convergence.

In order to explore the problem solving capabilities of the flow simulator for spatially variable unsaturated soils, we have simulated two-dimensional strip-source infiltration on horizontally and vertically layered soils. This could be viewed as an intermediate case between the ideal case of homogeneous soils, and the more realistic case of three-dimensional *random* soils to be analyzed in Chapter 7 (statistically layered soils in particular). Of course, we expect that the flow patterns will be

much easier to analyze for uniformly layered soils than for statistically layered (random) three-dimensional soils. That is precisely the reason for our choice here.

Three types of uniformly layered soil systems were considered for qualitative analysis: a horizontally layered system with mild contrast (sand/sand); another horizontally layered system with high contrast (sand/silt); and a vertically layered system with high contrast (sand/silt). Briefly, the sand/sand system corresponds to alternate layers of the Dek sand of Figure 5.3, and a somewhat coarser sand (Dieri sand, Ababou 1981). The sand/silt system corresponds to alternate layers of the Dek sand of Figure 5.3 and the Montfavet silt of Figure 5.4. The contrast for each layered system can be characterized by an index of variability of  $K_s$  and  $\alpha$ , the two parameters of the exponential  $K(h)$  curve, as follows:

$$\sigma_{\ln Y} = \left\{ \frac{(\ln Y_1/Y_G)^2 + (\ln Y_2/Y_G)^2}{2} \right\}^{1/2}$$

$$Y_G = \sqrt{Y_1 \cdot Y_2}$$

where  $Y$  is either  $K_s$  or  $\alpha$ , and the index (1,2) refers to the two soils composing the layered system. For the sand/sand system, the contrast was moderate:

$$\sigma_{\ell n} K_S \simeq 0.44$$

$$\sigma_{\ell n} \alpha \simeq 0.22$$

and, for the sand/silt system the contrast was quite high:

$$\sigma_{\ell n} K_S \simeq 2.60$$

$$\sigma_{\ell n} \alpha \simeq 0.87$$

Figure (5.22) shows pressure head contour lines obtained at time  $t = 1$  day for the sand/sand system with alternate horizontal layers of thickness 9 cm. The initial pressure was  $h = -150$  cm for figure (a), and  $h = -90$  cm for figure (b). The general shape of the wetted zone, apart from small scale oscillations, is quite similar to that obtained for either sand soil alone, that is, without alternate layering. But, for the highly contrasted sand/silt system shown in Figure (5.23), the pressure field looks quite different. In this case, the initial pressure ( $h = -150$  cm) was such that the initial conductivity was higher in the silt than in the sand, by two orders of magnitude. Consequently, as we have observed from detailed numerical outputs, the wetting front rested most of the time just above a sand layer, while moisture spread laterally within the silt layers.

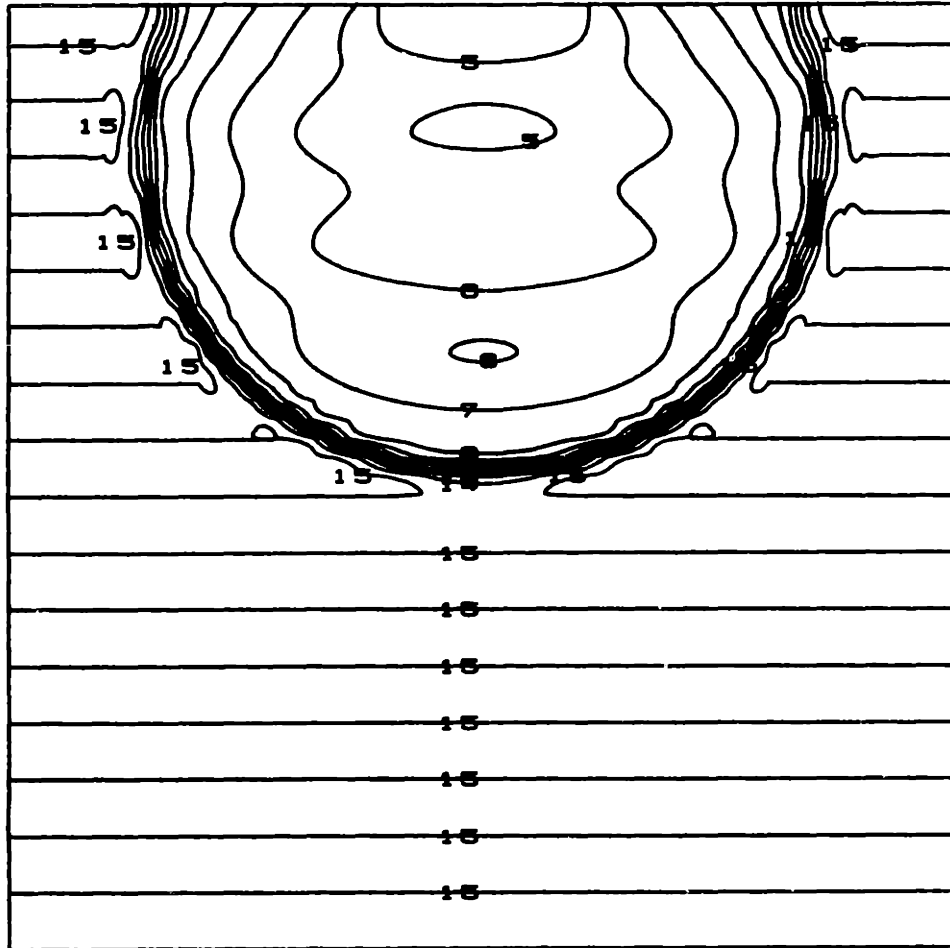


Figure 5.22 (a) Pressure head contour lines for 2D strip-source infiltration ( $q = 12$  cm/day) in a horizontally layered sand/sand system, at time  $t = 1$  day. The mesh size is 3 cm, the domain size  $150 \times 150$  cm, the strip width 33 cm, and the alternate layers thickness 9 cm. The initial pressure head was  $h_{in} = -150$  cm

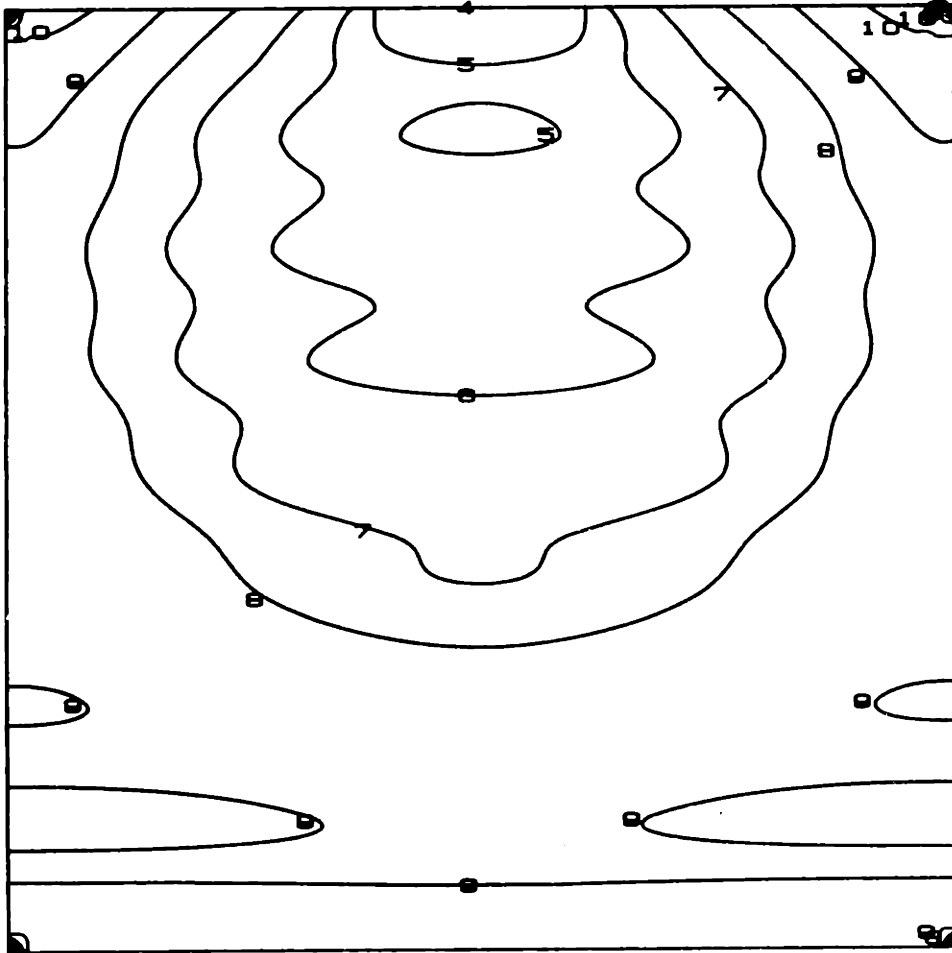


Figure 5.22(b) Same as Figure 5.22.a, but with a less dry initial state ( $h_{in} = -90$  cm).

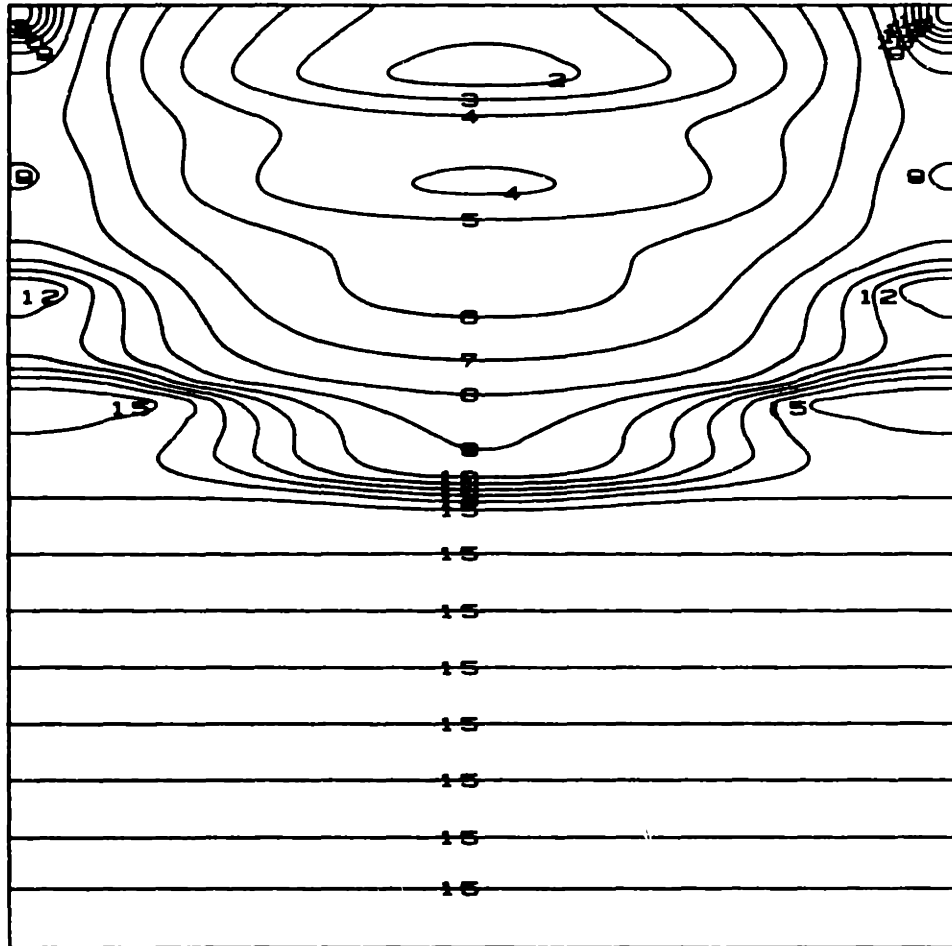


Figure 5.23 Pressure head contour lines for 2D strip-source infiltration ( $q = 12$  cm/day) in a horizontally layered sand/silt system, at time  $t = 1$  day. The mesh size is 3 cm, the domain size  $150 \times 150$  cm, the strip width 33 cm, and the alternate layers thickness 9 cm. The initial pressure was  $h_{in} = -150$  cm.

It should be noted that the mesh size in these examples was one third of the layers thickness, i.e.,  $\Delta x = 3$  cm. Figure (5.24) shows the solution obtained for the sand/silt system with a coarser grid equal to the layer thickness, i.e.,  $\Delta x = 9$  cm. The obvious effect of the coarse mesh is that it smears out the small scale fluctuations of pressure obtained with the finer grid (compare Figures 5.23 and 5.24). However, the overall shape and size of the wet zone are surprisingly well represented with the coarse grid simulation. This can be seen more easily by representing on the same plot the vertical pressure profiles obtained with the fine and coarse meshes (Figure 5.25). This relative agreement indicates that the grid resolution need not be much finer than the typical layer thickness in order to obtain realistic solutions. The grid Peclet number constraint (5.128) should be also kept in mind. In the present case, the coarse grid Peclet number (with  $\Delta x = 9$  cm) was about 0.6 for the sand layers, and 0.1 for the silt layers. Both these values satisfy the "nonlinear" stability constraint  $Pe \leq 2$ .

Finally, Figure (5.26) shows the pressure head contour lines obtained for the vertically layered sand/silt system, with alternate layers of thickness 9 cm. The non-symmetrical shape of the pressure field is due to the fact that the vertical axis

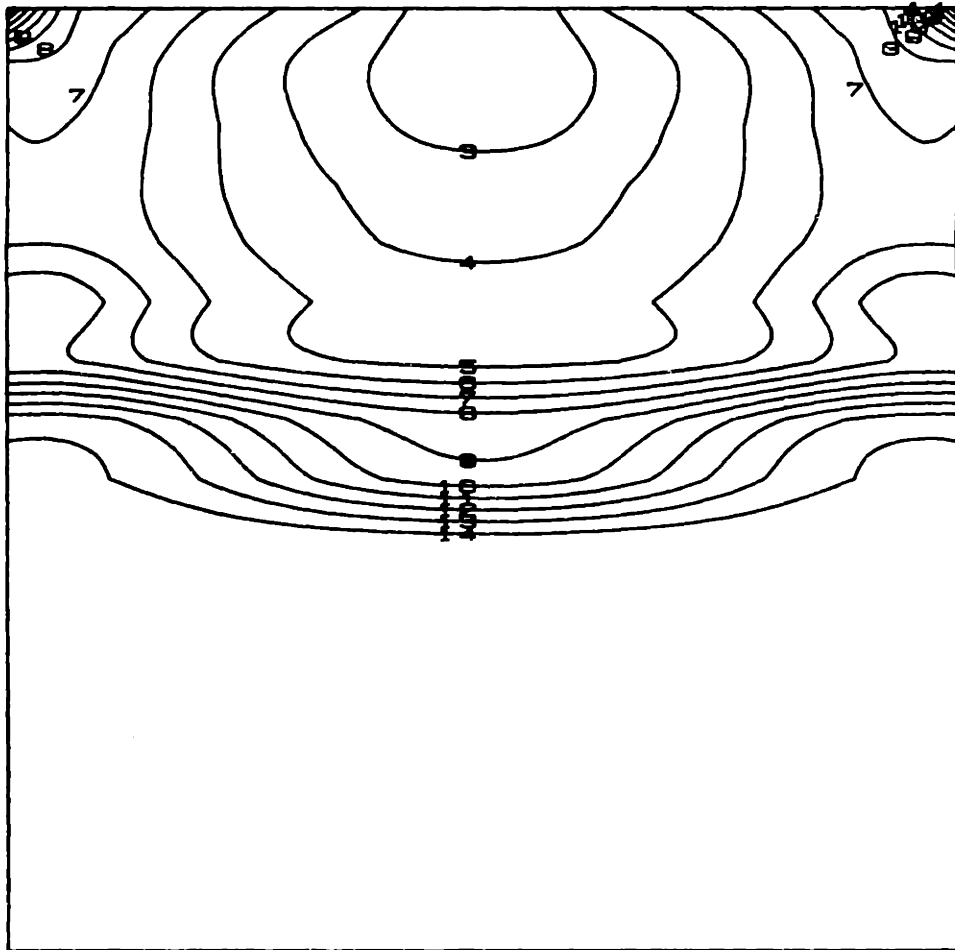


Figure 5.24 Same as Figure 5.23, but with a coarser mesh size  $\Delta x = 9$  cm equal to the layer thickness.



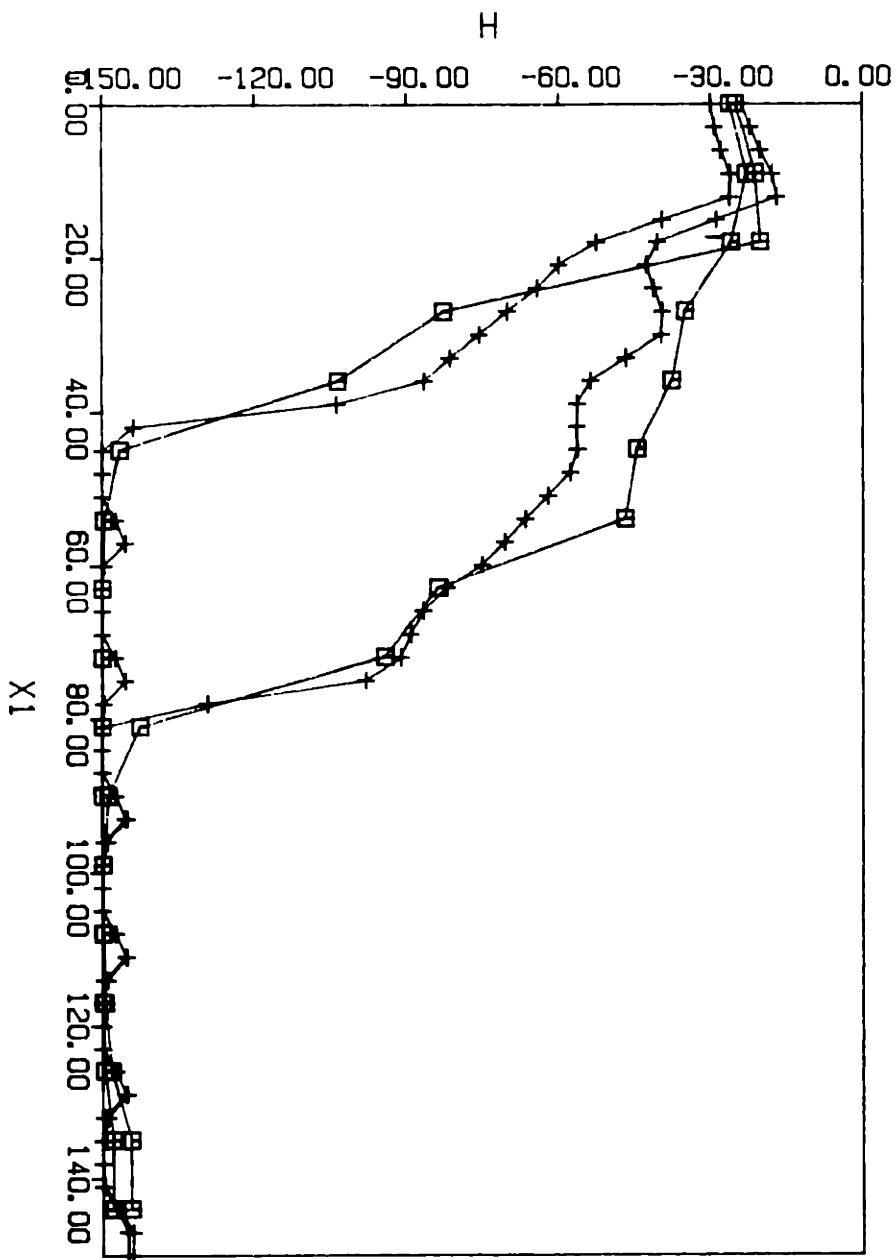


Figure 5.25 Vertical pressure profiles through the axis of symmetry of the strip source for the sand/silt system at times  $t = 0.3$  and 1 day. The crosses correspond to the fine mesh simulation (Figure 5.23 with  $\Delta x = 3\text{cm}$ ) and the square boxes to the coarse mesh simulation (Figure 5.24 with  $\Delta x = 9\text{cm}$ ).

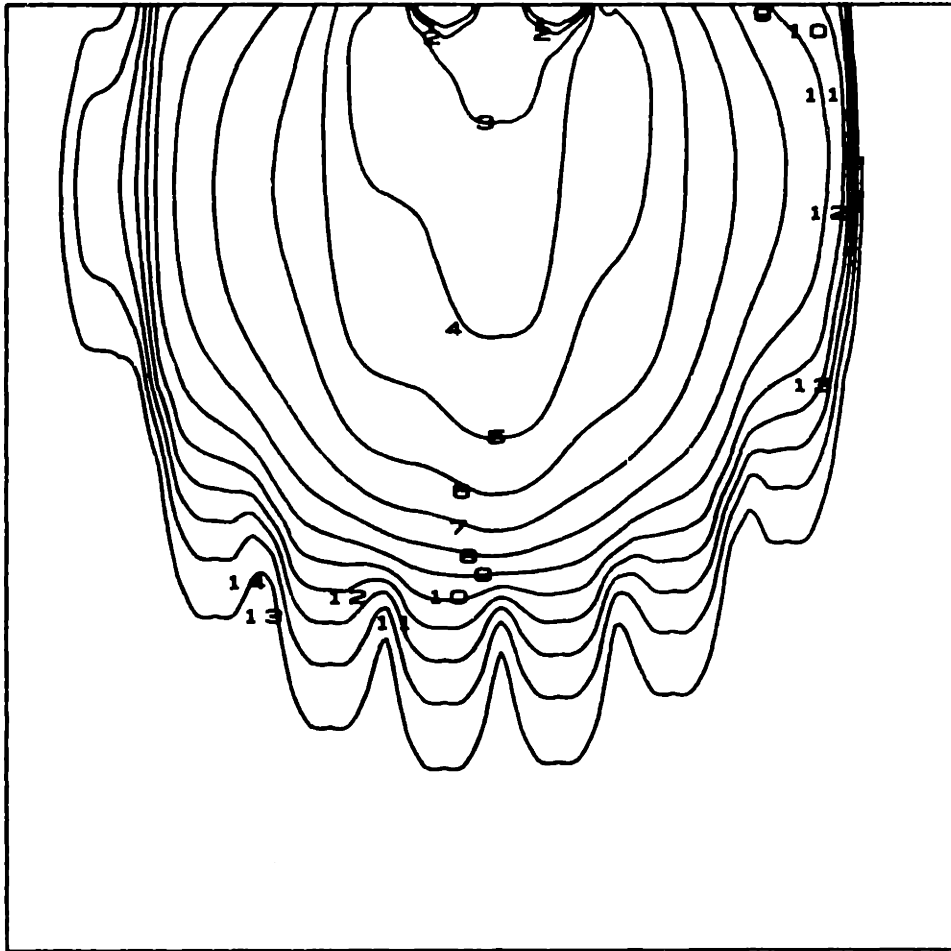


Figure 5.26 Vertically layered sand/silt soil system (strip source infiltration-time = 1day).

located at the mid-point of the strip-source does not constitute an axis of symmetry with respect to the vertical layers. One interesting feature in Figure (5.26) is that the spatial fluctuations of the wet pressure contours are more or less in opposite phase with the dry pressure contours (looking through vertical lines). This is due to the existence of a cross-over point ( $h = -90$  cm) below which  $K_{\text{silt}} < K_{\text{sand}}$ , and above which  $K_{\text{silt}} > K_{\text{sand}}$ . Thus, it should not be surprising to see that the particular contour line  $h = -90$  cm corresponding to  $K_{\text{silt}} = K_{\text{sand}}$  is almost perfectly smooth !

### 5.5 Summary and Conclusions on Numerics:

In this chapter, we have developed a multi-faceted analysis of the numerical issues related to the direct simulation of large and complex flow systems. It may be useful to briefly summarize the various approaches that were developed and the conclusions that were drawn from these analyses. To begin with, we developed in Section 5.1 the basic equations for the *finite difference* approximation of both saturated and unsaturated flow phenomena in spatially heterogeneous media. The particular choice of the finite difference model was motivated by considering the likely numerical requirements for simulating representative single realizations of random flow systems (high

resolution and large domain).

These considerations were confirmed by a more systematic theoretical analysis of the stochastic finite difference solution error arising from truncation errors (Section 5.2). The remarkable result obtained for the case of steady saturated flow, i.e., for the stochastic "heat equation" with 3D random field conductivities, was that the finite difference scheme is indeed a consistent approximation of the stochastic equation in the mean-square sense. Furthermore, it was shown that the order of accuracy is  $O(\Delta x/\lambda)^2$  for the hydraulic head and  $O(\Delta x/\lambda)$  for the flux vector, in the case of a smooth log-conductivity field with correlation length  $\lambda$  (e.g., random field with a Gauss-shaped spectrum). On the other hand, we found that the order of accuracy drops to  $O(\Delta x/\lambda)^{3/2}$  and  $O(\Delta x/\lambda)^{1/2}$  for the head and flux, in the case of a noisy log-conductivity such as the 3D Markov field with exponential covariance function. It is remarkable that the finite difference approximation is still consistent in this case, despite the fact that the log-conductivity is non-differentiable in the mean-square sense. These encouraging results were refined further by evaluating explicitly the leading order terms of the root-mean-square errors in the head and flux. It was found that both errors were proportional to the standard deviation of the log-conductivity field. One major conclusion from this

statistical truncation error analysis is that a relatively fine grid resolution is needed to obtain even moderately accurate solutions in terms of the flux vector field. Thus, when the log-conductivity is the "noisy" three-dimensional Markov field, the root-mean-square error on the flux is as large as 15-20% for  $\Delta x/\lambda = 1/3$ , and still about 10% for  $\Delta x/\lambda = 1/10$ .

However, it was also recognized that the numerical errors of the random flow simulator will be due in part to the difficulty of solving accurately very large matrix systems. Section 5.3 was devoted to the development of an adequate linear system solver for large sparse matrices. Our literature review focused on iterative solvers, and particularly the SIP and IOCG solvers based on approximate factorizations. The SIP solver was finally chosen for implementation and was described in some detail. The accuracy of the linear system solutions obtained with SIP were analyzed in a semi-empirical way by examining the rate of convergence of the SIP iterations both from a theoretical and "experimental" point of view.

Our conclusions, based on numerical experiments for large random systems of saturated flow (up to 1 million nodes), were quite favourable. It was found that the root-mean-square solution error could be reduced to very small values (typically less than 1%) in a few hundred up to one thousand iterations,

depending on the variability of the input log-conductivity field. The numerical simulations were carried out on a Cray 2 supercomputer, requiring CPU times of one to several hours for the most "difficult" random flow problems (1 million nodes). A Microvax 2 machine was used for medium size problems on the order of 1 to 2 hundred thousand nodes. One remarkable aspect of the proposed method of analysis was that the "true" solution error was evaluated indirectly by using information from the actual simulations (sequence of residual errors, and convergence rate). It was shown that in many cases the true error could be much larger than the apparent (residual) error, particularly for large and noisy systems where underrelaxation was needed to achieve convergence. Empirical analysis suggested that the number of iterations required to solve linear random flow problems could be proportional to  $n$ , the largest unidirectional size of the three-dimensional rectangular grid. However, it is still not clear at this time whether the SIP solver or any similar iterative solver will actually converge for very large random flow systems on the order of 10 million equations or more. Extrapolation of our results suggested that, in case of convergence, the solution of a highly variable saturated flow problem on a 10 million node grid could require about 1 day CPU time on the Cray 2 machine.

Finally Section 5.4 was devoted to the development and analysis of a nonlinear system solver for the case of unsaturated flow. The nonlinear SIP solver was developed by adding an iterative linearization scheme to the previous iterative matrix solver (nested Picard iterations). A preliminary analysis of numerical requirements suggested that, in the case of transient infiltration on dry soils, there could be a severe limitation on the time step size in order to ensure the convergence of the nonlinear iteration loop (outer iterations). On the other hand, the SIP matrix solver is likely to converge much faster for any given time step of a transient problem (particularly for small time steps) than for the single step of a steady state problem. Our discussion of these issues also included a brief literature review. Our attempt at elucidating the space-time resolution requirements by way of numerical analysis was not entirely successful. The most remarkable finding in that study was perhaps the *grid Peclet number constraint* ( $Pe = \alpha \Delta x_1 \leq 2$ ), which was obtained from a heuristic "nonlinear stability analysis" of the unsaturated finite difference system. This analysis also suggested that a very stringent requirement on the time step could result if the Peclet number constraint was not satisfied locally. The discussion included a physical interpretation of the Peclet number for unsaturated flow (gravity/diffusion), and focused on the possible divergence of the nonlinear solver in

severe cases such as infiltration in *dry heterogeneous soils* (sharp fronts).

It was felt that the complexity of the unsaturated flow problem, and the associated numerical issues, required a careful testing of the unsaturated flow simulator. The last part of Section 5.4 was devoted to numerical tests with increasingly complex problems of transient infiltration. These numerical experiments included specialized tests for checking certain features of the code such as the variable time step and the variable domain procedures, mass balance tests, comparisons with analytical solutions, and a number of infiltration experiments with homogeneous and uniformly layered soils, mostly in two dimensions. Our overall conclusion from these numerical experiments is that the unsaturated flow simulator appears as a reliable and flexible tool for the detailed simulation of fairly complex transient infiltration problems.

The encouraging results obtained here need however to be confirmed for the case of truly large realizations of random soil systems. This will be the subject of Chapter 7, where we will analyze in detail the solutions obtained from large single-realization simulations of flow in random soils, with three-dimensional grids on the order of ten thousand to several hundred thousand nodes. On the other hand, the forthcoming



Chapter 6 will be devoted to a systematic statistical analysis of the solutions obtained from large single-realization simulations of saturated flow. Note that both Chapter 6 and Chapter 7 will focus mostly on physical interpretation and mathematical analysis of numerical solutions, and only occasionally on some numerical issues. It is assumed at this stage that the flow simulator has been fully tested, both in the saturated and unsaturated flow regimes.

CHAPTER 6  
THREE-DIMENSIONAL SINGLE-REALIZATION  
SIMULATIONS OF SATURATED FLOW IN RANDOM POROUS MEDIA

6.1 Scope, Model Problems, and Methodology

This Chapter is devoted to the physical interpretation and statistical analysis of large realizations of steady state saturated flow fields in three-dimensional random porous media. In the single-realization approach, the hydraulic conductivity  $K(\underline{x})$  is generated as a particular replica of a statistically homogeneous random field in 3D space. In view of reproducing a relatively wide range of natural conditions, two main types of model problems (isotropic/anisotropic) were selected, with different subcases corresponding to various degrees of conductivity variability. In all cases, the random field conductivity was assumed *locally* isotropic, although the spatial structure could be statistically anisotropic as well as isotropic. This will be explained in more detail shortly.

[a] Model Problems.

The single-realization flow problems to be examined in this Chapter are listed in Table 6.1, with a summary of numerical and statistical input data in each case (problems A, B, E and F, to be analyzed in Sections 6.3, 6.2, 6.4, respectively).

TABLE 6.1  
 SYNOPSIS OF SINGLE-REALIZATION PROBLEMS OF STEADY SATURATED FLOW  
 WITH 3D RANDOM FIELD CONDUCTIVITIES  
 See Also Table 5.4

Category	Isotropic		Anisotropic	
	A #51, #52, #53	B #40, #30	E #42	F #43
Section	Section 6.3	Section 6.2	Section 6.4	Section 6.4
$\sigma_f$	1.0, 1.7, 2.3	1.0, 2.3	1.0	1.0
$\epsilon = \lambda_2/\lambda_1$	1	1	1/4	1/4
$(\lambda_i)$	(1., 1., 1.)	(1., 1., 1.)	(1., 1., 0.25)	(1., 1., 0.25)
$(L_i)$	(33.3, 33.3, 33.3)	(25., 25., 25.)	(30., 30., 7.5)	(30., 60., 60.)
$J_1$	0.004	0.004	0.004	0.0001
$\Delta x_i/\lambda_i$	(1/3, 1/3 1/3)	(1/2, 1/2, 1/2)	(1/2, 1/2, 1/2)	(1/2, 1.4)
$L_i/\lambda_i$	(33.3, 33.3, 33.3)	(25., 25., 25.)	(30., 30., 30.)	(30., 60., 240.)
$n_i$	(101, 101, 101)	(51, 51, 51)	(61, 61, 61)	(61, 61, 61)
$N$	1 Million	130000	220000	220000
Computer	Cray 2	Microvax 2	Microvax 2	Microvax 2

Note: The geometric mean conductivity was  $K_G = 1$  in all cases. The exact values used for  $\sigma_f$  were 1.0, 1.732, and 2.3025. Recall that  $\sigma_f$  is the standard deviation of the normally distributed log-conductivity (natural logarithm). For problems with more than one value of  $\sigma_f$ , the same realization of the  $\ln K$  field was used, provided appropriate rescaling in the obvious way.

In our view, these hypothetical flow problems cover a relatively wide range of field situations for groundwater flow applications, at least in a generic way. The selected set of input data does not correspond to any particular field site, but constitutes a fairly representative "sample" of known field cases, as can be seen from our review in Chapter 2 (Section 2.3).

The geometry, flow regime, and boundary conditions adopted in this work are represented graphically in Figure (6.1). The flow domain is a three-dimensional parallelepiped rectangle, defined by the size of its sides ( $L_1, L_2, L_3$ ). The flow regime corresponds to purely saturated steady flow, and the boundary conditions were chosen to mimick the case of a heterogeneous groundwater flow system driven by some large-scale regional hydraulic gradient ( $J_1$ ). Note that all lateral boundaries, including the top and bottom faces of the flow domain, were assumed to be impervious. Strictly speaking, this limits the applicability of the model to the case of *confined* groundwater flow.

Ideally, the case of *unconfined* groundwater flow could be simulated by taking into account the shape of the water table

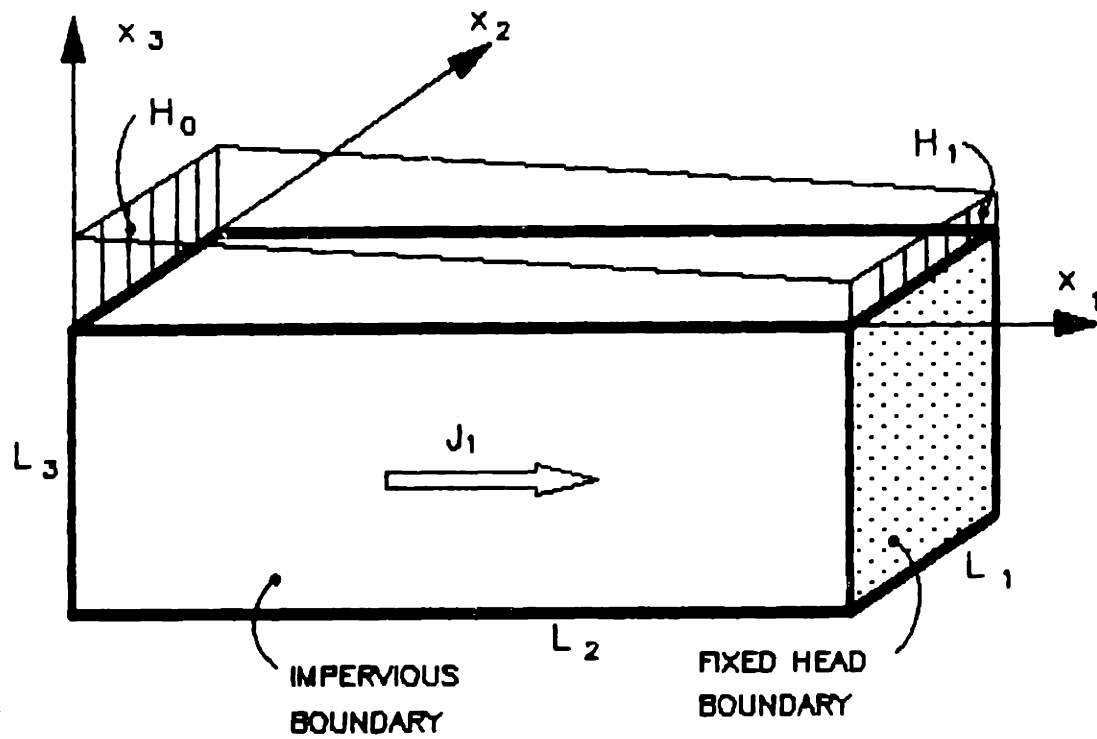


Figure 6.1 Schematic representation of flow domain geometry and boundary conditions used for single-realization simulations of steady-state saturated flow.

as part of the solution. However, there was no provision to do this in the *saturated* flow simulator developed in this work. To be fair, note that the flow simulator could also be run in the *partially saturated* mode to simulate unconfined flow, provided that the vadose zone above the water table be included in the flow domain. However, we have not tried this cumbersome approach. Instead, the case of unconfined flow could be approximated in the purely saturated flow regime by assuming a fixed, horizontal water table, through which some distributed recharge flux could be prescribed. The regional hydraulic gradient should be taken horizontal, and equal to the mean slope of the water table as measured in the field. In our view, the simulated flow fields obtained in this way could be fairly representative of natural unconfined groundwater flow systems, at least far enough below the water table. Thus, the model flow problem of Figure 6.1 could be interpreted alternatively as a confined flow system or as an unconfined flow system with zero recharge at the water table.

Let us now discuss our particular choice of boundary conditions (Figure 6.1) in the context of the single-realization approach to stochastic flow. We have indicated earlier that the flow was assumed to be driven at the large scale by some regional hydraulic gradient. This type of condition was modeled in an

indirect fashion by prescribing constant head conditions on two opposite faces of the flow domain, and zero flux conditions on all other lateral faces.

As a consequence, the regional or "mean" hydraulic gradient will be approximately aligned with the horizontal axis  $x_1$ , which also coincides exactly with the mean flow direction.

This property can be expressed more precisely by defining "regional" or "mean" quantities as three-dimensional spatial averages, e.g.:

$$\text{Mean Hydraulic Gradient: } \bar{J}_i = - \frac{1}{L_1 L_2 L_3} \cdot \iiint \frac{\partial H}{\partial x_i} \cdot d\mathbf{x} \quad (6.1)$$

$$\text{Mean Flux: } \bar{Q}_i = \frac{1}{L_1 L_2 L_3} \cdot \iiint Q_i \, d\mathbf{x} .$$

Due to the particular geometry and boundary conditions (impervious lateral boundaries), the mean transverse flux components necessarily vanish ( $\bar{Q}_2 = \bar{Q}_3 = 0$ ) and the mean flow is exactly horizontal. On the other hand, a simple manipulation of the triple volume integral defining  $\bar{J}_i$  shows that the longitudinal component  $\bar{J}_1$  is exactly equal to:

$$\boxed{\bar{J}_1 = - \frac{H_1 - H_0}{L_1}} \quad (6.2)$$

and the other gradient components are expected to vanish for sufficiently large domains ( $\bar{J}_2 \approx \bar{J}_3 \approx 0$ ). Note that the boundary conditions are such that the transverse components of the mean hydraulic gradient are only approximately null in a heterogeneous medium, whereas the mean transverse flux components are exactly zero by construction. It does not seem possible to ensure both conditions exactly with a consistent set of boundary conditions. Attempts to do so will lead to an ill-posed boundary value problem.

Equation (6.2) defines in a simple manner the longitudinal "mean" hydraulic gradient imposed on the flow in terms of the prescribed heads  $H_0$  and  $H_1$  at the left and right boundaries. One may conceptually relate this quantity to the ensemble mean hydraulic gradient that would obtain by taking  $L_1$  infinite while  $(H_1 - H_0)/L_1$  remains constant. Furthermore, we have seen that the average flux over the flow domain is necessarily aligned with the horizontal axis ( $x_1$ ), since all lateral boundaries are impervious. This property of the finite-domain flow field is consistent with the predictions of the infinite domain spectral theory in the special case where the log-conductivity field is statistically isotropic or has its



principal axis of anisotropy aligned with the mean gradient (horizontal axis  $x_1$ ).

Accordingly, the anisotropic model problems listed in Table 6.1 (E and F) were restricted to the case of horizontally stratified aquifers, with a zero dip angle between the mean flow and the principal axis of statistical anisotropy of the log-conductivity field. In the more general case of a non-zero dip angle (sloping stratification) the mean flux will not be aligned with the mean hydraulic gradient in general. Future work on this complex case should focus on the design of boundary conditions compatible with the infinite domain and ergodicity assumptions of the spectral theory. Briefly, there are at least two different ways in which a global flow condition can be prescribed over a finite domain of rectangular shape with a dip angle. A regional hydraulic gradient can be ascribed by assuming a linear head variation outside the computational domain (i.e., on all sloping boundaries). Alternatively, a regional discharge rate vector can be ascribed by assuming a constant discharge rate outside the computational domain. The first of these approaches is a generalization of the boundary conditions chosen in this work for the case of isotropic or horizontally stratified formations. It is not clear at this point which one of the two approaches will be the most advantageous for the simulation of groundwater flow in sloping stratified formations: we leave this

problem for future research.

[b] Random Conductivity Fields:

The random *log-conductivity field* used for each single-realization problem was a normally distributed three-dimensional Markov field. In short hand notation, the probability distribution function of  $\ell n K(\underline{x})$  can be defined as:

$$\text{pdf} = N(\ell n K_G, \sigma_f^2) \quad (6.3a)$$

where  $N$  indicates the standard normal distribution,  $K_G$  is the geometric mean conductivity:

$$K_G = \exp\langle \ell n K \rangle \quad (6.3b)$$

and  $\sigma_f^2$  is the variance of the log-conductivity perturbation  $f$ :

$$f(\underline{x}) = \ell n (K(\underline{x})/K_G) \quad (6.3c)$$

$$\sigma_f^2 = \langle f(\underline{x})^2 \rangle.$$

The spectral density  $S_{ff}(k)$  of the Markov field was given in Table 3.1 of Chapter 3 under the designation "3D Ellipsoidal

Markov". The covariance function of this random field is exponential, of the form:

$$\begin{aligned} R_{ff}(\underline{\xi}) &= \langle f(\underline{x}) \cdot f(\underline{x} + \underline{\xi}) \rangle \\ &= \sigma_f^2 \cdot \exp\left(-\sqrt{\sum_i \xi_i^2 / \lambda_i^2}\right) \end{aligned} \quad (6.3d)$$

where  $\xi_i$  is the separation vector, and  $\lambda_i$  is the integral correlation scale of the log-conductivity along the principal axis  $x_i$  ( $i = 1, 2, 3$ ). In the special isotropic case ( $\lambda_1 = \lambda_2 = \lambda_3$ ), the covariance function takes the simple form:

$$R_{ff}(\xi) = \sigma_f^2 \cdot e^{-\xi/\lambda} \quad (6.3.e)$$

where  $\xi$  is the separation distance, and  $\lambda$  the isotropic correlation length (same in all directions). For illustration, we show in [Figure \(6.2\)](#) a contour map of a three-dimensional isotropic Markov log-conductivity field in a two-dimensional slice. Only the low contour values (from  $K = K_G$  to  $K = K_G/100$ ) are represented. The size of the slice is about 43 correlation scales in each direction, the grid resolution is one third of the correlation scale, and there are 129 nodes on each side (about 16,600 grid points on the slice). Note the large number of very small regions of extreme conductivity. The areas devoid of contour lines indicate high permeability "pathways" for the flow:

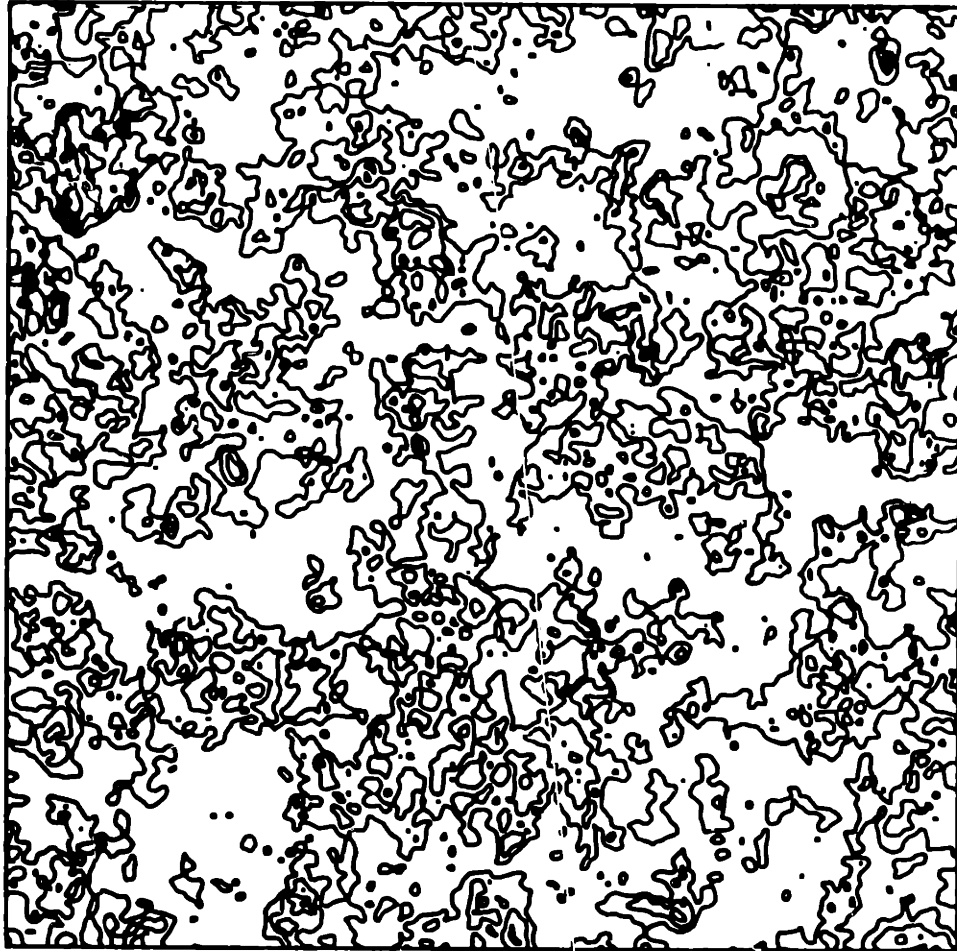


Figure 6.2 Typical high-resolution contour map of three-dimensional isotropic Markov log-conductivity field in a square two dimensional slice. Only the low contour values  $K/K_C = 1$  to  $1/100$  are represented ( $\sigma_f = 1..$ ,  $\Delta x_i/\lambda_i = 1/3$ ,  $L_i/\lambda_i = 43$ )

there is no preferential direction for these pathways since the field is statistically isotropic in this example.

It is important to note that the log-conductivity field just defined is, by construction, statistically homogeneous and ergodic in the strict sense. In other words, all n-point moments up to arbitrary order are statistically invariant by translation. Ergodicity guarantees the equivalence of infinite-domain spatial average with the ensemble means. For instance, the fact that:

$$\lim_{\|\xi\| \rightarrow \infty} R_{ff}(\xi) = 0$$

suffices to guarantee ergodicity in the first and second order moments (cf. Yaglom, 1962, 1.4). This is a desirable property to have in the context of the single-realization approach. In essence, ergodicity guarantees that, for sufficiently large domains ( $L_i \gg \lambda_i$ ) a single spatial realization of the log-conductivity field will carry almost all the information contained in an infinite number of replicas of the random field obtained in ensemble space. This will be illustrated later, by comparing in a specific case the ensemble and spatial moments of the input log-conductivity fields generated by the Turning Band Method (problem A, section 6.3).

[c] Statistical Analysis Methodology

Our methodology for estimating the statistical properties (moments) of single realizations of random fields was based on standard spatial average estimators applicable under the assumptions of spatial homogeneity and ergodicity. The precise procedure we used was not exactly the same for different types of random fields (input log-conductivity, output hydraulic head and output flux vector). The exact procedure used in each case is explained in more detail below.

The spatial moments of the prescribed homogeneous/ergodic log-conductivity field were computed by using standard unbiased estimators. Let  $\ell n(K_{i,j,k})$  be the discrete realization of the log-conductivity field over the grid. The mean and variance were computed by three-dimensional discrete averages as follows:

$$\text{Mean:} \quad \ell n \hat{K}_G = \frac{1}{N} \cdot \sum_{i,j,k} \ell n K_{i,j,k} \quad (6.4a)$$

$$\text{Perturbation:} \quad f_{i,j,k} = \ell n (K_{i,j,k} / \hat{K}_G) \quad (6.4b)$$

$$\text{Variance:} \quad \hat{\sigma}_f^2 = \frac{1}{N} \cdot \sum_{i,j,k} (f_{i,j,k})^2 \quad (6.4c)$$

where  $N$  is the total number of nodes on the grid ( $N = n_1 n_2 n_3$ ).

The two-point covariance functions along each of the axes  $(x_1, x_2, x_3)$  were computed for discrete values of the separation distance  $(\xi_1 = i_1 \Delta x_1, \xi_2 = i_2 \Delta x_2, \xi_3 = i_3 \Delta x_3)$  in a similar fashion. Note however that the fully three-dimensional function  $R_{ff}(\xi_1, \xi_2, \xi_3)$  was not directly computed. For example, the unidirectional covariance along  $x_1$  was evaluated by:

$$\hat{R}_{ff}(i_1, 0, 0) = \frac{1}{N(i_1)} \sum_{j_1, j_2, j_3} f(j_1, j_2, j_3) \cdot f(j_1 - i_1, j_2, j_3) \quad (6.4d)$$

where  $N(i_1)$  represents the number of pair of points with separation vector  $\xi = (i_1 \Delta x_1, 0, 0)$  on the grid, that is:

$$N(i_1) = (n_1 - i_1) \cdot n_2 \cdot n_3$$

Note that  $0 \leq i_1 \leq n_1 - 1$ . The triple index  $(j_1, j_2, j_3)$  in equation (6.4d) was from  $(1, 1, 1)$  through  $(n_1 - i_1, n_2, n_3)$ . The formulas used to compute the covariance function in the other directions are analogous.

For the particular single-realization problems examined in this work, it was found that the spatial moments (6.4) of the log-conductivity fields generated by the Turning Band Method were fairly close to the prescribed ensemble moments. More details will be given in later sections. Let us just mention here that the agreement was particularly good for the isotropic flow

problem A which had the finest resolution ( $\Delta x_i/\lambda_i = 1.3$ ) and the largest sample size ( $L_i/\lambda_i \approx 33.$ ). The reader is referred to Tompson, Ababou, and Gelhar (1987) for an evaluation of the capabilities of the Turning Band random field generator and a systematic comparison of ensemble versus spatial moments in a variety of cases.

The statistical properties of the simulated flow field ( $H(\underline{x}), Q_i(\underline{x})$ ) were evaluated in a similar fashion, for comparison with the ensemble moments predicted by the spectral theory. Note that the spectral theory itself is only approximate. In particular there is no guarantee that the variables  $H$  and  $Q_i$  describing the flow share the properties of homogeneity and ergodicity satisfied by the input log-conductivity field. Indeed, the hydraulic head field is obviously not homogeneous in the mean, since there is a non-vanishing mean head gradient in the longitudinal direction. Moreover, the zero-mean head perturbation:

$$h = H - \langle H \rangle$$

may not be second order stationary/ergodic as the spectral theory assumes, except perhaps asymptotically as  $\sigma_f \rightarrow 0$  (Chapter 4, Section 4.1). Finally, the correlation range of the head perturbation appears to be significantly larger than the



conductivity correlation scale  $\lambda$  (Chapter 3). As a consequence, to obtain a statistically meaningful realization of the hydraulic head field may require a domain much larger than what is needed for a representative realization of the conductivity field. The effect of boundary conditions renders this problem even more acute, as the deterministic constraint on the head near a boundary will tend to propagate towards the interior, in proportion to the correlation range of the hydraulic head.

Accordingly, our strategy for evaluating the statistical properties of the flow field was based on the premise that the flow variables of interest are not necessarily fully homogeneous in three-dimensional space. More precisely, we have found empirically that the preferential direction of spatial inhomogeneity for the finite-domain hydraulic head field was the longitudinal direction parallel to the mean flow. It should not be surprising that the flow be more nearly homogeneous in the direction transverse to the driving force. This was confirmed directly from the numerical solutions by examining the spatial variations of the cross-flow average of the head field as a function of the longitudinal coordinate.

$$\bar{H}(x_1) = \frac{1}{L_2 L_3} \cdot \iint H(\underline{x}) \, dx_2 dx_3 \quad (6.5a)$$

This function exhibited a few large scale fluctuations around the

theoretical linear mean  $\bar{H} = -J_1 \cdot x_1$ , with a wavelength typically on the order of the full domain length: see Figure 6.3 for illustration.

A zero-mean head perturbation  $h$  was then obtained by detrending the numerical head field with the nonlinear mean  $\bar{H}(x_1)$ :

$$h(\underline{x}) = H(\underline{x}) - \bar{H}(x_1) \quad (6.5b)$$

This quantity was assumed to be statistically homogeneous in all three space directions in the interior of the domain. Therefore, the head variance ( $\sigma_h^2$ ) and covariance function ( $R_{hh}$ ) were computed by using the standard spatial averaging procedure as described previously for the case of the log-conductivity field (replace  $f$  by  $h$  in equations 6.4c and 6.4d). The domain of integration was usually taken slightly smaller than the computational flow domain in order to avoid including data located near the boundaries.

The procedure used to analyze the statistical properties of the flux vector  $Q_1(\underline{x})$  was similar, however with one essential difference. By construction, the cross-flow average:

$$\bar{Q}_1(x_1) = \frac{1}{L_2 L_3} \cdot \iint Q_1(\underline{x}) \cdot dx_2 dx_3 \quad (6.7a)$$

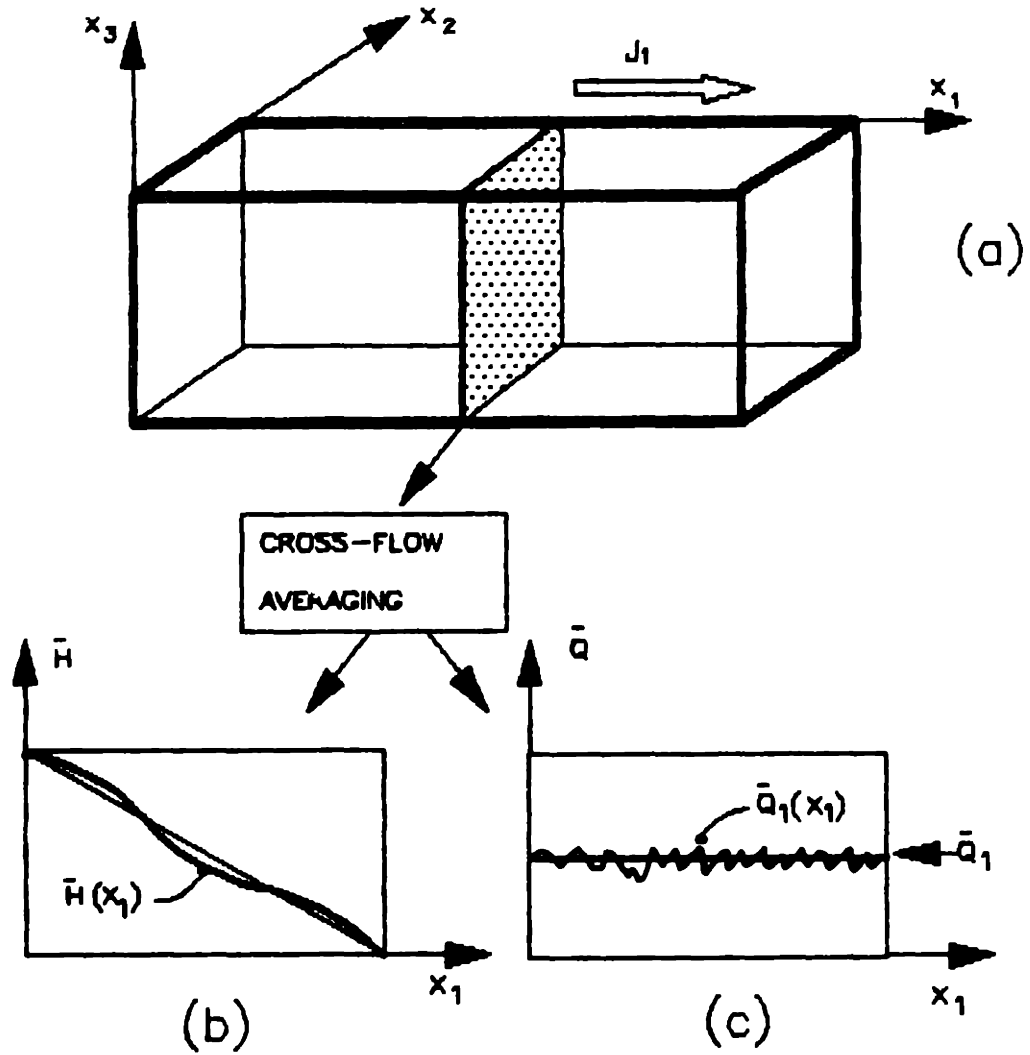


Figure 6.3 Illustration of the spatial averaging procedures used to detrend the hydraulic head field and the flux vector field: (a) Cross-flow averaging, (b) Nonlinear trend  $\bar{h}(x_1)$ , and (c) Approximately constant mean  $\bar{q}_1$ .

is in principle independent of the longitudinal coordinate  $x_1$ , and the transverse mean flux components  $\bar{Q}_2, \bar{Q}_3$  should vanish since all lateral boundaries are impervious. In actual practice, the "one-dimensional" conservative nature of the mean flow was not exactly satisfied by the numerical flux field due to the discrete nature of the solution (numerical errors) leading to slightly inaccurate mass balance. We have found that these discrepancies were sufficiently small to be neglected, particularly for the highest resolution problem A of Table 6.1. Thus  $\bar{Q}_1$  was approximately constant along  $x_1$ , which justified using a three-dimensional average to evaluate the constant mean flux as follows:

$$\bar{Q}_1 = \frac{1}{L_1 L_2 L_3} \cdot \iiint Q_1(x_1, x_2, x_3) dx_1 dx_2 dx_3$$

and similarly for  $\bar{Q}_2$  and  $\bar{Q}_3$ . The ratios  $\bar{Q}_i/\bar{Q}_1 (i=2,3)$  were used to evaluate the relative mass balance error of the numerical solution (ideally  $\bar{Q}_2 = \bar{Q}_3 = 0$ ).

In practice, the flux-integral above was converted into a discrete sum, and the fluxes were evaluated by a finite difference approximation of Darcy equation at mid-nodal locations (staggered grid  $(i_1+1/2, i_2, i_3)$ ) as explained in Chapter 5, equations (5.4) and (5.7). In certain cases (problem B), the

fluxes were evaluated as local cell-averages of neighboring mid-nodal fluxes, in order to obtain a tractable representation of the random velocity field for use in a particle-tracking simulator of solute transport (ongoing research by Gelhar and co-workers at MIT). Finally, the zero-mean flux perturbation:

$$q_i(\underline{x}) = Q_i(\underline{x}) - \bar{Q}_i \quad (6.7b)$$

was assumed to be statistically homogeneous in three-dimensional space. Consequently, the variances  $\sigma_{q_i}^2$  and covariance functions  $R_{q_i q_i}(\underline{\xi})$  were evaluated, for each flux component ( $i=1,2,3$ ), by the standard three-dimensional spatial averaging procedure described in equations (6.4c) and (6.4d), with  $f$  replaced by  $q_i$ . A similar procedure was also applied to the head gradient field  $G_i = \partial H / \partial x_i$  (replace  $Q_i$  by  $G_i$  in equations 6.7).

Last, but not least, the *effective conductivity* in the longitudinal direction was simply evaluated by:

$$\hat{K}_{11} = \frac{\bar{Q}_1}{\bar{J}_1} \quad (6.8)$$

where  $\bar{J}_1$  is the prescribed mean hydraulic gradient (6.2), and  $\bar{Q}_1$  the computed mean flux defined by (6.7a). In the special case of statistically isotropic log-conductivity field, equation (6.8) gives in fact the value of the effective conductivity along any

direction (problems A and B of Table 6.1). On the other hand, in the case of statistically anisotropic log-conductivity (with principal axis  $x_1$  aligned with the mean flow) the transverse components  $\hat{K}_{ii}$  ( $i = 2,3$ ) remain unknown. An additional flow simulation with the mean gradient oriented perpendicularly to the  $x_1$  axis would be needed to determine the effective conductivity perpendicular to stratification.

[d] Finite Size Effects on Estimated statistics

At this point, it may be instructive to examine the possible inaccuracies that may arise from the sampling of a single finite-domain realization of the flow field. We have already pointed out in particular that the hydraulic head field is inherently non-stationary in the mean (ideally linear) and has a larger correlation range than the input conductivity field. Therefore we expect that the computed mean and second order moments of the hydraulic head could be affected by finite-size sampling errors. We propose a simple evaluation of the "equivalent number of independent samples" (sample size) for evaluating sampling errors. Let  $Y(\underline{x})$  be a random field with constant mean,  $\lambda_y$  its correlation scale, and  $L$  the size of the domain of averaging used to estimate its moments. Intuitively, it seems reasonable to define the equivalent sample size as the size of the averaging domain expressed in correlation scale

units, that is:

$$N_Y = \left(\frac{L}{\lambda_Y}\right)^m \quad (6.9)$$

where  $m$  is the dimensionality of the averaging domain ( $m = 1, 2, 3$  for 1D, 2D, 3D averaging). According to standard sampling theory, (Appendix 2A), the sampling errors on the mean and on the standard deviation are of the form:

$$\begin{aligned} \text{Var}(\bar{Y}) &\approx \frac{\sigma^2}{N_Y} \\ \text{Var}(\sigma_Y) &\approx \frac{\sigma_Y^2}{2N_Y} \end{aligned}$$

to leading order in  $N_Y$ . This gives a rough estimate for the relative sampling errors ( $\epsilon$ ) in terms of the sample size ( $N_Y$ ) as follows:

$$\begin{aligned} \epsilon(\bar{Y}) &= \sqrt{\frac{\text{Var}(\bar{Y})}{\sigma^2}} \approx \frac{1}{\sqrt{N_Y}} \\ \epsilon(\sigma_Y) &= \sqrt{\frac{\text{Var}(\sigma_Y)}{\sigma_Y^2}} \approx \frac{1}{\sqrt{2N_Y}} \end{aligned} \quad (6.10)$$

Let us now illustrate the implications of (6.9) and (6.10) for the 1 million node single-realization problem A of Table 6.1 ( $\Delta x_i/\lambda_i = 1/3$  and  $L_i/\lambda_i \approx 33.3$ ). According to

equation (6.9), the sample size of the log-conductivity field is about 37,000 samples in 3D space. From equation (6.10), this implies that the sampling error on the mean ( $\ell n K_G$ ) and the standard deviation ( $\sigma_f$ ) should be on the order of 1% or less. On the other hand, for the hydraulic head field, the spectral theory predicts that the head correlation scales in the longitudinal ( $i=1$ ) and transverse ( $i=2,3$ ) directions are:

$$\begin{aligned} i = 1: \lambda_H^{(1)} &\approx 3.0\lambda \\ i = 2,3: \lambda_H^{(i)} &\approx 7.5\lambda \end{aligned}$$

Therefore, the three-dimensional size of the hydraulic head field is only about 220 independent samples. Moreover, in a 2D cross-section such as the one shown in Figure (6.3), the sample size drops to just about 20 independent head samples!

We may now apply equation (6.10) to evaluate, the sampling errors on the cross-sectional mean  $\bar{H}(x_1)$  and on the standard deviation  $\sigma_H$ . At each given location  $x_1$ , the mean trend  $\bar{H}(x_1)$  was evaluated by a 2D average as defined in equation (6.5a). Therefore, the sampling size is only 20 and the relative error on the mean will be quite large:

$$\epsilon(\bar{H}(x_1)) \approx \frac{1}{\sqrt{20}} \approx 20\%$$



For the head standard deviation, the averaging domain is three-dimensional. Applying equation (6.10) with sample size 220 gives:

$$\epsilon(\sigma_H) \approx \frac{1}{\sqrt{440}} \approx 5\%.$$

The relatively large sampling error on the mean  $\bar{H}(x_1)$  reflects the fact that, in any given cross-section  $x_1$ , the number of independent samples of the head field is quite low. To reduce the error  $\epsilon(\bar{H})$  to 5% would require increasing the lateral side of the domain by a factor of 4 in each transverse direction. This would lead to a grid size of 16 million nodes if the resolution  $\Delta x/\lambda = 1/3$  is kept fixed! Unfortunately, the truncation error analysis of Chapter 5 (Section 5.2) showed that a grid resolution on the order of  $1/3$  or less was required to obtain a reasonable numerical accuracy on the computed flux vector field, which has a much smaller correlation range than the head (typically on the order of  $\lambda$ ). The inherent disparity in the fluctuation scales of the flux and head fields is therefore the main cause of trouble in the single-realization approach, as will be seen.

In summary, we have found that the soundness of the single-realization approach depends on the competing requirements of large domain size (in order to obtain a large number of samples of the hydraulic head in space), and fine grid resolution (in order to capture the short range fluctuations of the

conductivity and flux vector). The situation will be even more severe in the case of statistically anisotropic log-conductivities, as will be seen later (section 6.4). Our particular choices of domain size and grid resolution (Table 6.1) usually tended to sacrifice sample size for resolution. The sampling errors due to modest domain size relative to the long range correlation of the hydraulic head, were alleviated in part by using the "ad hoc" detrending procedure of the head field as explained in equations (6.5) above.

In the sequel, we will rely on the methodology just described for analyzing the single-realization flow simulations listed in Table 6.1 above. The table also indicates the section where each particular flow simulation is being analyzed. Section 6.2 treats the medium-size isotropic problem B (130,000 nodes) and emphasizes some of the most obvious physical features of the flow field. The preliminary statistical analysis there does not include correlation functions. Section 6.3 develops a more comprehensive statistical analysis of the flow field for the isotropic problem A (1 million nodes), including a systematic comparison to spectral solutions in terms of single-point and two-point moments. Finally, Section 6.4 focuses on preliminary results obtained with the anisotropic problems E and F (220,000 nodes). The key results of these analyzes are summarized and discussed in the last section 6.5.

## 6.2 Preliminary Analysis of 3D Isotropic Flow Simulations (130,000 Nodes)

In this section, we analyze in some detail the numerical flow fields obtained for the isotropic problem (B) of Table 6.1 for two different values of the log-conductivity standard deviation ( $\sigma_f = 1.0$  and  $\sigma_f \simeq 2.3$ ). The statistical analysis will be limited here to single-point moments, due to the relatively modest size of the grid. On the other hand, we have chosen in this example to emphasize physical interpretation rather than statistical analysis, by using visual representations of the hydraulic head and flux vector fields. Some of the results discussed in this section were reported in a recent paper by Ababou et al. (1987).

### [a] Flow field visualization:

The method used here to visualize the three-dimensional flow fields relies heavily on "two-dimensional plots" showing contour lines in selected slices, and occasionally on "one-dimensional plots" of the solution along selected transects. In all cases, the slices and transects were selected at locations coinciding with the geometric center of the flow domain. For the

"isotropic" simulations at hand, the domain was a cube. Figure 6.4 shows the location and orientation of three different slices of interest. It is worth noting that the flow patterns in the horizontal slice parallel to flow (top) and in the vertical slice parallel to flow (centerpiece) should be statistically indistinguishable in the "isotropic" case. The flow pattern in the cross-flow slice (bottom) should look quite different, since the mean hydraulic gradient should be approximately zero in that plane.

In addition, we have included visual representations of the input conductivity fields in the form of 2D contour lines and, occasionally, 3D contour surfaces. We recognize that a three-dimensional representation of the flow fields could be also of interest, possibly in the form of contour surfaces of the hydraulic head and/or stream-surfaces of the flux vector field. This however was not attempted here. Nevertheless, we will see that a number of interesting features emerge from a visual inspection of low-dimensional plots of the random flow fields.

#### [b] Qualitative Analysis of the Flow Pattern

Let us now discuss the numerical solutions obtained for the isotropic problem "B" of Table 6.1. This flow problem was solved for two different values of the log-conductivity standard

deviation ( $\sigma_f = 1.0$  and  $\sigma_f = 2.3025$ ) on a cubic grid of size  $N \approx 130,000$  nodes. Recall that the boundary conditions were fixed heads on two opposite faces, and zero fluxes on all other boundaries (Figure 6.1). We have seen that this is equivalent to imposing a large-scale hydraulic gradient aligned with the mean flow direction. The value chosen for the hydraulic gradient ( $J_1 = 0.004$ ) is typical for natural groundwater flow systems. The random conductivity field was obtained from a single replica of the 3D isotropic Markov field, generated by the Turning Band Method. The grid resolution  $\Delta x_i / \lambda_i$  was taken equal to one half, and the cubic domain size was 25 correlation scales in each direction. About one hundred line processes were used in the Turning Band generator, with a random distribution of lines in space according to a uniform spherical distribution (see Chapter 2 and Tompson et al., 1987). The resulting  $\ln K$  field is Gaussian, with an isotropic exponential covariance function in 3D space, as explained in the previous section. Note that the same replica was used for the two sub-problems  $\sigma_f = 1.0$  and  $\sigma_f = 2.3025$ , by rescaling the  $\ln K$  field in the obvious way.

Figure 6.5 shows the low and high conductivity regions (respectively black and white patches) in a two-dimensional slice for the case  $\sigma_f \approx 2.3$ . The contouring routine we used for this and all other contour plots in this work was the Gconmap program

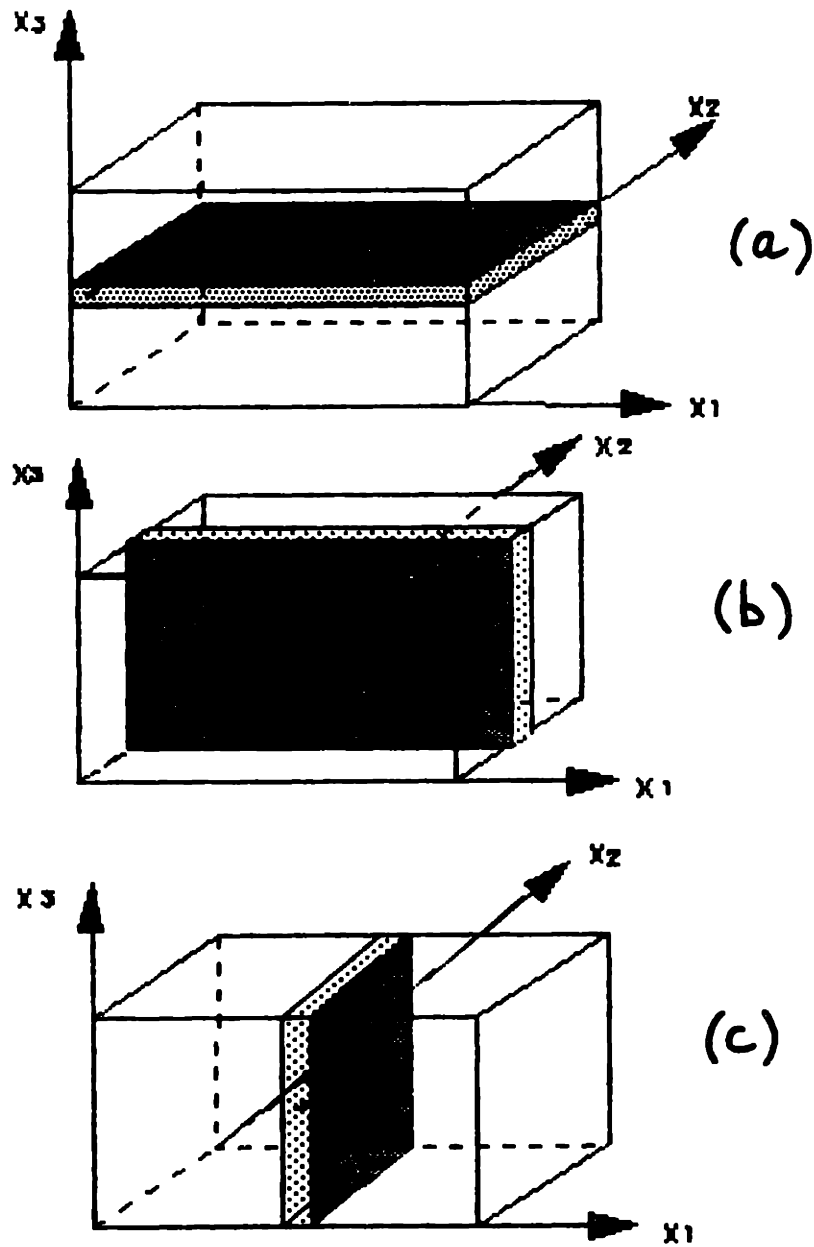


Figure 6.4 Sketch of the two-dimensional slices used for contour plots of the three-dimensional flow fields. The mean flow direction is  $x_1$ . From top to bottom: (a) Horizontal slice parallel to flow, (b) Vertical slice parallel to flow, and (c) Vertical slice orthogonal to flow

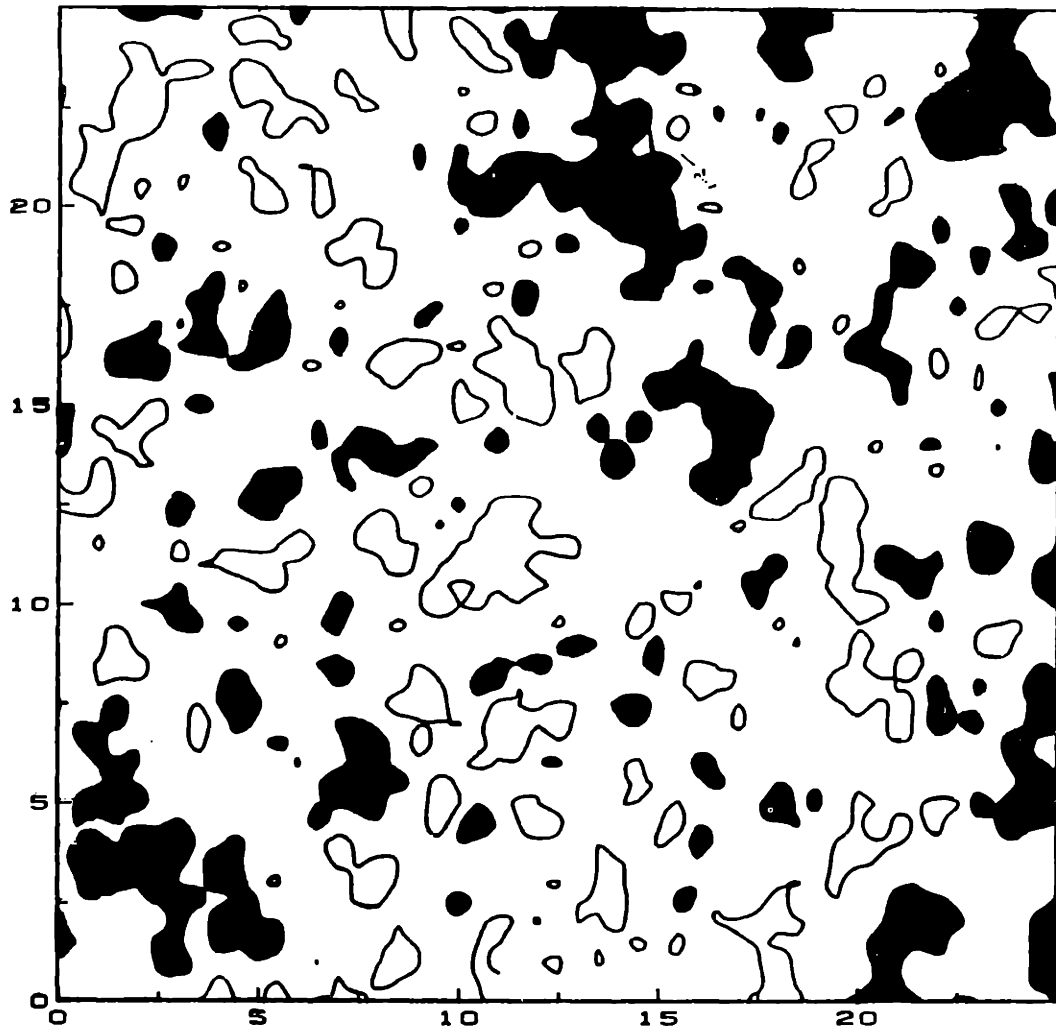


Figure 6.5 Two-dimensional excursion regions of the 3D random conductivity field in a slice (problem B with  $\sigma_f = 2.3025$ ). The black and white patches indicate regions where  $K/K_G \leq 0.1$  and  $K/K_G \geq 10$ , respectively.

(Dennis McLaughlin). The contours correspond to regions where the conductivity is one order of magnitude larger or one order of magnitude smaller than the geometric mean ( $K_G = 1$ ). For  $\sigma_f \simeq 2.3$ , about 30% of the whole space is occupied by such regions, equally distributed among low and high values (15% each). Note that some of the patches appear to be significantly larger than the correlation length ( $\lambda = 1$ ). As expected, they seem isotropically oriented in space.

Figure 6.6 shows an attempt at representing the corresponding high conductivity contour surfaces in three-dimensional space. Here, we have represented only those excursion regions where the conductivity is one order of magnitude larger than the geometric mean. The smallest excursion regions had to be filtered out in order to obtain a clearer representation. This was done by applying a linear filter based on a weighted local average of nearest neighbors. Even with this artificial device, the picture remains somewhat misleading: the excursion regions seem to crowd the page, although they really occupy only 15% of the three-dimensional cube. In order to give a feeling of the technical difficulty, we also show in Figure 6.7 a similar plot for the excursion regions corresponding approximately to  $K/K_G > 3$ . It may be hard to believe that these regions only occupy about 30% of the cubic domain. The "hidden



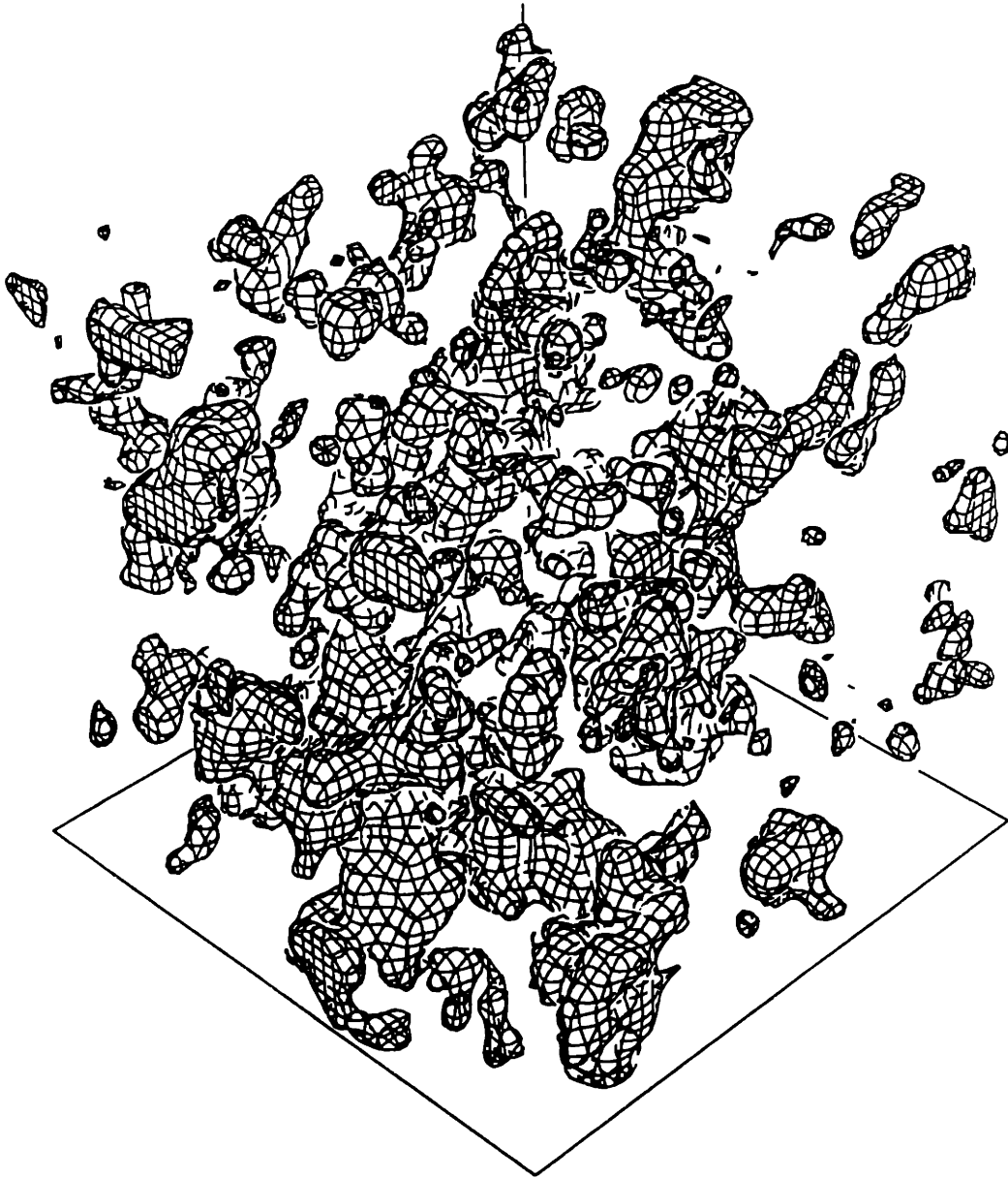


Figure 6.6 Three-dimensional excursion regions of the 3D random conductivity field in a cubic domain with 130,000 grid points (problem B with  $\sigma_f = 2.3025$ ). The regions correspond to high values of the conductivity such that  $K/K_G \geq 10$ .

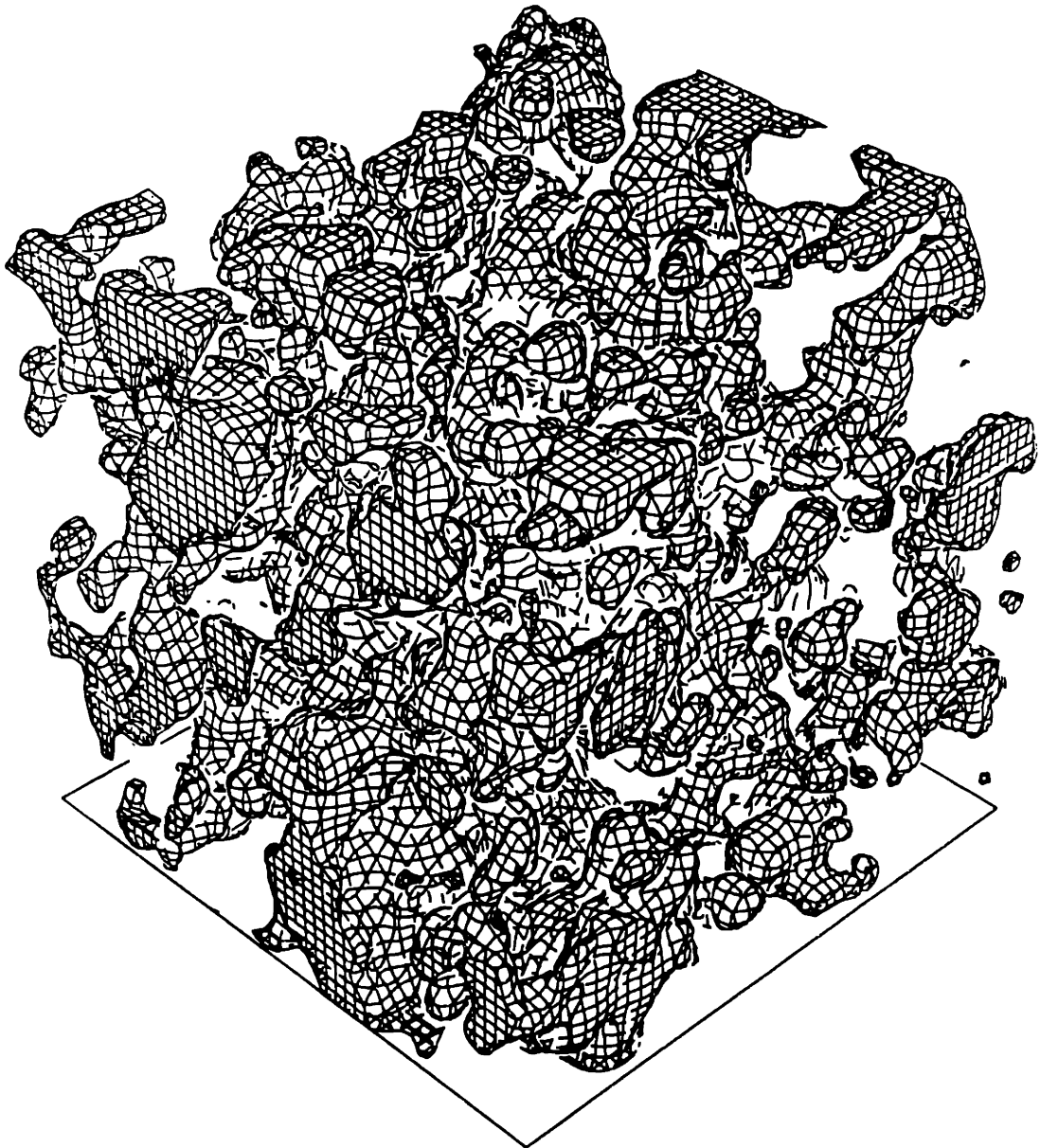


Figure 6.7 Same as Figure (6.6) except that  $K/K_G \geq \sqrt{10}$ .

lines algorithm" of the package we used (Graf Kit), did not seem able to handle properly such a contorted, random-like function of space. More advanced 3D contouring softwares should be used in these difficult cases.

Figure 6.8 displays the contour lines of the computed hydraulic head in a horizontal slice parallel to the mean flow, for  $\sigma_f \approx 2.3$ . Low conductivity contours are also shown in the background. The white areas, devoid of background conductivity contours, correspond to regions where the conductivity is greater than about 30% the geometric mean value (pathways for flow). It is worth noting that the head gradient steepens near local minima of the conductivity fields, and becomes flatter in the white areas corresponding to larger conductivities. This interesting behaviour could perhaps be deduced from the one-dimensional Darcy equation:

$$q = - K(x) \frac{dH}{dx} \text{ (constant)}$$

However, the generalization to three-dimensional flow is far from obvious. The observed one-dimensional behavior could be explained by the fact that the flow field in this example is globally one-dimensional, since all lateral boundaries are impervious. Incidentally, note that the head contour lines are

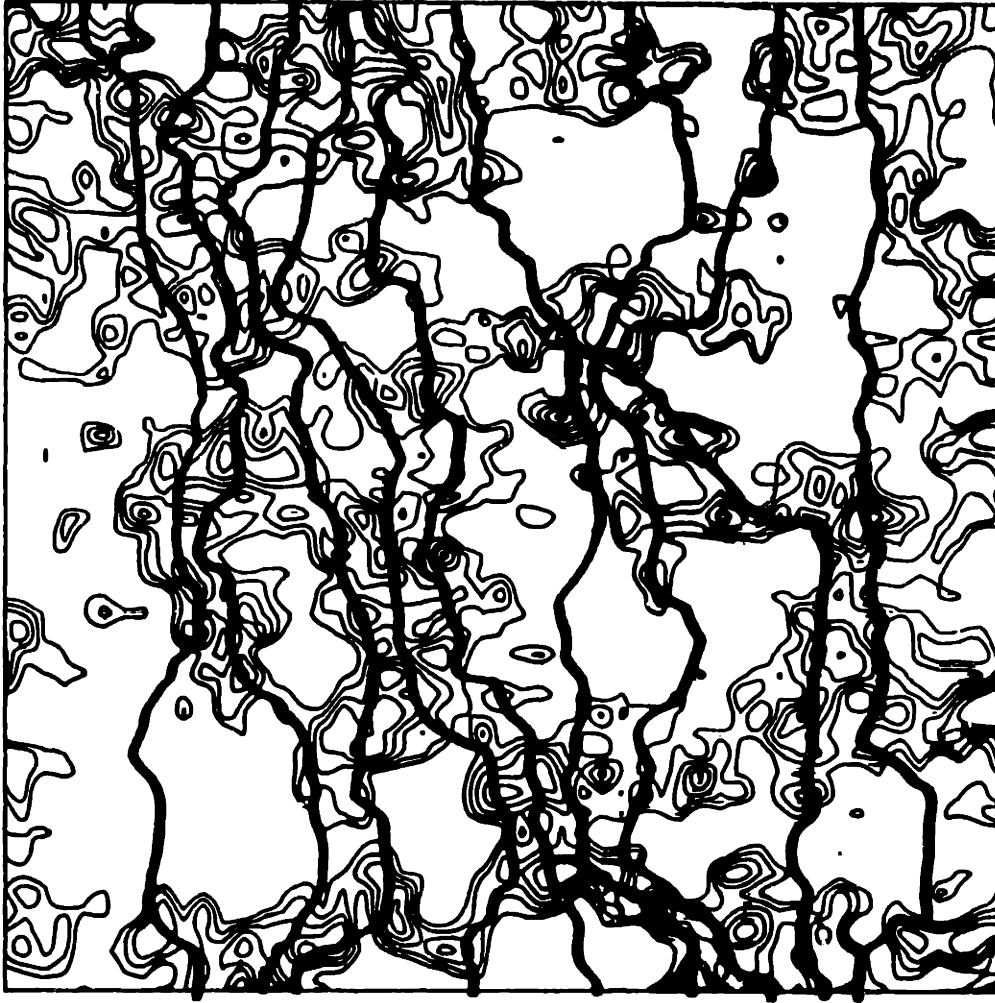


Figure 6.8 Hydraulic head contours in a horizontal slice parallel to the mean flow for problem B with  $\sigma_f = 2.3025$ . There are 10 contour lines of equally spaced head values including the right and left boundaries. Low conductivity contours are shown in the background ( $\log_{10}(K/K_G) = 0, -0.5, -1, -5, -2$ )

orthogonal to the lateral boundaries (as they should). The influence of such artificial boundaries on the fluctuations of the head in the interior does not seem overly important: see for instance how the left-most head contour line of Figure (6.8) joins the two lateral boundaries.

Figure 6.9 compares the hydraulic head contours for  $\sigma_f = 1.0$  and  $\sigma_f \simeq 2.3$  in the same horizontal slice as Figure (6.8). The influence of the log-conductivity variability ( $\sigma_f$ ) is quite dramatic: both the small scale and large scale fluctuations (wiggles and smooth undulations) of the head contour lines are significantly amplified when  $\sigma_f$  increases from 1.0 (top) to 2.3 (bottom). Note that the same replica of the log-conductivity field was used, so that the pattern of fluctuations of  $\ln K$  was the same for the top and bottom pictures of Figure (6.9). Another remarkable feature that emerges from these pictures is that the hydraulic head contours are relatively smooth compared to the noisy input conductivity. The typical fluctuations scale of the head contour lines in the cross-flow direction seems to be much larger than the  $\lambda$ -scale of conductivity. This feature is indeed predicted by the spectral theory.

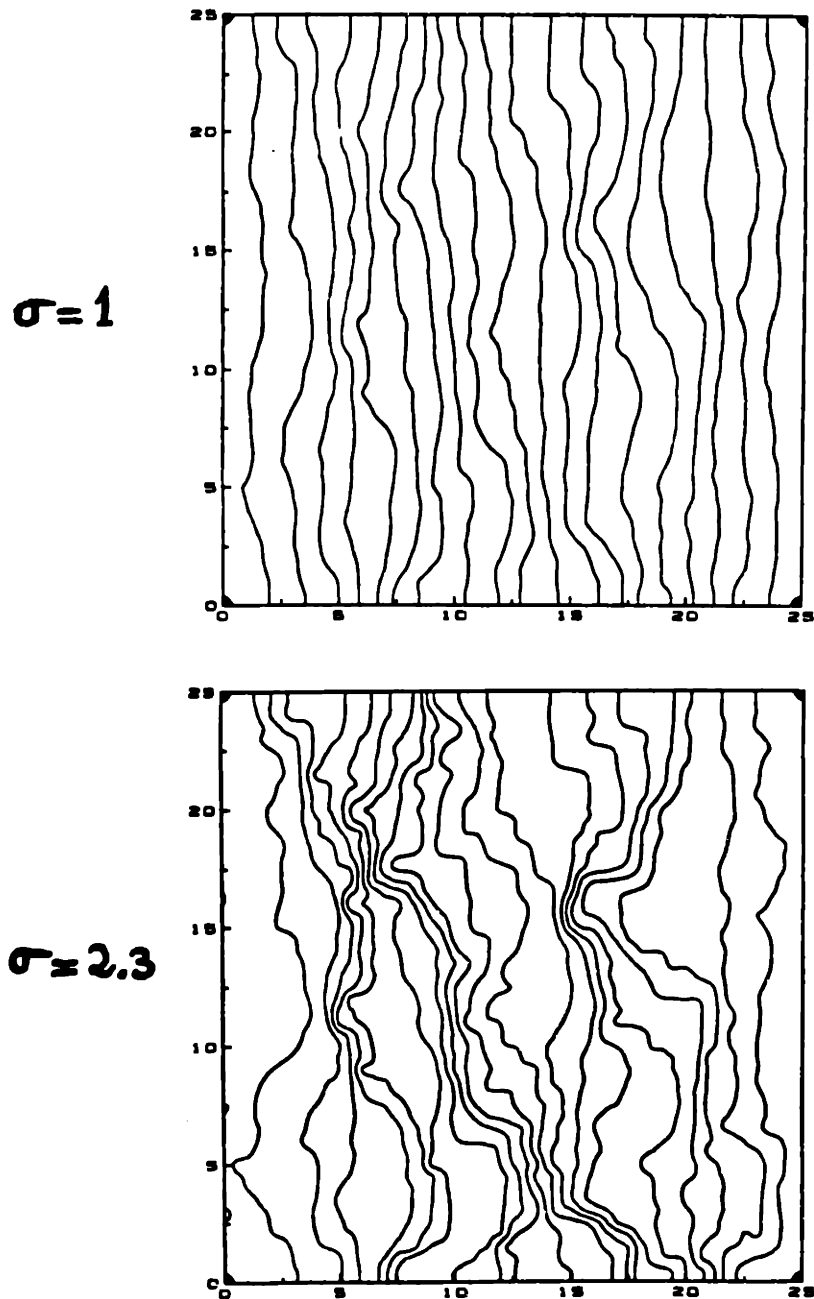


Figure 6.9 Comparison of hydraulic head contours in a horizontal slice parallel to flow for  $\sigma_f = 1$  (top) and  $\sigma_f \approx 2.3025$  (bottom) (Problem B). These are 21 contour lines of equally spaced head values, including the right and left boundaries.

More precisely, recall from Chapter 3 that the head correlation function predicted by the spectral theory has a larger correlation range than the input log-conductivity fields, about  $7.5\lambda$  in the transverse direction and  $3.0\lambda$  in the mean flow direction (see Figure 3.1). Our preliminary calculations of the head covariance function, based on the spatial averaging method outlined in the previous section (equations 6.4 and 6.6), showed approximately the same behaviour for the case of moderate variability  $\sigma_f = 1$ . However, the head covariance functions obtained for the case of higher variability did not agree with the spectral theory, probably due to the limited size of the domain and, perhaps, to the relatively coarse grid resolution (see problem B data in Table 6.1).

Nevertheless, it turns out that the computed head standard deviations matched to within 10% the values predicted by the spectral theory (equation 3.21) for both cases of moderate and high variability,  $\sigma_f = 1.0$  and  $\sigma_f \approx 2.3$ . Figure (6.10) shows the slowly fluctuating nonlinear trend around which the head variance was computed; a hypothetical linear mean head profile is superimposed for comparison (top picture). The bottom part of the figure displays a typical transect of the head process around the nonlinear trend. It is important to note that the computed head deviation would have been much larger than the

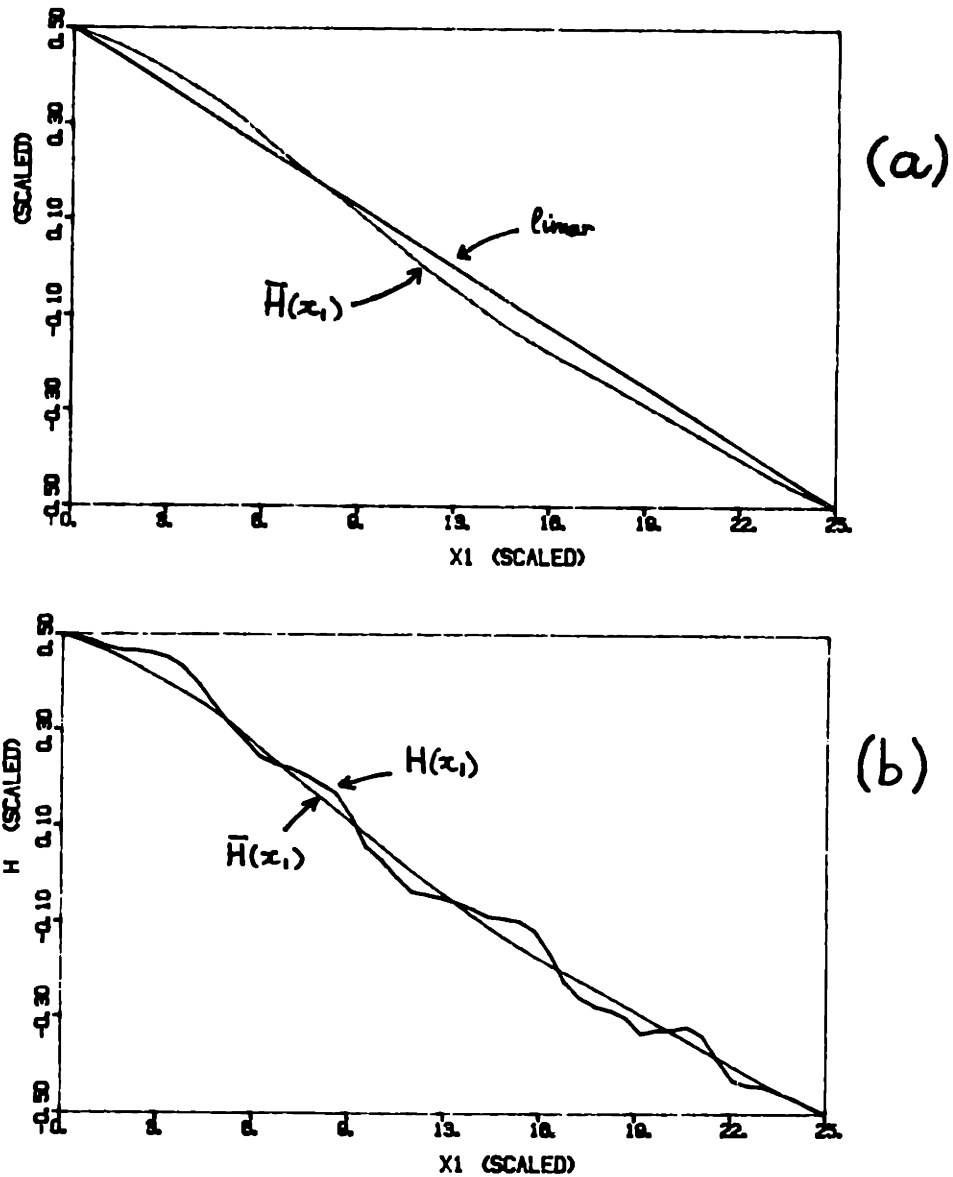


Figure 6.10 One-dimensional representation of the spatial fluctuations of the hydraulic head (Problem B -  $\sigma_f \approx 2.3$ ):

- (a) Comparison of computed trend  $\bar{H}(X_1)$  with hypothetical linear profile
- (b) Fluctuations of the head field around the trend for a particular transect parallel the mean flow



predicted spectral value if the hypothetical linear mean had been used instead. In our view, the head variance obtained in this way would be meaningless, since the whole method is based on the premise that the second order moments of the flow field are spatially homogeneous.

It is rather encouraging that our detrending technique leads to a close agreement between the theoretical (spectral) and numerical standard deviations of the head field, even for the relatively modest size problem at hand. This was confirmed for a number of other cases, isotropic and anisotropic, as will be seen in later sections.

### [c] Statistical Analysis of Single-point Moments

A more complete set of single-point moments of the numerical flow field is given in Table 6.2. The table lists the values of the head and flux vector standard deviations, as well as the effective conductivities, obtained by the spatial averaging techniques described in the previous section (equations 6.1-6.8). For comparison, the values predicted by the spectral theory are also listed in the same table (in parenthesis). The spectral formulas used to compute  $\sigma_H$ ,  $K_{eff}$ , and  $\sigma_{q_1}$ , were given in equations (3.21), (3.23) and (3.26) of Chapter 3. Note that

TABLE 6.2

COMPARISON OF NUMERICAL AND SPECTRAL THEORY STATISTICS FOR THE  
 "ISOTROPIC" FLOW PROBLEM B OF TABLE 6.1 ( $N \approx 130000$  NODES).  
 THE SPECTRAL THEORY STATISTICS ARE SHOWN IN PARENTHESIS.

	$\sigma_f = 1.0$	$\sigma_f = 2.3025$
$\sigma_f$	.002510 (.002309)	.005901 (.005317)
$\sigma_{q_1}$	.003820 ((.003451))	.04630 ((.01628))
$\sigma_{q_2}$	.001299 ((.001220))	.01959 ((.00576))
$\sigma_{q_3}$	.001313 ((.001220))	.02148 ((.00576))
$\sigma_{q_3}/\sigma_{q_1}$	.344 (.354)	.464 (.354)
$\bar{Q}_1$	.00527 (.00472)	.01604 (.00968)
$\bar{Q}_2/\bar{Q}_1$	.054 (.000)	.161 (.000)
$\bar{Q}_3/\bar{Q}_1$	-.066 (.000)	.011 (.000)
$K_{\text{eff}}$	1.318 (1.181)	4.010 (2.420)

the flux standard deviations  $\sigma_{q_1}$  shown in double parenthesis were computed from a modified version of the spectral theory of Geihar and Axness (1983), as explained in Section 4.3 of Chapter 4. The conclusions to be drawn from Table 6.2 are summarized below.

The most encouraging result from Table 6.2 is that all the statistics computed from the simulated flow field in the case of moderate variability ( $\sigma_f = 1.0$ ) agree with the spectral theory with a 10% margin of error. On the other hand, in the case of large variability ( $\sigma_f \approx 2.3$ ), there is a serious discrepancy for most of the statistics related to the flux vector. The most robust statistics appear to be the head standard deviation ( $\sigma_H$ ) and the ratio of transverse to longitudinal flux standard deviations ( $\sigma_{q_T} / \sigma_{q_L}$ ):

$$\sigma_H \approx \frac{1}{\sqrt{3}} \sigma_f J_1 \lambda$$

$$\frac{\sigma_{q_T}}{\sigma_{q_L}} \approx \frac{1}{\sqrt{8}}$$

It is remarkable that the ratio  $\sigma_{q_T} / \sigma_{q_L}$ , which indicates the relative variability of the transverse-versus-longitudinal flux

components, does not depend on  $\sigma_f$ . This particular property of the flow field predicted by the spectral theory, is approximately verified by the numerical solutions.

We believe that the discrepancies between the theoretical and numerical values of the flux deviation and effective conductivity obtained for  $\sigma_f \simeq 2.3$  are due to the combined effects of insufficient domain size ( $K_{eff}$ ), insufficient grid resolution ( $\sigma_{q_i}$  and  $K_{eff}$ ), and perhaps inaccurate first order spectral solution in cases of high variability (small  $\sigma_f$  assumption). The insufficient grid resolution (1/2) could be at the origin of the mass balance error indicated by the non-zero ratio  $\bar{Q}_2/\bar{Q}_1$  (11.6% for  $\sigma_f \simeq 2.3$ ); this significant error could also be explained by the fact that the fluxes were computed in this case as local "cell averages" of mid-nodal values, which might not be the best strategy. At any rate, the questions raised above motivated our subsequent use of supercomputing capabilities to simulate stochastic flow problems on larger and finer grids (1 million nodes); this will be examined separately in a forthcoming section. In comparison, recall that the grid size for the flow problem at hand was "only" 130,000 nodes.

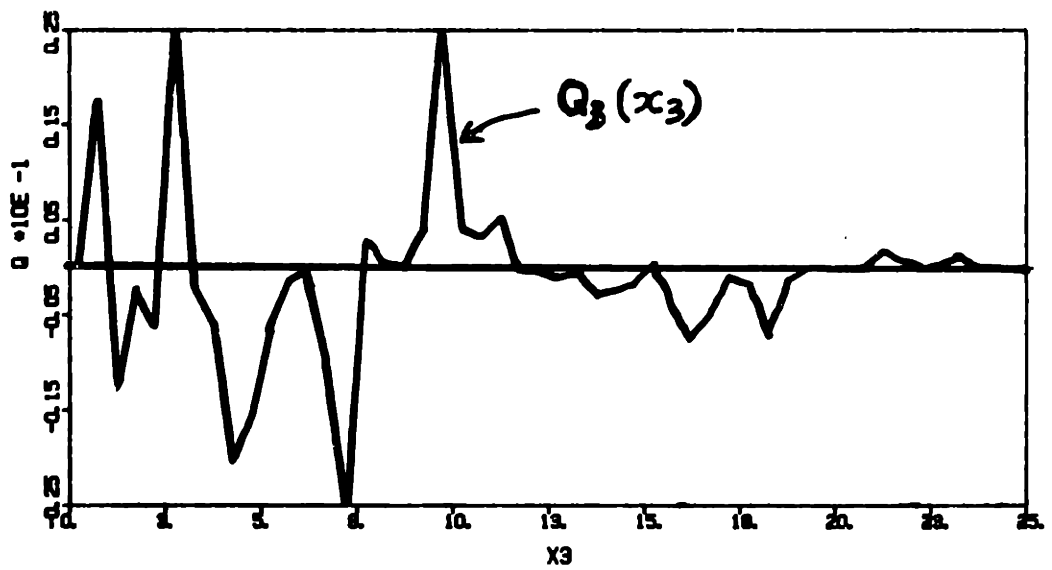


Figure 6.13 Transverse flux component  $Q_3$  along a transect  $x_3$  transverse to the mean flow (isotropic Problem B,  $\sigma_f = 2.3025$ )

[d] Qualitative Analysis of Flux Vector Field

In spite of the insufficient grid resolution, we found that the flow problem at hand was sufficiently representative to justify a preliminary qualitative analysis of the simulated flux vector field. Figures (6.11) to (6.15) depict the spatial variability of various flux components in the case  $\sigma_f \approx 2.3$ . The first three figures show the fluctuations of  $Q_i(\underline{x})$  along selected transects, and the next two figures display the pattern of  $Q_i(\underline{x})$  in selected slices. In Figure (6.11), the longitudinal flux component  $Q_1$  is plotted along the mean flow direction  $x_1$ ; the mean trend  $\bar{Q}_1(x_1)$  is also displayed for comparison. Observe the sharp peaks of  $Q_1(x_1)$  at local maxima, compared to the smooth local minima near zero. This behaviour indicates a positively skewed distribution, as would be the case for a positive log-normally distributed random function: see for instance the plot  $K(\underline{x})$  given in Figure 2.3 of Chapter 2. In contrast, the transverse flux components  $Q_2$  and  $Q_3$  depicted in Figure (6.12) and Figure (6.13) appear to fluctuate symmetrically around their zero mean value, as expected, due to the absence of a mean driving force in the transverse directions.

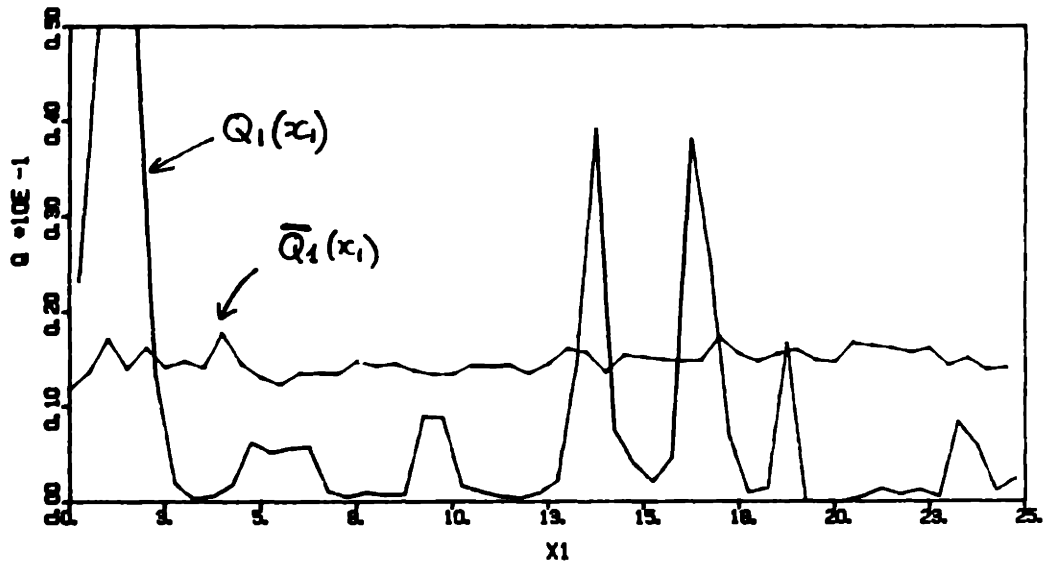


Figure 6.11 Longitudinal flux component  $Q_1$  along a transect parallel to the mean flow direction  $x_1$  (isotropic Problem B,  $\sigma_f = 2.3025$ )

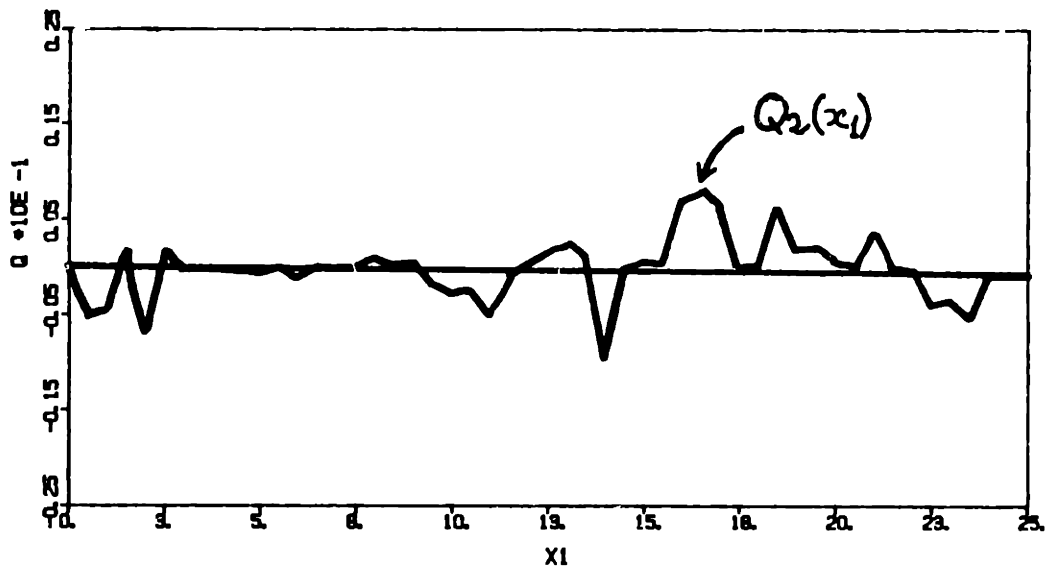


Figure 6.12 Transverse flux component  $Q_2$  along a transect parallel to the mean flow direction  $x_1$  (isotropic Problem B,  $\sigma_f = 2.3025$ )



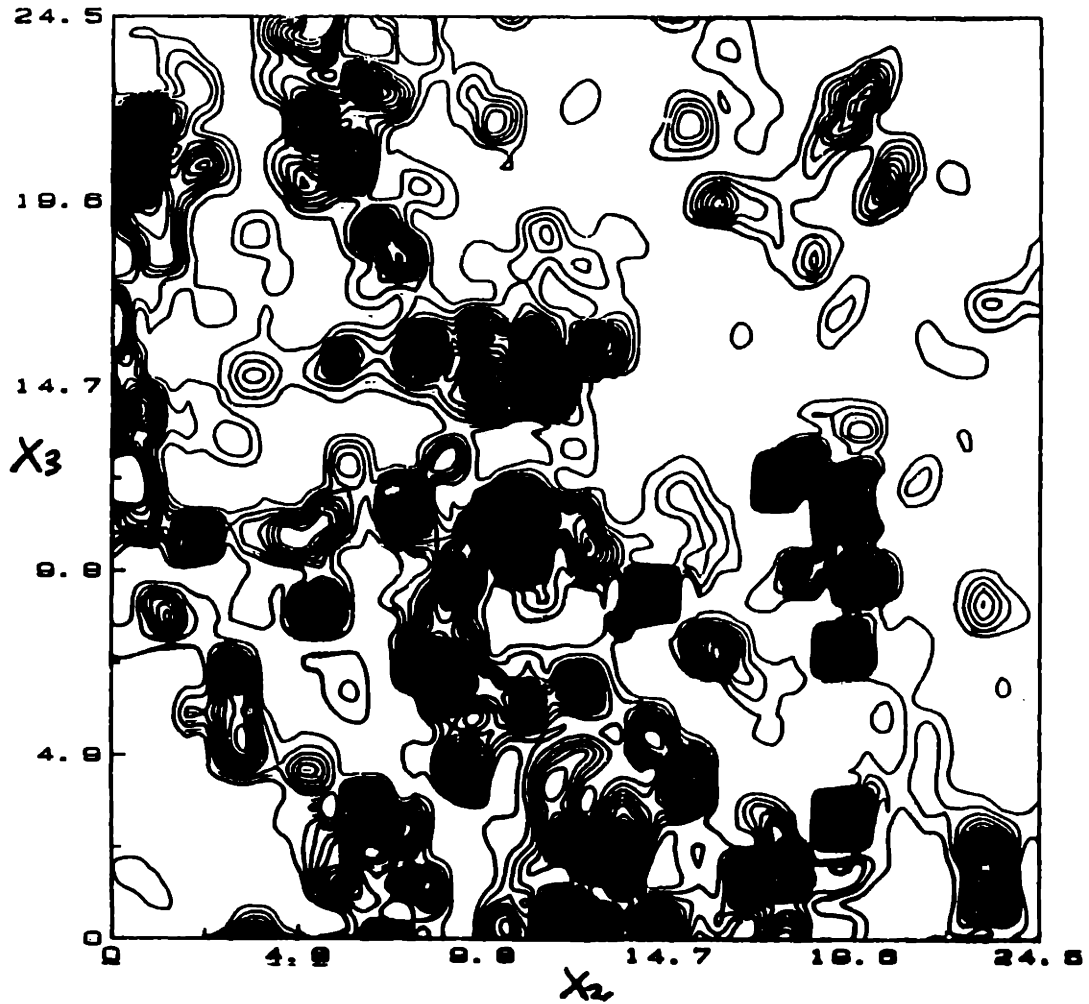


Figure 6.14 Contour lines of the longitudinal flux component  $Q_1$  in a vertical slice transverse to the mean flow (isotropic Problem B,  $\sigma_f = 2.3025$ ). The isovalues are equally spaced, from  $Q_1 = 0$  up; the black patches correspond to high values of  $Q_1$  well above the mean  $\bar{Q}_1$ .

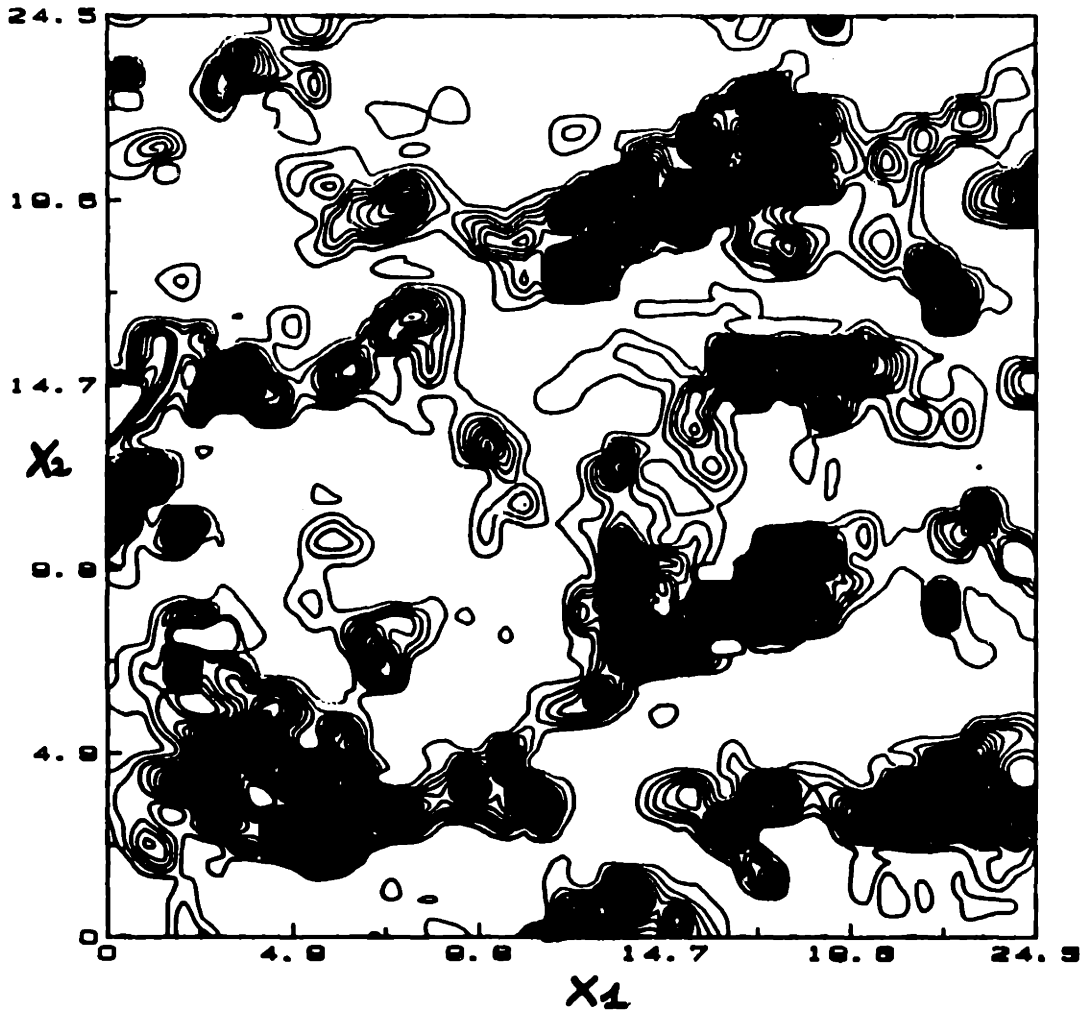


Figure 6.15 Same as Figure 6.14, except that the  $Q_1$ -contour lines are shown in a horizontal slice parallel to the mean flow (isotropic Problem B,  $\sigma_f = 2.3025$ ). The isovalues are equally spaced, from  $Q_1 = 0$  up; the black patches correspond to high values of  $Q_1$  well above the mean  $\bar{Q}_1$ .

Finally, let us comment on two more figures showing equally spaced isovalue contours of the longitudinal flux component  $Q_1$  in selected slices. Figure (6.14) shows  $Q_1(x)$  in a vertical plane transverse to the mean flow, i.e., such that the mean flow is orthogonal to the sheet of paper, pointing towards it. The regions of high "velocity" are highlighted in black: one might think of a sieve, with the black patches corresponding to holes or preferential pathways for flow. Two notable features emerge from this picture. First, it appears once again that local maxima (black patches) are much narrower than local minima (white areas). Second, the excursion regions of  $Q_1$  (e.g., the black patches) are more or less isotropically oriented in the cross-flow plane, as expected. However, note the quasi-rectangular shape of some of the smaller patches. This is probably due to insufficient grid resolution: the orthogonal geometry of the grid induces an artificial anisotropy of the flow field at the scale of the mesh.

It may be interesting to compare the near isotropic pattern of excursion regions of Figure (6.14) to those shown in the last Figure (6.15). In the latter case, the selected slice was in a horizontal plane parallel to flow (water moves from left to right in the plane of the sheet). The high excursion regions of  $Q_1$  appear to be elongated in the longitudinal direction.

This indicates that the longitudinal flux is more strongly correlated in the mean flow direction than across the flow. This property is indeed in agreement with the findings of the spectral theory (Figure 3.2 of Chapter 3). A direct comparison of numerical and theoretical flux correlation functions for the larger simulation (1 million node problem "A") will confirm these qualitative observations.

[e] Summary of Findings

In summary, we have found that the relatively modest size flow simulation at hand (130,000 nodes) produced a flow pattern in accordance with the findings of the spectral theory for a number of features, such as the head variance and, for moderate variability, the flux variance and the effective conductivity. The spatial structures of the hydraulic head and the longitudinal flux component were *qualitatively* in agreement with the behavior predicted by the spectral theory. It is remarkable that meaningful information could be obtained from a single realization of the flow field small enough to be produced on a minicomputer (Microvax 2).

However, we have also found some significant discrepancies between the spectral theory and the numerical solutions at high variability, particularly concerning the flux standard deviations  $\sigma_{q_1}$ , and the effective conductivity  $K_{\text{eff}}$ . The observed discrepancies could be due to a combination of truncation errors (insufficient resolution), sampling errors (finite size effects), and possibly to the increasing inaccuracy of the spectral theory as  $\sigma_f$  increases. This latter possibility may be indicated by the fact that the longitudinal flux component appeared to have a positively skewed distribution. This behavior seems to make sense intuitively, as the Darcy equation shows that  $Q_1$  can be expressed by Darcy's equations:

$$Q_1(\underline{x}) = K(\underline{x}) \cdot J_1 - K(\underline{x}) \cdot \frac{\partial h}{\partial x_1}$$

where the first term is a log-normally distributed random field. Now, the first order spectral theory obviously cannot take this kind of third order effect into account, since third order moments are ignored.

In order to try to resolve the questions of the accuracy of the spectral theory as  $\sigma_f$  increases, we proceed to

analyze in the next section a series of larger flow realizations on a 1 Million node grid.

### 6.3 Statistical Analysis of 3D Isotropic Flow Simulations (1 Million Nodes)

#### [a] Preliminary Considerations

The large single-realization flow problem to be analyzed here (problem A of Table 6.1) is similar to the previous one except for the finer grid resolution ( $\Delta x_i/\lambda_i = 1/3$  instead of  $1/2$ ) and larger domain size ( $L_i/\lambda_i = 33$  instead of 25). It may be instructive to begin by comparing how the difference in size could affect the statistical representativity of the flow field. For this purpose, let us use the simplified analysis of sampling errors outlined in section 6.1 (see equation 6.10 and the example below it). Thus, the sampling error on the mean hydraulic head  $\bar{H}(x_1)$  was evaluated as the inverse square-root of the number of head samples available in a cross-section transverse to the mean flow direction. This number is 20 for the problem (A) at hand,

compared to 10 for the previous problem (B). The relative sampling error on the mean  $\bar{H}(x_1)$ , according to equation (6.10), would then be about 20% for problem A, compared to about 30% for problem B. Thus, we expect that the fluctuations of the nonlinear trend  $\bar{H}(x_1)$  will be less pronounced for the larger problem A. In addition, we also expect a better accuracy on the flux variance due to the finer grid resolution. This point will be discussed in more detail later.

We focus now on the three single-realization flow fields ( $\sigma_f = 1.0, 1.732, 2.3025$ ) corresponding to the isotropic problem (A) of Table 6.1. On the numerical side, let us mention that the iterative solution of these 1 Million node problems was fully analyzed in Chapter 5 (Section 5.3, Table 5.4 and accompanying figures). Recall in particular that the three subproblems were solved in sequence on a Cray 2 machine, requiring a total of about four hours of CPU time. Finally, it may be worth noting that a single replica of the log-conductivity field was used for the three subproblems. This was done by rescaling  $\ln K(\underline{x})$  in the obvious way to accommodate different values of the log-conductivity standard deviation  $\sigma_f$ .

[b] Conductivity Field Generation and Analysis:

The conductivity field was generated, as before, by the three-dimensional Turning Band generator of Tompson, Ababou and Gelhar, 1987. For the case at hand, a three-dimensional isotropic Markov field  $\ln K(\underline{x})$  was generated over the  $101 \times 101 \times 101$  cubic finite difference grid. The particular data used in the Turning Band generator were as follows: 1000 lines distributed randomly in space ("turning band"), 300 harmonics per line for the generation of each line spectrum, and a few hundred points per line (up to 500) for the generation of the corresponding line processes. Thus, the spatial resolution on each line was about  $1/5$  relative to the mesh size. The resolution in Fourier space was  $\Delta \tilde{k} = 1/3$ , and the high wavenumber cut-off was  $\tilde{k}_{\max} = 100$  ( $\tilde{k}$  is a normalized wavenumber equal to  $\lambda k$ ). According to the empirical rules developed by Tompson et al. 1987, these parameters are quite conservative and should lead to statistically meaningful results as far as the conductivity field is concerned.

It may also be important to note that the random number generator we used was slightly different from Tompson et al. 1987. We took advantage of the fact that the largest integer on the 64-bit words Cray 2 machine is very large ( $N = 2^{63} \approx 9 \cdot 10^{18}$ ). In these conditions, our literature review indicated that one of



the most reliable random number generators available to date was the "Type 2" congruent method of Fishman and Moore (1986) as defined below. Let  $R$  be a random number uniformly distributed in  $[0,1]$ . Then a sequence of pseudo-random numbers  $R_k$  is obtained by:

$$\begin{cases} N_{k+1} = L \cdot N_k \pmod{M} \\ R_{k+1} = \text{Float}(N_{k+1})/\text{Float}(M) \end{cases} \quad (6.11a)$$

where the modulus ( $M$ ) and the multiplier ( $L$ ) are, respectively:

$$\begin{cases} M = 2^{31} - 1 = 2,147,483,647 \\ L = 950,706,376 \end{cases} \quad (6.11b)$$

and the initial seed  $N_0$  can be any number less than  $M$  (e.g.,  $N_0 = 1$ ). The advantage of this particular random number generator is that it is equidistributed and has a very large cycle length  $M - 1$ , i.e., about 2 billion numbers. The multiplier  $L$  given above was among the "best" in a series of tests developed by Fishman and Moore (1986).

To illustrate the soundness of the random field generator, we show in Table 6.3 a comparison between the

TABLE 6.3

COMPARISON OF THEORETICAL (ENSEMBLE) MOMENTS AND COMPUTED (SPATIAL) MOMENTS, FOR THE SINGLE REPLICA OF THE ISOTROPIC 3D MARKOV LOG-CONDUCTIVITY FIELD GENERATED BY THE TURNING BAND METHOD (1 MILLION NODE FLOW PROBLEM)

	INPUT Theoretical Values	OUTPUT Computed Values	RELATIVE ERROR
$\langle f \rangle$	0	0.1966	+2 %
$\sigma_f$	1.0	0.9983	-0.2%
$R_{ff}(\lambda, 0, 0)$	0.3679	0.3860	+5 %
$R_{ff}(0, \lambda, 0)$	0.3679	0.3785	+ 3 %
$R_{ff}(0, 0, \lambda)$	0.3679	0.3781	+ 3 %

Note: The relative error on the estimated mean was defined as  $(\bar{f} - \langle f \rangle) / \sigma_f$ . In this particular case,  $\sigma_f = 1$  and  $f = \ln(k/k_G)$  is a zero-mean Gaussian random field with isotropic correlation function  $e^{-\xi/\lambda}$ . At separation distance  $\xi = \lambda$ , the correlation is  $e^{-1} \approx 0.3679$ .

prescribed ensemble moments of the log-conductivity field and the computed spatial moments obtained by the spatial averaging method described previously (equations 6.4). Note that the relative errors on the mean and standard deviation are very small; the error on the covariance function at separation distance  $\lambda$  is also quite small. This excellent agreement indicates that the turning band generator can produce statistically accurate realizations of random fields at reasonable costs: the 1 million node realization at hand required only 10 minutes of CPU time on the Cray 2 machine (without the use of Fast Fourier Transforms). Furthermore, this also illustrates in a concrete way the equivalence of ensemble and spatial moments for large realizations of homogeneous-ergodic fields. In other words, the particular log-conductivity realization at hand appears to be fairly representative of the whole ensemble of possible realizations.

(c) Visual representation of the head field

The three flow realizations obtained by numerical simulation for the cases  $\sigma_f \approx 1.0, 1.7, 2.3$  were statistically analyzed by using the same spatial averaging procedures described in the methodology section (6.1). This will not be repeated

here; the reader is referred to equations (6.4)-(6.8). In order to illustrate concretely the spatial structure of the head field, we show in Figure 6.16, (a),(b),(c) the contour lines of the hydraulic head in a horizontal slice parallel to the mean flow, for each of the three cases  $\sigma_f \simeq 1.0, 1.7,$  and  $2.3$ . Note that each slice contains about ten thousand mesh points. The spatial structure of the head does not seem to differ much from the similar pictures obtained previously for a smaller flow problem (Section 6.2).

In addition, Figures 6.17 (a),(b),(c) show the fluctuations of the hydraulic head along a transect parallel to the mean flow. The nonlinear trend  $\bar{H}(x_1)$  obtained by cross-flow averaging was superimposed for comparison. It should be noted that the nonlinearity of  $\bar{H}(x_1)$  seems milder than it was for the smaller flow realizations analyzed previously: compare figure 6.17a to figure 6.10. This finding is in accordance with our previous evaluation of finite size sampling errors, at least qualitatively. The improvement seems to be even better than expected, due to the fact that boundary effects were not included directly in the aforementioned analysis of finite size effects.

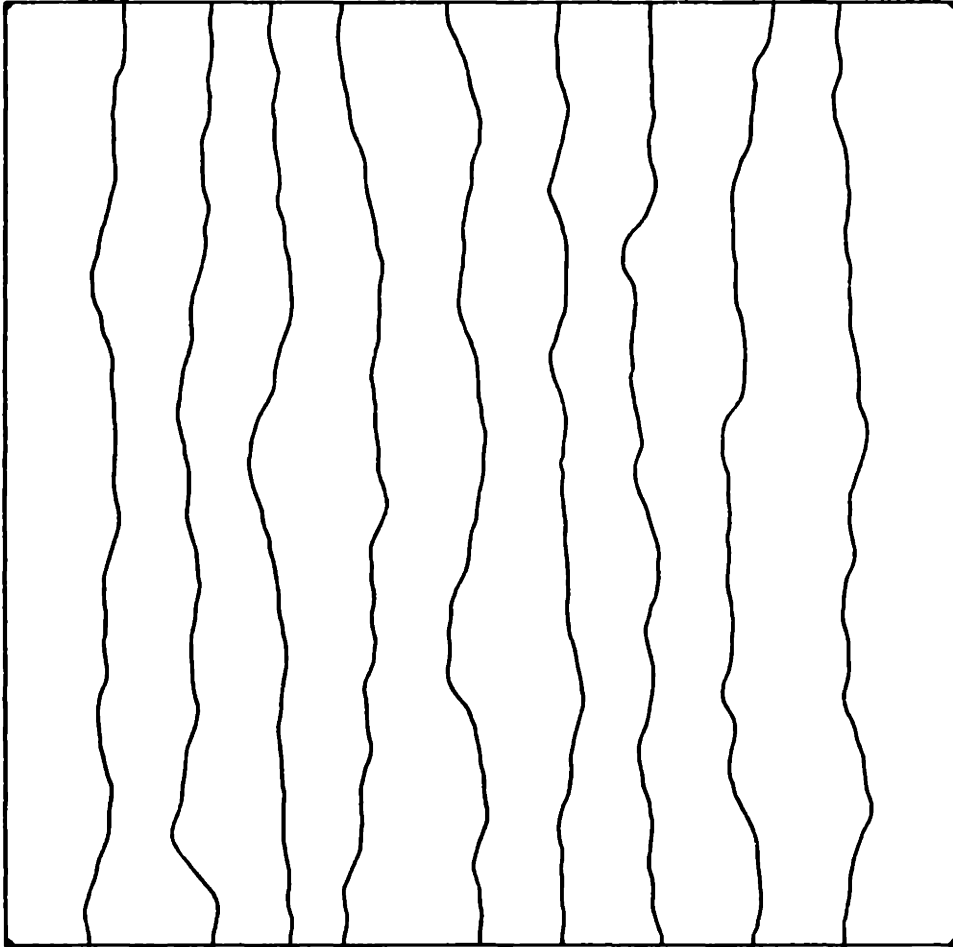


Figure 6.16 (a) Contour lines of the three-dimensional hydraulic head field in a horizontal slice parallel to the mean flow (pointing right). There are 11 iso-value contours including the left and right boundaries (equally spaced values). Flow problem A with 1 Million nodes: (a) case  $\sigma_f = 1.0$ .

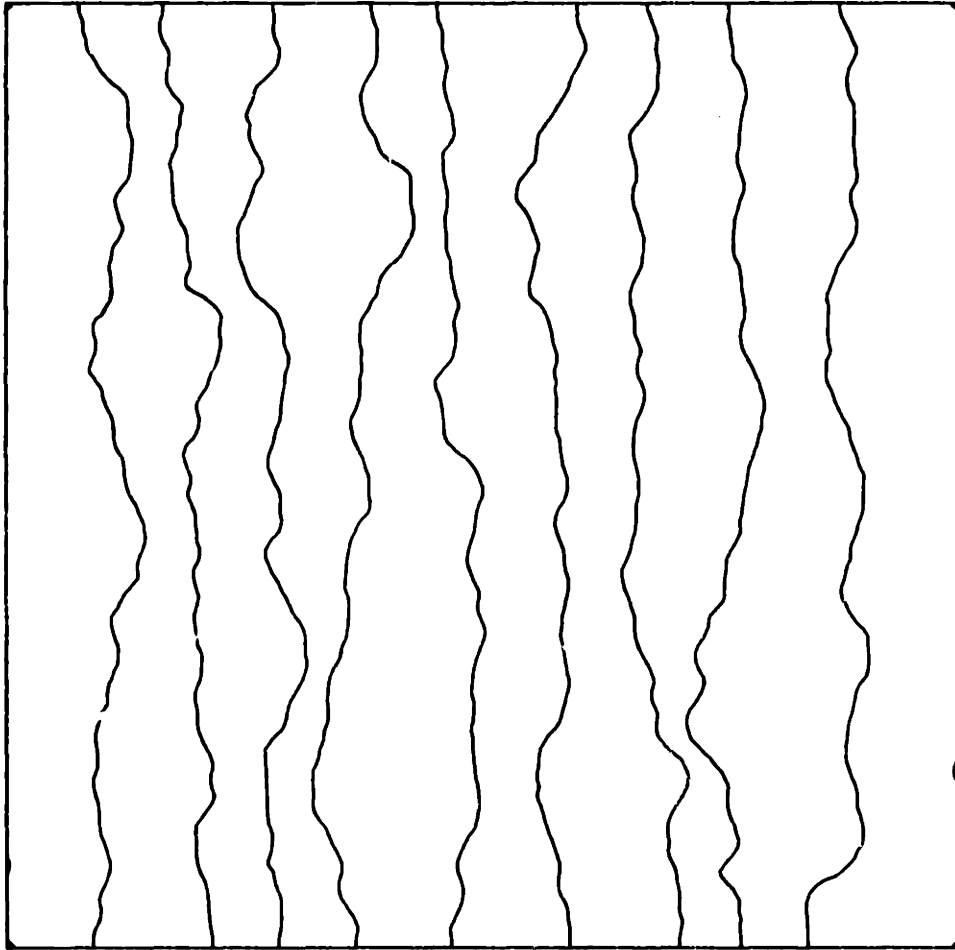


Figure 6.16 (b) Same as (a), with  $\sigma_f = 1.732$ .

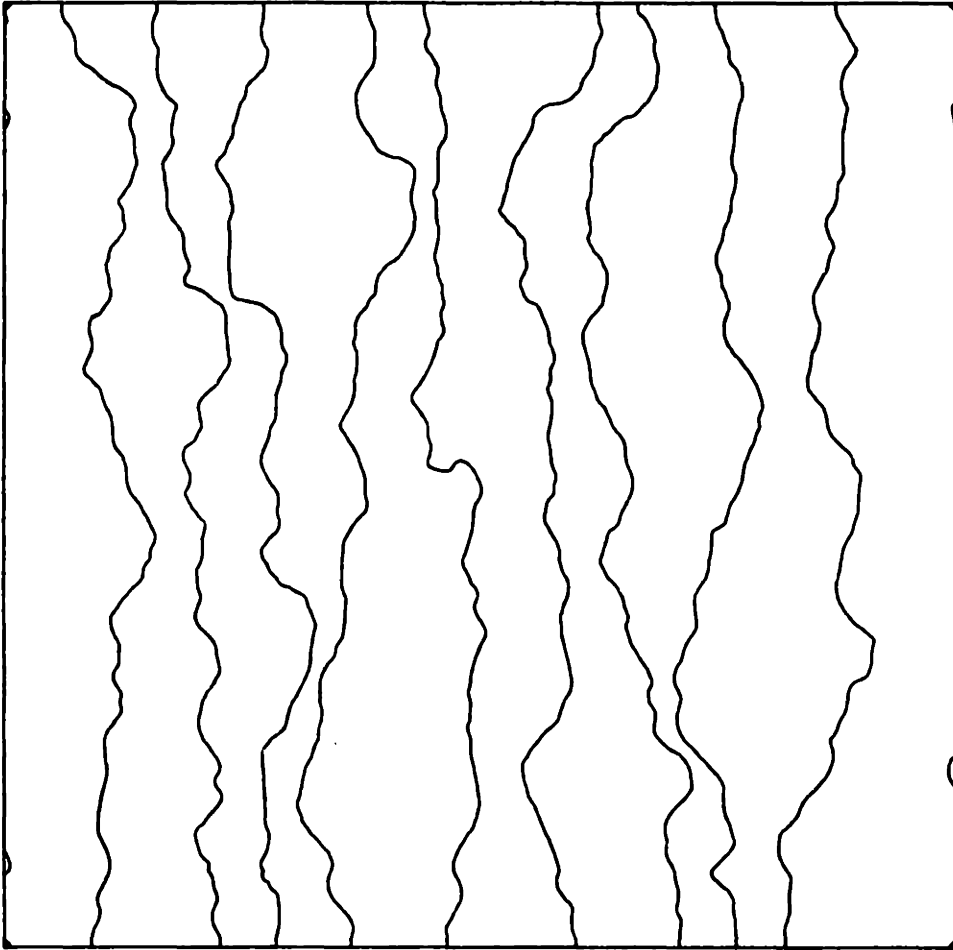


Figure 6.16 (c) Same as (a), with  $\sigma_f = 2.305$ .

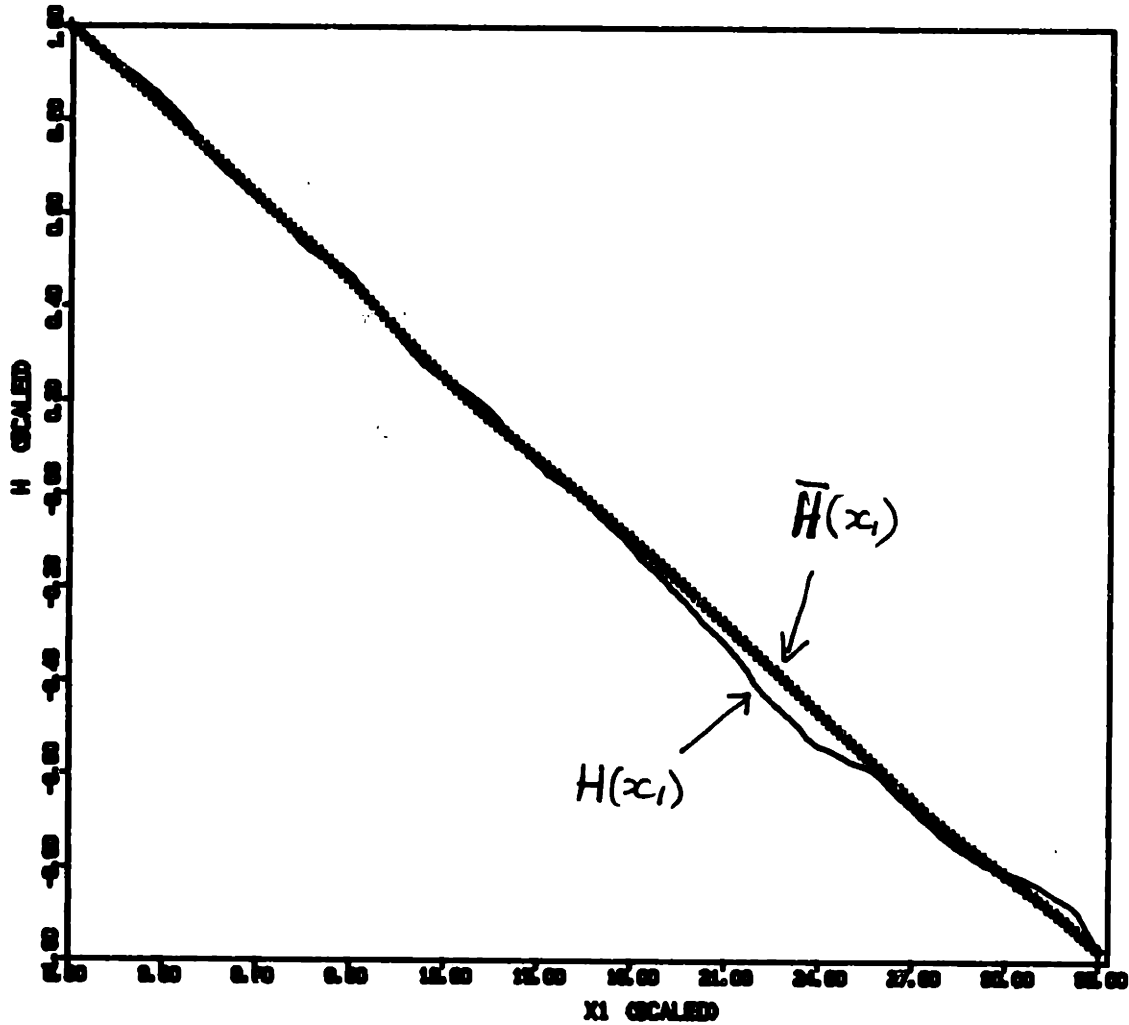


Figure 6.17 (a) One-dimensional representation of the head field (sample function  $H(x_1)$ , and nonlinear trend  $\bar{H}(x_1)$ ) along a transect parallel to the mean flow direction. Flow problem A with 1 Million nodes: (a) Case  $\sigma_f = 1.0$ .



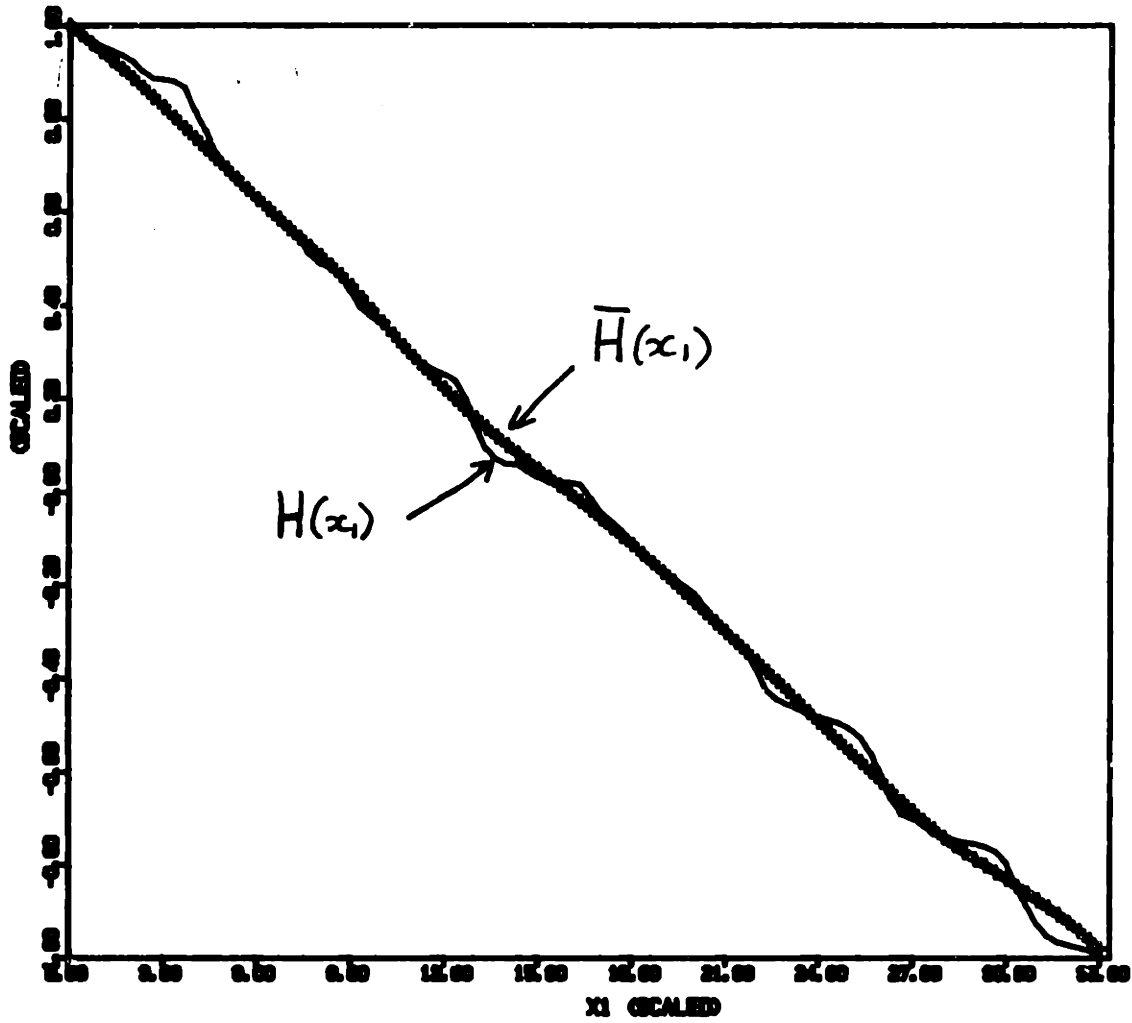


Figure 6.17 (b) Same as (a), with  $\sigma_f = 1.732$

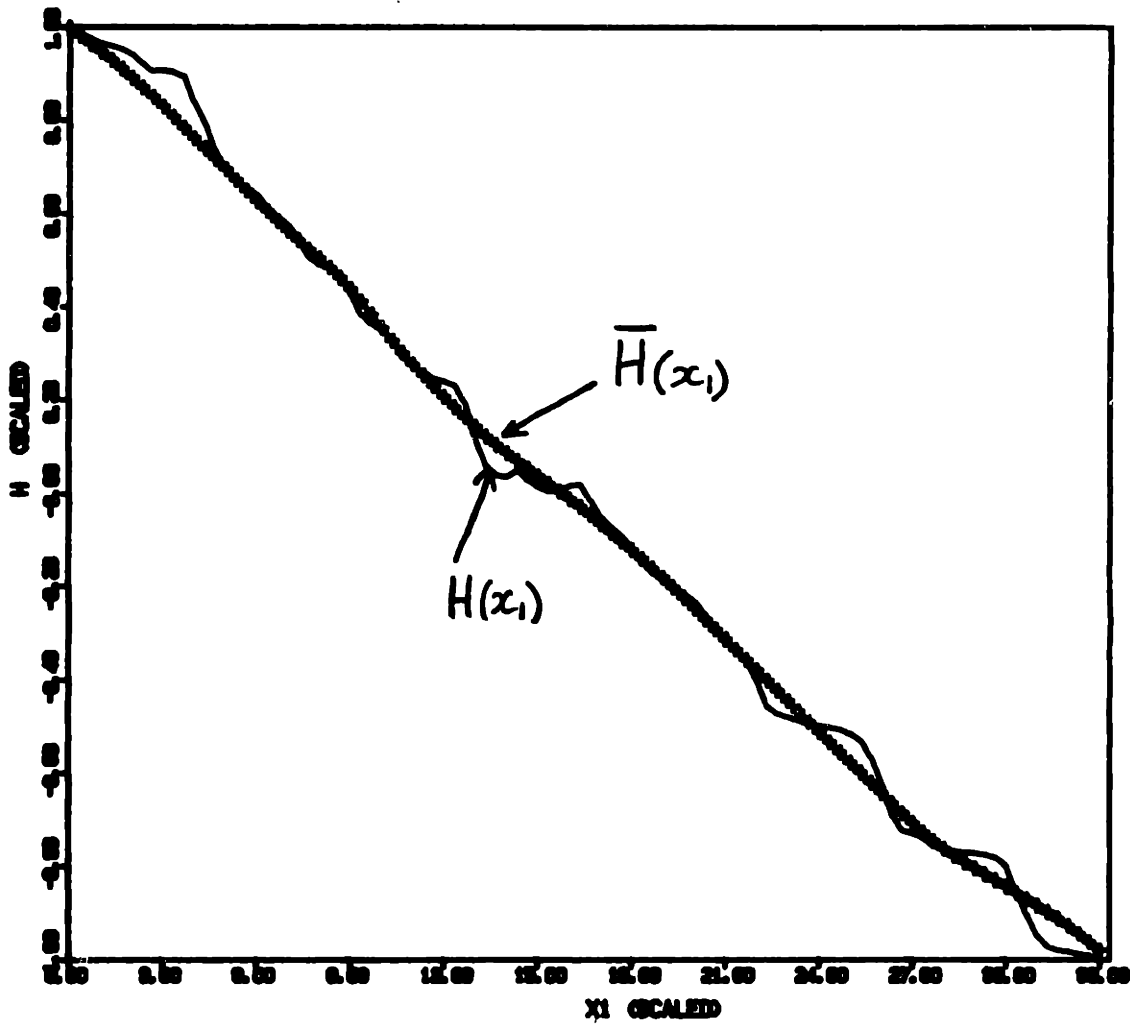


Figure 6.17 (c) Same as (a), with  $\sigma_f = 2.3205$ .

The flux vector field was not processed for graphic representations due to technical reasons. However, the reader is referred to the visual representations of the longitudinal flux component  $Q_1(\underline{x})$  obtained for the smaller flow realization of Section 6.2 (Figures 6.11-6.15). At any rate, it will be more informative to analyze the behavior of the flow fields in statistical terms. This is now examined.

[d] Single Point Statistics of the Flow Field.

The results of statistical analysis of the flow fields  $(H(\underline{x}), Q_1(\underline{x}))$  obtained for different values of  $\sigma_f$  are presented in the form of tables (for single-point statistics) and figures (for correlation functions). In each case, we develop a systematic comparison with the results of the infinite-domain spectral theory. For convenience the analytical results of the spectral theory concerning the single-point moments of the flow field are summarized in Table 6.4 below.

The numerical values of the single-point moments of the flow fields obtained in the cases  $\sigma_f \simeq 1.0, 1.7, \text{ and } 2.3$ , are summarized in a compact form in Table 6.5. The values predicted

TABLE 6.4  
 SUMMARY OF ANALYTICAL EXPRESSIONS FOR VARIOUS STATISTICS  
 FROM THE FIRST ORDER (·) AND HIGHER ORDER ((·)) SPECTRAL  
 SOLUTIONS, TO BE USED AS A REFERENCE FOR TABLES 6.5 AND 6.6  
 (CASE OF ISOTROPIC 3D MARKOV LOG CONDUCTIVITY)

Statistics	Expression	Equation Number	Other References
$(\sigma_H)$	$\frac{1}{\sqrt{3}} \sigma_F J_1 \lambda$	Equation (3.21)	Bakr et. al 1975
$((\sigma_H))$	$\sqrt{\frac{1 - .058\sigma_F^2}{3}} \cdot \sigma_F J_1 \lambda$	Equation (4.2)	Gelhar (pers. com.) Dagan (1985)
$(\sigma_{G_i})$	$i = 1: \frac{1}{\sqrt{5}} \sigma_F J_1$ $i = 2,3: \frac{1}{\sqrt{15}} \sigma_F J_1$	Equation (3.22)	Appendix 3.B
$(\sigma_{q_i})$	$i = 1: \sqrt{\frac{8}{15}} K_G \sigma_F J_1$ $i = 2,3: \sqrt{\frac{1}{15}} K_G \sigma_F J_1$	Equation (3.24)	Appendix 3.B
$((\sigma_{q_i}))$	$i = 1: \sqrt{\frac{8}{15}} \sigma_F \bar{Q}_1$ $i = 2,3: \sqrt{\frac{1}{15}} \sigma_F \bar{Q}_1$	Equation (3.26)	Chapter 4 (section 4.3)
$(\bar{Q}_1)$	$i = 1: K_{eff} J_1$ $i = 2,3: 0$	Equation (3.14)	Gelhar-Axness 1983
$(K_{eff})$	$K_G \exp(\sigma_F^2/6)$	Eqs. (3.19), (3.23)	Gelhar 1984

TABLE 6.5  
 SUMMARY OF COMPUTED STATISTICS OBTAINED FOR THE 1 MILLION NODE FLOW  
 SIMULATIONS (PROBLEM "A" WITH THREE VALUES OF LOG-CONDUCTIVITY  
 STANDARD DEVIATION), AND COMPARISON TO SPECTRAL THEORY (IN PARENTHESIS).  
 THE STATISTICAL QUANTITIES ARE DEFINED IN THE TEXT

Statistics	$\sigma_f = 1.0$	$\sigma_f = 1.732$	$\sigma_f = 2.3025$
$\sigma_H$	.002050 (.002309) ((.002241))	.003579 (.004000) ((.003635))	.004774 (.005317) ((.004425))
$\sigma_{G_1}$	.001558 (.001789)	.002711 (.003098)	.003625 (.004119)
$\sigma_{G_2}$	.000979 (.001033)	.001817 (.001789)	.002569 (.002378)
$\sigma_{G_3}$	.000975 (.001033)	.001793 (.001789)	.002518 (.002378)
$\sigma_{q_1}$	.003779 ((.003451))	.01103 ((.00834))	.02516 ((.01628))
$\sigma_{q_2}$	.001435 ((.001220))	.005075 ((.002950))	.01328 ((.00576))
$\sigma_{q_3}$	.001476 ((.001220))	.005285 ((.002950))	.01381 ((.00576))
$\sigma_{q_3}/\sigma_{q_1}$	.3906 ((.3536))	.4791 ((.3536))	.5489 ((.3536))
$\bar{Q}_1$	.004856 (.004725)	.006889 (.006595)	.01004 (.00968)
$\bar{Q}_2/\bar{Q}_1$	.004 (.000)	.009 .000	.013 (.000)
$\bar{Q}_3/\bar{Q}_1$	.013 ((.000))	.024 ((.000))	.033 ((.000))
$K_{eff}/K_G$	1.214 (1.181)	1.722 (1.645)	2.510 (2.420)

by the spectral theory are shown in parenthesis immediately below the numerical value. The values in single parenthesis (•) were obtained from the standard first order spectral theory of Bakr et. al. (1978) and Gelha and Axness (1983). On the other hand, the values in double parenthesis represent some higher order or improved spectral solutions, as defined in Table 6.4. In particular, note that the flux standard deviations ( $(\sigma_{q_i})$ ) were calculated from the improved spectral solutions developed in this work (Chapter 4, Section 4.3). The statistical quantities listed in Table 6.5 are as follows: standard deviations of the head ( $\sigma_H$ ), head gradient ( $\sigma_{G_i}$ ); ratio of transverse/longitudinal flux deviations ( $\sigma_{q_2}/\sigma_{q_1}$ ); mean longitudinal flux component ( $\bar{Q}_1$ ); relative mass balance errors ( $\bar{Q}_i/\bar{Q}_1$  for  $i=2,3$ ); and effective conductivity ( $K_{eff}$ ).

In order facilitate the comparison between numerical and spectral results, we also show in Table 6.6 the relative error on the spectral solutions for  $\sigma_H$  and  $\sigma_{q_i}$ , relative to the numerical solutions  $\hat{\sigma}_H$  and  $\hat{\sigma}_{q_i}$ . Our choice here has been to use the numerical solutions rather than the spectral solutions as a reference. Thus, the relative errors listed in the table were defined as:

$$e(\sigma_Y) = \frac{\sigma_Y - \hat{\sigma}_Y}{\hat{\sigma}_Y}$$

TABLE 6.6  
 COMPARISON OF FIRST ORDER ( $\cdot$ ) AND HIGHER ORDER ( $(\cdot)$ ) SPECTRAL SOLUTIONS  
 WITH NUMERICAL RESULTS. THE NUMBERS IN PARENTHESIS GIVE  
 THE RELATIVE ERROR ON  $\sigma_H$  AND  $\sigma_{q_1}$  WITH  
 RESPECT TO THE VALUES OBTAINED BY NUMERICAL SIMULATION

	$\sigma_f = 1.0$	$\sigma_f = 1.732$	$\sigma_f = 2.3025$
$e(\sigma_H)$	(+ 13%) ((+ 9%))	(+12%) ((+ 2%))	(+11%) ((- 7%))
$e(\sigma_{q_1})$	(- 23%) ((- 9%))	(-54%) ((-24%))	(-73%) ((-35%))
$e(\sigma_{q_2})$	(-28%) ((-15%))	(-65%) ((-42%))	(-82%) ((-57%))
$e(\sigma_{q_3})$	(-30%) ((-17%))	(-66%) ((-44%))	(-83%) ((-58%))

Note: The relative error  $e(\sigma_Y)$  is defined as the ratio  $(\sigma_Y - \hat{\sigma}_Y) / \hat{\sigma}_Y$  where  $\sigma_Y$  corresponds to the spectral theory, and  $\hat{\sigma}_Y$  is the value obtained from the numerical simulation. See also Table (6.4).

In addition, Table 6.6 allows for a direct comparison between the standard first order spectral solutions (single parenthesis) and higher order or modified spectral solutions ((double parenthesis)). The analytical form of each of these spectral solutions was given in Table 6.4 above.

Our observations based on Tables 6.4, 6.5 and 6.6, can now be summarized as follows:

- (i) The most robust statistics are  $\sigma_H$ ,  $\sigma_{G_1}$ , and  $K_{eff}$ . For these quantities, the values obtained with the spectral theory match the numerical results within 10% (5% for the effective conductivity), for the whole range of log-conductivity variability. The ratio of transverse to longitudinal flux standard deviations (e.g.,  $\sigma_{q_3} / \sigma_{q_1}$ ) is also relatively robust, although the spectral result is off the numerical value by (-35%) in the case of highest variability ( $\sigma_f \approx 2.3$ ). Note that these comparisons are based on the modified spectral solutions for the flux statistics.



- (ii) At moderate variability ( $\sigma_f = 1.0$ ), all the single-point statistics predicted by the spectral theory match the numerical results to within 15%, or 10% if the transverse flux deviations ( $\sigma_{q_2, q_3}$ ) are excluded. Again, these comparisons are based on the modified spectral solutions for the flux statistics.
- (iii) However, there are some significant discrepancies between the spectral theory and the numerical simulations concerning the values of the flux standard deviations at higher variability ( $\sigma_f \geq 1.7$ ). In the case of highest variability ( $\sigma_f \approx 2.3$ ) the error on the spectral results  $\sigma_{q_i}$  is quite high relative to the numerical results, particularly concerning the transverse flux standard deviations (-50% with the modified spectral theory, and as much as -83% with the standard spectral theory).
- (iv) The modified spectral theory proposed in this work for the flux spectrum (Chapter 4, Section 4.3) produces values of  $\sigma_{q_i}$  that are in closer agreement with the numerical simulations, than the standard spectral theory. The improvement is uniform over the whole

range of conductivity variability ( $\sigma_f \approx 1.0, 1.7, 2.3$ ), and is particularly significant for the longitudinal flux component ( $\sigma_{q_1}$ ).

- (v) Finally, the Gelhar-Dagan second order spectral solution for  $\sigma_H$  does not uniformly improve the standard spectral result over the whole range of conductivity variability. The agreement with the numerical results is not significantly better with the second order solution, except for a particular value of  $\sigma_f$  ( $\sigma_f \approx 1.7$ ). At any rate, the standard spectral solution  $\sigma_H$  was already quite close to the numerical values within the whole range  $\sigma_f \approx 1.0-2.3$ .

These observations lead us to the conclusion that the (modified) spectral theory and the numerical single-realization simulations produced nearly identical results for most of the single-point moments of the flow field, within a wide range of log-conductivity variability (up to  $\sigma_f \approx 2.3$ ). However, it should also be recognized that the predictions concerning the degree of variability of the flux components ( $\sigma_{q_i}$ ) were not in such a good agreement for medium to large log-conductivity

variability ( $\sigma_f \approx 1.7$  or larger). Nevertheless, the  $\sigma_{q_i}$ 's obtained from the modified spectral solutions developed in this work were significantly closer to the numerical results than those predicted by the standard spectral theory. It is also interesting to note that the second order spectral solution of Gelhar-Dagan for the standard deviation of the head did not significantly improve on the standard spectral solution relative to the numerical results. We conclude that the most important "high order effects" concern the degree of variability of the flux vector. This may have important implications for solute transport in a stochastic velocity field, and needs to be discussed further.

The observed discrepancy on the degree of variability (standard deviation) of the flux vector raises a question about the accuracy of the spectral theory and/or the numerical single-realization solution. The problem can be narrowed down further by observing that, for moderate variability  $\sigma_f = 1.0$ , the discrepancy between the two methods is on the same order as the estimated accuracy of the numerical solution (truncation error) when the modified spectral theory is used. This can be seen by comparing directly Table 6.6 to Table 5.2 of Chapter 5 (Section 5.2) for  $\sigma_f = 1.0$  and  $\Delta x/\lambda = 1/3$ , as will be explained below.

The result of this comparison is shown in Table 6.7. It is important to note that the *standard* spectral theory is off the numerical solution by an amount too large to be explained solely by numerical truncation errors. On the other hand, the *modified* spectral theory is close enough to the numerical solution that the discrepancy could be due solely to numerical truncation errors (for  $\sigma_f = 1.0$ ). Note that the relative truncation error approximates the relative error between the exact and numerical values of  $\sigma_{q_i}$ . Indeed, recall that the relative truncation error on the flux was defined as:

$$\frac{\sigma_{\delta q_i}}{\sigma_{q_i}}$$

where  $\delta q_i$  is the truncation error on the flux:

$$\delta q_i = \hat{q}_i - q_i.$$

$\hat{q}_i$  is the numerical solution while  $q_i$  is the exact (unknown) solution. Therefore, it is not difficult to see that:

TABLE 6.7

TRUNCATION ERROR AND DISCREPANCY BETWEEN THE SPECTRAL AND NUMERICAL SOLUTIONS, FOR THE FLUX STANDARD DEVIATIONS  $\sigma_{q_i}$

(1 Million node problem A  $\sigma_f = 1.00$  and  $\Delta x/\lambda = 1/3$ ).

	(1) Relative truncation error (exact/ numerical)	(2) Relative error (modified spectral/num.)	(3) Relative error (standard spectral/num.)...
$e(\sigma_{q_1})$	- 17%	- 9%	- 23%
$e(\sigma_{q_2})$	- 14%	- 15%	- 28%
$e(\sigma_{q_3})$	- 14%	- 17%	- 30%

Note: (1) Relative truncation error on the flux in the root-mean-square norm, approximating the relative error between the exact and numerical  $\sigma_{q_i}$ .

(2) Relative error between the modified spectral result and the numerical  $\sigma_{q_i}$ .

(3) Relative error between the standard spectral result and the numerical  $\sigma_{q_i}$ .

$$\hat{\sigma}_{q_i}^2 = \sigma_{q_i}^2 + 2 \langle q_i \cdot \delta q_i \rangle + \sigma_{\delta q_i}^2$$

Now, it seems reasonable to assume that the random error  $\delta q_i$  will be generally proportional to  $q_i$ . This yields:

$$\langle q_i \cdot \delta q_i \rangle \approx \sigma_{q_i} \cdot \sigma_{\delta q_i}$$

By using also the known fact that:

$$\sigma_{\delta q_i} \ll \sigma_{q_i}$$

we obtain finally the approximate relation:

$$\frac{\sigma_{q_i} - \hat{\sigma}_{q_i}}{\hat{\sigma}_{q_i}} \approx - \frac{\sigma_{\delta q_i}}{\sigma_{q_i}} \quad (6.12)$$

where the left term is the relative error listed in column (1) of Table 6.7, and the right term is just the relative truncation error of Chapter 5 (Table 5.2) with the sign reversed.

Thus, the result of Table 6.7 indicates that the values of  $\sigma_{q_i}$  obtained by the modified spectral theory are statistically indistinguishable from the numerical values, in the

case of  $\sigma_f = 1.0$ . (This does not hold when the standard spectral theory is used instead.) On the other hand, recall that all the other single-point statistics predicted by the spectral theory were quite close to the numerical results for  $\sigma_f = 1.0$  (and for larger variability as well). We conclude that, at least for moderate variability ( $\sigma_f \simeq 1$ ), both the modified spectral theory and the numerical simulations must be quite close to the unknown exact solution of the infinite-domain stochastic flow problem, as far as single-point moments are concerned (standard deviations of head and flux, and effective conductivity).

This encouraging conclusion seems justified if we reject the possibility of a mere chance coincidence, given the fact that the two methods are based on different kinds of approximations, as shown below:

Spectral Theory

- Infinite domain
- Small parameter expansion ( $\sigma_f$ )
- First or second order approximations
- Ensemble moments (Fourier integrals)

Single-realization Simulations:

- Finite domain
- Finite difference discretization
- Approximate factorization and iterative solution
- Spatial moments (physical space summation)

On the other hand, the discrepancy between the  $\sigma_q$ 's predicted by the (modified) spectral theory and the numerical simulations become statistically significant as  $\sigma_f$  increases over

unity ( $\sigma_f \approx 1.7$  and  $2.3$ ). Indeed, Table 6.6 shows that the relative error between the two solutions increases with  $\sigma_f$ , while we know from Chapter 5 (Section 5.2) that the relative truncation error does not increase with  $\sigma_f$  as a first approximation (i.e., to first order in  $\sigma_f$ ). If the results of the truncation error analysis are to be trusted, this implies that the *modified* spectral theory significantly underestimates the degree of variability of the flux vector as  $\sigma_f$  increases, say for  $\sigma_f > 1-1.5$ . It is also clear from Table 6.6 that the *standard* spectral theory leads to even more severe discrepancies, as noted previously.

Based on these remarks, we have obtained empirical expressions for the flux standard deviations ( $\sigma_{q_i}$ ) that fit extremely well the numerical results for the three values of  $\sigma_f$  tested in this work ( $\sigma_f \approx 1.0, 1.7, 2.3$ ). These conjectural expressions are simple and take a form similar to the spectral solutions, as follows:

$$\sigma_{q_1}^* = \sqrt{\frac{8}{15}} \sigma_f J_1 K_G e^{\sigma_f^2/4} \quad (6.13a)$$

$$\sigma_{q_2}^*, \sigma_{q_3}^* = \sqrt{\frac{1}{15}} \sigma_f J_1 K_G e^{\sigma_f^2/3}$$

Equivalently, by using the relation between the arithmetic and



geometric mean conductivities ( $K_A = K_G \exp(\sigma_f^2/2)$ ), these relations can be expressed as:

$$\sigma_{q_1}^* = \sqrt{\frac{8}{15}} \sigma_f K_G J_1 \left[ \frac{K_A}{K_G} \right]^{1/2} \quad (6.13b)$$

$$\sigma_{q_2}^* \cdot \sigma_{q_3}^* = \sqrt{\frac{1}{15}} \sigma_f K_G J_1 \left[ \frac{K_A}{K_G} \right]^{2/3}$$

Equations (6.13) agree with the numerical results listed in Table 6.5 within a margin of error of 3% ( $\sigma_{q_1}$ ) and 6% ( $\sigma_{q_2} \cdot \sigma_{q_3}$ ) for the whole range of conductivity variability up to  $\sigma_f \approx 2.3$ . These equations may be viewed as an empirical correction to the spectral theory to compensate for "unmodeled" high order effects in the case of large  $\sigma_f$ . It seems clear, at least from all our previous observations that the exact values of  $\sigma_{q_1}$  must lie between the values predicted by the modified spectral theory (Table 6.4) and the empirical relations (6.13) - presumably very close to the latter.

To complete our analysis of single-point moments of the flow field, let us recall from the previous section 6.2 that the longitudinal flux component was found to be positively skewed, based on a visual inspection of  $Q_1$  along selected transects and slices (Figures 6.11, 6.14, and 6.15). This, in our view, is another manifestation of high order effects not taken into

account by the spectral theory as it stands now. Thus, it should not be surprising that similar high order effects can contribute to the variance of the flux vector. The proposed correction (6.13) indicates that the effect of the high order terms, ignored by the spectral theory, is exponential in  $\sigma_f^2$ . With this correction, the  $\sigma_{q_i}$  and all other single-point statistics predicted by the spectral theory agreed well with the numerical results up to large conductivity variability ( $0 \leq \sigma_f \leq 2.3$ ). It will be interesting in the future to evaluate quantitatively the entire probability distribution of the flux components from the numerical results. Another key feature of the flow field is its spatial structure, which will be investigated next in connection with the predictions of the spectral theory.

[e] Spatial structure (two point correlations):

In the framework of the spectral theory, the spatial structure of the flow field can be described by the three-dimensional two-point correlation functions of the flow variables  $H(\underline{x})$  and  $Q_1(\underline{x})$ . Although we have seen that this information may not be sufficient ( $Q_1(\underline{x})$  has a skewed distribution, requiring three-point correlation functions), it will nevertheless be instructive to determine the two-point correlation functions of the numerical flow field and compare with the results of the spectral theory.

In the present case, we have evaluated the unidirectional correlation functions:

$$R(\xi_1) = R(\xi_1, 0, 0)$$

$$R(\xi_2) = R(0, \xi_2, 0)$$

$$R(\xi_3) = R(0, 0, \xi_3)$$

for each of the flow variables:

- hydraulic head H
- flux vector components  $Q_1, Q_2, Q_3$
- (head gradient components  $G_1, G_2, G_3$ )

In actual practice, we computed first the covariance functions by using the spatial averaging procedure explained previously in equations (6.4, 6.5, 6.7) of Section (6.1). The correlation functions were then simply obtained by dividing the covariances by the variances (covariances at lag zero). Thus, we obtained the correlation functions  $R_{HH}(\xi_j)$ ,  $R_{Q_i Q_i}(\xi_j)$ , and  $R_{G_i G_i}(\xi_j)$  for  $i = 1, 2, 3$  and  $j = 1, 2, 3$ . Note that we use here the notation  $R(\xi_j)$  to denote unidirectional correlation functions (equal to unity at lag zero), although the notation  $R(\xi)$  was used elsewhere to designate covariance functions.

Figures (6.18) and (6.19) show the correlation structure of the hydraulic head field and a comparison with the head correlation functions predicted by the spectral theory (see Chapter 3, Section 3.3, Figure 3.1). The unidirectional correlation functions from the numerical head field are shown in Figures 6.18(a), (b), (c) for the cases  $\sigma_f = 1.0, 1.7, 2.3$ , respectively. In all three cases, the head correlation structure appears to be nearly isotropic in the cross-flow plane, as it should, i.e.:

$$R_{HH}(0, \xi_2, 0) \simeq R_{HH}(0, 0, \xi_3)$$

In addition, the head correlation range is larger in the cross-flow plane than in the longitudinal direction  $\xi_1$ , parallel to the mean flow. This feature is indeed predicted by the spectral theory.

However, the agreement with the spectral theory is only qualitative, as can be seen from the comparison of numerical and spectral head correlations show in Figure (6.19) for the case  $\sigma_f \simeq 1.0$ . It is clear from this figure that the numerical result underestimates the correlation range of the head field with respect to the spectral result, particularly in the cross-flow directions. This is presumably due to the limited size of the flow domain, as can be seen by examining the number of available

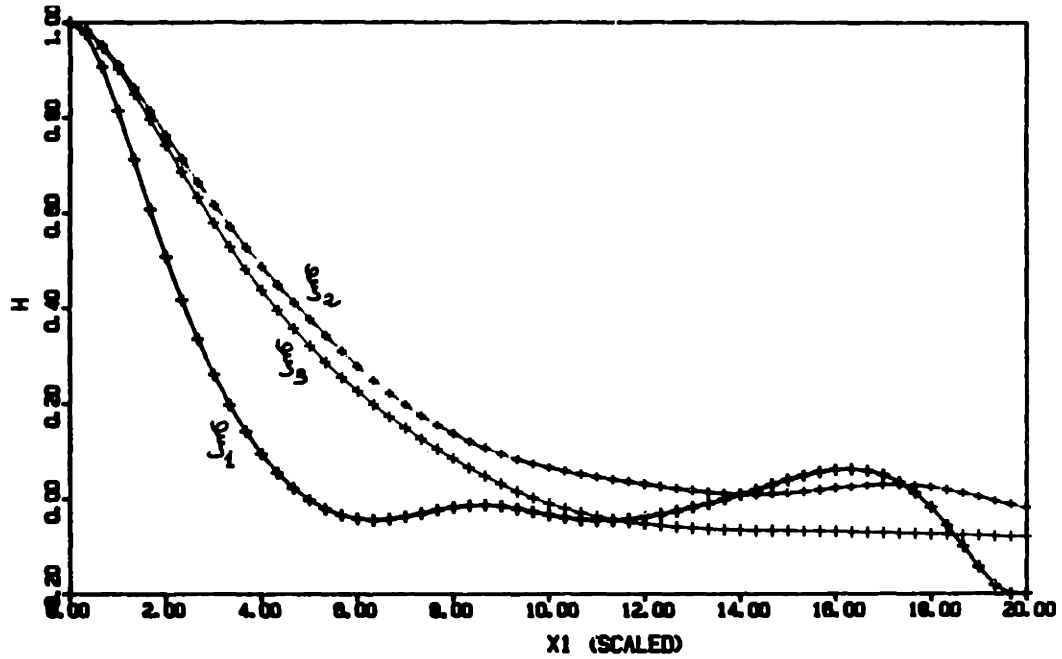


Figure 6.18 (a) Numerical head correlation functions along three directions, for the 1 Million node "isotropic" problem A ( $\sigma_f = 1.0$ ).

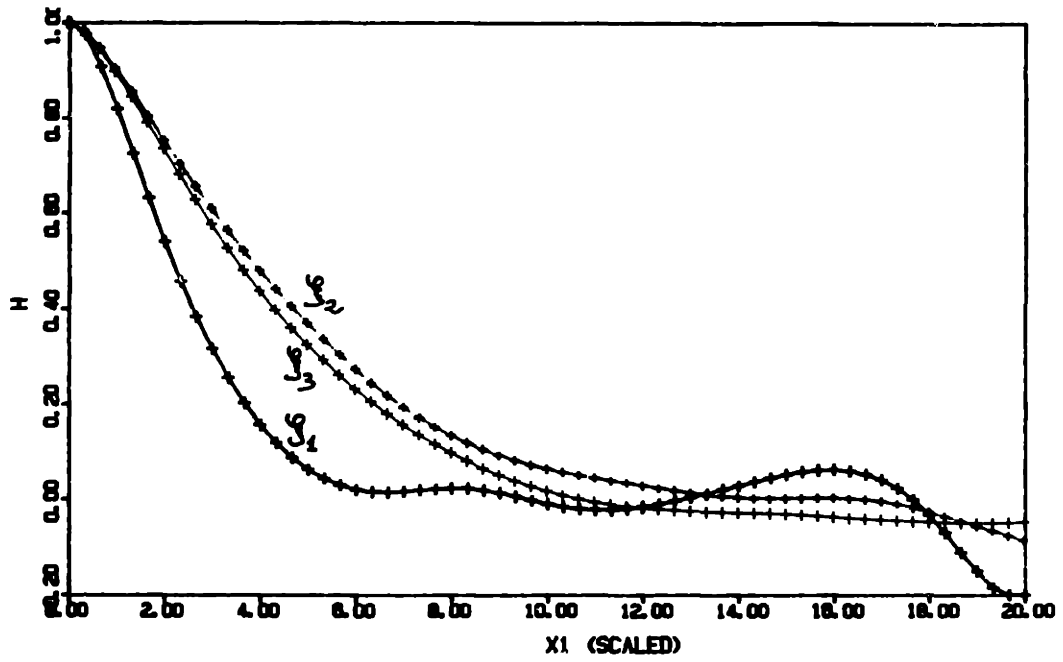


Figure 6.18 (b) Same as (a), with  $\sigma_f = 1.732$ .

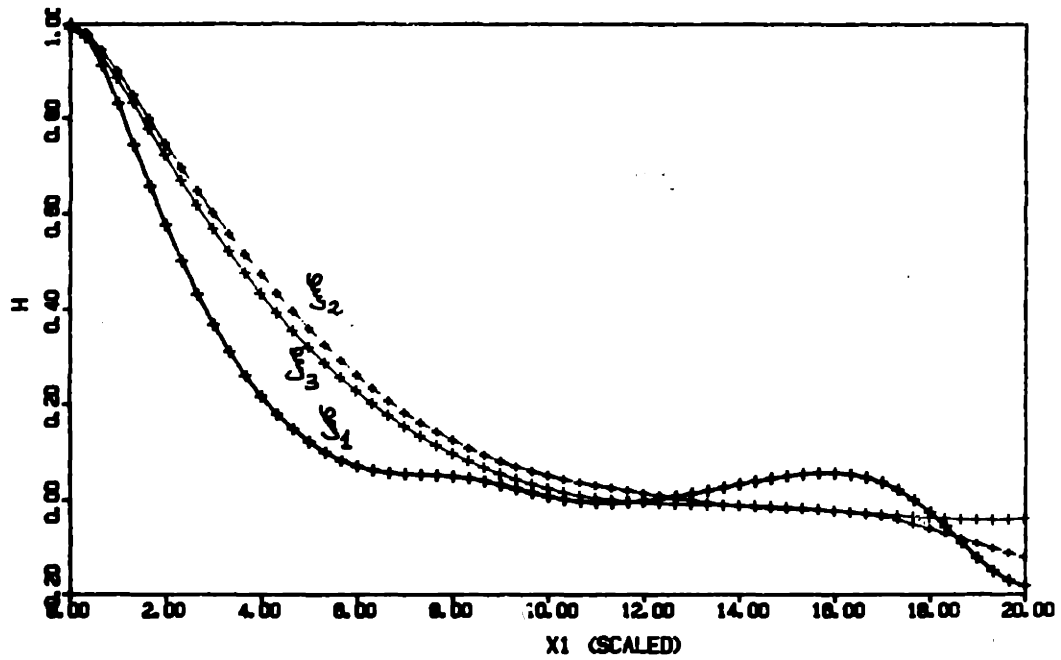


Figure 6.18 (c) Same as (a), with  $\sigma_f = 2.3025$ .

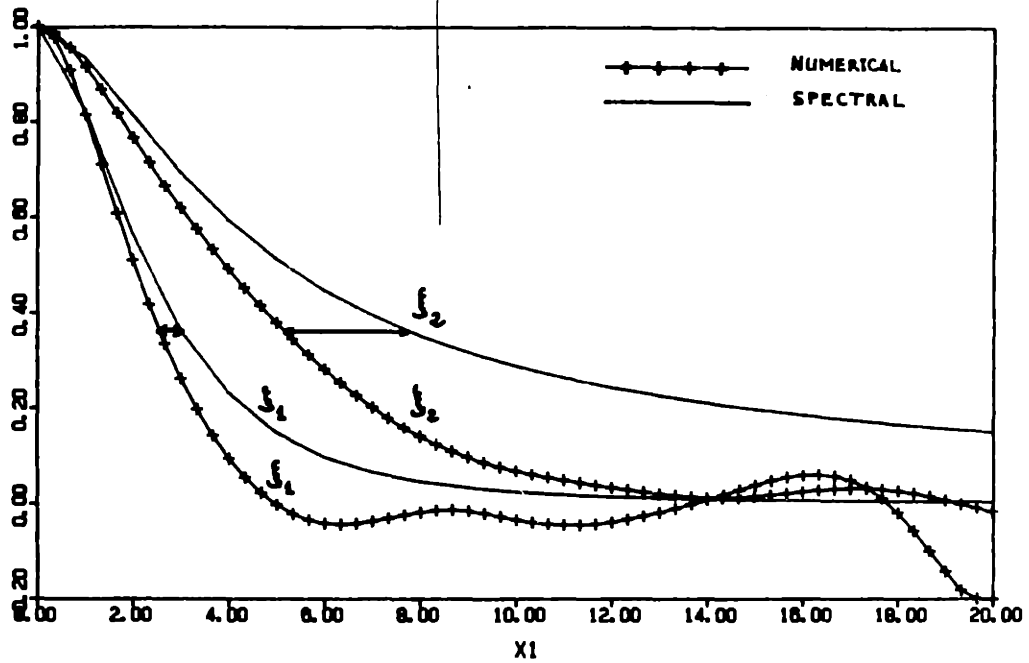


Figure 6.19 Comparison of numerical and theoretical (spectral) head correlation functions in the longitudinal and transverse directions  $\xi_1$  and  $\xi_2$  (1 Million node isotropic Problem A, with  $\sigma_f = 1.0$ ).



"head samples" along the three axes. The transverse sample size is:

$$\frac{L}{7.5\lambda} \approx \frac{33.3}{7.5} \approx 4.5$$

while the longitudinal sample size is:

$$\frac{L}{30.\lambda} \approx \frac{33.3}{3.0} \approx 11.$$

Therefore, it is not surprising that the numerical head correlation functions obtained by finite-domain averaging differ somewhat from the results of the infinite-domain spectral theory, particularly in the transverse direction where the equivalent number of head samples is so small. See Appendix 2A for more rigorous statements on sampling uncertainty.

It may be also instructive to compare directly the head correlations in terms of correlation scales. Table 6.8 compares the e-correlation scales of the head field for the spectral and numerical solutions ( $\sigma_f \approx 1.0, 1.7, 2.3$ ). The e-correlation scale was defined as the distance at which the correlation drops to  $e^{-1} \approx 0.3679$ . Note that this definition coincides with the integral correlation length in the case of the Markov log-conductivity field (but not for other random fields such as

TABLE 6.8

CORRELATION SCALES OF THE HYDRAULIC HEAD FIELD ALONG THREE DIRECTIONS:  
COMPARISON OF SPECTRAL SOLUTION WITH THE NUMERICAL RESULTS OF THE  
1 MILLION NODE "ISOTROPIC" FLOW PROBLEM A.

Correlation Function	Spectral theory for $\sigma_f$	Numerical Results		
		( $\sigma_f=10$ )	( $\sigma_f=1.7$ )	( $\sigma_f=2.3$ )
$R_{HH}(\xi_1)$	3.0	2.5	2.7	3.0
$R_{HH}(\xi_2)$	7.5	5.1	5.0	4.9
$R_{HH}(\xi_3)$	7.5	4.6	4.6	4.6

Note: The numbers give the e-correlation scale  $\lambda_e$ , defined by

$R(\lambda_e) = e^{-1} \approx 0.3679$ . Since the e-correlation scale  $\lambda$  of the log-conductivity was unity, the numbers can also be viewed as dimensionless ratios ( $\lambda_e/\lambda$ ).

the hydraulic head). This table shows that, depending on  $\sigma_f$ , the longitudinal head correlation length obtained numerically is 0% - 15% smaller than the spectral theory predicts. For the transverse head correlation length, the numerical value is about 40% smaller than predicted by the spectral theory. Although this is a serious discrepancy, the spatial structure of the numerical head field is qualitatively similar to that predicted by the spectral theory. Incidentally, it may be surprising that the numerical head correlation lengths appear to increase with  $\sigma_f$ , thus getting closer to the spectral values as  $\sigma_f$  increases. The reason for this behavior is not all clear, and might result from complex interactions between different kinds of sampling errors in the numerical approach (finite domain effects, nonhomogeneous head field, empirical detrending).

At any rate, it seems very likely that the observed differences in the head correlation structure are due to the limited size of the domain with respect to the head correlation range, as explained above. Due to this limitation, we can only conclude here that the numerical results do not invalidate the predictions of the spectral theory concerning the infinite-domain correlation structure of the hydraulic head. In practice however, the spectral theory may not be applicable to flow systems of limited size. In the case of a confined aquifer for instance, our results suggest that the depth of the aquifer must

be several tens of conductivity correlation scales (say 50-100) in order to satisfy approximately the assumption of infinite domain. This kind of limitation will be discussed again with the anisotropic flow simulations presented in the next section.

Let us now focus on the correlation structure of the flux vector field, which has important implications for solute transport macrodispersion. Figures (6.20) through (6.28) show various components of the numerical flux correlation tensor along three directions. Each of these figures includes also a comparison with the results of the spectral theory. But first, it may be useful to provide some background on the method used to represent the flux correlation structure.

For a vector field like the flux, the correlation structure is defined by the tensor function  $R_{ij}(\xi)$  of the log vector  $\xi$  in 3D space. The more restricted subset of correlation functions discussed below corresponds to the diagonal components of this tensor, with separation vectors parallel to any of the three principal axes ( $x_1, x_2, x_3$ ): unidirectional functions  $R_{ii}(\xi_j)$ . The physical meaning of these correlation functions can be better apprehended by examining Figure (6.20). For instance, the function  $R_{11}(\xi_1)$  is the longitudinal flux correlation in the longitudinal direction, while the function  $R_{22}(\xi_3)$  is the transverse flux correlation in the other transverse direction.

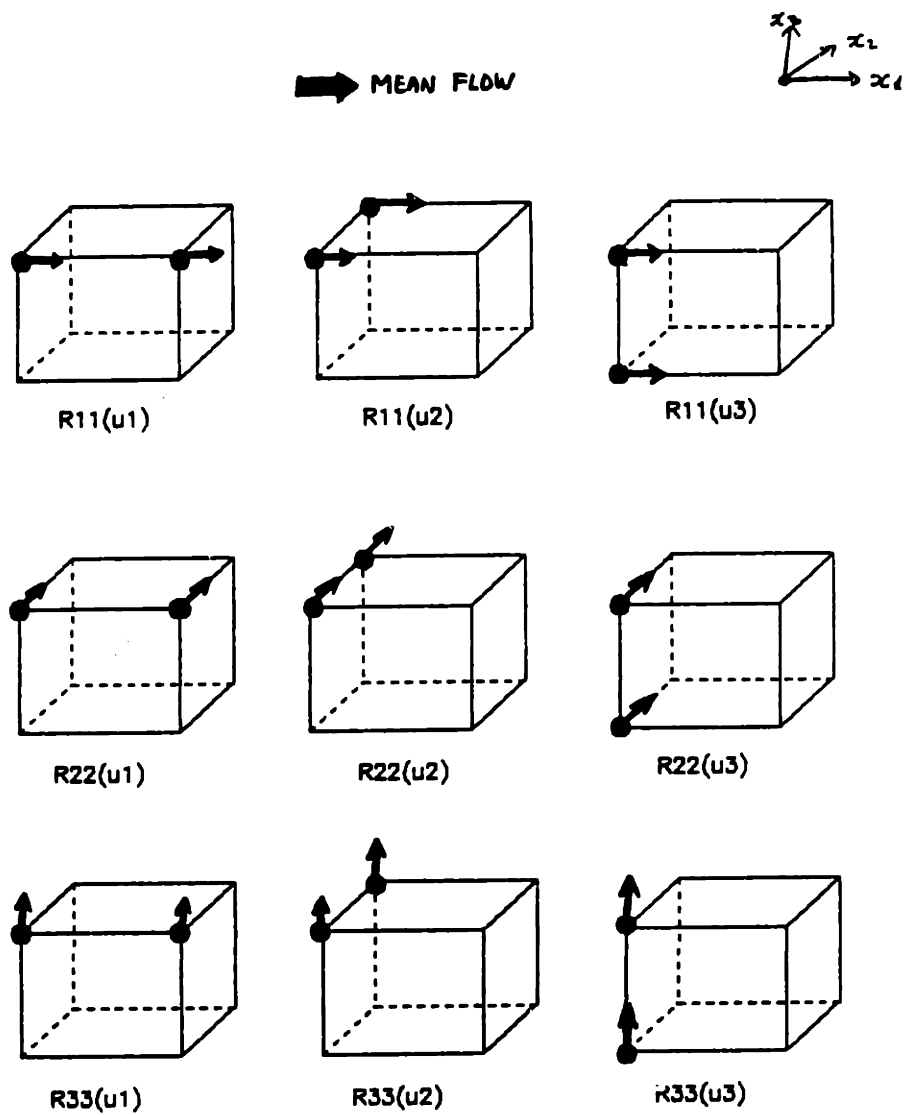


Figure 6.20 Subset of vector-vector correlation functions, restricted to the diagonal components of the correlation tensor and to separation vectors parallel to the principal axes.

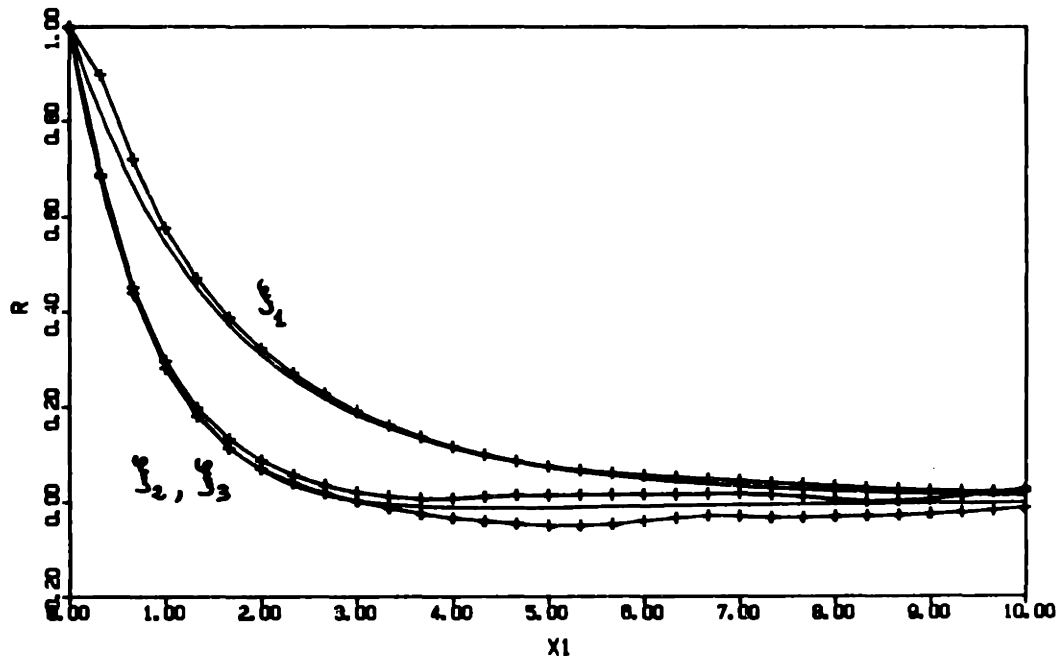


Figure 6.21: Flux correlation functions  $R_{Q_1 Q_1}(\xi_j)$  for  $\sigma_f = 1.0$  (solid lines: spectral theory; crosses; numerical simulation).

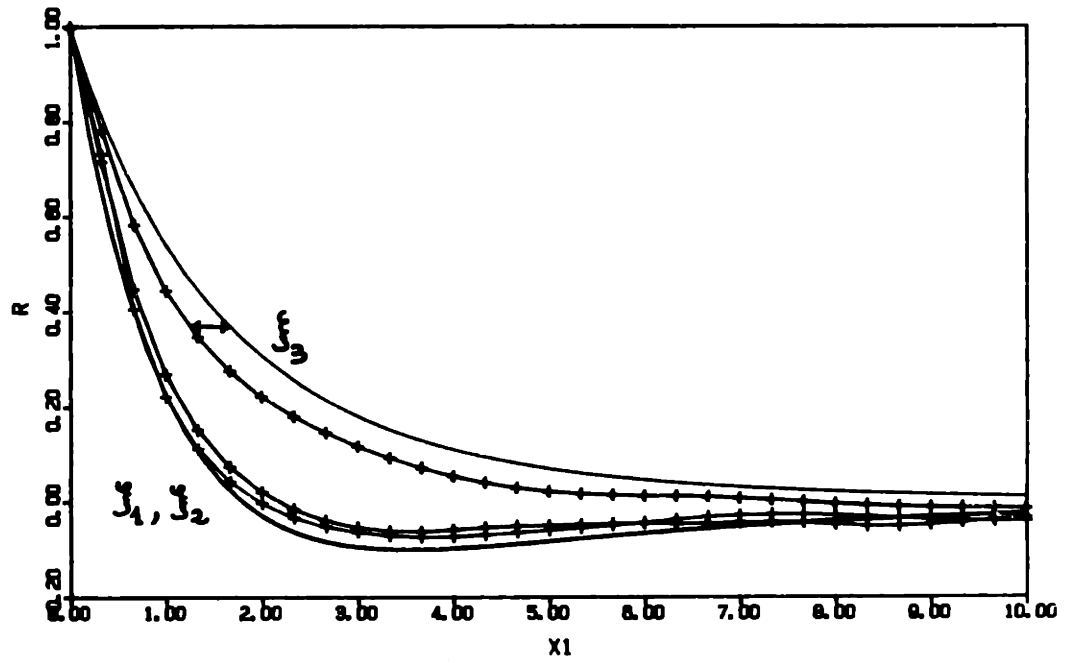


Figure 6.22 Flux correlation functions  $R_{Q_2 Q_2}(\xi_j)$  for  $\sigma_f = 1.0$  (solid lines: spectral theory; crosses: numerical simulation).

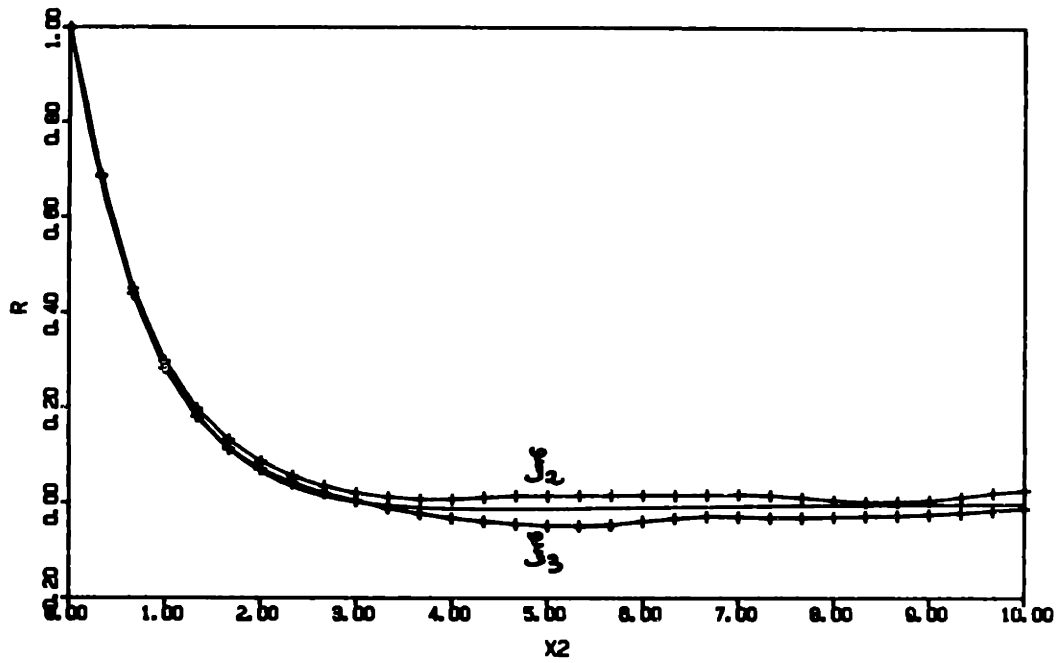


Figure 6.23 Verification of statistical symmetries on the numerical flux correlation functions ( $\sigma_f = 1.0$ ):

$$R_{Q_1 Q_1}(F_2) \approx R_{Q_1 Q_1}(F_3).$$



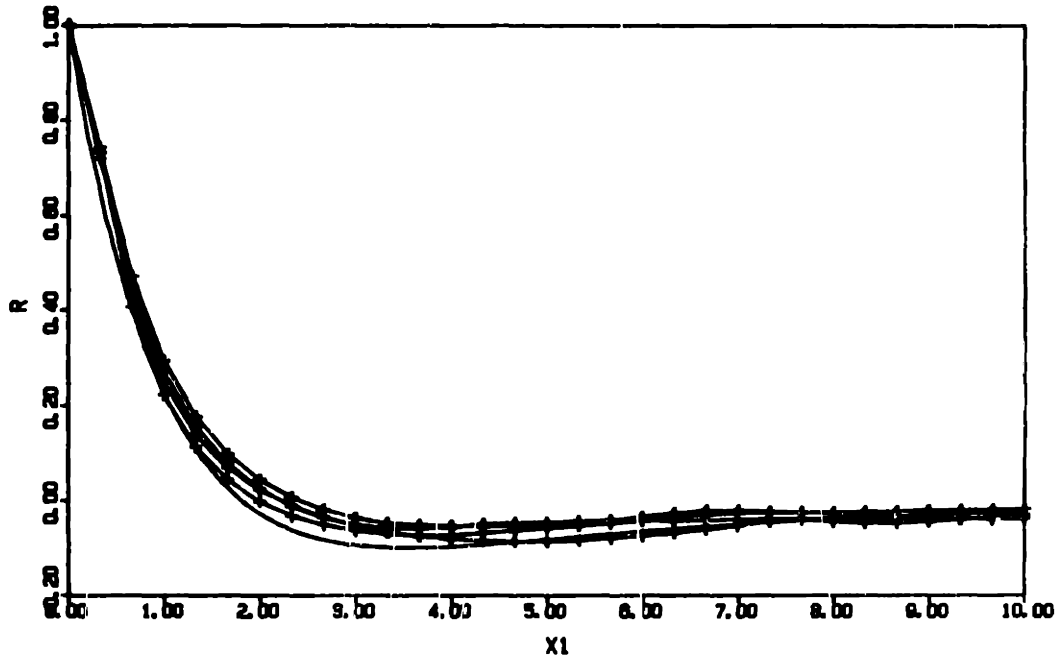


Figure 6.24 Verification of statistical symmetries of the numerical flux correlation functions ( $\sigma_f = 1.0$ ):  $R_{Q_2Q_2}(\xi_1)$ ,  $R_{Q_2Q_2}(\xi_2)$ ,  $R_{Q_3Q_3}(\xi_1)$ ,  $R_{Q_3Q_3}(\xi_2)$  are nearly identical.

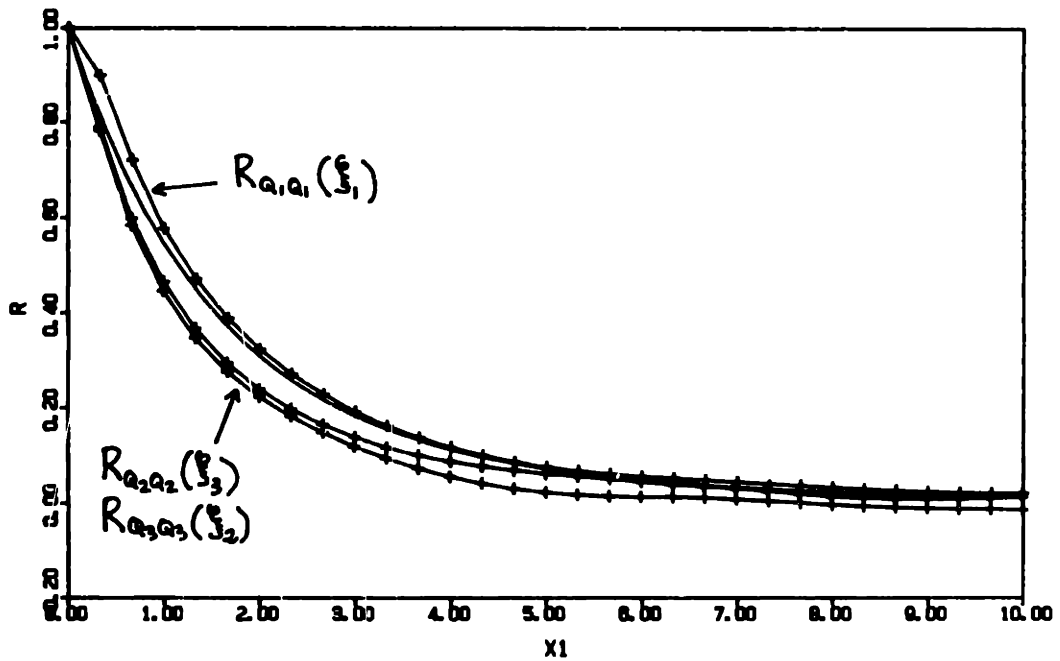


Figure 6.25 Verification of statistical symmetries on the numerical flux correlation functions ( $\sigma_f = 1.0$ ):

$$R_{Q_2 Q_2}(\xi_2) \approx R_{Q_3 Q_3}(\xi_3) \approx R_{Q_1 Q_1}(\xi_1).$$

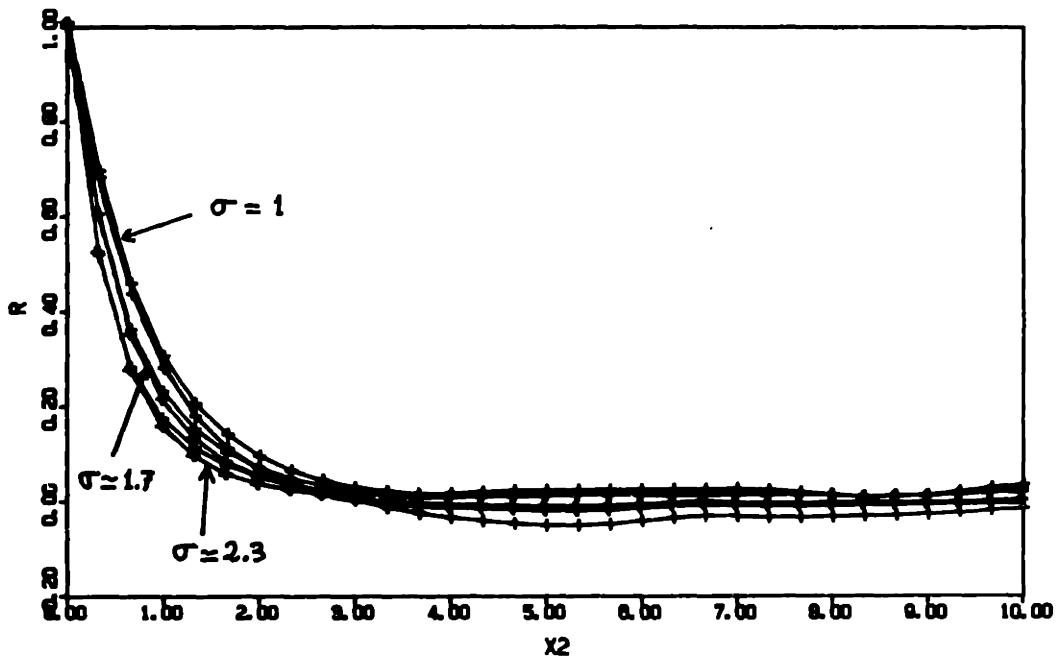


Figure 6.26 Numerical flux correlation functions  $R_{Q_1 Q_2}(\xi_2)$ , and  $R_{Q_1 Q_1}(\xi_3)$  for  $\sigma_f \approx 1.0, 1.7$  and  $2.3$ .

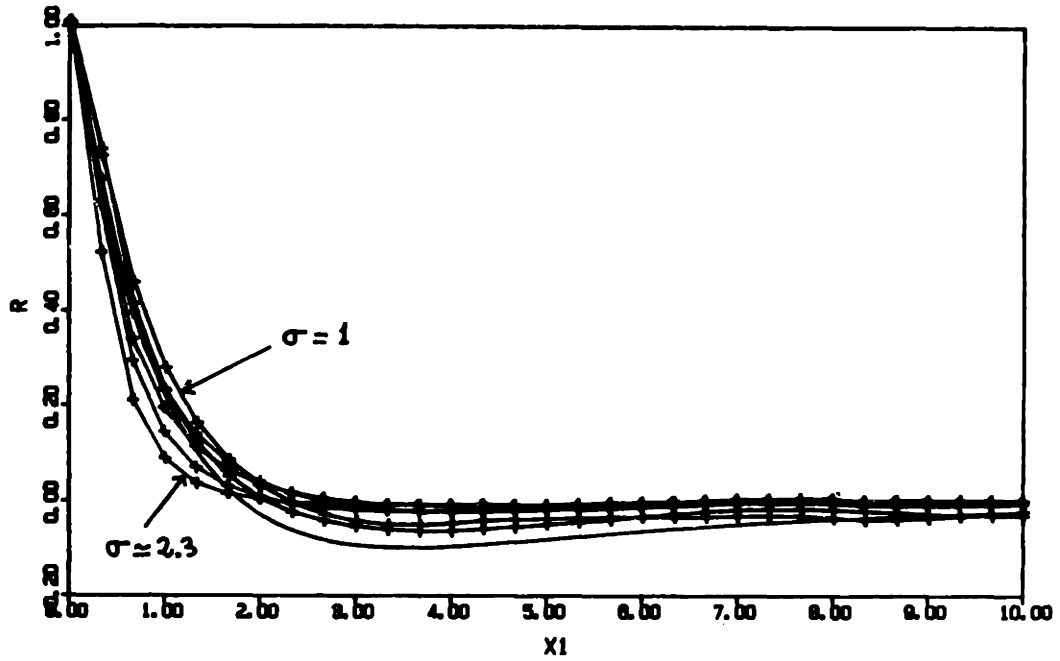


Figure 6.27 Numerical flux correlation functions  $R_{Q_2Q_2}(\xi_1)$ , and  $R_{Q_2Q_2}(\xi_2)$  for  $\sigma_f \approx 1.0, 1.7$ , and  $2.3$ .

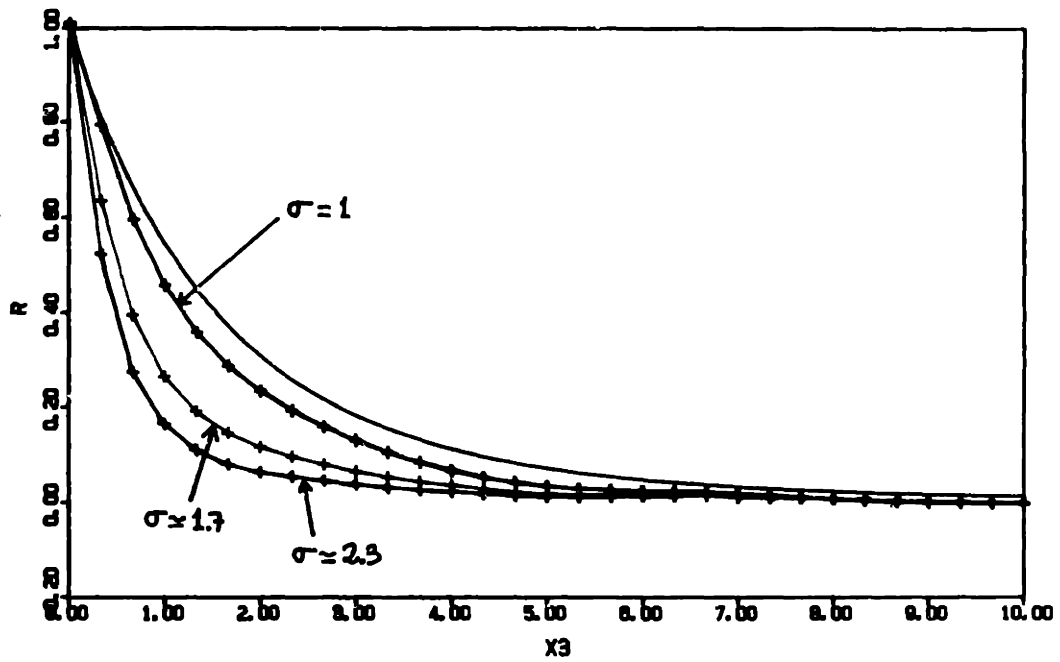


Figure 6.28 Numerical flux correlation function  $R_{Q_2 Q_2}(\xi_3)$ , for  $\sigma_f \approx 1.0, 1.7, \text{ and } 2.3$ . The solid line corresponds to the result of the spectral theory, independent of  $\sigma_f$ .

These functions satisfy a number of symmetry relations which were discussed in Chapter 4 (Section 4.2).

With this in mind, let us now focus on the results obtained for the flux vector correlation functions. For moderate variability  $\sigma_f = 1.0$ , Figures 6.21 and 6.22 show a surprisingly good agreement between the flux correlation function obtained numerically and those predicted by the spectral theory (Chapter 3, Section 3.3, Figures 3.2 and 3.3). There is in particular an excellent agreement for the correlation functions of the longitudinal flux component in any direction ( $R_{Q_1 Q_1}(\xi_j)$  in Figure 6.21). The agreement is also excellent for the correlation functions  $R_{Q_2 Q_2}(\xi_1)$  and  $R_{Q_2 Q_2}(\xi_2)$  shown in Figure (6.22). Finally, note that the numerical solution slightly underestimates the correlation  $R_{Q_2 Q_2}(\xi_3)$  with respect to the spectral theory, although the agreement is still fairly good.

Furthermore, it is also important to note that the correlation structure of the numerical flux vector field appears to satisfy the symmetry relations implied by the statistical isotropy of the input log-conductivity field (Chapter 4, Section 4.2). This can be verified by assembling on the same plot the numerical correlation functions that should be identical in theory. The results of these comparisons are shown in Figures (6.23, (6.24), and (6.25) for the case  $\sigma_f = 1.0$ . The theoretical

symmetry identities (listed below) are indeed satisfied quite accurately by the numerical results:

Figure (6.23):  $R_{Q_1 Q_1}(\xi_2) = R_{Q_1 Q_1}(\xi_3)$

Figure (6.24):  $R_{Q_2 Q_2}(\xi_1) = R_{Q_2 Q_2}(\xi_2)$   
 $= R_{Q_3 Q_3}(\xi_1)$   
 $= R_{Q_3 Q_3}(\xi_3)$

Figure (6.25):  $R_{Q_2 Q_2}(\xi_3) = R_{Q_3 Q_3}(\xi_2)$

Overall, these encouraging results lead us to conclude that the correlation structure of the flux vector field predicted by the spectral theory must be fairly close to the exact result in the case  $\sigma_f = 1.0$ . This conclusion is warranted if one rejects the possibility of a mere chance coincidence between the spectral solutions and the numerical single-realization simulations. The reliability of the numerical flux correlations does not seem questionable, in view of the fact that they satisfied fundamental symmetry relations with excellent accuracy. Thus, our simulation results confirm the validity of the Gelhar-Axness spectral theory (Gelhar and Axness, 1983) concerning the correlation structure, or shape of the flux spectrum, at least for moderate variability ( $\sigma_f \leq 1$ ). Note that the same remark applies to the modified spectral solutions developed in this work, since the proposed modification (Chapter

4, Section 4.3) did not affect the shape of the flux spectrum, but only the flux variances.

Let us now focus on the effect of increasing log-conductivity variability on the correlation structure of the flux vector field. First of all, note that the flux correlations obtained from the spectral theory are independent of  $\sigma_f$ . Now, this appears to be approximately satisfied by the numerical flux correlation functions  $R_{Q_i Q_i}(\xi_j)$ , except for one particular correlation function  $R_{Q_2 Q_1}(\xi_3)$ , as shown in Figures (6.26), (6.27), and (6.28). In each figure, the numerical correlation functions obtained for the three cases  $\sigma_f \simeq 1.0, 1.7, 2.3$  were superimposed. It seems clear that the only significant departure from the spectral theory concerns the "correlation of the transverse flux component in the other transverse direction",  $R_{Q_2 Q_1}(\xi_3)$ , as depicted in Figure (6.28). Nevertheless, the other flux correlation functions appeared to be relatively stable with respect to  $\sigma_f$ , in accordance with the spectral theory.

Again, these results suggest that the spectral theory of Gelhar and Axness (1983) is remarkably robust as far as the flux correlation structure or shape of the flux spectrum is concerned. The agreement between the numerical and "spectral" flux correlation functions was reasonably good within the whole range of log-conductivity variability up to  $\sigma_f \simeq 2.3$ . This can



be seen more directly by inspection of Table 6.9, where the correlation scales of various flux correlation functions are compared to those predicted by the spectral theory. However, this kind of comparison does not fully reflect the good agreement observed from the plots. In our view, the only major point of concern here is the behavior of the flux correlation  $R_{Q_2Q_2}(\xi_2)$ , and its identical "twin"  $R_{Q_3Q_3}(\xi_3)$ . The reason for the discrepancy on this particular correlation is not clear to us at this point, although the theoretical results of Chapter 4 might provide a clue for future investigation.

Finally, it might also be of interest to mention, without going into details, that the correlation functions of the head gradient ( $G_i$ ) were also in good agreement with the spectral theory. At large variability, there was a closer agreement between the numerical and spectral correlations of the head gradient than between the numerical and spectral correlations of the flux. Since we also found that the standard deviations of the head gradient predicted by the theory were quite close to the numerical results for all values of  $\sigma_f$ , we conclude that the head gradient field is not affected much by high order effects. This finding might be useful for further refinement of the spectral theory.

TABLE 6.9

CORRELATION SCALES OF THE FLUX VECTOR COMPONENTS ALONG THREE DIRECTIONS  
 $(R_{Q_i Q_i}(\xi_j))$ : COMPARISON OF SPECTRAL SOLUTION WITH THE NUMERICAL  
 RESULTS OF THE 1 MILLION NODE "ISOTROPIC" FLOW PROBLEM A

Correlation Function	Spectral theory for all $\sigma_f$	Numerical Results		
		$(\sigma_f=1.0)$	$(\sigma_f=1.7)$	$(\sigma_f=2.3)$
$R_{Q_1 Q_1}(\xi_1)$	1.70	1.75	1.41	1.16
$R_{Q_2 Q_2}(\xi_3)$	1.70	1.26	0.71	0.53
$R_{Q_3 Q_3}(\xi_2)$	1.70	1.33	0.77	0.55
$R_{Q_1 Q_1}(\xi_2)$	0.80	0.83	0.65	0.54
$R_{Q_1 Q_1}(\xi_3)$	0.80	0.85	0.64	0.52
$R_{Q_2 Q_2}(\xi_1)$	0.72	0.72	0.58	0.49
$R_{Q_2 Q_2}(\xi_2)$	0.72	0.81	0.71	0.63
$R_{Q_3 Q_3}(\xi_1)$	0.72	0.78	0.60	0.51
$R_{Q_3 Q_3}(\xi_3)$	0.72	0.85	0.76	0.66

Note: The numbers give the e-correlation scale  $\lambda_e$  defined by  $R(\lambda_e) = e^{-1} \approx 0.3679$ .  
 The correlation scale of the log-conductivity field was equal to unity.

[f] Summary of results:

The single-realization results obtained in this section confirmed many aspects of the spectral theory previously developed by Bakr et al. (1978) and Gelhar and Axness (1983). Our arguments to accept (or reject) the single-realization simulation results were based on a number of criteria: evaluation of sampling errors for the head field, truncation errors for the flux field, symmetry relations for the flux correlation functions, and, last but not least, agreement with spectral theory.

Some of our conclusions in particular seem beyond doubt in view of the close agreement with the spectral theory for a wide range of conductivity variability. Thus, it seems that the standard spectral theory gives essentially exact solutions for the standard deviations of the head ( $\sigma_H$ ) and head gradient ( $\sigma_{G_i}$ ), as well as the effective conductivity ( $K_{eff}$ ), up to large variability  $\sigma_f \simeq 2.3$ . Furthermore, the results also indicate that the flux correlation structure predicted by the spectral theory is very accurate at  $\sigma_f = 1.0$ , and remains still fairly reliable up to large conductivity variability ( $\sigma_f \simeq 2.3$ ) except perhaps for one particular flux correlation function.

On the other hand, our analysis suggested that the

standard spectral theory significantly underestimates the degree of variability of the flux vector ( $\sigma_{q_i}$ ) even in the case of moderate variability ( $\sigma_f = 1.0$  and larger). When the *modified* spectral theory developed in Chapter 4 (Section 4.3) was used instead, the theoretical values of  $\sigma_{q_i}$  became closer to the numerical ones. However the discrepancy was still larger than the allowable margin of error (numerical truncation error on the flux) in the case of large variability  $\sigma_f \geq 1.7$ . New analytical expressions (6.13) were proposed for the  $\sigma_{q_i}$  in order to compensate for unmodeled high order effects. It may be more than a coincidence that these expressions, which involve combinations of arithmetic and geometric mean conductivities, fit the numerical results with very good accuracy for  $\sigma_f = 1.0, 1.7$  and 2.3 as well. We therefore conclude that it may be important to consider higher order spectral solutions of the flux vector (such as those proposed in this work) for applications to groundwater flow and transport in highly heterogeneous aquifers (say  $\sigma_f \approx 1-1.5$  or larger).

In addition, we have found that the spatial structure of the head field could be significantly different from that predicted by the spectral theory in the case of finite size flow domains, although the magnitude and anisotropy of the head correlations were qualitatively in accordance with the spectral theory. For the isotropic flow problem at hand, our analysis of

finite size effects suggests that the "infinite domain" assumption of the spectral theory will hold in cases where the longitudinal size is on the order of  $25-50\lambda$ , and the transverse size  $50-100\lambda$ . This might be important for applications involving confined aquifers with finite thickness.

Apart from the above reservations concerning the flux standard deviations and the head correlations, it seems that all other large scale flow properties predicted by the spectral theory are reasonably accurate within a wide range of log-conductivity standard deviations, say up to  $\sigma_f \approx 2$  or so.

#### **6.4 Summary Analysis of 3D Anisotropic Flow Simulations (220,000 Nodes)**

This section is devoted to the analysis of single-realization flow simulations in the case of a statistically anisotropic log-conductivity field (3D Markov ellipsoidal) with principal axis parallel to the mean hydraulic gradient. The "anisotropic" flow problems E and F of Table 6.1 were designed to mimic the case of horizontal groundwater flow in a horizontally "stratified" aquifer, with anisotropy ratio  $\epsilon = 1/4$  (ratio of vertical to horizontal correlation scales of log-conductivity). Observe that the variability of the log-conductivity field is the same for both problems ( $\sigma_f = 1.0$ )

but the geometry of the discrete grid differs.

For Problem E, the grid resolution was taken to be one-half with respect to the conductivity correlation scales in each direction ( $\Delta x_i/\lambda_i=1/2$ ). On the other hand, for problem F, the grid resolution in the vertical was much coarser ( $\Delta x_3/\lambda_3=4$ ) but, as a result, the vertical size of the domain was much larger. The total number of nodes was the same for both problems (220,000 nodes). These problems were designed to test the applicability of the single-realization approach in the case of statistically anisotropic media, and notably to evaluate the numerical requirements implied by anisotropy. These *preliminary results* are presented here because of their relevance for practical applications, in view of the fact that most natural formations exhibit some kind of stratification (see Figure 2.3. of Chapter 2 for a comparison of the anisotropic Markov conductivity with field measurements). However, there will be no attempt here at obtaining an exhaustive statistical description of the flow field, as was done in the case of isotropic conductivities. The reasons for the limited scope of this study may become clearer in the sequel.

In what follows, it will be convenient to designate the anisotropic problem (E) as the "shallow stratified aquifer" flow problem, and the anisotropic problem (F) as the "deep stratified

aquifer" flow problem. Indeed, it can be seen from Table 6.1 that the aquifer thickness is just 7.5 units in the first case, compared to 60 units in the second case, in units of the horizontal correlation scale  $\lambda$  of the log-conductivity field. By the same token, recall that Problem E (shallow aquifer) has a much finer grid resolution than problem F (deep aquifer), particularly in the vertical direction. Despite these differences, recall that the size of the grid was the same for each case, comprising 61 nodes in each direction (220,000 nodes).

With this distinction in mind, we now proceed to develop a succinct analysis of the simulated flow fields, limited to the study of spatial variability of the hydraulic head. The spatial variation of the head is depicted graphically in Figures (6.29), (6.30), (6.31) along selected slices (respectively: horizontal parallel to flow, vertical parallel to flow, and vertical transverse to flow). Each of these figures shows the numerical head fields obtained for:

- (a) -- the "shallow stratified aquifer" problem (E)
- (b) -- the "deep stratified aquifer" problem (F)

Figures 6.31(a), (b) in particular seem to indicate that the pattern of hydraulic heads in the cross-flow plane perpendicular to stratification is more anisotropic for the "shallow stratified

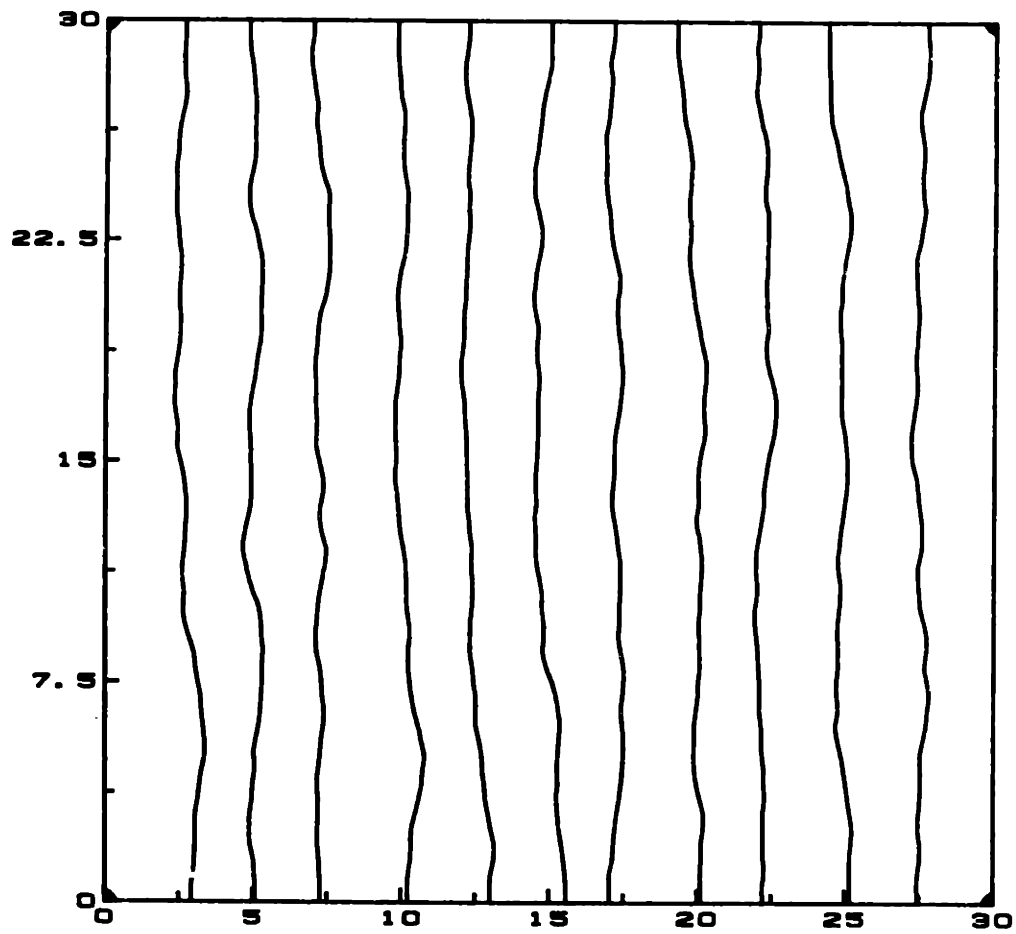


Figure 6.29 (a) Hydraulic head contours in a horizontal slice parallel to the mean flow, for a "shallow stratified aquifer" (Problem E)



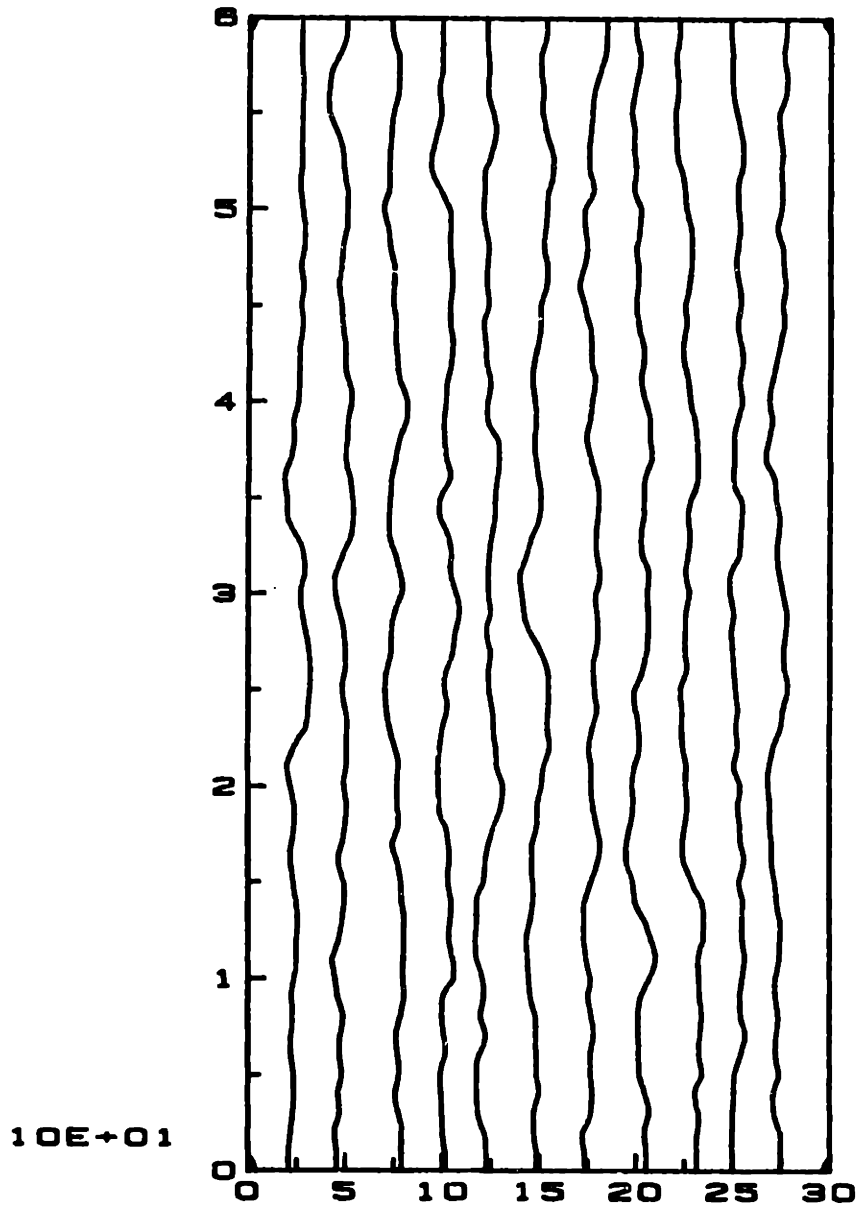


Figure 6.29 (b) Same as (a), for a "deep stratified aquifer" (Problem F)

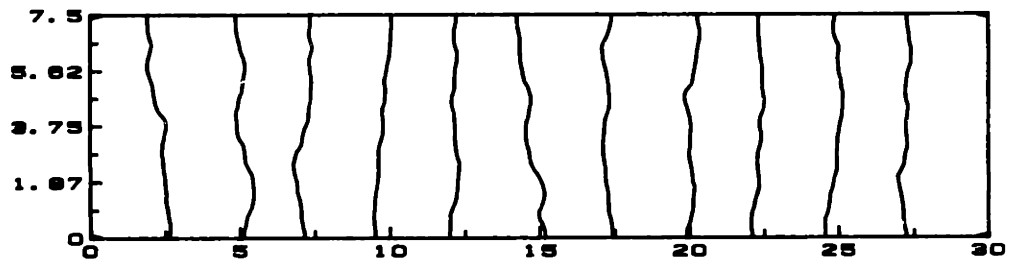


Figure 6.30 (a) Hydraulic head contours in a vertical slice parallel to the mean flow, for a "shallow stratified aquifer" (Problem E)

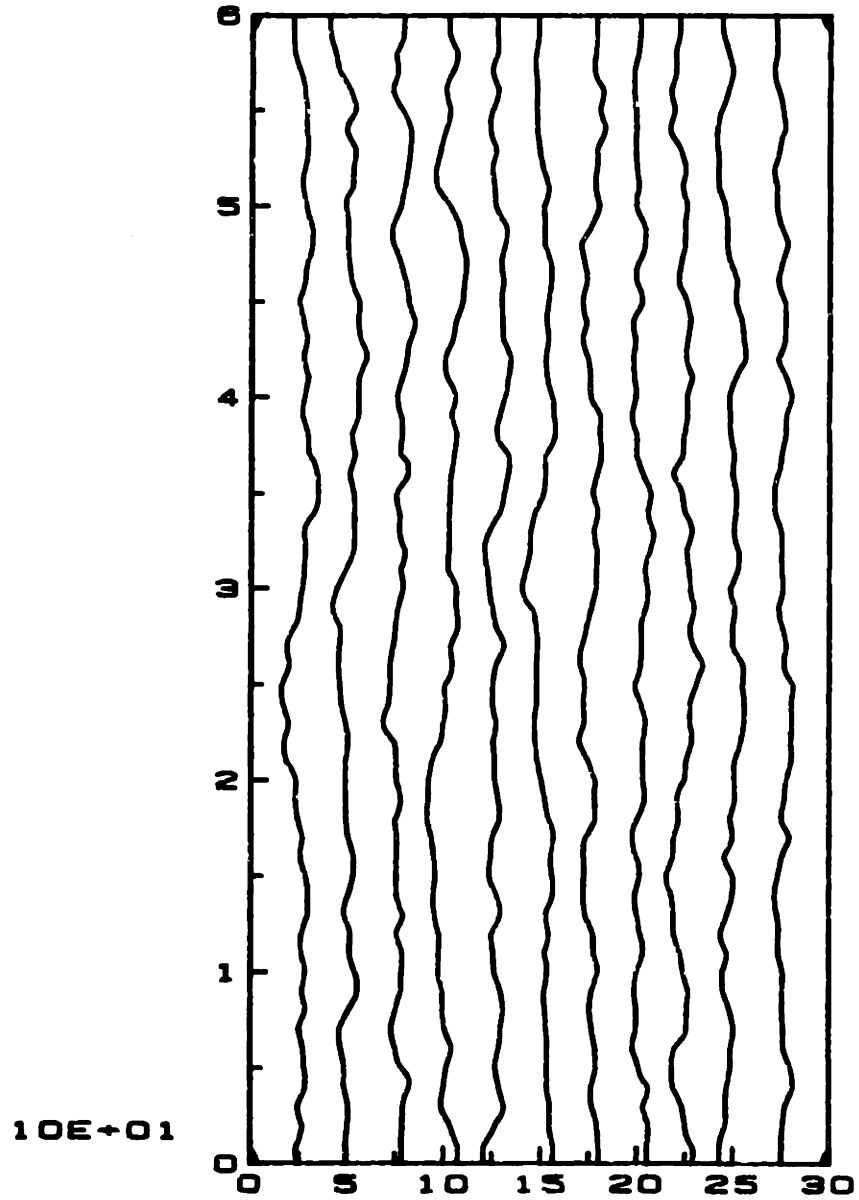


Figure 6.30 (b) Same as (a), for a "deep stratified aquifer" (Problem F).



Figure 6.31 (a) Hydraulic head contours in a vertical slice transverse to the mean flow, for a "shallow stratified aquifer" (Problem E)

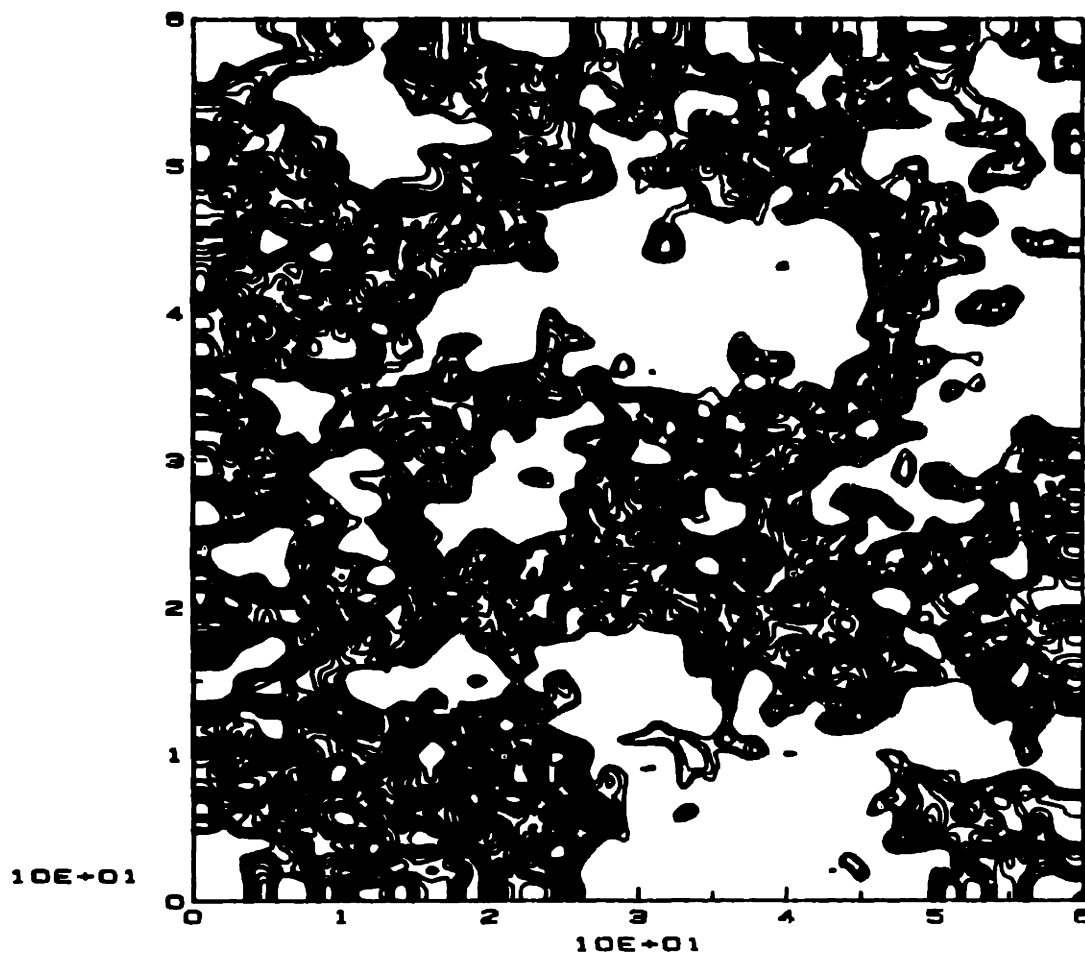


Figure 6.31 (b) Same as (a), for a "deep stratified aquifer" (Problem F).

aquifer" (a), than for the "deep stratified aquifer" (b). It may be preposterous to draw any definite conclusions from such limited observations, however we will see shortly that the above conclusion is confirmed by statistical analysis.

The standard deviation and correlation functions of the head were computed in each case by using the same longitudinal detrending technique as in the previous sections (see section 6.1 on methodology). Figure (6.32) shows in each case (a) and (b) a typical sample function of the head  $H(x_1)$  along the mean flow direction, superimposed on the cross-flow average  $\bar{H}(x_1)$  as defined in equation (6.5). These pictures suggest that the head variability around the nonlinear trend is smaller for the shallow aquifer (a) than for the deep aquifer (b).

Indeed, Table 6.10 (top) shows that the head standard deviation for (a) is significantly smaller than for (b). The infinite-domain spectral theory (equation 3.28 of Section 3.4, Chapter 3) gives the same value of  $\sigma_H$  in both cases. Furthermore, it appears that the value predicted by the spectral theory lies in between the numerical solutions of (a) and (b). This might be explained by the fact that, in (a), the flow domain was too small to allow for fully three-dimensional fluctuations of the hydraulic head whereas in (b), the grid resolution was coarse enough to generate significant numerical noise that may

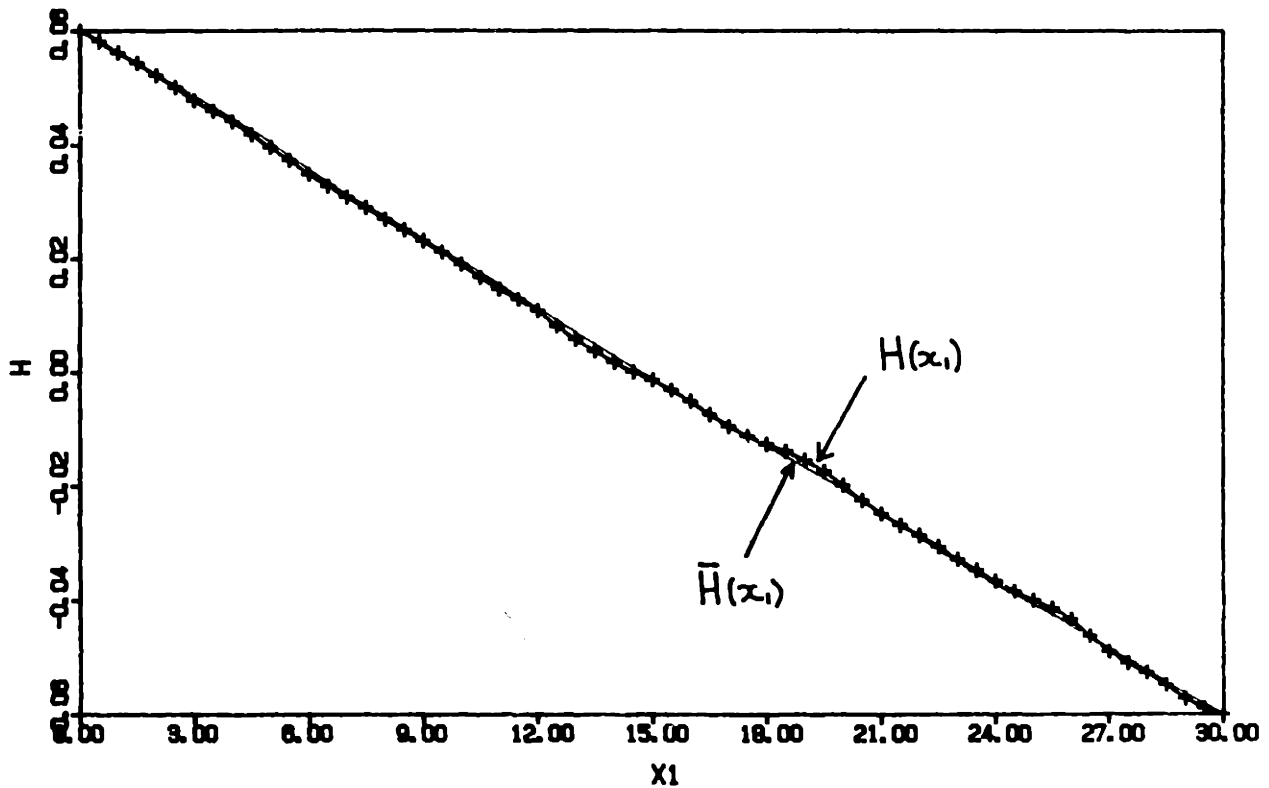


Figure 6.32 (a) Sample function of the head field  $H(x_1)$  along a selected transect parallel to the mean flow, and cross flow average  $\bar{H}(x_1)$ : case of the "shallow aquifer" Problem E.

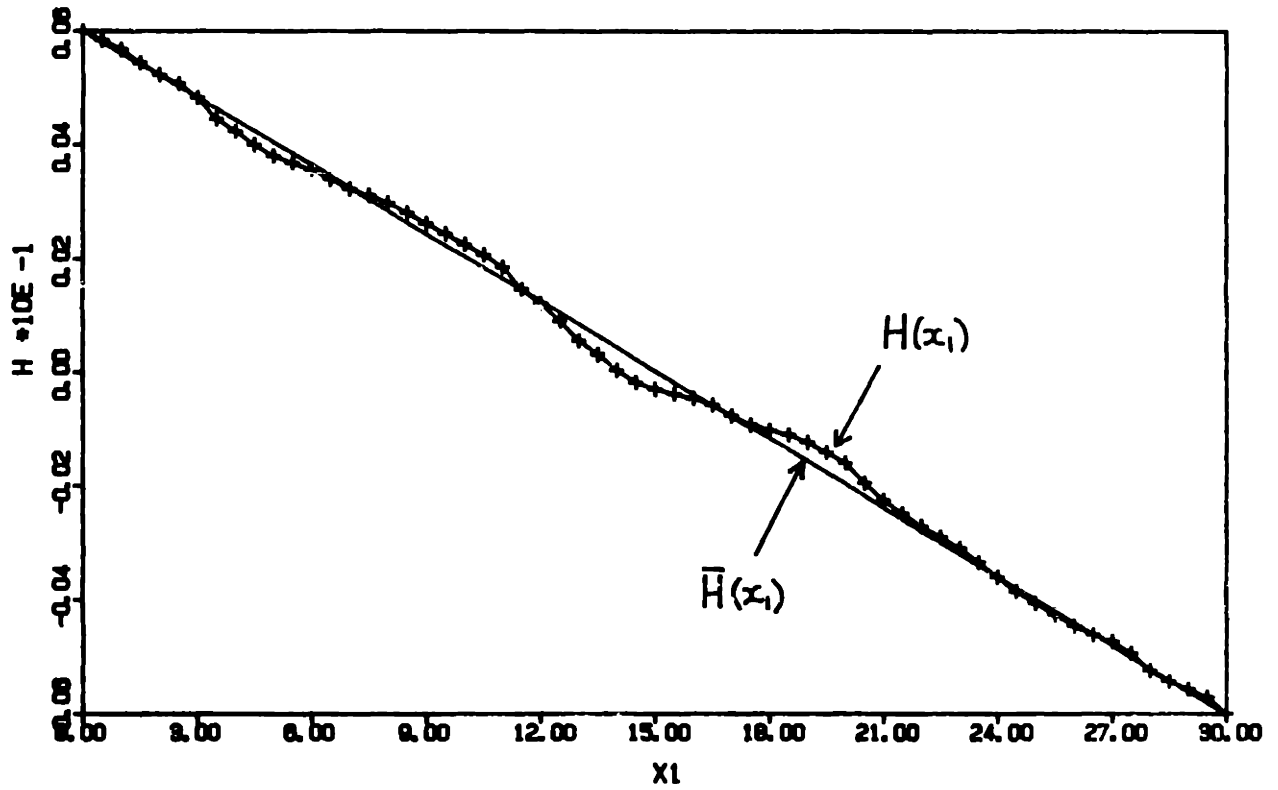


Figure 6.32 (b) Same as (a) for the "deep aquifer" Problem F.



TABLE 6.10  
 COMPARISON OF PRELIMINARY "ANISOTROPIC FLOW SIMULATIONS"  
 WITH THE RESULTS OF THE SPECTRAL THEORY:  
 HEAD STANDARD DEVIATION AND CORRELATION SCALES  
 (220,000 NODE FLOW PROBLEMS E AND F,  $\sigma_f = 1.0$  and  $\epsilon = 1/4$ ).

Normalized Head Standard Deviation	Spectral Theory	(a): Shallow Aquifer (Problem E)	(b): Deep Aquifer (Problem F)
$\sigma_H/J_1$	0.3100	0.2654	0.3678
$\frac{\hat{\sigma}_H - \sigma_H}{\sigma_H}$	---	-14%	+18%

Correlation Scales	Longitudinal (i=1)	Transverse Horizontal (i = 2)	Transverse Vertical (i = 3)
$\lambda_{\ln K}$	1.00	1.00	0.25
$\lambda_H$ (spectral)	3.0	7.5	7.0
(a): $\lambda_H$ (Problem E)	2.2	3.7	2.6
(b): $\lambda_H$ (Problem F)	2.2	5.7	3.7

have contributed to the standard deviation of the head. Thus,  $\sigma_H$  was underestimated in the first case and overestimated in the second case, with respect to the spectral result. Note that  $\sigma_H$  was normalized by the mean head gradient, which was not the same in the two simulations.

Let us now focus on the statistical correlation structure of the simulated hydraulic head fields. It may be instructive to examine first the correlation structure of the single realization log-conductivity fields generated in each case. Figures 6.33 (a) and (b) show the computed log-conductivity correlation functions along the three principal directions, respectively for the "shallow aquifer problem" (a) and the "deep aquifer problem" (b). It is interesting to note that, in the latter case, the  $\ell n K$ -correlations along the vertical axis are not very well captured due to the coarse grid resolution  $\Delta x_3/\lambda_3=4$ . Nevertheless, in both cases (a) and (b), the computed correlations agree with the theoretical anisotropic Markov correlation function. In addition, the computed standard deviation of  $\ell n K$  were in each case very close to the theoretical value  $\sigma_f=1.0$ , with a 2% margin of error.

The unidirectional head correlation functions were computed from the detrended head fields according to the procedure outlined in Section 6.1 (same procedure used for

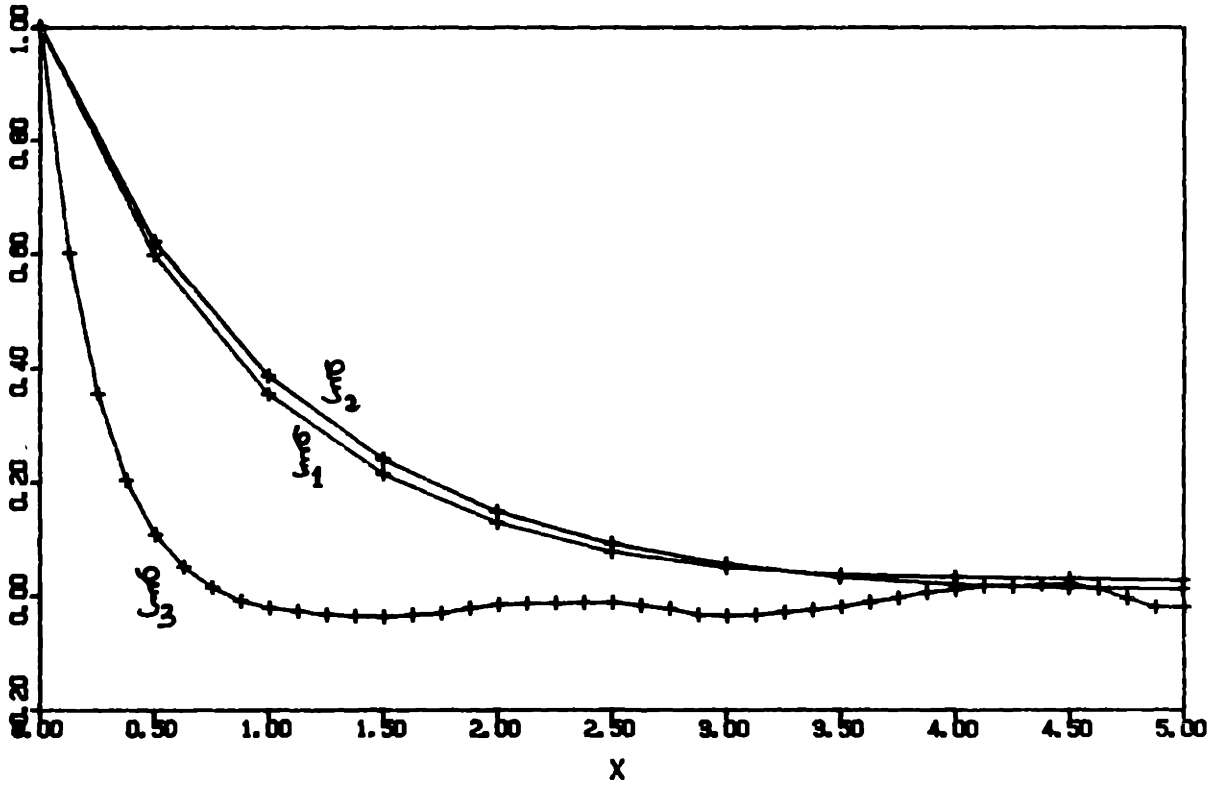


Figure 6.33 (a) Computed log-conductivity correlation functions for the single-realization anisotropic Problem E (shallow aquifer, fine grid)

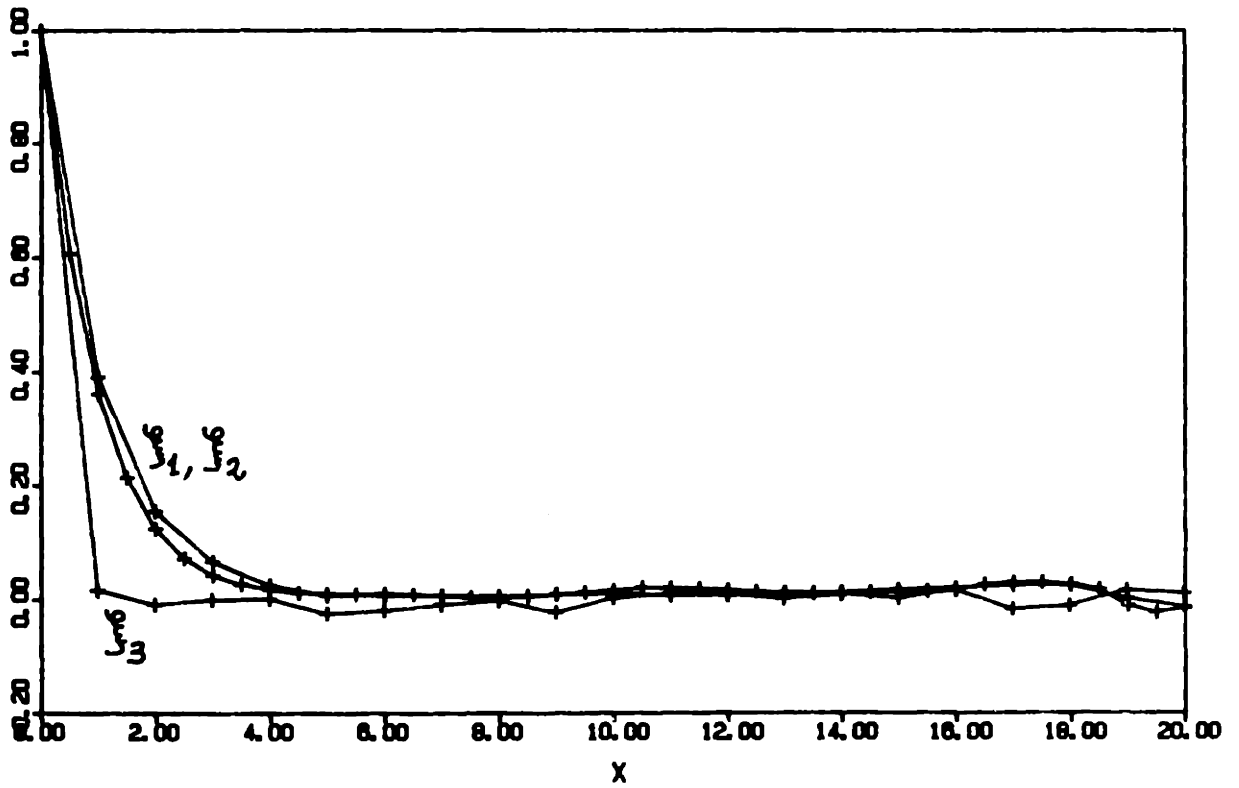


Figure 6.33 (b) Computed log-conductivity correlation functions for the single-realization anisotropic Problem F (deep aquifer coarse grid)

analyzing the isotropic flow problems in previous sections). The numerical head correlation functions corresponding to the "shallow" and "deep" aquifer problems (a) and (b) are shown in Figures 6.34(a) and (b). For comparison, the correlation functions obtained from the spectral theory (Chapter 3, section 3.4) are also displayed in Figure 6.34(c).

As expected, it appears that the head correlation structure obtained for the "shallow stratified aquifer" (a) disagrees more strongly with the infinite-domain spectral theory than the correlations obtained for the "deep stratified aquifer" (b). This can be also seen by comparing directly the head correlation scales  $\lambda_H^{(i)}$ , as shown in Table 6.10 (bottom).

Thus the simulation results at hand confirm our previous conclusions about the applicability of the spectral theory in the case of stratified aquifers (Chapter 3, section 3.5). It seems clear that the spatial structure of the head field in the case of the shallow stratified aquifer could not be adequately modeled by the infinite-domain spectral theory, since the aquifer thickness ( $7.5 \lambda$ ) was on the same order as the vertical correlation range of the head field (about  $7.0 \lambda$  according to the spectral theory, or  $2.0 \lambda$  according to the finite domain simulation). In these conditions, the hydraulic head field obtained for the shallow case (a) may not be

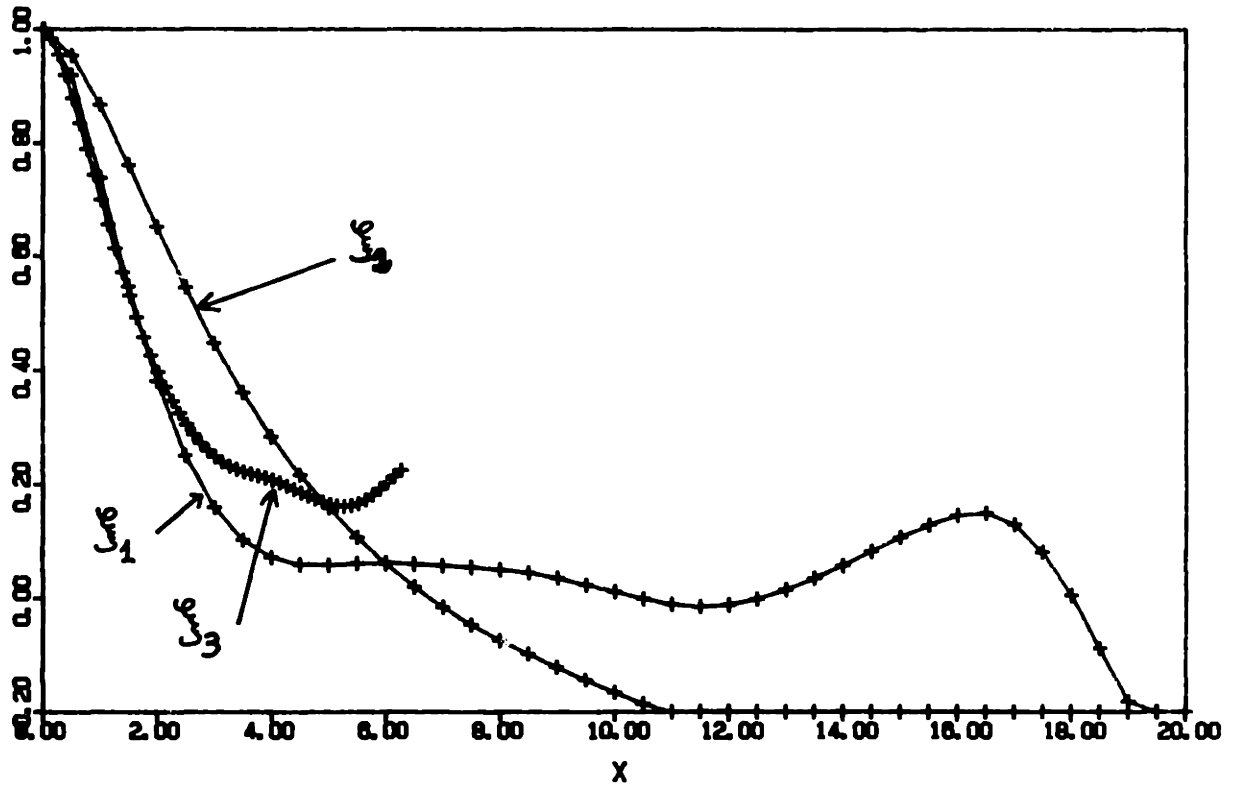


Figure 6.34 (a) Computed head correlation functions for the single-realization anisotropic flow Problem E (shallow aquifer, fine grid)

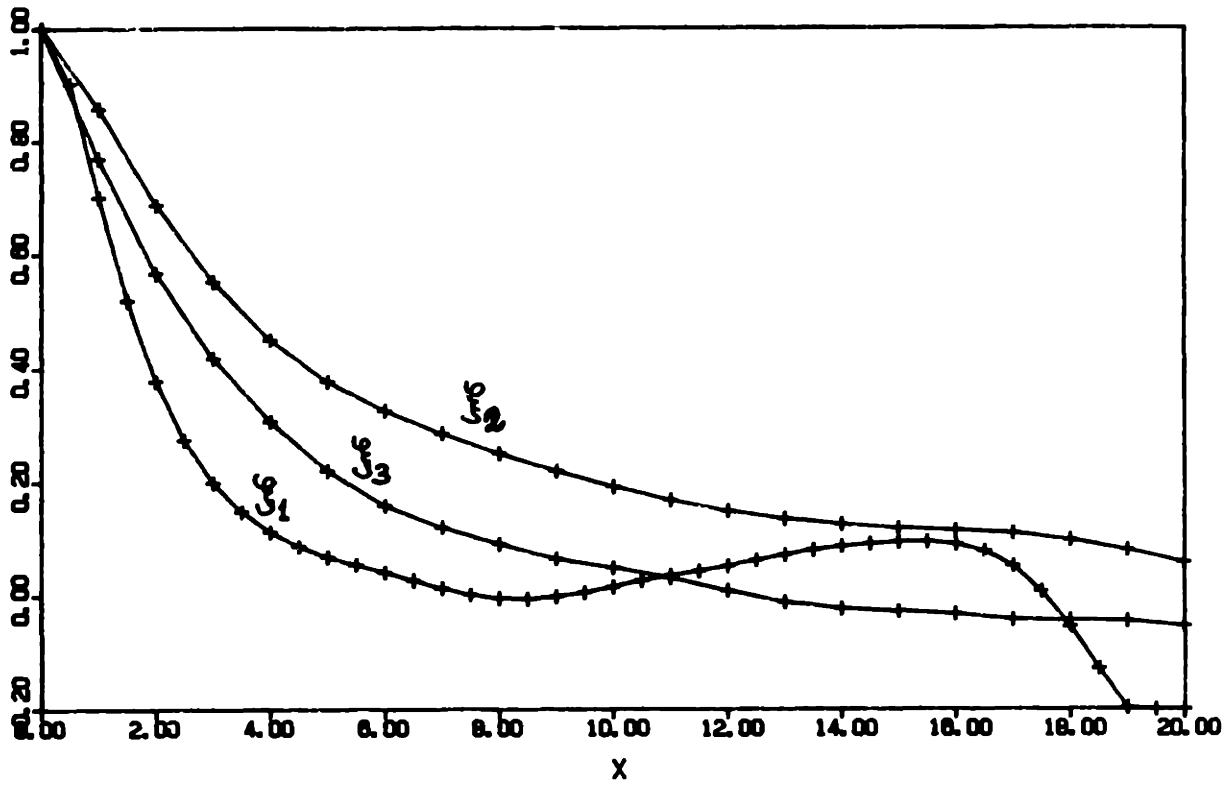


Figure 6.34 (b) Computed head correlation functions for the single-realization anisotropic flow problem F(deep aquifer, coarse grid).

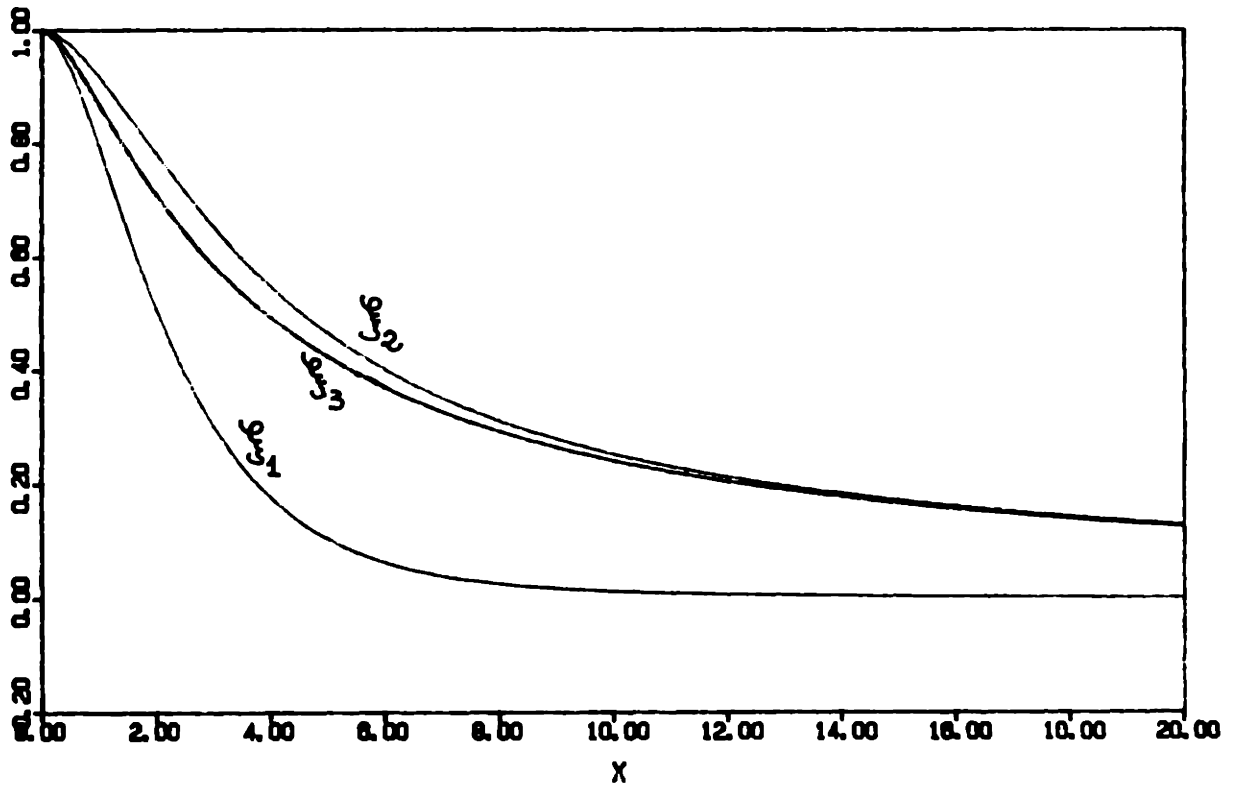


Figure 6.34 (c) Theoretical head correlation functions as predicted by the spectral theory for anisotropy ratio  $\epsilon = 1/4$  ( $\lambda_i = 1, 1, .025$ ).



representative of the ensemble of possible flow realizations, and the stochastic single-realization approach becomes meaningless.

On the other hand, the head correlations obtained for the "deep stratified aquifer" case (b) agree more closely with the infinite-domain spectral theory. This leads us to believe that the predictions of the spectral theory (near-isotropy of the head in the vertical and horizontal directions transverse to the mean flow) could be confirmed more conclusively with a larger flow domain and improved geometry/resolution of the grid.

To obtain also an accurate statistical representation of the flux vector field, however, the grid resolution may have to be fine in proportion to the smallest correlation scale of the input conductivity field ( $\lambda_3 = \lambda/4$ ). Indeed, our previous discussion of stratified flow systems (Chapter 3, sections 3.4 and 3.5) suggested that the correlation scales of the transverse flux components could be only a fraction of the geometric mean of horizontal and vertical conductivity scales ( $\lambda_G = \sqrt{\lambda \cdot \lambda_3}$ ). The reader is referred in particular to Figures (3.5) to (3.7) and equation (3.22). The latter equation can be used to evaluate the fluctuations scales  $\Lambda_{ii}$  corresponding to the flux correlations  $R_{Q_i Q_i}(\xi_i)$ . For the case at hand, this yields:

$$\Lambda_{11} \simeq \lambda = \lambda_1$$

$$\Lambda_{22} \simeq 0.15 = 0.15\lambda_2$$

$$\Lambda_{33} \simeq 0.30\lambda = 1.20\lambda_3$$

In comparison, remember that the finest mesh size in the simulations at hand was  $\Delta x_i = 0.5\lambda_i$  ("shallow aquifer" problem E of Table 6.1). Thus, it appears that the grid resolution was probably much too coarse in the horizontal cross-flow direction ( $x_2$ ) to be able to capture the fluctuations of the transverse flux  $Q_2(\underline{x})$ . Moreover, the grid resolution used for the "deep aquifer" problem was even coarser.

For "anisotropic" media, we conclude that the grid size may have to be exceedingly large in order to obtain a statistically representative flow realization (*hydraulic head H*) while capturing the finest fluctuations of the flow field (*transverse flux component  $Q_2$* ). The severe requirements of the single realization approach for stratified flow systems could possibly lead to prohibitive grid sizes in regard to current numerical/computing capabilities (i.e., well above 1-10 million nodes). This question could be examined further in the future by analyzing the numerical flux vector fields for the currently available "modest size" flow realizations (220,000 nodes), or perhaps from new simulations with improved grid resolution and geometry.

## 6.5 Summary and Discussion:

The stochastic flow simulations analyzed in this chapter were aimed at evaluating the range of validity of the spectral theory in the case of groundwater flow in finite (but large) realizations of random porous formations. The assumptions of the spectral theory, infinite domain and homogeneity-ergodicity of the flow field, were not required in the direct simulation approach. Thus, the simulated flow fields were statistically analyzed by using spatial averaging and detrending techniques very much like those frequently used to analyze field data. Furthermore, the small parameter expansions in the log-conductivity standard deviation ( $\sigma_f$ ) required in the spectral theory, were not needed in the direct numerical simulation approach. Admittedly, the latter approach introduces new kinds of errors, such as truncation errors, solution errors due to approximate factorization of the matrix system and incomplete convergence of iterations, and round-off errors. However, these were presumably kept under control by using various tools from numerical analysis and by numerical experimentation (Chapter 5). In contrast, the accuracy of the spectral solutions was essentially unknown before the present research was initiated, except for a few special cases where exact solutions were available (effective conductivities for one-dimensional, and two-dimensional isotropic, random media).

The most significant results in this chapter were those obtained from large flow simulations with statistically isotropic log-conductivities (3D Markov field with exponential covariance) in section 6.3. The numerical flow fields obtained on a large three-dimensional grid (1 million nodes) were compared to the spectral solutions, via statistical analysis, for a wide range of conductivity variability ( $1 \leq \sigma_f \leq 2.3$ ). There was a surprisingly good agreement for the effective conductivity ( $K_{eff}$ ) and the degree of variability of the hydraulic head (standard deviation  $\sigma_H$  around the empirical trend) for all values of  $\sigma_f$ . On the other hand, the degree of variability of the flux vector field  $Q_i$  was significantly underestimated by the spectral theory for large variability ( $\sigma_f > 1.7$ ). In addition, our visual observations for the flux field (section 6.2) strongly suggested that the probability distribution of the longitudinal flux  $Q_1$  was significantly skewed positively. Both these effects are presumably due to high order interactions not taken into account by the first order spectral theory.

Nevertheless, the flux standard deviations  $\sigma_{q_i}$  predicted by the modified (higher order) spectral solutions of Chapter 4 (section 4.3) were more closely in agreement with the numerical results, than the standard spectral theory of Gelhar and Axness (1983). A further empirical modification of the spectral theory to account for high-order effects at large values

of  $\sigma_f$  finally produced a near-perfect fit with the numerical results. The empirical analytical expressions for  $\sigma_{q_1}$  were given in equations (6.13), to be compared to the standard and modified spectral solutions listed in Table 6.4.

On the other hand, the flux correlation functions (related to the shape of the flux spectrum) obtained from the Gelhar-Axness spectral theory agreed remarkably well with the numerical flux correlations in the case of moderate variability ( $\sigma_f = 1.0$ ). Even for higher variability, there was still a fair qualitative agreement between the spectral and numerical flux correlation structures, except for one particular component of the flux correlation tensor,  $R_{Q_2 Q_3}(\xi_3)$ . These results are particularly important for applications to stochastic solute transport. For instance, Gelhar (1987) shows that the macrodispersivity of a solute convected in a random velocity field  $Q_1(\underline{x})$  is proportional to the integrated velocity covariance (see for instance equations 4.64-4.65 of Chapter 4). Overall, our results strongly suggest that the flux covariance predicted by the spectral theory will be accurate for a wide range of conductivity variability, provided the use of high-order corrections for the flux variance as explained above. The Gelhar-Axness theory of macrodispersion may have to be modified accordingly, especially for cases of large variability.

The hydraulic head correlation functions obtained numerically did not agree so well with the spectral results, even for moderate conductivity variability. In view of the very good agreement observed for the flux correlation functions, we conclude that the discrepancies concerning the spatial structure of the head field were mainly due to the large fluctuation scales of the head relative to the size of the flow domain. Thus, we conjectured from a simplified analysis of sampling errors that the infinite-domain spectral theory ideally requires a domain size on the order of 25-50 correlation scales in the mean flow direction, and as much as 50-100 correlation scales in the transverse directions, in order to be applicable to practical field situations (*isotropic case*). In fact, the spatial structure of the head field obtained on a domain of size  $(33\lambda)^3$  still agreed reasonably well with the spectral theory, at least qualitatively. Thus, in the *isotropic case*, the numerical head field appeared to be statistically anisotropic as predicted by the theory, although the numerical correlation ranges were systematically smaller.

For the *anisotropic case* on the other hand, the restrictions on the range of applicability of the spectral solutions seemed to be more severe (see Section 6.4). First of all, it appeared that even for fairly large size flow problems (the "deep aquifer" case), there was still a significant

finite-size effect, resulting in smaller head correlations and more pronounced head anisotropy than predicted by the spectral theory (see Figures 6.34). Furthermore, we conjectured that a severe restriction on the mesh size may have to be satisfied in order to obtain a meaningful numerical solution for the flux vector field. The strict resolution requirement is due to the very small fluctuation scales of the transverse flux in the case of a stratified aquifer (small vertical/horizontal anisotropy ratio). Overall, the requirements of large domain size and very fine grid resolution may lead to discrete systems too large to be handled with current machine capabilities and/or with the class of numerical methods considered in this work. At any rate, the numerical simulations of Section 6.4 concerning the cases of "deep" and "shallow" stratified aquifers, seem to confirm our previous concerns about the possible inapplicability of the three-dimensional anisotropic spectral solutions in the case of confined aquifers of moderate thickness (Chapter 3, section 3.5).

Note finally that these possible limitations of the spectral theory concern only the correlation structure of the hydraulic head, not its global variability. Thus, we have found that, for all domain sizes and in all cases of anisotropy and variability, the head standard deviation  $\sigma_H$  calculated by empirical detrending of the numerical solution, matched to within 10-15% the spectral result. The fact that this worked also for

the case of the "shallow" stratified aquifer indicates that the spectral solution for  $\sigma_H$  can be quite robust, i.e., unaffected by finite size effects and/or domain scale inhomogeneities, provided that appropriate detrending techniques be used to smooth out the observed inhomogeneities. More generally, our results strongly suggest that the spectral theory provides an essentially correct description of the correlation structure of the flow in sufficiently large flow domains (deep aquifers), provided that the effects of domain scale or large scale inhomogeneities be smoothed out by detrending the observed hydraulic head field. In actual practice, such inhomogeneities could be caused by the presence of natural boundaries (or artificial boundaries in a numerical model), and/or distributed sources, and/or inherent inhomogeneities of the porous formation at the scale of the domain or larger. This should be taken into account in particular in the solution of the inverse problem based on field measurements of conductivity (or transmissivity) and of hydraulic head.

In summary, our direct simulations of single-realization stochastic flow problems in finite domains have helped defining the range of applicability of the infinite-domain spectral perturbation solutions (Gelhar and Axness, 1983, and this work, Chapters 3 and 4). Some of the limitations of the spectral theory may have implications for the



solution of inverse flow problems (correlation structure of the head field), and for the theory of stochastic solute transport (macrodispersion of a solute convected in a random velocity field). Our results show that the restrictions of the spectral theory, large domain and small variability, may be loosened greatly by using appropriate detrending techniques to evaluate the spatial structure of the head perturbations, and by using higher order approximations for the flux variance as proposed in this work. More research will be needed to evaluate the applicability of the Gelhar-Axness theory for stratified aquifers, particularly in the case of a dip angle between the mean flow and the principal axis of statistical anisotropy, which was not explored in this work (see indications in Section 6.1).

## CHAPTER 7: THREE-DIMENSIONAL SINGLE-REALIZATION SIMULATIONS OF UNSATURATED INFILTRATION IN RANDOM SOILS

### 7.1 Scope and Objectives

This chapter is devoted to the numerical simulation and interpretation of large scale realizations of stochastic unsaturated flow in random soils. The principle of the single-realization approach was explained in Chapter 2, and the related numerical issues were discussed in Chapter 5. The statistical aspects of the method were illustrated quite concretely in Chapter 6 for the case of steady state groundwater flow under a given regional hydraulic gradient.

However, here, a new difficulty arises due to the severe nonlinearity and inhomogeneity of the infiltration problem. For example, the preliminary infiltration experiments presented in Chapter 5 (section 5.4.3) clearly demonstrated the strongly inhomogeneous nature of the pressure field during the early stages of infiltration from a local strip source (evolving wetting front). When strong nonlinearity dominates the flow process, the assumptions of the linearized spectral theory of Mantoglou and Gelhar (1987) may be too constraining to warrant a precise quantitative comparison between the ensemble moments

obtained by the theory, and the spatial moments obtained from the numerical solutions. Therefore, unlike the case of groundwater flow, we do not have here the support of a robust analytical theory to guide our numerical experiments. For instance, little is known about the behavior of the wetting front in the presence of random heterogeneities. The reader is referred to Mantoglou (1984) and the above-quoted work, for a detailed account of the assumptions of homogeneity and the various linearization and "small parameter" approximations involved in their spectral solutions of transient unsaturated flow.

In addition, there is another difficulty inherent to the single-realization approach when dealing with localized and inhomogeneous transient flow processes, as occurs during infiltration from a local source. In such cases, the actual size of the flow domain (evolving wet zone) is regulated by the physics and depends on the time scale of interest. Thus, a single realization solution may not be statistically representative of the ensemble of possible realizations unless the time scale is large and/or the size of the source is large.

Our choice of strip-source infiltration problems was motivated in part by this kind of limitation. In the strip-source case, the source and the flow domain can be taken arbitrarily large in the longitudinal direction parallel to the

strip, at least within the limits imposed by computing capabilities. By symmetry arguments, we expect the flow field to be statistically homogeneous in the longitudinal direction, as illustrated in Figure 7.1. By sampling the solution along the longitudinal axis, one may obtain a representative picture of the effects of spatial variability from a single realization of the strip-source flow.

Accordingly, the next two sections will be devoted to the study of transient strip-source infiltration in random soils. In section 7.2, we investigate specifically the influence of the variability of the unsaturated conductivity curve on the flow pattern for a statistically isotropic soil. In section 7.3, we analyze one very large realization of strip-source infiltration in a statistically anisotropic soil, designed to mimic an on-going experiment at the Las Cruces experimental farm of the University of New Mexico. In either case, however, direct statistical analysis of the pressure field will not be attempted, due to the limitations mentioned above.

In addition, Section 7.4 is devoted to a class of infiltration problems where the solution is expected to be statistically homogeneous in all three space directions. Thus, we have chosen to study the case of steady state infiltration from a uniform plane source of constant intensity (uniform

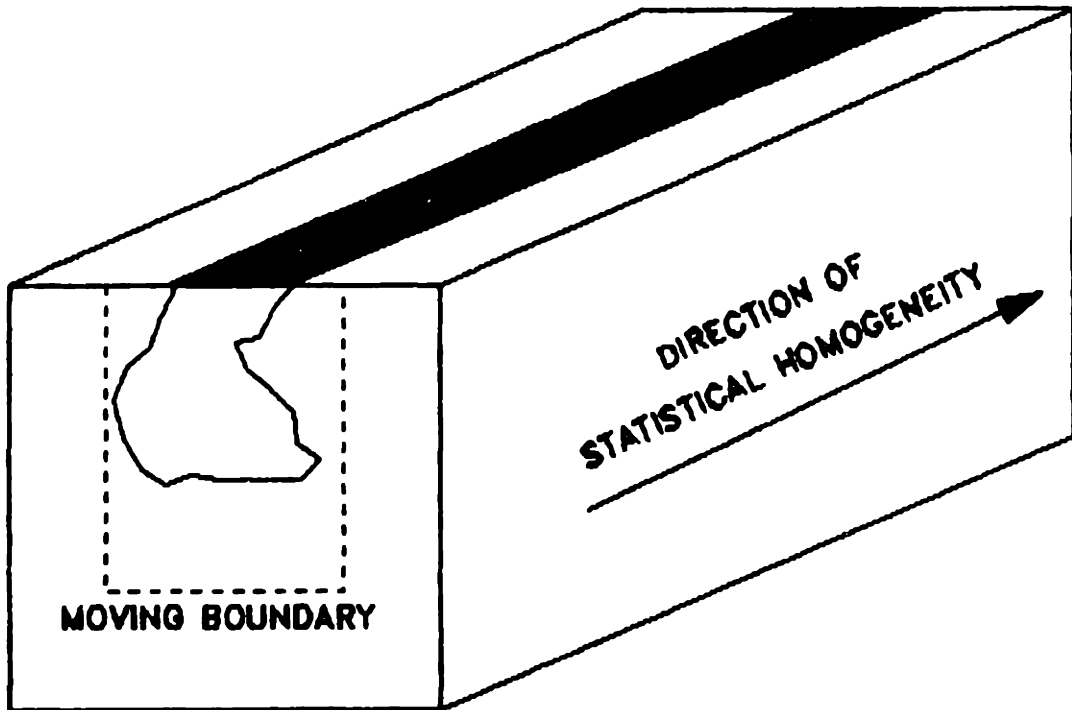


Figure 7.1 Illustration of a strip-source infiltration problem having one spatial direction of statistical homogeneity (longitudinal direction).

"rainfall"). Some preliminary statistical analysis will be briefly presented, for comparison with the results of the steady state linearized spectral theory of Yeh et al. (1985), later extended by Mantoglou and Gelhar (1987).

The strip-source and the steady uniform infiltration problems of Sections 7.3 and 7.4 were solved for the same large realization of a statistically anisotropic random soil, over a grid of size 300,000 nodes. To run these two problems required a CPU time on the order of 10 hours on a Cray 2 machine, including trial and errors for adjusting the time steps. Note that the steady state infiltration problem of section 7.4 was in fact solved by way of transient simulation up to a relatively large time of infiltration (3 months), and required about 3 CPU hours on the Cray 2 machine. In contrast, the preliminary strip-source infiltration problems presented in section 7.2 were solved on relatively "modest" grid sizes (25,000 nodes) using the Microvax 2 minicomputer. It should be noted that the purposes of the three sets of simulations (sections 7.2, 7.3, 7.4) were somewhat different. The contents of each section are summarized below for convenience.

Section 7.2 (25,000 nodes/transient):

Preliminary simulations of transient strip-source

infiltration on statistically isotropic soils for relatively small time and length scales (3 days of infiltration, 1.4 x 4 x 4 meters domain). Test of different assumptions concerning the variability of the  $\ln K(h)$  curve, and qualitative interpretation of simulation results.

Section 7.3 (300,000 nodes/transient):

Single-realization simulation of transient strip-source infiltration and drainage on a statistically anisotropic soil for relatively large time and length scales (20 days of infiltration and drainage, 5 x 15 x 15 meters domain). The geometry, boundary conditions, hydraulic properties, and spatial variability data were selected to mimick the on-going "trench" experiment at Las Cruces. Qualitative interpretation of simulation results.

Section 7.4 (300,000 nodes/steady):

Single-realization simulation of steady state infiltration from a plane source of constant intensity (uniform rainfall). Same geometry, grid size, and soil data as in the previous strip-source "experiment". Qualitative interpretation and preliminary statistical analysis of pressure head variability and effective conductivity. Comparison with linearized spectral solutions.

A few additional comments may be useful to complete this summary. In all cases, the unsaturated conductivity curve was assumed to vary randomly in space (one different curve for each node of the grid), while the water retention curve was assumed to be the same at all locations (deterministic). The unsaturated conductivity-pressure relation was assumed to be exponential, and the water retention curve was represented by the Van Genuchten function, as explained in Chapter 5 (section 5.1.3). The precise data and the assumed stochastic properties of the conductivity curve will be given in more detail in the sequel: see in particular the next section (7.2) concerning the method used to generate random conductivity parameters. On the whole, the single realization solutions presented in this chapter constitute, as far as we know, the largest high-resolution representations of heterogeneous three-dimensional unsaturated flow systems available to date.

## **7.2 Strip Source Infiltration in Statistically Isotropic Soils (25,000 nodes):**

### **7.2.1 Model problems and input data**

The nonlinear conductivity and water retention curves adopted in the sequel are, respectively, the exponential and the Van Genuchten functions (see Chapter 5):



$$K(h, \underline{x}) = \begin{cases} K_s(\underline{x}) \exp(\alpha(\underline{x})h) & \text{if } h \leq 0 \\ K_s(\underline{x}) & \text{if } h \geq 0 \end{cases} \quad (7.1)$$

$$\theta(h) = \theta_s + \frac{\theta_s - \theta_r}{(1 + (-\beta h)^n)^{1-1/n}} \quad (7.2)$$

Both parameters  $K_s(\underline{x})$  and  $\alpha(\underline{x})$  of the unsaturated conductivity curve (7.1) are assumed to be random functions of three-dimensional space. On the other hand, we assume that the water retention curve (7.2) is deterministic, i.e., the same at all spatial locations. This simplifying assumption was motivated by the findings of Mantoglou (1984) and Mantoglou and Gelhar (1987), whose linearized spectral results suggest that the variability of  $\theta(h, \underline{x})$  plays a minor role compared to the variability of  $K(h, \underline{x})$ . Their results also indicate that the statistical properties of the flow will be quite sensitive to the mean and variance of  $\alpha(\underline{x})$ .

The parameter  $\alpha$  corresponds to the slope of the log-conductivity curve, obtained by differentiating  $\ln K(h, \underline{x})$  with  $\underline{x}$  fixed. Various physical interpretations of  $\alpha$  were discussed in Chapter 5 (section 5.4.2), e.g. inverse height of the capillary fringe, pore size distribution index, or convection/diffusion ratio. Field data concerning the variability of the conductivity curve were discussed in

Chapter 2 (section 2.3.2, table 2.2). It should be pointed out that the degree of correlation between  $K_s(\underline{x})$  and  $\alpha(\underline{x})$  remains unknown. On the other hand, the linearized spectral solutions of Mantoglou and Gelhar (1987) seem to be fairly sensitive to the assumed correlation between these two random field parameters (correlated/uncorrelated) and very sensitive to the degree of variability of the  $\alpha$ -parameter in particular.

In the present section, we propose to investigate directly the effect of variability of the  $\alpha$ -parameter and of the correlation between  $\alpha$  and  $K_s$ , by way of numerical simulations of strip-source infiltration for relatively modest time and length scales. The relevant input data used in these simulations are summarized in Table 7.1 below. Three types of variability were assumed for the random conductivity curve of equation (7.1):

Case (1):  $K_s(\underline{x})$  random,  $\alpha$  constant.

Case (2):  $(K_s(\underline{x}), \alpha(\underline{x}))$  random and perfectly correlated.

Case (3):  $(K_s(\underline{x}), \alpha(\underline{x}))$  random and perfectly uncorrelated.

In each case, the parameters  $\ln K$  and/or  $\ln \alpha$  were assumed to be statistically isotropic Markov random fields in three-dimensional space, with a constant-mean Gaussian distribution. Thus, defining  $K_G$  and  $\alpha_G$  the geometric means of  $K_s(\underline{x})$  and  $\alpha(\underline{x})$ , we used the turning band method (Chapter 2 and

**TABLE 7.1**  
**SUMMARY OF INPUT DATA FOR THE SINGLE-REALIZATION**  
**SIMULATIONS OF STRIP-SOURCE INFILTRATION IN STATISTICALLY ISOTROPIC SOILS**  
**(25,000 NODES)**

Type of Data	Description	Value
Domain Geometry, Boundary Conditions, and Initial Conditions	Vertical domain size Transverse horizontal domain size Transverse longitudinal domain size Strip source width Flux at the surface of the strip Condition at the bottom boundary Initial pressure head	$L_1 = 1.40$ m $L_2 = 4.00$ m $L_3 = 4.00$ m $W_s = 1.10$ m $q_0 \cong 2$ cm/day $q_1 = -K(h)$ $h_{in} = -150$ cm
Space-Time Discretization	Time step Mesh size $\Delta x_i$ ( $i=1,2,3$ ) Unidirectional number of nodes $n_i$ Total number of nodes of 3D grid	Variable $\Delta x_i = 0.10$ m $n_i = (5, 41, 41)$ $N = 25215$
Exponential Conductivity Curve (Random)	Geometric mean saturated conductivity Standard deviation of $\ln K_s$ Geometric mean of the $\ln K$ -slope Standard deviation of $\ln \alpha$ Isotropic correlation scales $\lambda_i$	$K_G = 541$ cm/d $\sigma_f = 0.7$ $\alpha_G = 0.09$ cm <sup>-1</sup> $\sigma_a = 0.3$ $\lambda_i = 0.20$ m
Van-Genuchten Water retention Curve (Deterministic)	Saturated moisture content Residual moisture content Scaling parameter Shape factor (real number)	$\theta_s = 0.38$ $\theta_r = 0.07$ $\beta = 0.05$ cm <sup>-1</sup> $n = 2.00$

Chapter 6) to generate the zero-mean Gaussian random fields:

$$f(\underline{x}) = \ln(K_s(\underline{x})/K_G)$$

$$a(\underline{x}) = \ln(\alpha(\underline{x})/\alpha_G)$$
(7.3)

with isotropic exponential covariance function. The corresponding spectral density can be found in Table 3.1 of Chapter 3 (special case of ellipsoidal Markov-spectrum, with equal correlation lengths in all three directions).

Note that we assumed the log-normality of the  $\alpha$ -parameter. This differs from the assumption of normality implicit in the theoretical work of Mantoglou and Gelhar (1987). In our opinion, the log-normal behavior of  $\alpha$  makes sense in view of the fact that this parameter, like  $K_s$ , is necessarily positive for all usual types of rigid porous media. This is also supported by the experimental observations discussed in the data survey section of Chapter 2. In particular, Russo (1983) found that  $\alpha(\underline{x})$  followed a log-normal distribution with skewness coefficient equal to 1.36 (similarly,  $K_s(\underline{x})$  was log-normal with skewness 2.49). Now, equations (2.19-2.21) can be used to relate the mean and variance of a log-normal variable ( $Y$ ) to the geometric mean ( $Y_G$ ) and the variance of  $\ln Y$ . These equations also show that the skewness of a log-normal variable is always

positive and increases rapidly with its coefficient of variation. On the other hand, in the case of mild variability ( $\sigma_{\ln Y} \ll 1$ ) the skewness of  $Y$  becomes negligible, the standard deviation of  $\ln Y$  becomes approximately equal to the coefficient of variation ( $\sigma_Y/\bar{Y}$ ), and the geometric mean ( $Y_G$ ) becomes close to the mean ( $\bar{Y}$ ). These simple observations may help compare our simulation data to other data or theories published in the literature.

A few single-realizations of the log-normal random fields  $K_s(\underline{x})$  and  $\alpha(\underline{x})$  were produced in order to simulate the three cases outlined above. In case (1), only  $K_s$  was random. The turning band method was used to generate one realization of a Gaussian random field, say  $u_1(\underline{x})$ , and the desired  $K_s$ -field was obtained by rescaling  $u_1(\underline{x})$  and applying an exponential transform in the obvious way. In case (2), where  $\ln K_s$  and  $\ln \alpha$  were perfectly correlated random fields, the same realization  $u_1(\underline{x})$  was used to obtain both  $K_s(\underline{x})$  and  $\alpha(\underline{x})$  after rescaling and exponentiating. Finally, in case (3), two independent realizations  $u_1(\underline{x})$  and  $u_2(\underline{x})$  were used to obtain  $K_s(\underline{x})$  and  $\alpha(\underline{x})$  independently from each other. The procedures just described are summarized below for convenience, along with a possible generalization to handle the case of imperfect correlation, as may be needed in the future when more data become available.

Case (1):

$$K_s(\underline{x}) = K_G \cdot \exp(\sigma_f \cdot u_1(\underline{x})) \quad (7.4)$$

$$\alpha(\underline{x}) = \alpha_G$$

Case (2):

$$K_s(\underline{x}) = K_G \cdot \exp(\sigma_f \cdot u_1(\underline{x})) \quad (7.5)$$

$$\alpha(\underline{x}) = \alpha_G \cdot \exp(\sigma_a \cdot u_1(\underline{x}))$$

Case (3):

$$K_s(\underline{x}) = K_G \cdot \exp(\sigma_f \cdot u_1(\underline{x})) \quad (7.6)$$

$$\alpha(\underline{x}) = \alpha_G \cdot \exp(\sigma_a \cdot u_2(\underline{x}))$$

General case (imperfect correlation):

$$K_s(\underline{x}) = K_G \exp(\sigma_f \cdot u_1(\underline{x})) \quad (7.7)$$

$$\alpha(\underline{x}) = \alpha_G \exp\{\sigma_a(\rho u_1(\underline{x}) + \sqrt{1-\rho^2} u_2(\underline{x}))\}$$

In the latter case,  $\rho$  designates the correlation coefficient between  $f(\underline{x})$  and  $a(\underline{x})$  ( $-1 \leq \rho \leq 1$ ). More precisely, the covariance tensor of the jointly Gaussian random fields  $(a(\underline{x}), f(\underline{x}))$  is of the form:

$$\begin{bmatrix} R_{aa}(\xi) & R_{af}(\xi) \\ R_{fa}(\xi) & R_{ff}(\xi) \end{bmatrix} = \begin{bmatrix} \sigma_a^2/\sigma_f^2 & \rho\sigma_a/\sigma_f \\ \rho\sigma_a/\sigma_f & 1 \end{bmatrix} \cdot R_{ff}(\xi)$$

Accordingly, case (1) obtains by taking  $\sigma_a = 0$ , case (2) by taking  $\rho = 1$ , and case (3) by taking  $\rho = 0$ . The two special cases  $\rho = 1$  and  $\rho = 0$  were motivated by the observation that  $(\alpha, K_s)$  should be positively correlated ( $0 \leq \rho \leq 1$ ) since both  $\alpha$  and  $K_s$  generally increase with soil coarseness, and decrease with clay content.

Figure 7.2 illustrates the two extreme assumptions of perfect correlation and perfect independence ( $\rho = 1$  and  $\rho = 0$ ) corresponding to cases (2) and (3). The  $\ln K(h)$  functions were plotted schematically for different spatial locations. The log-conductivity curves shown in the top part of Figure 7.2 have perfectly correlated slope and intercept ( $\ln \alpha$  and  $\ln K_s$ ). Their envelope has the shape of a hyperbole. On the bottom part of the figure, the case of perfect independence between  $\ln \alpha$  and  $\ln K_s$  is represented in the same fashion. There is no well-defined envelope in this case. Figure (2.2) of Chapter 2 suggests that a reasonable description of natural conductivity variability stands somewhere between these two cases. Admittedly, more work is needed to refine these simplified representations of unsaturated soil variability (see discussion of field data in Chapter 2).

Let us now comment briefly on our choice of some of the other data of Table 7.1, in relation with numerical and statistical issues. First of all, observe that the statistical

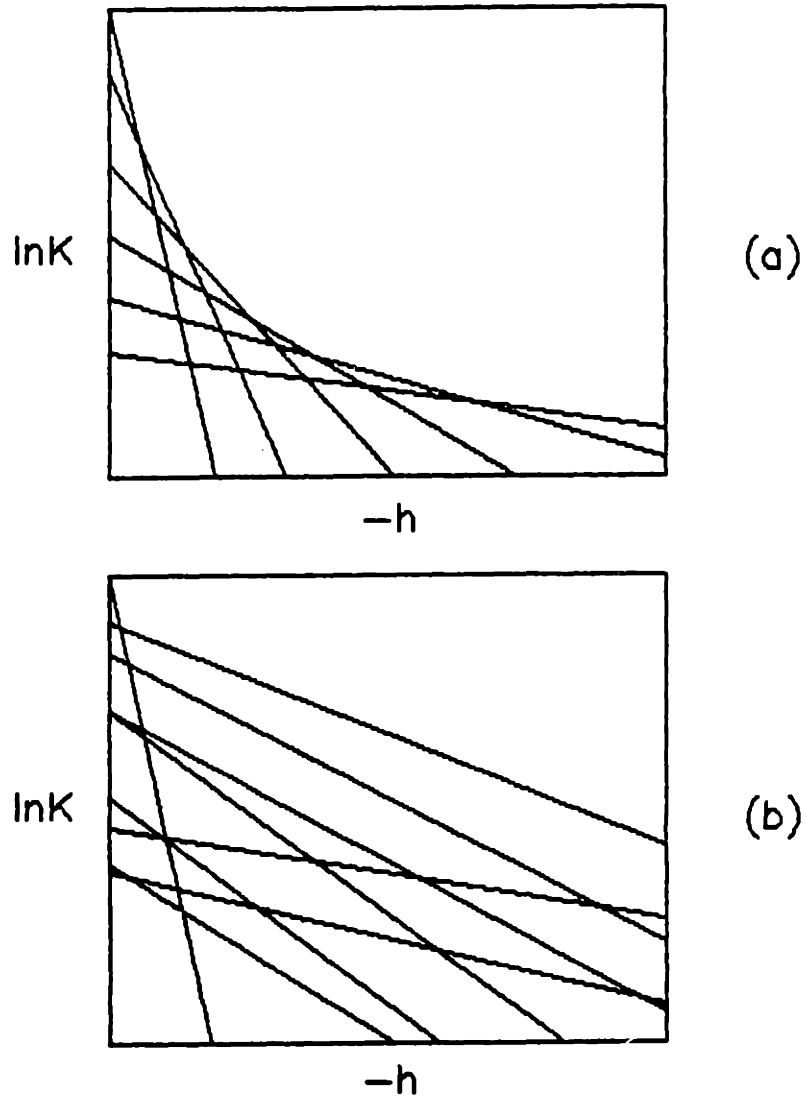


Figure 7.2 Schematic representation of unsaturated log-conductivity variability in two cases. On top, the parameters  $\ln K_s$  and  $\ln \alpha$  are perfectly correlated (Case 2 in the text). On bottom, they are perfectly uncorrelated (Case 3 in the text).



resolution of the grid is moderate:

$$\frac{\Delta x_i}{\lambda_i} = \frac{1}{2},$$

and isotropic in space (same in all directions). Second, note that the Peclet number constraint:

$$Pe = \alpha \Delta x_1 \leq 2$$

which arose as a "nonlinear stability condition" in Chapter 5 (section 5.4.2, equation 5.128) seems to be satisfied if  $\alpha$  is replaced by its geometric mean value  $\alpha_G$ . Thus, we obtain for the  $\alpha_G$  of Table 7.1:

$$\bar{Pe} = \alpha_G \cdot \Delta x_1 = 0.9 \leq 2.$$

The procedure used to control the size of the variable time step was described in Chapter 5 (section 5.4.3). In no case was the time step allowed to grow at a rate faster than  $\Delta t_{n+1}/\Delta t_n = 1.25$ . The initial time step size was  $\Delta t_{in} = 0.003$  day (4mm 20 sec). Infiltration lasted for about 3 days, after which the simulation was halted. The results shown in this section were obtained with a fixed domain size, but similar results were also obtained by using the variable domain size algorithm (see Figures 5.11-5.13 of Chapter 5). Finally, it

is worth noting that the size of the domain is relatively small: the "sample size"  $L_i/\lambda_i$  is 7 in the vertical, and 20 in both horizontal directions. The infiltration experiment was stopped at  $t = 3$  days because the flow domain was too small to approximate a "semi-infinite" medium for larger times. The selected output times were  $t = 0.5, 1.0, 2.0$  and  $3.0$  days. The resulting three-dimensional pressure head fields are being analyzed below.

### 7.2.2 Simulation results

We now discuss the simulation results (pressure head fields) obtained for the three cases of unsaturated conductivity variability described above (equations 7.4, 7.5, 7.6 and Figure 7.2). The geometry and boundary conditions were illustrated in Figure 7.1, and the complete set of input data was given in Table 7.1. Recall in particular that the initial pressure  $h_{in}$  was  $-150$  cm.

Figures 7.3, 7.4 and 7.5 give three-dimensional views of a single pressure contour surface obtained after two days of infiltration. These figures show essentially the shape of the wet zone ( $h \geq -90$  cm) in perspective view. Figure 7.3 corresponds to  $K_s$  random and  $\alpha$  constant (case 1), Figure 7.4 to  $\ln K_s$  and  $\ln \alpha$  random but perfectly correlated (case 2).

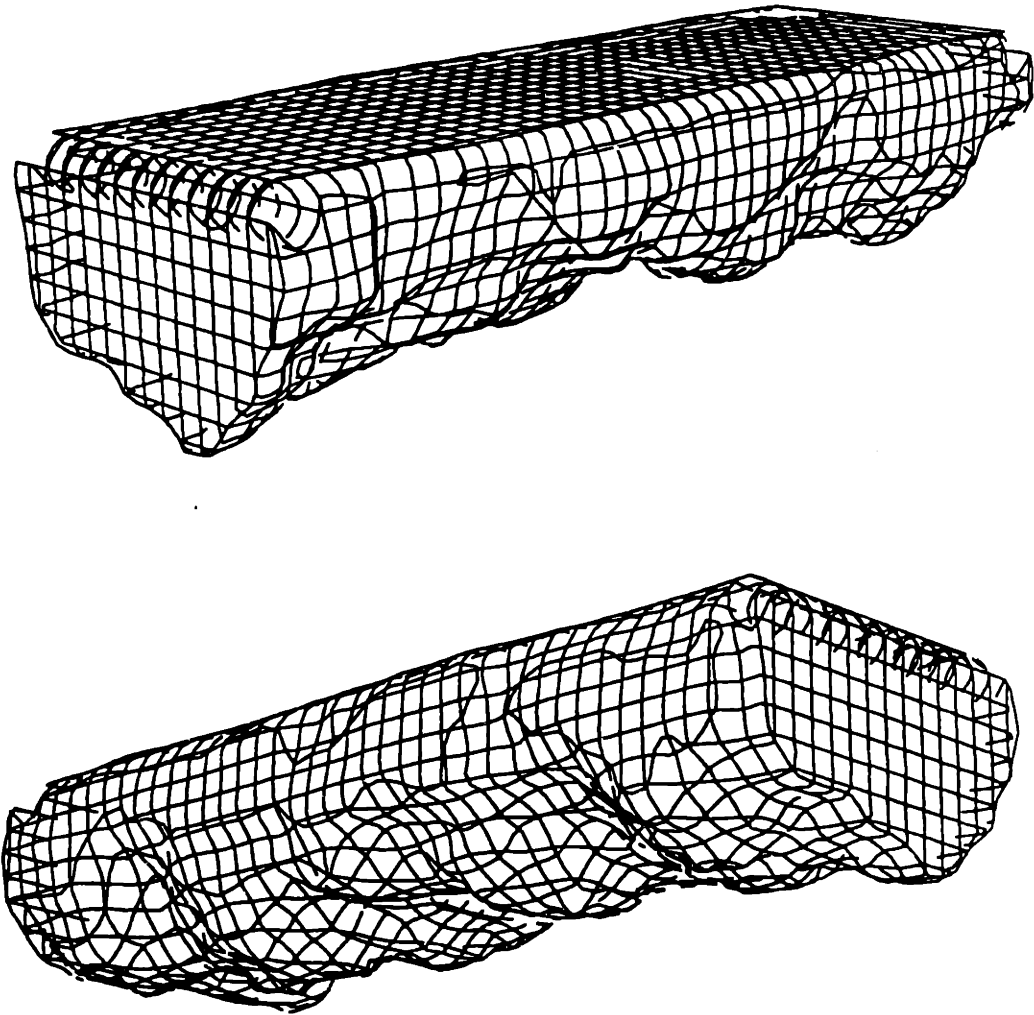


Figure 7.3: Two perspective views of the pressure contour surface  $h = -90$  cm at  $t = 2$  days for strip-source infiltration in a statistically isotropic soil with initial pressure  $h_{in} = -150$  cm (Case 1:  $K_s$  random,  $\alpha$  constant)

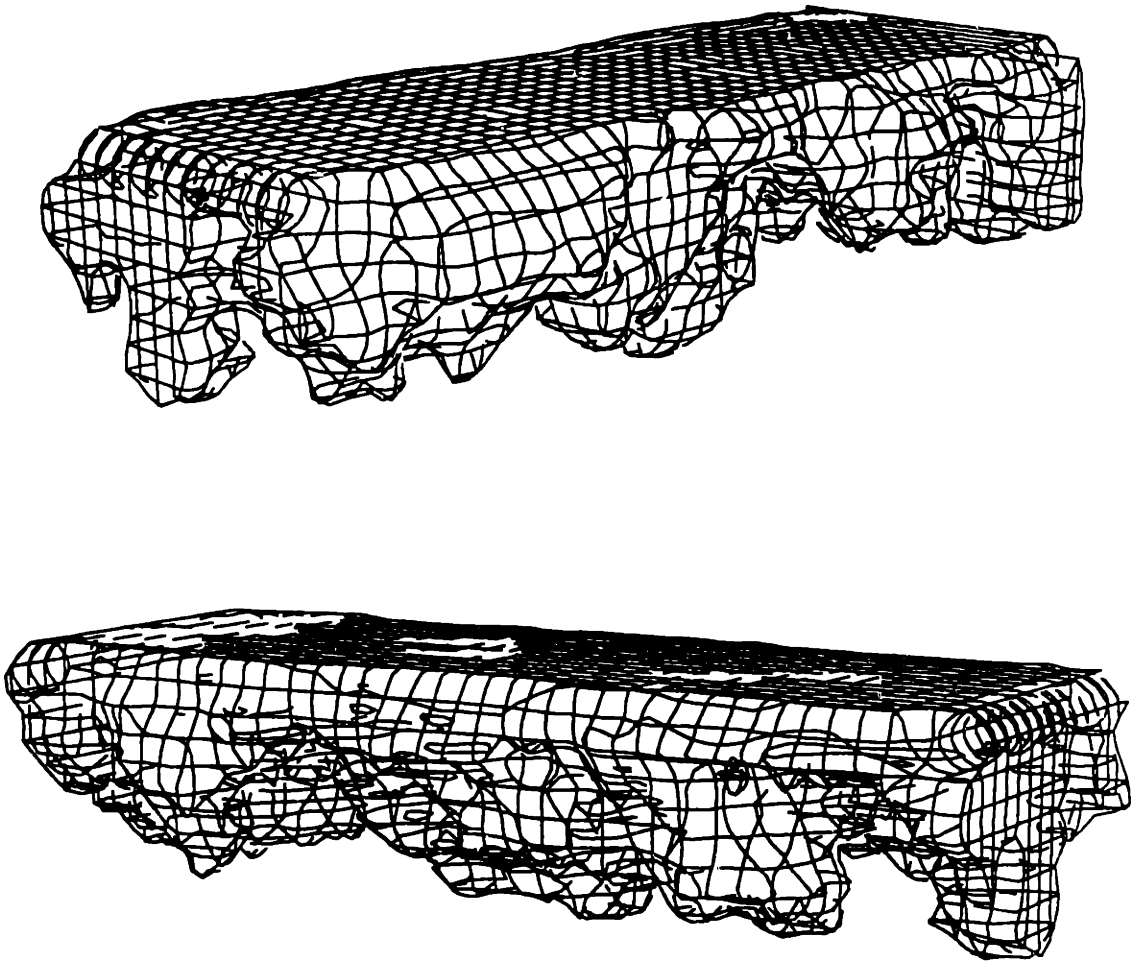


Figure 7.4 Two perspective views of the pressure contour surface  $h = -90$  cm at  $t = 2$  days for strip-source infiltration in a statistically isotropic soil with initial pressure  $h_{in} = -150$  cm (Case 2:  $K_s$  and  $\alpha$  random, perfectly correlated).

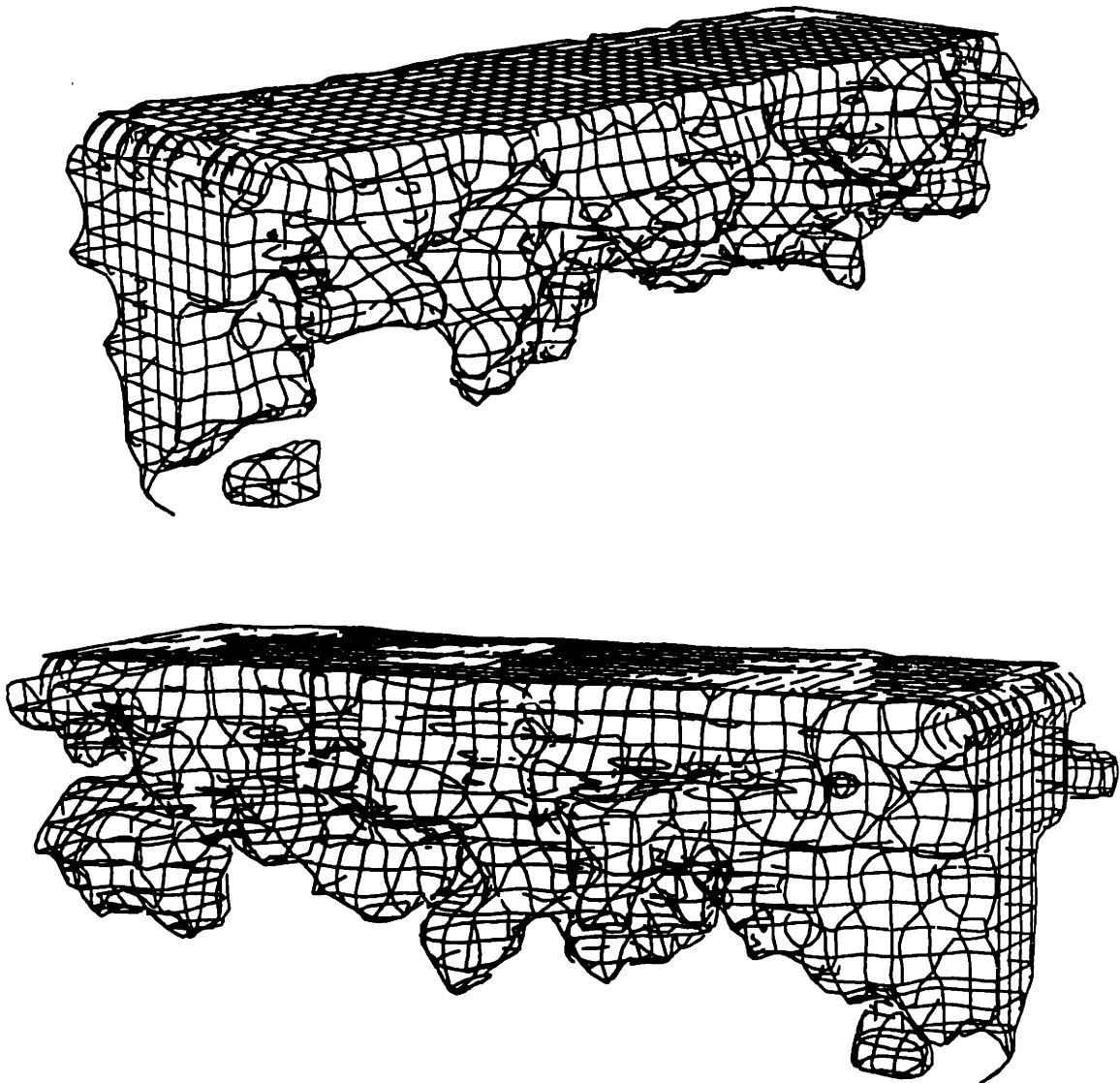


Figure 7.5 Two perspective views of the pressure contour surface  $h = -90$  cm at  $t = 2$  days for strip-source infiltration in a statistically isotropic soil with initial pressure  $h_{in} = -150$  cm (Case 3:  $K_s$  and  $\alpha$  random, perfectly independently).

and Figure 7.5 to  $\ln K_s$  and  $\ln \alpha$  random and perfectly uncorrelated (case 3).

Comparing figures 7.3 and 7.4 (cases 1 and 2) clearly shows that the variability of the log-conductivity slope ( $\alpha$ ) plays a more important role than the variability of the saturated conductivity ( $K_s$ ). Despite the relatively small variability of  $\alpha$  in Figure 7.4 ( $\sigma_{\ln \alpha} = 0.3$ ) the shape of the wet zone is much more contorted than in Figure 7.3 where only  $K_s$  is variable ( $\sigma_{\ln K_s} = 0.7$ ). Furthermore, comparing figures 7.4 and 7.5 (cases 2 and 3) indicates that the spatial variability of the wet zone is increased further when  $\alpha$  is allowed to vary independently from  $K_s(\underline{x})$ . In the latter case (Figure 7.5) the wet zone at  $t = 2$  days appears to be extremely contorted, and even disconnected. This indicates that soil heterogeneity can induce the creation of local wet regions entirely surrounded by dryer regions, at least in the transient flow regime.

Some of these observations are also illustrated by Figure 7.6, which depicts the pattern of pressure head contours in a vertical plane transverse to the strip-source for the three cases discussed above. Note the separation of the wet plume in two distinct plumes on the bottom part of Figure 7.6 (case 3,  $K_s(x)$  and  $\alpha(x)$  independent). The two "halves" of the wet plume could perhaps reconnect at a later time. Incidentally, our

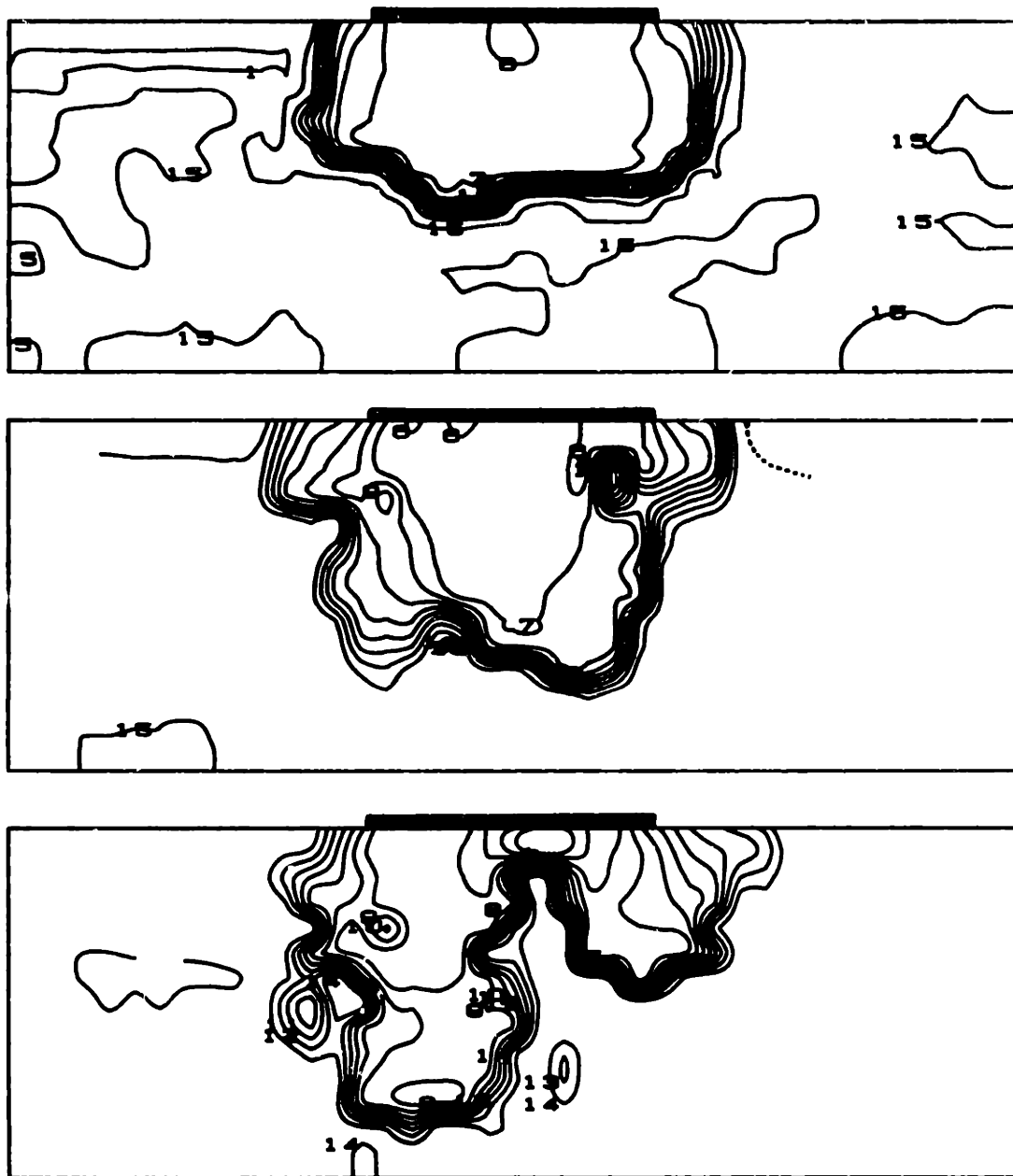


Figure 7.6 Pressure head contour lines in a vertical plane transverse to the strip source for cases (1), (2), (3) as in Figures (7.3), (7.4), (7.5). The pressure contours are labelled every 10 cm, e.g., contour #6 corresponds to - 60 cm, and contour #9 to - 90 cm.

choice of the value  $h = -90$  cm to represent the 3D pressure surfaces in the previous plots, was motivated by the fact that this value corresponds fairly well to the wetting fronts appearing in the 2D contour maps of Figure 7.6. The wetting fronts are sharply defined in all three cases, as could be expected for early times of infiltration in a relatively dry soil.

Overall, these pictures clearly show that the pressure field becomes increasingly variable and "chaotic" as the log-conductivity slope  $\alpha(\underline{x})$  becomes more variable and independent of  $K_s(\underline{x})$ . When  $\alpha$  is constant, the variability of  $K_s(x)$  produces only mild variability of the unsaturated pressure field. When  $\alpha(\underline{x})$  is variable, the unsaturated plume develops mushroom-shaped regions oriented downwards, especially in the longitudinal direction (as can be seen from Figures 7.4 and 7.5), but also in the transverse direction (Figure 7.6 bottom). The size of these "mushrooms" seems to be on the order of 0.6-1.0 m, or about 3-5 correlation scales ( $\lambda = 0.2$  m).

These observations lead us to think that the typical scale of fluctuation of the pressure field could be on the order of 1 meter, or 5 correlation scales. However, the pressure fluctuations are too large, and the domain too small, to permit a meaningful statistical analysis in the case of random  $\alpha(\underline{x})$ .



Furthermore, it is not clear how the length and width of the strip influence the flow pattern at early times. It seems possible that the width of the strip imposes a definite length scale to the fluctuating pressure field, both in the longitudinal and transverse directions (in the present case, the strip width is 1.1 m, or 5.5 correlation scales). At any rate, the influence of the strip source width could be considerably reduced for large times of infiltration and large wet zones, as far as the fluctuation scales are concerned.

To verify these conjectures would require simulations on larger domains, and for larger times of infiltration. The transverse size of the domain should be taken larger in order to avoid interactions between the wet zone and the lateral (no-flow) boundaries as the unsaturated plume evolves. In addition, the length of the strip should be taken much larger than the typical fluctuation scale of the pressure field in order to obtain meaningful spatial moments by longitudinal averaging (i.e., by averaging in the direction of statistical homogeneity as illustrated in Figure 7.1). It seems reasonable to require that the strip length be at least  $10^2$ - $10^3$  pressure correlation scales. For a grid resolution  $\Delta x/\lambda$  equal to one-half, and assuming a pressure fluctuation scale on the order of  $5\lambda$ , this would lead to  $10^3$ - $10^4$  mesh points in the longitudinal direction. In comparison, there were only 41 nodes along the strip length in

the case at hand, and a total of 25,000 nodes in 3D space. To obtain statistically meaningful large-time solutions (in the sense defined above) would therefore require a three-dimensional grid size of at least 1-10 million nodes for the isotropic case at hand, and probably even more for the anisotropic case.

In this discussion, we assumed implicitly that a mesh size equal to one-half the correlation scale of input hydraulic properties provided adequate resolution. It may be instructive to examine the grid resolution problem more closely here. Inspection of the pressure contours shown in Figure 7.6, suggests that the 10 cm mesh was perhaps too coarse to resolve the smallest scales of fluctuations of the pressure field (see the rectangular and straight-line shapes of the pressure contour fluctuations at the small scale). This is even more apparent in the pressure contour plot of Figure 7.7, which represents the pressure field in the vertical plane coinciding with the longitudinal axis of the strip source (case 1:  $\ln K_s$  and  $\ln a$  perfectly correlated). This indicates that grid resolution may have to be refined further, especially in view of analyzing the flux vector field and the related convection-dispersion pattern of a contaminant carried in the flow.

On the other hand, the chosen grid resolution of one half was perhaps fine enough to obtain a reasonably accurate

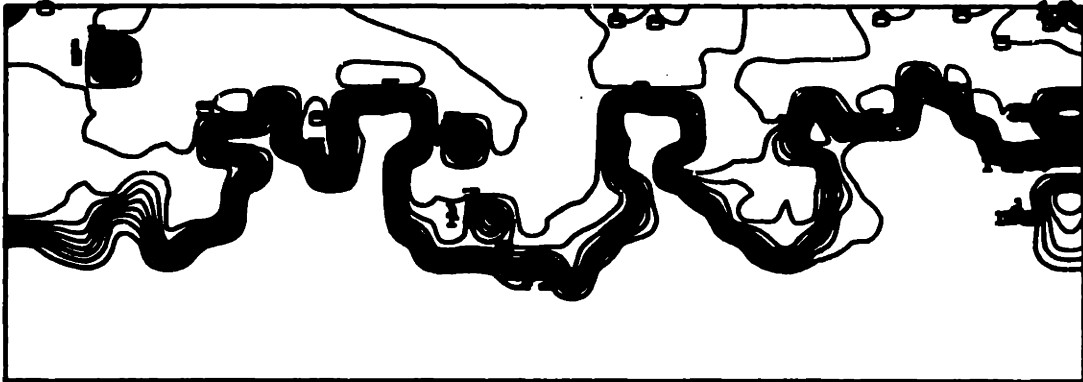


Figure 7.7 Pressure head contour lines in a vertical plane parallel to the strip source for case (2) as in Figure (7.4). The pressure contours are labelled every 10 cm, e.g., contour #6 corresponds to -60 cm, and contour #9 to -90 cm.

picture of pressure variability. The numerical experiments of Chapter 5 with uniformly layered soils showed that the mesh size could be taken equal to layer thickness without distorting the overall pattern of the pressure fields (see Figures 5.23, 5.24 and 5.25 of Chapter 5, section 5.4.3). There is also the remaining constraint of a low Peclet number, or small vertical mesh size, that must be satisfied in order to avoid instabilities. There were no particular instability problems in the case at hand.

### **7.3 Strip Source Infiltration in a Statistically Anisotropic Soil (300,000 nodes)**

#### **7.3.1 Model problem and input data**

##### **[a] - Overview of data**

In this section, we present the results of a single-realization simulation of strip source infiltration in a more realistic case than before. The soil data, geometry, and boundary conditions were chosen to mimic an on-going "trench experiment" at the New Mexico State University College Ranch of Las Cruces, New Mexico (Wierenga, Gelhar et. al. 1986, and Wierenga, Porro et. al. 1986). The major differences with the simulations of the previous section are the following:

- the strip source does not span the whole length of the computational domain
- the soil is *statistically anisotropic*, with a larger correlation scale in the horizontal than in the vertical.
- the space-time scales of simulation are relatively large (5 m x 15 m x 15 m and 20 days)
- both the infiltration phase and the *natural drainage after the end of infiltration* are being simulated (10 days of infiltration followed by 10 more days of drainage).

Figure 7.8 shows a schematic representation of the computational flow domain in perspective view. Its size is 5 m in the vertical, and 15 m in both horizontal directions. However, note that the strip source only extends over a length of 9.8 m in the longitudinal direction (4 m in width). The vertical plane in the forefront represents the face of the trench in the experimental set-up of Wierenga et al. (1986). This was approximated as a "no-flow" boundary in our simulation, despite evidence that some evaporation actually occurred in the field experiment. The other vertical faces of the domain were assumed also to be "no-flow" boundaries; they did not seem to interfere with the infiltration and drainage processes at the time scale of the simulation. The bottom boundary, however, was not deep

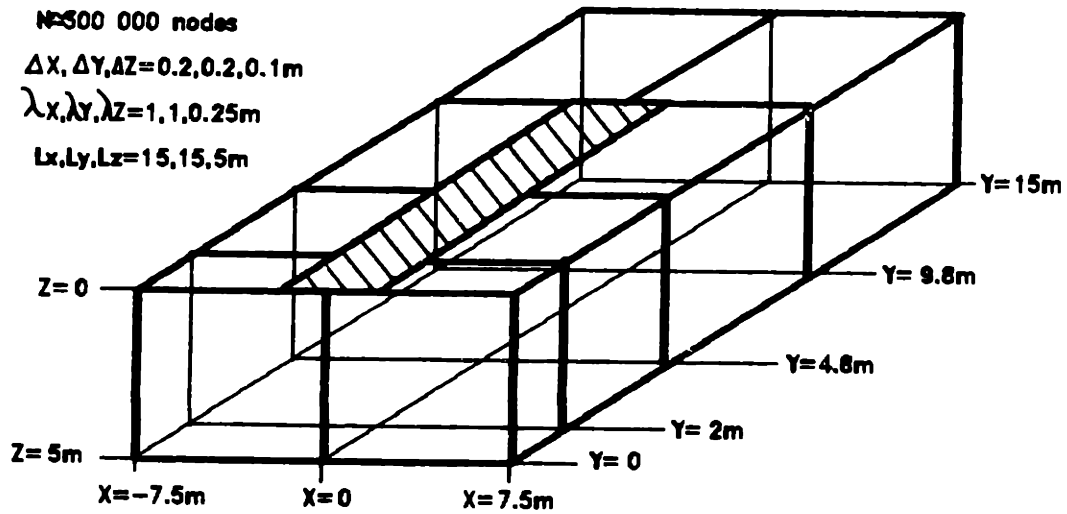


Figure 7.8 Schematic representation of the flow domain geometry for the 300,000 node simulation of strip-source infiltration in a statistically anisotropic soil ("trench experiment"). The numerical solution was sampled along certain slices ( $Y = 2, 4.8, 9.8\text{m}$  and  $X = 0$ ).

enough to avoid interactions with the evolving wet zone during the last part of the drainage phase (more on this later). The flux at the surface of the strip was 2 cm/day during infiltration, and zero during the redistribution phase. A zero flux was imposed over the remaining part of the soil surface at all times.

Table 7.2 summarizes the input data used for the simulated "trench experiment" just described, including geometry, initial and boundary conditions, space-time discretization, and hydraulic properties of the hypothetically random soil. Some of these data were chosen in accordance with available field observations or were imposed by the experimental set-up (the infiltration experiment at the Las Cruces site was in fact designed in part for purposes of comparison with mathematical models like ours). However, some of the other data of Table 7.2 were only indirectly related to field observations, or were imposed by numerical constraints. The rationale behind the selected inputs shown in Table 7.2 is explained in more detail below for each category of data.

#### [b] Space-time discretization and computational issues

The three-dimensional mesh size was chosen as a compromise between the numerical constraints (Peclet number

TABLE 7.2  
SUMMARY OF INPUT DATA FOR THE SINGLE-REALIZATION SIMULATION OF STRIP-SOURCE  
INFILTRATION IN A STATISTICALLY ANISOTROPIC SOIL ("TRENCH EXPERIMENT")

Type of Data	Description	Value
Domain Geometry, Boundary Conditions, and Initial Conditions	Vertical domain size Transverse horizontal domain size Transverse longitudinal domain size Strip source width Strip source length Flux at the surface of the strip Condition at the bottom boundary Initial pressure head	$L_1 = 5.0$ m $L_2 = 15.0$ m $L_3 = 15.0$ m $W_s = 4.0$ m $L_s = 9.9$ m $q_0 = 2$ cm/day $q_1 = -K(h)$ $h_{in} = -150$ cm
Space-Time Discretization	Time step Mesh size $\Delta x_i$ ( $i=1,2,3$ ) Unidirectional number of nodes $n_i$ Total number of nodes of 3D grid	Variable $\Delta x_i = 0.10, 0.20, 0.20$ m $n_i = 52, 76, 76$ $N = 300352$
Exponential Conductivity Curve (Random)	Geometric mean saturated conductivity Standard deviation of $\ln K_s$ Geometric mean of the $\ln K$ -slope Standard deviation of $\ln \alpha$ Anisotropic correlation scales $\lambda_i$	$K_G = 100$ cm/d $\sigma_f = 0.6083$ $\alpha_G = 0.0494$ cm <sup>-1</sup> $\sigma_a = 0.2202$ $\lambda_i = 0.25, 1.0, 1.0$ m
Van-Genuchten Retention Curve (Deterministic)	Saturated moisture content Residual moisture content Scaling parameter Shape factor (real number)	$\theta_s = 0.368$ $\theta_r = 0.102$ $\beta = 0.0334$ cm <sup>-1</sup> $n = 1.982$



constraint  $\alpha\Delta x_i \ll 2$  in the vertical, and statistical resolution requirement  $\Delta x_i/\lambda_i \ll 1$  in all three directions) and computational feasibility (total number of nodes on the order of  $10^5$ - $10^6$  at most). In addition, we rejected any solution that would have resulted in a large discrepancy between  $\Delta x_1$ ,  $\Delta x_2$ ,  $\Delta x_3$  by a factor of more than 2. Our choice  $\Delta x_i = (10 \text{ cm}, 20 \text{ cm}, 20 \text{ cm})$  seems to satisfy approximately all these requirements. Note that the statistical resolution of the grid in the vertical direction (2/5) is coarser than in the horizontal directions (1/5). There are 52 nodes in the vertical, and 76 nodes in each horizontal direction, resulting in a total of about 300,000 nodes in three dimensions.

On the other hand, the time-step was variable, typically on the order of 5 minutes initially, up to several hours towards the end of the drainage phase ( $t = 20$  days). As a consequence, the computational work was mostly consumed by the early stages of the infiltration phase. For example, the simulation of the first quarter of the infiltration stage, from  $t = 0$  to 2.5 days, consumed 1.5 hour of CPU time on a Cray 2 machine (NASA Ames Research Center). For the whole infiltration phase,  $t = 0$  to 10 days, the computational work was about 4 CPU hours. Only one additional hour was consumed in the simulation of 10 days of natural drainage after the end of infiltration ( $t = 10$  to  $t = 20$  days). Therefore, the total computational

work was about 5 hours of Cray 2 CPU time for the whole 20 day simulation.

[c] Soil properties and spatial variability

As before, we assumed that the water retention curve  $\theta(h)$  was deterministic, i.e. independent of spatial location. The  $\theta(h)$  curve was assumed to follow the Van Genuchten relation (equation 7.2 in the previous section). The "mean" parameters of  $\theta(h)$  were obtained by fitting the Van Genuchten function to a set of measured values  $\theta_i(h_i)$  obtained from samples taken within the upper soil layer (0-75 cm). Figure 7.9 shows the data points and the fitted "mean"  $\theta(h)$  curve, from Wierenga, Porro et al. (1986) and D. Polmann (personal communication).

The unsaturated conductivity was assumed to be an exponential function of pressure, as in equation 7.1 in the previous section, with random saturated conductivity  $K_s(\underline{x})$  and random slope  $\alpha(\underline{x})$  of the  $\ln K(h)$  curve. Furthermore,  $\alpha(\underline{x})$  and  $K_s(\underline{x})$  were assumed to be statistically independent (i.e. uncorrelated). This corresponds to "case 3" of the previous section (see bottom part of Figure 7.2), which produced a greater variability of the flow pattern than the case of perfect correlation. The standard deviations of  $\ln K_s$  was evaluated from field measurements and, indirectly, by relating the spatial

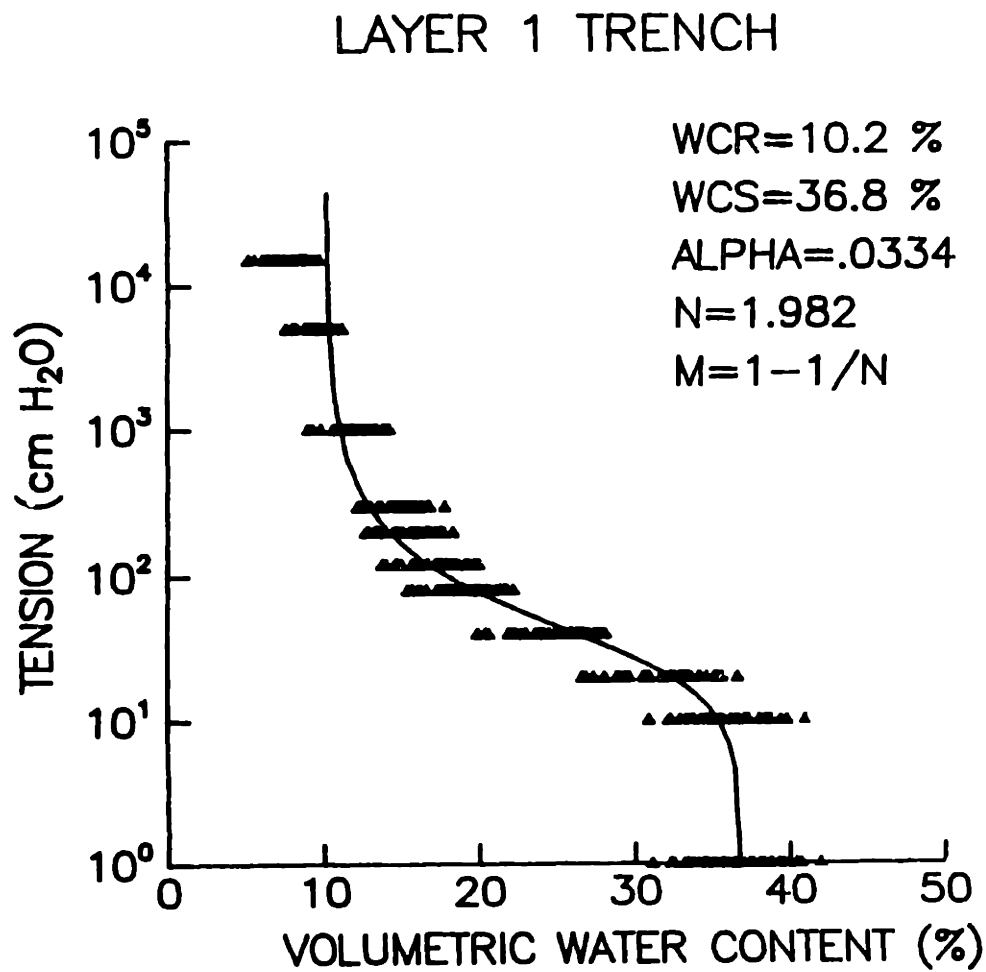


Figure 7.9 Water retention curve (tension versus volumetric moisture content) for the soil of the strip-source simulation ("trench experiment", Wierenga, et. al., 1986).

variability of  $K(h)$  to that of  $\theta(h)$  through a conceptual model (Mualem-Van Genuchten). The latter procedure was also used to evaluate the standard deviation of  $\ln \alpha$ , since direct measurements of  $\ln \alpha$  were not available. In addition, the geometric means  $K_G$  and  $\alpha_G$  were evaluated indirectly by fitting a tangent straight-line to the Mualem-Van Genuchten log-conductivity function at  $K = 2$  cm/day (value of the infiltration flux at the strip source) as shown in Figure 7.10. Note that the unsaturated conductivity values predicted by the two models are roughly in agreement (same order of magnitude) within the range of pressures  $-150 \text{ cm} \leq h \leq -50 \text{ cm}$ .

The  $\ln \alpha$  and  $\ln K_s$  random fields were assumed to be independent Markov fields with anisotropic correlation lengths  $\lambda_1 = 0.25 \text{ m}$ ,  $\lambda_2 = \lambda_3 = 1 \text{ m}$ . These values were chosen based in part on variograms of  $\ln K_s$  measured in the field (Wierenga et al., personal communication). However, note that the same anisotropic correlation scales were used for  $\ln \alpha$ , for which no data were available. Although there is a great part of subjectivity in this choice, it seems reasonable to assume the same anisotropy ratio ( $\lambda_1/\lambda_3 = 1/4$ ) for both parameters of the conductivity curve. The turning band method was used to generate two independent realizations of the 3D anisotropic Markov random fields  $\ln K_s$  and  $\ln \alpha$  over the 300,000 node grid. In actual practice, two isotropic fields were generated, and the

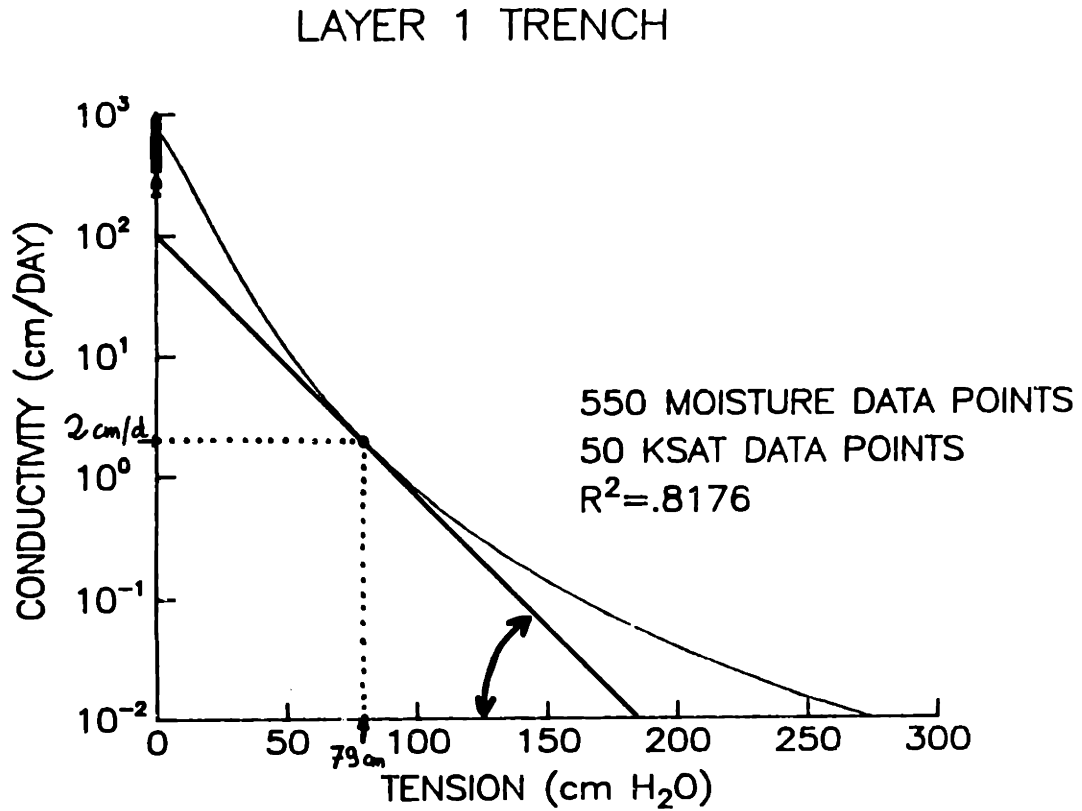


Figure 7.10 Mean unsaturated conductivity curve  $K(h)$  for the soil of the strip-source "trench experiment": the straight line corresponds to the exponential model actually used in the numerical simulation; the other curve is the Mualem-Van Genuchten model indirectly fitted to field data by Wierenga et. al., 1986.

desired anisotropy was obtained by rescaling the three coordinate axes (see Chapter 2, equation 2.18).

[d] Initial conditions:

Selecting an adequate initial condition in agreement with field observations proved to be a major difficulty, due to the restricted range of applicability of the exponential conductivity model used in the flow simulator. Field observations based on direct measurements of in-situ moisture contents suggested that the soil was initially very dry, near its residual moisture content (negative pressures on the order of  $10^4$  cm). However, preliminary numerical experiments with an initial pressure  $h_{in} = -300$  cm, corresponding to  $K_{in} = 3 \cdot 10^{-5}$  cm/day in the mean, showed that there was a severe restriction on the time step size in order to avoid divergence of the nonlinear system solver (nonlinear SIP, based on Picard iterations for linearization). The initial pressure was finally revised to a higher value  $h_{in} = -150$  cm, corresponding to  $K_{in} = 0.06$  cm/day in the mean.

For further reference, we give below a list of numerical values of some "mean" hydraulic properties corresponding to the initial state of the soil:

- Pressure:  $h_{in} = -150$  cm
- Relative conductivity:  $K_{in}/K_G = 0.6 \cdot 10^{-3}$
- Conductivity/flux ratio:  $K_{in}/q_o = 0.03$
- Moisture content:  $\theta_{in} = 0.155$
- Degree of saturation:  $S_{in} = \frac{\theta_{in} - \theta_r}{\theta_s - \theta_r} = 0.20$ .

Note that the soil is relatively dry, since only 20% of the porosity is initially filled with water. In addition, the following parameters may help evaluate, in different ways, the downward velocity of the wet zone:

- Maximum pressure at the source:  $h_{max} = -79.2$  cm
- Maximum moisture content at the source:  $\theta_{max} = 0.198$
- Downward velocity (mass balance):

$$V = \frac{q_o - K_{in}}{\theta_{max} - \theta_{in}} = 20.2 \text{ cm/day}$$

- Downward velocity (wetting front):

$$v = \left( \frac{dK}{d\theta} \right)_{in} = 8.8 \text{ cm/day}$$

The so-called maximum pressure  $h_{max}$  was evaluated by solving the equation:

$$K(h_{max}) = q_o$$

and the velocity  $v$  was evaluated by using the following

identities:

$$v = \left( \frac{dK}{d\theta} \right)_{in} = \alpha \left( K \frac{dh}{d\theta} \right)_{in} = \frac{\alpha K_{in}}{C_{in}}$$

In the case at hand,  $\alpha = 0.0494 \text{ cm}^{-1}$ ,  $K_{in} = 0.06 \text{ cm/day}$ , and  $C_{in} = 0.00034 \text{ cm}^{-1}$ . The result for  $v$ , given above, follows immediately. These relations are only intended to provide "order of magnitude" estimates of the downward velocity of the wet zone for mean values of the hydraulic parameters of the soil.

[e] Boundary conditions:

As stated earlier, all lateral boundaries were assumed impervious (including the face of the trench). The boundary conditions at the soil surface were a fixed flux ( $q = q_0$  on the strip source, and  $q = 0$  elsewhere). During infiltration the source flux was  $q_0 = 2 \text{ cm/day}$ . The condition at the bottom boundary was variable. During the early stages of infiltration, the moving boundary algorithm was used (see Chapter 5, section 5.4.3, Figure 5.11). However, this procedure proved to be inefficient, as the artificial bottom boundary moved rapidly downwards to reach the maximum prescribed depth (5m). After that time, a zero pressure gradient was imposed at the fixed bottom boundary:



$$\frac{\partial h}{\partial z} = 0 \rightarrow q = -K(h)$$

Since the initial conductivity was quite small ( $K_{in} = 0.06$  cm/day, compared to  $q_0 = 2$  cm/day) the downward flux through the bottom boundary was essentially negligible as long as the wet zone had not reached that boundary (infiltration phase and part of the drainage phase). The influence of the zero-pressure gradient boundary during the passage of the downward moving wet zone will be discussed later, based on visual inspection of the simulated pressure field.

### 7.3.2 Simulation Results

#### [a] Infiltration Phase:

The simulated infiltration phase lasted for 10 days, at a specific discharge rate of  $q_0 = 2$  cm/day over the strip source. Given the width and length of the strip (4 m x 9.9 m) the total quantity of water applied to the soil was about 7.9 m<sup>3</sup> (2100 gallons). A simple calculation shows that, if this amount of water was distributed uniformly beneath the strip-source (without lateral spread) over a 4 meter deep layer, the increase in volumetric soil moisture in that region would be 0.05, which approximately brings the moisture content to its potential maximum ( $\theta_{max}$ ) as evaluated in the previous sub-section. The

corresponding degree of saturation in that region of soil would be 40%, compared to 20% initially, still a moderate amount. These preliminary considerations may give an idea of the meaning of the term "wet zone" in this case of relatively slow-rate infiltration. Indeed, the so-called "wet zone" will presumably be only moderately wet, i.e., quite drier than the saturation point on average. This should be kept in mind when the terms "wet zone" and "wetting front" are being employed in the sequel.

The simulated three-dimensional pressure head fields (300,000 nodal values) were saved at times 1.0, 2.5, 5.0, 7.5, 10, 15, and 20 days. A post-processor code was used to sample the three-dimensional pressure fields along certain slices (2D) and transects (1D). The location of some of the selected slices was outlined in Figure 7.8 above. Three vertical slices transverse to the strip source, and one vertical slice coinciding with the longitudinal axis of the strip, were selected in order to display the transverse and longitudinal pressure field patterns at different times of infiltration and drainage. In addition, certain transects were selected along these slices in order to display in a single graph the time evolution of unidirectional pressure profiles. Occasionally, we will also show the pressure pattern in a horizontal slice or along a horizontal transect located at a given depth. For clarity of

exposition, let us define below our terminology concerning the sampled slices and transects (see Figure 7.8):

-- X, Y, Z coordinates:

X = lateral coordinate (horizontal, transverse to strip)

Y = longitudinal coordinate (horizontal, parallel to strip)

Z = vertical coordinate (depth below soil surface)

-- "Transverse" slices:

Vertical slices transverse to the strip source:

Y = 2 m (near trench face)

Y = 4.8 m (mid-point along the strip)

Y = 9.8 m (free edge of the strip)

-- Vertical transect:

Vertical transect located in the transverse slice

Y = 4.8 m, and passing approximately through the geometric center of the strip

(X = 0, Y = 4.8 m)

-- "Longitudinal" slice:

Vertical slice parallel to the strip and coinciding with its longitudinal axis of symmetry (X=0)

-- "Longitudinal" transect:

Horizontal transect lying in the horizontal slice  
 $X = 0$ , at some specified depth  $Z$ .

-- "Transverse" transect:

Horizontal transect lying in the transverse slice  
 $Y = 4.8$  m, at some specified depth  $Z$ .

-- Horizontal slice:

Horizontal slice located at some specified depth  $Z$   
( $Z = 0.5$  m: "shallow";  $Z = 2.0$  m: "deep").

A fairly representative picture of the three-dimensional pressure field can be obtained by looking at the pressure contours in three different "transverse slices" on the same page. This is shown in Figures 7.11, 7.12, 7.13, and 7.14 at times  $t = 5$  days,  $t = 10$  days,  $t = 10 + 5$  days, and  $t = 10 + 10$  days, respectively. A general observation that can be made is that the lateral edges of the wetted zone have a propension to spread laterally (see the contour line  $h = -125$  cm during infiltration, or  $h = -70$  cm during drainage). In contrast, there are some isolated (disconnected?) wet regions of high pressure which seem to be quite stable throughout the process of infiltration and drainage. A localized region of high pressure can be observed just beneath the center of the source

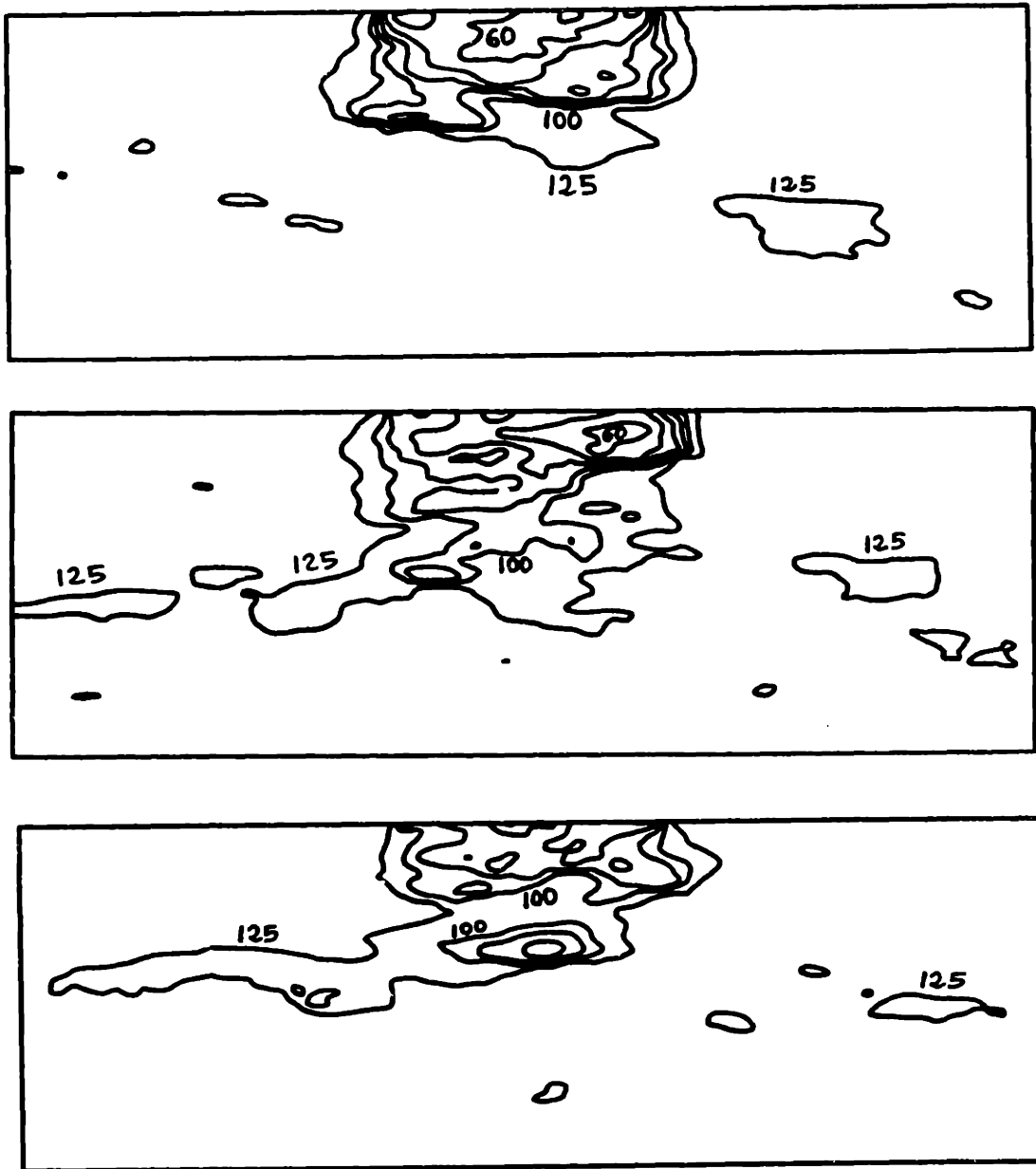


Figure 7.11 Contour lines of pressure head in three vertical-transverse slices during the simulated strip-source experiment after 5 days of infiltration ( $t=5$  days). From top to bottom: Slices  $Y = 2\text{m}$ ,  $Y = 4.8\text{m}$ ,  $Y = 9.8\text{m}$ .

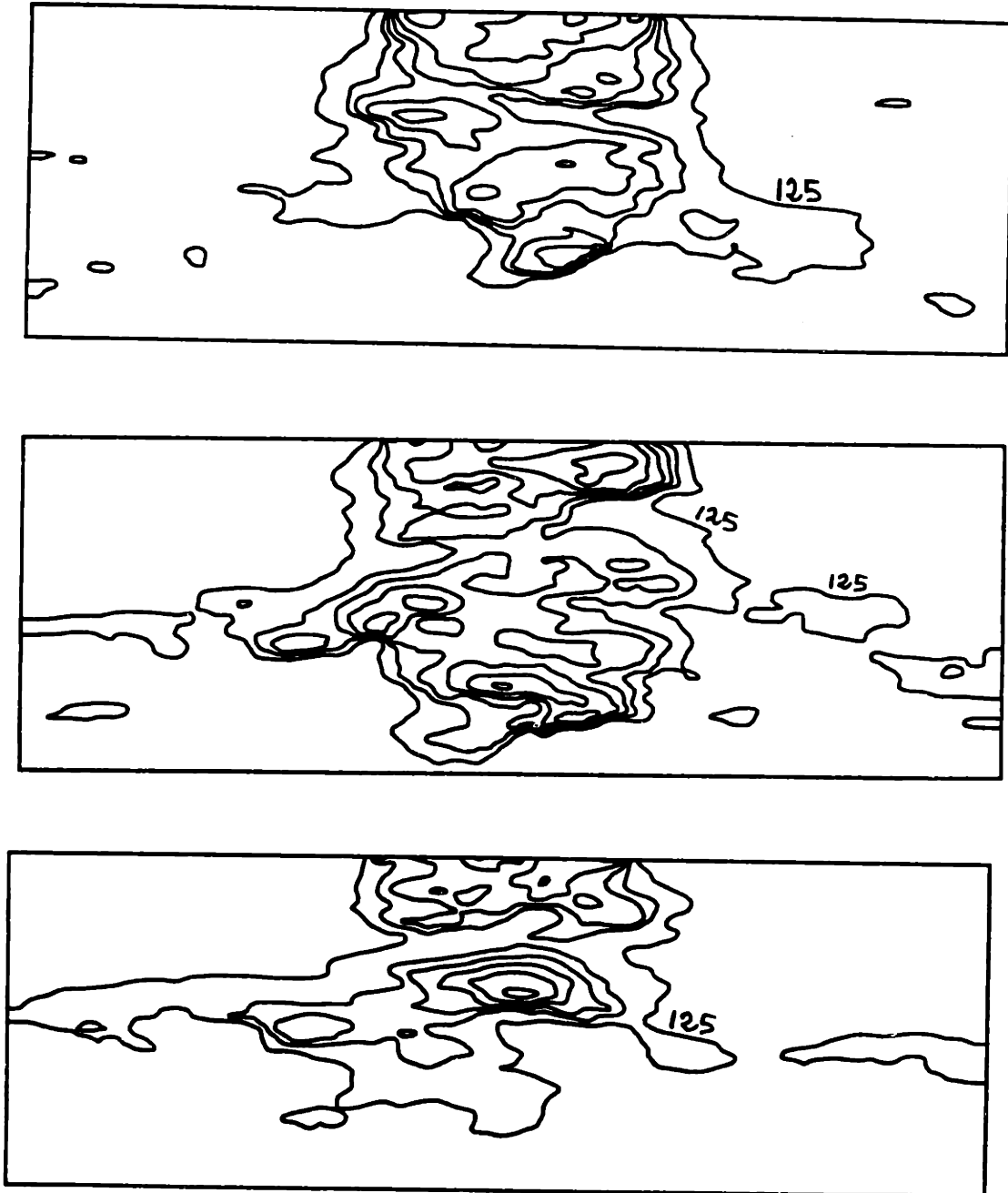


Figure 7.12 Contour lines of pressure head in three vertical-transverse slices during the simulated strip-source experiment after 10 days of infiltration ( $t = 10$  days). From top to bottom: slices  $Y = 2\text{m}$ ,  $Y = 4.8\text{m}$ ,  $Y = 9.8\text{m}$ .

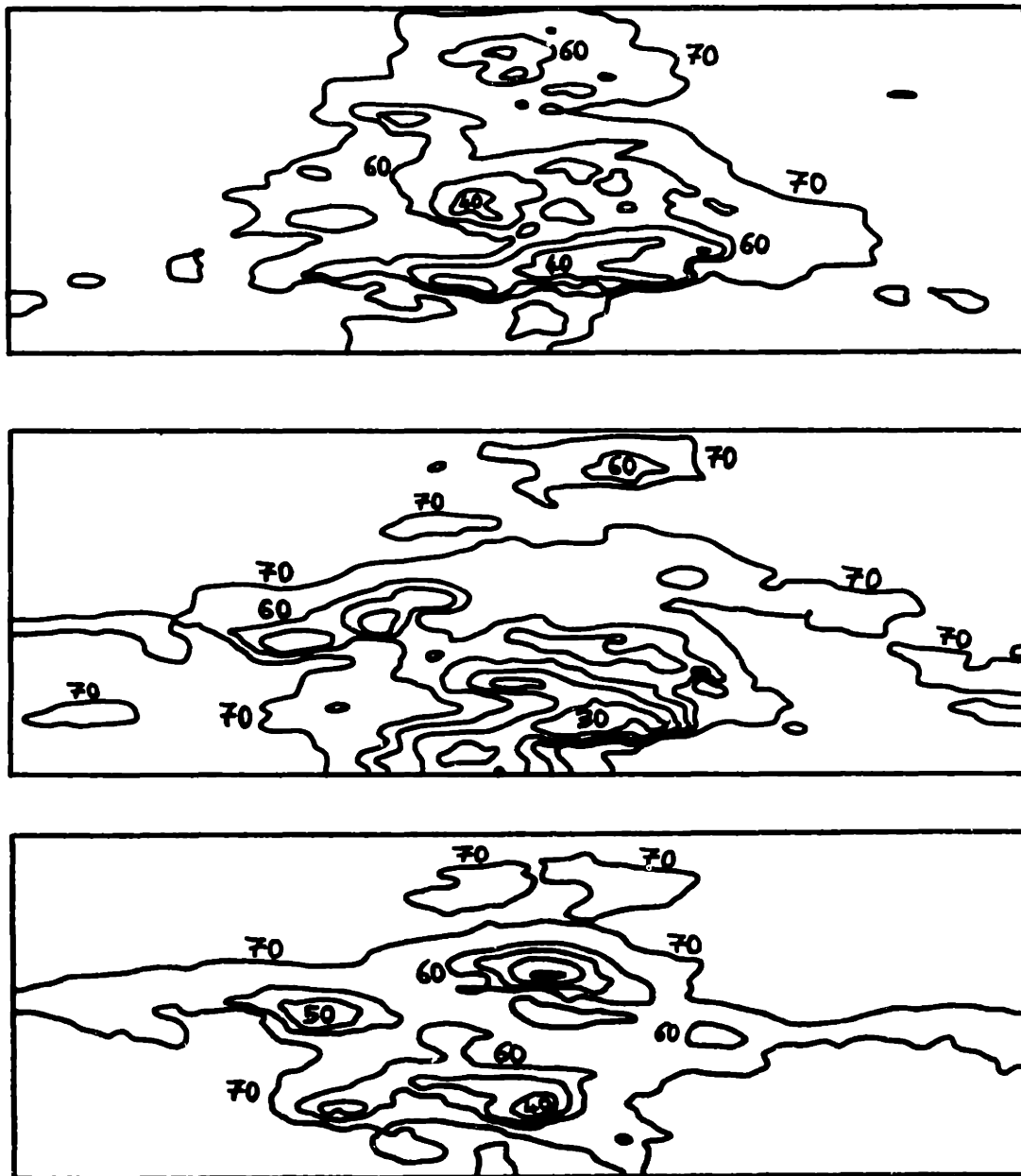


Figure 7.13 Contour lines of pressure head in three vertical-transverse slices during the simulated strip-source experiment after 10 days of infiltration and 5 days of drainage ( $t = 15$  days). From top to bottom: slices  $Y = 2\text{m}$ ,  $Y = 4.8\text{m}$ ,  $Y = 9.8\text{m}$ .

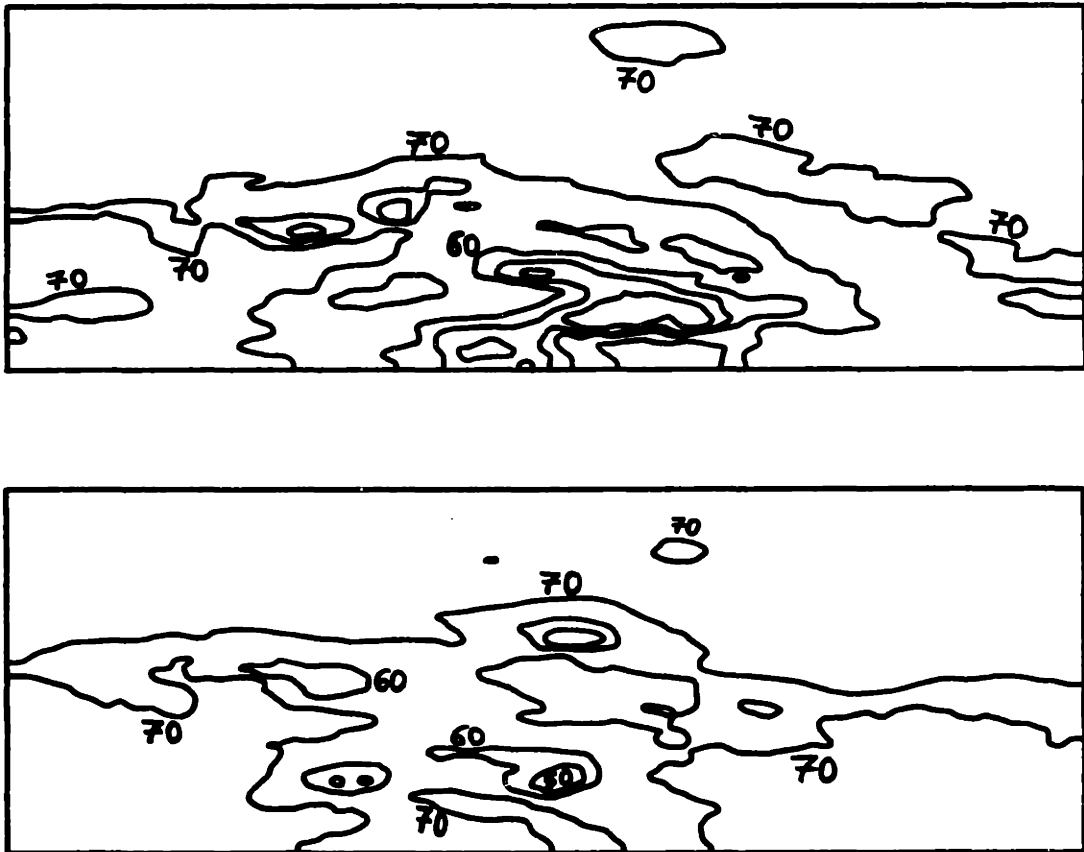


Figure 7.14 Contour lines of pressure head in three vertical-transverse slices during the simulated strip-source experiment after 10 days of infiltration and 10 days of drainage ( $t = 20$  days). From top to bottom, slices  $Y = 4.8$  m and  $Y = 9.8$  m.



(approximately 2 m deep) in the bottom parts of figures 7.11 through 7.14. Overall, these pictures leave the impression that the stratified structure of the soil (i.e., the statistical anisotropy of the conductivity curve) produces a differentiated anisotropy of the wetted zone, with a more pronounced lateral spreading of soil moisture in marginally wet regions than in the core of the wetted zone.

The evolution of the wetted zone can be followed by looking at a single "transverse slice" at successive times, as depicted in Figure 7.15. The pressure contours are shown at times  $t = 5$  days,  $t = 10$  days, and  $t = 10 + 5$  days (from top to bottom) for the "transverse slice" located near the free edge of the strip source ( $Y = 9.8$  m). During infiltration, the flow pattern beneath the strip source seems to be quasi-one dimensional down to a depth of approximately one meter, below which lateral spreading takes place. The same feature can also be observed at other locations along the strip (see previous figures 7.11-7.14). During the drainage phase, the wet region just beneath the strip source moves downward, and diffuses away laterally as well.

It may be also instructive to examine the evolution of the wetted zone in a longitudinal slice. This is shown in Figure 16 at three different times during infiltration and

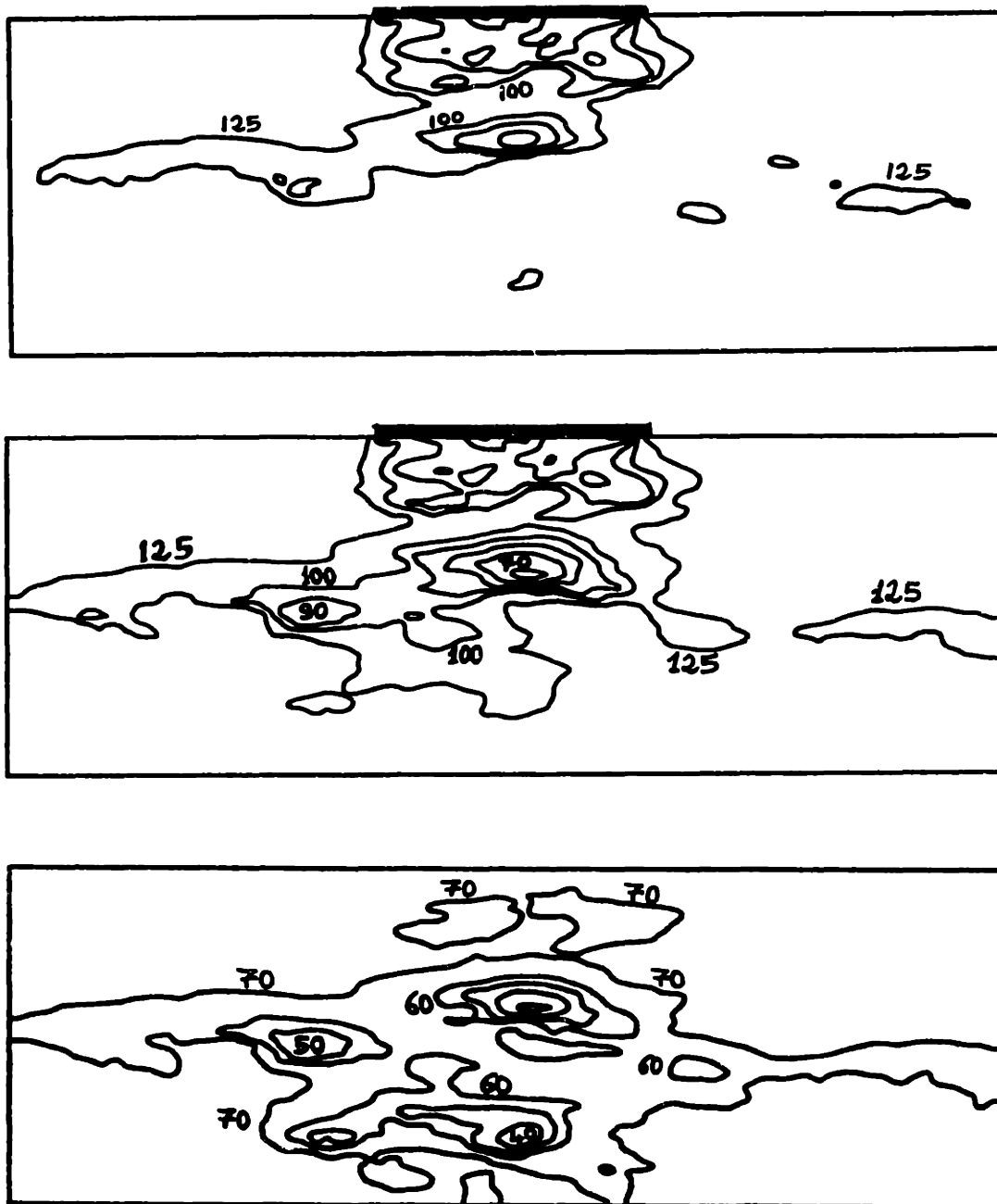


Figure 7.15 Contour lines of pressure head in the vertical-transverse slice located near the free edge of the strip ( $Y = 9.8$  m) at three different times. From top to bottom:  $t = 5$  days,  $t = 10$  days, and  $t = 15$  days (10 days infiltration + 5 days drainage).

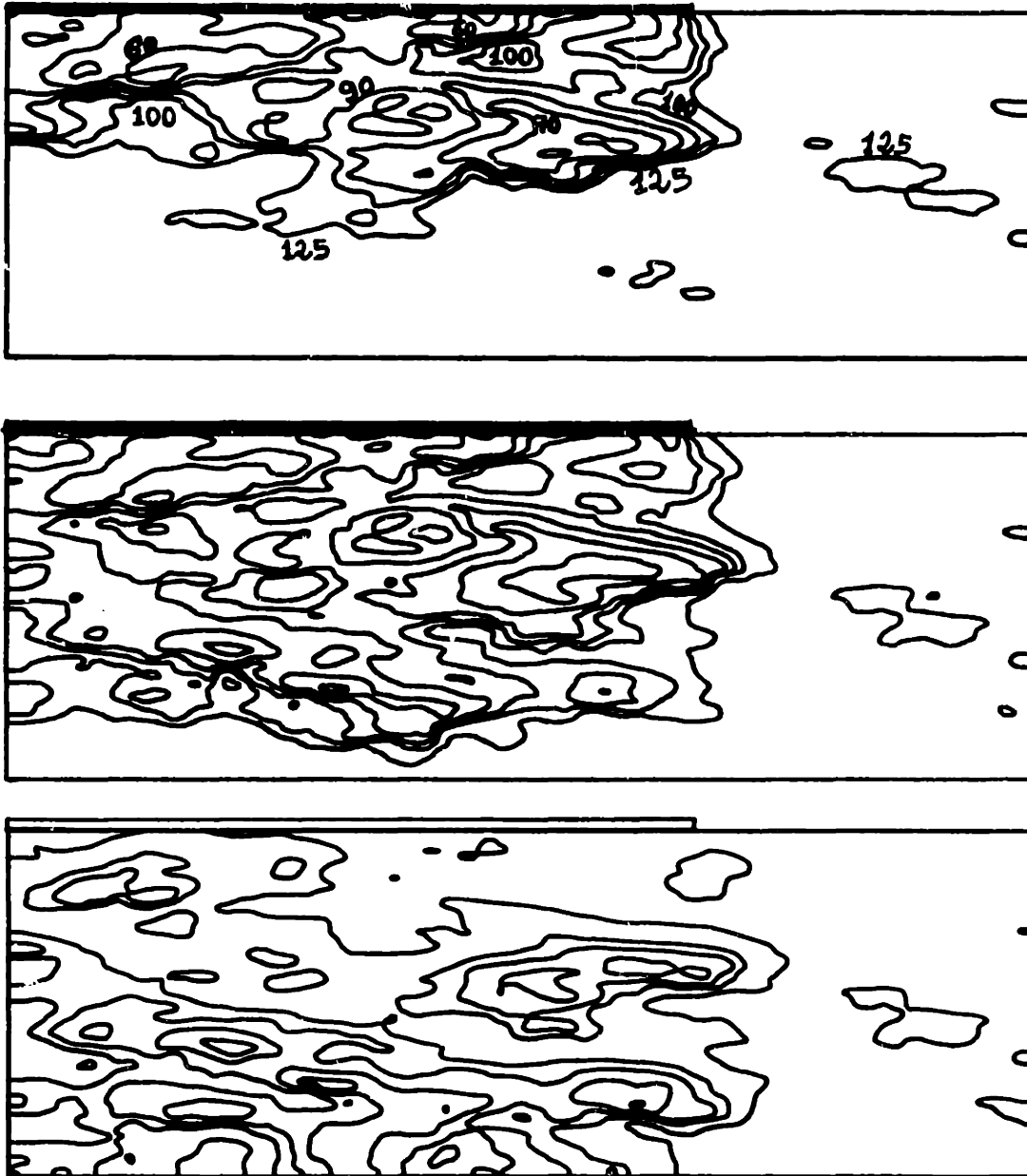


Figure 7.16 Contour lines of pressure head in the vertical-longitudinal slice ( $X=0$ ) at three different times. From top to bottom:  $t = 5$  days,  $t = 10$  days, and  $t = 15$  days (10 days infiltration and 5 days drainage).

drainage, for the vertical-longitudinal slice coinciding with the axis of symmetry of the strip . This figure illustrates the complex three-dimensional nature of the flow system. In a homogeneous soil, the flow pattern along the strip (from left to right on Figure 7.16) would be quasi uniform, except for a possible edge effect on the free end of the strip (right part of the graphs). This edge effect, i.e., diffusion of moisture away from the free edge of the strip, seems to be minimal during infiltration, but more pronounced during natural drainage. In any case, the influence of vertical/horizontal anisotropy appears once again to be quite important, as can be seen from the elongated shape of pressure contour lines below the strip. Note that the length of the strip is only ten times larger than the horizontal correlation scale  $\lambda$  of  $\ln K_s$  and  $\ln \alpha$ , i.e. much too short for a statistical analysis of the (presumably homogeneous) longitudinal fluctuations of pressure.

To complete our visual representation of the three-dimensional pressure pattern, we show in Figure 7.17 (a) and (b) the pressure contour lines in two horizontal slices, located respectively at depth  $Z = 0.5$  m and  $Z = 2.0$  m, during the drainage phase (time  $t = 15$  days). These figures should be compared to the vertical-longitudinal pressure map of Figure 7.16 at the same time  $t = 15$  days. The horizontal pressure map obtained at shallow depth  $Z = 0.5$  m (Figure 7.17a)

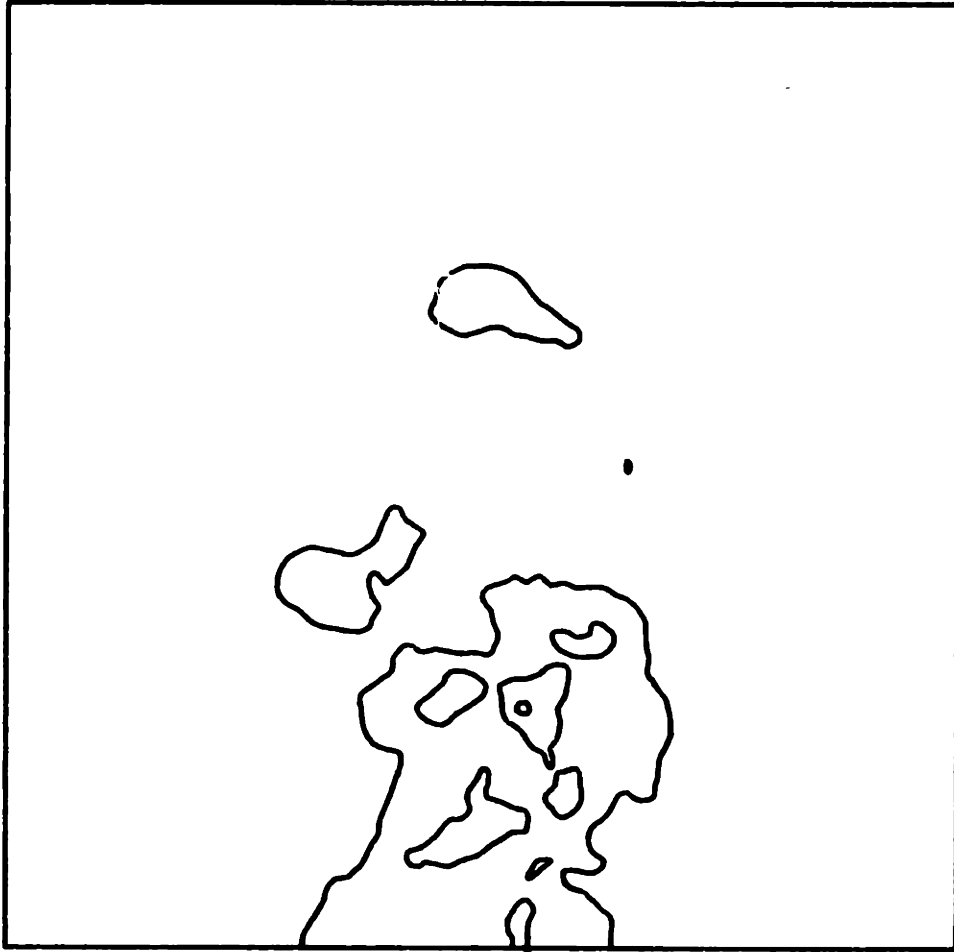


Figure 7.17 (a) Contour lines of pressure head in a horizontal slice at shallow depth  $Z = 0.5$  m. Time  $t = 15$  days (10 days of infiltration and 5 days drainage).

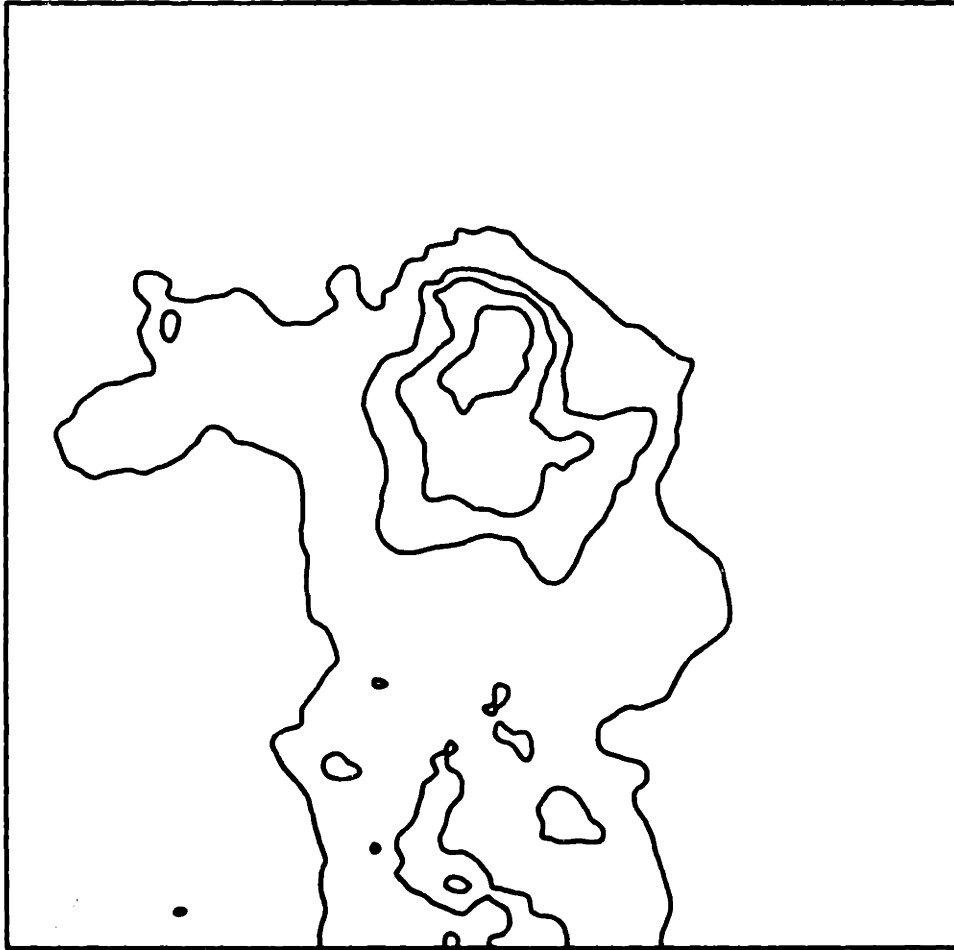


Figure 7.17 (b) Same as (a), for a horizontal slice at a larger depth  $Z = 2.0m$ .

is not surprising in view of the previous figure. For the larger depth  $Z = 2.0$  m (Figure 7.17 b), the horizontal pressure map reveals previously unnoticed features: non-symmetric spreading of the relatively "dry" part of the moisture plume in the transverse direction, compared to the nearly axi-symmetric pattern of "wet" pressure contours. It is not clear whether these features are due to a three-dimensional edge effect, or merely to the particular soil heterogeneity below the free edge of the strip at that depth.

Finally, it is also instructive to examine the evolution of pressure profiles along selected transects in the vertical, transverse, and longitudinal directions. This is shown in the following figures: vertical pressure profiles during the infiltration phase (Figure 7.18) and the drainage phase (Figure 7.19); horizontal-transverse pressure profiles during the drainage phase at depth 0.5 m and 2.0 m (Figure 7.20 (a) and (b)); and horizontal-longitudinal pressure profiles during the drainage phase at depths 0.5 m and 2.0 m (Figure 7.21 (a) and (b)).

The vertical pressure profiles of Figure 7.18 depict the downward movement of the local "wetting front" at that particular location. A simple calculation shows that the downward velocity of the front decreased with time, from

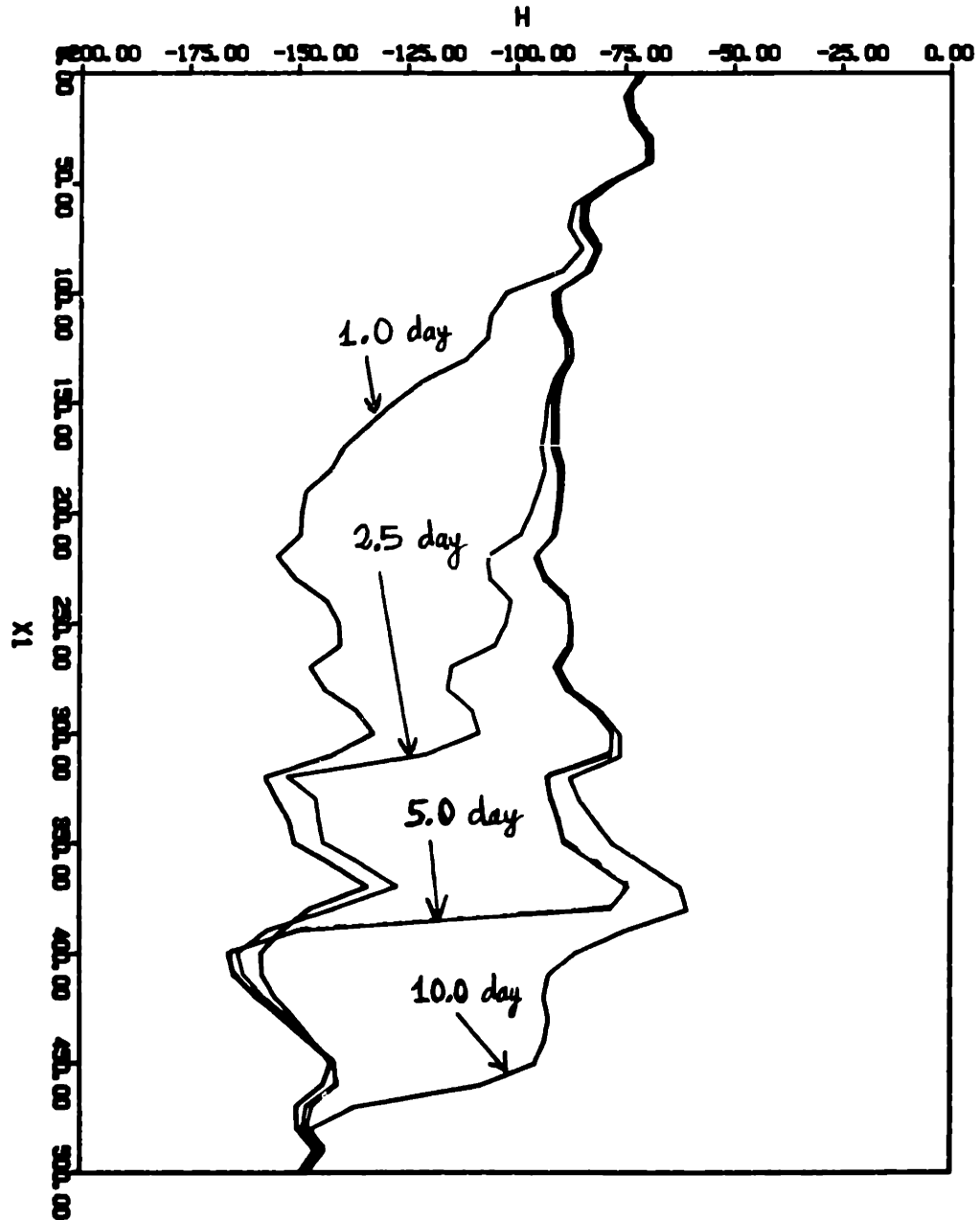


Figure 7.18 Pressure head profiles in the vertical direction during infiltration (times  $t = 1.0, 2.5, 5.0$  and  $10$  days). The vertical transect is located near the geometric center of the strip ( $X=0, Y=4.8\text{m}$ ).



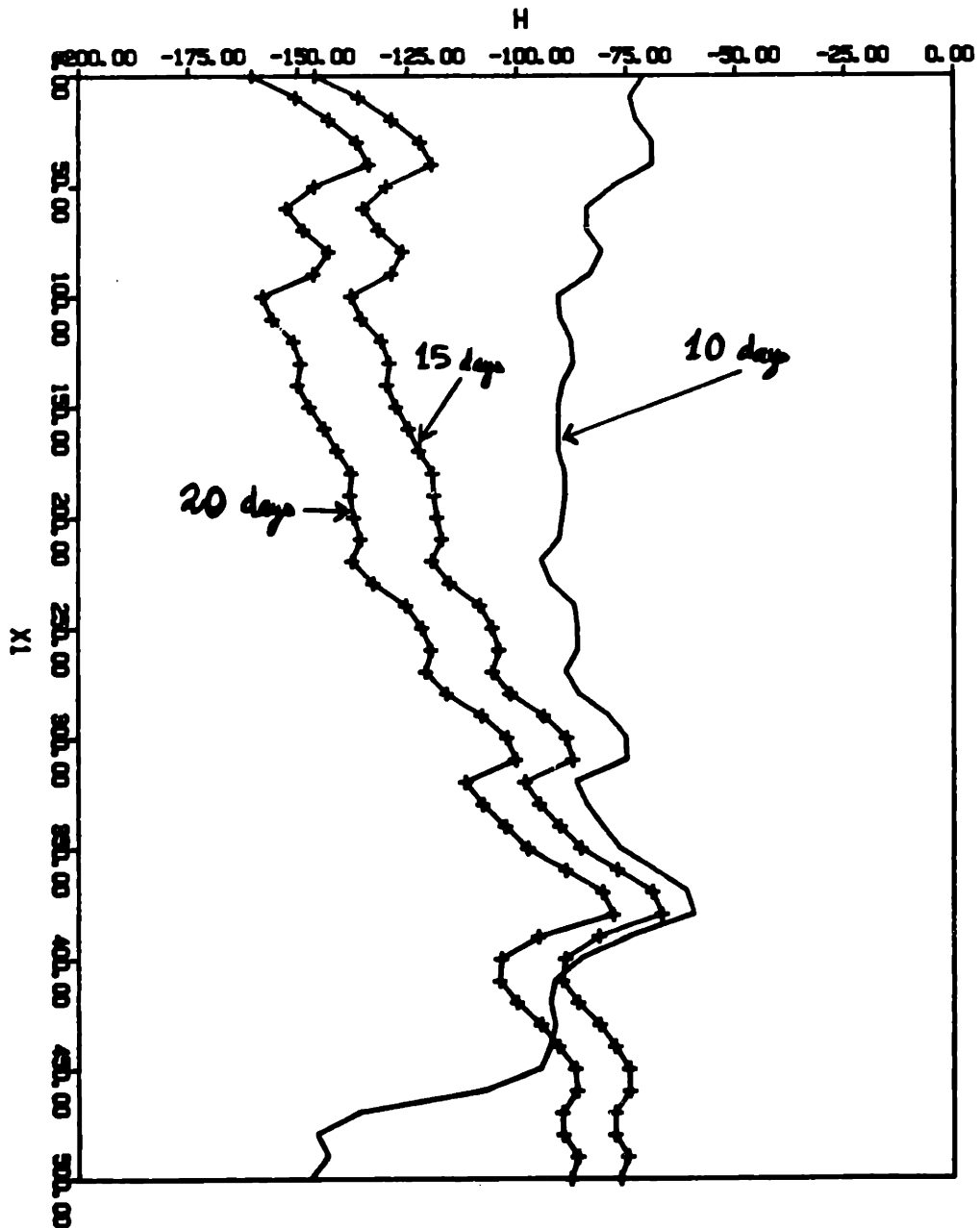


Figure 7.19 Pressure head profiles in the vertical direction during drainage (times  $t = 10, 15$  and  $20$  days). The vertical transect is located near the geometric center of the strip ( $X = 0, Y = 4.8\text{m}$ ).

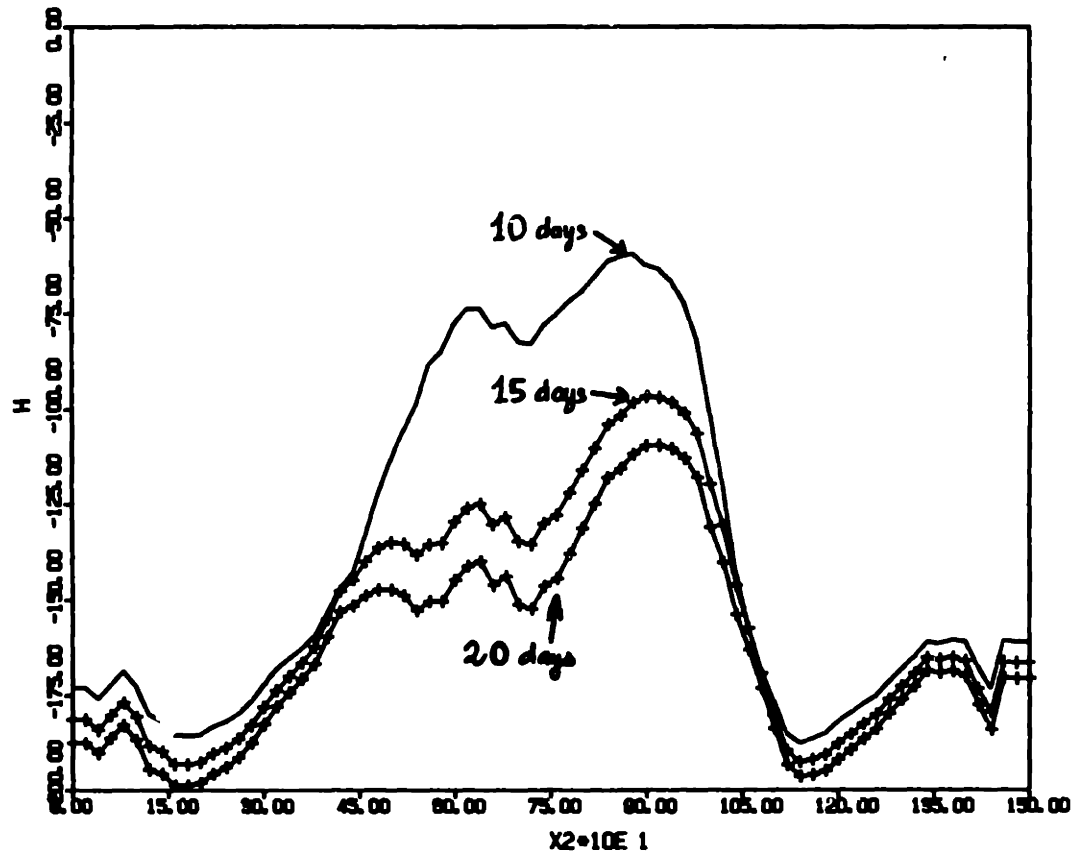


Figure 7.20 (a) Pressure head profiles in the horizontal-transverse direction during drainage (times  $t = 10, 15$  and  $20$  days). The transect is located at depth  $Z = 0.5$  m beneath the strip source.

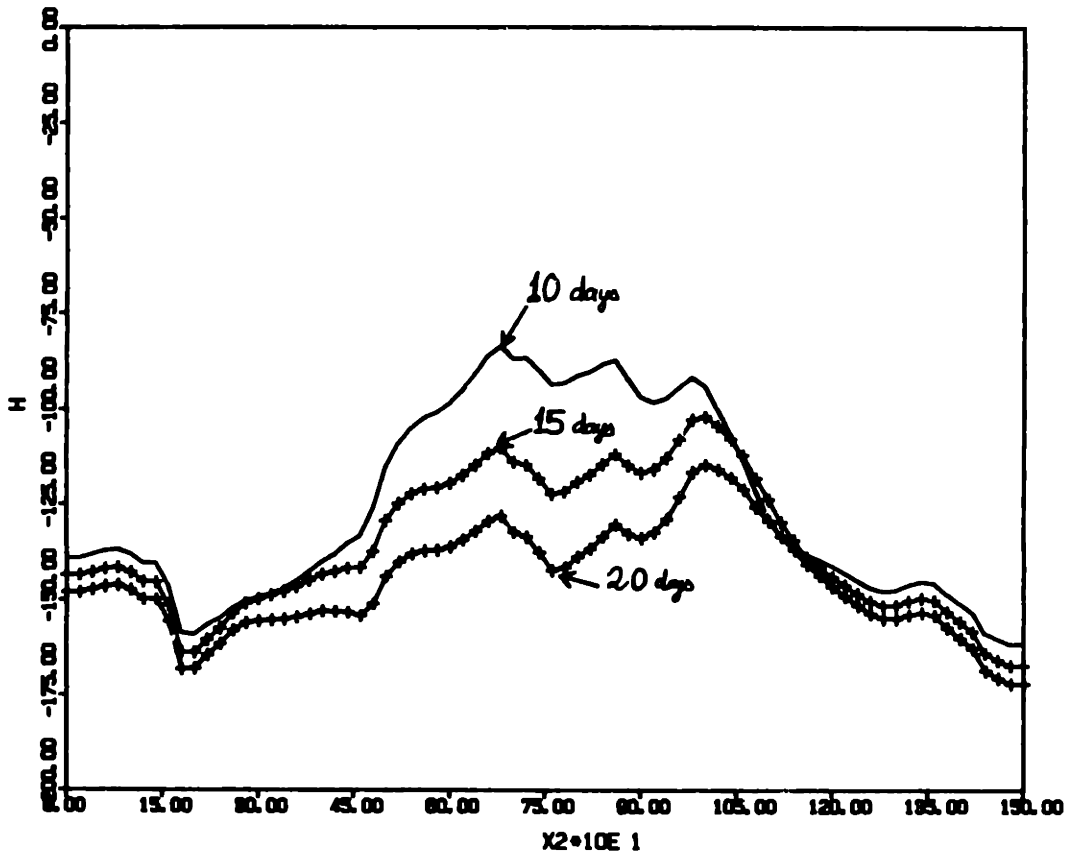


Figure 7.20 (b) Same as (a), for a larger depth  $Z = 2.0\text{m}$ .

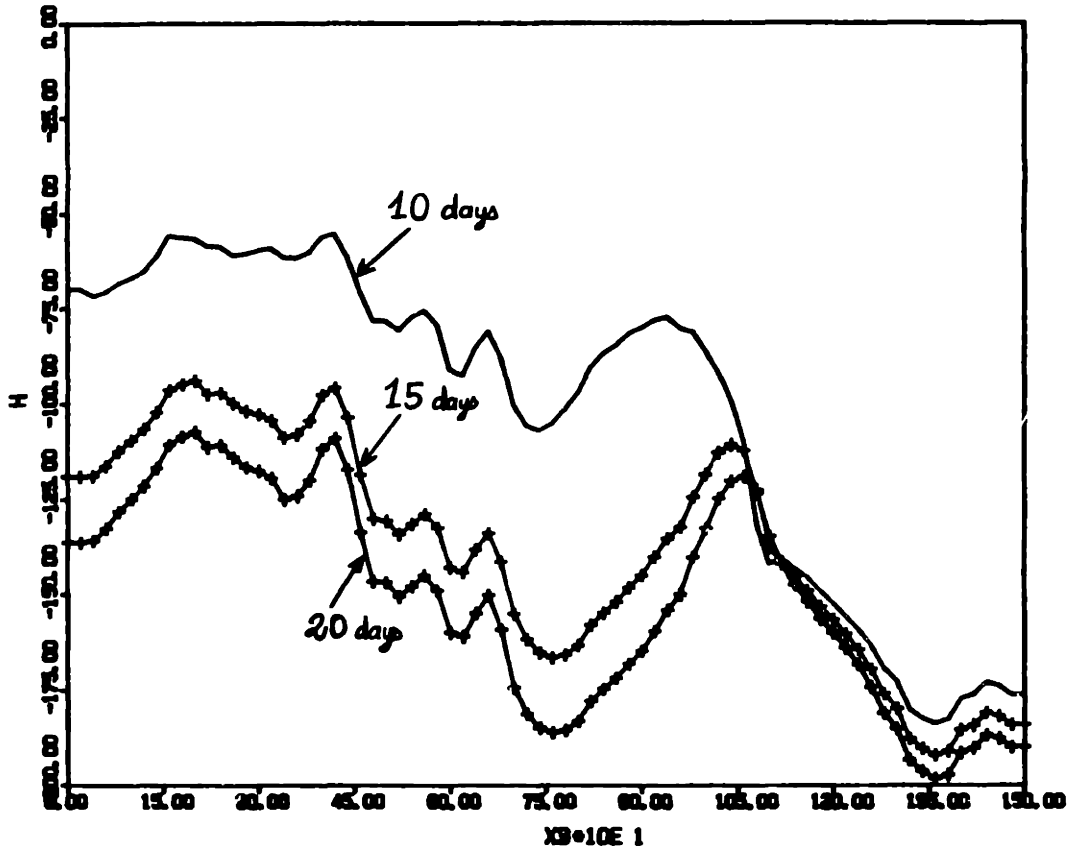


Figure 7.21 (a) Pressure head profiles in the horizontal-longitudinal direction during drainage (times  $t = 10, 15$  and  $20$  days). The transect is located at depth  $Z = 0.5\text{m}$ .

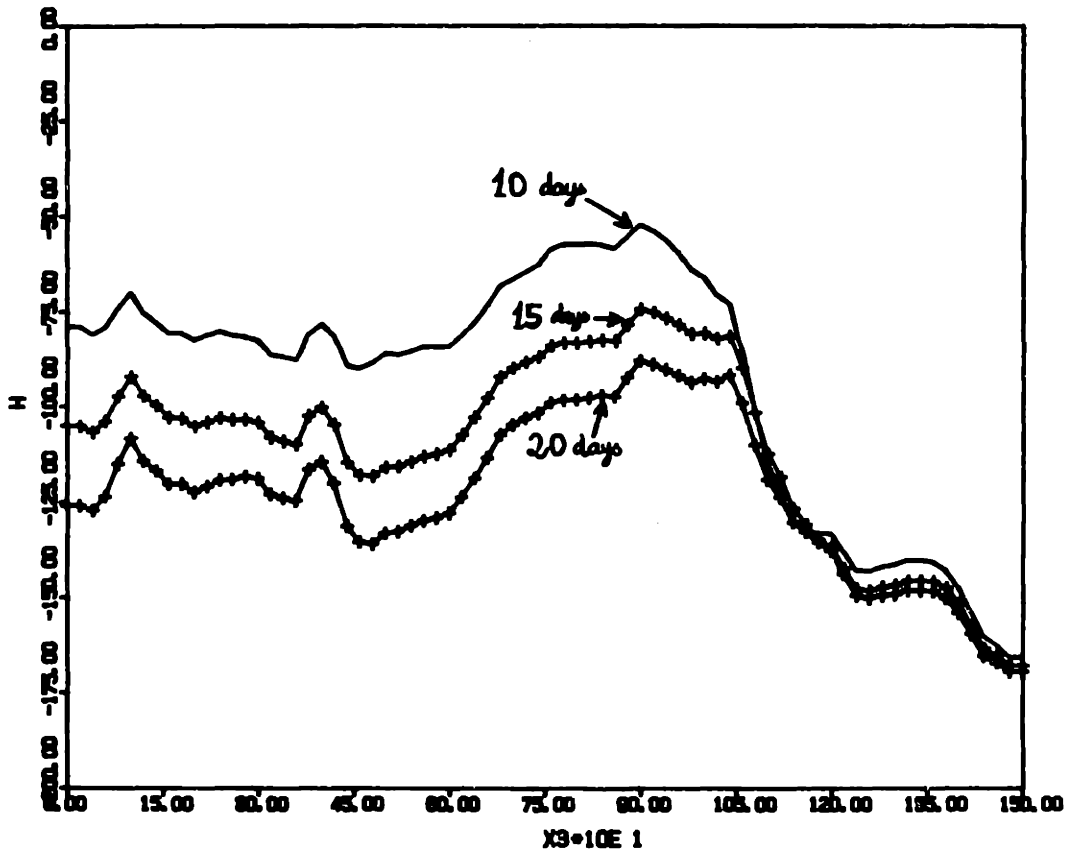


Figure 7.21 (b) Same as (a), for a larger depth  $Z = 2.0\text{m}$ .

1.5 m/day during the first day, to 1.1 m/day during the next 1.5 days, then 0.3 m/d during the next 2.5 days, and finally 0.2 m/day during the last 5 days of infiltration. The latter value coincides with our previous estimate ( $V$ ) based on mass balance:

$$V = \frac{q_0 - K_{in}}{\theta_{max}} - \frac{K_{in}}{\theta_{in}} \simeq 0.2 \text{ m/day.}$$

but is still higher than the asymptotic velocity ( $v$ ) of the wetting front, previously evaluated as:

$$v = \left( \frac{dK}{d\theta} \right)_{in} \simeq 0.1 \text{ m/day.}$$

At any rate, it seems that the pressure profiles of Figure 7.18 tend to a quasi-steady downward translation as time evolves (compare  $t = 2.5, 5.0,$  and  $10.0$  days). This, however, could be particular to the soil region traversed by the vertical transect located at the center of the strip. The seemingly one-dimensional behavior of the transient wetting front along that transect could be perhaps explained by the large width of the strip source, on the same order as the total depth of the flow domain (4 m compared to 5 m).

The remaining figures (7.19, 7.20, 7.21), shown just above, depicted the evolution of pressure profiles during the

drainage phase. Figure (7.19) shows that the soil was constantly drying above depth 3.5-4.0 m, and wetting below 4.0 m depth. The "gravity-driven" flow condition imposed at the bottom boundary ( $q = -K(h)$  at depth  $Z = 5.0$  m) allowed water to cross that boundary downward as natural drainage took place. Figure (7.20) clearly shows the persistent effect of the strip-source infiltration phase during drainage: the soil remains wetter beneath the strip source during the whole drainage period, particularly at shallow depth  $Z = 0.5$  m (Figure 7.20 (a)). At larger depth  $Z = 2.0$  m, the contrast of pressures beneath and away from the strip is milder due to lateral spreading (Figure 7.20 (b)). However, this kind of effect is not observed in the longitudinal direction parallel to the strip (Figure 7.21): the longitudinal wetting front near the free edge of the strip does not seem to smooth out with depth and/or with time. The dimensions of the strip are such that there is little lateral diffusion at the edge of the strip (apparently no more than 1 m). See however Figure (7.17 b) for a two-dimensional picture of edge effects.

Some other observations on the statistical nature of pressure variability can be made, in view of the one-dimensional pressure profiles just discussed. The vertical profiles of Figure (7.18) display quasi-homogeneous pressure fluctuations over several meters (below the wetting front for  $t = 1$  day, and

above the wetting front for  $t = 10$  days). It can be seen by visual inspection that the amplitude of pressure fluctuations is larger on average for dryer soil:

$$\Delta h \simeq 25 \text{ cm} \quad \text{for} \quad \bar{h} \simeq -150 \text{ cm}$$

$$\Delta h \simeq 5-10 \text{ cm} \quad \text{for} \quad \bar{h} \simeq -80 \text{ cm.}$$

This observation agrees qualitatively with the findings of the linearized spectral theory of Mantoglou and Gelhar (1987).

Incidentally, it is also interesting to note that the mean pressure  $\bar{h} \simeq -80$  cm ( $t = 10$  days) coincides with our previous estimate of the maximum asymptotic pressure  $h_{\text{max}}$ . This implies that the "mean" conductivity of the wetted soil beneath the center of the strip becomes about equal to the infiltration flux at the surface of the strip, after a sufficiently large time of infiltration. Note that the mean conductivity is defined here at the deterministic  $K(h)$  curve corresponding to geometric mean parameters  $K_G$  and  $\alpha_G$ . Now, the fact that the mean vertical pressure gradient is zero (Figure 7.18 at  $t = 10$  days) suggests that the "mean" conductivity coincides with the large-scale effective conductivity in the vertical, i.e.:



$$\hat{K}_{11}(\bar{h}) \simeq K_G \cdot \exp(\alpha_G \cdot \bar{h}).$$

Finally, it should also be noted that the pressure fluctuations in the vertical appear to have a relatively small length scale (on the order of  $\lambda_1 = 0.25$  m) whenever a relatively constant mean pressure can be identified (Figure 7.18). In contrast, the pressure fluctuations in the horizontal directions appear to have a more complex structure, with a superposition of small and large scales of fluctuations: see in particular Figure (7.20 a) and Figure (7.21 a). The largest scale of fluctuations of pressure (apparently several meters) may reflect the large horizontal correlation scale of the anisotropic soil (1 m). However, these large scale fluctuations could also be due to a phenomenon of "scale selection" in relation to the size of the strip source itself (4 m x 9.8 m).

The ensemble of observations presented just above will be summarized in the last section of this chapter (section 7.5: summary and discussion). Before this, we present below the results of another large infiltration simulation on the same random soil, but for a very different type of flow conditions.

## 7.4 Steady "Rainfall" Infiltration in a Statistically Anisotropic Soil (300,000 nodes)

### 7.4.1 Model problem and input data:

In this section, we present the results of a large single-realization of steady state infiltration from a uniform planar source with constant flux. The geometry of the flow domain as well as the random soil properties are the same as in the previous section. In particular, we use here the same realization of a statistically anisotropic random conductivity curve on the 300,000 node grid, as previously. See subsection 7.3.1, Figure 7.8, and Table 7.2 concerning input data (except for boundary conditions).

The steady state solution was obtained by running the flow simulator in the transient regime until a steady state was reached beyond "reasonable doubt". The boundary condition over soil surface was a uniform constant flux  $q_0 = 0.060517$  cm/day, approximately equivalent to a mean "rainfall" rate of 213 mm per year (arid climate). The condition at the bottom boundary ( $Z = 5$ m) was a zero pressure gradient, i.e., by Darcy equation:

$$q = -K(h, \underline{x}).$$

The initial condition was a uniform pressure:

$$h_{in} = -150 \text{ cm.}$$

Note that  $q_0$  and  $h_{in}$  were chosen in such a way that the final solution should be close to the "initial guess" ( $h_{in}$ ) on average:

$$q_0 = K_G \exp(\alpha_G h_{in}) = \bar{K}(h_{in}).$$

All lateral boundaries were assumed impervious (zero flux).

The transient simulation was conducted in several pieces, with intermediate solutions saved at times:

$$t = 4.92, \quad 14.44, \quad 44.03, \quad 64.33, \quad 74.31, \quad \text{and} \quad 114.00 \text{ days}$$

The flow had clearly reached a nearly steady state regime by the time  $t \approx 114$  days (approximately 4 months of infiltration). This was attested by the insignificant changes of pressure observed along a selected transect, beyond the first 2 weeks of infiltration. An example is shown in [Figure 7.22](#) for a vertical transect located at the geometric center of the domain. The pressure profiles at times  $t \approx 44, 64, 74$  and 114 days were almost indistinguishable (only the last of these is represented in the figure). Moreover, the mass balance routine (Chapter 5, section 5.4.3) was used to monitor the global convergence of the

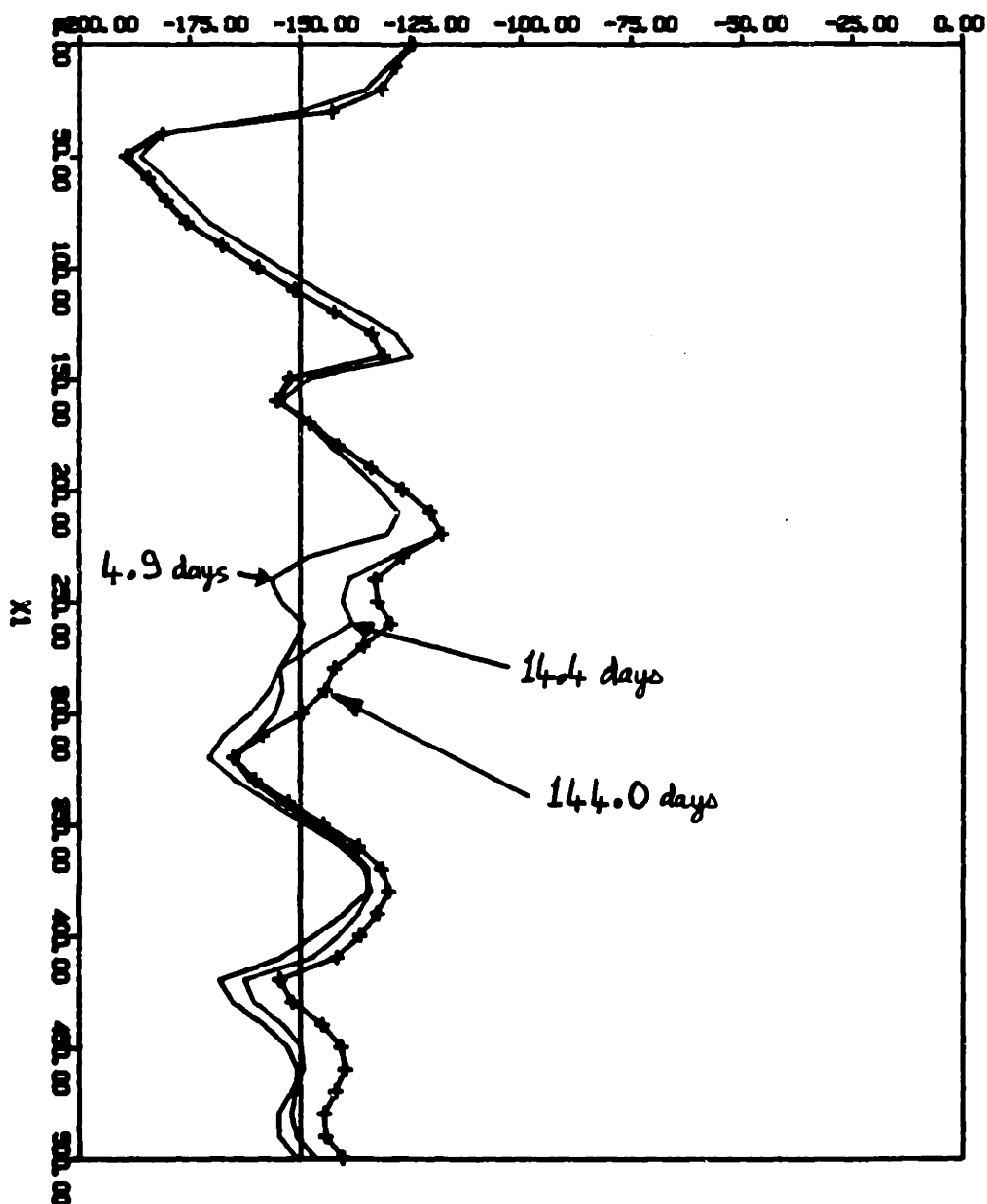


Figure 7.22 Vertical pressure head profiles obtained at different times during the transient simulation towards a steady state solution of the "rainfall infiltration" problem. Times  $t = 4.9$  day, 14.4 day and 114 day: the crosses indicate the quasi-steady solution at  $t = 114$  days. The vertical transect is near the center of the domain.

solution towards a steady state. The relative mass balance error:

$$E = \frac{Q_{in} - Q_{out}}{Q_{in}}$$

was only about +2% at time  $t = 114$  days. Thus, it seems beyond doubt that a steady state flow regime was actually reached, at least in a mean sense.

#### 7.4.2 Simulation Results and Statistical Analysis:

The steady-state three-dimensional pressure field was sampled along selected slices and transects, all traversing the geometric center of the flow domain. [Figure 7.23](#) depicts the pressure head contour lines in a vertical slice and located midway between lateral boundaries, and [Figure 7.24](#) shows the pressure contours in a horizontal slice located at mid-distance between the top and bottom boundaries. In both cases, the pressure contour values are equally spaced and range from -110 cm to -190 cm (recall that  $h_{in} = -150$  cm). The contour values were not shown on these figures; some comments will help clarify their meaning.

The most striking feature in the vertical slice of [Figure 7.23](#) is the presence of narrow-elongated "fronts" (nearly



Figure 7.23 Pressure head contour lines in a vertical slice for the steady state "rainfall" infiltration in a statistically anisotropic soil (300,000 nodes). The slice approximately crosses the geometric center of the domain ( $Y = 7.4\text{m}$ ).

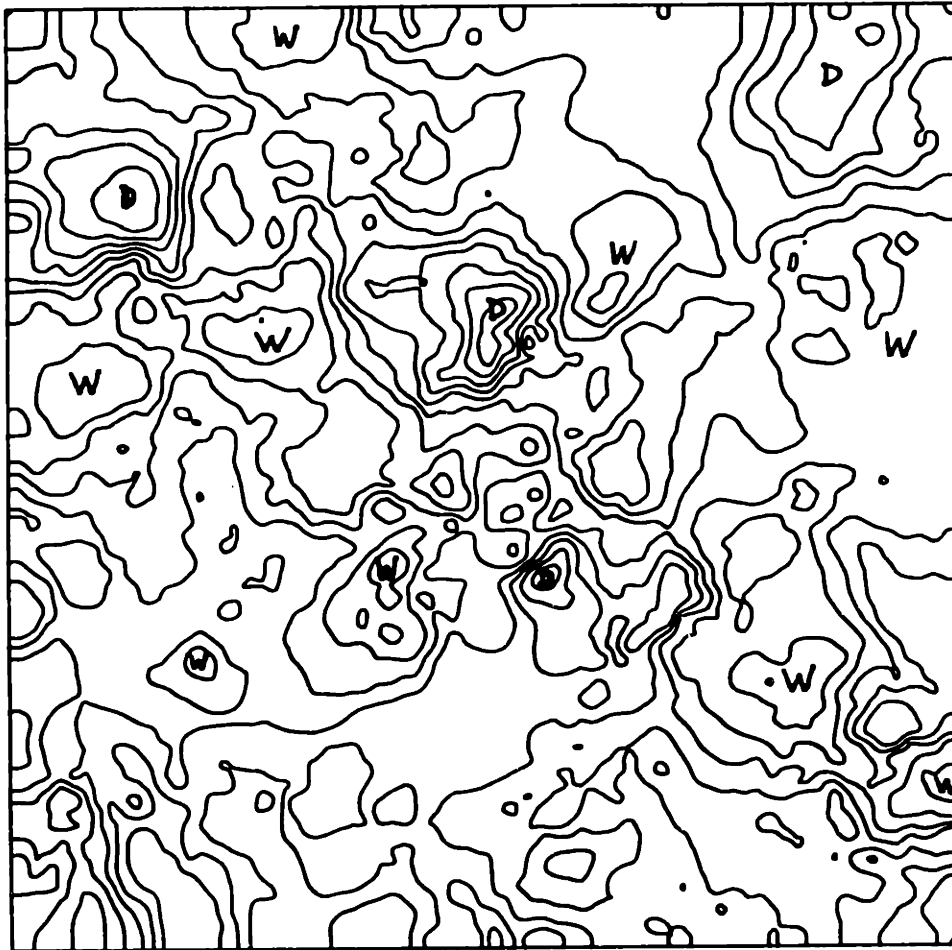


Figure 7.24 Pressure head contour lines in a horizontal slice for the steady state "rainfall" infiltration in a statistically anisotropic soil (300,000 nodes). The slice is approximately located at the mid-point between soil surface and bottom boundary ( $z = 2.5\text{m}$ ).

black on the picture) separating two regions of local maxima of pressure, above and below. Inspection of contour values reveals that in most cases, the regions just above the horizontal fronts have a local maximum of pressure (relatively wet), and those below have a local minimum of pressure (relatively dry). See for instance the two zones marked "W" and "D" ("wet" and "dry") in Figure 7.23. The important role of statistical anisotropy of the soil parameters is quite evident. In its downward movement driven by gravity, water tends to accumulate above elongated lenses of low unsaturated conductivity, and spreads laterally from there by a kind of "diffusion" process.

On the other hand, the horizontal slice of Figure 7.24 displays a fairly isotropic pattern of pressure heads, as could be expected due to the horizontal isotropy of the soil and the horizontal uniformity of boundary conditions. The labels "W" and "D" were used here again to designate regions of maximum pressure (wet) and minimum pressure (dry). It seems that most of the relatively "wet" regions are larger and have smoother pressure gradients than the locally "dry" zones. This may indicate an assymetry in the probability distribution of pressure, with negative skewness. Equivalently, the tension  $\psi = -h$  could perhaps be represented by a log-normal random function having positive skewness. Another possible interpretation of the observed assymetry (?) of the pressure field around the value



$h_{in} = -150$  cm could be that the actual mean  $\bar{h}$  was in fact higher (wetter) than the initial state.

In order to obtain a more synthetic characterization of the steady pressure field, we have attempted a summary statistical analysis of  $h(\underline{x})$  based on the assumption of statistical homogeneity of first and second moments in all three spatial directions. This was also complemented by a second statistical analysis of  $h(\underline{x})$ , assuming that the perturbation:

$$h'(\underline{x}) = h(\underline{x}) - \bar{h}(x_1)$$

is homogeneous in 3D space. The spatially variable mean  $\bar{h}(x_1)$  intervening in this expression was obtained empirically by averaging the pressure in the horizontal plane at each different depth  $x_1$ . The results obtained by the two methods were fairly close, as shown in Table 7.3. However, the empirical mean  $\bar{h}(x_1)$  was quite variable with depth.

Interpreting the statistical results of Table 7.3 to their face value, it appears that the pressure head standard deviation was about 20 cm around the constant mean  $\bar{h} \simeq h_{in} = -150$  cm. Furthermore, it turns out that  $h(\underline{x})$  was negatively skewed (or  $\psi = -h$  positively skewed) as conjectured earlier based on pressure contour maps. Finally, it appears that

TABLE 7.3  
 SINGLE-POINT MOMENTS AND CORRELATION FUNCTION  
 OF THE PRESSURE HEAD FIELD FOR THE  
 SINGLE-REALIZATION "RAINFALL INFILTRATION"  
 SIMULATION ON A STATISTICALLY ANISOTROPIC SOIL  
 (300,000 NODE GRID)

Pressure Moments	$h'(\underline{x}) = h(\underline{x}) - \bar{h}$ $\bar{h} = 3D \text{ average}$	$h'(\underline{x}) = h(\underline{x}) - \bar{h}(x_1)$ $\bar{h}(x_1) = 2D \text{ average}$
Mean $\bar{h}$	- 147.5 cm	---
Stand. Dev. $\sigma_h$	19.1 cm	17.9 cm
Skewness $\gamma_h$	- 0.27	- 0.22
Kurtosis $\kappa_h$	+ 0.30	+ 0.22
$\rho(1.6\lambda_1)$	+ 0.352	+ 0.311
$\rho(1.6\lambda_2)$	+ 0.386	+ 0.298
$\rho(1.6\lambda_3)$	+ 0.381	+ 0.287

Note:  $\rho(1.6\lambda_i)$  indicates the value of the pressure correlation function at lag  $\xi_i = 1.6\lambda_i$  along the  $x_i$  axis ( $\lambda_1 = 0.25$  m vertically, and  $\lambda_2 = \lambda_3 = 1$  m horizontally).

the correlation scales of pressure in the vertical and horizontal directions are proportional to the soil parameter correlation scales. Thus, if  $\lambda_i^h$  designates the e-correlation scale of pressure (such that the correlation drops to  $e^{-1} \approx 0.37$ ), then we have from Table 7.3:

$$\lambda_i^h / \lambda_i \approx 1.6$$

$$\rightarrow \begin{cases} \lambda_i^h \approx 0.4\text{m vertically} \\ \lambda_i^h \approx 1.6\text{m horizontally} \end{cases}$$

These results seem to be confirmed in part by the behavior of the fluctuating pressure head along selected transects. Figure 7.25 displays the vertical pressure profile along the transect located at the center of the domain, and Figure 7.26 shows two perpendicular transects in the horizontal plane. The degree of variability of pressure along these transects seems to agree with the computed standard deviation (amplitude of oscillations about  $\pm 20$  cm around the local mean). However, the spatial pattern of pressure along these transects does not seem to quite agree with the computed correlation scales, 0.4 m in the vertical and 1.6 m in the horizontal. There are apparently some very long range fluctuations of pressure along the selected transects. More work is needed before definite conclusions can be drawn regarding the anisotropic correlation structure of the steady pressure field.

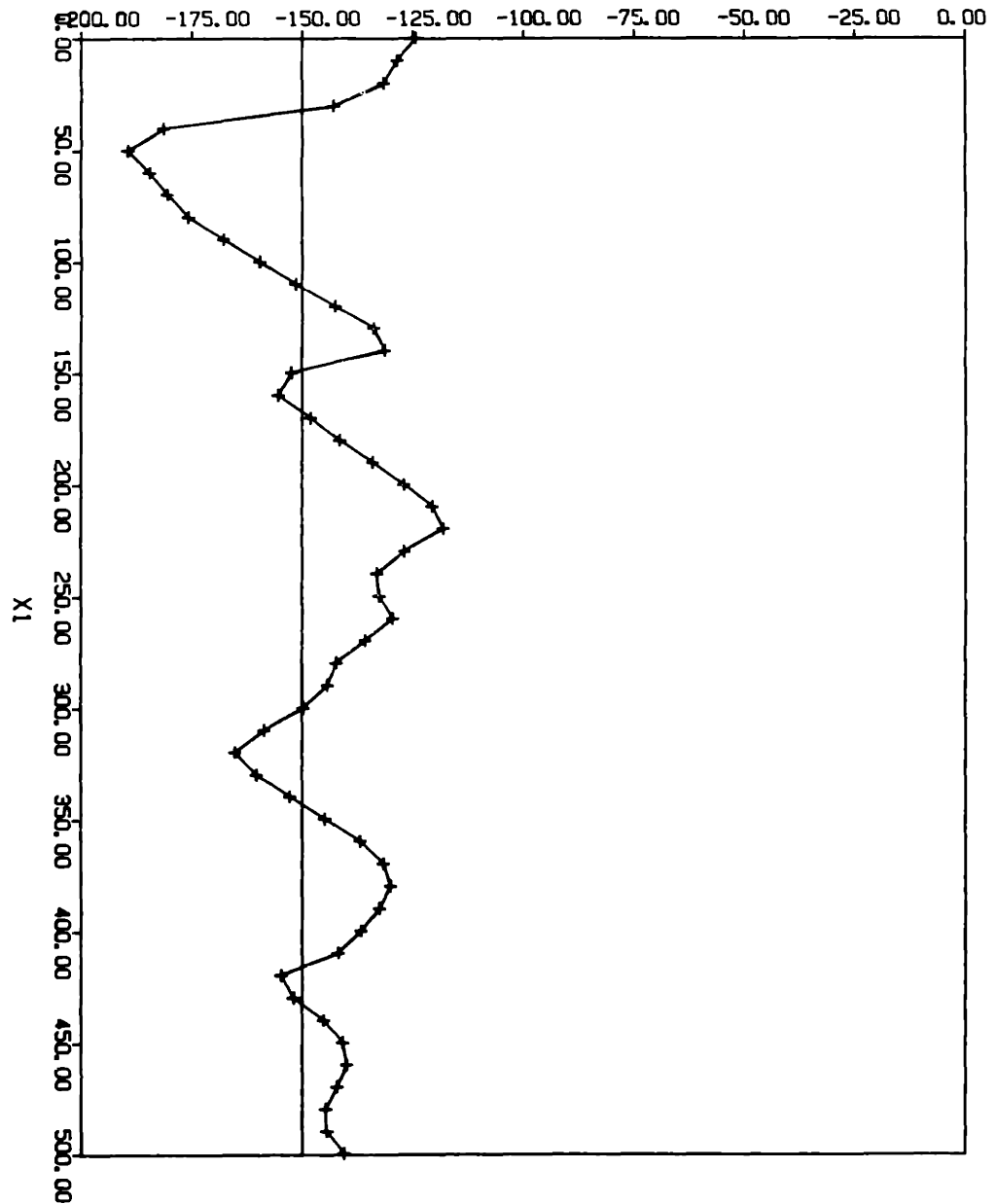


Figure 7.25 Pressure head profile in the vertical direction for the steady state "rainfall" infiltration simulation. The transect is located near the geometric center of the domain ( $X = 0$ ,  $Y = 7.4\text{m}$ ).

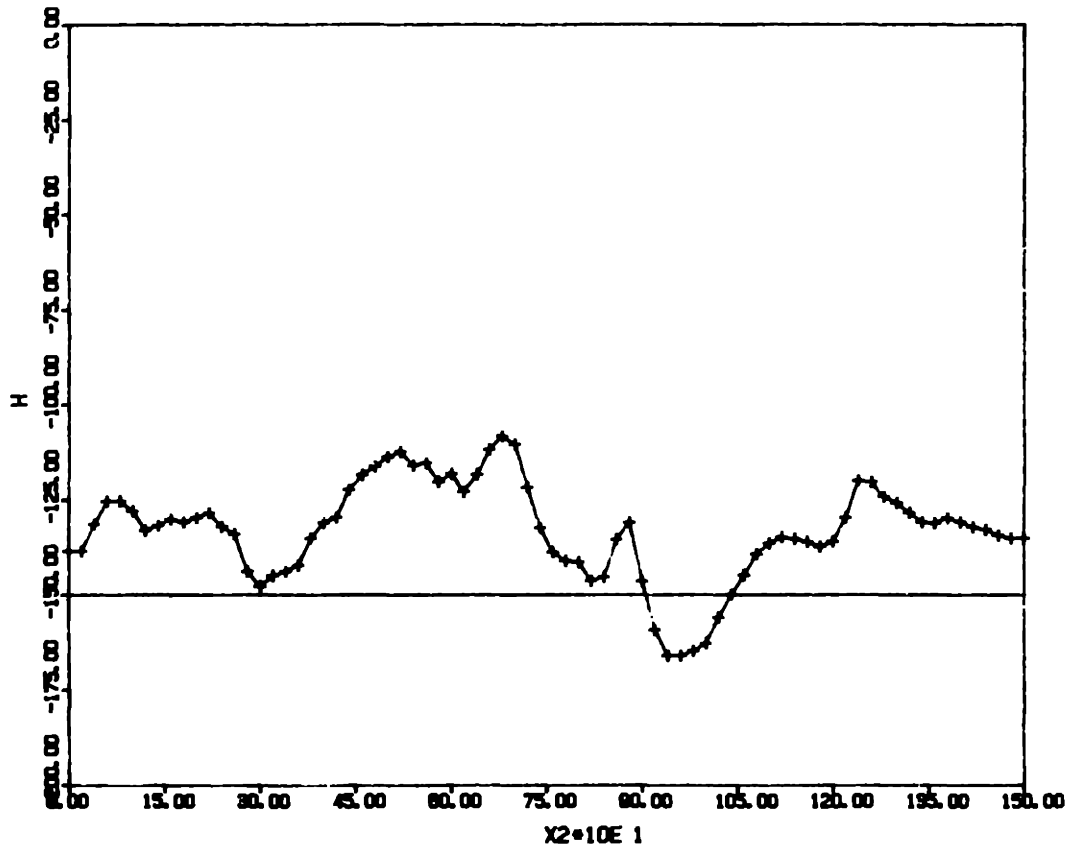


Figure 7.26 (a) Pressure head profile in the horizontal direction for the steady state "rainfall" infiltration simulation. The transect crosses the center of the domain and is oriented in the "transverse" direction ( $Y = 7.4\text{m}$ ,  $Z = 2.5\text{m}$ ).

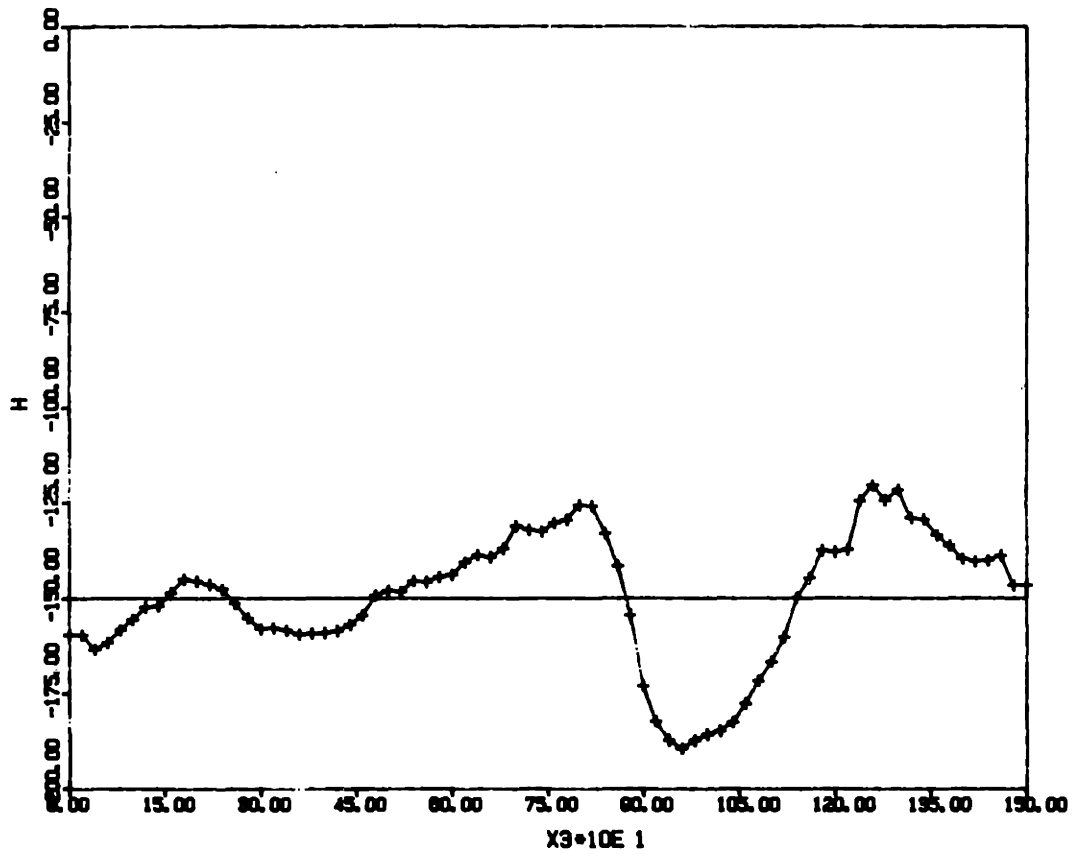


Figure 7.26 (b) Same as (a), for another horizontal transect crossing the center of the domain and oriented in the "longitudinal" direction ( $X=0$ ,  $Z=-2.5\text{m}$ ).

On the other hand, a preliminary estimate of the effective unsaturated conductivity in the vertical direction was obtained by assuming a zero mean pressure gradient vertically. Using a "large scale Darcy equation", this gives the simple equation:

$$\hat{K}_{1,1}(\bar{h}) = -\bar{q}_1.$$

The mean downward flux  $\bar{q}_1$  was evaluated by using the boundary flux calculations generated by the mass balance subroutine of the flow simulator ( $\bar{q}_1 = -0.059974$  cm/day). This eventually leads to an effective unsaturated conductivity of the form:

$$\hat{K}_{1,1}(\bar{h}) = 0.88 \cdot \bar{K}(\bar{h})$$

where the so-called "mean" unsaturated conductivity  $\bar{K}$  is the deterministic function:

$$\bar{K}(\bar{h}) = K_G \cdot \exp(\alpha_G \bar{h})$$

Now, Mantoglou and Gelhar (1987c) obtained the steady state effective conductivity as a solution of linearized spectral equations. In the case of independent  $(K_s, \alpha)$  parameters and extreme anisotropy ( $\epsilon = \lambda_1/\lambda \rightarrow 0$ ) they obtained a relation for  $\hat{K}_{1,1}(\bar{h})$  in the form of an expression that depends on soil

variability, multiplied by the deterministic conductivity  $\bar{K}(\bar{h})$  defined above. Using their equation (34.b) with  $J_1 = L_1 = 1$ , corresponding to a zero mean pressure gradient, we obtain the theoretical relation:

$$\hat{K}_{1,1}(\bar{h}) = \exp \left[ -\frac{1}{2} \cdot \frac{\sigma_f^2 + \sigma_\alpha^2 \cdot (\bar{h}^2 - 2\lambda_1 \bar{h})}{1 + \bar{\alpha}\lambda_1} \right] \cdot \bar{K}(\bar{h})$$

For the case at hand, the single-point moments of  $f = \ell_n K_s$  and  $a = \ell_n \alpha$  were given in Table 7.2 of the previous section (shown below for convenience):

$$\sigma_f = \sigma_{\ell_n K_s} = 0.6083; \quad K_G = 100 \text{ cm/d}$$

$$\sigma_a = \sigma_{\ell_n \alpha} = 0.2202; \quad \alpha_G = 0.0494 \text{ cm}^{-1}$$

By using also some previously established identities (equations 2.19-2.21 of Chapter 2) we obtain:

$$\sigma_\alpha = 0.01128 \text{ cm}^{-1}$$

$$\bar{\alpha} = 0.0506 \text{ cm}^{-1}$$

With  $\lambda_1 = 25 \text{ cm}$ , and  $\bar{h} = -147.5 \text{ cm}$  (after Table 7.3 just above), this gives the theoretical result:



$$\hat{K}_{1,1}(\bar{h}) = 0.62 \bar{K}(\bar{h})$$

Now, according to the previous numerical result, the coefficient 0.62 becomes 0.88. This can be regarded as a mild discrepancy between the theoretical and numerical effective conductivities, given the many assumptions that were made. In fact, we expected a theoretical value smaller than the numerical one, since we assumed  $\epsilon \rightarrow 0$  for the spectral solution (asymptotic case of perfectly stratified soils), whereas the numerical simulation was carried out for a finite anisotropy ratio  $\epsilon = 1/4$  (imperfectly stratified soil). The vertical conductivity must indeed be smallest in a perfectly stratified soil.

Similarly, the pressure head standard deviation ( $\sigma_h \simeq 20$  cm in Table 7.3) can be compared to the steady state spectral solution obtained by Mantoglou and Gelhar [1987b, equation (28)]:

$$\sigma_h = \frac{1}{\alpha} \cdot \left[ \frac{\bar{\alpha}\bar{\lambda}_1}{1+\bar{\alpha}\bar{\lambda}_1} \right]^{1/2} \cdot (\sigma_f^2 + \sigma_\alpha^2 \bar{h}^2)^{1/2}$$

With the data at hand, this gives the theoretical value:

$$\sigma_h = 26.2 \text{ cm.}$$

Again, this compares very well with the numerical result

$\sigma_h \approx 20$  cm; the slightly higher value of  $\sigma_h$  predicted by the theory could be due again to its asymptotic character (limit of perfectly stratified soil  $\epsilon \rightarrow 0$ , compared to  $\epsilon = 1/4$  in the numerical simulation).

We conclude that the numerical single-realization solution of steady state rainfall infiltration was large enough to be statistically meaningful as far as the single-point moments of the pressure field are concerned. Indeed, we presume that the relatively good agreement between the spectral theory and the single-realization statistics could not be purely coincidental (mean pressure gradient *and* mean flux, intervening in the effective conductivity, and standard deviation of pressure). However, there remains a gray zone concerning the correlation structure of the pressure field. The flow domain may have been too small, despite the large size of the grid (300,000 nodes), to accurately represent the spatial structure of pressure in free space. More work is needed here in order to evaluate the statistical representativity of the observed spatial structure of the pressure field ( $\lambda_i^h \approx 1.6 \lambda_i$ ?). Our results also showed that the probability distribution of tension head ( $\psi = -h$ ) was positively skewed; it seems likely that the skewness would increase with increasing variability and/or increasing mean tension head. This complication reflects the complexity of stochastic unsaturated flow systems due to highly nonlinear

coefficients.

### 7.5 Summary and Discussion:

It may be useful to summarize the main results of the different single-realization simulations of unsaturated flow systems presented in this Chapter. The modest size simulations of strip-source infiltration in statistically isotropic soils (section 7.2) were intended to explore the sensitivity of the solution to different hypotheses of conductivity variability. It was clear, from the three hypothesis tested, that the spatial variability of the wetted zone was extremely sensitive to the degree of variability of the slope  $\alpha$  of the log-conductivity curve  $\ln K(h)$ . In addition, the degree of correlation between  $\ln K_s$  and  $\ln \alpha$  also had an important effect. For early times of infiltration ( $t \approx 2$  days) it was found that the 3D wetted zone was sharply defined (steep wetting front), and was extremely heterogeneous and contorted in the case of statistically independent parameters  $K_s$  and  $\alpha$  (with  $\sigma_{\ln K_s} = 0.7$ , and  $\sigma_{\ln \alpha} = 0.3$ ).

These findings suggest that future research on large scale flow and solute transport in the vadose zone should focus on the development of practical methods and/or conceptual models for determining the spatial variability of the nonlinear

conductivity curve. For instance, it could be useful to search for possible correlations between the slope of  $\ln K(h)$  and other hydraulic soil parameters (saturated conductivity, pore size distribution, etc.) or by using certain similarity assumptions (relation between  $\theta(h)$  and  $K(h)$ ).

In the case of isotropic soils, reviewed just above, the heterogeneity of the wet zone was manifested by the appearance of mushroom-shaped bulbs that evolved more or less independently, at least until reconnection occurred. The spatial pattern of the wet zone for a statistically anisotropic, imperfectly layered soil was visually quite different, as shown in section 7.3. Indeed, the large single-realization solution obtained for 20 days of strip source infiltration and drainage (300,000 node simulation) exhibited pronounced lateral spreading of the edges of the wet zone. After a few days of infiltration, there appeared also several isolated wet regions of ellipsoidal shape. The vertical/horizontal aspect ratio of the marginally wet periphery of the unsaturated plume was much smaller than the aspect ratio of high moisture regions. This seemed to confirm the findings of Mantoglou and Gelhar (1987) concerning the pressure-dependent anisotropy of the effective conductivity for stochastic unsaturated flow systems.

Some other features of the heterogeneous flow system of section 7.3 seemed to be more specific to the particular boundary conditions and the geometry of the strip source, which were chosen to mimick an on-going field experiment. For instance, it appeared that the flow pattern beneath the center of the strip-source was fairly "one-dimensional" during the infiltration phase. The pattern of lateral diffusion around the free edge of the strip was also discussed. See subsection 7.3.2 for a detailed presentation of the 3D pressure field sampled at various locations of the 300,000 node grid during the 20 day simulation.

For applications to vadose zone contamination (say, resulting from the leak of a buried radioactive waste) it may be important to examine the possible effects of *anisotropy* over much larger time and length scales than those considered in our numerical simulations. The results obtained in section 7.3 suggest that the downward movement of the core of the unsaturated plume may continue to slow down indefinitely during the redistribution phase, while the marginally wet edges of the plume diffuse laterally and the mean moisture content of the plume decreases. This simplified "picture" may also indicate the possible behaviour of a contaminant carried in the unsaturated moisture plume. However, to simulate this type of phenomenon over three-dimensional length scales on the order of 100 m and time scales on the order of months or years may be too

prohibitive with the numerical single-realization approach adopted in this work, unless some new simplifying assumptions are adopted.

In addition, there is also the need for investigating the sensitivity of the wetting/drainage pattern with respect to initial conditions. In particular, the interpretation of our transient simulation results was somewhat obscured by the fact that a uniform pressure was prescribed initially. This simplifying assumption should be revised, as it ignores the past history of the heterogeneous flow system under natural conditions. Nevertheless, despite the limitations just discussed, the 20 day simulation of section 7.3 provided, for the first time, a detailed picture of a relatively large transient unsaturated flow system ( $5\text{m} \times 15\text{m} \times 15\text{m}$ ) with highly variable nonlinear soil properties (random curve  $K(h, \underline{x})$ ) and an unusually high grid resolution in 3D space ( $52 \times 76 \times 76 \simeq 300,000$  nodes). The results of this direct simulation could serve as a proving ground for future conceptual models.

In section 7.4, we showed more concretely how the single realization approach could be used to test current theories of spatially variable unsaturated flow. The statistically anisotropic soil of the previous section (7.3) was used to simulate a steady state infiltration under a uniform

constant flux at soil surface (uniform "rainfall"). The inherent statistical homogeneity of this type of infiltration problem justified our attempt at a direct statistical comparison with available spectral solutions (Mantoglou and Gelhar, 1987). The standard deviation of the pressure head and the effective unsaturated conductivity of the vertical infiltration system agreed with the spectral solutions within a margin of error of 20%.

This agreement is quite encouraging, but needs to be confirmed for a wider range of conditions, i.e., for other flow rates or mean pressure head values. Our results also suggested that the probability distribution of tension head ( $\psi = -h$ ) was positively skewed. If the hypothesis of a log-normal distribution of the tension head was retained, the skewness would increase rapidly with the coefficient of variation of tension head (equation 2.19 of Chapter 2), which itself is known to increase with mean tension (spectral theory of Mantoglou and Gelhar, 1987). Therefore, it is possible that, for very dry soils, a second order moment description of tension head variability will not be sufficient to completely characterize the actual distribution of tensions. A log transform could be used, but third order moments may eventually be required.

Finally, it should be emphasized that the correlation scales of the pressure head random field were found to be proportional to the  $\lambda_i$  scales of the random soil parameters ( $\lambda_i^h \simeq 1.6 \lambda_i$ ). However, this result may not be representative of truly "infinite domain" pressure fluctuations, given the limited size of the flow domain with respect to the computed pressure correlation scales (about  $10 \lambda_i^h$  in each direction). Note that the total CPU time required to solve this steady state problem on a Cray 2 machine was not overly prohibitive. In spite of the large 300,000 node grid, only 3 CPU hours were required to converge to a steady solution (in 85 time steps or 114 days of infiltration). It seems feasible to simulate such statistically homogeneous unsaturated flow systems over larger grids, on the order of 1 million nodes or more.

In conclusion, the application of the numerical single-realization approach to stochastic unsaturated flow problems provided a means of direct visualization of plausible heterogeneous pressure fields in three-dimensional space, with a degree of detail unattainable by current field measurement techniques. A few numerical experiments unveiled the complex nature of unsaturated flow systems. One of the most striking features of the transient strip-source infiltration problem was its great sensitivity to the degree of variability of the conductivity curve (particularly its slope  $\alpha$ ) and to statistical



anisotropy. The complex interactions between the homogeneous random field fluctuations of hydraulic properties and the evolving nonlinear wetting front (and drying front) seem to defy current stochastic analyses. However, the good agreement obtained between the linearized spectral theory and the numerical solution of steady state "rainfall" infiltration suggests that a simplified conceptual model like the spectral theory can provide reliable predictions of unsaturated flow variability in certain cases. The encouraging results obtained in the steady state case may possibly be extrapolated (confirmed) for transient flow systems after sufficiently large times and/or in the absence of sharp wetting fronts.

**CHAPTER 8: CONCLUSIONS**

A number of approaches were developed in this work for the characterization of three-dimensional flow fields in randomly heterogeneous porous media. For the most part, this problem was tackled under the assumption that naturally heterogeneous subsurface formations can be realistically modeled in the form of statistically homogeneous random functions of space. Our focus on a fully three-dimensional representation of subsurface flow phenomena was motivated by experimental as well as theoretical evidence on the artificial character of lower dimensional representations. Most of our results confirm indeed that, in the general case, fluid pathways are inherently three-dimensional in heterogeneous porous media. On the other hand, experimental evidence supporting the assumptions of randomness and statistical homogeneity of the hydraulic properties of natural porous formations was discussed in the data survey section of Chapter 2.

These assumptions were at the basis of most of the conceptual approaches pursued in this work. For instance, statistically homogeneous (and ergodic) random hydraulic properties were postulated in most of the analytical contributions of chapters 3 and 4, except in the spectral conditioning approach. In a certain sense, the postulate of a homogeneous/ergodic porous medium was also used for the numerical

simulations of single-realization flow fields in chapters 6 and 7. With this in mind, we now proceed to summarize and discuss the interrelated results obtained in different parts of this work, as well as some practical consequences in the area of subsurface hydrology. The discussion will be followed by a "summary of contributions", and a brief epilogue presenting a more general assessment of the outlook for stochastic approaches to subsurface flow and contaminant transport.

[a] Discussion of results:

One of the main motivations of this work was to assess the range of validity of the spectral solutions of stochastic subsurface flow developed by Gelhar and others during the past decade (Bakr et al. 1978; Gelhar and Axness 1983; Mantoglou and Gelhar 1987; Gelhar 1986). The spectral theory of stochastic flow (and mass transport) relies on the postulate of statistical homogeneity of the random flow field (hydraulic or pressure head perturbation, and water flux or velocity vector). In addition, this approach implicitly assumes the existence of ergodic solutions, since it purports to characterize unique "effective" transport properties for infinite-domain realizations of the flow field. Finally, the spectral solution method also requires small parameter expansions and various linearization approximations, in order to arrive at tractable closed-form solutions of the

governing stochastic partial differential equations. Let us point out that similar approximate expansions were also required in other analytical and numerical stochastic approaches published in the literature (see review in Chapter 2).

The existing "spectral theory" developed by the above-mentioned authors was expounded in detail in Chapter 3 for the case of stochastic groundwater flow. The approximate nature of the spectral solutions was made clearer by using  $\sigma$ -expansions, where  $\sigma$  is the standard deviation of the random log-conductivity field. The modern formalism of Fourier space representations of statistically homogeneous random fields was heavily used, and served as a background for subsequent developments. Some particular restrictions on the properties of the log-conductivity spectrum were discussed, in view of previous results obtained in the literature. In particular, we concluded that, in order to obtain a statistically homogeneous hydraulic head solution around its linear mean, the random conductivity field must be taken more nearly "periodic" as the degree of freedom of flow decreases, from fully three-dimensional and isotropic formations to the extreme case of one-dimensional flow, with all the conceivable intermediate cases corresponding to various configurations of stratified flow systems.

Furthermore, some new closed form results were inferred

by applying the spectral solution method to a variety of specific cases, in particular for horizontally stratified aquifers. Our findings regarding the correlation structure of the flow field led us to restrict the range of validity of the infinite-domain spectral solutions (aquifer thickness must be much larger than the horizontal fluctuation scales of the conductivity field). For stratified aquifers, the hydraulic head field was found to be nearly isotropic in vertical planes, and only moderately anisotropic in horizontal planes. An approximate analysis also suggested that the flux or velocity vector was much more strongly anisotropic in 3D space than the head field. These previously unknown results were confirmed in part by subsequent numerical experiments.

However, we recognize that more work will be needed in order to fully characterize the correlation structure of the velocity field in the case of stastically anisotropic aquifers. This may have important consequences regarding the validity of two-dimensional representations of groundwater flow and transport phenomena commonly used in engineering practice. In addition, we expect that stringent grid resolution constraints will be required for the numerical simulation of strongly anisotropic flow systems due to the disparity of fluctuation scales involved. Moreover, note that the analytical results just discussed were obtained within the framework of the spectral theory, based on

"small parameter" approximations, and on the assumption of statistical homogeneity of the input conductivity and the output flow field.

In contrast, we have developed in Chapter 4 new stochastic solutions of the groundwater flow equation without some of the limiting assumptions of the spectral theory (see discussion in section 4.1). Thus, the "small parameter" approximation was dropped altogether in section 4.2, devoted to the development of non-perturbative spectral solutions. In addition, we obtained in section 4.3 an "improved" spectral solution for the groundwater velocity spectrum, by linearizing the equations for the velocity components rather than that for head. Finally, the assumptions of infinite domain and statistical homogeneity of the flow field were abandoned in section 4.4, where a new "spectral conditioning" approach was developed to treat the case of finite size flow and transport phenomena. It may be worthwhile to recapitulate here on some of the main results obtained by these alternative spectral approaches.

The non-perturbative spectral relations obtained in section 4.2 were derived from fundamental statistical symmetries and other "exact" properties of the flow field in the case of statistically isotropic and homogeneous random conductivity. In

the 3D case, mass conservation and statistical axial symmetry were used to infer relations on the covariance or spectral structure of the flow field. A special conjugacy relation was found in the 2D case, leading to a statistical identity relating the head gradient and velocity fields. It was found that the previous first order spectral solutions (e.g. Gelhar and Axness, 1983) were consistent with these statistical identities in any number of dimensions (for isotropic media). However, a close inspection of the first order spectral solutions also revealed that the degree of variability of groundwater velocity was probably underestimated in the 3D case. A new, presumably "improved" spectral approximation, was developed in Section 4.3 for arbitrary conductivity spectrum. The new spectral solution, although not exact, turned out to agree better with subsequent numerical results, and was also consistent with the previous non-perturbative spectral relations for 3D isotropic media. Some of the implications of these results will be discussed shortly.

In the general case of statistically anisotropic aquifers, exact statistical identities of the type mentioned just above were not obtained, due to the lack of symmetry of the flow pattern. In any case, recall our previous finding that the infinite-domain spectral theory may not be directly applicable to shallow aquifers unless their thickness is much greater than the horizontal fluctuation scales of natural heterogeneities. Some

of the numerical experiments, to be discussed later in this chapter, suggested indeed that the aquifer thickness must be on the order of several tens of horizontal fluctuation scales for the spectral theory to be applicable. When this is the case, the spectral results of Gelhar and Axness (1983) can be used to infer the effective conductivity of the groundwater flow system at the large scale. These authors showed in particular that, as a first order approximation in  $\sigma$ , the effective conductivity is a second rank symmetric tensor whose degree of anisotropy depends (in a seemingly complex position) on the variance and statistical anisotropy of the underlying random conductivity field. Their result takes the form of complicated Fourier integrals, although some simplifications occur in asymptotic cases of perfect stratification (infinitely small or infinitely large anisotropy ratio) and in the isotropic case (anisotropy ratio equal to unity).

In contrast, we proposed in this work a simple analytical expression for the effective conductivity in the general anisotropic case, based on an empirical generalization of a previous conjecture by Matheron (1967). This author observed that, for isotropic formations, the effective conductivity seems to depend in a simple fashion on spatial dimension. Our generalization by way of induction, led to an expression relating the effective conductivity component  $K_{11}$  to the log-conductivity



variance  $\sigma^2$ , the correlation scale  $\lambda_1$ , and the geometric and arithmetic averages of the three correlation scales ( $\lambda_1, \lambda_2, \lambda_3$ ), as shown in equations (4.48-4.49) of Chapter 4, section 4.2.6. For illustration, let us use an example taken from a field contamination study discussed in Gelhar (1986). The three correlation scales, in the same order as above, were 60 m and 15 m (horizontal) and 1 m (vertical), and the log-conductivity variance was 4.2. By using the Gelhar-Axness formula, Gelhar (1986) was able to evaluate the anisotropy ratios of the effective conductivity (horizontal/vertical:  $K_{11}/K_{33}$ ; horizontal/horizontal:  $K_{11}/K_{22}$ ). His values were 47 and 1.3, respectively. By using instead the simple relation proposed in his work, the conductivity anisotropy ratios are found to be 45 and 1.2, very close to the values predicted by the Gelhar-Axness first order spectral theory. The proposed relation also coincides with the effective conductivity result of Bakr et al. (1978) in the 3D isotropic case. In addition, this relation coincides with all results known to be exact, such as the arithmetic and harmonic means for flow parallel and orthogonal to perfect stratification, and the geometric mean for two-dimensional isotropic media).

Some of the new analytical results established in this work may have direct implications for the study of solute transport in randomly heterogeneous groundwater flow systems. If

molecular diffusivity is neglected, the pathways of nonreactive solutes convected in the flow are the same as those of tagged fluid particles. Therefore, the variability and spatial structure of the groundwater velocity field determine entirely the overall transport properties of the flow, like "macrodispersivity". Furthermore, assuming for convenience that the porosity of the aquifer is approximately constant, the groundwater velocity is simply proportional to the Darcy flux. The two vector fields, velocity and flux, are therefore equivalent if one ignores the constant of proportionality. With this in mind, let us examine more specifically some of the consequences of our analytical results in the area of groundwater solute transport.

Approximate spectral solutions of stochastic groundwater solute transport were developed by Gelhar and Axness (1983) and others. Subsequently, Gelhar (1987) pointed out that the asymptotic or "large time" longitudinal macrodispersivity ( $A_{11}$ ) was proportional to the correlation scale of the longitudinal velocity component in the longitudinal direction. The factor of proportionality was the longitudinal velocity variance divided by the square of the mean velocity. By plugging in this relation the Gelhar-Axness spectral solutions of stochastic groundwater flow, one obtains a simple closed form expression for  $A_{11}$  in the 3D isotropic case. Surprisingly, it

turns out that the resulting macrodispersivity has a maximum at some moderate value of the log-conductivity variance ( $\sigma^2 = 3$ ) and tends to zero as  $\sigma$  goes to infinity. Now, this seemingly unphysical behavior disappears when the "improved" velocity spectrum proposed in this work (section 4.3) is used instead of the Gelhar-Axness spectrum. For 3D isotropic formations in particular, the large time macrodispersivity obtained with the higher order solution takes the simple form  $A_{1,1} = \sigma^2\lambda$ , where  $\lambda$  is the integral correlation scale of the isotropic log-conductivity field.

It is particularly instructive to note that the product of  $\sigma^2\lambda$  is invariant under local averaging of the underlying conductivity field. Thus, Vanmarcke (1983) observed that the product "variance-correlation scale" quantifies the intrinsic amount of uncertainty carried by a homogeneous random field, independently of the scale of measurement. Our result concerning macrodispersivity suggests a parallel interpretation. The large time longitudinal macrodispersivity of a solute, convected over infinite distances in a statistically homogeneous groundwater velocity field, quantifies in effect the intrinsic variability of the porous formation independently of the scale at which this variability is "measured".

However, it should be emphasized that these results on

contaminant macrodispersion rely on quite stringent hypotheses: the large time and infinite domain assumptions, the postulate of a statistically homogeneous porous formation, and the first order perturbation approximations of the solute transport equation. Intuitively, the "large time" assumption means that the contaminant plume must have encountered a large number of conductivity fluctuations or formation heterogeneities. Assuming that the formation is statistically homogeneous, this becomes equivalent to requiring that the size of the plume or the mean travel distance ( $L$ ) be much larger than the formation's correlation length ( $\lambda$ ). In actual practice however, there may not exist a uniquely defined correlation length valid for a sufficiently large range of plume sizes or travel distances. It is this particular problem that was addressed in section 4.4 of Chapter 4 (Finite size effects: band-pass self-similar spectra, spectral conditioning and uncertainty).

The "spectral conditioning" approach was developed in order to characterize finite-size and evolving phenomena in stochastic flow and transport problems. This approach avoids the elusive concepts of correlation scales, infinite domains, and statistical homogeneity, while still retaining some of the analytical simplicity of the spectral solution method. By applying first the standard spectral solution method in conjunction with a band-pass self-similar model of

random field heterogeneity, based on data published in the literature, we evaluated explicitly the dependence of statistical properties on domain size (1- and 3-dimensional head variance, effective conductivity, and macrodispersivity). This motivated further development of the spectral conditioning approach for a consistent characterization of the effects of domain size on the mean, variance, and effective conductivity of the flow field. In particular, the uncertainty on these parameters was shown to be directly related to domain size, i.e. to the typical length scale of the phenomenon of interest. Although closed form solutions were limited to the case of one-dimensional flow, it seems that a similar spectral conditioning approach could be developed in order to quantify the effective transport coefficients and the uncertainty of evolving contaminant plumes in three-dimensional groundwater flow systems. Some of our preliminary results suggest that, for statistically isotropic 3D formations, both the macrodispersivity and the effective conductivity will grow with plume size, while the uncertainty on these coefficients will decrease (at least up to a certain cut-off scale many times larger than the largest size of geological heterogeneities). With some further refinements, it seems that this approach could provide an analytically tractable model of the process of evolving macrodispersion with only minimal assumptions on the random nature of the underlying porous formation.

Much of the remaining part of this work was devoted to the development and application of a *numerical approach* to saturated as well as unsaturated stochastic flow, under the postulate of statistically homogeneous random field properties of the porous medium. The proposed approach required solving numerically the governing flow equation for a single realization of random field properties in a large but finite domain, with approximate boundary conditions. Observe that no assumption whatsoever was made on the nature of the flow at the solution stage. The motivation behind this numerical "single-realization" approach was two-fold. First of all, our expectation was that the single-realization flow fields obtained numerically could be statistically analyzed by using standard detrending and spatial averaging methods under some weak assumptions of statistical homogeneity (section 6.1 of Chapter 6). In this way, the numerical simulations could be compared directly to available spectral results (second order moments of the flow field, and effective conductivity) like the Gelhar-Axness groundwater flow spectral solutions and the *unsaturated flow* spectral solutions of Mantoglou and Gelhar (1987). Moreover, because the single-realization method does not entail any a priori assumptions concerning the random nature of the simulated flow field, it lends itself naturally to an empirical evaluation of the validity of the homogeneity/ergodicity assumptions of the spectral theory. As will be seen, these assumptions may not be

justified in certain cases, but the single-realization approach can still be used as a means of obtaining, by way of direct numerical solution, a plausible realization of the detailed flow pattern in a typical heterogeneous or random porous formation.

To be successful, the proposed numerical approach must obviously take into account the specific numerical issues associated with the discrete solution of highly variable, random-like flow equations on large three-dimensional grids with fine mesh resolution. The saturated/unsaturated flow simulator developed and tested in Chapter 5 was designed specifically for that purpose ("Bigflo" code). An efficient finite difference system solver (the "strongly implicit procedure" or SIP method) was used to solve the saturated (linear) as well as unsaturated (nonlinear) flow equations, for large realizations of random hydraulic coefficients on three-dimensional grids as large as one million nodes. The largest simulations of Chapter 6 (saturated flow) and Chapter 7 (unsaturated flow) required the use of the Cray 2 supercomputer, with typical CPU times of a few hours per simulation. However, a number of meaningful "medium size" simulations were also obtained on a Microvax 2 minicomputer.

Typically, a "medium size" numerical problem in this work could involve a grid size of tens of thousands of nodes for unsaturated flow, and up to two hundred thousand nodes for steady

saturated flow. The largest numerical problems involved grid sizes of several hundred thousand nodes for unsaturated flow, and one million nodes for saturated flow. To obtain meaningful numerical solutions for such large random flow problems required a certain amount of numerical analysis and experimentation, the results of which are now being discussed. However, the reader is referred to Chapter 5 for details. See in particular Appendix 5D for an abstract of the "Bigflo" simulator used to generate all the numerical solutions analyzed in this work.

One important new result of numerical analysis concerned the question of consistency and accuracy of finite difference approximations of stochastic partial differential equations. This theoretical problem was tackled by developing a spectral method of truncation error analysis, leading to closed form expressions for the root-mean-square finite difference error in the case of stochastic groundwater flow with a statistically isotropic three-dimensional random conductivity field. More precisely, the Fourier-space spectrum of the stochastic error (difference between the discrete solution and the exact solution of the continuous equation) was explicitly evaluated - at least to the leading order of a double expansion in terms of the mesh size ( $\Delta x$ ) and log-conductivity standard deviation ( $\sigma$ ). The relative root-mean-square error was defined as the ratio of standard deviations of the error to that of the variable itself



(the variables of interest were the hydraulic head and the flux vector). It was found that the relative error was in general proportional to a fractional power ( $p$ ) of the mesh resolution ratio ( $\Delta x/\lambda$ ), where  $\lambda$  is some fluctuation scale or correlation scale of the conductivity field. The exponent  $p$  defines the order of accuracy of the finite difference scheme in a mean-square sense.

For the hydraulic head, the order of accuracy was 2 for a "smooth" log-conductivity field but dropped to 3/2 for a "noisy" log-conductivity field (respectively Hole-Gaussian and Markov three-dimensional spectra). For the flux or groundwater velocity vector, the order of accuracy was 1 in the "smooth" case, and only 1/2 in the "noisy" case. These previously unknown results show that the seven point centered finite difference scheme yields a consistent approximation of the exact hydraulic head and flux vector for a wide range of random log-conductivity fields, including the case of the "noisy" three-dimensional Markov field (non-differentiable in the mean-square sense). The specific results obtained for the isotropic Markov field indicated that a good accuracy on the hydraulic head, and a reasonable accuracy on the flux vector, could be obtained with a statistical grid resolution ( $\Delta x/\lambda$ ) on the order of 1/3. Note however that these results may hold only for moderate conductivity variability (presumably for  $\sigma$  not much greater than

unity). These indications were used in Chapter 6 to design the numerical simulations of stochastic groundwater flow, and to evaluate confidence intervals on the numerical solutions for comparison with the results of the spectral theory.

In addition, we also developed in Chapter 5 a particularly cautious approach for estimating the error due to the approximate iterative solution of the finite difference system (SIP solver, based on approximate factorization of the coefficient matrix and Picard iterations). Thus, we used standard results of linear algebra to show that the Euclidian norm of the residual error may significantly underestimate the true root-mean-square solution error, particularly in cases of slow convergence. An approximate upper bound on the true error was evaluated in terms of the residual error and mean convergence rate of the iterative solver. Numerical experiments for steady state stochastic groundwater flow (similar to a "random heat equation") were conducted for values of  $\sigma$  up to 2.3 and grid sizes on the order of 100,000 to 1 million nodes, using a Cray 2 machine for the largest problems. Briefly, these experiments indicated that the convergence rate of the SIP solver was roughly proportional to the unidirectional size of the grid, a number presumably related to the square-root of the condition number of the random conductivity matrix. For the degree of variability and the problem sizes investigated, it was concluded that the

matrix system could be solved with 1% relative accuracy on the hydraulic head with a few hundred to a thousand underrelaxed iterations.

Overall, these results of truncation error analysis and iterative solver convergence lead us to believe that the stochastic groundwater flow simulations presented in Chapter 6 were generally quite accurate, particularly concerning the largest simulations with statistically isotropic conductivity (1 million nodes, with grid resolution  $1/3$ ). Likewise, the "turning band method" used to generate discrete realizations of random conductivities seemed adequate, since the spatial statistics of large conductivity realizations appeared to be very close to the prescribed ensemble statistics. These indications appear quite useful in view of the fact that there is no known *exact* solution to the stochastic groundwater flow equation.

Some aspects of the numerical/statistical methodology adopted in this work could be quite useful in other contexts. For example, our numerical approach and results on stochastic groundwater flow could be extended to other physical problems involving random conduction phenomena (thermal and electrical conduction in composite materials, and random resistance networks). In addition, our spectral analysis of stochastic truncation errors could perhaps be extended to other

discretization methods (weighted residuals and pseudo-spectral) and to other stochastic equations (convection-diffusion in random media). This may be particularly important for assessing the feasibility of direct numerical simulations of solute transport in random porous media.

Other numerical contributions of this work concerned the numerical solution of randomly heterogeneous unsaturated flow systems, involving highly nonlinear and spatially variable hydraulic coefficients. In the transient case, a fully implicit time discretization scheme was used. The method used to solve the resulting nonlinear finite difference system was basically the same as for linear flow problems, however with an additional outer Picard iteration loop to sequentially linearize the system (nonlinear SIP solver). A heuristic stability analysis of the nonlinear finite difference equations suggested that a severe constraint on the time step ( $\Delta t/\Delta x^2$ ) may be required, unless a grid Peclet number condition be satisfied at each node of the grid ( $\alpha\Delta x_1 \leq 2$ , where  $\alpha$  is the slope of the unsaturated log-conductivity function of pressure, and  $\Delta x_1$  the vertical mesh size). However, any truly rigorous statements on numerical requirements were precluded by the complexity of the spatially variable unsaturated flow equation.

In view of these difficulties, the problem solving

capabilities of the transient unsaturated flow simulator were tested in an empirical fashion by way of numerical experimentation (comparisons with analytical solutions, mass balance checks, and other tests). In the process, some instructive observations were made on the physics of two-dimensional strip source infiltration in uniformly stratified soils with horizontal or vertical layers (cf. last section of Chapter 5). More importantly, some truly large simulations of three-dimensional infiltration in "random soils" were analyzed at length, in Chapter 7.

From a numerical viewpoint, the most difficult random infiltration problem was the case of transient strip source infiltration in a statistically stratified soil, with a different unsaturated conductivity curve defined at each mesh point of the 300,000 node grid in three-dimensional space. It may be of interest here to recall some of the details of this numerical experiment (see Chapter 7). About 5 CPU hours of Cray 2 time were consumed in the simulation of 10 days of infiltration and 10 subsequent days of drainage in a moderately dry soil, with initially small but increasing time step size. The exact size of the time step at initial time and at a few intermediate times, was set empirically by trial and error, although an automatic adjustment was also made by the code during simulation. Overall, our experience with this numerical experiments indicates that a

very severe constraint on the time step could be required for convergence of the nonlinear iterations in the case of dry soils. In the case at hand, the initial degree of saturation was only moderately low, about 20%.

Thus, it may be questioned whether a fully implicit finite difference method such as used in this work is truly adapted to the simulation of extremely sharp infiltration fronts in "air dry" soils, particularly in the presence of random heterogeneities. On the other hand, the extreme nonlinearity of the exponential conductivity-pressure relation assumed in this work may also be called into question. In any case, it should be kept in mind that, in spite of these difficulties, the flow code was efficient enough to simulate some rather large and highly heterogeneous unsaturated flow systems, with grid sizes on the order of tens of thousands of nodes (Microvax 2) to several hundred thousand nodes (Cray 2)... in reasonable amounts of CPU time. Some of the most important results of stochastic flow simulations will now be discussed, both for saturated and unsaturated flow.

The large high-resolution simulations of stochastic groundwater flow and unsaturated flow in random media were thoroughly analyzed and discussed in Chapter 6 and Chapter 7, respectively. Each of these chapters included a "summary and

discussion" section, of which some essential points are recalled here. Starting with the case of groundwater flow in statistically isotropic aquifers, it should be emphasized that a remarkably good agreement was found between the single-realization simulations and the spectral solutions, particularly concerning the effective conductivity and the head variance. For the latter quantities, the agreement between simulations and theory was quite good up to large conductivity variability ( $\sigma = 2.3$ , where  $\sigma$  is the standard deviation of  $\ln K$ ). However, the single-realization head variance was computed about a slightly nonlinear trend of hydraulic head in the mean flow direction, in contrast with the linear mean head assumed by the first order spectral theory. There was some evidence that the discrepancy in the mean head was due to the "modest size" of the flow domain relative to the large correlation range of the hydraulic head. As a consequence, the computed head correlations were systematically smaller than the theoretical ones, although there was a broad agreement concerning the three-dimensional structure of the head field. On the other hand, a similar but more pronounced discrepancy was observed in two cases involving statistically anisotropic conductivities ("shallow" and "deep" stratified aquifers). In the case of a shallow stratified aquifer, the spatial structure of the simulated head field did not agree with the infinite domain spectral result. This confirms our previous discussion

concerning potential restrictions on the range of applicability of the spectral theory.

With these results in mind, it might be useful at this point to discuss some implications for practical issues like the solution of inverse flow problems, or other questions where the spatial structure of the hydraulic head field (measured or predicted) may intervene. Broadly speaking, our numerical results indicate that the spectral theory is essentially correct for the head variance, and to a lesser degree the head correlation structure, provided that the effects of large scale inhomogeneities be removed by empirical detrending of measured hydraulic heads. In actual practice, statistical inhomogeneity can be equated to the nonlinearity of the observed mean head field. We expect that the head covariance function predicted by the spectral theory be relatively accurate when this nonlinearity is mild. In the case of shallow aquifers however, the predicted head covariance function may not be realistic if aquifer thickness is on the order of ten horizontal correlation scales or less. These indications may be particularly useful for the solution of inverse flow problems, where prior knowledge of the cross-correlation between heads and log-conductivities will be required.

The case of statistically anisotropic log-conductivity



fields is important for applications, as most natural geological formations appear to be stratified. In the case of horizontal stratification, the theoretical (spectral) results obtained in Chapter 3 suggested that the groundwater velocity vector was strongly anisotropic in proportion with the degree of anisotropy of the porous formation. However, recall that the hydraulic head appears to be only mildly anisotropic, independent of the formation's anisotropy (from theoretical and simulation results). Thus, it can be inferred that the hydraulic head carries little information about the covariance structure of groundwater velocities, which ultimately determines the fate of contaminants (dispersion). Now, since detailed measurements of groundwater velocities are rarely feasible in practice, it seems particularly important to ascertain the validity of the spectral results concerning the correlation structure of the flux or velocity field. This question remains open in the case of stratified aquifers; however, encouraging results were obtained in the special case of statistically isotropic aquifers as explained below.

In the case of statistically isotropic aquifers, the groundwater velocity correlation functions (tensor) obtained numerically agreed very closely with the spectral results of Gelhar and Axness (1983) for moderate log-conductivity variability ( $\sigma = 1$ ), and were still in reasonable agreement for

higher variability (up to  $\sigma = 2.3$ ). However, the Gelhar-Axness solutions appeared to underestimate the velocity variances, especially for high variability ( $\sigma > 1$ ). The discrepancy was milder for the "improved" velocity spectrum proposed in this work, although still significant. The numerical values obtained for the velocity variances suggested that the high order terms neglected in the standard and "improved" spectral solutions grow exponentially with the log-conductivity variance. Equations 6.13 give empirical expressions fitted to the numerical velocity variances. Finally, a visual inspection of the numerical velocity vector field also revealed that the longitudinal component had a positively skewed probability distribution, possibly close to a lognormal distribution.

These findings should motivate future research towards a higher order characterization of the random groundwater velocity field, as this may have consequences for stochastic solute transport. Our finding that the first order spectral solutions underestimate the velocity variance with respect to numerical solutions, also imply that contaminant macrodispersivity (over large time scale) will be higher than predicted by the spectral theory. Admittedly, more work is needed in order to assess more precisely the accuracy of our numerical evaluation of the variances of groundwater velocity. The effect of numerical noise was taken into account in our

comparisons of numerical/spectral solutions by using the previous results of truncation error analysis. It seems also important to evaluate the possible effects of the shape of the input log-conductivity (a Markov spectrum was used in the case at hand). The influence of the log-conductivity spectrum on stochastic flow and transport solutions was discussed in section 3.2 of Chapter 3 ("infrared" and "ultraviolet" divergences of Fourier integrals). At any rate, the simulation results of Chapter 6, section 6.3, clearly show that the "improved" spectral theory provides a reasonably accurate approximation of the groundwater velocity covariance for a wide range of conductivity variability, at least for the specific case of an isotropic Markov log-conductivity field with exponential covariance.

Overall, we may conclude that the single-realization approach to stochastic groundwater flow led to statistical results similar to those obtained by the infinite-domain spectral theory, at least for a choice of domain size and boundary conditions that guaranteed the approximate statistical homogeneity of second order moments of the flow field (after empirical detrending). This encouraging result seems to confirm the operational character of the homogeneity/ergodicity hypothesis on which the spectral theory depends, at least for steady state groundwater flow in sufficiently deep aquifers and

approximately constant "regional" hydraulic gradient. On the other hand, the limitations of the homogeneity/ergodicity hypothesis appeared to be much more severe in the case of complex nonlinear flow systems, such as infiltration in randomly heterogeneous unsaturated soils (Chapter 7). The numerical single-realization solutions of infiltration are now being discussed.

In the case of transient infiltration from localized (strip) source in moderately dry random soils, it seemed quite obvious that no large three-dimensional flow region of approximate statistical homogeneity developed during the time scales of simulations (on the order of days or weeks). Nevertheless, visual inspection of the time-dependent three-dimensional pressure fields revealed some global features of evolving unsaturated plumes in heterogeneous soils. It was observed that maximum variability of the pressure field occurred when the level and the slope of the unsaturated log-conductivity curve were both random and statistically independent. In the case of statistically isotropic soil, the shape of the wetted zone at early times of strip-source infiltration appeared to be extremely contorted in 3D space, but with little lateral spreading. On the other hand, there was a pronounced lateral spreading away from the strip source in the case of statistically stratified soils (vertical/horizontal anisotropy ratio equal to

1/4). Based on the spatial pattern of pressure contours observed during infiltration and drainage, the anisotropy of the flow field appeared to be pressure-dependent, with a more pronounced lateral spreading of the edges of the moisture plume (marginally wet) than inside the core of the plume (wet). This is qualitatively similar to the behavior predicted by Mantoglou and Gelhar (1987) based on their linearized spectral solutions of transient unsaturated flow (the anisotropy of the wetting effective conductivity is more pronounced in dry regions than in wet regions).

In spite of the large size of the grid (300,000 nodes) it seemed preposterous to attempt a quantitative statistical analysis of the above strip-source experiment, as the unsaturated plume remained too small to sample a sufficiently large "spectrum" of soil heterogeneities. Indeed, some of the features of the simulated moisture pattern seemed to be specifically related to the idiosyncracies of the heterogeneous environment (the particular random field realization of hydraulic parameters) and to boundary and initial conditions (strip width, input flux and initial pressure head). In view of these limitations, it may be useful to examine from a more general point of view the possibility of obtaining statistically meaningful realizations of transient unsaturated flow in typical situations.

The case of the accidental spill of a radioactive liquid at the Hanford site can be used here for illustration (see Chapter 1, and the report by Rouston et al. 1979 for details). As a first approximation - although admittedly a crude one - let us assume that the contaminant plume can be equated to the unsaturated plume. The source located near soil surface, can be assimilated to a disc with a diameter of a few meters. Due to the axi-symmetry of the source, we expect that the moisture or contamination pattern be more nearly statistically homogeneous tangentially around the axis of the source than along any other direction ("axi-symmetric homogeneity"). Finally, note that the time and length scales of interest could be a few decades and several tens or hundreds of meters, or perhaps much more. In comparison, the natural fluctuation scales of the formation heterogeneities could be on the order of a fraction of a meter or perhaps several meters.

The key question is whether the statistical properties of the three-dimensional unsaturated plume (real or simulated) will converge to some stable quantities as time goes on. Unfortunately, it seems clear from our example that a direct numerical simulation similar to the highly detailed simulations of strip source infiltration obtained in this work, will be extraordinarily prohibitive given the time and length scales of interest: perhaps tens of millions of mesh points, and hundreds

of hours of supercomputer time on a Cray 2 machine). Thus our hypothetical example leads us to conclude that some of the features of the current single realization approach may have to be altered before a meaningful and accurate characterization of evolving unsaturated plumes can be achieved for the very large time and length scales of interest. Essentially the same remarks apply to the similar problem of evolving contaminant plumes in groundwaters. To our knowledge, there exists at present no satisfactory simulation (high resolution -- large time scale) of these types of phenomena that could be used for testing existing analytical theories.

On the other hand, in the case of a steady state unsaturated flow ("rainfall" infiltration), we have found a relatively good agreement between numerical results and the linearized spectral solutions of Mantoglou and Gelhar (1987) and Yeh et al. (1985). The steady state pressure field obtained for a statistically anisotropic soil was analyzed by the same spatial averaging method used in groundwater flow simulations, assuming a statistically homogeneous random field of pressure in all three space directions. The pressure head standard deviation and the vertical component of the effective unsaturated conductivity were both within 20% of the theoretical spectral solutions. This encouraging result is of interest for applications involving toxic wastes buried in dry formations characterized by a very

slow (downward?) flow of water, as in the hypothetical scenario discussed by Winograd (1981). In such cases, the simulated unsaturated water velocity field, if obtained on sufficiently large high-resolution grid, could be used to simulate the transport of a radioactive solute leaking from the buried source. Note that the present "rainfall" infiltration experiment on a 300,000 node grid involved a relatively "modest" domain size (5m x 15m x 15m) and a relatively high downward flux (213 mm/year) compared to only 2 mm/year at the Yucca Flat site in Nevada (approximate evaluation by Winograd, 1981). The time scale of interest for contaminant transport could be thousands of years or more.

It remains to be seen whether detailed simulations of very large steady state unsaturated flow fields in extremely dry heterogeneous formations can be obtained at reasonable costs with the present version of our unsaturated flow simulator. At any rate, the present results strongly suggest that the linearized spectral solutions of Mantoglou and Gelhar (1987) may provide an adequate characterization of pressure variability and effective conductivity in such cases. This is in contrast with the case of transient infiltration/drainage from localized sources, where the question of the validity of the homogeneity/ergodicity postulate remains open.



[b] Summary of contributions

It may be useful at this point to recapitulate in a compact form the main findings of this work, with a highlight on new approaches and results. For convenience, we follow the order of exposition adopted in this report; analytical results of Chapters 3 and 4, numerical analyses of Chapter 5, and statistical analyses and interpretation of single-realization simulations in Chapters 6 and 7. A header is used to indicate the nature of the results being summarized (analytical results, numerical analysis, simulation results):

*Analytical Results:* Explicit characterization of the stochastic hydraulic head and groundwater velocity fields by using the spectral solution method of Gelhar and Axness (1983) in the case of statistically stratified aquifers: new results concerning the statistical anisotropy of the flow field and the applicability of the theory for finite-thickness aquifers.

*Analytical Results:* Non-perturbative spectral relations for stochastic groundwater flow in statistically isotropic formulations. Test of first order spectral solutions: they satisfy all the non-perturbative

spectral relations between the flux and head spectra in 1,2,3 dimensions. In particular, an equation relating the flux and head spectra is shown to be "exact" in the 2D case.

*Analytical Result:* New closed form expression for the effective conductivity of stochastic groundwater flow systems in the general case of 3D statistical anisotropy. This conjectural expression fits most of previously established results (Matheron 1967; Gelhar and Axness 1983), including those known to be exact.

*Analytical Result:* "Improved" spectral approximation for the groundwater velocity spectrum based on a system of equations governing the velocity or flux vector. The velocity variances and the resulting macrodispersivity differ from the standard spectral results of Gelhar and Axness (1983). The behavior of both statistical properties appear more realistic with the new solutions. Numerical flow simulations also showed a better agreement with the new expressions for velocity variance.

*Analytical Results:* Self-similar model of randomness

and "spectral conditioning" approach for the characterization of stochastic flow and transport phenomena over finite and time dependent length scales. Quantification of effective flow and transport coefficients over finite size domains, and the uncertainty on these coefficients. For evolving phenomena such as a growing concentration plume in a 3D isotropic medium, the preliminary results suggest that macrodispersivity and effective conductivity increase while their uncertainty decreases.

*Numerical Analysis:* Truncation error analysis for the finite difference approximation of stochastic groundwater flow equation (a model of "random heat equation"). Explicit closed form evaluation of the root-mean-square error on the hydraulic head potential and on the water flux vector, for different types of random log-conductivity fields. The order of accuracy is fractional in the case of a "noisy" log-conductivity field such as the non-differentiable 3D isotropic

*Markov field:*  $3/2$  for the head and  $1/2$  for the flux, in terms of the mesh size resolution  $(\Delta x/\lambda)$ .

*Numerical Analysis:* Evaluation of the true solution

error due to the approximate factorization and iterative solution of the finite difference system with the SIP solver. The residual error underestimate the true error in cases of slow convergence. Applications and numerical experiments for stochastic groundwater flow systems with grid size up to 1 million nodes. Analysis of convergence rate (inversely proportional to the unidirectional size of the grid).

*Numerical Analysis:* Non-standard stability analysis of the time-implicit finite difference approximation of the nonlinear unsaturated flow equation. A Peclet number constraint  $Pe \leq 2$  is required for nonlinear stability. Note  $Pe = \alpha \Delta x_1$ , where  $\alpha$  is the slope of the log-conductivity function of pressure, and  $\Delta x_1$  the vertical mesh size. A severe constraint on the time step size could result if this Peclet condition was not satisfied everywhere, as may occur when  $\alpha$  is a random field.

*Simulation Results:* Most of the spectral results of stochastic groundwater flow were confirmed by statistical analysis of single-realization flow fields, with random hydraulic conductivities generated by the 3D turning band method. The limitations of the

spectral results in the case of high variability and finite domains (shallow aquifers) were analyzed in detail. The simulations involved 3D grids of size 100,000 to 1 million nodes, and statistically isotropic as well as anisotropic random log-conductivities with standard deviations from  $\sigma = 1$  up to 2.3. In the isotropic case, both the hydraulic head and the velocity field were thoroughly analyzed.

**Simulation Results:** The case of localized infiltration in three-dimensional heterogeneous soils with random unsaturated conductivity curves was explored by the single-realization approach with exceptionally fine grid resolution (from 25,000 up to 300,000 nodes). The wetting pattern appeared to be very sensitive to the variability and anisotropy of the conductivity parameters (especially the slope of the log-conductivity curve). The study includes in particular a comprehensive qualitative analysis of infiltration and drainage on a statistically stratified soil (20 days, 5m x 15m x 15m, and 300,000 nodes).

**Simulation Results:** Steady state "rainfall" infiltration (213 mm/year) on a statistically stratified soil (5m x 15m x 15m, and 300,000 nodes).

The results of statistical analysis were in agreement with the linearized spectral solutions of Mantoglou and Gelhar 1987 (pressure head variance, and unsaturated effective conductivity).

[c] Outlook of stochastic approaches:

Some of the new methods and results developed in this work, particularly the approach of "spectral conditioning" and the results obtained by single-realization simulations, suggest some possible modifications of current conceptual approaches of naturally heterogeneous subsurface flow and transport phenomena. Originally, one of the leitmotives of this work was that such phenomena can be represented by single spatial replicas of statistically homogeneous and ergodic random fields. At first sight, the single replica postulate seems to be a natural working hypothesis for the study of randomly heterogeneous phenomena, since events actually take place in a "single world" rather than through some hypothetical ensemble space. Furthermore, the homogeneity-ergodicity postulate can be justified intuitively by the observation that such physical phenomena, taking place in heterogeneous environments over large length scales, may become globally homogeneous after many natural fluctuations have been encountered. The idea of balanced compensation is in fact at the root of our intuitive understanding of the concept of "chance"

(law of large numbers: stable and equal frequencies for head or tail in a game of coin tossing).

Accordingly, the "ergodic" or "single realization" approach purports that spatially heterogeneous subsurface phenomena may be characterized uniquely by a few statistical parameters. These parameters describe spatial fluctuations in a synthetic manner, in the same sense that the mean, amplitude, and wavelength characterize entirely a sinusoidal signal. In the language of random fields, the equivalent statistical quantities are the mean, standard deviation, and correlation lengths. Similarly, the concept of cross-correlation between two random fields can be related to the phase difference between two periodic signals. This simple analogy illustrates the fact that deterministic (periodic) as well as random (ergodic) spatial fluctuations can be characterized in terms of spatial moments without any explicit recourse to a hypothetical ensemble space. In summary, the ergodic "single-world" approach focuses on a single flow/transport event, taking place in "infinite" physical space, and whose statistical properties describe uniquely the spatial structure and global transport properties of the phenomenon at hand.

However, the single-world approach might be challenged on the grounds that natural flow and transport phenomena take place over finite or evolving length scales rather than in

infinite space. A difficulty of this nature was encountered with some of the numerical single-realization simulations analyzed in this work, particularly for steady groundwater flow in shallow stratified aquifers, and for transient infiltration from localized sources (evolving moisture plume over a time scale of days or weeks). In the latter case in particular, it seemed clear that the assumptions of infinite domain, homogeneity and ergodicity, were not operational. In view of this crucial difficulty, it may be useful to consider alternative methodologies.

Some alternative stochastic approaches proposed in the literature do not have recourse to the postulate of homogeneity/ergodicity of subsurface flow/transport phenomena. Broadly speaking, these approaches are based on an ensemble characterization of the statistical properties of random phenomena, and rely more or less explicitly on the notions of uncertainty and risk. The case of stochastic groundwater flow was tackled along these lines by Dagan (1982), Townley (1983), McLaughlin (1985), and Ma et al. (1987), using various mathematical methods (approximate Green functions, numerical solution of approximate moment equations, Monte-Carlo simulations). In these ensemble approaches, the concept of uncertainty seems to play a major role, particularly for phenomena of a local nature (e.g. uncertainty of drawdowns near a



pumping well). Nevertheless, there remains some ambiguity concerning the physical meaning of the statistical results obtained by the proponents of the ensemble approach in some applications (uncertainty or spatial variability?). This question might be clarified by a simple hypothetical example in the area of groundwater contamination.

Consider the case of an evolving concentration plume due to the continuous release of a contaminant from a local source in a heterogeneous aquifer. Depending on the configuration of local heterogeneities near the source, the plume may initially take an extremely asymmetrical shape, or even split in two distinct parts. An example of plume splitting can be seen for instance in Figure 7.6 (bottom) in the case of a moisture plume during strip source infiltration. See also the very different moisture patterns observed in two distant vertical planes along a strip source (top and bottom parts of Figure 7.12). Now, it seems possible that some of the asymmetry and inhomogeneity observed at early times will persist as time goes on, despite increasing homogenization and mixing with increasing travel distance. The peculiar features of the evolving plume are determined by the idiosyncracies of the heterogeneous formation in the neighborhood of the source, and depend on the exact location of the source in situ. With these considerations in mind, it seems clear that localized or evolving

flow and transport phenomena can be characterized by a certain degree of uncertainty. At the same time, the concept of "effective" or "large scale" transport properties (like effective conductivity and macrodispersivity) may still be relevant, provided that the particular length scale of interest be taken into account.

The analytical approach of spectral conditioning, developed in this work, may be one consistent way of combining the ensemble and single world approaches. The ensemble viewpoint enters into play by assigning uncertainty to the actual location of the contamination event in a single, randomly heterogeneous formation. The single world approach intervenes in the definition of global or effective transport properties at the scale of interest. Along these lines, it seems possible to design, in parallel to the spectral conditioning approach, a numerical simulation method somewhat similar to the single-realization approach implemented in this work. For instance, the fate of a contaminant released from a local source could be studied by solving numerically the flow and transport equations in a single realization of the random formation, using Monte-Carlo simulations to sample several possible locations of the source with respect to the detailed configuration of the heterogeneous porous formation.



## REFERENCES

- R. Ababou, (1981), "Modélisation Des Transferts Hydrauliques Dans Le Sol En Irrigation Localisée"; Dr.-Ing. Thesis, Inst. Nat. Polytech. and Univ. of Grenoble. France, (218 pp).
- R. Ababou, D. McLaughlin, L. W. Gelhar, and A. F. B. Tompson, (1985), "Numerical Simulation of Saturated Flow Fields in Randomly Heterogeneous Porous Media"; in *The Stochastic Approach to Subsurface Flow*, pre-prints International Symposium, A.I.R.H., Montvillargennes, France, June, 1985.
- R. Ababou, (1986), "Self-Similar Random Fields", Unpublished report (written under the advisorship of B. Mandelbrot), M.I.T. and Harvard University, 25 pp.
- R. Ababou, D. McLaughlin, L. W. Gelhar, A. F. B. Tompson, (1987), "Numerical Simulation of Three-Dimensional Saturated Flow in Randomly Heterogeneous Porous Media", paper submitted to the *Journal of Transport in Porous Media*, J. Bear, ed.
- R. J. Adler, (1981), *The Geometry of Random Fields*, Wiley, New York, 280 pp.
- A. A. Bakr, (1976), "Stochastic Analysis of the Effect of Spatial Variations of Hydraulic Conductivity on Groundwater Flow," PhD Thesis, New Mexico Instit. of Mining and Technology, Socorro, New Mexico.
- A. A. Bakr, L. W. Gelhar, A. L. Gutjahr, and R. J. McMillan, (1978), "Stochastic Analysis of Spatial Variability in Subsurface Flow (1) - Comparison of One and Three Dimensional Flows"; *Water Res. Res.* 14(2).
- F. Ballhaus, A. Jameson, and J. Albert, (1977), "Implicit Approximate-Factorization Schemes for the Efficient Solution of Steady Transonic Flow Problems," AIAA Paper, 77-634, 8 pp.
- M. S. Bartlett, (1946), "On the Theoretical Specification and Sampling Properties of Autocorrelated Times Series", *J. Royal Stat. Soc.*, Vol. 38, No. 27.
- G. K. Batchelor, (1953), *The Theory of Homogeneous Turbulence*, Cambridge Univ. Press (197 pp.).
- J. Bear, (1972), *Dynamics of Fluids in Porous Media*, American Elsevier, New York (746 pp).

C. M. Bender and S. A. Orszag, (1978), **Advanced Mathematical Methods for Scientists and Engineers**, McGraw-Hill, New York, (593 pp).

A. A. Binsariti, (1980), "Statistical Analyzes and Stochastic Modelling of the Contaro Aquifer in Southern Arizona", PhD dissertation, Dept. of Hydrol. and Water Resour., Univer. Ariz., Tucson.

C. Birkhoff and A. Schoenstadt, (1984), **Elliptic Problem Solvers II**, (*Proc. Elliptic Problem Solvers Conf.*, Monterey, California, January, 1983), Acad. Press, 573 pp.

J. Bjordammen and K. H. Coats, (1969), "Comparison of Alternative-Direction and Successive Overrelaxation Techniques in Simulation of Reservoir Fluid Flow", *Trans. Soc. Petrol. Eng.*, March, 1969.

A. Brandt, (1977), "Multi-Level Adaptive Solutions for Boundary Value Problems"; *Mathematics of Computations*, 31,(138), 333-390 pp, April, 1977.

P. A. Burrough, (1981), "Fractal Dimensions of Landscapes and Other Environmental Data", *Nature*, Vol. 294, 238-242, 19 November, 1981.

H. S. Carslaw, and J. C. Jaeger, (1959), **Conduction of Heat in Solids**, Oxford Univ. Press (510 pp).

M. Celia and G. Pinder, (1985), "An Analysis of Alternate Directions Methods for Parabolic Equations," *Journal of Numerical Methods for Partial Differential Equations*, Vol. 1, 57-70 pp.

P. M. Clifton, S. P. Neuman, 1982, "Effects of Kriging and Inverse Modeling on Conditional Simulation of the Arra Valley Aquifer in Southern Arizona", *Water Res. Res.*, 18 (4), 1215-1234.

R. Cooley, (1974), "Finite Element Solutions for the Equations of Groundwater Flow"; Tech. Report series H-W, No. 18, Center for Water Res. Res., University of Nevada, Desert Research Institute, Nevada, 1974.

R. Cooley, (1983), "Some New Procedures for the Numerical Solution of Variably Saturated Flow Problems"; *Water Res. Res.* 19(5), 1271-1285 pp, 1983.

H. S. M. Coxeter, (1973), **Regular Polytopes**. Dover, 321 pp.

G. Dagan, (1981), "Analysis of Flow Through Heterogeneous Random Aquifers by the Method of Embedding Matrix, 1: Steady Flow"; *Water Res. Res.*, 17(1), 107-121, 1981.

G. Dagan, (1982), "Stochastic Modeling of Groundwater Flow by Unconditional and Conditional Probabilities: (1) Conditional Simulation and the Direct Problem"; *Water Res. Res.* 18(4), 813-833 pp, 1982.

G. Dagan, and E. Bresler, (1983), "Unsaturated Flow in Spatially Variable Fields, (1) Derivation of Models of Infiltration and Redistribution"; *Water Res. Res.* 19(2), 413-420 pp.

G. Dagan, (1985), "A Note on the Higher-Order Corrections of the Head Covariances in Steady Aquifer Flow", *Water Res. Res.* 21(4), 573-578 pp.

G. Dagan, (1987), "Solute Transport in Groundwater", to be published in *Annual Review of Fluid Mechanics*, 19, 1987.

H. P. G. Darcy, (1856), "Les Fontaines Publiques de la Ville de Dijon, Exposition et Application des Principes à Suivre et des Formules à Employer dans les Questions de Distribution d'Eau", Victor Dalmont, Paris, 1856.

L. A. Davis and S. P. Neuman, (1983), "Documentation and User's Guide: UNSAT2-Variably Saturated Flow Model", Final Report WWL/TM-1791-1, W.W.L., Inc. (for U.S.N.R.C.) Fort-Collins, December, 1983.

J. P. Delhomme, (1979), "Spatial Variability and Uncertainty in Groundwater Flow Parameters: A Geostatistical Approach", *Water Res. Res.* 15, 269-280 pp, 1979.

J. L. Devary, P. G. Doctor, 1982, "Pore Velocity Estimation Uncertainties", *Water Res. Res.*, 18(4), 1157-1164.

J. Douglas, (1962), "Alternating Direction Methods for Three Space Variables", *Numerische Mathematik*, 4, 411-463 pp.

T. DuPont, R. P. Kendall and H. H. Rachford, (1968), "An Approximate Factorization Procedure for Solving Self-Adjoint Elliptic Difference Equations", *SIAM J. Numer. Anal.*, Vol. 5, No. 3, September, 1968.

T. Dupont, (1968), "A Factorization Procedure for the Solution of Elliptic Difference Equations", *SIAM J. Numer. Anal.*, Vol. 5, No. 4, December, 1968.

D. J. Evans, (1981), "On Preconditioned Iterative Methods for Elliptic PDE's" in *Elliptic Problem Solver I*, Academic Press, New York.

D. J. Evans, (1983), **Preconditioning Methods: Analysis and Applications**, Ed. D. J. Evans, Gordon and Breach, New York, 1983.

D. J. Evans, (1984), "Implicit Block Explicit Overrelaxation Schemes" in *Elliptic Problem Solver II*, (*Proc. Elliptic Problem Solvers Conf.*, Monterey, Calif., Jan. 1983), Academic Press, 573 pp.

G. S. Fishman, L. R. Moore, (1986), "An Exhaustive Analysis of Multiplicative Congruential Random Number Generators with Modulus  $2^{31}-1$ ", *SIAM J. Sci. Stat. Comput.*, Vol. 7, No. 1, January.

G. E. Forsythe and W. R. Wasow, (1960), **Finite-Difference Methods for Partial Differential Equations**, Wiley and Sons, New York.

R. A. Freeze, (1971), "Three-Dimensional Transient, Saturated Unsaturated Flow in a Groundwater Basin", *Water Res. Res.*, 7(2), 1971.

R. A. Freeze, (1975), "Stochastic-Conceptual Analysis of One Dimensional Groundwater Flow in Nonuniform Homogeneous Media", *Water Res. Res.* 11, 725-741 pp., 1975.

Y. M. Gajem, A. W. Warrick, and D. E. Myers, (1981), "Spatial Dependence of Physical Properties of a Typic Torrifluent Soil", *Soil Sci. Soc. Am. J.*, Vol. 45, 709-715 pp.

G. Gambolati and A.M. Perdon, (1984), "The Conjugate Gradients in Subsurface Flow and Land Subsidence Modelling", in **Fundamentals of Transport Phenomena in Porous Media**, J. Bear and M. Y. Corapcioglu, Eds., The Hague, 1984.

L. W. Gelhar, (1976), "Stochastic Analysis of Flow in Aquifers", *Advances in Groundwater Hydrology, Proceedings, 1976 Symposium of the Amer. Water Resources Assoc.*, Minneapolis, Minnesota.

L. W. Gelhar, (1984), "Stochastic Analysis of Flow in Heterogeneous Porous Media" in **Selected Topics in Mechanics of Fluids in Porous Media**, *Proceedings NATO Symposium*, Eds. Bear and Corapcioglu, Martinus Nijhoff publishers, Dordrecht, The Netherlands, 673-718.

- L. W. Gelhar, P. J. Wierenga, K. R. Rehfeldt, C. J. Duffy, M. J. Simonett, T.-C. Yeh, and W.R. Strong, (1982), "Irrigation Return Flow Water Quality Monitoring, Modeling, and Variability in the Middle Rio Grande Valley, New Mexico", EPA Report 600/2-83-072, New Mexico Inst. of Mining and Tech., Socorro, New Mexico.
- L. W. Gelhar, and C. L. Axness, (1983), "Three Dimensional Stochastic Analysis of Macrodispersion in Aquifers", *Water Res. Res.* 19(1), 161-180 pp.
- L. W. Gelhar, A. Mantoglou, C. Welty, and K. Rehfeldt, (1984), "A Review of Field Scale Subsurface Solute Transport Processes Under Saturated and Unsaturated Conditions", Report RP-22485-05, Electrical Power Research Institute.
- L. W. Gelhar, (1986), "Stochastic Subsurface Hydrology from Theory to Applications", *Water. Res. Res.*, 22(99), 135-145 pp.
- L. W. Gelhar, (1987), "Stochastic Analysis of Solute Transport in Saturated and Unsaturated Porous Media", *Fundamentals of Transport in Porous Media*, ed. J. Bear and M. Y. Corapcioglu, Martinus Nijhoff publishers, Dordrecht, The Netherlands, 657-700.
- S. Godunov, (1973), *Equations de la Physique Mathematique*, ed. MIR, Moscow (French translation from Russian).
- G. H. Golub and C. F. Van Loan, (1983), *Matrix Computations*, The John Hopkins Univ. Press, Baltimore
- I. S. Gradshteyn and I. M. Ryzhik, (1980), *Table of Integrals, Series, and Products*, (ed. A. Jeffrey), Academic Press, New York (1160 pp).
- I. Gustafsson, (1978), "A Class of First Order Factorization Methods," *BIT (Nordisk Tidskrift for Inform. Behandling)*, 18, 1442-156 pp.
- A. L. Gutjahr, L. W. Gelhar, A. A. Bakr, and R. J. MacMillan, (1978), "Stochastic Analysis of Spatial Variability in Subsurface Flows, (2) Evaluation and Application", *Water Res. Res.*, 14(5), 953-959 pp.
- A. L. Gutjahr, and L. W. Gelhar, (1981), "Stochastic Models for Subsurface Flow; Infinite Versus Finite Domains and Stationarity", *Water Res. Res.* 17(2), 337-350 pp.
- A. L. Gutjahr, (1984), "Stochastic Models of Subsurface Flow: Log Linearized Gaussian Models are Exact for Covariances", *Water Res. Res.*, 20, 1909-1912 pp.



- L. A. Hageman and D. M. Young, (1981). **Applied Iterative Methods**, Acad. Press, New York.
- R. Haverkamp and M. Vauclin, (1979), "A Note on Estimating Finite Difference Interblock Hydraulic Conductivity Value for Transient Unsaturated Flow Problems", *Water Res. Res.* 15(1).
- M. R. Hestenes and E. Stiefel, (1952). "Method of Conjugate Gradients for Solving Linear Systems", Nat. Bureau of Standards, *J. Res.*, 49, 409-436.
- R. J. Hoeksema, and P. K. Kitanidis, (1985), "Analysis of the Spatial Structure of Properties of Selected Aquifers", *Water Res. Res.* 21(4), 563-572 pp.
- A. S. Householder, (1964), **The Theory of Matrices in Numerical Analysis**, Dover Publications, New York, 1964 and 1975.
- P. Hufschmied, (1985), "Estimation of Three Dimensional Statistically Anisotropic Hydraulic Conductivity Field by Means of Single Well Pumping Tests Combined with Flowmeter Measurements", in **The Stochastic Approach to Subsurface Flow**, pre-prints International Symposium, A.I.R.H., Montvillargenne, France, June 1985.
- P. S. Huyakorn and G. F. Pinder, (1983), **Computational Methods in Subsurface Flow**, Academic Press, New York
- P. S. Huyakorn , S. D. Thomas, and B. M. Thompson, (1984), "Techniques for Making Finite Elements Competitive in Modeling Flow in Variably Saturated Porous Media" , *Water Res. Res.* 20(8), 1099-1115 pp.
- C. P. Jackson and P. C. Robinson, (1985), "A Numerical Study of Various Algorithms Related to the Preconditioned Conjugate Gradient Method", *Int. J. Num. Methods in Eng.*, Vol. 21, 1315-1338.
- D. A. H. Jacobs, (1981), "The Exploitation of Sparsity by Iterative Methods in **Sparse Matrices and their Use**, *Proceedings* edited by C. S. Duff, Academic Press, New York.
- A. H. Jacobs, (1983). "Preconditioned Conjugate Gradient Algorithms for Solving Finite Difference Systems", in **Preconditioning Methods: Analysis and Applications**, Ed. D. J. Evans, Gordon and Breach, New York, 1983.
- W. A. Jury, and L. H. Stolzy, (1982), "A Field Test of the Transfer Function Model for Predicting Solute Transport", *Water Res. Res.* 18(2), 369-375 pp., 1982.

- W. A. Jury, G. Sposito, and White, (1986), "A Transfer Function Model of Solute Transport Thru Soil: (1) Fundamental Concepts", *Water Res. Res.* 22(2), 243-247 pp.
- M. G. Kendall, A. Stuart, (1977), "The Advanced Theory of Statistics", Vol. 1, *Distribution Theory*, MacMillan, New York, 472 pp.
- B. C. Kent, C. R. Mauldin, M. W. Cooper, (1982), "Evaluation of Subsurface Migration from Solar Ponds", *Underground Resource Management Report*, Austin, TX.
- D. S. Kershaw, (1978), "The Incomplete Choleski-Conjugate Gradient Method for the Iterative Solution of Systems of Linear Equations", *J. Comput. Physics*, 2-6, 43-65 pp.
- G. R. Kirchhoff, (1894), "Vorlesungen uber die Theorie der Wärme".
- G. A. Korn and T. M. Korn, (1968), *Mathematical Handbook for Scientists and Engineers*, McGraw-Hill, New York, 2nd Edition, (1130 pp).
- L. K. Kuiper, (1981), "A Comparison of the Incomplete Choleski-Conjugate Gradient Method with the Strongly Implicit Method as Applied to the Solution of Two-Dimensional Groundwater Flow Equations", *Water Res. Res.* 17(6), pp 1082-1086.
- L. K. Kuiper, (1987), "A Comparison of Iterative Methods as Applied to the Solution of the Nonlinear Three-Dimensional Groundwater Flow Equation" *SIAM Journal on Sci. Stat. Computing*, 8(4), July, 1987.
- M. T. Landahl and E. Mollo-Christensen, (1986), *Turbulence and Random Processes in Fluid Mechanics*, Cambridge Univ. Press. (154 pp.).
- M. Loève, (1963, 1978), *Probability Theory, Vol. II*; Springer-Verlag, 1978.
- R. J. Luxmoore, B. P. Spaulding, I. M. Munro, (1981), "Areal Variation and Chemical Modification of Weathered Shale Infiltration Characteristics", *Soil Sci. Soc. Am. J.*, 45, 687-691.
- F. Ma, M. S. Wei, W. H. Mills, (1987), "Correlation Structuring and the Statistical Analysis of Steady-State Groundwater Flow", *SIAM J. Sci. Stat. Comput.*, Vol. 8, No. 5, 848-867.

- B. B. Mandelbrot and J. W. Van Ness, (1968), "Fractional Brownian Motions, Fractional Noises and Applications", *SIAM Review*, Vol. 10, No. 4, 422-437.
- B. B. Mandelbrot and J. R. Wallis, (1969), "Some Long-Run Properties of Geophysical Records", *Water Resource Research*, Vol. 5, No. 2, pp. 321-340.
- B. B. Mandelbrot, (1983), *The Fractal Geometry of Nature*, Freeman and Co., New York, (468 pp)
- B. B. Mandelbrot, D. E. Passoja, A. J. Paullay, (1984), "Fractal Character of Fracture Surfaces of Metals," *Nature*, Vol. 308, No. 5961, pp. 721-722, 19 April 1984.
- A. Mantoglou, and J. Wilson, (1982), "The Turning Bands Method for Simulation of Random Fields using Line Generation by a Spectral Method", *Water Res. Res.* 18(5), 1379-1394 pp.
- A. Mantoglou, (1984), "Large-Scale Models of Transient Unsaturated Flow and Contaminant Transport Using Stochastic Methods", Ph.D. Thesis, M.I.T., Cambridge, Massachusetts.
- A. Mantoglou, (1987), "Digital Simulation of Multivariate Two- and Three-Dimensional Stochastic Processes with a Spectral Turning Bands Method", *Mathematical Geology*, Vol. 19, No. 2, 129-149.
- A. Mantoglou and L. W. Gelhar, (1987a), "Stochastic Modeling of Large-Scale Transient Unsaturated Flow Systems", *Water Res. Res.*, 23(1), 37-46.
- A. Mantoglou and L. W. Gelhar, (1987b), "Capillary Tension Head Variance, Mean Soil Moisture Content, and Effective Specific Soil Moisture Capacity of Transient Unsaturated Flow in Stratified Soils", *Water Res. Res.*, 23(1), 47-56.
- A. Mantoglou and L. W. Gelhar (1987c), "Effective Hydraulic Conductivities of Transient Unsaturated Flow in Stratified Soils", *Water Res. Res.*, 23(1), 57-67.
- J. Marchant and R. Gabillard, (1975), Sur le calcul d'un réseau résistif aléatoire, Short Note in C.R.A.S.(Comptes-Rendus. Acad. Sci.), Paris, Vol. 281, Série B, 261-264, 6 Oct. 1975.
- G. Matheron, (1967), *Elements Pour une Théorie des Milieux Poreux*, Masson et Cie, Paris, 1967 (164 pp).
- G. Matheron, (1973), "The Intrinsic Random Functions and their Applications", *Adv. Appl. Prob.*, 5, 439-468 pp.

- G. Matheron, (1984), "L'Emergence de la Loi de Darcy", *Annales des Mines*, No. 5-6, pp. 11-16, May-June, 1984, Paris School of Mines, France.
- M. G. McDonald, and A. W. Harbaugh, (1984), "A Modular Three Dimensional Finite-Difference Groundwater Flow Model", U. S. Dept. Interior, and U. S. Geol. Survey, Nat. Center, Reston, Virginia (528 pp.).
- D. McLaughlin, (1985), "A Distributed Parameter State Space Approach for Evaluating the Accuracy of Groundwater Predictions", Ph.D. thesis, Princeton Univ., Princeton, New Jersey.
- J. A. Meijerink and H. A. Van der Vorst, (1977), "An Iterative Method for Linear Systems of which the Coefficient Matrix is a Symmetric M-Matrix", *Math. Comp.*, Jan. 1977.
- P. C. D. Milly, (1985), "A Mass-Conservative Procedure for Time-Stepping in Models of Unsaturated Flow", *Adv. Water Resources*, Vol. 8, March, 32-36.
- A. S. Monin and A. M. Yaglom, (1965), **Statistical Fluid Mechanics: Mechanics of Turbulence** (Volume 2), Ed. J. L. Lumley, The MIT Press, Cambridge, MA (874 pp).
- R. L. Naff and A. V. Vecchia, (1986), "Stochastic Analysis of Three-Dimensional Flow in a Bounded Domain", *Water Resour. Res.*, 22(5), 695-704 pp.
- D. R. Nielsen, J. W. Biggar, and K. T. Ehr, (1973), "Spatial Variability of Field-Measured Soil Water Properties", *Hilgardia*, 42, 215-260 pp., 1973.
- S. A. Orszag, (1977), "Numerical Simulation of Turbulent Flows; Chapter 10" in **Handbook of Turbulence, Vol. 1: Fundamentals and Applications**, Plenum Press, Eds. Frost and Moulden, New York.
- J. M. Ortega, and W. C. Rheinboldt, (1970), **Iterative Solution of Nonlinear Equations in Several Variables**, Academic Press, New York
- J. Y. Parlange, (1972), "Theory of Water Movement in Soils: (5) Unsteady infiltration from Spherical Cavities", *Soil Sci.*, 113, 156-161 pp.
- D. W. Peaceman, and H. H. Rachford, (1955), "The Numerical Solution of Parabolic and Elliptic Differential Equation", *J. SIAM*, 3, 1, 28-41 pp.
- J. R. Philip, (1969) "Theory of Infiltration" in **Advances in Hydroscience**, 5, 1969, Acad. Press; N.Y.

P. A. C. Raats, (1971), "Some Properties of Flows in Unsaturated Soils with an Exponential Dependence of Hydraulic Conductivity upon the Pressure Head", *J. of Hydrology*, 14, 129-138 pp.

A. E. Reisenauer, K. T. Key, T. N. Narasimhan and R. W. Nelson, (1982), "TRUST: A Computer Program for Variably Saturated Flow in Multidimensional, Deformable Media", Pacific Northwest Lab. Rep. NUREG/CR-2360, (for U.S. N.R.C.), Washington, D. C. January 1982.

I. Remson, G. M. Hornberger, and F. J. Molz, (1971), **Numerical Methods in Subsurface Hydrology**, Wiley-Interscience, New York.

R. C. Routson, W. H. Price, D. J. Brown, and K. R. Fecht, (1979), "High-Level Waste Leakage from the 241-T-106 Tank at Hanford"; Report RHO-ST-14, U. S. Department of Energy/Rockwell International, Richland, WA.

D. Russo, and E. Bresler, (1980), "Scaling Soil Hydraulic Properties of a Heterogeneous Field", *Soil Soc. Am. J.*, 44, 681-684.

D. Russo, and E. Bresler, (1981), "Soil Hydraulic Properties as Stochastic Processes. I: An Analysis of Field Spatial Variability", *Soil Soc. Am. J.*, 45, 682-687.

D. Russo, (1983), "A Geostatistical Approach to the Trickle Irrigation Design in Heterogeneous Soils, (1): Theory", *Water Res. Res.*, 19, 632-642 pp.

J. B. Scisson, and P. J. Wierenga, (1981), "Spatial Variability of Steady State Infiltration Rate as a Stochastic Process", *Soil Sci. Soc. Am. Journal*, 45 699-704 pp.

M. L. Sharma, G. A. Gander, C. G. Hunt, (1980), "Spatial Variability of Infiltration in a Watershed", *J. of Hydrology*, 45, 101-122.

M. Shinozuka, C. M. Jan, (1972), "Digital Simulation of Random Processes and its Applications" *J. Sound Vib.*, 25 (1), p. 111.

M. Shultz (editor), (1981), **Elliptic Problem Solver**, I, Acad. Press, New York.

C. S. Simmons, D. R. Nielsen, J. W. Biggar, (1979), "Scaling of Field-Measured Soil Water Properties", *Hilgardia*, 47 (4), 77-173, Sept. 1979.

- M. Sivapalan, E. F. Wood, (1986), "Stochastic Description and Simulation of Nonstationary Space-Time Rainfall at the Catchment Scale", Chapman Conference on Modeling of Rainfall Fields, Proceedings, Caracas, 1986.
- L. Smith, R. A. Freeze, (1979a), "Stochastic Analysis of Steady State Groundwater Flow in a Bounded Domain, 1: One-Dimensional Simulations", *Water Res.*, 15 (3), 521-528.
- L. Smith, R. A. Freeze, (1979b), "Stochastic Analysis of Steady State Groundwater Flow in a Bounded Domain, 2: Two-Dimensional Simulations", *Water Res.*, 15(6), 1543-1559.
- H. L. Stone, (1968), "Iterative Solution of Implicit Approximations of Multi-Dimensional Partial Differential Equations", *S.I.A.M. Journal Num. Anal.*, 5(3), Sept. 1968.
- E. A. Sudicky, (1986), "A Natural Gradient Experiment on Solute Transport in a Sand Aquifer: Spatial Variability of Hydraulic Conductivity and its Role in the Dispersion Process", *Water Res. Res.*, 22 (13), 2069-2082.
- A. F. B. Tompson, R. Ababou, and L. W. Gelhar, (1987), "Applications and Use of the Three-Dimensional Turning Band Random Field Generator in Hydrology: Single Realization Problems", Tech. Report. #313, Parsons Laboratory, M.I.T., Cambridge, MA (March, 1987).
- L. Townley, (1983), "Numerical Models of Groundwater Flow: Prediction and Parameter Estimation in the Presence of Uncertainty", Ph.D. thesis, M.I.T., Cambridge, Mass., 1983.
- S. J. Trauntwein, D. E. Daniel, and H. W. Cooper, (1983), "Case History Study of Water Flow Through Unsaturated Soils", in *The Role of the Unsaturated Zone in Radioactive Hazardous Waste Disposal*, Mercer et. al., Ann Arbor Science, Ann Arbor, MI.
- P. C. Trescott, (1975), "Documentation of Finite-Difference Model for Simulation of Three-Dimensional Groundwater Flow", U.S. Geol. Survey, Open File Report 75-438 pp, Sept. 1975.
- P. C. Trescott, and S. P. Larson, (1977), "Comparison of Iterative Methods of Solving Two-Dimensional Flow Equations", *Water Res. Res.* 13(1), 1977.
- R. Van Genuchten, (1978), "Calculating the Unsaturated Hydraulic Conductivity with a New Closed-Form Analytical Model," *Water Res. Program*, Princeton University. (65 p)

- M. Th. Van Genuchten, (1980). "A Closed Form Equation for Predicting the Hydraulic Conductivity of Unsaturated Soils," *Soil Sci. Soc. Am., J.*, 44, 892-898 pp.
- E. Vanmarcke, (1983). **Random Fields Analysis and Synthesis**, The MIT Press, Cambridge, MA (382 pp).
- R. Varga, (1962). **Matrix Iterative Analysis**, Prentice-Hall, Englewood Cliffs, N.J.
- M. Vauclin, R. Haverkamp, and G. Vachaud, (1979), **Résolution Numérique d'une Equation de Diffusion Nonlinéaire**, P.U.G., Grenoble, 183 p.
- M. Vauclin, J. Imbernon, and G. Vachaud, (1981), "Spatial Variability of Some Soil Physical Properties over One-Hectar Field Plot", AGU Chapman Conference, Fort-Collins, Colorado, July, 1981.
- M. Vauclin, (1982), "Méthode d'étude de la Variabilité Spatiale des Propriétés d'un Sol", in **Variabilité Spatiale des Processus de Transfert dans les Sols** Avignon, France, June 1982, Ed. INRA publ., No. 15 9-43 pp.
- S.R. Vieira, D. R. Nielsen and J. W. Biggar, (1981), "Spatial Variability of Field-Measured Infiltration Rate", *Soil Sci. Soc. Am. J.*, 45, 1040-1048.
- E. Vomvoris, (1986). "Concentration Variability in Transport in Heterogeneous Aquifers: A Stochastic Analysis", Ph.D. thesis, Parsons Laboratory, M.I.T., Cambridge, MA.
- A. W. Warrick, and D. O. Lomen, (1976). "Time Dependent Linearized Infiltration (III): Strip and Disc Sources)", *Soil Sci. Soc. Am. J.*, 40.
- A. W. Warrick, G. J. Mullen and D. R. Nielsen, (1977), "Scaling Field-Measured Soil Hydraulic Properties Using a Similar Media Concept," *Water Res. Res.*, 13, 355-362.
- A. W. Warrick, and Amoozegar-Fard, (1979), "Infiltration and Drainage Calculations Using a Similar Media Concept", *Water Res. Res.*, 13, 355-362 pp., 1977.
- J. W. Watts, (1971), "An Iterative Matrix Solution Method Suitable for Anisotropic Problems", *Trans. Soc. Petrol. Eng.*, March 1971, 47-51 pp.

- H. G. Weinstein, H. L. Stone, and T. V. Kwan, (1969), "Iterative Procedure for Solution of Systems of Parabolic and Elliptic Equations in Three Dimensions", *Industr. Engin. Chem., Fundamentals*, 8(2), 281-187 pp., 1969.
- I. White and M. J. Sully, (1987), "Macroscopic and Microscopic Capillary Length and Time Scales from Field Infiltration", *Water Res. Res.*, 23, (8), 1516-1522.pp.
- P. J. Wierenga, L. W. Gelhar, C. S. Simmons, G. W. Gee, and T. J. Nicholson (1986), "Validation of Stochastic Flow and Transport Models for Unsaturated Soils: A Comprehensive Field Study", Report NUREG/CR-4622 (U.S. Nuclear Regulatory Commission), Pacific Northwest Lab., Richland, WA.
- P. J. Wierenga, I. Porro, W. Strong, J. Vinson, D. Hudson, M. Nash, and A. Schneeberger, (1986), "Validation of Stochastic Flow and Transport for Unsaturated Soils", Research Report 86-SS-01, Dept. Agronomy Agric., New Mexico State University, Las Cruces, NM.
- K. G. Wilson and J. Kogut, (1974), "The Renormalization Group and the  $\epsilon$  Expansion", *Physics Reports (Section C of Physics Letters)* 12 (2), 75-200.
- K. G. Wilson, (1979) "Problems in Physics with Many Scales of Length", *Scientific American*, Vol. 241, No. 2, August, 1979.
- K. G. Wilson, (1983), "The Renormalization Group and Critical Phenomena", *Review of Modern Physics*, 55(3), p. 583.
- I. J. Winograd, (1981), "Radioactive Waste Disposal in Thick Unsaturated Zones," *Science*, Vol. 212, No. 4502, 1457-1464, June 26, 1981.
- R. A. Wooding, (1968), "Steady Infiltration from a Shallow Circular Pond", *Water Res. Res.*, 4, No. 6, 1259-1273 pp.
- G. T. Yeh and R. J. Luxmoore, (1983), "MATTUM: A Multidimensional Model for Simulating Moisture and Thermal Transport in Unsaturated Porous Media", *Env. Sci. Div. Publ. No. 2009*, Oak Ridge Nat. Lab. (for the U.S. Dept. of Energy).
- G. T. Yeh (1985) "Comparisons of Successive Iteration and Direct Methods to Solve Finite Element Equations of Aquifer Contaminant Transport", *Water Res. Res.*, 21(3), 272-280 pp.
- T.-C. Yeh, L. W. Gelhar, and A. L. Gutjhar, (1982), "Stochastic Analysis of Effects of Spatial Variability on Unsaturated Flow", Report No. H-11, New Mexico Institute of Mining and Technology, Socorro, N.M., July, 1982, (228 pp).



T.-C. Yeh, L. W. Gelhar, and A. L. Gutjhar, (1985a), "Stochastic Analysis of Unsaturated Flow in Heterogeneous Soils: (1) Statistically Anisotropic Media", *Water Res. Res.*, 21(4), 447-456 pp., 1985.

T.-C. Yeh, L. W. Gelhar, and A. L. Gutjhar, (1985b), "Stochastic Analysis of Unsaturated Flow in Heterogeneous Soils: (2) Statistically Anisotropic Media with Variable  $\alpha$ ", *Water Res. Res.*, 21((4), 457-464 pp.

T.-C. Yeh, L. W. Gelhar, and A. L. Gutjhar, (1985c), "Stochastic Analysis of Unsaturated Flow in Heterogeneous Soils: (3): Observations and Applications", *Water Res. Res.*, 21(4), 465-471 pp.

D. M. Young, (1971), *Iterative Solution of Large Linear Systems*, Academic Press, New York.

**APPENDIX 2A:  
UNCERTAINTY OF SAMPLE STATISTICS FOR RANDOM  
VARIABLES AND RANDOM FIELDS**

This appendix gives a brief overview of finite sample statistics for random variables, and adds further indications in the more general case of random fields. This may serve as a reference for parts of chapters 2 and 6 where some of the sample statistics are used to evaluate confidence intervals on spatial moments of single replicas of random fields. However, the present review is not meant to be a complete summary of available results in the literature.

**1. Random variables:**

The statistics of finite size samples of a random variable ( $y$ ) are themselves random variables, whose variances quantify the uncertainty of finite size sample statistics. In the case where the sample size is reasonably large (say  $n > 50$ ) the sample mean and the sample variance are defined, respectively, by:

$$\hat{\mu} = \frac{1}{n} \sum_i y_i$$

$$\hat{\sigma}^2 = \frac{1}{n-1} \sum_i (y_i - \hat{\mu})^2$$

and follow approximately the normal distributions:

$$\begin{aligned}\hat{\mu} &: N(\mu, \sigma^2/n) \\ \hat{\sigma}^2 &: N(\sigma^2, 2\sigma^4/n)\end{aligned}$$

Moreover, the sample standard derivation  $\hat{\sigma}$  also follows approximately a normal distribution for sufficiently large  $n$ , as shown below:

$$\hat{\sigma}: N(\sigma, \sigma^2/2n)$$

These results can be found in many textbooks, for instance Kendall and Stuart (1977). Note that all three estimators are unbiased and convergent.

For practical applications, it may be useful to quantify the uncertainty of these sample statistics by defining a "relative error" ( $\epsilon$ ) as follows:

$$\begin{aligned}\epsilon(\mu) &= \frac{(\text{Var}(\hat{\mu}))^{1/2}}{\sigma} \\ \epsilon(\sigma^2) &= \frac{(\text{Var}(\hat{\sigma}^2))^{1/2}}{\sigma^2}\end{aligned}$$

$$\epsilon(\sigma) = \frac{(\text{Var}(\hat{\sigma}))^{1/2}}{\sigma}$$

Plugging the previous results in these expressions gives the relative errors on the sample mean, variance, and standard deviation as follows:

$$\epsilon(\mu) = \sqrt{1/n}$$

$$\epsilon(\sigma^2) = \sqrt{2/n}$$

$$\epsilon(\sigma) = \sqrt{1/2n}$$

As suggested in chapters 2 and 6, these formulas can be used also to evaluate (crudely) the uncertainty of sample statistics of finite size realizations of correlated random functions, with an appropriate definition of the "equivalent" number of independent samples (e.g.  $n = L/\lambda$  for one-dimensional space).

## 2. Correlated random variables and random functions:

Let us point out other results of interest in the case of correlated random functions or discrete random processes (sequence of correlated random variables). Beginning with the case of two correlated random variables  $(y_1, y_2)$  following a bivariate normal distribution, Kendall and Stuart (1977) show that the variance of the sample correlation coefficient  $(\hat{\rho})$  is given by:

$$\text{Var}(\hat{\rho}) = \frac{1}{n} (1-\rho)^2$$

However, Kendall and Stuart also point out that the sampling distribution of  $\hat{\rho}$  tends very slowly to normality as  $n$  increases, so that using this formula to estimate confidence intervals on the true value ( $\rho$ ) may be misleading.

For a discrete random process or a sequence of random variables, the sample correlation coefficient:

$$\hat{\rho}_i = \frac{1}{n-j} \sum_{i=1}^{n-j} Y_i Y_{i+j} / \frac{1}{n} \sum_{i=1}^n U_i^2$$

is unbiased for sufficiently large  $n$ , and its variance is given by:

$$\text{Var}(\hat{\rho}_i) = \frac{1}{n} \sum_{i=-\infty}^{+\infty} [\rho_i^2 + \rho_{i-j}\rho_{i+j} - 4\rho_i\rho_j\rho_{i+j} + 2\rho_i^2\rho_j^2].$$

The latter formula is due to Bartlett (1946).

Finally, for a stationary random function  $Y(x)$  of one-dimensional space (or time), the sample covariance function could be evaluated as:

$$\hat{R}(\xi) = \frac{1}{L} \int_0^{L-\xi} (Y(x) - \hat{\mu})(Y(x+\xi) - \hat{\mu}) dx$$

for lag distance  $\xi \leq L$ , where  $L$  is the size of the available sample. The above estimator is unbiased. Bartlett (1946) gave the ensemble covariance between two values of the estimated covariance function at different lags (see also Vanmarcke, 1983). In particular, this yields the variance of the estimated covariance function:

$$\text{Var}(\hat{R}(\xi)) = \frac{1}{L^2} \cdot \int_0^{L-\xi} \int_0^{L-\xi} \text{Cov}(Y(x_1-\xi) \cdot Y(x_1), Y(x_2-\xi) \cdot Y(x_2)) dx_1 dx_2$$

Alternatively, the domain of integration ( $L-\xi$ ) could be replaced by ( $L$ ) to obtain unbiased estimates. With this modification and some further manipulations, it is easily shown that:

$$\text{Var}(\hat{R}(\xi)) = \frac{1}{L} \int_{-L}^{+L} \left(1 - \frac{|s|}{L}\right) (R(s+\xi) \cdot R(s-\xi) + R^2(s)) ds$$

The latter formula gives explicitly the ensemble variance of the estimated covariance function at any lag distance  $\xi \leq L$ . Note

that an a-priori knowledge of the true covariance function is required.

It may be useful to illustrate the above formula in a simple case. Let  $Y(x)$  be a one-dimensional random function with exponential covariance function:

$$R(\xi) = \sigma^2 e^{-|\xi|/\lambda}$$

where  $\sigma^2$  is the variance and  $\lambda$  the integral correlation scale of  $Y(x)$ . After some tedious but straightforward integrations, we obtained a closed-form expression for the squared relative error defined as:

$$\epsilon^2(\xi) = \text{Var}(\hat{R}(\xi))/R(\xi)^2.$$

In particular, that expression could be simplified in the case  $L \gg \lambda$  (large number of equivalent independent samples). The result is given below:

$$\epsilon^2(\xi) \approx \frac{2\lambda}{L} \cdot \left[ 1 - \frac{1}{2} \frac{\xi}{L} - \frac{1}{4} \frac{\lambda}{L} + \frac{\xi}{\lambda} \left( 1 - \frac{\xi}{2L} \right) \right].$$

At zero lag ( $\xi = 0$ ) this gives the relative error on the estimated variance:

$$\epsilon^2(0) \simeq 2 \frac{\lambda}{L} \left(1 - \frac{1}{4} \frac{\lambda}{L}\right)$$

which, by comparison with the result obtained for the estimated variance of a single random variable ( $\epsilon^2 = 2/n$ ), illustrates that for  $\lambda/L \ll 1$  the number of independent samples becomes  $n = L/\lambda$ . For intermediate lag distances, say  $\xi = \lambda$ , the relative error is approximately (using  $\lambda \ll L$ ):

$$\epsilon^2(\lambda) \simeq 4 \frac{\lambda}{L}.$$

Finally, at large lag distances  $\xi \gg \lambda$ , one obtains a large relative error that goes to unity (100%) as  $\xi$  goes to  $L$ . These simple results could probably be generalized to treat the case of discrete finite realizations of three-dimensional fields.





## APPENDIX 3.A

CLOSED FORM EVALUATION OF THE HEAD GRADIENT VARIANCES FOR THE  
3D ISOTROPIC MARKOV SPECTRUM

Assuming for convenience that the mean hydraulic gradient  $\underline{J}$  is aligned with the  $x_1$  axis, and denoting  $h_i = \frac{\partial h}{\partial x_i}$  the gradient of head perturbation, the spectrum of the head gradient field is, from Section 3.1:

$$S_{h_i, h_j}(\underline{k}) = k_i k_j \frac{J_1^2 k_1^2}{k^4} S_{ff}(\underline{k}).$$

In particular, this gives:

$$\sum_i S_{h_i, h_i}(\underline{k}) = \frac{J_1^2 k_1^2}{k^2} S_{ff}(\underline{k})$$

$$\sum_i \sigma_{h_i}^2 = \sigma_{h_1}^2 + \sigma_{h_2}^2 + \sigma_{h_3}^2 = \iiint_{-\infty}^{+\infty} \frac{J_1^2 k_1^2}{k^2} S_{ff}(\underline{k}) d\underline{k}.$$

Plugging this expression in the 3D Markov isotropic spectrum, one obtains:

$$\sum_i \sigma_{h_i}^2 = \frac{\sigma_f^2 \lambda^3 J_1^2}{\pi^2} \iiint_{-\infty}^{+\infty} \frac{k_1^2}{k^2} \frac{1}{(1+\lambda^2 k^2)^2} d\mathbf{k}.$$

Using spherical coordinates, this gives:

$$\begin{aligned} \sum_i \sigma_{h_i}^2 &= \frac{\sigma_f^2 \lambda^3}{\pi^2} J_1^2 \int_{\theta=0}^{\theta=2\pi} \int_{\varphi=0}^{\varphi=\pi} \int_{k=0}^{k=+\infty} \frac{\cos^2 \theta \sin^2 \varphi \cdot k^2 \sin \varphi}{(1+\lambda^2 k^2)^2} d\theta d\varphi dk \\ &= \frac{\sigma_f^2 \lambda^3 J_1^2}{\pi^2} \cdot \int_{\theta=0}^{\theta=2\pi} \cos^2 \theta d\theta \int_{\varphi=0}^{\varphi=\pi} \sin^3 \varphi d\varphi \int_{k=0}^{k=+\infty} \frac{k^2}{(1+\lambda^2 k^2)^2} dk \\ &= \frac{4}{3} \frac{\sigma_f^2 J_1^2}{\pi} \int_{-\infty}^{+\infty} \frac{u^2}{(1+u^2)} du \end{aligned}$$

The integral above, is equal to  $\pi/4$ , whence the final result:

$$\sum_{i=1,2,3} \sigma_{h_i}^2 = \frac{1}{3} \sigma_f^2 J^2 \Rightarrow \boxed{\sqrt{\sigma_{h_1}^2 + \sigma_{h_2}^2 + \sigma_{h_3}^2} = \frac{1}{\sqrt{3}} \sigma_f J}$$

On the other hand, the transverse head gradient variance can be

obtained directly as follows:

$$\begin{aligned}\sigma_{h_2}^2 &= \iiint S_{h_2 h_2}(\underline{k}) \, d\underline{k} \\ &= J_1^2 \iiint \frac{k_1^2 k_2^2}{k^4} S_{ff}(\underline{k}) \, d\underline{k}\end{aligned}$$

Plugging the 3D isotropic Markov spectrum above and integrating yields finally:

$$\boxed{\sigma_{h_2}^2, \sigma_{h_3}^2 = \frac{1}{15} J_1^2 \sigma_f^2}$$

The longitudinal head variance obtains readily from previous results, using the fact  $\sigma_{h_2} = \sigma_{h_3}$  by symmetry. Whence:

$$\begin{aligned}\sigma_{h_1}^2 &= \sum_1 \sigma_{h_i}^2 - (\sigma_{h_2}^2 + \sigma_{h_3}^2) \\ &= \frac{1}{3} \sigma_f^2 J^2 - \frac{2}{15} \sigma_f^2 J^2 \\ &= \frac{3}{15} \sigma_f^2 J^2\end{aligned}$$

$$\Rightarrow \boxed{\sigma_{h_1}^2 = \frac{1}{5} \sigma_f^2 \cdot J^2}$$

In summary, the head gradient standard deviations are:

$$\boxed{\sigma_{h_1} = \frac{1}{\sqrt{5}} \sigma_f J} \quad \text{and} \quad \boxed{\sigma_{h_2} = \sigma_{h_3} = \frac{1}{\sqrt{15}} \sigma_f J}$$

## APPENDIX 3.B

CLOSED FORM EVALUATION OF FLUX VARIANCES AND CROSS-COVARIANCES  
AT LAG ZERO, FOR THE 3D ISOTROPIC MARKOV SPECTRUM

In order to evaluate  $R_{q_i q_j}(\underline{0})$ , we use the flux spectrum of the standard first order spectral theory, given by equation (3.18):

$$S_{q_i q_j}(\underline{k}) = K_G^2 J_i^2 \left[ \delta_{i1} - \frac{k_i k_1}{k^2} \right] \left[ \delta_{j1} - \frac{k_j k_1}{k^2} \right] S_{ff}(\underline{k})$$

where  $S_{ff}$  is the 3D isotropic Markov spectrum:

$$S_{ff}(\underline{k}) = \frac{\sigma_F^2 \lambda^3}{\pi^2} \cdot \frac{1}{(1 + \lambda^2 k^2)^2}$$

and  $k$  is the radial wavenumber:

$$k^2 = k_1^2 + k_2^2 + k_3^2.$$

The cross-covariances are given by

$$R_{q_i q_j}(\underline{0}) = \iiint_{-\infty}^{+\infty} S_{q_i q_j}(\underline{k}) d\underline{k}. \quad (i=1,2,3 \text{ and } j=1,2,3)$$

By using certain symmetry properties of the flow as explained in Section 4.2, only the following spectra need to be integrated:

$$S_{q_1 q_1}(\mathbf{k}) = K_G^2 J_1^2 \sigma_f^2 \left[ 1 - \frac{k_1^2}{k^2} \right]^2 \cdot \frac{\lambda^3}{\pi^2 (1 + \lambda^2 k^2)^2}$$

$$j \neq 1: \quad S_{q_1 q_j}(\mathbf{k}) = K_G^2 J_1^2 \sigma_f^2 \left[ 1 - \frac{k_1^2}{k^2} \right] \cdot \left[ -\frac{k_1 k_j}{k^2} \right] \frac{\lambda^3}{\pi^2 (1 + \lambda^2 k^2)^2}$$

$$S_{q_2 q_3}(\mathbf{k}) = K_G^2 J_1^2 \sigma_f^2 \frac{k_1^2 k_2 k_3}{k^4} \frac{\lambda^3}{\pi^2 (1 + \lambda^2 k^2)^2}$$

$$j \neq 1: \quad S_{q_j q_j}(\mathbf{k}) = K_G^2 J_1^2 \sigma_f^2 \frac{k_1^2 k_j^2}{k^4} \frac{\lambda^3}{\pi^2 (1 + \lambda^2 k^2)^2}$$

### 1. Transverse Flux Variance:

$$\sigma_{q_T}^2 = R_{q_j q_j}(0) \quad (j = 2, 3):$$

$$\frac{\sigma_{q_T}^2}{K_G^2 J_1^2 \sigma_f^2} = \iiint_{-\infty}^{+\infty} \frac{k_1^2 k_2^2}{k^4} \frac{\lambda^3}{\pi^2 (1 + \lambda^2 k^2)^2} dk_1 dk_2 dk_3$$

$$\dots = \frac{\lambda^3}{\pi^2} \int_{\varphi=0}^{\pi} \int_{\theta=0}^{2\pi} \int_{k=0}^{+\infty} dk d\theta d\varphi \cdot k^2 \sin\varphi.$$

$$\cdot \frac{\sin^2 \varphi \cos^2 \theta \cdot \sin^2 \varphi \sin^2 \theta}{(1 + \lambda^2 k^2)^2}$$

$$\dots = \frac{\lambda^3}{\pi^2} \int_{\varphi=0}^{\pi} \sin^5 \varphi d\varphi \cdot \int_{\theta=0}^{2\pi} \cos^2 \theta \sin^2 \theta d\theta \cdot \int_{k=0}^{+\infty} \frac{k^2}{(1 + \lambda^2 k^2)^2} dk$$

$$\dots = \frac{\lambda^3}{\pi^2} \cdot \frac{16}{5} \cdot \frac{\pi}{4} \frac{\pi}{4\lambda^3}$$

$$\dots = \frac{1}{15} \Rightarrow$$

$$\boxed{\sigma_{q_T}^2 = \frac{1}{15} K_G^2 J_1^2 \sigma_f^2}$$

## 2. Longitudinal Flux Variance:

$$\sigma_{q_L}^2 = R_{q_1 q_1}(0):$$

$$\frac{\sigma_{q_L}^2}{K_G^2 J_1^2 \sigma_f^2} = \frac{\lambda^3}{\pi^2} \iiint_{-\infty}^{+\infty} \frac{(1 - k_1^2/k^2)^2}{(1 + \lambda^2 k^2)^2} dk_1 dk_2 dk_3$$

$$\dots = \frac{\lambda^3}{\pi^2} \int_{\varphi=0}^{\pi} \int_{\theta=0}^{2\pi} \int_{k=0}^{+\infty} [1 - \sin^2 \varphi \cos^2 \theta]^2 \cdot \frac{k^2 \sin \varphi}{(1 + \lambda^2 k^2)^2} dk d\theta d\varphi.$$

Expanding:

$$(1 - \sin^2 \varphi \cos^2 \theta)^2 \cdot \sin \varphi \equiv \sin \varphi - 2 \sin^3 \varphi \cos^2 \theta + \sin^5 \varphi \cdot \cos^4 \theta$$



and plugging this in the integral gives:

$$\dots = \frac{\lambda^3}{\pi^2} \cdot \left\{ \int_0^{2\pi} d\theta \times \int_0^{\pi} \sin\varphi d\varphi - 2 \int_0^{2\pi} \cos^2\theta d\theta \times \int_0^{\pi} \sin^3\varphi d\varphi \right. \\ \left. + \int_0^{2\pi} \cos^4\theta d\theta \times \int_0^{\pi} \sin^5\varphi d\varphi \right\} \times \left\{ \int_0^{+\infty} \frac{k^2}{(1+\lambda^2 k^2)^2} dk \right\}$$

$$\dots = \frac{\lambda^3}{\pi^2} \cdot \left\{ 2\pi \times 2 - 2 \times \pi \times 4/3 + \frac{3\pi}{4} \times \frac{16}{15} \right\} \times \left\{ \frac{\pi}{4\lambda^3} \right\}$$

$$\dots = \frac{8}{15} \Rightarrow \boxed{\sigma_{q_L}^2 = \frac{8}{15} K_G^2 \sigma_f^2 J_1^2} .$$

### 3. Cross-Covariances Between Different Flux Components at Lag Zero:

These cross-variances vanish due to the fact that the spectral integrand is odd. Precisely,  $R_{q_2 q_3}(0)$  vanishes since  $S_{q_2 q_3}(\underline{k})$  is odd in  $k_2$  and  $k_3$ ; similarly,  $R_{q_1 q_2}(0)$  vanishes because  $S_{q_1 q_2}(\underline{k})$  is odd in  $k_1$  and  $k_2$ . Whence the result:

$$\boxed{R_{q_i q_j}(0) \text{ is } 0 \text{ for } i \neq j.}$$

## APPENDIX 3.C

CLOSED FORM EVALUATION OF CERTAIN CORRELATION  
FUNCTIONS OF THE FLUX AND HEAD GRADIENT VECTORS, FOR THE 3D  
ISOTROPIC MARKOV SPECTRUM

## 1. Transverse Flux Correlation Function

Here, we focus on the correlation of the transverse flux component  $q_2$  along the other transverse direction  $x_3$ . This correlation function is defined as:

$$\tilde{R}_{q_2 q_2}(\xi_3) = \frac{R_{q_2 q_2}(0, 0, \xi_3)}{\sigma_{q_2}^2}$$

From (3.18) and (3.24) we have:

$$S_{q_i q_j}(\underline{k}) = K_G^2 J_1^2 \left[ \delta_{i1} - \frac{k_i k_1}{k^2} \right] \left[ \delta_{j1} - \frac{k_j k_1}{k^2} \right] S_{ff}(k)$$

$$\sigma_{q_2}^2 = \frac{1}{15} K_G^2 \sigma_f^2 J_1^2$$

which gives for the correlation function:

$$\tilde{R}_{q_2 q_2}(\xi_3) = \frac{15}{\sigma_f^2} \iiint e^{jk_3 \xi_3} \frac{k_1^2 k_2^2}{k^4} S_{ff}(\underline{k}) d\underline{k}$$

Plugging the 3D isotropic Markov spectrum:

$$S_{ff}(\underline{k}) = \frac{\sigma_f^2 \lambda^3}{\pi^2} \frac{1}{(1+\lambda^2 k^2)^2}$$

in the integral above yields:

$$\tilde{R}_{q_2 q_2}(\xi_3) = \frac{15\lambda^3}{\pi^2} \iiint e^{jk_3 \xi_3} \frac{k_1^2 k_2^2}{k^4} \frac{1}{(1+\lambda^2 k^2)^2} d\underline{k}.$$

Using spherical coordinates we obtain finally the double-integral:

$$\tilde{R}_{q_2 q_2}(\xi_3) = \frac{15\lambda^3}{4\pi} \int_0^\pi \sin^5 \varphi \, d\varphi \int_0^\infty \frac{k^2 \cos(k\xi_3 \cos \varphi)}{(1+\lambda^2 k^2)^2} dk.$$

Equivalently, by letting  $u = \lambda k$  and  $a = \xi_3/\lambda$  this gives:

$$\tilde{R}_{q_2 q_2}(\xi_3) = \frac{15}{4\pi} \int_0^\pi \sin^5 \varphi \, d\varphi \int_0^\infty \frac{u^2 \cos(ua \cos \varphi)}{(1+u^2)^2} du$$

Finally, taking symmetries into account and letting  $v = \sin \varphi$  or  $\cos \varphi$ , and  $\sqrt{1-v^2} = \cos \varphi$  or  $\sin \varphi$ , with  $0 \leq \varphi \leq \pi/2$ , we obtain:

$$\tilde{R}_{q_2 q_2}(\xi_3) = \frac{15}{2\pi} \cdot \int_0^1 (1-v^2)^2 \, dv \int_0^\infty \frac{u^2 \cos(uv a)}{(1+u^2)^2} du$$

From Gradshteyn and Ryzhik (3.728.3), we have for the inner

integral:

$$\int_0^{\infty} \frac{x^2 \cos Ax}{(1+x^2)^2} dx = \frac{\pi}{4}(1-A)e^{-A} .$$

Note that as  $A \rightarrow 0$  the result above converges to  $\pi/4$  as expected (good check). Plugging this result in the double-integral above yields:

$$\tilde{R}_{q_2 q_2}(\xi_3) = \frac{15}{8} \int_0^1 [1 - av - 2v^2 + 2av^3 + v^4 - av^5] e^{-av} dv$$

where  $a = \xi_3/\lambda$  is the dimensionless separation distance. After integration, this gives:

$$\begin{aligned} \tilde{R}_{q_2 q_2}(a) = & \frac{15}{8} \left\{ \frac{1}{a}(1 - e^{-a}) + e^{-a} \left( 1 + \frac{1}{a} \right) - \frac{1}{a} \right. \\ & + 2e^{-a} \left[ \frac{1}{a} + \frac{2}{a^2} + \frac{2}{a^3} \right] - \frac{4}{a^3} \\ & - 2e^{-a} \left[ 1 + \frac{3}{a} + \frac{6}{a^2} + \frac{6}{a^3} \right] + \frac{12}{a^3} \\ & - e^{-a} \left[ \frac{1}{a} + \frac{4}{a^2} + \frac{12}{a^3} + \frac{24}{a^4} + \frac{24}{a^5} \right] + \frac{24}{a^5} \\ & \left. - e^{-a} \left[ \frac{1}{a} + \frac{5}{a} + \frac{20}{a^2} + \frac{60}{a^3} + \frac{120}{a^4} + \frac{120}{a^5} \right] - \frac{120}{a^5} \right\} \end{aligned}$$

This expression finally reduces to:

$$\tilde{R}_{q_2 q_2}(0,0,\xi_3) = \frac{15}{a^2} \cdot \left\{ \frac{1}{a} \left( 1 - \frac{12}{a^2} \right) + e^{-a} \cdot \left( 1 + \frac{5}{a} + \frac{12}{a^2} + \frac{12}{a^3} \right) \right\}$$

where  $a \equiv \xi_3/\lambda$ . It can be checked that this correlation function goes to one as  $a \rightarrow 0$ , as it should. This can be shown by using a Taylor development of  $e^{-a}$  up to fifth order.

## 2. Head Gradient Correlation Functions:

The correlation functions  $\tilde{R}_{h_i h_j}(\xi)$  for the head gradient vector  $h_i = \partial h / \partial x_i$  can be obtained similarly by integrating the spectrum  $S_{h_i h_j}(\mathbf{k})$  given in Chapter 3. It turns out that some of the directional correlations thus obtained are identical to certain flux correlations. In particular, we obtain:

$$\boxed{\tilde{R}_{h_1 h_1}(0,0,\xi_3) = \tilde{R}_{q_2 q_2}(0,0,\xi_3).}$$

A more general closed form expression for  $\tilde{R}_{h_i h_j}(\xi)$  could be obtained directly by differentiating the known head correlation  $\tilde{R}_{hh}(\xi)$  as explained in Chapter 3:

$$R_{h_i h_j}(\xi) = - \frac{\partial^2 R_{hh}(\xi)}{\partial \xi_i \partial \xi_j}.$$

By carrying out differentiation with respect to  $\xi_1$  and to  $r = \sqrt{\xi_2^2 + \xi_3^2}$ , one obtains equation (4.14) in the text. The final closed form result, not reproduced here, would obtain by plugging  $R_{hh}(\xi)$  of equation (3.22) into equation (4.14).

**APPENDIX 3.D**  
**HEAD COVARIANCE FUNCTION FOR THE 3D ANISOTROPIC**  
**MARKOV SPECTRUM (INDICATIONS FOR NUMERICAL INTEGRATION)**

In this appendix, we explain how the head covariance functions shown in Figure 3.4 were obtained for arbitrary anisotropy ratio, in the form of double Fourier integrals to be *integrated numerically*.

Assume  $\ell_1 = \ell_2 = \ell$  and let  $\epsilon = \ell_3/\ell$  be the arbitrary, anisotropy ratio in the 3D anisotropic Markov spectrum of log-conductivity  $S_{ff}$  (Table 1 of Chapter 3). The relation between the head and log-conductivity spectra is:

$$S_{hh}(\underline{k}) = J_1^2 \frac{k_1^2}{k^4} S_{ff}(\underline{k})$$

The head covariance function is just the Fourier Transform of  $S_{hh}$ :

$$R_{hh}(\underline{\xi}) = \iiint e^{j\underline{k}\underline{\xi}} S_{hh}(\underline{k}) d\underline{k}$$

which finally leads to an expression of the form:

$$R_{hh}(\xi) = \frac{\pi}{8} \sigma_f^2 J_1^2 \ell \ell_3 \cdot I(\xi)$$

where  $I(\xi)$  is the triple integral:

$$I(\xi) = \left(\frac{2}{\pi \ell}\right)^3 \iiint_{-\infty}^{+\infty} \frac{k_1^2 \cdot \cos(\underline{k} \cdot \xi)}{k^4 [\ell^{-2} + k_1^2 + k_2^2 + \epsilon^2 k_3^2]^2} d\underline{k}.$$

We now express  $I(\xi)$  by using spherical coordinates in Fourier space:

$$\begin{aligned} k &= \sqrt{k_1^2 + k_2^2 + k_3^2} & 0 \leq k < +\infty \\ k_1 &= k \cos\theta \sin\phi & 0 \leq \phi < 2\pi \\ k_2 &= k \sin\theta \sin\phi & 0 \leq \theta < \pi \\ k_3 &= k \cos\theta. \end{aligned}$$

The Jacobian of the transformation (from Cartesian to spherical coordinates) is:

$$\frac{\partial(k_1, k_2, k_3)}{\partial(k, \theta, \phi)} = k^2 \cdot \sin\theta.$$

After some manipulations, this gives:



$$I(\xi) = \left(\frac{2}{\pi\ell}\right)^3 \cdot \int_0^{2\pi} \cos^2\theta \cdot d\theta \int_0^{\pi} \sin^3\phi d\phi \int_0^{+\infty} \frac{\cos(k \cdot A)}{[k^2 B^2 + \ell^{-2}]^2} dk$$

where:

$$A(\theta, \phi) = (\xi_1 \cos\theta + \xi_2 \sin\theta) \sin\phi + \xi_3 \cdot \cos\phi$$

$$B(\phi) = \sqrt{\sin^2\phi + \epsilon^2 \cdot \cos^2\phi}.$$

Generalizing a formula given by Gradshteyn and Ryzik (3.729.1)

we obtained for the k-integral above:

$$\int_0^{+\infty} \frac{\cos(k \cdot A)}{[k^2 B^2 + \ell^{-2}]^2} dk = \frac{\pi}{4\ell^{-3}} \frac{1+C}{B} e^{-C}$$

where:

$$C = \ell^{-1} \cdot \left| \frac{A}{B} \right|.$$

This leads to the expression given in the text:

$$I(\xi) = \frac{2}{\pi^2} \cdot \int_0^{2\pi} \cos^2\theta \cdot d\theta \int_0^\pi F(\theta, \phi) d\phi$$

$$F(\theta, \phi) = \sin^3\phi \cdot \left[ \frac{1+C(\theta, \phi)}{B(\phi)} \right] e^{-C(\theta, \phi)}$$

which was finally integrated numerically as explained in the text.

The head variance in particular obtains by letting the separation vector go to zero:

$$\sigma_h^2 = R_{hh}(\underline{0}) .$$

In this case, the integral  $I(\underline{0})$  above comes much simpler:

$$I(\underline{0}) = \frac{2}{\pi^2} \cdot \int_0^{2\pi} \cos^2\theta \cdot d\theta \int_0^\pi \frac{\sin^3\phi \, d\phi}{\sqrt{\sin^2\phi + \epsilon^2 \cdot \cos^2\phi}} .$$

This integral (or another equivalent integral) has already been evaluated by Naff and Vecchia (1986). The resulting head variance is given in close form in the text (equation 3.26).

## APPENDIX 3.E

QUASI-ANALYTICAL EVALUATION OF THE HEAD COVARIANCE  
 $R_{hh}(0,0,\xi_3)$  FOR THE 3D ANISOTROPIC MARKOV SPECTRUM WITH  
 SMALL ANISOTROPY RATIO

In this appendix, we compute the vertical head covariance function in the anisotropic case with small anisotropy ratio ( $\epsilon \ll 1$ ), in order to check the more general results obtained by numerical integration. The result given in Section 3.4 for the 3D anisotropic Markov spectrum was:

$$R_{hh}(\xi) = \frac{\pi}{8} \sigma_f^2 J^2 \ell \ell_3 \cdot I(\xi)$$

where  $I(\xi)$  had to be evaluated numerically.

In the case  $\epsilon \ll 1$ , we let  $\epsilon = 0$  in  $I(\xi)$  and restrict the analysis to the case of a vertical separation vector  $(0,0,\xi_3)$ . This gives a more tractable integral as shown below (for  $\xi_3 \geq 0$ ):

$$\begin{aligned}
I(\xi_3) &= \frac{2}{\pi^2} \int_0^{2\pi} \cos^2\theta \cdot d\theta \\
&\cdot \left\{ \int_0^{\pi/2} \sin^2\phi \cdot \left[ 1 + \frac{\xi_3}{\ell} \cotg \phi \right] \exp\left[-\frac{\xi_3}{\ell} \cotg \phi\right] d\phi \right. \\
&+ \left. \int_{\pi/2}^{\pi} \sin^2\phi \cdot \left[ 1 + \frac{\xi_3}{\ell} \cotg \phi \right] \exp\left[-\frac{\xi_3}{\ell} \cotg \phi\right] d\phi \right\}.
\end{aligned}$$

Now, let:

$$u = \pm \cotg \phi$$

$$a = \xi_3/\ell$$

After some manipulations, we obtain:

$$I(\xi_3) = \frac{4}{\pi} \left\{ \int_0^{+\infty} \frac{e^{-au} du}{(1+u^2)^2} + a \cdot \int_0^{+\infty} \frac{ue^{-au}}{(1+u^2)^2} du \right\}$$

where  $a = \xi_3/\ell$  is the dimensionless separation distance in the vertical. We now use a result from Gradshteyn and Ryzik (3.355.1 and 2):

$$\int_0^{\infty} \frac{e^{-au} du}{(1+u^2)^2} = \frac{1}{2} \{ci(a) \cdot \sin(a) - si(a) \cdot \cos(a)\} \\ - a \cdot [ci(a) \cdot \cos(a) + si(a) \cdot \sin(a)]$$

$$\int_0^{\infty} \frac{ue^{-au} du}{(1+u^2)^2} = \frac{1}{2} \{1 - a \cdot [ci(a) \cdot \sin(a) - si(a) \cdot \cos(a)]\}$$

The special functions  $si(x)$  and  $ci(x)$  are the sine and cosine integrals:

$$si(x) = - \int_x^{\infty} \frac{\sin t}{t} dt = - \frac{\pi}{2} + \int_0^x \frac{\sin(t)}{t} dt$$

$$ci(x) = - \int_x^{\infty} \frac{\cos t}{t} dt = C + \ln x + \int_0^x \cos(t) - 1 dt$$

where  $C$  is the Euler constant:

$$C = 0.577215\dots$$

Using a Table of sine-cosine integrals (Korn and Korn, 1968, Appendix F.6) we obtain in particular:

$$I(0,0,\xi_3) = \frac{4}{\pi} \cdot 0.6717 \text{ for } \xi_3 = \ell$$

$$I(0,0,\xi_3) = \frac{4}{\pi} \cdot 0.2529 \text{ for } \xi_3 = 7\ell.$$

Plugging these values into the relation given on top of this appendix gives the head correlation for two different separation distances in the vertical:

$$\frac{R_{hh}(0,0,\ell)}{\sigma_h^2} \simeq 0.8552$$

$$\frac{R_{hh}(0,0,7\ell)}{\sigma_h^2} \simeq 0.3220.$$

The results obtained by numerical integration agreed closely with these analytical values (see Figure 3.4 with  $\epsilon \ll 1$ ).

## APPENDIX 3.F

## CLOSED FORM EVALUATION OF THE FLUX VARIANCE FOR THE 3D ANISOTROPIC MARKOV SPECTRUM WITH SMALL ANISOTROPY RATIO

In this Appendix, we compute the variance of the flux vector components for a small anisotropy ratio ( $\epsilon \ll 1$ ), using the 3D anisotropic Markov spectrum of Table 3.1 (Chapter 3). For completeness, we also compute the *macrodispersivity* according to Gelhar and Axness (1983), for arbitrary anisotropy ratio.

The flux spectrum obtained by the standard first order spectral theory is given generally by equation (3.18) in the text. For the case at hand, we define for convenience a rescaled flux spectrum as follows:

$$\tilde{S}_{q_i q_i} = S_{q_i q_i} / \left\{ \frac{\ell^2 \ell_3}{\pi^2} \cdot \sigma_f^2 K_G^2 J^2 \right\}.$$

The resulting expression for the rescaled flux spectrum is:

$$\tilde{S}_{q_i q_i}(\mathbf{k}) = \left[ \delta_{i1} - \frac{k_i k_1}{k^2} \right]^2 \cdot \frac{1}{[1 + \ell^2(k_1^2 + k_2^2 + \epsilon^2 k_3^2)]^2}$$

where  $\epsilon = \ell_3/\ell$  is the (small) anisotropy ratio. The flow statistics of interest can now be expressed as:

$$\tilde{\sigma}_{q_i}^2 = \iiint \tilde{S}_{q_i q_i}(\underline{k}) d\underline{k}$$

$$\tilde{A}_{ii} = \frac{\pi}{Q^2} \cdot \iint \tilde{S}_{q_i q_i}(0, k_2, k_3) dk_2 dk_3$$

where  $\tilde{\sigma}_{q_i}^2$  is a scaled flux variance, and  $\tilde{A}_{ii}$  a scaled macrodispersivity for solute transport at large times in the absence of local dispersion (see Gelhar and Axness, 1983, and Gelhar, 1985).

Using spherical coordinates in Fourier space (see for instance Appendix 3.D), we obtain the scaled flux variances in the form:

$$\tilde{\sigma}_{q_i}^2 = \int_0^{2\pi} d\theta \int_0^\pi B'_i(\theta, \phi) d\phi \int_0^\infty \frac{k^2 dk}{[1 + \ell^2(\sin^2\phi + \epsilon^2 \cos^2\phi)k^2]^2}$$

The k-integral can be worked out by using a formula given in Gradshtein and Rhyzik (3.241.5):

$$\int_0^\infty \frac{x^2 dx}{(1+x^2)^2} = \pi/4.$$

This gives finally:



$$\tilde{\sigma}_{q_i}^2 = \frac{\pi}{4\ell^3} \int_0^{2\pi} d\theta \int_0^\pi B_i(\theta, \phi) d\phi$$

where the integrand  $B_i$  takes the form:

$$i=1: B_1(\theta, \phi) = (1 - 2 \cos^2\theta \sin^2\phi + \cos^4\theta \sin^4\phi) \frac{\sin\phi}{(\sin^2\phi + \epsilon^2 \cos^2\phi)^{3/2}}$$

$$i=2: B_2(\theta, \phi) = \cos^2\theta \cdot \sin^2\phi \frac{\sin^5\phi}{(\sin^2\phi + \epsilon^2 \cos^2\phi)^{3/2}}$$

$$i=3: B_3(\theta, \phi) = \cos^2\theta \cdot \cos^2\phi \frac{\sin^3\phi}{(\sin^2\phi + \epsilon^2 \cos^2\phi)^{3/2}}$$

For  $\epsilon \ll 1$ , it turns out that the approximation  $\epsilon \simeq 0$  can be used in the integrals involving  $B_2$  and  $B_3$ , but not in the integral involving  $B_1$  (this would lead to an indeterminacy of the type "zero divided by zero"). Beginning with the components  $i = 2$ , and  $i = 3$ , we plug  $\epsilon \simeq 0$  in  $B_2$  and  $B_3$  to obtain, after some simple integrations:

$$\tilde{\sigma}_{q_2}^2 \simeq \frac{\pi^3}{32\ell^3} \quad (\epsilon \simeq 0)$$

$$\tilde{\sigma}_{q_3}^2 \simeq \frac{\pi^3}{8\ell^3} \quad (\epsilon \simeq 0)$$

For the longitudinal flux component, we obtain after integrating over  $\theta$  and keeping  $\epsilon \neq 0$  in some of the intermediate expressions:

$$\tilde{\sigma}_{q_1}^2 \approx \frac{\pi}{4\ell^3} \left\{ 4\pi \int_0^{\pi/2} \frac{\sin\phi \, d\phi}{(\sin^2\phi + \epsilon^2 \cos^2\phi)^{3/2}} - \frac{13}{8} \pi^2 \right\}.$$

However note that we used  $\epsilon \approx 0$  to evaluate an intermediate expression ( $\phi$ -integral) that resulted in the term  $13\pi^2/8$ .

To evaluate the remaining  $\phi$ -integral above, let us take  $u = \cos \phi$  as the new variable of integration and use a result by Gradshteyn and Ryzik (2.271.5). This yields for the  $\phi$ -integral above:

$$\begin{aligned} \int_0^{\pi/2} \dots \, d\phi &= \int_0^1 \frac{du}{(1-(1-\epsilon^2)u^2)^{3/2}} \\ &= \left[ \frac{u}{\sqrt{1-(1-\epsilon^2)u^2}} \right]_0^1 \\ &= \frac{1}{\epsilon}. \end{aligned}$$

This leads finally to a close form expression for the scaled

longitudinal flux variance:

$$\tilde{\sigma}_{q_1}^2 \simeq \frac{\pi^2}{\ell^3} \left( \frac{1}{\epsilon} - \frac{13}{32\pi} \right)$$

Finally, the flux variances are readily obtained by observing that:

$$\sigma_{q_i}^2 = \tilde{\sigma}_{q_i}^2 \cdot \left\{ \frac{\ell^2 \ell_3}{\pi} \sigma_f^2 K_G^2 J_1^2 \right\}$$

This gives finally:

$$\begin{aligned} \sigma_{q_1}^2 &\simeq \sigma_f^2 K_G^2 J_1^2 \left( 1 - \frac{13}{32} \pi \epsilon \right) \\ \sigma_{q_2}^2 &\simeq \sigma_f^2 K_G^2 J_1^2 \frac{\pi}{32} \epsilon \\ \sigma_{q_3}^2 &\simeq \sigma_f^2 K_G^2 J_1^2 \frac{\pi}{8} \epsilon \end{aligned}$$

provided that  $\epsilon \ll 1$ . This result was given in equation 3.31.

Note that  $\sigma_{q_1}$  tends to a non-zero constant value as  $\epsilon \rightarrow 0$ , while

$\sigma_{q_2}$  and  $\sigma_{q_3}$  vanish as  $\epsilon \rightarrow 0$ .

The scaled macrodispersivity  $\tilde{A}_{ii}$  defined at the beginning of this appendix is easily computed for arbitrary values of the anisotropy ratio ( $\epsilon \leq 1$ ), as shown below:

$$\frac{\pi}{Q_1^2} \tilde{A}_{ii} = \iint_{-\infty}^{+\infty} \frac{\delta_{i1}}{[1 + \ell^2(k_2^2 + \epsilon^2 k_3^2)]^2} dk_2 dk_3 .$$

This gives immediately:

$$\boxed{A_{22} = A_{33} = 0} .$$

For the longitudinal component of macrodispersing, let us use circular coordinates in the transverse plane  $(k_2, k_3)$ :

$$k_2 = k_0 \cos \theta$$

$$k_3 = k_0 \sin \theta$$

$$k_0 = \sqrt{k_2^2 + k_3^2}$$

$$\text{Jacobian} = k_0$$

This yields:

$$\tilde{A}_{11} = \frac{\pi}{Q_1^2} \int_0^{2\pi} d\theta \int_0^{\infty} \frac{k_0 dk_0}{[1 + B(\theta) \cdot k_0^2]^2}$$

$$B(\theta) = \ell^2 \cdot [1 - (1 - \epsilon^2) \sin^2 \theta] \geq 0$$

The  $k_0$ -integral is easily worked out by using the variable of

integration:

$$W = 1 + B(\theta) \cdot k_0^2$$

We obtained after integration:

$$\tilde{A}_{11} = \frac{2}{\ell^2} \frac{\pi}{\bar{Q}_1^2} \cdot \int_0^{\pi/2} \frac{d\theta}{1-\gamma \cdot \sin^2 \theta}$$

where  $\gamma = 1 - \epsilon^2$  ( $0 \leq \gamma < 1$ ). From Gradshtein and Ryzik (2.562.1) we get for  $\theta$ -integral:

$$\int_0^x \frac{d\theta}{1-\gamma \sin^2 \theta} = \frac{1}{\sqrt{1-\gamma}} \operatorname{arctg} (\sqrt{1-\gamma} \operatorname{tg} x) .$$

This gives:

$$\tilde{A}_{11} = \frac{2}{\ell^2} \frac{\pi}{\bar{Q}_1^2} \cdot \frac{1}{\epsilon} \cdot [\operatorname{arctg}(\epsilon \operatorname{tg} x)]_0^{\pi/2} .$$

After rescaling  $\tilde{A}_{11}$ , we obtain finally the dimensional macrodispersivity:

$$\boxed{A_{11} = \left[ \frac{K_{GJ}}{\bar{Q}_1} \right]^2 \cdot \sigma_f^2 \cdot \ell}$$

It is worth mentioning that a correction to the

standard first order spectral method was proposed in Section 4.3 of this work. Accordingly, the term  $(K_G J)$  should be replaced by  $(\bar{Q}_1)$  in all the results obtained in this Appendix. In particular, the macrodispersivity becomes

$$A_{11} = \sigma_f^2 \cdot \ell$$

The major difference between this and the previous expression is that  $A_{11}$  increases monotonously with  $\sigma_f$  in the modified result just above. In addition, note that  $A_{11}$  is independent of the anisotropy ratio ( $0 \leq \epsilon \leq 1$ ). However,  $A_{11}$  becomes indeterminate if  $\epsilon = 0$ .

**APPENDIX 3.G**  
**CLOSED FORM EVALUATION OF THE HEAD VARIANCE AND COVARIANCE**  
**FUNCTION FOR THE 3D HOLE-MARKOV SPECTRUM**  
**(ISOTROPIC AND ANISOTROPIC CASES)**

In this Appendix, we evaluate the head variance for the Hole-Markov spectrum with arbitrary anisotropy ratio. In addition, we also evaluate in closed form the head correlation function along the vertical direction (in the isotropic case only). These results are used in the text for comparison with the standard Markov spectrum without a "hole". Note that the effect of the "hole" is to decrease the low-wavenumber content of the log-conductivity spectrum.

The head covariance  $R_{hh}(\xi)$  is proportional to a certain triple Fourier integral  $I(\xi)$ , given in Section 3.6. By using spherical wavenumber coordinates as in Appendix 3.D, we obtain after some manipulations:

$$R_{hh}(\xi) = \left(\frac{\pi}{8}\right) \sigma_f^2 J_1^2 \ell \ell_3 \cdot I(\xi)$$

$$I(\xi) = \left(\frac{\pi}{2\ell}\right)^3 \cdot \int_0^{+\infty} \cos^2\theta \cdot d\theta \int_0^\pi \frac{\sin^3\phi \cdot K(\theta, \phi) d\phi}{[\sin^2\phi + \epsilon^2 \cos^2\phi]^2}$$

$$K(\theta, \phi) = \int_0^{+\infty} \frac{k^2 \cos(ak) dk}{(k^2 + b^2)^3}$$

$$a = |(\xi_1 \cos\theta + \xi_2 \sin\theta) \sin\phi + \xi_3 \cos\phi|$$

$$b = \frac{1}{\rho \cdot \sqrt{\sin^2\phi + \epsilon^2 \cos^2\phi}}$$

By using a number of intermediate results from Gradshteyn and Ryzik (3.737.1) we obtained a closed form expression for the  $K(\theta, \phi)$  integral as shown below. First, let us define a class of integrals of the form:

$$J_n = \int_0^{+\infty} \frac{\cos(ak) dk}{(k^2 + b^2)^n}$$

Then we have:

$$K(\theta, \phi) = J_2 - b^2 \cdot J_3$$

On the other hand, the  $J_n$  integrals are known in closed form:

$$J_n = \frac{\pi e^{-ab}}{(2b)^{2n-1} \cdot (n-1)!} \cdot \sum_{k=0}^{n-1} \frac{(2n-k-2)! (2ab)^k}{k! (n-k-1)!}$$

Plugging  $J_n$  into  $K$  finally leads to



$$K(\theta, \phi) = \frac{\pi}{16} \cdot \frac{1+ab-(ab)^2}{b^3} \cdot e^{-ab}$$

Plugging  $K(\theta, \phi)$  in  $I(\xi)$  above leaves a fairly complicated double integral to be evaluated in the general anisotropic case with arbitrary separation vector  $\xi$ . To arrive at a useful close form result for the correlation function, let us focus on the isotropic case, and let  $\xi$  be a vertical separation vector  $(0, 0, \xi_3)$ . The anisotropic case will also be considered later for variance calculations.

#### 1. Isotropic Case: Covariance $R_{hh}(0, 0, \xi_3)$ :

Letting  $\epsilon = \ell_3/\ell = 1$  and  $\xi_1 = \xi_2 = 0$ , the expression for the  $I(\xi)$  integral reduces to:

$$I(\xi_3) = \frac{\pi}{16} \cdot \left(\frac{\pi}{2}\right)^3 \cdot \int_0^{2\pi} \cos^2\theta \cdot d\theta \cdot L(\xi_3)$$

$$L(\xi_3) = 2 \int_0^1 (1-u^2) (1+s_3u-(s_3 \cdot u)^2) e^{-au} du$$

where  $s_3 = \xi_3/\ell$  is the dimensionless separation distance in the vertical. Note that the integral  $L$  was obtained after changing a variable of integration ( $u = \sin\phi$ ). This integral can be worked out without difficulty (the details are tedious and will

not be shown here):

$$L(\xi_3) = \frac{16}{s_3} \left\{ \frac{2}{s_3} \left[ \frac{1-e^{-s_3}}{s_3} - e^{-s_3} \right] - \left( 1 + \frac{s_3}{4} \right) e^{-s_3} \right\}.$$

Eventually, we find that the head covariance can be related directly to  $L(\xi_3)$  via:

$$R_{hh}(0,0,\xi_3) = \frac{1}{16} \left( \frac{\pi}{2} \right)^6 \sigma_f^2 J^2 \ell^2 \cdot L(\xi_3) .$$

In particular, taking  $\xi_3 = 0$  gives the head variance in the isotropic case. The value of  $L(0)$  can be found by using a Taylor development of  $L(\xi_3)$  as  $\xi_3 \rightarrow 0$ ; the result is:

$$L(0) = 4/3.$$

This gives immediately the head variance for the isotropic case:

$$\boxed{\sigma_h^2 = \frac{1}{12} \left( \frac{\pi}{2} \right)^6 \cdot \sigma_f^2 J^2 \ell^2} \quad (\epsilon=1)$$

The head correlation function in the vertical direction can now be expressed as:

$$\boxed{\frac{R_{hh}(0,0,\xi_3)}{\sigma_h^2} = \frac{12}{s^3} \left\{ \frac{2}{s^3} \left[ \frac{1-e^{-s_3}}{s_3} - e^{-s_3} \right] - \left[ 1 - \frac{s_3}{4} \right] e^{-s_3} \right\}} \quad (\epsilon = 1)$$

where  $s_3 = \xi_3/\ell$ . These two equations, taken together, give in closed form the head covariance in the cross-flow direction for the isotropic Hole-Markov spectrum.

## 2. Anisotropic Case: Head Variance $\sigma_h^2$ :

In the general anisotropic case, the head variance obtains by taking  $\underline{\xi} = \underline{0}$  in the general expression given for  $I(\underline{\xi})$  at the beginning of this appendice. The integral  $K(\theta, \phi)$  now becomes more tractable since the term  $\cos(ak)$  is eliminated from the integrand:

$$K(\theta, \phi) = \int_0^{+\infty} \frac{k^2}{(k^2+b^2)^3} dk$$

After Gradshteyn and Ryzik (3.241.4) we obtain:

$$K(\theta, \phi) = \frac{\pi}{16 \cdot b^3}$$

where  $b$  is a function of  $\phi$  alone, as defined earlier.

Plugging this expression into the integral  $I(\xi)$  evaluated at zero separation distance gives finally:

$$I(0) = \frac{1}{4} \left(\frac{\pi}{2}\right)^5 \int_0^\pi \frac{\sin^3 \phi \, d\phi}{\sqrt{\sin^2 \phi + \epsilon^2 \cos^2 \phi}}$$

$$\sigma_h^2 = \frac{\pi}{8} \sigma_f^2 J^2 \ell^2 \cdot I(0).$$

It turns out that the  $\phi$ -integral above can be computed in closed form, separately, for  $\epsilon > 1$ ,  $\epsilon = 1$  and  $\epsilon < 1$ . For the simplest case  $\epsilon = 1$ , we obtain the same head variance as already found above (isotropic case). For  $\epsilon < 1$ , the  $\phi$ -integral can be rewritten as:

$$\frac{1}{\epsilon} \cdot \int_0^\pi \frac{\sin^3 \phi \, d\phi}{\sqrt{1 + \gamma^2 \sin^2 \phi}}$$

where  $\gamma^2 = (1 - \epsilon^2)/\epsilon^2$ . This integral can be evaluated from two results of Gradshteyn and Ryzik (2.584.7 and 2.598). We give below the final result for  $\sigma_h^2$ :

$$\boxed{\begin{aligned} \sigma_h^2 &= \frac{\pi}{8} \sigma_f^2 J^2 \ell^2 \cdot I(0) \\ I(0) &= \frac{1}{4} \left(\frac{\pi}{2}\right)^5 \frac{1}{\sqrt{1 - \epsilon^2}} \left\{ \frac{\epsilon}{\sqrt{1 - \epsilon^2}} + \frac{1 - 2\epsilon^2}{1 - \epsilon^2} \cdot \arcsin(\sqrt{1 - \epsilon^2}) \right\} \quad (\epsilon < 1) \end{aligned}}$$

For  $\epsilon > 1$  the  $\phi$ -integral can be expressed as:

$$\int_0^{\pi} \frac{\sin^3 \phi \, d\phi}{\sqrt{1-\omega^2 \cdot \sin^2 \phi}}$$

where  $\omega^2 = (\epsilon^2 - 1)/\epsilon^2$ . Using again a few intermediate results of Gradshteyn and Ryzik, we obtain finally:

$$\sigma_h^2 = \frac{\pi}{8} \sigma_f^2 J^2 \ell \ell_G \cdot I(0)$$

$$I(0) = \frac{1}{4} \left(\frac{\pi}{2}\right)^5 \frac{\epsilon^2}{\epsilon^2 - 1} \left\{ -\frac{1}{\epsilon} + \frac{2\epsilon^2 - 1}{\epsilon^2 \sqrt{\epsilon^2 - 1}} \cdot \ln \left[ \frac{\epsilon + \sqrt{\epsilon^2 - 1}}{\epsilon - \sqrt{\epsilon^2 - 1}} \right] \right\} \quad (\epsilon > 1)$$

It is interesting to note that  $\sigma_h^2$  tends to a non-zero constant as  $\epsilon \rightarrow 0$  if the geometric mean correlation scale  $\ell_G = \sqrt{\ell \ell_3}$  is held fixed. On the other hand, the last equation above shows that  $\sigma_h^2 \rightarrow 0$  as  $\epsilon \rightarrow \infty$  while  $\ell_G$  is held fixed.

## APPENDIX 5.A

CLOSED FORM EVALUATION OF THE NUMERICAL HEAD ERROR  
 $\sigma(\delta H)$  FOR THE 3D MARKOV SPECTRUM OF LOG-CONDUCTIVITY

In this Appendix, we describe in some detail the analytical integrations needed to obtain the root-mean-square norm of the numerical head error  $\delta H(\underline{x})$  (truncation error) in the case where the log-conductivity is an isotropic 3D Markov random field. The final result was given in the text (equation 5.63 top: "noisy input"). The next appendix (5.B) presents similar calculations in the case of a Gaussian log-conductivity spectrum ("smooth input"). Recall that these results were obtained by a stochastic analysis of the truncature errors arising from the finite difference discretization of the groundwater flow equation.

Our starting point is equation (5.59) in the text, which gives the variance of  $\delta H(\underline{x})$  obtained by Fourier integration of the  $\delta H$ -spectrum up to wavenumbers  $|k| \simeq \pi/\Delta x$ . That equation is reproduced below for convenience:

$$\text{Var}(\hat{\delta H}_i) \simeq \left[ J_1 \frac{\Delta x^2}{24} \right]^2 \cdot I$$

where  $I$  is the 3D integral:

$$I = \int_{0 \leq k \leq \pi/\Delta x} k_1^2 \left[ \frac{3k_1^2}{k^2} + \frac{(k_m^2 \cdot k_m^2)}{k^4} \right]^2 \cdot \frac{S_{ff}(\underline{k})}{\sigma_f^2} d\underline{k}.$$

Note that  $k$  is the radial wavenumber  $(k_1 \cdot k_1)^{1/2}$ , and that summation over repeated indices is implicit, unless stated otherwise.

In the case of the isotropic 3D Markov spectrum, the last term in the integrand of  $I$  takes the form:

$$\frac{S_{ff}(\underline{k})}{\sigma_f^2} = \frac{\lambda^3}{\pi^2} \cdot \frac{1}{(1+\lambda^2 k^2)^2}.$$

By using spherical coordinates as defined, for instance, in Appendix 3D, we obtain:

$$I = I' \cdot I''$$

where the integrals  $I'$  and  $I''$  are respectively:

$$I' = \frac{\lambda^3}{\pi^2} \int_0^{\pi/\Delta x} \frac{k^4}{(1+\lambda^2 k^2)^2} dk$$

$$I'' = \int_0^{2\pi} d\theta \cdot \int_0^{\pi} A(\theta, \phi) d\phi$$

$$A(\theta, \phi) = \cos^2\theta \cdot \sin^3\phi \cdot [3\cos^2\theta \cdot \sin^2\phi + \cos^4\theta \cdot \sin^4\phi + \sin^4\theta \cdot \sin^4\phi + \cos^4\phi]^2$$

Now, the first integral  $I'$  can be rewritten by using the transformation  $u = \lambda k$  as follows:

$$I' = \frac{1}{(\lambda\pi)^2} \cdot \int_0^{\frac{\lambda\pi}{\Delta x}} \frac{u^4}{(1+u^2)^2} du.$$

This integral was already computed in the text by using identities from Gradshteyn and Ryzik 1980 (2.174 and 2.175): see above equations (5.61) in the text for details. The resulting expression for the  $I'$  integral is finally:

$$I' = \frac{1}{(\lambda\pi)^2} \cdot \frac{1}{R} \cdot \left[ \frac{1}{1+R^2} + \frac{3}{2} \cdot \frac{R^2}{1+R^2} - \frac{3}{2} R \operatorname{arctg} \left( \frac{1}{R} \right) \right]$$

where  $R$  is the radial grid resolution parameter defined as:



$$l_1 = \frac{\Delta x}{\lambda \pi}$$

For the second integral  $I''$ , the integrand  $A(\theta, \phi)$  can be decomposed in the form:

$$A(\theta, \phi) = [a+b+c+d]^2 = a^2+b^2+c^2+d^2+2(ab+bc+cd+da+ac+bd)$$

This gives  $A(\theta, \phi)$  in the form:

$$\begin{aligned} A(\theta, \phi) = & 9 \cos^6 \theta \cdot \sin^7 \phi + \cos^{10} \theta \cdot \sin^{11} \phi \\ & + \cos^2 \theta \cdot \sin^8 \theta \cdot \sin^{11} \phi + \cos^2 \theta \cdot \sin^3 \phi \cdot \cos^8 \phi \\ & + 6 \cos^8 \theta \sin^9 \phi + 2 \cos^6 \theta \cdot \sin^4 \theta \cdot \sin^{11} \phi \\ & + 6 \cos^4 \theta \cdot \sin^5 \phi \cdot \cos^4 \phi + 6 \cos^4 \theta \sin^4 \theta \cdot \sin^9 \phi \\ & + 2 \cos^6 \theta \cdot \sin^7 \phi \cdot \cos^4 \phi + 2 \cos^2 \theta \cdot \sin^4 \theta \cdot \sin^7 \phi \cdot \cos^4 \phi \end{aligned}$$

To obtain a close-form expression for the double-integral of  $A(\theta, \phi)$ , we used the following identities from Gradshteyn and Ryzik, 1980 (2.510 - 511-512-513):

$$\int_0^{2\pi} \cos^{2p}\theta \cdot d\theta = 2\pi \cdot \frac{(2p-1)!!}{p!2^p}$$

$$\int_0^{2\pi} \cos^p\theta \cdot \sin^{2n}\theta \cdot d\theta = \frac{(2n-1)!!}{(2n+p)(2n+p-2)\cdots(p+2)} \cdot \int_0^{2\pi} \cos^p\theta \cdot d\theta$$

$$\int_0^\pi \sin^{2n+1}\phi \cdot d\phi = \frac{2^{n+1}}{2n+1} \cdot \frac{n!}{(2n-1)(2n-3)\cdots 1} \quad (n \geq 1)$$

$$\int_0^\pi \cos^p\phi \cdot \sin^{2n+1}\phi \cdot d\phi = 0 \quad (n \geq 1, p \text{ odd})$$

$$\int_0^\pi \cos^p\phi \cdot \sin^{2n+1}\phi \cdot d\phi = (n \geq 1, p \text{ even})$$

$$\frac{1}{2n+p+1} \cdot \left[ \frac{4n}{2n+p-1} \cdot \delta_{1n} + 2^{n+1} \cdot \frac{n!}{(2n+p-1)(2n+p-3)\cdots(p+1)} \right]$$

In these expressions, we used the following notations:

$$(2n-1)!! = (2n-1)(2n-3)\cdots 1$$

$$\delta_{1n} = 1 \text{ if } n = 1$$

$$\delta_{1n} = 0 \text{ if } n \neq 1.$$

Using these identities finally led to a closed form (exact) expression for  $I'' = \iint A(\theta, \phi) d\theta d\phi$  in the form of a sum of ten rational numbers (fractions) multiplied by the number  $\pi$ . The

approximate value of  $I''$  is finally:

$$I'' \approx 3.85\pi \approx 4\pi.$$

This gives immediately the desired result for  $\text{Var}(\delta H)$ .  
 Multiplying  $I'$  by  $I''$  above and using the first equation of this  
 appendix gives a closed form expression for  $\text{Var}(\delta H)$ .  
 Furthermore, to obtain the relative root-mean-square error:

$$\epsilon(\delta H) = \frac{\sigma(\delta H)}{\sigma_H}$$

we also need the following result already obtained in the text  
 (equation 3.21 or Bakr et al. 1978):

$$\sigma_H = \frac{1}{\sqrt{3}} \sigma_f J_1 \lambda$$

This gives finally the desired result for the relative  
 root-mean-square error on the head, as follows:

$$\boxed{\frac{\sigma(\delta H)}{\sigma(H)} \approx \frac{\sqrt{3}}{12} \cdot \left(\frac{\Delta x}{\lambda}\right)^{3/2} \cdot G\left(\frac{\Delta x}{\pi\lambda}\right)}$$

where the function  $G(y)$  is defined by:

$$G(y) = \left[ \frac{1}{1+y^2} + \frac{3}{2} \cdot \frac{y^2}{1+y^2} - \frac{3}{2} y \arctg\left(\frac{1}{y}\right) \right]^{1/2}$$

Note that, for  $y = \frac{\Delta x}{\lambda \pi} \ll 1$  we obtain:

$$G\left(\frac{\Delta x}{\lambda \pi}\right) \approx \sqrt{1 + 0 \left(\frac{\Delta x}{\lambda \pi}\right)} \approx 1 + 0 \left(\frac{\Delta x}{\lambda \pi}\right).$$

Therefore, replacing the term  $G\left(\frac{\Delta x}{\lambda \pi}\right)$  by one in the above result gives the leading order term of the relative head error, as shown in the text.

## APPENDIX 5.B

CLOSED FORM EVALUATION OF THE NUMERICAL HEAD ERROR  
 $\sigma(\delta H)$  FOR THE 3D HOLE-GAUSSIAN SPECTRUM OF LOG-CONDUCTIVITY

This Appendix follows a development parallel to that of Appendix 5A, but with a Hole-Gaussian spectrum rather than a Markov spectrum for the 3D isotropic log-conductivity field. Therefore, we will refer to some of the notations used in Appendix 5A in the sequel. However, let us first define the Hole-Gaussian spectrum, since it was not used anywhere else in this work.

The Hole-Gaussian ellipsoidal log-conductivity spectrum, with "rational hole" of order  $m$ , was defined and used by Vomvoris (1986) to obtain spectral solutions of stochastic solute transport. The general form of this spectrum is:

$$S_{ff}(\underline{k}) = \sigma_f^2 \frac{\ell_1 \ell_2 \ell_3}{(2\pi)^{3/2}} \cdot \frac{(\ell_i^2 k_i^2)^m}{(2m+1)!!} \cdot \exp\left(-\frac{1}{2} \ell_i^2 k_i^2\right)$$

with implicit summation on repeated indices, and:

$$(2m+1)!! = 1.3.5 \cdots (2m+1).$$

In the particular case at hand, we used the isotropic

Hole-Gaussian spectrum of order one ( $m = 1$ ):

$$S_{ff}(\underline{k}) = \frac{\sigma_f^2 \ell^3}{3(2\pi)^{3/2}} \cdot \ell^2 k^2 \cdot e^{-\ell^2 k^2/2}$$

Now, in order to evaluate the relative head error  $\sigma(\delta H)/\sigma(H)$ , we need to evaluate the standard deviation  $\sigma(H)$  of the head solution by using the results of the spectral theory of stochastic flow (equations 3.18 of Chapter 3). The head spectrum is related to the log-conductivity spectrum by:

$$S_{hh}(\underline{k}) = \frac{J_1^2 k_1^2}{k^4} S_{ff}(\underline{k}).$$

The head variance  $\sigma_H^2$  obtains by integrating the head spectrum in Fourier space ( $-\infty \leq k_i \leq +\infty$ ). Plugging the Hole-Gaussian  $S_{ff}$  spectrum on the right-hand side gives:

$$\sigma_H^2 = \frac{\sigma_f^2 J_1^2 \ell^5}{3(2\pi)^{3/2}} \cdot I_1$$

$$I_1 = \iiint_{-\infty}^{+\infty} \frac{k_1^2}{k^2} e^{-\ell^2 k^2/2} d\underline{k} .$$

The  $I_1$  integral is easily worked out by using spherical coordinates. We obtained after some manipulations:

$$\begin{aligned} I_1 &= \frac{4\pi}{3} \cdot \int_0^{+\infty} k^2 e^{-\ell^2 k^2/2} dk \\ &= \frac{4\pi}{3\ell^3} \cdot \int_0^{+\infty} u^2 e^{-u^2/2} du \\ &= \frac{4\pi}{3\ell^3} \cdot \sqrt{\frac{\pi}{2}} \end{aligned}$$

where we used the identity:

$$\int_0^{\infty} u^{2n} e^{-pu^2} du = \frac{(2n-1)!!}{2(2p)^n} \cdot \sqrt{\frac{\pi}{p}}$$

after Gradshteyn and Ryzhik 1980 (3.461.2). This gives finally the first order spectral solution for the head variance in the case of a Hole-Gaussian isotropic log-conductivity field in 3D space:

$$\sigma_H^2 = \frac{1}{9} \sigma_f^2 J_1^2 \ell^2$$

Let us now evaluate the standard deviation of the head

error,  $\sigma(\delta H)$ , as in Appendix 5A. Briefly, our starting point is the relation:

$$\sigma(\delta H)^2 \approx \frac{\sigma_f^2 J_1^2 \ell^6}{3(2\pi)^{3/2}} \left[ \frac{\Delta x^2}{24} \right]^2 \cdot I$$

$$I = \int_{0 \leq k \leq \pi/\Delta x} \left[ \frac{3k_i^3}{k} + \frac{k_i(k_m^2 \cdot k_m^2)}{k^3} \right]^2 \cdot e^{-\ell^2 k^2/2} \cdot d\underline{k} .$$

Note that the exponential term in the integrand above resulted from plugging the Hole-Gaussian spectrum in equation (5.59) given in the text. Now, by using spherical coordinates, the I-integral above takes the form:

$$I = I' \cdot I''$$

where the I' integral is:

$$I' = \int_0^{\pi/\Delta x} k^6 \cdot e^{-\ell^2 k^2/2} dk$$

and the I'' integral is the same as that of Appendix 5A:



$$I'' = \int_0^{2\pi} d\theta \int_0^{\pi} d\phi A(\theta, \phi) \simeq 4\pi$$

For the  $I'$ -integral, we use the transformation  $u = k\ell$  to obtain, after some manipulation:

$$I' = \frac{4\pi}{\ell^7} \cdot \left[ \int_0^{\infty} u^6 \cdot e^{-u^2/2} du - \int_{\frac{\pi\ell}{\Delta x}}^{\infty} u^6 \cdot e^{-u^2/2} du \right]$$

Using again the Gradshteyn-Ryzik identity given above, we obtain by taking  $n = 3$  and  $p = 1/2$ :

$$\int_0^{\infty} u^6 \cdot e^{-u^2/2} du = \frac{15}{2} \sqrt{2\pi} .$$

Now, the second integral intervening in  $I'$  is always positive, and goes to zero as the radial resolution:

$$R = \frac{\Delta x}{\pi\ell}$$

goes to zero. This gives a relatively tight upper bound on the  $I'$  integral:

$$I' \leq \frac{4\pi}{\ell^7} \cdot \frac{15}{2} \sqrt{2\pi} .$$

Using intermediate results above finally leads to a similar upper bound estimate of the variance of  $\delta H$ :

$$\sigma(\delta H)^2 \leq \frac{5\sigma_f^2 J_1^2 \ell^2}{(24)^2} \cdot \left(\frac{\Delta x}{\ell}\right)^4$$

with equality in the limit as the grid resolution  $R$  goes to zero. Combining this result with the previous equation for  $\sigma_H^2$  finally gives a tight upper bound for the relative error on the head in the case of a Hole-Gaussian log-conductivity spectrum:

$$\left| \frac{\sigma(\delta H)}{\sigma(H)} \leq \frac{\sqrt{5}}{8} \left(\frac{\Delta x}{\ell}\right)^2 \right| .$$

This inequality was given in the text in equation (5.63) under the designation "smooth input". Recall that the inequality becomes equality asymptotically as the radial grid resolution  $R = \Delta x/(\pi\ell)$  goes to zero. In practice, approximate equality holds for  $R \ll 1$ , say  $\Delta x \leq 0.5\lambda$ .

## APPENDIX 5.C

## CLOSED FORM EVALUATION OF THE NUMERICAL ERROR ON THE FLUX VECTOR AND HEAD GRADIENT FOR THE 3D MARKOV SPECTRUM OF LOG-CONDUCTIVITY

In this Appendix, we evaluate the root-mean-square error on the flux vector  $q_m$  and the head gradient  $G_m$ , using equations (5.73) and (5.77) in the text. Recall that Appendix 5.A evaluated the error on the hydraulic head in the case of the isotropic 3D Markov log-conductivity spectrum. The same spectrum is used here to evaluate  $\sigma(\delta q_m)$  and  $\sigma(\delta G_m)$ .

According to equations (5.73) and (5.77), the expression for  $\text{Var}(\delta q_m)$  will involve a sum of three sets of integrals  $L_m^{(1)}$ ,  $L_m^{(2)}$ ,  $L_m^{(3)}$ . The  $L_1$  integral taken alone will also give the value of  $\text{Var}(\delta G_m)$ . These integrals are three-dimensional Fourier space integrals, with domain of integration  $0 \leq \|k_m\| \leq \pi/\Delta x$ . For simplicity, we will approximate this rectangular domain as the sphere  $0 \leq k \leq \pi/\Delta x$ , where  $k$  is the three-dimensional radial wavenumber.

More precisely, we have:

$$\text{Var}(\delta q_m) = \left[ \frac{K_G \sigma_f J_1 \Delta x^2}{24} \right]^2 \cdot (L_m^{(1)} + L_m^{(2)} + L_m^{(3)})$$

$$\text{Var}(\delta G_m) = \left[ \frac{J_1 \sigma_f \Delta x^2}{24} \right]^2 \cdot L_m^{(1)}$$

where the  $L_m^{(1)}$ ,  $L_m^{(2)}$ ,  $L_m^{(3)}$  integrals are defined as follows for each component  $m = 1, 2, 3$  of the flux or head gradient vectors:

$$L_m^{(1)} = \frac{1}{\sigma_f^2} \cdot \iiint I_m^2(\underline{k}) S_{ff}(\underline{k}) d\underline{k}$$

$$L_m^{(2)} = \frac{1}{\sigma_f^2} \cdot \iiint \frac{2k_1 k_m^3}{k^2} \cdot I_m(\underline{k}) S_{ff}(\underline{k}) d\underline{k}$$

(no summation implied over  $m$ )

$$L_m^{(3)} = \frac{1}{\sigma_f^2} \cdot \iiint \frac{k_1^2 k_m^6}{k^4} S_{ff}(\underline{k}) d\underline{k}$$

and the  $I_m(\underline{k})$  terms appearing in the integrand are of the form:

$$I_m(\underline{k}) = k_1 k_m \cdot \left[ \frac{3k_1^2}{k^2} + \sum_{i=1,2,3} k_i^4 / k^4 \right]$$

We now proceed to evaluate these integrals after plugging the 3D isotropic Markov spectrum:

$$S_{ff}(\underline{k}) = \sigma_f^2 \frac{\lambda^3}{\pi^2} \frac{1}{(1+\lambda^2 k^2)^2} .$$

Let us focus first on the  $L_m^{(1)}$  integral. By using spherical coordinates, we obtained after some manipulation a tractable expression for the first "component" of  $L_m^{(1)}$  (i.e., with  $m = 1$ ) as follows:

$$L_i^{(1)} = L_o \cdot L_i^{(1)''}$$

$$L_o = \frac{1}{\pi^2 \lambda^4} \cdot \int_0^{\frac{\pi \lambda}{\Delta x}} \frac{u^6}{(1+u^2)^2} du$$

$$L_i^{(1)''} = \int_0^{2\pi} d\theta \int_0^\pi d\phi \cdot A(\theta, \phi)$$

$$\begin{aligned} A(\theta, \phi) = & 9 \cos^8 \theta \cdot \sin^9 \phi + \cos^{12} \theta \cdot \sin^{13} \phi \\ & + \cos^4 \theta \cdot \sin^8 \theta \cdot \sin^{13} \phi \\ & + 2 \cos^8 \theta \cdot \sin^4 \theta \cdot \sin^{13} \phi \\ & + \cos^4 \theta \cdot \sin^5 \phi \cdot \cos^8 \phi \\ & + 2 \cos^8 \theta \cdot \sin^9 \phi \cdot \cos^4 \phi \\ & + 2 \cos^4 \theta \cdot \sin^4 \theta \cdot \sin^9 \phi \cdot \cos^4 \phi \\ & + 6 \cos^{10} \theta \cdot \sin^{11} \phi \\ & + 6 \cos^6 \theta \cdot \sin^4 \theta \cdot \sin^{11} \phi \\ & + 6 \cos^6 \theta \cdot \sin^7 \phi \cdot \cos^4 \phi \end{aligned}$$

For  $L_0$ , we obtained by using identities from Gradshteyn and Ryzik 1980 (2.174 and 2.175):

$$L_0 = \frac{1}{\pi^2 \lambda^4} \cdot \left[ \frac{1}{1+R^{-2}} \left( \frac{R^{-5}}{3} - \frac{5R^{-3}}{3} - \frac{5R^{-1}}{2} \right) + \frac{5}{2} \operatorname{arctg} (R^{-1}) \right]$$

in terms of the radial resolution ratio:

$$\boxed{R = \frac{\Delta x}{\pi \lambda}}$$

For  $R \ll 1$  (say  $R \leq 0.2$  or so) this gives approximately:

$$\boxed{L_0 \simeq \frac{1}{3\pi^2 \lambda^4 R^3}}$$

On the other hand, evaluating the double integral  $L_1^{(1)}$  requires some straightforward but tedious trigonometric integrations, similar to those developed in Appendix 5.A. Without going into details, we give below the final result.

$$\boxed{L_1^{(1)} \simeq 7.35\pi \simeq \frac{22\pi}{3}}$$

Combining the two previous results gives finally, for a

resolution  $R = \Delta x / (\lambda \pi)$  reasonably smaller than unity (say  $R \leq 0.2$  or  $\Delta x / \lambda \leq 0.5$ ):

$$\boxed{m = 1: L_1^{(1)} \approx \frac{22}{9\pi} \frac{1}{\lambda^4 R^3}}$$

For  $m = 2$ , the evaluation of  $L_2^{(1)}$  requires integrations similar to those developed above. Briefly, this integral can be cast into the form:

$$L_2^{(1)} = L_0 \cdot L_2^{(1)''}$$

where  $L_0$  was defined and evaluated previously, and  $L_2^{(1)''}$  is a double trigonometric integral similar (but not identical) to the previous  $L_1^{(1)''}$ . The final result is written below for the case  $R \ll 1$  (as explained previously):

$$\boxed{m = 2: L_2^{(1)} \approx \frac{2}{15\pi\lambda^4 R^3}}$$

where we used for convenience the approximation  $0.41 \approx 2/5$ .

We now focus on the second set of integrals,  $L_m^{(2)}$ . Using again spherical coordinates, we obtained these integrals in the form:

$$L_m^{(2)} = L_0 \cdot L_m^{(2)''}$$

where  $L_0$  was defined (and evaluated) previously, and the  $L_m^{(2)''}$  are trigonometric integrals similar in form to the  $L_m^{(1)''}$  integrals, but simpler. They are given below:

$$\begin{aligned} \underline{m = 1}: L_1^{(2)''} &= \int_0^{2\pi} d\theta \int_0^\pi d\phi \\ &[\cos^8\theta \cdot \sin^9\phi + \cos^{10}\theta \cdot \sin^{11}\phi \\ &+ \cos^6\theta \cdot \sin^4\theta \cdot \sin^{11}\phi + \cos^6\theta \cdot \sin^7\phi \cdot \cos^4\phi] \end{aligned}$$

$$\begin{aligned} \underline{m = 2}: L_2^{(2)''} &= \int_0^{2\pi} d\theta \int_0^\pi d\phi \\ &[\cos^4\theta \cdot \sin^4\theta \cdot \sin^9\phi \\ &+ \cos^8\theta \cdot \sin^2\theta \cdot \sin^{11}\phi + \cos^4\theta \cdot \sin^6\theta \cdot \sin^{11}\phi \\ &+ \cos^4\theta \cdot \sin^2\theta \cdot \sin^7\phi \cdot \cos^4\phi] \end{aligned}$$

This gives finally:

$$\begin{aligned} L_1^{(2)''} &\simeq 0.84\pi \\ L_2^{(2)''} &\simeq 0.10\pi. \end{aligned}$$

Multiplying by  $L_0$  and using again the approximation  $R = \Delta x / (\lambda\pi) \ll 1$  as explained previously gives finally the  $L_m^{(2)}$



integrals:

$$\boxed{L_1^{(2)} \approx \frac{2}{3} \frac{0.84}{\pi} \frac{1}{\lambda^4 R^3}}$$

$$\boxed{L_2^{(2)} \approx \frac{2}{3} \frac{0.10}{\pi} \frac{1}{\lambda^4 R^3}}$$

For the  $L_m^{(3)}$  integrals, we use again spherical coordinates to obtain after some manipulations:

$$\begin{aligned} \underline{m = 1}: \quad \boxed{L_1^{(3)}} &= L_0 \cdot \int_0^\pi \sin^3 \phi \, d\phi \cdot \int_0^{2\pi} \cos^2 \theta \cdot d\theta \\ &\approx \frac{1}{3\pi^2 \lambda^4 R^3} \cdot \frac{8}{9} \frac{32}{35} \cdot \frac{35}{64} \pi \\ &\approx \boxed{\frac{4}{27\pi} \frac{1}{\lambda^4 R^3}} \quad (\text{for } R \ll 1) \end{aligned}$$

and:

$$\begin{aligned} \underline{m = 2}: \quad \boxed{L_2^{(3)}} &= L_0 \cdot \int_0^\pi \sin^3 \phi \cdot \int_0^{2\pi} \cos^2 \theta \sin^6 \theta \, d\theta \\ &\approx \frac{1}{3\pi^2 \lambda^4 R^3} \cdot \frac{8}{9} \frac{32}{35} \cdot \frac{5\pi}{64} \\ &\approx \boxed{\frac{1}{49\pi} \frac{28}{27} \frac{1}{\lambda^4 R^3}} \quad (\text{for } R \ll 1) \end{aligned}$$

We have therefore obtained closed form expressions for the three sets of integrals  $L_m^{(1)}$ ,  $L_m^{(2)}$  and  $L_m^{(3)}$  involved in the variance of the flux error and head gradient error, as defined at the beginning of this Appendix. Note that each set of integral was evaluated for the longitudinal component ( $m = 1$ ) and for the transverse component ( $m = 2$ ). The result for  $m = 3$  is identical to  $m = 2$  by symmetry, due to the statistical isotropy of the flow in the cross-flow plane. The final results given in the text (equations 5.78 - 5.79) were obtained as follows:

- Assemble the integrals above to compute  $\text{Var}(\delta Y_m)$  as indicated on top of this Appendix ( $Y_m$  stands for the components of the flux vector or of the head gradient).
- Use the known spectral solutions  $\text{Var}(Y_m)$  to evaluate the ratio  $\text{Var}(\delta Y_m)/\text{Var}(Y_m)$ .
- Take the square-root of the above expression to obtain the final result  $\sigma(\delta Y_m)/\sigma(Y_m)$ , which gives the root-mean-square norm of the error relative to the root-mean-square norm of the variable itself.

**APPENDIX 5.D**  
**"BIGFLO" CODE ABSTRACT**

**A High Resolution, Three Dimensional, Saturated/Unsaturated  
Flow Simulator**

1.       **Program Name:** BIGFLO
2.       **Auxiliary Programs:**
  - Combig (Set of common blocks for BIGFLO.)
  - Floproc (Large set of Data Processing Routines)
  - Cturn or TB3 (Turning Band Generator of 3D Random  
                  Fields)
3.       **Programming Language:** Fortran 77
4.       **Computers and Operating Systems:**

BIGFLO has been developed on a Microvax minicomputer running the VMS operating system; it was subsequently modified to run on a Cray 2 supercomputer running the UNICOS (UNIX) operating system, and the CFT77 Fortran compiler. These modifications eliminated a few minor non-standard features, such as instructions with more than 20 continuation lines, and the "INCLUDE" statement used on the Microvax to include the set of common blocks COMBIG (same for all subroutines).

5. **Machine Requirements:**

BIGFLO contains about 12,000 lines of instructions and comments. Most of the storage required at execution time is taken up by the master array ABIG defined in the main program MAINFLO. The size of this array can be modified as needed in the main program; the parameter LPAR located just below the dimension statement must take exactly the same value as the dimension (otherwise the results could be unpredictable). No other modification will be needed in the BIGFLO code in order to run a particular problem.

The actual size of the master array required to solve a particular problem is proportional to the size ( $N$ ) of the three-dimensional grid: typically about  $12 N$  for a saturated flow problem with spatially variable conductivity. On a Microvax 2, a practical limit for the size of the master array is about 1 -1.5 Million; on the four-quadrant Cray 2, the size could be as large as 250 Million words in principle. The code will issue an error message and stop execution if the prescribed size of the master array is insufficient to solve the problem.

6. **Program Description:**

BIGFLO is a three-dimensional porous medium flow simulator, handling steady, transient saturated, and partially saturated or unsaturated flow, with spatially variable or randomly distributed hydraulic coefficients.

The code is based on a finite difference approximation of the equation governing the hydraulic head (saturated flow) or the pressure head (partially saturated or unsaturated flow). The governing flow equation was obtained from the (generalized) Darcy equation and the continuity equation without source terms. The computational flow domain is a three-dimensional parallelepiped rectangle, discretized into an orthogonal grid of mesh points.

For transient unsaturated flow in dry soils, or any similar evolution problems, the actual size of the computational domain can be time-dependent (automatically controlled by the code). For one and two-dimensional problems, the size of the grid can be shrunk to just 5 nodes (3 internal nodes and 2 boundary nodes) along the unmodeled directions.

The boundary conditions accepted by the code are, respectively, a fixed flux normal to the boundary, a fixed head, or a zero head gradient. The prescribed fluxes and heads can vary arbitrarily over the boundaries, as well as the type of boundary condition (flux, head, or zero head gradient). In the case of unsaturated or partially saturated flow, the direction of the gravity vector with respect to the axes of the flow domain can be arbitrary, as prescribed by the user.

The hydraulic properties of the porous medium required for saturated flow problems are the saturated hydraulic conductivity ( $K_s$ ) and the specific storativity ( $S_s$ ). Both can vary arbitrarily in space as needed. For partially saturated or unsaturated flow, the hydraulic conductivity ( $K$ ) is assumed to be an exponential function of pressure head ( $h$ ) with a given slope ( $\alpha$ ), up to a given bubbling pressure ( $h_b$ ) where  $K$  reaches the saturation value  $K_s$ . All three coefficients,  $K_s$ , and  $h_b$  can be spatially variable over the 3D grid of mesh points. The soil moisture retention curve  $\theta(h)$  can be an arbitrary function with several parameters (two of which can be spatially variable). The current version of the code includes subroutines for  $\theta(h)$

piecewise linear, exponential, and "Van Genuchten function". The soil moisture capacity is computed by a chord slope (finite difference) differentiation of the  $\theta(h)$  function. Finally, the specific storativity  $S_s$  is taken into account in regions of positive pressures (partially saturated flow). In this case, unlike the case of purely saturated flow,  $S_s$  must be assumed constant in space.

7. **Solution Method:**

The governing equation is discretized by a seven-point centered finite difference scheme in 3D space, and a fully implicit backwards Euler finite difference scheme in time. The code accomodates both transient and steady solution algorithms for the linear saturated flow problem. A steady state option also exists for the nonlinear unsaturated flow problem, however the best strategy in this case seems to obtain the steady state by running the transient solution algorithm for large times.

The nonlinear flow problem is approximately linearized by a modified Picard iteration scheme. Thus, an approximate linear system has to be solved for each

iteration step, and this is repeated several times at each time step.

The linear or linearized finite difference system is solved iteratively by using a preconditioned iterative method. For the nonlinear case, this gives a doubly iterative loop: outer iteration loop for linearization, and inner iteration loop for solution of the linear system. The available matrix solvers used in this code are variants of the Strongly Implicit Procedure (SIP solver), based on an approximate LU factorization, and on a modified Picard iteration scheme to converge to the exact solution. Other routines corresponding to the ICCG solver (Incomplete Choleski-Conjugate Gradients) have been introduced in the code, but are not fully debugged at this time.

#### 8. **Problem Restrictions:**

Some of the limitations of the BIGFLO simulator are listed below:

- Geometry: The 3D domain must be a parallelepiped rectangle.
- Source terms: There are no source terms in the interior of the domain.



-- Water table: The familiar 2D equation of unconfined flow with a water table is not included (use instead the partially saturated flow option).

9. **I/O Data Processing:**

Most of the inputs/outputs of the BIGFLO code can be processed interactively by using the companion code FLOPROC, a special-purpose data processor for creating the basic input file of BIGFLO and processing 1D, 2D, 3D data fields (including statistical analysis). The generation of random field parameters inputs is handled separately by using the 3D Turning Band code (CTURN or TB3). BIGFLO can be run as a batch process (non-interactively). The required input files required have the logical names INPUTj (j=1,...9). The basic input file INPUT1 contains the actual names chosen by the user for all the other input files, as well as the basic description of the flow problem and a number of numerical options. INPUT1 can be created interactively by using the data processor FLOPROC.

The numerical outputs from the BIGFLO code can be quite large. A short file containing basic information on the simulation is created at the start (OUT10) as well as a short error file named OUTBAD. The output files

OUT11 and OUT12 contain numerical information such as the residual iteration errors; the output file OUT13 contains mass balance errors and other information required at each time step (depending on options). The three-dimensional head field (solution) is stored in a data file named HEAD-T0 for steady flow, or in several data files named HEAD\_Tn or H\_Tnnn for transient flow problems (at selected times prescribed by the user).

The format of these files can be either ASCII (formatted) or BINARY (unformatted). The latter option is strongly recommended in the case of large simulations. However, binary data files are not easily transportable among different operating systems. It is recommended to rename all output files after completion of a BIGFLO run, since the code uses always the same file names for its outputs.

The data processor FLOPROC can be used to obtain other information from the 3D head field, such as: 3D flux vector field, 3D head gradient field, transects and plane sections of three-dimensional fields, and statistical properties (mean, variance, covariance functions).

10. **Practical Implementation:**

The tasks required to execute the BIGFLO code are summarized below:

(a) Create basic input data file INPUT1 by using the interactive FLOPROC code.

(b) Find out which other input files are needed. The FLOPROC processor can be used to generate the initial condition (INPUT2) and the boundary conditions (INPUT3) if they are spatially variable. The other input files INPUT4-INPUT9 correspond to spatially variable hydraulic properties. In certain simple cases, only the INPUT1 file is required. Example: saturated or unsaturated flow with uniform initial condition, uniform boundary conditions, on each face of the domain, and spatially constant hydraulic coefficients.

(c) If necessary, specify the names of the additional input files in the basic input file INPUT 1 created previously.

(d) Run BIGFLO: for complex problems, it is advised to execute the code with the option LRUN = 0 as a test; a full simulation LRUN = 1 can then be launched after inspection of the output (OUT10) of the previous test.

(e) Error messages from the BIGFLO code will appear in the output file OUTBAD in cases of abnormal termination. Three types of errors (usually detected after a short time of execution) will cause the program to stop executing:

- Insufficient dimension of the master array ABIG
- Erroneous or incompatible set of data in the basic input file INPUT 1; the error code LBAD = -n will help locate the cause of the problem, e.g. by scanning the source code for the string "LBAD = ".
- Erroneous or non-existent data file INPUTj( $2 \leq j \leq 9$ ): the first digit of the error code LBAD will help locate the problem (e.g., LBAD = - 52 indicates a problem with INPUT5).

11. **Author and Reference:**

R. Ababou, "Three-Dimensional Flow in Random Porous Media", PhD Thesis, Parsons Laboratory, MIT, Cambridge, Massachusetts, January 1988.